arXiv:1201.3084v1 [hep-ph] 15 Jan 2012

Handbook of LHC Higgs cross sections: 2. Differential Distributions

Report of the LHC Higgs Cross Section Working Group

Editors: S. Dittmaier
C. Mariotti
G. Passarino
R. Tanaka

Conveners

Gluon-fusion process: M. Grazzini, F. Petriello, J. Qian, F. Stöckli

Vector-boson-fusion process: A. Denner, S. Farrington, C. Hackstein, C. Oleari, D. Rebuzzi

$\mathrm{WH/ZH}$ *production mode*: S. Dittmaier, R. Harlander, C. Matteuzzi, J. Olsen, G. Piacquadio

ttH *process*: C. Neu, C. Potter, L. Reina, M. Spira

MSSM neutral Higgs: M. Spira, M. Vazquez Acosta, M. Warsinsky, G. Weiglein

MSSM charged Higgs: M. Flechl, S. Heinemeyer, M. Krämer, S. Lehti

PDF: S. Forte, J. Huston, K. Mazumdar, R. Thorne

Branching ratios: A. Denner, S. Heinemeyer, I. Puljak, D. Rebuzzi

NLO MC: M. Felcini, F. Krauss, F. Maltoni, P. Nason, J. Yu

Higgs pseudo-observables: M. Dührssen, M. Felcini, G. Passarino

$\gamma\gamma$ *decay:* S. Gascon-Shotkin, M. Kado

ZZ^* *decay:* N. De Filippis, S. Paganis

WW^* *decay:* J. Cuevas, T. Dai

$\tau\tau$ *decay:* A. Nikitenko, M. Schumacher

$\mathrm{b\bar{b}}$ *decay:* C. Matteuzzi, J. Olsen, C. Potter

$\mathrm{H}^{\pm}$ *decay:* M. Flechl, S. Lehti

Abstract

This Report summarises the results of the second year's activities of the LHC Higgs Cross Section Working Group. The main goal of the working group was to present the state of the art of Higgs Physics at the LHC, integrating all new results that have appeared in the last few years. The first working group report *Handbook of LHC Higgs Cross Sections: 1. Inclusive Observables* (CERN-2011-002) focuses on predictions (central values and errors) for total Higgs production cross sections and Higgs branching ratios in the Standard Model and its minimal supersymmetric extension, covering also related issues such as Monte Carlo generators, parton distribution functions, and pseudo-observables. This second Report represents the next natural step towards realistic predictions upon providing results on cross sections with benchmark cuts, differential distributions, details of specific decay channels, and further recent developments.

We, the authors, would like to dedicate this Report to the memory of
Robert Brout and Simon van der Meer.

S. Dittmaier[1], C. Mariotti[2,3], G. Passarino[2,4] and R. Tanaka[5] (eds.);
S. Alekhin[6,7], J. Alwall[8], E. A. Bagnaschi[9,10], A. Banfi[11], J. Blümlein[6], S. Bolognesi[12], N. Chanon[11], T. Cheng[13], L. Cieri[14], A. M. Cooper-Sarkar[15], M. Cutajar[16], S. Dawson[17], G. Davies[16], N. De Filippis[18], G. Degrassi[19], A. Denner[20], D. D'Enterria[3], S. Diglio[21], B. Di Micco[3], R. Di Nardo[22], R. K. Ellis[23], A. Farilla[19], S. Farrington[15], M. Felcini[24], G. Ferrera[9], M. Flechl[1], D. de Florian[14], S. Forte[9], S. Ganjour[25], M. V. Garzelli[26,27], S. Gascon-Shotkin[28], S. Glazov[29], S. Goria[2,4], M. Grazzini[30,†], J.-Ph. Guillet[31], C. Hackstein[32], K. Hamilton[3], R. Harlander[33], M. Hauru[34], S. Heinemeyer[24], S. Höche[35], J. Huston[36], C. Jackson[37], P. Jimenez-Delgado[30], M. D. Jorgensen[38], M. Kado[5], S. Kallweit[30], A. Kardos[26,37], N. Kauer[40], H. Kim[37], M. Kovac[41], M. Krämer[42], F. Krauss[43], C.-M. Kuo[44], S. Lehti[34], Q. Li[45], N. Lorenzo[5], F. Maltoni[46], B. Mellado[47], S. O. Moch[6], A. Mück[42], M. Mühlleitner[32], P. Nadolsky[48], P. Nason[49], C. Neu[50], A. Nikitenko[16], C. Oleari[49], J. Olsen[51], S. Palmer[32], S. Paganis[52], C. G. Papadopoulos[53], T .C. Petersen[38], F. Petriello[54,55], F. Petrucci[19], G. Piacquadio[3], E. Pilon[31], C. T. Potter[56], J. Price[57], I. Puljak[41], W. Quayle[47], V. Radescu[58], D. Rebuzzi[59], L. Reina[60], J. Rojo[3], D. Rosco[2,4], G. P. Salam[51,3,10], A. Sapronov[61], J. Schaarschmidt[5], M. Schönherr[43], M. Schumacher[1], F. Siegert[1], P. Slavich[10], M. Spira[62], I. W. Stewart[63], W. J. Stirling[64], F. Stöckli[63], C. Sturm[65], F. J. Tackmann[29,63], R. S. Thorne[66], D. Tommasini[30,67], P. Torrielli[68], F. Tramontano[69], Z. Trócsányi[26,39], M. Ubiali[42], S. Uccirati[20], M. Vazquez Acosta[16], T. Vickey[70,15], A. Vicini[9], W. J. Waalewijn[71], D. Wackeroth[72], M. Warsinsky[1], M. Weber[65], M. Wiesemann[33], G. Weiglein[29], J. Yu[37] and G. Zanderighi[15].

[1] Physikalisches Institut, Albert-Ludwigs-Universität Freiburg, D-79104 Freiburg, Germany
[2] INFN, Sezione di Torino, Via P. Giuria 1, 10125 Torino, Italy
[3] CERN, CH-1211 Geneva 23, Switzerland
[4] Dipartimento di Fisica Teorica, Università di Torino, Via P. Giuria 1, 10125 Torino, Italy
[5] Laboratoire de l'Accélérateur Linéaire, CNRS/IN2P3, F-91898 Orsay CEDEX, France
[6] DESY, Zeuthen, Platanenallee 6, D-15738 Zeuthen, Germany
[7] Institute for High Energy Physics, 142281 Protvino, Moscow region, Russia
[8] Theoretical Physics Department, Fermi National Accelerator Laboratory MS 106, Batavia, IL 60510-0500, USA
[9] Dipartimento di Fisica, Università degli Studi di Milano and INFN, Sezione di Milano, Via Celoria 16, I-20133 Milan, Italy
[10] Laboratoire de Physique Théorique et des Hautes Energies, 4 Place Jussieu, F-75252 Paris CEDEX 05, France
[11] Zurich, ETH CH-8093 Zurich, Schafmattstrasse 16, 8093, Zurich, Switzerland
[12] Johns Hopkins University, Baltimore, Maryland. 410-516-8000, USA
[13] University of Florida, 215 Williamson Hall, P.O. Box 118440 Gainesville, FL 32611
[14] Departamento de Física, Facultad de Ciencias Exactas y Naturales Universidad de Buenos Aires, Pabellon I, Ciudad Universitaria (1428) Capital Federal, Argentina
[15] Department of Physics, University of Oxford, Denys Wilkinson Building, Keble Road, Oxford OX1 3RH, UK
[16] Physics Dept., Blackett Laboratory, Imperial College London, Prince Consort Rd, London SW7 2BW, UK
[17] Department of Physics, Brookhaven National Laboratory, Upton, NY 11973, USA
[18] Dipartimento Interateneo di Fisica dell'Università e del Politecnico di Bari, INFN Sezione di Bari, Via Orabona 4, 70125 Bari, Italy

[19] Università degli Studi di "Roma Tre" Dipartimento di Fisica
Via Vasca Navale 84, 00146 Rome, Italy

[20] Institut für Theoretische Physik und Astrophysik, Universität Würzburg,
Emil-Hilb-Weg 22, D-97074 Würzburg, Germany

[21] School of Physics, University of Melbourne, Victoria, Australia

[22] Univversità di Roma 'Tor Vergata' Dipartimento di Fisica
Via della Ricerca Scientifica, 1 I-00133 Rome, Italy

[23] Theoretical Physics Department, Fermi National Accelerator Laboratory
MS 106, Batavia, IL 60510-0500, USA

[24] Instituto de Física de Cantabria (IFCA), CSIC-Universidad de Cantabria,
Santander, Spain

[25] CEA - Centre d'Etudes de Saclay, France

[26] Institute of Physics, University of Debrecen H-4010 Debrecen P.O.Box 105, Hungary

[27] University of Nova Gorica, Laboratory for Astroparticle Physics
SI-5000 Nova Gorica, Slovenia

[28] Université Claude Bernard Lyon 1, CNRS-IN2P3, Institut de Physique Nucleaire de Lyon (IPNL)
4, rue Enrico Fermi F-69622 Villeurbanne, CEDEX, France

[29] DESY, Notkestrasse 85, D-22607 Hamburg, Germany

[30] Institute for Theoretical Physics University of Zurich
Winterthurerstrasse 190, CH-8057 Zurich, Switzerland

[31] LAPTH, Université de Savoie and CNRS, Annecy-le-Vieux, France

[32] Institut für Theoretische Physik und Institut für Experimentelle Teilchenphysik,
Karlsruhe Institut of Technology, D-76131 Karlsruhe, Germany

[33] Bergische Universität Wuppertal, D-42097 Wuppertal, Germany

[34] Helsinki Institute of Physics, P.O. Box 64, FIN-00014 University of Helsinki, Finland

[35] SLAC National Accelerator Laboratory, Menlo Park, CA 94025 USA

[36] Department of Physics and Astronomy, Michigan State University,
East Lansing, MI 48824, USA

[37] Department of Physics, Univ. of Texas at Arlington, SH108, University of Texas,
Arlington, TX 76019, USA

[38] Niels Bohr Institute (NBI) University of Copenhagen
Blegdamsvej 17 DK-2100 Copenhagen DENMARK

[39] Institute of Nuclear Research of the Hungarian Academy of Sciences, Hungary

[40] Department of Physics, Royal Holloway, University of London Egham TW20 0EX, UK

[41] University of Split, FESB, R. Boskovica bb, 21 000 Split, Croatia

[42] Institut für Theoretische Teilchenphysik und Kosmologie, RWTH Aachen University,
D-52056 Aachen, Germany

[43] Institute for Particle Physics Phenomenology, Department of Physics,
University of Durham, Durham DH1 3LE, UK

[44] National Central University, Chung-Li, Taiwan

[45] School of Physics, and State Key Laboratory of Nuclear Physics and Technology,
Peking University, China

[46] Centre for Cosmology, Particle Physics and Phenomenology (CP3),
Université Catholique de Louvain, B-1348 Louvain-la-Neuve, Belgium

[47] Univ. of Wisconsin Dept. of Physics, High Energy Physics
2506 Sterling Hall 1150 University Ave, Madison, WI 53706

[48] Southern Methodist University Dept. of Physics, Dallas, TX 75275, USA
[49] Università di Milano-Bicocca and INFN, Sezione di Milano-Bicocca,
Piazza della Scienza 3, 20126 Milan, Italy
[50] University of Virginia, Charlottesville, VA 22906, USA
[51] Department of Physics, Princeton University, Princeton, NJ 08542, USA
[52] Dept. of Physics and Astronomy University of Sheffield, Sheffield S3 7RH, UK
[53] NCSR Demokritos, Institute of Nuclear Physics, Athens, Greece
[54] High Energy Physics Division, Argonne National Laboratory, Argonne, IL 60439, USA
[55] Department of Physics & Astronomy, Northwestern University, Evanston, IL 60208, USA
[56] Department of Physics, University of Oregon, Eugene, OR 97403-1274, USA
[57] University of Liverpool Dept. of Physics Oliver Lodge Lab,
Oxford St. Liverpool L69 3BX UK
[58] Physikalisches Institut, Universität Heidelberg, Heidelberg, Germany
[59] Università di Pavia and INFN, Sezione di Pavia
Via A. Bassi, 6, 27100 Pavia, Italy
[60] Physics Department, Florida State University
Tallahassee, FL 32306-4350, USA
[61] Joint Institute for Nuclear Research (JINR), Joliot-Curie st., 6,
Dubna, 141980 Moscow region, Russia
[62] Paul Scherrer Institut, CH–5232 Villigen PSI, Switzerland
[63] Massachusetts Institute of Technology 77 Massachusetts Avenue
Cambridge, MA 02139-4307 USA
[64] Cambridge University Dept. of Physics Cavendish Laboratory
Cambridge CB3 0HE, UK
[65] Max-Planck-Institut für Physik, Werner-Heisenberg-Institut,
Föhringer Ring 6, D-80805 München, Germany
[66] Department of Physics and Astronomy, University College London,
Gower Street, London WC1E 6BT, UK
[67] INFN, Sezione di Firenze and Dipartimento di Fisica e Astronomia, Università di Firenze,
I-50019 Sesto Fiorentino, Florence, Italy
[68] ITPP, Lausanne CH-1015 Lausanne, PHB - Ecublens, 1015, Lausanne, Switzerland
[69] Università di Napoli Federico II Dipartimento di Scienze Fisiche
via Cintia I-80126 Napoli, Italy
[70] School of Physics, University of the Witwatersrand, Private Bag 3,
Wits 2050, Johannesburg, South Africa
[71] Department of Physics, University of California at San Diego,
La Jolla, CA 92093, USA
[72] Department of Physics, SUNY at Buffalo, Buffalo, NY 14260-1500, USA
† On leave of absence from INFN, Sezione di Firenze, Italy

Prologue

The implementation of spontaneous symmetry breaking in the framework of gauge theories in the 1960s triggered the breakthrough in the construction of the standard electroweak theory, as it still persists today. The idea of driving the spontaneous breakdown of a gauge symmetry by a self-interacting scalar field, which thereby lends mass to gauge bosons, is known as the *Higgs mechanism* and goes back to the early work of Refs. [1–6]. The postulate of a new scalar neutral boson, known as the *Higgs particle*, comes as a phenomenological imprint of this mechanism. Since the birth of this idea, the Higgs boson has successfully escaped detection in spite of tremendous search activities at the high-energy colliders LEP and Tevatron, leaving open the crucial question whether the Higgs mechanism is just a theoretical idea or a 'true model' for electroweak symmetry breaking.

The experiments at the Large Hadron Collider (LHC) have made an impressive step forward in answering this question, by closing down the space available for the long sought Higgs and supersymmetric particles to hide in, putting the Standard Model of particle physics through increasingly gruelling tests. Results based on the analysis of considerably more data than those presented at the Summer Conferences are sufficient to make significant progress in the search for the Higgs boson, but not enough to make any conclusive statement on the existence or non-existence of the Higgs. The outcome of the Higgs search at the LHC will either carve our present understanding of electroweak interactions in stone or will be the beginning of a theoretical revolution.

Contents

1 Introduction[1] . . . 1
2 Branching ratios[2] . . . 4
2.1 SM Higgs branching ratios with uncertainties . . . 4
2.2 MSSM Higgs branching ratios . . . 12
3 Parton distribution functions[3] . . . 18
3.1 PDF set updates . . . 18
3.2 Correlations . . . 18
4 NLO parton shower[4] . . . 32
4.1 Introduction . . . 32
4.2 POWHEG BOX and MC@NLO comparison with HQT[5] . . . 33
4.3 Uncertainties in $\mathrm{gg} \to \mathrm{H} \to \mathrm{WW}^{(*)}$[6] . . . 37
4.4 Systematic studies of NLO MC tools in experimental implementations . . . 47
4.5 Guidelines for the use of HQT results to improve NLO+PS programs . . . 50
4.6 Guidelines to estimate non-perturbative uncertainties . . . 52
4.7 Higgs production via gluon fusion: finite-mass effects[7] . . . 53
4.8 Scale and PDF uncertainties in MC@NLO . . . 56
4.9 On-going debates and open issues . . . 56
5 The gluon-fusion process[8] . . . 59
5.1 Finite-quark-mass effects in the SM gluon-fusion process in POWHEG[9] . . . 60
5.2 Perturbative uncertainties in exclusive jet bins[10] . . . 64
5.3 Perturbative uncertainties in jet-veto efficiencies[11] . . . 70
5.4 The Higgs p_{T} spectrum and its uncertainties[12] . . . 73
5.5 Monte Carlo and resummation for exclusive jet bins[13] . . . 77
6 VBF production mode[14] . . . 84
6.1 Theoretical framework . . . 84
6.2 VBF parameters and cuts . . . 86
6.3 Results . . . 87

[1] S. Dittmaier, C. Mariotti, G. Passarino and R. Tanaka.

[2] A. Denner, S. Heinemeyer, I. Puljak, D. Rebuzzi (eds.); S. Dittmaier, M. Mühlleitner, A. Mück, M. Spira, M.M. Weber and G. Weiglein.

[3] S. Forte, J. Huston and R. S. Thorne (eds); S. Alekhin, J. Blümlein, A.M. Cooper-Sarkar, S. Glazov, P. Jimenez-Delgado, S. Moch, P. Nadolsky, V. Radescu, J. Rojo, A. Sapronov and W.J. Stirling.

[4] M. Felcini, F. Krauss, F. Maltoni, P. Nason and J. Yu. (eds.); J. Alwall, E. Bagnaschi, G. Degrassi, M. Grazzini, K. Hamilton, S. Höche, C. Jackson, H. Kim, Q. Li, F. Petriello, M. Schönherr, F. Siegert, P. Slavich, P. Torrielli and A. Vicini.

[5] K. Hamilton, F. Maltoni, P. Nason and P. Torrielli.

[6] M. Grazzini, H. Hoeth, F. Krauss, F. Petriello, M. Schönherr and F. Siegert.

[7] J. Alwall, Q. Li and F. Maltoni.

[8] M. Grazzini, F. Petriello (eds.); E.A. Bagnaschi, A. Banfi, D. de Florian, G. Degrassi, G. Ferrera, G. P. Salam, P. Slavich, I. W. Stewart, F. Stoeckli, F. J. Tackmann, D. Tommasini, A. Vicini, W. J. Waalewijn and G. Zanderighi.

[9] E.A. Bagnaschi, G. Degrassi, P. Slavich and A. Vicini.

[10] I. W. Stewart and F. J. Tackmann.

[11] A. Banfi, G. P. Salam and G. Zanderighi.

[12] D. de Florian, G.Ferrera, M.Grazzini and D.Tommasini.

[13] I. W. Stewart, F. Stöckli, F. J. Tackmann and W. J. Waalewijn.

[14] A. Denner, S. Farrington, C. Hackstein, C. Oleari, D. Rebuzzi (eds.); S. Dittmaier, A. Mück, S. Palmer and W. Quayle.

7 WH/ZH production mode[15] . . . 95
7.1 Theoretical developments . . . 95
7.2 Numerical results . . . 95
8 ttH Process[16] . . . 102
8.1 NLO distributions for $\mathrm{t\bar{t}H}$ associated production . . . 102
8.2 Interface of NLO $\mathrm{t\bar{t}H}$ and $\mathrm{t\bar{t}A}$ calculations with parton-shower Monte Carlo programs . 105
8.3 The $\mathrm{pp} \to \mathrm{t\bar{t}b\bar{b}}$ background . . . 111
9 $\gamma\gamma$ decay mode[17] . . . 114
9.1 Introduction . . . 114
9.2 Sets of acceptance criteria used . . . 114
9.3 Signal modelling and differential K-factors . . . 114
9.4 Background extraction and modelling . . . 117
10 WW* decay mode[18] . . . 122
10.1 Introduction . . . 122
10.2 Jet bin categorisation and uncertainties . . . 122
10.3 Discussion about the 2-jet bin . . . 124
10.4 Backgrounds . . . 124
10.5 Theoretical uncertainties on the extrapolation parameters α for the 0j and 1j analyses . . 127
10.6 Contribution from the $\mathrm{gg} \to \mathrm{WW}$ process . . . 129
10.7 WW background estimate for the high-mass selection . . . 130
10.8 PDF errors . . . 132
11 ZZ* decay mode[19] . . . 133
11.1 Introduction . . . 133
11.2 The $\mathrm{H} \to \mathrm{ZZ}$ signal process . . . 133
11.3 The ZZ background process . . . 137
11.4 Angular distributions in $\mathrm{H} \to \mathrm{ZZ}$ decays . . . 147
12 Neutral-Higgs-boson production in the MSSM[20] . . . 150
12.1 The MSSM Higgs sector: general features . . . 150
12.2 Status of inclusive calculations . . . 151
12.3 Status of differential cross sections . . . 158
13 Charged-Higgs-boson production and decay[21] . . . 178
13.1 Light charged Higgs boson . . . 178

[15] S. Dittmaier, R.V. Harlander, J. Olsen, G. Piacquadio (eds.); A. Denner, G. Ferrera, M. Grazzini, S. Kallweit, A. Mück and F. Tramontano.

[16] L. Reina, M. Spira (eds.); S. Dawson, R. Frederix, M. V. Garzelli, A. Kardos, C. G. Papadopoulos, Z. Trócsányi and D. Wackeroth.

[17] S. Gascon-Shotkin, M. Kado (eds.); N. Chanon, L. Cieri, G. Davies, D. D'Enterria, D. de Florian, S. Ganjour, J. -Ph. Guillet, C. -M. Kuo, N. Lorenzo,E. Pilon and J. Schaarschmidt.

[18] S. Diglio, B. Di Micco, R. Di Nardo, A. Farilla, B. Mellado and F. Petrucci (eds.).

[19] N. De Filippis, S. Paganis (eds.), S. Bolognesi, T. Cheng, R. K. Ellis, M.D. Jorgensen, N. Kauer, M. Kovac, C. Mariotti, P. Nason, T.C. Petersen, J. Price and I. Puljak.

[20] M. Spira, M. Vazquez Acosta, M. Warsinsky, G. Weiglein (eds.); E.A. Bagnaschi, M. Cutajar, G. Degrassi, R. Harlander, S. Heinemeyer, M. Krämer, A. Nikitenko, S. Palmer, M. Schumacher, P. Slavich, A. Vicini, T. Vickey and M. Wiesemann.

[21] M. Flechl, S. Heinemeyer, M. Krämer, S. Lehti (eds.); M. Hauru, M. Spira and M. Ubiali.

13.2 Heavy charged Higgs boson . . . 181
14 Predictions for Higgs production and decay with a 4th SM-like fermion generation[22] . . . 188
14.1 General setup . . . 188
14.2 Higgs production via gluon fusion . . . 188
14.3 NLO corrections to $\mathrm{H} \to 4\mathrm{f}$ in SM4 . . . 192
14.4 $\mathrm{H} \to \mathrm{f}\bar{\mathrm{f}}$ . . . 193
14.5 $\mathrm{H} \to \mathrm{gg}, \gamma\gamma, \gamma\mathrm{Z}$ . . . 193
14.6 Numerical results . . . 195
15 The (heavy) Higgs-boson lineshape[23] . . . 204
15.1 Introduction . . . 204
15.2 Propagation . . . 205
15.3 Production and decay . . . 208
15.4 Numerical results . . . 212
15.5 QCD scale error . . . 218
15.6 Concluding remarks . . . 219
16 Conclusions[24] . . . 223
Appendices . . . 248
A SM Higgs branching ratios . . . 248
B Weights for POWHEG by HQT program . . . 269
C 2D K-factors for gluon-fusion Higgs signal production and prompt diphoton backgrounds . 269

[22] A. Denner, S. Dittmaier, A. Mück, G. Passarino, M. Spira, C. Sturm, S. Uccirati and M.M. Weber.
[23] G. Passarino (ed.), S. Goria and D. Rosco.
[24] S. Dittmaier, C. Mariotti, G. Passarino and R. Tanaka.

1 Introduction[1]

The quest for the origin of electroweak symmetry breaking is one of the major physics goals of the Large Hadron Collider (LHC) at CERN. After the successful start of pp collisions in 2009 and 2010, the LHC machine has been operated at the centre-of-mass energy of 7 TeV in 2011, and data corresponding to a luminosity of 5.7 fb^{-1} have been delivered. The LHC is expected to operate at $\sqrt{s} = 7$ or 8 TeV in 2012 and a long shutdown (2013–2014) is scheduled to prepare for the run at the design centre-of-mass energy of 14 TeV.

At the LHC, the most important Standard Model (SM) Higgs-boson production processes are: the gluon-fusion process ($\mathrm{gg} \to \mathrm{H}$), where a gg pair annihilates into the Higgs boson through a loop with heavy-quark dominance; vector-boson fusion ($\mathrm{qq}' \to \mathrm{qq}'\mathrm{H}$), where vector bosons are radiated off quarks and couple to produce a Higgs boson; vector-boson associated production ($\mathrm{q\overline{q}} \to \mathrm{WH/ZH}$), where the Higgs boson is radiated off a gauge boson; top-quark pair associated production ($\mathrm{q\overline{q}/gg} \to \mathrm{t\overline{t}H}$), where the Higgs boson is radiated of a top quark.

ATLAS and CMS, with data currently analysed, are able to exclude a substantial region of the possible Higgs-boson mass range. The results that were presented in December 2011 show that the region of Higgs masses between approximately 116 and 127 GeV is not excluded, and the excess of events observed for hypothesised Higgs-boson masses at this low end of the explored range makes the observed limits weaker than expected. To ascertain the origin of this excess, more data are required. With much more data accumulated in 2012, one may eventually reach the discovery of the Higgs boson. For this, predictions with the highest precision for Higgs-boson production and decay rates and associated uncertainty estimates are crucial. If there is a discovery then theoretical predictions for Higgs-boson property measurements will become even more important. This is the reason why the LHC Higgs Cross Section Working Group has been created in 2010 as the joint forum of the experimental collaborations (ATLAS, CMS, and LHCb) and the theory communities.

In the LHC Higgs Cross Section Working Group, there are 16 subgroups. The first four address different Higgs-boson production modes: $\mathrm{gg} \to \mathrm{H}$, $\mathrm{qq}' \to \mathrm{qq}'\mathrm{H}$, $\mathrm{q\overline{q}} \to \mathrm{WH/ZH}$, and $\mathrm{q\overline{q}/gg} \to \mathrm{t\overline{t}H}$ processes. Two more subgroups are focusing on MSSM neutral- and MSSM charged-Higgs production. In addition, six new subgroups were created in 2010 to study the Higgs-boson decay modes: $\mathrm{H} \to \gamma\gamma, \mathrm{W^+W^-}, \mathrm{ZZ}, \tau^+\tau^-, \mathrm{b\overline{b}}$, and $\mathrm{H}^\pm$. Four subgroups discuss common issues across the various production modes: Higgs-boson decay branching ratios (BR) in the SM and in the Minimal Supersymmetric Standard Model (MSSM), parton distribution functions (PDFs), next-to-leading order (NLO) Monte Carlo (MC) generators for both Higgs signal and SM backgrounds and, finally, the definition of Higgs pseudo-observables, in particular, the heavy-Higgs-boson lineshape.

In the first Report [7], the state-of-the-art inclusive Higgs-boson production cross sections and decay branching ratios have been compiled. The major part of the Report was devoted to discussing the computation of cross sections and branching ratios for the SM and MSSM Higgs bosons. The related theoretical uncertainties due to QCD scale and PDF were discussed. The Higgs-boson production cross sections are calculated with varying precision in the perturbative expansion. For total cross sections, the calculations are performed up to the next-to-next-to-leading-order (NNLO) QCD correction for the $\mathrm{gg} \to \mathrm{H}$, $\mathrm{qq}' \to \mathrm{qq}'\mathrm{H}$, and $\mathrm{q\overline{q}} \to \mathrm{WH/ZH}$ processes, while up to NLO for $\mathrm{q\overline{q}/gg} \to \mathrm{t\overline{t}H}$ process. In most cases, the NLO electroweak (EW) corrections have been applied assuming factorisation with the QCD corrections. The Higgs-boson decay branching ratios take into account the recently calculated higher-order NLO QCD and EW corrections in each Higgs-boson decay mode. The resulting SM Higgs-boson production cross sections times branching ratios are shown in Figure 1. For these calculations, the common SM input parameter set has been used as given in Ref. [8]. The coherent theory results to the experimental collaborations facilitated the first LHC combination of the Higgs-boson search results, as described in Ref. [9].

[1] S. Dittmaier, C. Mariotti, G. Passarino and R. Tanaka.

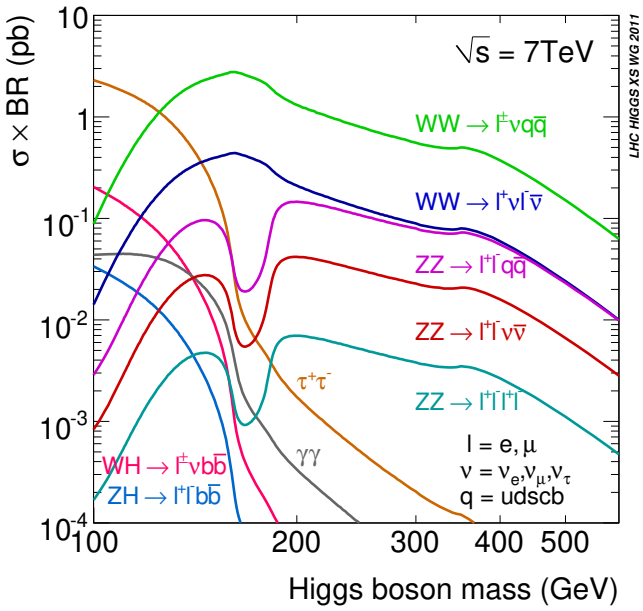

Fig. 1: The SM Higgs-boson production cross sections multiplied by decay branching ratios in pp collisions at $\sqrt{s} = 7$ TeV as a function of Higgs-boson mass. All production modes are summed in the channels of $\mathrm{H} \to \tau^+\tau^-$, $\gamma\gamma$, or $\mathrm{WW/ZZ}(\to 4\ \mathrm{fermions})$. In the $\mathrm{H} \to \mathrm{b\bar{b}}$ channel, only the vector-boson associated production is considered.

The present Report, in particular, covers updates on inclusive observables. The goal of this second Report is to extend the previous study of inclusive cross sections to differential distributions. The experimental analysis must impose cuts on the final state in order to extract the signal from background: a precise determination of the corresponding signal acceptance is therefore necessary.

Various studies are performed in different Higgs-boson production modes ($\mathrm{gg} \to \mathrm{H}$, $\mathrm{qq'} \to \mathrm{qq'H}$, $\mathrm{q\bar{q}} \to \mathrm{WH/ZH}$, and $\mathrm{q\bar{q}/gg} \to \mathrm{t\bar{t}H}$ processes); the benchmark cuts for these processes have been defined, and the differential distributions have been compared at various levels of theoretical accuracy, i.e., at NLO/NNLO and with MC generators:

- In addition, many search modes for the Higgs boson are carried out in the exclusive mode, i.e., by separating the events according to number of jets or the transverse momentum (p_{T}) of the Higgs boson. A particularly important channel is $\mathrm{H} \to \mathrm{WW} \to \mathrm{l}\nu\mathrm{l}\nu$ in $\mathrm{gg} \to \mathrm{H}$ process, where the events are classified in $\mathrm{H}{+}0,1,2$-jet multiplicity bins to improve the signal-to-noise ratio. There are large logarithms associated with the ratio of the Higgs-boson mass over the defining p_{T} of the jet: the theoretical error assignment in the exclusive jet bins has been extensively discussed, and a precise prescription is given in this Report.
- The p_{T} of the Higgs boson is a particularly interesting quantity, as it can be used as the discriminant variable against the SM backgrounds. Possible large logarithms that can occur when cuts are imposed should be studied carefully: for instance, the Higgs-boson transverse-momentum spectrum in $\mathrm{gg} \to \mathrm{H}$ process has been studied at NLO accuracy and supplemented with next-to-next-to-leading logarithmic (NNLL) resummation of small-p_{T} logarithms. A systematic study of the uncertainties of the shape of the resummed Higgs-boson p_{T} spectrum has also been carried out.
- The differential distributions of the SM backgrounds (in particular the irreducible backgrounds to Higgs-boson searches) have been studied extensively in this Report. In the searches at LHC, most of the backgrounds in the signal regions are derived from measurements in control regions

(so-called "data-driven" methods); the extrapolation to the signal region relies on MC simulations, and the related theoretical uncertainty is usually estimated by comparing different MC generators and by varying the QCD scales. Whenever possible, not only the normalisation, but also the parametrisation of the background shape should be taken from the control region. However, there are backgrounds for which one must rely on theoretical predictions; the main example is represented by di-boson backgrounds $\mathrm{q\overline{q}/gg} \to \mathrm{WW/ZZ}$ where data control regions cannot be used, due to the limited size of the data sample that is available.

– In addition, the interference between the Higgs-boson signal in $\mathrm{gg} \to \mathrm{H} \to \mathrm{WW/ZZ}$ and the gluon-induced continuum $\mathrm{WW/ZZ}$ production may not be negligible after introducing experimental cuts. It will be important to compute the interference between signal and background and to try to access this at NLO level. The NLO Monte Carlo's will be used to simulate this background and to determine how the K-factor is changing with the chosen kinematic cuts.

This Report also discusses issues common to different Higgs-boson search channels.

– The Higgs-boson BRs are the important ingredients for Higgs physics. Their most precise estimate with the state-of-the-art calculations for SM and MSSM is presented and the associated uncertainties are discussed.
– PDFs are crucial for the prediction of Higgs-boson production processes, hence PDFs and their uncertainties are of particular significance. At present, these PDFs are obtained from fits to data from deep-inelastic scattering, Drell–Yan processes, and jet production from a wide variety of different experiments. Upon arrival of new LHC data, significant improvements are expected for the PDF predictions. Different groups have produced publicly available PDFs using different data sets and analysis frameworks, and updates are reported.
– NLO MCs are now widely used at LHC; the main progress is represented by a consistent inclusion of exact NLO corrections matched to the parton-shower (PS) simulations. At present, all the main Higgs-boson production channels ($\mathrm{gg} \to \mathrm{H}$, $\mathrm{qq'} \to \mathrm{qq'H}$, $\mathrm{q\overline{q}} \to \mathrm{WH/ZH}$, and $\mathrm{q\overline{q}/gg} \to \mathrm{t\overline{t}H}$) are simulated with NLO+PS, together with most important SM backgrounds, like $\mathrm{q\overline{q}/gg} \to \mathrm{WW/ZZ, Wb\overline{b}/Zb\overline{b}, t\overline{t}}$, etc. Tuning of NLO+PS generators is an important issue, and particularly relevant is the p_{T} of the Higgs boson. Estimates of uncertainties in NLO+PS simulations due to QCD scale uncertainties or different matching procedures are also reported, and uncertainties due to hadronisation and underlying events are discussed.
– The current searches for a heavy Higgs boson assume on-shell (stable) Higgs-boson production. The production cross section is then sampled over a Breit–Wigner distribution (either fixed-width or running-width scheme), as implemented in the MC simulations. Recent studies have shown that the effects due to off-shell Higgs-boson production and decay and to interference of the signal with the SM backgrounds may become sizable for Higgs-boson masses $M_{\mathrm{H}} > 300$ GeV; the Higgs-boson lineshape is expected to be altered as well. Thus concrete theoretical predictions for the heavy-Higgs-boson lineshape is discussed in this Report.

Several models beyond the SM are also discussed in this Report: in the MSSM the Higgs-boson sector contains, two scalar doublets, accommodating five physical Higgs bosons of the light and heavy CP-even h and H, the CP-odd A, and the charged Higgs bosons $\mathrm{H}^{\pm}$; BRs and various kinematical distributions are discussed. A model which contains a 4th generation of heavy fermions, consisting of an up- and a down-type quark $(\mathrm{t'}, \mathrm{b'})$, a charged lepton $(\mathrm{l'})$, and a massive neutrino $(\mathrm{\nu_l'})$ has been studied: a large effect of the higher-order electroweak corrections has been found.

This Report is based upon the outcome of a series of workshops throughout 2010–2011, joint effort for Higgs-boson cross sections between ATLAS, CMS, LHCb collaborations, and the theory community. These results are recommended as the common inputs to the experimental collaborations, and for the Higgs combinations at LHC [2].

[2] Any updates will be bade available at the TWiki page: https://twiki.cern.ch/twiki/bin/view/LHCPhysics/CrossSections

2 Branching ratios[3]

For a correct interpretation of experimental data precise calculations not only of the various production cross sections, but also for the relevant decay widths are essential, including their respective uncertainties. Concerning the SM Higgs boson in Ref. [7] a first precise estimate of the branching ratios was presented. In Section 2.1 we update this prediction and supplement it with an estimate of the various uncertainties. For the lightest Higgs boson in the MSSM in Ref. [7] preliminary results for $\mathrm{BR}(\mathrm{H} \to \tau^+\tau^-)$ ($\phi = \mathrm{h}, \mathrm{H}, \mathrm{A}$) were given. In Section 2.2 we present a prediction for all relevant decay channels evaluated in the $m_{\mathrm{h}}^{\mathrm{max}}$ scenario [10].

2.1 SM Higgs branching ratios with uncertainties

In this section we present an update of the BR calculation as well as results for the uncertainties of the decay widths and BRs for a SM Higgs boson. Neglecting these uncertainties would yield in the case of negative search results too large excluded regions of the parameter space. In case of a Higgs-boson signal these uncertainties are crucial to perform a reliable and accurate determination of M_{H} and the Higgs-boson couplings [11–13]. The uncertainties arise from two sources, the missing higher-order corrections yield the "theoretical" uncertainties, while the experimental errors on the SM input parameters, such as the quark masses or the strong coupling constant, give rise to the "parametric" uncertainties. Both types of uncertainty have to be taken into account and combined for a reliable estimate. We investigate all relevant channels for the SM Higgs boson, $\mathrm{H} \to \mathrm{t\bar{t}}$, $\mathrm{H} \to \mathrm{bb}$, $\mathrm{H} \to \mathrm{c\bar{c}}$, $\mathrm{H} \to \tau^+\tau^-$, $\mathrm{H} \to \mu^+\mu^-$, $\mathrm{H} \to \mathrm{gg}$, $\mathrm{H} \to \gamma\gamma$, $\mathrm{H} \to \mathrm{Z}\gamma$, $\mathrm{H} \to \mathrm{WW}$ and $\mathrm{H} \to \mathrm{ZZ}$ (including detailed results also for the various four-fermion final states). We present results for the total width, Γ_{H}, as well as for various BRs. These results have also been published in Ref. [14].

2.1.1 Programs and Strategy for Branching Ratio Calculations

The branching ratios of the Higgs boson in the SM have been determined using the programs HDECAY [15–17] and PROPHECY4F [18–20]. In a first step, all partial widths have been calculated as accurately as possible. Then the branching ratios have been derived from this full set of partial widths. Since the widths are calculated for on-shell Higgs bosons, the results have to be used with care for a heavy Higgs boson ($M_{\mathrm{H}} \gtrsim 500$ GeV).

- HDECAY calculates the decay widths and branching ratios of the Higgs boson(s) in the SM and the MSSM. For the SM it includes all kinematically allowed channels and all relevant higher-order QCD corrections to decays into quark pairs and into gluons. Below the thresholds for two-particle decays, the corresponding three-particle decays are used, e.g., below the $\mathrm{t\bar{t}}$ threshold the branching ratio for $\mathrm{H} \to \mathrm{t\bar{t}}$ is calculated from the three-body decay $\mathrm{H} \to \mathrm{tbW}$ including finite-width effects. More details are given below.
- PROPHECY4F is a Monte Carlo event generator for $\mathrm{H} \to \mathrm{WW/ZZ} \to 4\mathrm{f}$ (leptonic, semi-leptonic, and hadronic) final states. It provides the leading-order (LO) and next-to-leading-order (NLO) partial widths for any possible 4-fermion final state. It includes the complete NLO QCD and electroweak corrections and all interferences at LO and NLO. In other words, it takes into account both the corrections to the decays into intermediate WW and ZZ states as well as their interference for final states that allow for both. The dominant two-loop contributions in the heavy-Higgs-mass limit proportional to $G_F^2 M_{\mathrm{H}}^4$ are included according to Refs. [21, 22]. Since the calculation is consistently performed with off-shell gauge bosons without any on-shell approximation, it is valid above, near, and below the gauge-boson pair thresholds. Like all other light quarks and leptons, bottom quarks are treated as massless. Using the LO/NLO gauge-boson widths in the LO/NLO

[3] A. Denner, S. Heinemeyer, I. Puljak, D. Rebuzzi (eds.); S. Dittmaier, M. Mühlleitner, A. Mück, M. Spira, M.M. Weber and G. Weiglein.

calculation ensures that the effective branching ratios of the W and Z bosons obtained by summing over all decay channels add up to one.

– Electroweak NLO corrections to the decays $\mathrm{H} \to \gamma\gamma$ and $\mathrm{H} \to \mathrm{gg}$ have been calculated in Refs. [23–29]. They are implemented in HDECAY in form of grids based on the calculations of Refs. [28, 29].

The results presented below have been obtained as follows. The Higgs total width resulting from HDECAY has been modified according to the prescription

$$\Gamma_{\mathrm{H}} = \Gamma^{\mathrm{HD}} - \Gamma^{\mathrm{HD}}_{\mathrm{ZZ}} - \Gamma^{\mathrm{HD}}_{\mathrm{WW}} + \Gamma^{\mathrm{Proph.}}_{\mathrm{4f}} \,, \tag{1}$$

where Γ_{H} is the total Higgs width, Γ^{HD} the Higgs width obtained from HDECAY, $\Gamma^{\mathrm{HD}}_{\mathrm{ZZ}}$ and $\Gamma^{\mathrm{HD}}_{\mathrm{WW}}$ stand for the partial widths to ZZ and WW calculated with HDECAY, while $\Gamma^{\mathrm{Proph.}}_{\mathrm{4f}}$ represents the partial width of $\mathrm{H} \to \mathrm{4f}$ calculated with PROPHECY4F. The latter can be split into the decays into ZZ, WW, and the interference,

$$\Gamma^{\mathrm{Proph.}}_{\mathrm{4f}} = \Gamma_{\mathrm{H}\to\mathrm{W}^*\mathrm{W}^*\to\mathrm{4f}} + \Gamma_{\mathrm{H}\to\mathrm{Z}^*\mathrm{Z}^*\to\mathrm{4f}} + \Gamma_{\mathrm{WW/ZZ-int.}} \,. \tag{2}$$

2.1.2 The SM input-parameter set

The production cross sections and decay branching ratios of the Higgs bosons depend on a large number of SM parameters. For our calculations, the input-parameter set as defined in Appendix A of Ref. [7] has been used.

As input values for the gauge-boson masses we use the pole masses $M_{\mathrm{Z}} = 91.15349$ GeV and $M_{\mathrm{W}} = 80.36951$ GeV, derived from the PDG values given in Appendix A of Ref. [7]. The gauge-boson widths have been calculated at NLO from the other input parameters resulting in $\Gamma_{\mathrm{Z}} = 2.49581$ GeV and $\Gamma_{\mathrm{W}} = 2.08856$ GeV.

It should be noted that for our numerical analysis we have used the one-loop pole masses for the charm and bottom quarks and their uncertainties, since these values do not exhibit a significant dependence on the value of the strong coupling constant α_{s} in contrast to the $\overline{\mathrm{MS}}$ masses [30].

2.1.3 Procedure for determining uncertainties

We included two types of uncertainty: Parametric uncertainties (PU), which originate from uncertainties in input parameters, and theoretical uncertainties (THU), which arise from unknown contributions to the theoretical predictions, typically missing higher orders. Here we describe the way these uncertainties have been determined.

2.1.3.1 Parametric uncertainties

In order to determine the parametric uncertainties of the Higgs-decay branching ratios we took into account the uncertainties of the input parameters α_{s}, m_{c}, m_{b}, and m_{t}. The considered variation of these input parameters is given in Table 1. The variation in α_{s} corresponds to three times the error given in Refs. [31, 32]. The uncertainties for m_{b} and m_{c} are a compromise between the errors of Ref. [32] and the errors from the most precise evaluations [33–35]. For m_{c} our error corresponds roughly to the one obtained in Ref. [36]. Finally, the assumed error for m_{t} is about twice the error from the most recent combination of CDF and DØ [37].

We did not consider parametric uncertainties resulting from experimental errors on G_F, M_{Z}, M_{W}, and the lepton masses, because their impact is below one per mille. We also did not include uncertainties for the light quarks $\mathrm{u}, \mathrm{d}, \mathrm{s}$ as the corresponding branching ratios are very small and the impact on other branching ratios is negligible. Since we used G_F to fix the electromagnetic coupling α, uncertainties in the hadronic vacuum polarisation do not matter.

Table 1: Input parameters and their relative uncertainties, as used for the uncertainty estimation of the branching ratios. The masses of the central values correspond to the 1-loop pole masses, while the last column contains the corresponding $\overline{\mathrm{MS}}$ mass values.

Parameter	Central value	Uncertainty	$\overline{\mathrm{MS}}$ masses $m_{\mathrm{q}}(m_{\mathrm{q}})$
$\alpha_{\mathrm{s}}(M_{\mathrm{Z}})$	0.119	± 0.002	
m_{c}	1.42 GeV	± 0.03 GeV	1.28 GeV
m_{b}	4.49 GeV	± 0.06 GeV	4.16 GeV
m_{t}	172.5 GeV	± 2.5 GeV	165.4 GeV

Given the uncertainties in the parameters, the parametric uncertainties have been determined as follows. For each parameter $p = \alpha_{\mathrm{s}}, m_{\mathrm{c}}, m_{\mathrm{b}}, m_{\mathrm{t}}$ we have calculated the Higgs branching ratios for p, $p + \Delta p$ and $p - \Delta p$, while all other parameters have been left at their central values. The error on each branching ratio has then been determined by

$$\begin{aligned} \Delta^p_+ \mathrm{BR} &= \max\{\mathrm{BR}(p+\Delta p), \mathrm{BR}(p), \mathrm{BR}(p-\Delta p)\} - \mathrm{BR}(p), \\ \Delta^p_- \mathrm{BR} &= \mathrm{BR}(p) - \min\{\mathrm{BR}(p+\Delta p), \mathrm{BR}(p), \mathrm{BR}(p-\Delta p)\}. \end{aligned} \tag{3}$$

Note that this definition leads to asymmetric errors. The total parametric errors have been obtained by adding the parametric errors from the four parameter variations in quadrature. This procedure ensures that the branching ratios add up to unity for all parameter variations individually.

The uncertainties of the partial and total decay widths have been obtained in an analogous way,

$$\begin{aligned} \Delta^p_+ \Gamma &= \max\{\Gamma(p+\Delta p), \Gamma(p), \Gamma(p-\Delta p)\} - \Gamma(p), \\ \Delta^p_- \Gamma &= \Gamma(p) - \min\{\Gamma(p+\Delta p), \Gamma(p), \Gamma(p-\Delta p)\}, \end{aligned} \tag{4}$$

where Γ denotes the partial decay width for each considered decay channel or the total width, respectively. The total parametric errors have been derived by adding the individual parametric errors in quadrature.

2.1.3.2 Theoretical uncertainties

The second type of uncertainty for the Higgs branching ratios results from approximations in the theoretical calculations, the dominant effects being due to missing higher orders. Since the decay widths have been calculated with HDECAY and PROPHECY4F the missing contributions in these codes are relevant. For QCD corrections the uncertainties have been estimated by the scale dependence of the widths resulting from a variation of the scale up and down by a factor 2 or from the size of known omitted corrections. For electroweak corrections the missing higher orders have been estimated based on the known structure and size of the NLO corrections. For cases where HDECAY takes into account the known NLO corrections only approximatively the accuracy of these approximations has been used. The estimated relative theoretical uncertainties for the partial widths resulting from missing higher-order corrections are summarised in Table 2. The corresponding uncertainty for the total width is obtained by adding the uncertainties for the partial widths linearly.

Specifically, the uncertainties of the partial widths calculated with HDECAY are obtained as follows: For the decays $\mathrm{H} \to \mathrm{b}\overline{\mathrm{b}}, \mathrm{c}\overline{\mathrm{c}}$, HDECAY includes the complete massless QCD corrections up to and including NNNNLO, with a corresponding scale dependence of about 0.1% [38–45]. The NLO electroweak corrections [46–49] are included in the approximation for small Higgs masses [50] which has an accuracy of about $1-2\%$ for $M_{\mathrm{H}} < 135$ GeV. The same applies to the electroweak corrections to $\mathrm{H} \to \tau^+\tau^-$. For Higgs decays into top quarks HDECAY includes the complete NLO QCD corrections

Table 2: Estimated theoretical uncertainties from missing higher orders.

Partial width	QCD	electroweak	total
$\mathrm{H} \to \mathrm{b\bar{b}}/\mathrm{c\bar{c}}$	$\sim 0.1\%$	$\sim$ 1–2% for $M_\mathrm{H} \lesssim 135$ GeV	$\sim 2\%$
$\mathrm{H} \to \tau^+\tau^-/\mu^+\mu^-$		$\sim$ 1–2% for $M_\mathrm{H} \lesssim 135$ GeV	$\sim 2\%$
$\mathrm{H} \to \mathrm{t\bar{t}}$	$\lesssim 5\%$	$\lesssim$ 2–5% for $M_\mathrm{H} < 500$ GeV	$\sim 5\%$
		$\sim 0.1(\frac{M_\mathrm{H}}{1\ \mathrm{TeV}})^4$ for $M_\mathrm{H} > 500$ GeV	$\sim$ 5–10%
$\mathrm{H} \to \mathrm{gg}$	$\sim 3\%$	$\sim 1\%$	$\sim 3\%$
$\mathrm{H} \to \gamma\gamma$	$< 1\%$	$< 1\%$	$\sim 1\%$
$\mathrm{H} \to \mathrm{Z}\gamma$	$< 1\%$	$\sim 5\%$	$\sim 5\%$
$\mathrm{H} \to \mathrm{WW/ZZ} \to 4\mathrm{f}$	$< 0.5\%$	$\sim 0.5\%$ for $M_\mathrm{H} < 500$ GeV	$\sim 0.5\%$
		$\sim 0.17(\frac{M_\mathrm{H}}{1\ \mathrm{TeV}})^4$ for $M_\mathrm{H} > 500$ GeV	$\sim$ 0.5–15%

[51–57] interpolated to the large-Higgs-mass results at NNNNLO far above the threshold [38–45]. The corresponding scale dependence is below 5%. Only the NLO electroweak corrections due to the self-interaction of the Higgs boson are included, and the neglected electroweak corrections amount to about $2{-}5\%$ for $M_\mathrm{H} < 500$ GeV, where 5% refers to the region near the $\mathrm{t\bar{t}}$ threshold and 2% to Higgs masses far above. For $M_\mathrm{H} > 500$ GeV higher-order heavy-Higgs corrections [58–63] serve as error estimate, resulting in an uncertainty of about $0.1 \times (M_\mathrm{H}/1\ \mathrm{TeV})^4$ for $M_\mathrm{H} > 500$ GeV. For $\mathrm{H} \to \mathrm{gg}$, HDECAY uses the NLO [64–66], NNLO [67], and NNNLO [68] QCD corrections in the limit of heavy top quarks. The uncertainty from the scale dependence at NNNLO is about 3%. The NLO electroweak corrections are included via an interpolation based on a grid from Ref. [29]; the uncertainty from missing higher-order electroweak corrections is estimated to be 1%. For the decay $\mathrm{H} \to \gamma\gamma$, HDECAY includes the full NLO QCD corrections [66, 69–74] and a grid from Ref. [28, 29] for the NLO electroweak corrections. Missing higher orders are estimated to be below 1%. The contribution of the $\mathrm{H} \to \gamma\mathrm{e}^+\mathrm{e}^-$ decay via virtual photon conversion, evaluated in Ref. [75] is not taken into account in the following results. Its correct treatment and its inclusion in HDECAY are in progress.[4] The partial decay width $\mathrm{H} \to \mathrm{Z}\gamma$ is included in HDECAY at LO including the virtual W, top, bottom, and τ loop contributions. The QCD corrections are small in the intermediate-Higgs-mass range [76] and can thus safely be neglected. The associated theoretical uncertainty ranges at the level below one per cent. The electroweak corrections to this decay mode are unknown and thus imply a theoretical uncertainty of about 5% in the intermediate-Higgs-mass range.

The decays $\mathrm{H} \to \mathrm{WW/ZZ} \to 4\mathrm{f}$ are based on PROPHECY4F, which includes the complete NLO QCD and electroweak corrections with all interferences and leading two-loop heavy-Higgs corrections. For small Higgs-boson masses the missing higher-order corrections are estimated to roughly 0.5%. For $M_\mathrm{H} > 500$ GeV higher-order heavy-Higgs corrections dominate the error leading to an uncertainty of about $0.17 \times (M_\mathrm{H}/1\ \mathrm{TeV})^4$.

Based on the error estimates for the partial widths in Table 2, the theoretical uncertainties for the branching ratios are determined as follows. For the partial widths $\mathrm{H} \to \mathrm{b\bar{b}}, \mathrm{c\bar{c}}, \tau^+\tau^-, \mathrm{gg}, \gamma\gamma$ the total uncertainty given in Table 2 is used. For $\mathrm{H} \to \mathrm{t\bar{t}}$ and $\mathrm{H} \to \mathrm{WW/ZZ} \to 4\mathrm{f}$, the total uncertainty is used for $M_\mathrm{H} < 500$ GeV, while for higher Higgs masses the QCD and electroweak uncertainties are added linearly. Then the shifts of all branching ratios are calculated resulting from the scaling of an individual partial width by the corresponding relative error (since each branching ratio depends on all partial widths, scaling a single partial width modifies all branching ratios). This is done by scaling each partial width separately while fixing all others to their central values, resulting in individual theoretical uncertainties of each branching ratio. However, since the errors for all $\mathrm{H} \to \mathrm{WW/ZZ} \to 4\mathrm{f}$ decays

[4] The contribution of $\mathrm{H} \to \gamma\mathrm{e}^+\mathrm{e}^-$ is part of the QED corrections to $\mathrm{H} \to \gamma\gamma$ which are expected to be small in total.

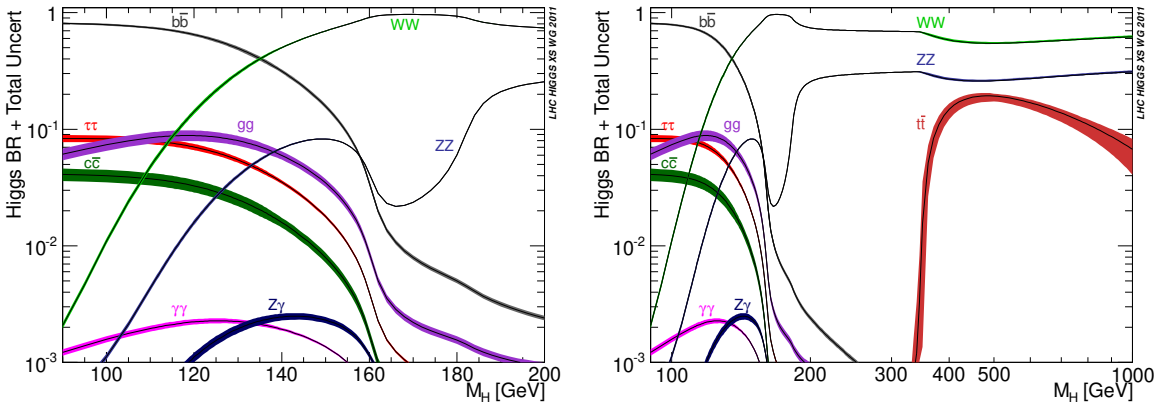

Fig. 2: Higgs branching ratios and their uncertainties for the low mass range (left) and for the full mass range (right).

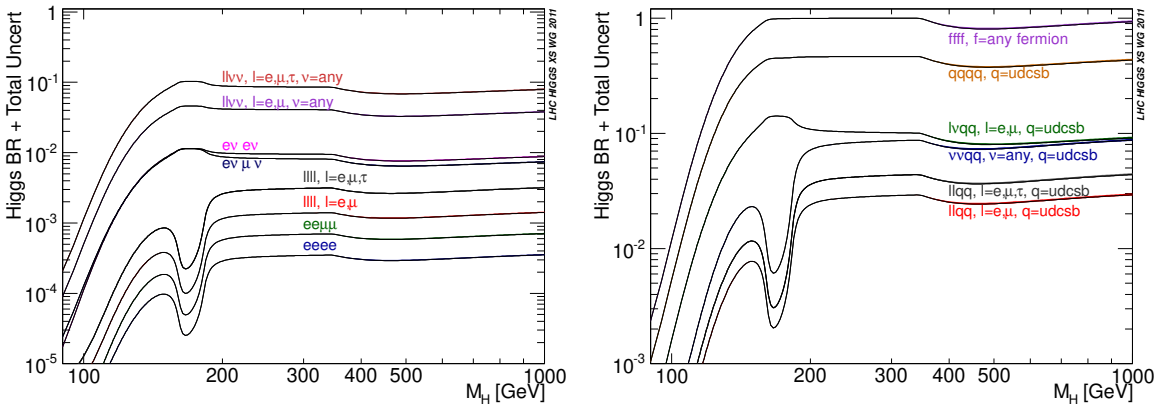

Fig. 3: Higgs branching ratios for the different $\mathrm{H} \to 4\mathrm{l}$ and $\mathrm{H} \to 2\mathrm{l}2\nu$ final states (left) and for $\mathrm{H} \to 4\mathrm{q}$, $\mathrm{H} \to 4\mathrm{f}$ and $\mathrm{H} \to 2\mathrm{q}2\mathrm{l}, 2\mathrm{q}\mathrm{l}\nu, 2\mathrm{q}2\nu$ final states (right) and their uncertainties for the full mass range.

are correlated for $M_{\mathrm{H}} > 500$ GeV or small below, we only consider the simultaneous scaling of all 4-fermion partial widths. The thus obtained individual theoretical uncertainties for the branching ratios are combined linearly to obtain the total theoretical uncertainties.

Finally, the total uncertainties are obtained by adding linearly the total parametric uncertainties and the total theoretical uncertainties.

2.1.4 Results

In this section the results of the SM Higgs branching ratios, calculated according to the procedure described above, are shown and discussed. Figure 2 shows the SM Higgs branching ratios in the low mass range, 100 GeV $< M_{\mathrm{H}} < 200$ GeV, and in the "full" mass range, 100 GeV $< M_{\mathrm{H}} < 1000$ GeV, as solid lines. The (coloured) bands around the lines show the respective uncertainties, estimated considering both the theoretical and the parametric uncertainty sources (as discussed in Section 2.1.3). More detailed results on the decays $\mathrm{H} \to \mathrm{WW}$ and $\mathrm{H} \to \mathrm{ZZ}$ with the subsequent decay to $4\mathrm{f}$ are presented in Figures 3. The largest "visible" uncertainties are found for the channels $\mathrm{H} \to \tau^+\tau^-$, $\mathrm{H} \to \mathrm{gg}$, $\mathrm{H} \to \mathrm{c}\overline{\mathrm{c}}$, and $\mathrm{H} \to \mathrm{t}\overline{\mathrm{t}}$, see below.

In the following we list the branching ratios for the Higgs two-body fermionic and bosonic final states, together with their uncertainties, estimated as discussed in Section 2.1.3. Detailed results for four representative Higgs-boson masses are given in Table 3. Here we show the BR, the PU separately for

the four parameters as given in Table 1, the total PU, the theoretical uncertainty THU as well as the total uncertainty on the Higgs branching ratios. The THU are most relevant for the $\mathrm{H} \to \mathrm{gg}$, $\mathrm{H} \to \mathrm{Z}\gamma$, and $\mathrm{H} \to \mathrm{t}\bar{\mathrm{t}}$ branching ratios, reaching $\mathcal{O}(10\%)$. For the $\mathrm{H} \to \mathrm{bb}$, $\mathrm{H} \to \mathrm{c}\bar{\mathrm{c}}$, and $\mathrm{H} \to \tau^+\tau^-$ branching ratios they remain below a few per cent. PU are relevant mostly for the $\mathrm{H} \to \mathrm{c}\bar{\mathrm{c}}$ and $\mathrm{H} \to \mathrm{gg}$ branching ratios, reaching up to $\mathcal{O}(10\%)$ and $\mathcal{O}(5\%)$, respectively. They are mainly induced by the parametric uncertainties in α_s and m_c. The PU resulting from m_b affect the $\mathrm{BR}(\mathrm{H} \to \mathrm{bb})$ at the level of 3%, and the PU from m_t influences in particular the $\mathrm{BR}(\mathrm{H} \to \mathrm{t}\bar{\mathrm{t}})$ near the $\mathrm{t}\bar{\mathrm{t}}$ threshold. For the $\mathrm{H} \to \gamma\gamma$ channel the total uncertainty can reach up to about 5% in the relevant mass range. Both THU and PU on the important channels $\mathrm{H} \to \mathrm{ZZ}$ and $\mathrm{H} \to \mathrm{WW}$ remain at the level of 1% over the full mass range, giving rise to a total uncertainty below 3% for $M_\mathrm{H} > 135$ GeV. In Tables A.1–A.10 (see Appendix) we list the branching ratios for the Higgs two-body fermionic and bosonic final states, together with their total uncertainties, for various Higgs-boson masses.[5] Tables A.6–A.10 also contain the total Higgs width Γ_H in the last column.

Finally, Tables A.11–A.15 and Tables A.16–A.20, list the branching ratios for the most relevant Higgs decays into four-fermion final states. The right column in these tables shows the total relative uncertainties on these branching ratios in per cent. These are practically equal for all the $\mathrm{H} \to 4\mathrm{f}$ branching ratios and the same as those for $\mathrm{H} \to \mathrm{WW/ZZ}$. It should be noted that the charge-conjugate state is not included for $\mathrm{H} \to \mathrm{l}\nu\mathrm{q}\bar{\mathrm{q}}$.

We would like to remark that, when possible, the branching ratios for Higgs into four fermions, explicitly calculated and listed in Tables A.11–A.20, should be preferred over the option of calculating

$$\mathrm{BR}(\mathrm{H} \to \mathrm{VV}) \times \mathrm{BR}(\mathrm{V} \to \mathrm{f}\bar{\mathrm{f}}) \times \mathrm{BR}(\mathrm{V} \to \mathrm{f}\bar{\mathrm{f}}) \times \text{(statistical factor)} \tag{5}$$

where $\mathrm{V} = \mathrm{W}, \mathrm{Z}$, and $\mathrm{BR}(\mathrm{H} \to \mathrm{VV})$ is estimated by PROPHECY4F, while $\mathrm{BR}(\mathrm{V} \to \mathrm{f}\bar{\mathrm{f}})$ are from Particle Data Group (PDG). The formula (5) is based on the narrow-Higgs-width approximation and supposes the W and Z gauge bosons to be on shell and thus neglects, in particular, all interferences between different four-fermion final states. This approximation is generally not accurate enough for Higgs masses below and near the $\mathrm{WW/ZZ}$ thresholds. For precision Higgs physics, it is strongly recommended to use $\mathrm{H} \to 4\mathrm{f}$ BRs whenever possible. The ratio of above approximation (5) over PROPHECY4F prediction is shown in Figure 4. For $\mathrm{H} \to \mathrm{e}^+\mathrm{e}^-\mathrm{e}^+\mathrm{e}^-$ or $\mu^+\mu^-\mu^+\mu^-$ there is a large enhancement in the BR due to interference for $M_\mathrm{H} < 200$ GeV (i.e. below $\mathrm{WW/ZZ}$ thresholds). Approximation (5) underestimates the BR for $\mathrm{H} \to \mathrm{e}^+\mathrm{e}^-\mathrm{e}^+\mathrm{e}^-$ or $\mu^+\mu^-\mu^+\mu^-$ by 11% at $M_\mathrm{H} = 120$ GeV. For $\mathrm{H} \to \mathrm{e}^+\nu_\mathrm{e}\mathrm{e}^-\bar{\nu}_\mathrm{e}$ or $\mathrm{H} \to \mu^+\nu_\mu\mu^-\bar{\nu}_\mu$ there is an interference effect for $M_\mathrm{H} < 200$ GeV. Approximation (5) overestimates the BR for $\mathrm{H} \to \mathrm{e}^+\nu_\mathrm{e}\mathrm{e}^-\bar{\nu}_\mathrm{e}$ or $\mathrm{H} \to \mu^+\nu_\mu\mu^-\bar{\nu}_\mu$ by 5.4% at $M_\mathrm{H} = 120$ GeV. Above the $\mathrm{WW/ZZ}$ threshold, the approximation agrees with PROPHECY4F at the level of 1%. For $\mathrm{H} \to \mathrm{ZZ} \to \mathrm{l}\bar{\mathrm{l}}\mathrm{q}\bar{\mathrm{q}}, \mathrm{H} \to \mathrm{WW} \to \mathrm{l}^\pm\nu\mathrm{q}\bar{\mathrm{q}}$, and $\mathrm{H} \to \mathrm{ZZ} \to \nu\bar{\nu}\mathrm{q}\bar{\mathrm{q}}$ the agreement is at the 1% level. For $\mathrm{H} \to \mathrm{WW/ZZ} \to \mathrm{q}\bar{\mathrm{q}}\mathrm{q}\bar{\mathrm{q}}$ there is an interference effect for $M_\mathrm{H} < 200$ GeV.

A comparison of our results with previous calculations can be found in Ref. [14].

[5] The value 0.0% means that the uncertainty is below 0.05%.

Table 3: SM Higgs branching ratios and their relative parametric (PU), theoretical (THU) and total uncertainties for a selection of Higgs masses. For PU, all the single contributions are shown. For these four columns, the upper percentage value (with its sign) refers to the positive variation of the parameter, while the lower one refers to the negative variation of the parameter.

Channel	$M_{\rm H}$ [GeV]	BR	$\Delta m_{\rm c}$	$\Delta m_{\rm b}$	$\Delta m_{\rm t}$	$\Delta\alpha_{\rm s}$	PU	THU	Total
$\rm H \to bb$	120	$6.48{\cdot}10^{-1}$	$^{-0.2\%}_{+0.2\%}$	$^{+1.1\%}_{-1.2\%}$	$^{+0.0\%}_{-0.0\%}$	$^{-1.0\%}_{+0.9\%}$	$^{+1.5\%}_{-1.5\%}$	$^{+1.3\%}_{-1.3\%}$	$^{+2.8\%}_{-2.8\%}$
	150	$1.57{\cdot}10^{-1}$	$^{-0.1\%}_{+0.1\%}$	$^{+2.7\%}_{-2.7\%}$	$^{+0.1\%}_{-0.1\%}$	$^{-2.2\%}_{+2.1\%}$	$^{+3.4\%}_{-3.5\%}$	$^{+0.6\%}_{-0.6\%}$	$^{+4.0\%}_{-4.0\%}$
	200	$2.40{\cdot}10^{-3}$	$^{-0.0\%}_{+0.0\%}$	$^{+3.2\%}_{-3.2\%}$	$^{+0.0\%}_{-0.1\%}$	$^{-2.5\%}_{+2.5\%}$	$^{+4.1\%}_{-4.1\%}$	$^{+0.5\%}_{-0.5\%}$	$^{+4.6\%}_{-4.6\%}$
	500	$1.09{\cdot}10^{-4}$	$^{-0.0\%}_{+0.0\%}$	$^{+3.2\%}_{-3.2\%}$	$^{+0.1\%}_{-0.1\%}$	$^{-2.8\%}_{+2.8\%}$	$^{+4.3\%}_{-4.3\%}$	$^{+3.0\%}_{-1.1\%}$	$^{+7.2\%}_{-5.4\%}$
$\rm H \to \tau^+\tau^-$	120	$7.04{\cdot}10^{-2}$	$^{-0.2\%}_{+0.2\%}$	$^{-2.0\%}_{+2.1\%}$	$^{+0.1\%}_{-0.1\%}$	$^{+1.4\%}_{-1.3\%}$	$^{+2.5\%}_{-2.4\%}$	$^{+3.6\%}_{-3.6\%}$	$^{+6.1\%}_{-6.0\%}$
	150	$1.79{\cdot}10^{-2}$	$^{-0.1\%}_{+0.1\%}$	$^{-0.5\%}_{+0.5\%}$	$^{+0.1\%}_{-0.1\%}$	$^{+0.3\%}_{-0.3\%}$	$^{+0.6\%}_{-0.6\%}$	$^{+2.5\%}_{-2.5\%}$	$^{+3.0\%}_{-3.1\%}$
	200	$2.87{\cdot}10^{-4}$	$^{-0.0\%}_{+0.0\%}$	$^{-0.0\%}_{+0.0\%}$	$^{+0.0\%}_{-0.1\%}$	$^{+0.0\%}_{-0.0\%}$	$^{+0.0\%}_{-0.1\%}$	$^{+2.5\%}_{-2.5\%}$	$^{+2.5\%}_{-2.6\%}$
	500	$1.53{\cdot}10^{-5}$	$^{-0.0\%}_{+0.0\%}$	$^{-0.0\%}_{+0.0\%}$	$^{+0.1\%}_{-0.1\%}$	$^{-0.1\%}_{+0.0\%}$	$^{+0.1\%}_{-0.1\%}$	$^{+5.0\%}_{-3.1\%}$	$^{+5.0\%}_{-3.2\%}$
$\rm H \to \mu^+\mu^-$	120	$2.44{\cdot}10^{-4}$	$^{-0.2\%}_{+0.2\%}$	$^{-2.0\%}_{+2.1\%}$	$^{+0.1\%}_{-0.1\%}$	$^{+1.4\%}_{-1.3\%}$	$^{+2.5\%}_{-2.5\%}$	$^{+3.9\%}_{-3.9\%}$	$^{+6.4\%}_{-6.3\%}$
	150	$6.19{\cdot}10^{-5}$	$^{-0.0\%}_{+0.0\%}$	$^{-0.5\%}_{+0.5\%}$	$^{+0.1\%}_{-0.1\%}$	$^{+0.3\%}_{-0.3\%}$	$^{+0.6\%}_{-0.6\%}$	$^{+2.5\%}_{-2.5\%}$	$^{+3.1\%}_{-3.2\%}$
	200	$9.96{\cdot}10^{-7}$	$^{-0.0\%}_{-0.0\%}$	$^{-0.0\%}_{+0.0\%}$	$^{+0.1\%}_{-0.1\%}$	$^{+0.0\%}_{-0.0\%}$	$^{+0.1\%}_{-0.1\%}$	$^{+2.5\%}_{-2.5\%}$	$^{+2.6\%}_{-2.6\%}$
	500	$5.31{\cdot}10^{-8}$	$^{-0.0\%}_{+0.0\%}$	$^{-0.0\%}_{+0.0\%}$	$^{+0.1\%}_{-0.1\%}$	$^{-0.0\%}_{+0.0\%}$	$^{+0.1\%}_{-0.1\%}$	$^{+5.0\%}_{-3.1\%}$	$^{+5.1\%}_{-3.1\%}$
$\rm H \to c\overline{c}$	120	$3.27{\cdot}10^{-2}$	$^{+6.0\%}_{-5.8\%}$	$^{-2.1\%}_{+2.2\%}$	$^{+0.1\%}_{-0.1\%}$	$^{-5.8\%}_{+5.6\%}$	$^{+8.5\%}_{-8.5\%}$	$^{+3.8\%}_{-3.7\%}$	$^{+12.2\%}_{-12.2\%}$
	150	$7.93{\cdot}10^{-3}$	$^{+6.2\%}_{-6.0\%}$	$^{-0.6\%}_{+0.6\%}$	$^{+0.1\%}_{-0.1\%}$	$^{-6.9\%}_{+6.8\%}$	$^{+9.2\%}_{-9.2\%}$	$^{+0.6\%}_{-0.6\%}$	$^{+9.7\%}_{-9.7\%}$
	200	$1.21{\cdot}10^{-4}$	$^{+6.2\%}_{-6.1\%}$	$^{-0.2\%}_{+0.1\%}$	$^{+0.1\%}_{-0.2\%}$	$^{-7.2\%}_{+7.2\%}$	$^{+9.5\%}_{-9.5\%}$	$^{+0.5\%}_{-0.5\%}$	$^{+10.0\%}_{-10.0\%}$
	500	$5.47{\cdot}10^{-6}$	$^{+6.2\%}_{-6.0\%}$	$^{-0.1\%}_{+0.1\%}$	$^{+0.1\%}_{-0.1\%}$	$^{-7.6\%}_{+7.6\%}$	$^{+9.8\%}_{-9.7\%}$	$^{+3.0\%}_{-1.1\%}$	$^{+12.8\%}_{-10.7\%}$
$\rm H \to t\overline{t}$	350	$1.56{\cdot}10^{-2}$	$^{+0.0\%}_{+0.0\%}$	$^{-0.0\%}_{+0.0\%}$	$^{+120.9\%}_{-78.6\%}$	$^{+0.9\%}_{-0.9\%}$	$^{+120.9\%}_{-78.6\%}$	$^{+6.9\%}_{-12.7\%}$	$^{+127.8\%}_{-91.3\%}$
	360	$5.14{\cdot}10^{-2}$	$^{-0.0\%}_{-0.0\%}$	$^{-0.0\%}_{+0.0\%}$	$^{-36.2\%}_{+35.6\%}$	$^{+0.7\%}_{-0.7\%}$	$^{+35.6\%}_{-36.2\%}$	$^{+6.6\%}_{-12.2\%}$	$^{+42.2\%}_{-48.4\%}$
	400	$1.48{\cdot}10^{-1}$	$^{+0.0\%}_{+0.0\%}$	$^{-0.0\%}_{+0.0\%}$	$^{-6.8\%}_{+6.2\%}$	$^{+0.4\%}_{-0.3\%}$	$^{+6.2\%}_{-6.8\%}$	$^{+5.9\%}_{-11.1\%}$	$^{+12.2\%}_{-17.8\%}$
	500	$1.92{\cdot}10^{-1}$	$^{-0.0\%}_{+0.0\%}$	$^{-0.0\%}_{+0.0\%}$	$^{-0.3\%}_{+0.1\%}$	$^{+0.1\%}_{-0.2\%}$	$^{+0.1\%}_{-0.3\%}$	$^{+4.5\%}_{-9.5\%}$	$^{+4.6\%}_{-9.8\%}$
$\rm H \to gg$	120	$8.82{\cdot}10^{-2}$	$^{-0.2\%}_{+0.2\%}$	$^{-2.2\%}_{+2.2\%}$	$^{-0.2\%}_{+0.2\%}$	$^{+5.7\%}_{-5.4\%}$	$^{+6.1\%}_{-5.8\%}$	$^{+4.5\%}_{-4.5\%}$	$^{+10.6\%}_{-10.3\%}$
	150	$3.46{\cdot}10^{-2}$	$^{-0.1\%}_{+0.1\%}$	$^{-0.7\%}_{+0.6\%}$	$^{-0.3\%}_{+0.3\%}$	$^{+4.4\%}_{-4.2\%}$	$^{+4.4\%}_{-4.3\%}$	$^{+3.5\%}_{-3.5\%}$	$^{+7.9\%}_{-7.8\%}$
	200	$9.26{\cdot}10^{-4}$	$^{-0.0\%}_{-0.0\%}$	$^{-0.1\%}_{+0.1\%}$	$^{-0.6\%}_{+0.6\%}$	$^{+3.9\%}_{-3.8\%}$	$^{+3.9\%}_{-3.9\%}$	$^{+3.7\%}_{-3.7\%}$	$^{+7.6\%}_{-7.6\%}$
	500	$6.04{\cdot}10^{-4}$	$^{-0.0\%}_{+0.0\%}$	$^{-0.0\%}_{+0.0\%}$	$^{+1.6\%}_{-1.6\%}$	$^{+3.4\%}_{-3.3\%}$	$^{+3.7\%}_{-3.7\%}$	$^{+6.2\%}_{-4.3\%}$	$^{+9.9\%}_{-7.9\%}$
$\rm H \to \gamma\gamma$	120	$2.23{\cdot}10^{-3}$	$^{-0.2\%}_{+0.2\%}$	$^{-2.0\%}_{+2.1\%}$	$^{+0.0\%}_{+0.0\%}$	$^{+1.4\%}_{-1.3\%}$	$^{+2.5\%}_{-2.4\%}$	$^{+2.9\%}_{-2.9\%}$	$^{+5.4\%}_{-5.3\%}$
	150	$1.37{\cdot}10^{-3}$	$^{+0.0\%}_{+0.1\%}$	$^{-0.5\%}_{+0.5\%}$	$^{+0.1\%}_{-0.0\%}$	$^{+0.3\%}_{-0.3\%}$	$^{+0.6\%}_{-0.6\%}$	$^{+1.6\%}_{-1.5\%}$	$^{+2.1\%}_{-2.1\%}$
	200	$5.51{\cdot}10^{-5}$	$^{-0.0\%}_{-0.0\%}$	$^{-0.0\%}_{+0.0\%}$	$^{+0.1\%}_{-0.1\%}$	$^{+0.0\%}_{-0.0\%}$	$^{+0.1\%}_{-0.1\%}$	$^{+1.5\%}_{-1.5\%}$	$^{+1.6\%}_{-1.6\%}$
	500	$3.12{\cdot}10^{-7}$	$^{-0.0\%}_{+0.0\%}$	$^{-0.0\%}_{+0.0\%}$	$^{+8.0\%}_{-6.5\%}$	$^{-0.7\%}_{+0.7\%}$	$^{+8.0\%}_{-6.6\%}$	$^{+4.0\%}_{-2.1\%}$	$^{+11.9\%}_{-8.7\%}$
$\rm H \to Z\gamma$	120	$1.11{\cdot}10^{-3}$	$^{-0.3\%}_{+0.2\%}$	$^{-2.1\%}_{+2.1\%}$	$^{+0.0\%}_{-0.1\%}$	$^{+1.4\%}_{-1.4\%}$	$^{+2.5\%}_{-2.5\%}$	$^{+6.9\%}_{-6.8\%}$	$^{+9.4\%}_{-9.3\%}$
	150	$2.31{\cdot}10^{-3}$	$^{-0.1\%}_{+0.0\%}$	$^{-0.6\%}_{+0.5\%}$	$^{+0.0\%}_{-0.1\%}$	$^{+0.2\%}_{-0.3\%}$	$^{+0.5\%}_{-0.6\%}$	$^{+5.5\%}_{-5.5\%}$	$^{+6.0\%}_{-6.2\%}$
	200	$1.75{\cdot}10^{-4}$	$^{-0.0\%}_{-0.0\%}$	$^{-0.0\%}_{+0.0\%}$	$^{+0.0\%}_{-0.1\%}$	$^{+0.0\%}_{-0.0\%}$	$^{+0.0\%}_{-0.1\%}$	$^{+5.5\%}_{-5.5\%}$	$^{+5.5\%}_{-5.6\%}$
	500	$7.58{\cdot}10^{-6}$	$^{-0.0\%}_{+0.0\%}$	$^{-0.0\%}_{+0.0\%}$	$^{+0.8\%}_{-0.6\%}$	$^{-0.0\%}_{+0.0\%}$	$^{+0.8\%}_{-0.6\%}$	$^{+8.0\%}_{-6.1\%}$	$^{+8.7\%}_{-6.7\%}$
$\rm H \to WW$	120	$1.41{\cdot}10^{-1}$	$^{-0.2\%}_{+0.2\%}$	$^{-2.0\%}_{+2.1\%}$	$^{-0.0\%}_{+0.0\%}$	$^{+1.4\%}_{-1.4\%}$	$^{+2.5\%}_{-2.5\%}$	$^{+2.2\%}_{-2.2\%}$	$^{+4.8\%}_{-4.7\%}$
	150	$6.96{\cdot}10^{-1}$	$^{-0.1\%}_{+0.1\%}$	$^{-0.5\%}_{+0.5\%}$	$^{-0.0\%}_{+0.0\%}$	$^{+0.3\%}_{-0.3\%}$	$^{+0.6\%}_{-0.6\%}$	$^{+0.3\%}_{-0.3\%}$	$^{+0.9\%}_{-0.8\%}$
	200	$7.41{\cdot}10^{-1}$	$^{-0.0\%}_{-0.0\%}$	$^{-0.0\%}_{+0.0\%}$	$^{-0.0\%}_{+0.0\%}$	$^{+0.0\%}_{-0.0\%}$	$^{+0.0\%}_{-0.0\%}$	$^{+0.0\%}_{-0.0\%}$	$^{+0.0\%}_{-0.0\%}$
	500	$5.46{\cdot}10^{-1}$	$^{-0.0\%}_{+0.0\%}$	$^{-0.0\%}_{+0.0\%}$	$^{+0.1\%}_{-0.0\%}$	$^{-0.0\%}_{+0.0\%}$	$^{+0.1\%}_{-0.1\%}$	$^{+2.3\%}_{-1.1\%}$	$^{+2.4\%}_{-1.1\%}$
$\rm H \to ZZ$	120	$1.59{\cdot}10^{-2}$	$^{-0.2\%}_{+0.2\%}$	$^{-2.0\%}_{+2.1\%}$	$^{-0.0\%}_{+0.0\%}$	$^{+1.4\%}_{-1.4\%}$	$^{+2.5\%}_{-2.5\%}$	$^{+2.2\%}_{-2.2\%}$	$^{+4.8\%}_{-4.7\%}$
	150	$8.25{\cdot}10^{-2}$	$^{-0.1\%}_{+0.1\%}$	$^{-0.5\%}_{+0.5\%}$	$^{+0.0\%}_{+0.0\%}$	$^{+0.3\%}_{-0.3\%}$	$^{+0.6\%}_{-0.6\%}$	$^{+0.3\%}_{-0.3\%}$	$^{+0.9\%}_{-0.8\%}$
	200	$2.55{\cdot}10^{-1}$	$^{-0.0\%}_{+0.0\%}$	$^{-0.0\%}_{+0.0\%}$	$^{+0.0\%}_{-0.0\%}$	$^{+0.0\%}_{-0.0\%}$	$^{+0.0\%}_{-0.0\%}$	$^{+0.0\%}_{-0.0\%}$	$^{+0.0\%}_{-0.0\%}$
	500	$2.61{\cdot}10^{-1}$	$^{+0.0\%}_{-0.0\%}$	$^{-0.0\%}_{+0.0\%}$	$^{+0.0\%}_{+0.0\%}$	$^{-0.0\%}_{+0.0\%}$	$^{+0.1\%}_{-0.0\%}$	$^{+2.3\%}_{-1.1\%}$	$^{+2.3\%}_{-1.1\%}$

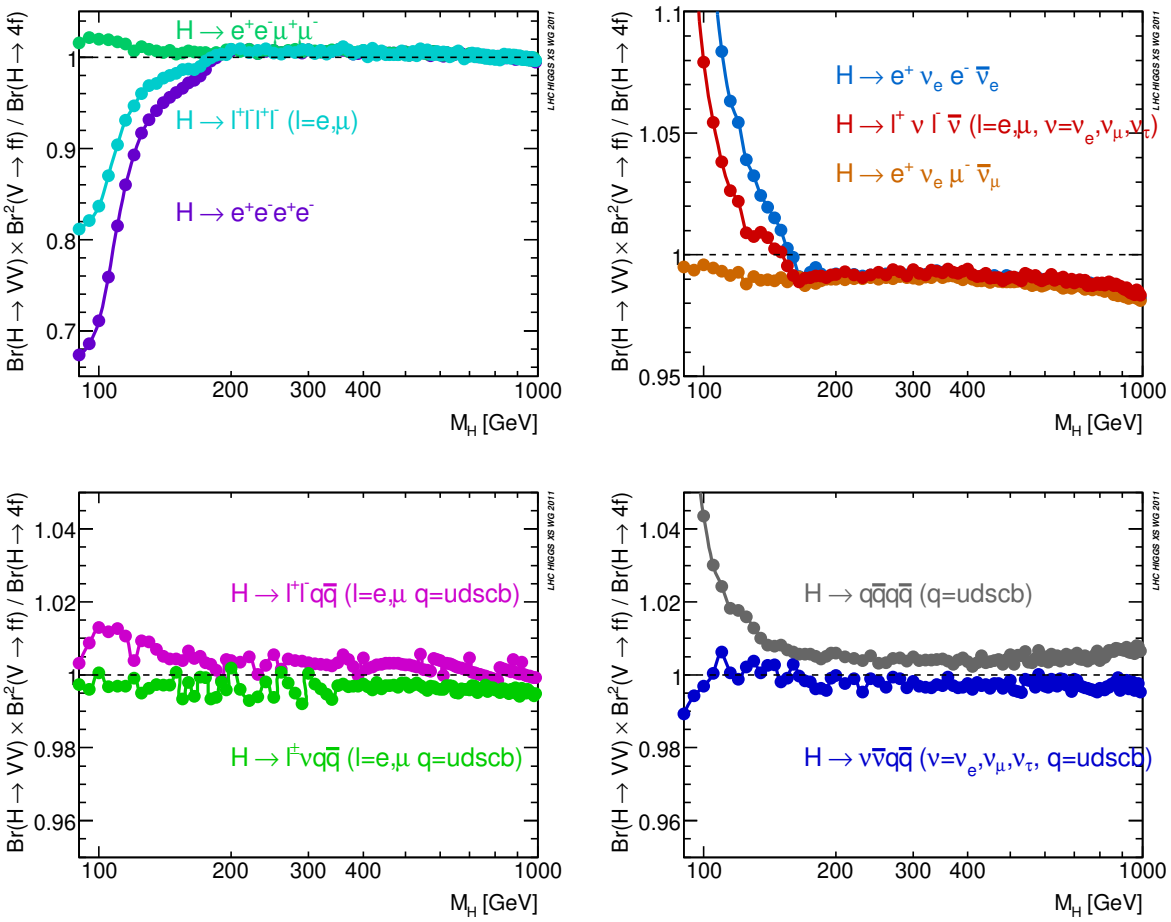

Fig. 4: The ratio between formula (5) and PROPHECY4F for $H \to ZZ \to l\bar{l}l\bar{l}$ (top-left), $H \to WW/ZZ \to l\nu l\nu$ (top-right), $H \to ZZ \to l\bar{l}q\bar{q}$, $H \to WW \to l\nu q\bar{q}$ (bottom-left), and $H \to ZZ \to \nu\bar{\nu}q\bar{q}$, $H \to WW/ZZ \to q\bar{q}q\bar{q}$ (bottom-right).

2.2 MSSM Higgs branching ratios

In the MSSM the evaluation of cross sections and of branching ratios have several common issues as outlined in Section 12.1. It was discussed that *before* any branching-ratio calculation can be performed in a first step the Higgs-boson masses, couplings, and mixings have to be evaluated from the underlying set of (soft SUSY-breaking) parameters. A brief comparison of the dedicated codes that provide this kind of calculations (FEYNHIGGS [77–80] and CPSUPERH [81, 82]) was been given in Ref. [7], where it was concluded that in the case of real parameters more corrections are included into FEYNHIGGS. Consequently, FEYNHIGGS was chosen for the corresponding evaluations in this Report. The results for Higgs-boson masses and couplings can be provided to other codes (especially HDECAY [15–17]) via the SUSY Les Houches Accord [83, 84].

In the following subsections we describe how the relevant codes for the calculation of partial decay widths, FEYNHIGGS and HDECAY, are combined to give the most precise result for the Higgs-boson branching ratios in the MSSM. Numerical results are shown within the $m_{\rm h}^{\rm max}$ scenario [10], where it should be stressed that it would be desirable to interpret the model-independent results of various Higgs-boson searches at the LHC also in other benchmark models, see for instance Refs. [10, 85]. We restrict the evaluation to $\tan\beta = 1 \ldots 60$ and $M_{\rm A} = 90$ GeV $\ldots$ 500 GeV.

2.2.1 Combination of calculations

After the calculation of Higgs-boson masses and mixings from the original SUSY input the branching-ratio calculation has to be performed. This can be done with the codes CPSUPERH and FEYNHIGGS for real or complex parameters, or HDECAY for real parameters. The higher-order corrections included in the calculation of the various decay channels differ in the three codes.

Here we concentrate on the MSSM with real parameters. We combine the results from HDECAY and FEYNHIGGS on various decay channels to obtain the most accurate result for the branching ratios currently available. In a first step, all partial widths have been calculated as accurately as possible. Then the branching ratios have been derived from this full set of partial widths. Concretely, we used FEYNHIGGS for the evaluation of the Higgs-boson masses and couplings from the original input parameters, including corrections up to the two-loop level. FEYNHIGGS results are furthermore used for the channels ($\phi = {\rm h}, {\rm H}, {\rm A}$),

- $\Gamma({\rm H} \to \tau^+\tau^-)$: a full one-loop calculation of the decay width is included [86].
- $\Gamma({\rm H} \to \mu^+\mu^-)$: a full one-loop calculation of the decay width is included [86].
- $\Gamma({\rm H} \to {\rm V}^{(*)}{\rm V}^{(*)})$, $V = {\rm W}^\pm, {\rm Z}$: results for a SM Higgs boson, taken from PROPHECY4F [18–20] and based on a full one-loop calculation, are dressed with effective couplings for the respective coupling of the MSSM Higgs boson to SM gauge bosons, see Section 12.3.1. It should be noted that this does not correspond to a full one-loop calculation in the MSSM, and the approximation may be insufficient for very low values of $M_{\rm A}$.

The results for the Higgs-boson masses and couplings are passed to HDECAY via the SUSY Les Houches Accord [83, 84]. Using these results the following channels have been evaluated by HDECAY,

- $\Gamma({\rm H} \to {\rm b}\overline{\rm b})$: SM QCD corrections are included up to the four-loop level [38–45]. The full SUSY-QCD corrections [87–90] matched to the resummed bottom Yukawa coupling with respect to $\Delta_{\rm b}$ terms have been included. The $\Delta_{\rm b}$ terms are included up to the leading two-loop corrections [91–93] within the resummed Yukawa coupling.
- $\Gamma({\rm H} \to {\rm t}\overline{\rm t})$: SM QCD corrections are included up to NLO [51–57] interpolated to the massless four-loop result [38–45] far above the threshold, while no MSSM specific corrections are taken into account.

– $\Gamma(\mathrm{H} \to \mathrm{c\overline{c}})$: SM QCD corrections are included up to the four-loop level [38–45], while no MSSM specific corrections are taken into account.
– $\Gamma(\mathrm{H} \to \mathrm{gg})$: SM QCD corrections are included up to four-loop order in the limit of heavy top quarks [64–68]. The squark-loop contributions including the NLO QCD corrections [94] in the limit of heavy squarks but no genuine MSSM corrections are taken into account.
– $\Gamma(\mathrm{H} \to \gamma\gamma)$: The full SM QCD corrections are included up to NLO [66, 69–74]. The additional charged Higgs, squark, and chargino loop contributions including the full NLO QCD corrections to the squark loops [94] are taken into account, but no genuine MSSM corrections.
– $\Gamma(\mathrm{H} \to \mathrm{Z}\gamma)$: No higher-order corrections are included. The additional charged Higgs, squark, and chargino loop contributions are taken into account at LO.

Other decay channels such as $\mathrm{H} \to \mathrm{s\overline{s}}$ and the decays to lighter fermions are not included since they are neither relevant for LHC searches, nor do they contribute significantly to the total decay width. With future releases of FeynHiggs, HDECAY, and other codes the evaluation of individual channels might change to another code.

The total decay width is calculated as,

$$\begin{aligned}\Gamma_\phi = {} & \Gamma^{\mathrm{FH}}_{\mathrm{H}\to\tau^+\tau^-} + \Gamma^{\mathrm{FH}}_{\mathrm{H}\to\mu^+\mu^-} + \Gamma^{\mathrm{FH/P4f}}_{\mathrm{H}\to\mathrm{W}^{(*)}\mathrm{W}^{(*)}} + \Gamma^{\mathrm{FH/P4f}}_{\mathrm{H}\to\mathrm{Z}^{(*)}\mathrm{Z}^{(*)}} \\ & + \Gamma^{\mathrm{HD}}_{\mathrm{H}\to\mathrm{b\overline{b}}} + \Gamma^{\mathrm{HD}}_{\mathrm{H}\to\mathrm{t\overline{t}}} + \Gamma^{\mathrm{HD}}_{\mathrm{H}\to\mathrm{c\overline{c}}} + \Gamma^{\mathrm{HD}}_{\mathrm{H}\to\mathrm{gg}} + \Gamma^{\mathrm{HD}}_{\mathrm{H}\to\gamma\gamma} + \Gamma^{\mathrm{HD}}_{\mathrm{H}\to\mathrm{Z}\gamma}\,, \end{aligned} \tag{6}$$

followed by a corresponding evaluation of the respective branching ratio. Decays to strange quarks or other lighter fermions have been neglected. Due to the somewhat different calculation compared to the SM case in Section 2.1.1 no full decoupling of the decay widths and branching ratios of the light MSSM Higgs to the respective SM values can be expected.

2.2.2 Results in the $m_h^{\max}$ scenario

The procedure outlined in the previous subsection can be applied to arbitrary points in the MSSM parameter space. Here we show representative results in the $m_{\mathrm{h}}^{\max}$ scenario. In Figure 5 the branching ratios for the light MSSM Higgs boson are shown as a function of M_{A} for $\tan\beta = 10(50)$ in the left (right) plot. For low M_{A} a strong variation of the branching ratios is visible, while for large M_{A} the SM limit is reached.

More detailed sample results for the branching ratio of the lightest MSSM Higgs boson to $\mathrm{b\overline{b}}$, $\tau^+\tau^-$, $\mu^+\mu^-$, $\gamma\gamma$, $\mathrm{W}^{(*)}\mathrm{W}^{(*)}$, and $\mathrm{Z}^{(*)}\mathrm{Z}^{(*)}$ are shown in Tables 4–9. As before they have been obtained in the $m_{\mathrm{h}}^{\max}$ scenario with M_{A} and $\tan\beta$ varied (as indicated in the tables).

Table 4: MSSM Higgs branching ratio BR($\mathrm{h} \to \mathrm{b\bar{b}}$) in the $m_{\mathrm{b}}^{\max}$ scenario as a function of M_{A} [GeV] and $\tan\beta$. The format in each cell is M_{h} [GeV], BR.

M_{A}	$\tan\beta = 20$		$\tan\beta = 30$		$\tan\beta = 40$		$\tan\beta = 50$		$\tan\beta = 60$	
90	89.6	$9.02 \cdot 10^{-1}$	89.8	$9.00 \cdot 10^{-1}$	89.9	$8.97 \cdot 10^{-1}$	89.9	$8.94 \cdot 10^{-1}$	89.9	$8.91 \cdot 10^{-1}$
100	99.4	$9.01 \cdot 10^{-1}$	99.7	$8.98 \cdot 10^{-1}$	99.9	$8.95 \cdot 10^{-1}$	99.9	$8.92 \cdot 10^{-1}$	99.9	$8.89 \cdot 10^{-1}$
110	109.0	$8.99 \cdot 10^{-1}$	109.6	$8.96 \cdot 10^{-1}$	109.8	$8.93 \cdot 10^{-1}$	109.8	$8.90 \cdot 10^{-1}$	109.9	$8.87 \cdot 10^{-1}$
120	118.2	$8.98 \cdot 10^{-1}$	119.1	$8.95 \cdot 10^{-1}$	119.5	$8.92 \cdot 10^{-1}$	119.7	$8.89 \cdot 10^{-1}$	119.7	$8.86 \cdot 10^{-1}$
130	125.2	$8.95 \cdot 10^{-1}$	126.9	$8.91 \cdot 10^{-1}$	127.8	$8.86 \cdot 10^{-1}$	128.4	$8.78 \cdot 10^{-1}$	128.9	$8.62 \cdot 10^{-1}$
140	128.1	$8.89 \cdot 10^{-1}$	129.3	$8.87 \cdot 10^{-1}$	129.8	$8.86 \cdot 10^{-1}$	130.2	$8.84 \cdot 10^{-1}$	130.5	$8.84 \cdot 10^{-1}$
150	128.9	$8.75 \cdot 10^{-1}$	129.7	$8.73 \cdot 10^{-1}$	130.1	$8.71 \cdot 10^{-1}$	130.4	$8.69 \cdot 10^{-1}$	130.6	$8.68 \cdot 10^{-1}$
160	129.2	$8.54 \cdot 10^{-1}$	129.9	$8.52 \cdot 10^{-1}$	130.2	$8.49 \cdot 10^{-1}$	130.4	$8.47 \cdot 10^{-1}$	130.6	$8.45 \cdot 10^{-1}$
170	129.4	$8.30 \cdot 10^{-1}$	130.0	$8.27 \cdot 10^{-1}$	130.2	$8.25 \cdot 10^{-1}$	130.4	$8.22 \cdot 10^{-1}$	130.6	$8.20 \cdot 10^{-1}$
180	129.5	$8.06 \cdot 10^{-1}$	130.0	$8.03 \cdot 10^{-1}$	130.2	$8.00 \cdot 10^{-1}$	130.4	$7.97 \cdot 10^{-1}$	130.6	$7.94 \cdot 10^{-1}$
190	129.6	$7.82 \cdot 10^{-1}$	130.0	$7.78 \cdot 10^{-1}$	130.2	$7.75 \cdot 10^{-1}$	130.4	$7.72 \cdot 10^{-1}$	130.6	$7.69 \cdot 10^{-1}$
200	129.7	$7.60 \cdot 10^{-1}$	130.1	$7.56 \cdot 10^{-1}$	130.2	$7.52 \cdot 10^{-1}$	130.4	$7.49 \cdot 10^{-1}$	130.6	$7.46 \cdot 10^{-1}$
210	129.7	$7.39 \cdot 10^{-1}$	130.1	$7.35 \cdot 10^{-1}$	130.2	$7.31 \cdot 10^{-1}$	130.4	$7.28 \cdot 10^{-1}$	130.6	$7.24 \cdot 10^{-1}$
220	129.7	$7.20 \cdot 10^{-1}$	130.1	$7.15 \cdot 10^{-1}$	130.3	$7.12 \cdot 10^{-1}$	130.4	$7.08 \cdot 10^{-1}$	130.6	$7.05 \cdot 10^{-1}$
230	129.8	$7.02 \cdot 10^{-1}$	130.1	$6.98 \cdot 10^{-1}$	130.3	$6.94 \cdot 10^{-1}$	130.4	$6.91 \cdot 10^{-1}$	130.6	$6.87 \cdot 10^{-1}$
240	129.8	$6.86 \cdot 10^{-1}$	130.1	$6.82 \cdot 10^{-1}$	130.3	$6.78 \cdot 10^{-1}$	130.4	$6.75 \cdot 10^{-1}$	130.6	$6.71 \cdot 10^{-1}$
250	129.8	$6.72 \cdot 10^{-1}$	130.1	$6.68 \cdot 10^{-1}$	130.3	$6.64 \cdot 10^{-1}$	130.4	$6.60 \cdot 10^{-1}$	130.6	$6.56 \cdot 10^{-1}$
260	129.8	$6.59 \cdot 10^{-1}$	130.1	$6.55 \cdot 10^{-1}$	130.3	$6.51 \cdot 10^{-1}$	130.4	$6.47 \cdot 10^{-1}$	130.6	$6.43 \cdot 10^{-1}$
270	129.8	$6.48 \cdot 10^{-1}$	130.1	$6.43 \cdot 10^{-1}$	130.3	$6.39 \cdot 10^{-1}$	130.4	$6.36 \cdot 10^{-1}$	130.6	$6.32 \cdot 10^{-1}$
280	129.8	$6.37 \cdot 10^{-1}$	130.1	$6.33 \cdot 10^{-1}$	130.3	$6.29 \cdot 10^{-1}$	130.4	$6.25 \cdot 10^{-1}$	130.6	$6.21 \cdot 10^{-1}$
290	129.8	$6.28 \cdot 10^{-1}$	130.1	$6.23 \cdot 10^{-1}$	130.3	$6.19 \cdot 10^{-1}$	130.4	$6.16 \cdot 10^{-1}$	130.6	$6.11 \cdot 10^{-1}$
300	129.8	$6.19 \cdot 10^{-1}$	130.1	$6.14 \cdot 10^{-1}$	130.3	$6.11 \cdot 10^{-1}$	130.4	$6.07 \cdot 10^{-1}$	130.6	$6.02 \cdot 10^{-1}$

Table 5: MSSM Higgs branching ratio BR($\mathrm{h} \to \tau^+\tau^-$) in the $m_{\mathrm{h}}^{\max}$ scenario as a function of M_{A} [GeV] and $\tan\beta$. The format in each cell is M_{h} [GeV], BR.

M_{A}	$\tan\beta = 20$		$\tan\beta = 30$		$\tan\beta = 40$		$\tan\beta = 50$		$\tan\beta = 60$	
90	89.6	$9.50 \cdot 10^{-2}$	89.8	$9.77 \cdot 10^{-2}$	89.9	$1.01 \cdot 10^{-1}$	89.9	$1.03 \cdot 10^{-1}$	89.9	$1.06 \cdot 10^{-1}$
100	99.4	$9.68 \cdot 10^{-2}$	99.7	$9.96 \cdot 10^{-2}$	99.9	$1.02 \cdot 10^{-1}$	99.9	$1.05 \cdot 10^{-1}$	99.9	$1.08 \cdot 10^{-1}$
110	109.0	$9.84 \cdot 10^{-2}$	109.6	$1.01 \cdot 10^{-1}$	109.8	$1.04 \cdot 10^{-1}$	109.8	$1.07 \cdot 10^{-1}$	109.9	$1.1 \cdot 10^{-1}$
120	118.2	$1.00 \cdot 10^{-1}$	119.1	$1.03 \cdot 10^{-1}$	119.5	$1.06 \cdot 10^{-1}$	119.7	$1.09 \cdot 10^{-1}$	119.7	$1.12 \cdot 10^{-1}$
130	125.2	$1.02 \cdot 10^{-1}$	126.9	$1.06 \cdot 10^{-1}$	127.8	$1.12 \cdot 10^{-1}$	128.4	$1.20 \cdot 10^{-1}$	128.9	$1.36 \cdot 10^{-1}$
140	128.1	$1.01 \cdot 10^{-1}$	129.3	$1.04 \cdot 10^{-1}$	129.8	$1.06 \cdot 10^{-1}$	130.2	$1.07 \cdot 10^{-1}$	130.5	$1.08 \cdot 10^{-1}$
150	128.9	$9.83 \cdot 10^{-2}$	129.7	$1.00 \cdot 10^{-1}$	130.1	$1.02 \cdot 10^{-1}$	130.4	$1.04 \cdot 10^{-1}$	130.6	$1.05 \cdot 10^{-1}$
160	129.2	$9.54 \cdot 10^{-2}$	129.9	$9.70 \cdot 10^{-2}$	130.2	$9.86 \cdot 10^{-2}$	130.4	$1.00 \cdot 10^{-1}$	130.6	$1.02 \cdot 10^{-1}$
170	129.4	$9.25 \cdot 10^{-2}$	130.0	$9.38 \cdot 10^{-2}$	130.2	$9.52 \cdot 10^{-2}$	130.4	$9.65 \cdot 10^{-2}$	130.6	$9.79 \cdot 10^{-2}$
180	129.5	$8.95 \cdot 10^{-2}$	130.0	$9.06 \cdot 10^{-2}$	130.2	$9.18 \cdot 10^{-2}$	130.4	$9.31 \cdot 10^{-2}$	130.6	$9.43 \cdot 10^{-2}$
190	129.6	$8.67 \cdot 10^{-2}$	130.0	$8.76 \cdot 10^{-2}$	130.2	$8.86 \cdot 10^{-2}$	130.4	$8.97 \cdot 10^{-2}$	130.6	$9.08 \cdot 10^{-2}$
200	129.7	$8.42 \cdot 10^{-2}$	130.1	$8.48 \cdot 10^{-2}$	130.2	$8.58 \cdot 10^{-2}$	130.4	$8.67 \cdot 10^{-2}$	130.6	$8.77 \cdot 10^{-2}$
210	129.7	$8.18 \cdot 10^{-2}$	130.1	$8.23 \cdot 10^{-2}$	130.2	$8.31 \cdot 10^{-2}$	130.4	$8.40 \cdot 10^{-2}$	130.6	$8.49 \cdot 10^{-2}$
220	129.7	$7.96 \cdot 10^{-2}$	130.1	$8.00 \cdot 10^{-2}$	130.3	$8.08 \cdot 10^{-2}$	130.4	$8.15 \cdot 10^{-2}$	130.6	$8.23 \cdot 10^{-2}$
230	129.8	$7.77 \cdot 10^{-2}$	130.1	$7.80 \cdot 10^{-2}$	130.3	$7.86 \cdot 10^{-2}$	130.4	$7.93 \cdot 10^{-2}$	130.6	$8.01 \cdot 10^{-2}$
240	129.8	$7.59 \cdot 10^{-2}$	130.1	$7.62 \cdot 10^{-2}$	130.3	$7.67 \cdot 10^{-2}$	130.4	$7.74 \cdot 10^{-2}$	130.6	$7.81 \cdot 10^{-2}$
250	129.8	$7.43 \cdot 10^{-2}$	130.1	$7.45 \cdot 10^{-2}$	130.3	$7.50 \cdot 10^{-2}$	130.4	$7.56 \cdot 10^{-2}$	130.6	$7.62 \cdot 10^{-2}$
260	129.8	$7.28 \cdot 10^{-2}$	130.1	$7.30 \cdot 10^{-2}$	130.3	$7.34 \cdot 10^{-2}$	130.4	$7.40 \cdot 10^{-2}$	130.6	$7.45 \cdot 10^{-2}$
270	129.8	$7.15 \cdot 10^{-2}$	130.1	$7.16 \cdot 10^{-2}$	130.3	$7.20 \cdot 10^{-2}$	130.4	$7.25 \cdot 10^{-2}$	130.6	$7.30 \cdot 10^{-2}$
280	129.8	$7.03 \cdot 10^{-2}$	130.1	$7.04 \cdot 10^{-2}$	130.3	$7.07 \cdot 10^{-2}$	130.4	$7.12 \cdot 10^{-2}$	130.6	$7.17 \cdot 10^{-2}$
290	129.8	$6.92 \cdot 10^{-2}$	130.1	$6.92 \cdot 10^{-2}$	130.3	$6.96 \cdot 10^{-2}$	130.4	$7.00 \cdot 10^{-2}$	130.6	$7.05 \cdot 10^{-2}$
300	129.8	$6.82 \cdot 10^{-2}$	130.1	$6.82 \cdot 10^{-2}$	130.3	$6.85 \cdot 10^{-2}$	130.4	$6.90 \cdot 10^{-2}$	130.6	$6.94 \cdot 10^{-2}$

Table 6: MSSM Higgs branching ratio BR($\mathrm{h} \to \mu^+\mu^-$) in the $m_{\mathrm{h}}^{\max}$ scenario as a function of M_{A} [GeV] and $\tan\beta$. The format in each cell is M_{h} [GeV], BR.

M_{A}	$\tan\beta = 20$		$\tan\beta = 30$		$\tan\beta = 40$		$\tan\beta = 50$		$\tan\beta = 60$	
90	89.6	$3.30 \cdot 10^{-4}$	89.8	$3.39 \cdot 10^{-4}$	89.9	$3.49 \cdot 10^{-4}$	89.9	$3.59 \cdot 10^{-4}$	89.9	$3.68 \cdot 10^{-4}$
100	99.4	$3.36 \cdot 10^{-4}$	99.7	$3.46 \cdot 10^{-4}$	99.9	$3.56 \cdot 10^{-4}$	99.9	$3.66 \cdot 10^{-4}$	99.9	$3.76 \cdot 10^{-4}$
110	109.0	$3.42 \cdot 10^{-4}$	109.6	$3.52 \cdot 10^{-4}$	109.8	$3.62 \cdot 10^{-4}$	109.8	$3.72 \cdot 10^{-4}$	109.9	$3.82 \cdot 10^{-4}$
120	118.2	$3.47 \cdot 10^{-4}$	119.1	$3.58 \cdot 10^{-4}$	119.5	$3.68 \cdot 10^{-4}$	119.7	$3.78 \cdot 10^{-4}$	119.7	$3.89 \cdot 10^{-4}$
130	125.2	$3.54 \cdot 10^{-4}$	126.9	$3.69 \cdot 10^{-4}$	127.8	$3.87 \cdot 10^{-4}$	128.4	$4.17 \cdot 10^{-4}$	128.9	$4.72 \cdot 10^{-4}$
140	128.1	$3.5 \cdot 10^{-4}$	129.3	$3.59 \cdot 10^{-4}$	129.8	$3.67 \cdot 10^{-4}$	130.2	$3.72 \cdot 10^{-4}$	130.5	$3.75 \cdot 10^{-4}$
150	128.9	$3.41 \cdot 10^{-4}$	129.7	$3.48 \cdot 10^{-4}$	130.1	$3.54 \cdot 10^{-4}$	130.4	$3.60 \cdot 10^{-4}$	130.6	$3.65 \cdot 10^{-4}$
160	129.2	$3.31 \cdot 10^{-4}$	129.9	$3.36 \cdot 10^{-4}$	130.2	$3.42 \cdot 10^{-4}$	130.4	$3.47 \cdot 10^{-4}$	130.6	$3.53 \cdot 10^{-4}$
170	129.4	$3.21 \cdot 10^{-4}$	130.0	$3.25 \cdot 10^{-4}$	130.2	$3.30 \cdot 10^{-4}$	130.4	$3.35 \cdot 10^{-4}$	130.6	$3.40 \cdot 10^{-4}$
180	129.5	$3.11 \cdot 10^{-4}$	130.0	$3.14 \cdot 10^{-4}$	130.2	$3.18 \cdot 10^{-4}$	130.4	$3.23 \cdot 10^{-4}$	130.6	$3.27 \cdot 10^{-4}$
190	129.6	$3.01 \cdot 10^{-4}$	130.0	$3.04 \cdot 10^{-4}$	130.2	$3.07 \cdot 10^{-4}$	130.4	$3.11 \cdot 10^{-4}$	130.6	$3.15 \cdot 10^{-4}$
200	129.7	$2.92 \cdot 10^{-4}$	130.1	$2.94 \cdot 10^{-4}$	130.2	$2.97 \cdot 10^{-4}$	130.4	$3.01 \cdot 10^{-4}$	130.6	$3.04 \cdot 10^{-4}$
210	129.7	$2.84 \cdot 10^{-4}$	130.1	$2.86 \cdot 10^{-4}$	130.2	$2.88 \cdot 10^{-4}$	130.4	$2.91 \cdot 10^{-4}$	130.6	$2.94 \cdot 10^{-4}$
220	129.7	$2.76 \cdot 10^{-4}$	130.1	$2.78 \cdot 10^{-4}$	130.3	$2.80 \cdot 10^{-4}$	130.4	$2.83 \cdot 10^{-4}$	130.6	$2.86 \cdot 10^{-4}$
230	129.8	$2.69 \cdot 10^{-4}$	130.1	$2.70 \cdot 10^{-4}$	130.3	$2.73 \cdot 10^{-4}$	130.4	$2.75 \cdot 10^{-4}$	130.6	$2.78 \cdot 10^{-4}$
240	129.8	$2.63 \cdot 10^{-4}$	130.1	$2.64 \cdot 10^{-4}$	130.3	$2.66 \cdot 10^{-4}$	130.4	$2.68 \cdot 10^{-4}$	130.6	$2.71 \cdot 10^{-4}$
250	129.8	$2.58 \cdot 10^{-4}$	130.1	$2.58 \cdot 10^{-4}$	130.3	$2.60 \cdot 10^{-4}$	130.4	$2.62 \cdot 10^{-4}$	130.6	$2.64 \cdot 10^{-4}$
260	129.8	$2.53 \cdot 10^{-4}$	130.1	$2.53 \cdot 10^{-4}$	130.3	$2.55 \cdot 10^{-4}$	130.4	$2.56 \cdot 10^{-4}$	130.6	$2.59 \cdot 10^{-4}$
270	129.8	$2.48 \cdot 10^{-4}$	130.1	$2.48 \cdot 10^{-4}$	130.3	$2.50 \cdot 10^{-4}$	130.4	$2.51 \cdot 10^{-4}$	130.6	$2.53 \cdot 10^{-4}$
280	129.8	$2.44 \cdot 10^{-4}$	130.1	$2.44 \cdot 10^{-4}$	130.3	$2.45 \cdot 10^{-4}$	130.4	$2.47 \cdot 10^{-4}$	130.6	$2.49 \cdot 10^{-4}$
290	129.8	$2.40 \cdot 10^{-4}$	130.1	$2.40 \cdot 10^{-4}$	130.3	$2.41 \cdot 10^{-4}$	130.4	$2.43 \cdot 10^{-4}$	130.6	$2.45 \cdot 10^{-4}$
300	129.8	$2.37 \cdot 10^{-4}$	130.1	$2.37 \cdot 10^{-4}$	130.3	$2.38 \cdot 10^{-4}$	130.4	$2.39 \cdot 10^{-4}$	130.6	$2.41 \cdot 10^{-4}$

Table 7: MSSM Higgs branching ratio BR($\mathrm{h} \to \gamma\gamma$) in the $m_{\mathrm{h}}^{\max}$ scenario as a function of M_{A} [GeV] and $\tan\beta$. The format in each cell is M_{h} [GeV], BR.

M_{A}	$\tan\beta = 20$		$\tan\beta = 30$		$\tan\beta = 40$		$\tan\beta = 50$		$\tan\beta = 60$	
90	89.6	$9.76 \cdot 10^{-7}$	89.8	$6.73 \cdot 10^{-7}$	89.9	$5.83 \cdot 10^{-7}$	89.9	$5.48 \cdot 10^{-7}$	89.9	$5.34 \cdot 10^{-7}$
100	99.4	$1.19 \cdot 10^{-6}$	99.7	$7.24 \cdot 10^{-7}$	99.9	$5.90 \cdot 10^{-7}$	99.9	$5.36 \cdot 10^{-7}$	99.9	$5.12 \cdot 10^{-7}$
110	109.0	$1.70 \cdot 10^{-6}$	109.6	$8.76 \cdot 10^{-7}$	109.8	$6.48 \cdot 10^{-7}$	109.8	$5.56 \cdot 10^{-7}$	109.9	$5.13 \cdot 10^{-7}$
120	118.2	$3.43 \cdot 10^{-6}$	119.1	$1.45 \cdot 10^{-6}$	119.5	$9.04 \cdot 10^{-7}$	119.7	$6.91 \cdot 10^{-7}$	119.7	$5.89 \cdot 10^{-7}$
130	125.2	$1.37 \cdot 10^{-5}$	126.9	$6.88 \cdot 10^{-6}$	127.8	$4.24 \cdot 10^{-6}$	128.4	$2.89 \cdot 10^{-6}$	128.9	$2.07 \cdot 10^{-6}$
140	128.1	$6.25 \cdot 10^{-5}$	129.3	$5.22 \cdot 10^{-5}$	129.8	$4.79 \cdot 10^{-5}$	130.2	$4.54 \cdot 10^{-5}$	130.5	$4.36 \cdot 10^{-5}$
150	128.9	$1.60 \cdot 10^{-4}$	129.7	$1.51 \cdot 10^{-4}$	130.1	$1.47 \cdot 10^{-4}$	130.4	$1.45 \cdot 10^{-4}$	130.6	$1.44 \cdot 10^{-4}$
160	129.2	$2.88 \cdot 10^{-4}$	129.9	$2.80 \cdot 10^{-4}$	130.2	$2.77 \cdot 10^{-4}$	130.4	$2.77 \cdot 10^{-4}$	130.6	$2.77 \cdot 10^{-4}$
170	129.4	$4.28 \cdot 10^{-4}$	130.0	$4.21 \cdot 10^{-4}$	130.2	$4.20 \cdot 10^{-4}$	130.4	$4.21 \cdot 10^{-4}$	130.6	$4.22 \cdot 10^{-4}$
180	129.5	$5.70 \cdot 10^{-4}$	130.0	$5.63 \cdot 10^{-4}$	130.2	$5.63 \cdot 10^{-4}$	130.4	$5.65 \cdot 10^{-4}$	130.6	$5.68 \cdot 10^{-4}$
190	129.6	$7.06 \cdot 10^{-4}$	130.0	$7.00 \cdot 10^{-4}$	130.2	$7.00 \cdot 10^{-4}$	130.4	$7.03 \cdot 10^{-4}$	130.6	$7.07 \cdot 10^{-4}$
200	129.7	$8.33 \cdot 10^{-4}$	130.1	$8.28 \cdot 10^{-4}$	130.2	$8.29 \cdot 10^{-4}$	130.4	$8.32 \cdot 10^{-4}$	130.6	$8.37 \cdot 10^{-4}$
210	129.7	$9.50 \cdot 10^{-4}$	130.1	$9.45 \cdot 10^{-4}$	130.2	$9.47 \cdot 10^{-4}$	130.4	$9.51 \cdot 10^{-4}$	130.6	$9.56 \cdot 10^{-4}$
220	129.7	$1.06 \cdot 10^{-3}$	130.1	$1.05 \cdot 10^{-3}$	130.3	$1.05 \cdot 10^{-3}$	130.4	$1.06 \cdot 10^{-3}$	130.6	$1.06 \cdot 10^{-3}$
230	129.8	$1.15 \cdot 10^{-3}$	130.1	$1.15 \cdot 10^{-3}$	130.3	$1.15 \cdot 10^{-3}$	130.4	$1.16 \cdot 10^{-3}$	130.6	$1.16 \cdot 10^{-3}$
240	129.8	$1.24 \cdot 10^{-3}$	130.1	$1.24 \cdot 10^{-3}$	130.3	$1.24 \cdot 10^{-3}$	130.4	$1.24 \cdot 10^{-3}$	130.6	$1.25 \cdot 10^{-3}$
250	129.8	$1.32 \cdot 10^{-3}$	130.1	$1.32 \cdot 10^{-3}$	130.3	$1.32 \cdot 10^{-3}$	130.4	$1.32 \cdot 10^{-3}$	130.6	$1.33 \cdot 10^{-3}$
260	129.8	$1.39 \cdot 10^{-3}$	130.1	$1.39 \cdot 10^{-3}$	130.3	$1.39 \cdot 10^{-3}$	130.4	$1.39 \cdot 10^{-3}$	130.6	$1.4 \cdot 10^{-3}$
270	129.8	$1.46 \cdot 10^{-3}$	130.1	$1.45 \cdot 10^{-3}$	130.3	$1.45 \cdot 10^{-3}$	130.4	$1.46 \cdot 10^{-3}$	130.6	$1.47 \cdot 10^{-3}$
280	129.8	$1.51 \cdot 10^{-3}$	130.1	$1.51 \cdot 10^{-3}$	130.3	$1.51 \cdot 10^{-3}$	130.4	$1.52 \cdot 10^{-3}$	130.6	$1.52 \cdot 10^{-3}$
290	129.8	$1.57 \cdot 10^{-3}$	130.1	$1.56 \cdot 10^{-3}$	130.3	$1.56 \cdot 10^{-3}$	130.4	$1.57 \cdot 10^{-3}$	130.6	$1.58 \cdot 10^{-3}$
300	129.8	$1.61 \cdot 10^{-3}$	130.1	$1.61 \cdot 10^{-3}$	130.3	$1.61 \cdot 10^{-3}$	130.4	$1.62 \cdot 10^{-3}$	130.6	$1.62 \cdot 10^{-3}$

Table 8: MSSM Higgs branching ratio BR($\mathrm{h} \to \mathrm{W}^{(*)}\mathrm{W}^{(*)}$) in the $m_{\mathrm{h}}^{\max}$ scenario as a function of M_{A} [GeV] and $\tan\beta$. The format in each cell is M_{h} [GeV], BR.

M_{A}	$\tan\beta = 20$		$\tan\beta = 30$		$\tan\beta = 40$		$\tan\beta = 50$		$\tan\beta = 60$	
90	89.6	$6.95 \cdot 10^{-8}$	89.8	$1.54 \cdot 10^{-8}$	89.9	$5.21 \cdot 10^{-9}$	89.9	$2.28 \cdot 10^{-9}$	89.9	$1.1 \cdot 10^{-9}$
100	99.4	$9.14 \cdot 10^{-7}$	99.7	$2.04 \cdot 10^{-7}$	99.9	$6.91 \cdot 10^{-8}$	99.9	$2.96 \cdot 10^{-8}$	99.9	$1.49 \cdot 10^{-8}$
110	109.0	$8.19 \cdot 10^{-6}$	109.6	$1.89 \cdot 10^{-6}$	109.8	$6.41 \cdot 10^{-7}$	109.8	$2.75 \cdot 10^{-7}$	109.9	$1.37 \cdot 10^{-7}$
120	118.2	$7.36 \cdot 10^{-5}$	119.1	$1.93 \cdot 10^{-5}$	119.5	$6.85 \cdot 10^{-6}$	119.7	$2.96 \cdot 10^{-6}$	119.7	$1.45 \cdot 10^{-6}$
130	125.2	$8.81 \cdot 10^{-4}$	126.9	$4.46 \cdot 10^{-4}$	127.8	$2.58 \cdot 10^{-4}$	128.4	$1.60 \cdot 10^{-4}$	128.9	$1.02 \cdot 10^{-4}$
140	128.1	$6.29 \cdot 10^{-3}$	129.3	$5.79 \cdot 10^{-3}$	129.8	$5.55 \cdot 10^{-3}$	130.2	$5.41 \cdot 10^{-3}$	130.5	$5.31 \cdot 10^{-3}$
150	128.9	$1.84 \cdot 10^{-2}$	129.7	$1.85 \cdot 10^{-2}$	130.1	$1.87 \cdot 10^{-2}$	130.4	$1.88 \cdot 10^{-2}$	130.6	$1.9 \cdot 10^{-2}$
160	129.2	$3.48 \cdot 10^{-2}$	129.9	$3.57 \cdot 10^{-2}$	130.2	$3.63 \cdot 10^{-2}$	130.4	$3.68 \cdot 10^{-2}$	130.6	$3.74 \cdot 10^{-2}$
170	129.4	$5.31 \cdot 10^{-2}$	130.0	$5.47 \cdot 10^{-2}$	130.2	$5.58 \cdot 10^{-2}$	130.4	$5.67 \cdot 10^{-2}$	130.6	$5.77 \cdot 10^{-2}$
180	129.5	$7.18 \cdot 10^{-2}$	130.0	$7.40 \cdot 10^{-2}$	130.2	$7.54 \cdot 10^{-2}$	130.4	$7.66 \cdot 10^{-2}$	130.6	$7.79 \cdot 10^{-2}$
190	129.6	$9.00 \cdot 10^{-2}$	130.0	$9.26 \cdot 10^{-2}$	130.2	$9.43 \cdot 10^{-2}$	130.4	$9.59 \cdot 10^{-2}$	130.6	$9.75 \cdot 10^{-2}$
200	129.7	$1.07 \cdot 10^{-1}$	130.1	$1.10 \cdot 10^{-1}$	130.2	$1.12 \cdot 10^{-1}$	130.4	$1.14 \cdot 10^{-1}$	130.6	$1.16 \cdot 10^{-1}$
210	129.7	$1.23 \cdot 10^{-1}$	130.1	$1.26 \cdot 10^{-1}$	130.2	$1.28 \cdot 10^{-1}$	130.4	$1.30 \cdot 10^{-1}$	130.6	$1.33 \cdot 10^{-1}$
220	129.7	$1.37 \cdot 10^{-1}$	130.1	$1.41 \cdot 10^{-1}$	130.3	$1.43 \cdot 10^{-1}$	130.4	$1.45 \cdot 10^{-1}$	130.6	$1.48 \cdot 10^{-1}$
230	129.8	$1.50 \cdot 10^{-1}$	130.1	$1.54 \cdot 10^{-1}$	130.3	$1.57 \cdot 10^{-1}$	130.4	$1.59 \cdot 10^{-1}$	130.6	$1.62 \cdot 10^{-1}$
240	129.8	$1.62 \cdot 10^{-1}$	130.1	$1.66 \cdot 10^{-1}$	130.3	$1.69 \cdot 10^{-1}$	130.4	$1.71 \cdot 10^{-1}$	130.6	$1.74 \cdot 10^{-1}$
250	129.8	$1.73 \cdot 10^{-1}$	130.1	$1.77 \cdot 10^{-1}$	130.3	$1.80 \cdot 10^{-1}$	130.4	$1.82 \cdot 10^{-1}$	130.6	$1.85 \cdot 10^{-1}$
260	129.8	$1.83 \cdot 10^{-1}$	130.1	$1.87 \cdot 10^{-1}$	130.3	$1.89 \cdot 10^{-1}$	130.4	$1.92 \cdot 10^{-1}$	130.6	$1.95 \cdot 10^{-1}$
270	129.8	$1.91 \cdot 10^{-1}$	130.1	$1.95 \cdot 10^{-1}$	130.3	$1.98 \cdot 10^{-1}$	130.4	$2.01 \cdot 10^{-1}$	130.6	$2.04 \cdot 10^{-1}$
280	129.8	$1.99 \cdot 10^{-1}$	130.1	$2.03 \cdot 10^{-1}$	130.3	$2.06 \cdot 10^{-1}$	130.4	$2.09 \cdot 10^{-1}$	130.6	$2.12 \cdot 10^{-1}$
290	129.8	$2.06 \cdot 10^{-1}$	130.1	$2.11 \cdot 10^{-1}$	130.3	$2.14 \cdot 10^{-1}$	130.4	$2.17 \cdot 10^{-1}$	130.6	$2.20 \cdot 10^{-1}$
300	129.8	$2.13 \cdot 10^{-1}$	130.1	$2.17 \cdot 10^{-1}$	130.3	$2.20 \cdot 10^{-1}$	130.4	$2.23 \cdot 10^{-1}$	130.6	$2.26 \cdot 10^{-1}$

Table 9: MSSM Higgs branching ratio BR($\mathrm{h} \to \mathrm{Z}^{(*)}\mathrm{Z}^{(*)}$) in the $m_{\mathrm{h}}^{\max}$ scenario as a function of M_{A} [GeV] and $\tan\beta$. The format in each cell is M_{h} [GeV], BR.

M_{A}	$\tan\beta = 20$		$\tan\beta = 30$		$\tan\beta = 40$		$\tan\beta = 50$		$\tan\beta = 60$	
90	89.6	$1.79 \cdot 10^{-9}$	89.8	$1.79 \cdot 10^{-9}$	89.9	$1.79 \cdot 10^{-9}$	89.9	$1.79 \cdot 10^{-9}$	89.9	$1.79 \cdot 10^{-9}$
100	99.4	$5.91 \cdot 10^{-8}$	99.7	$1.35 \cdot 10^{-8}$	99.9	$4.60 \cdot 10^{-9}$	99.9	$1.99 \cdot 10^{-9}$	99.9	$1.99 \cdot 10^{-9}$
110	109.0	$7.34 \cdot 10^{-7}$	109.6	$1.70 \cdot 10^{-7}$	109.8	$5.82 \cdot 10^{-8}$	109.8	$2.49 \cdot 10^{-8}$	109.9	$1.24 \cdot 10^{-8}$
120	118.2	$7.95 \cdot 10^{-6}$	119.1	$2.13 \cdot 10^{-6}$	119.5	$7.61 \cdot 10^{-7}$	119.7	$3.30 \cdot 10^{-7}$	119.7	$1.62 \cdot 10^{-7}$
130	125.2	$1.09 \cdot 10^{-4}$	126.9	$5.65 \cdot 10^{-5}$	127.8	$3.31 \cdot 10^{-5}$	128.4	$2.07 \cdot 10^{-5}$	128.9	$1.32 \cdot 10^{-5}$
140	128.1	$8.11 \cdot 10^{-4}$	129.3	$7.56 \cdot 10^{-4}$	129.8	$7.30 \cdot 10^{-4}$	130.2	$7.14 \cdot 10^{-4}$	130.5	$7.03 \cdot 10^{-4}$
150	128.9	$2.39 \cdot 10^{-3}$	129.7	$2.43 \cdot 10^{-3}$	130.1	$2.46 \cdot 10^{-3}$	130.4	$2.49 \cdot 10^{-3}$	130.6	$2.52 \cdot 10^{-3}$
160	129.2	$4.55 \cdot 10^{-3}$	129.9	$4.69 \cdot 10^{-3}$	130.2	$4.79 \cdot 10^{-3}$	130.4	$4.87 \cdot 10^{-3}$	130.6	$4.96 \cdot 10^{-3}$
170	129.4	$6.96 \cdot 10^{-3}$	130.0	$7.20 \cdot 10^{-3}$	130.2	$7.36 \cdot 10^{-3}$	130.4	$7.05 \cdot 10^{-3}$	130.6	$7.64 \cdot 10^{-3}$
180	129.5	$9.42 \cdot 10^{-3}$	130.0	$9.74 \cdot 10^{-3}$	130.2	$9.96 \cdot 10^{-3}$	130.4	$1.01 \cdot 10^{-2}$	130.6	$1.03 \cdot 10^{-2}$
190	129.6	$1.18 \cdot 10^{-2}$	130.0	$1.22 \cdot 10^{-2}$	130.2	$1.25 \cdot 10^{-2}$	130.4	$1.27 \cdot 10^{-2}$	130.6	$1.29 \cdot 10^{-2}$
200	129.7	$1.40 \cdot 10^{-2}$	130.1	$1.45 \cdot 10^{-2}$	130.2	$1.48 \cdot 10^{-2}$	130.4	$1.51 \cdot 10^{-2}$	130.6	$1.53 \cdot 10^{-2}$
210	129.7	$1.61 \cdot 10^{-2}$	130.1	$1.66 \cdot 10^{-2}$	130.2	$1.70 \cdot 10^{-2}$	130.4	$1.73 \cdot 10^{-2}$	130.6	$1.76 \cdot 10^{-2}$
220	129.7	$1.80 \cdot 10^{-2}$	130.1	$1.86 \cdot 10^{-2}$	130.3	$1.89 \cdot 10^{-2}$	130.4	$1.92 \cdot 10^{-2}$	130.6	$1.96 \cdot 10^{-2}$
230	129.8	$1.98 \cdot 10^{-2}$	130.1	$2.03 \cdot 10^{-2}$	130.3	$2.07 \cdot 10^{-2}$	130.4	$2.10 \cdot 10^{-2}$	130.6	$2.14 \cdot 10^{-2}$
240	129.8	$2.13 \cdot 10^{-2}$	130.1	$2.19 \cdot 10^{-2}$	130.3	$2.23 \cdot 10^{-2}$	130.4	$2.27 \cdot 10^{-2}$	130.6	$2.31 \cdot 10^{-2}$
250	129.8	$2.27 \cdot 10^{-2}$	130.1	$2.33 \cdot 10^{-2}$	130.3	$2.37 \cdot 10^{-2}$	130.4	$2.41 \cdot 10^{-2}$	130.6	$2.45 \cdot 10^{-2}$
260	129.8	$2.4 \cdot 10^{-2}$	130.1	$2.46 \cdot 10^{-2}$	130.3	$2.5 \cdot 10^{-2}$	130.4	$2.54 \cdot 10^{-2}$	130.6	$2.59 \cdot 10^{-2}$
270	129.8	$2.51 \cdot 10^{-2}$	130.1	$2.58 \cdot 10^{-2}$	130.3	$2.62 \cdot 10^{-2}$	130.4	$2.66 \cdot 10^{-2}$	130.6	$2.71 \cdot 10^{-2}$
280	129.8	$2.62 \cdot 10^{-2}$	130.1	$2.68 \cdot 10^{-2}$	130.3	$2.73 \cdot 10^{-2}$	130.4	$2.77 \cdot 10^{-2}$	130.6	$2.81 \cdot 10^{-2}$
290	129.8	$2.71 \cdot 10^{-2}$	130.1	$2.78 \cdot 10^{-2}$	130.3	$2.82 \cdot 10^{-2}$	130.4	$2.86 \cdot 10^{-2}$	130.6	$2.91 \cdot 10^{-2}$
300	129.8	$2.80 \cdot 10^{-2}$	130.1	$2.86 \cdot 10^{-2}$	130.3	$2.91 \cdot 10^{-2}$	130.4	$2.95 \cdot 10^{-2}$	130.6	$3.00 \cdot 10^{-2}$

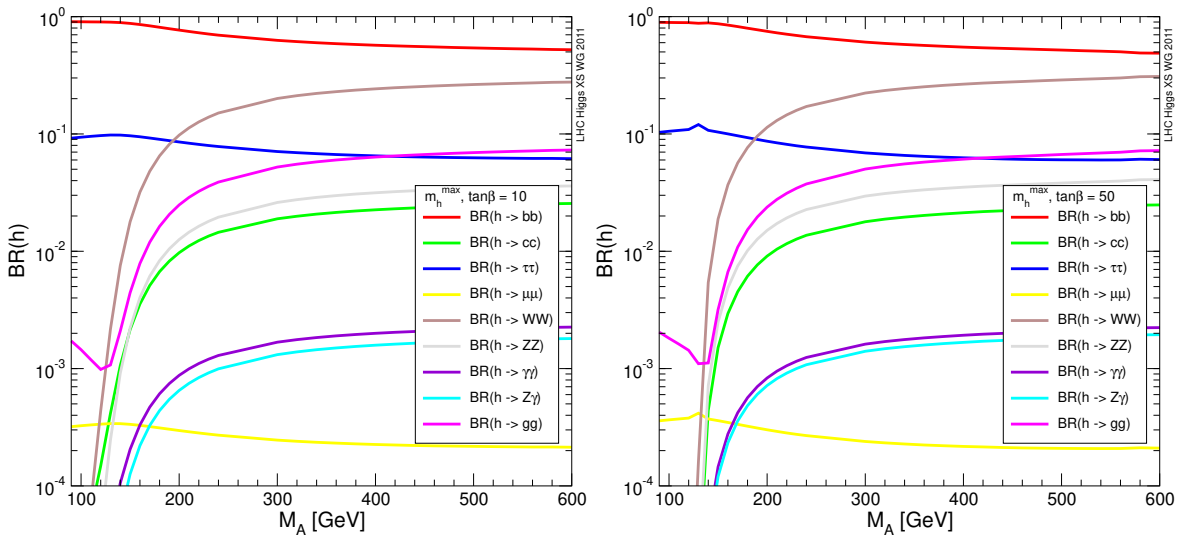

Fig. 5: Higgs branching ratios for the light MSSM Higgs boson for the relevant final states. The parameters are chosen according to the $m_{\rm h}^{\rm max}$ scenario, see Eq. (82), with $\tan\beta = 10(50)$ in the left (right) plot.

3 Parton distribution functions[6]

3.1 PDF set updates

Several of the PDF sets which were discussed in the previous Yellow Report [7] have been updated since. NNPDF2.1 [95] is an updated version of NNPDF2.0 [96] which uses the FONLL general mass VFN scheme [97] instead of a zero-mass scheme. There are also now NNPDF NNLO and LO sets [98], which are based on the same data and methodology as NNPDF2.1. The HERA PDF group now use HERAPDF1.5 [99], which contains more data than HERAPDF1.0 [100], a wider examination of parameter dependence, and an NNLO set with uncertainty. This set is available in LHAPDF, however it is partially based on preliminary HERA-II structure-function data.

The current PDF4LHC prescription [101, 102] for calculating a central value and uncertainty for a given process should undergo the simple modification of using the most up-to-date relevant set from the relevant group, i.e., NNPDF2.0 should be replaced with NNPDF2.1 [95] and CTEQ6.6 [103] with CT10 [104]. At NNLO the existing prescription should be used, but with the uncertainty envelope calculated using the up-to-date sets noted above.

3.2 Correlations

The main aim of this section is to examine the correlations between different Higgs production processes and/or backgrounds to these processes. The PDF uncertainty analysis may be extended to define a *correlation* between the uncertainties of two variables, say $X(\vec{a})$ and $Y(\vec{a})$. As for the case of PDFs, the physical concept of PDF correlations can be determined both from PDF determinations based on the Hessian approach and on the Monte Carlo approach. For convenience and commonality, all physical processes were calculated using the MCFM NLO program (versions 5.8 and 6.0) [105, 106] with a common set of input files for all groups.

We present the results for the PDF correlations at NLO for Higgs production via gluon–gluon fusion, vector-boson fusion, in association with W or with a $\mathrm{t\bar{t}}$ pair at masses $M_{\mathrm{H}} = 120$ GeV, $M_{\mathrm{H}} = 160$ GeV, $M_{\mathrm{H}} = 200$ GeV, $M_{\mathrm{H}} = 300$ GeV, $M_{\mathrm{H}} = 500$ GeV. We also include a wide variety of background processes and other standard production mechanisms, i.e., W, WW, WZ, Wγ, $\mathrm{Wb\bar{b}}$, $\mathrm{t\bar{t}}$, $\mathrm{t\bar{b}}$ and the t-channel $\mathrm{t}(\to \mathrm{\bar{b}}) + \mathrm{q}$, where W denotes the average of W^+ and W^-.

For MSTW2008 [107], CT10 [104], GJR08 [108, 109], and ABKM09 [110] PDFs the correlations of any two quantities X and Y are calculated using the standard formula [111]

$$\rho\,(X,Y) \equiv \cos\varphi = \frac{\sum_i (X_i - X_0)(Y_i - Y_0)}{\sqrt{\sum_i (X_i - X_0)^2 \sum_i (Y_i - Y_0)^2}}. \tag{7}$$

The index in the sum runs over the number of free parameters and X_0, Y_0 correspond to the values obtained by the central PDF value. When positive and negative direction PDF eigenvectors are used this is equivalent to (see e.g., Ref. [103])

$$\begin{aligned} \cos\varphi &= \frac{\vec{\Delta}X \cdot \vec{\Delta}Y}{\Delta X \Delta Y} = \frac{1}{4\Delta X \Delta Y} \sum_{i=1}^{N} \left(X_i^{(+)} - X_i^{(-)}\right)\left(Y_i^{(+)} - Y_i^{(-)}\right), \\ \Delta X &= \left|\vec{\Delta}X\right| = \frac{1}{2}\sqrt{\sum_{i=1}^{N}\left(X_i^{(+)} - X_i^{(-)}\right)^2}, \end{aligned} \tag{8}$$

where the sum is over the N pairs of positive and negative PDF eigenvectors. For MSTW2008 and CT10 the eigenvectors by default contain only PDF parameters, and α_{s} variation may be considered separately. For GJR08 and ABKM09, α_{s} is one of the parameters used directly in calculating the correlation coefficient, with the central value and variation determined by the fit.

[6] S. Forte, J. Huston and R. S. Thorne (eds); S. Alekhin, J. Blümlein, A.M. Cooper-Sarkar, S. Glazov, P. Jimenez-Delgado, S. Moch, P. Nadolsky, V. Radescu, J. Rojo, A. Sapronov and W.J. Stirling.

Due to the specific error calculation prescription for HERAPDF1.5 which includes parametrisation and model errors, the correlations can not be calculated in exactly the same way. Rather, a formula for uncertainty propagation can be used in which correlations can be expressed via relative errors of compounds and their combination:

$$\left[\sigma\left(\frac{X}{\sigma(X)}+\frac{Y}{\sigma(Y)}\right)\right]^2 = 2+2\cos\varphi, \tag{9}$$

where $\sigma(O)$ is the PDF error of observable O calculated using the HERAPDF prescription.

The correlations for the NNPDF prescription are calculated as discussed in Ref. [112], namely

$$\rho\left(X,Y\right) = \frac{\langle XY\rangle_{\rm rep} - \langle X\rangle_{\rm rep}\langle Y\rangle_{\rm rep}}{\sigma_X\sigma_Y} \tag{10}$$

where the averages are performed over the $N_{\rm rep} = 100$ replicas of the NNPDF2.1 set.

For all sets the correlations are for the appropriate value of $\alpha_{\rm s}$ for the relevant PDF set.

3.2.1 Results for the correlation study

Our main result is the computation of the correlation between physical processes relevant to Higgs production, either as signal or as background. It is summarised in Tables 10 and 11, where we show the PDF4LHC average for each of the correlations between signal and background processes considered. These tables classify each correlation in classes with $\Delta\rho = 0.2$, that is, if the correlation is $1 > \rho > 0.9$ the processes is assigned correlation 1, if $0.9 > \rho > 0.7$ the processes is assigned correlation 0.8 and so on. The class width is typical of the spread of the results from the PDF sets, which are in generally very good, but not perfect agreement. The average is obtained using the most up-to-date PDF sets (CT10, MSTW2008, NNPDF2.1) in the PDF4LHC recommendation, and it is appropriate for use in conjunction with the cross-section results obtained in Ref. [7], and with the background processes listed; the change of correlations due to updating the prescription is insignificant in comparison to the class width.

We have also compared this PDF4LHC average to the average using all six PDF sets. In general there is rather little change. There are quite a few cases where the average moves into a neighbouring class but in many cases due to a very small change taking the average just over a boundary between two classes. There is only a move into the next-to-neighbouring class, i.e., a change of more than 0.2, in a very small number of cases. For the VBF–Wγ correlation at $M_{\rm H} = 120, 160$ GeV it reduces from 0.6 to 0.2, for the VBF–W correlation at $M_{\rm H} = 500$ GeV it reduces from 0.4 to 0, for the Wγ–$\rm t\overline{b}$ correlation it reduces from 0.8 to 0.4, for WZ–$\rm t\overline{t}H$ at $M_{\rm H} = 120$ GeV it increases from -0.4 to 0.0, and for $\rm Wb\overline{b}$–$\rm t\overline{t}H$ at $M_{\rm H} = 200$ GeV it increases from -0.2 to 0.2.

A more complete list of processes, with results for each individual PDF set, may be found in the tables on the webpage at the LHC Higgs Cross Section Working Group TWiki [113]. Note, however, that there is a high degree of redundancy in the approximate correlations of many processes. For example W production is very similar to Z production, both depending on partons (quarks in this case) at very similar hard scales and x values. Similarly for WW and ZZ, and the subprocesses $\rm gg \to WW(ZZ)$ and Higgs production via gluon–gluon fusion for $M_{\rm H} = 200$ GeV.

More detailed results are presented for the MSTW2008, NNPDF2.1, CT10, HERAPDF1.5, GJR08, and ABKM09 PDFs in Figures 6–21. The result using each individual PDF sets is compared to the (updated) PDF4LHC average. There is usually a fairly narrow clustering of the individual results about the average, with a small number of cases where there is one, or perhaps two outliers. The sets with the largest parametrisations for the PDFs generally tend to give smaller magnitude correlations or anticorrelations, but this is not always the case, e.g., NNPDF2.1 gives the largest anti-correlation for VBF–$\rm t\overline{t}H$. There are some unusual features, e.g., for HERAPDF1.5 and high values of $M_{\rm H}$, the $\rm t\overline{t}H$ correlations with quantities depending on the high-x gluon, e.g., $\rm ggH$ and $\rm t\overline{t}$ is opposite to the other sets

Table 10: The up-to-date PDF4LHC average for the correlations between all signal processes with other signal and background processes for Higgs production considered here. The processes have been classified in correlation classes, as discussed in the text.

$M_{\mathrm{H}} = 120$ GeV	ggH	VBF	WH	$\mathrm{t\bar{t}H}$
ggH	1	−0.6	−0.2	−0.2
VBF	−0.6	1	0.6	−0.4
WH	−0.2	0.6	1	−0.2
$\mathrm{t\bar{t}}H$	−0.2	−0.4	−0.2	1
W	−0.2	0.6	0.8	−0.6
WW	−0.4	0.8	1	−0.2
WZ	−0.2	0.4	0.8	−0.4
Wγ	0	0.6	0.8	−0.6
$\mathrm{Wb\bar{b}}$	−0.2	0.6	1	−0.2
$\mathrm{t\bar{t}}$	0.2	−0.4	−0.4	1
$\mathrm{t\bar{b}}$	−0.4	0.6	1	−0.2
$\mathrm{t}(\rightarrow \bar{\mathrm{b}})\mathrm{q}$	0.4	0	0	0

$M_{\mathrm{H}} = 160$ GeV	ggH	VBF	WH	$\mathrm{t\bar{t}H}$
ggH	1	−0.6	−0.4	0.2
VBF	−0.6	1	0.6	−0.2
WH	−0.4	0.6	1	0
$\mathrm{t\bar{t}H}$	0.2	−0.2	0	1
W	−0.4	0.4	0.6	−0.4
WW	−0.4	0.6	0.8	−0.2
WZ	−0.4	0.4	0.8	−0.2
Wγ	−0.4	0.6	0.6	−0.6
$\mathrm{Wb\bar{b}}$	−0.2	0.6	0.8	−0.2
$\mathrm{t\bar{t}}$	0.4	−0.4	−0.2	0.8
$\mathrm{t\bar{b}}$	−0.4	0.6	1	0
$\mathrm{t}(\rightarrow \bar{\mathrm{b}})\mathrm{q}$	0.6	0	0	0

$M_{\mathrm{H}} = 200$ GeV	ggH	VBF	WH	$\mathrm{t\bar{t}H}$
ggH	1	−0.6	−0.4	0.4
VBF	−0.6	1	0.6	−0.2
WH	−0.4	0.6	1	0
$\mathrm{t\bar{t}H}$	0.4	−0.2	0	1
W	−0.6	0.4	0.6	−0.4
WW	−0.4	0.6	0.8	−0.2
WZ	−0.4	0.4	0.8	−0.2
Wγ	−0.4	0.4	0.6	−0.6
$\mathrm{Wb\bar{b}}$	−0.2	0.6	0.8	−0.2
$\mathrm{t\bar{t}}$	0.6	−0.4	−0.2	0.8
$\mathrm{t\bar{b}}$	−0.4	0.6	0.8	0
$\mathrm{t}(\rightarrow \bar{\mathrm{b}})\mathrm{q}$	0.6	−0.2	0	0

$M_{\mathrm{H}} = 300$ GeV	ggH	VBF	WH	$\mathrm{t\bar{t}H}$
ggH	1	−0.4	−0.2	0.6
VBF	−0.4	1	0.4	−0.2
WH	−0.2	0.4	1	0.2
$\mathrm{t\bar{t}H}$	0.6	−0.2	0.2	1
W	−0.6	0.4	0.4	−0.6
WW	−0.4	0.6	0.8	−0.2
WZ	−0.6	0.4	0.6	−0.4
Wγ	−0.6	0.4	0.4	−0.6
$\mathrm{Wb\bar{b}}$	−0.2	0.4	0.8	−0.2
$\mathrm{t\bar{t}}$	1	−0.4	0	0.8
$\mathrm{t\bar{b}}$	−0.4	0.4	0.8	−0.2
$\mathrm{t}(\rightarrow \bar{\mathrm{b}})\mathrm{q}$	0.4	−0.2	0	−0.2

$M_{\mathrm{H}} = 500$ GeV	ggH	VBF	WH	$\mathrm{t\bar{t}H}$
ggH	1	−0.4	0	0.8
VBF	−0.4	1	0.4	−0.2
WH	0	0.4	1	0
$\mathrm{t\bar{t}H}$	0.8	−0.2	0	1
W	−0.6	0.4	0.2	−0.6
WW	−0.4	0.6	0.6	−0.4
WZ	−0.6	0.4	0.6	−0.4
Wγ	−0.6	0.4	0.2	−0.6
$\mathrm{Wb\bar{b}}$	−0.4	0.4	0.6	−0.4
$\mathrm{t\bar{t}}$	1	−0.4	0	0.8
$\mathrm{t\bar{b}}$	−0.4	0.4	0.8	−0.2
$\mathrm{t}(\rightarrow \bar{\mathrm{b}})\mathrm{q}$	0.2	−0.2	0	−0.2

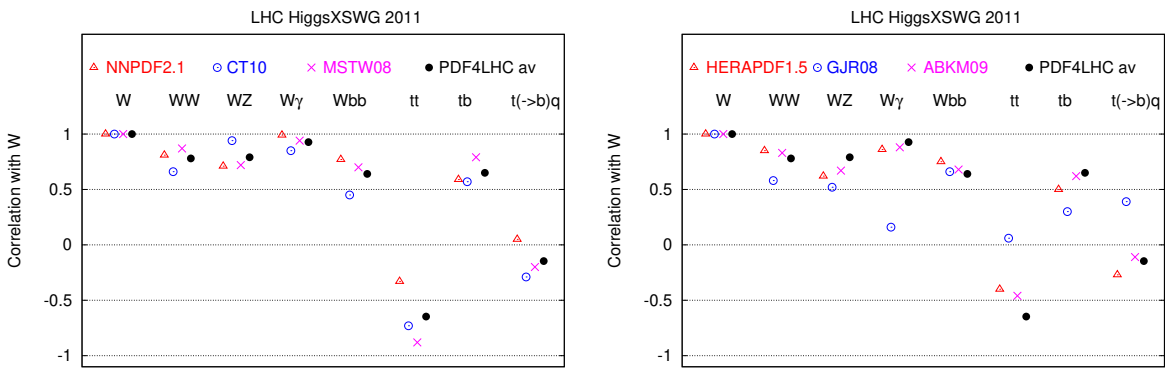

Fig. 6: The correlations between W production and the other background processes considered. We show the results for NNPDF2.1, CT10 and MSTW2008 in the left plot, and HERAPDF, JR and ABKM in the right plot. In both cases we show the up-to-date PDF4LHC average result.

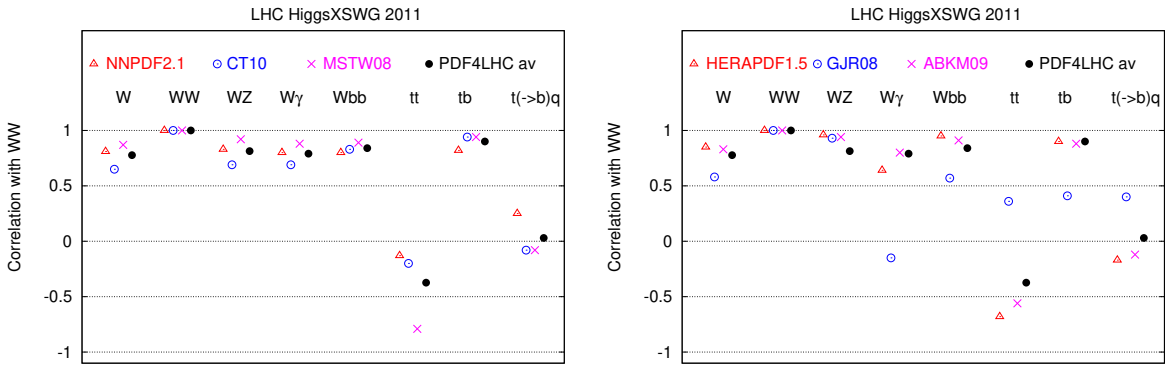

Fig. 7: The same as Figure 6 for WW production.

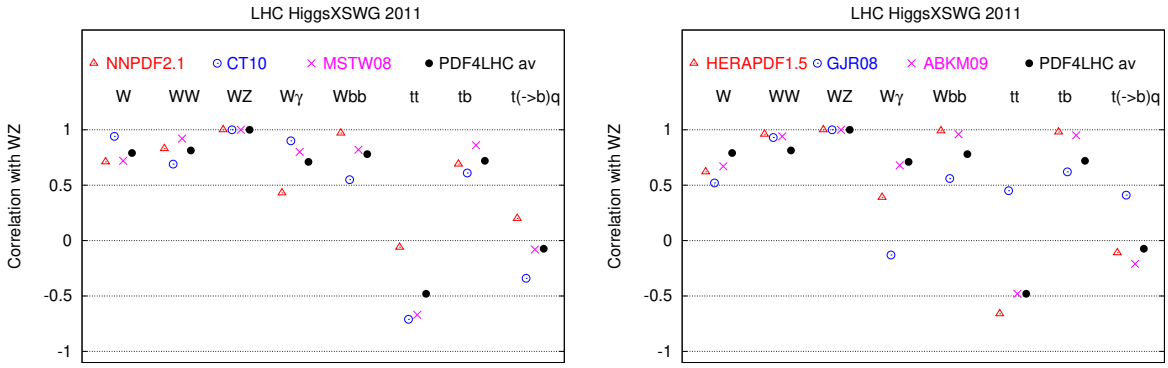

Fig. 8: The same as Figure 6 for WZ production.

Table 11: The same as Table 10 for the correlations between background processes.

	W	WW	WZ	$\mathrm{W\gamma}$	$\mathrm{Wb\bar{b}}$	$\mathrm{t\bar{t}}$	$\mathrm{t\bar{b}}$	$\mathrm{t(\to \bar{b})q}$
W	1	0.8	0.8	1	0.6	−0.6	0.6	−0.2
WW	0.8	1	0.8	0.8	0.8	−0.4	0.8	0
WZ	0.8	0.8	1	0.8	0.8	−0.4	0.8	0
$\mathrm{W\gamma}$	1	0.8	0.8	1	0.6	−0.6	0.8	0
$\mathrm{Wb\bar{b}}$	0.6	0.8	0.8	0.6	1	−0.2	0.6	0
$\mathrm{t\bar{t}}$	−0.6	−0.4	−0.4	−0.6	−0.2	1	−0.4	0.2
$\mathrm{t\bar{b}}$	0.6	0.8	0.8	0.8	0.6	−0.4	1	0.2
$\mathrm{t(\to \bar{b})q}$	−0.2	0	0	0	0	0.2	0.2	1

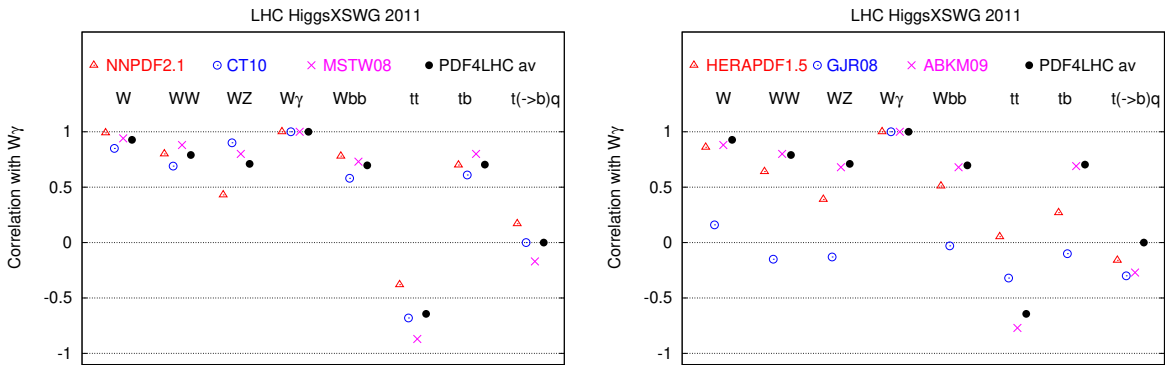

Fig. 9: The same as Figure 6 for $\mathrm{W\gamma}$ production.

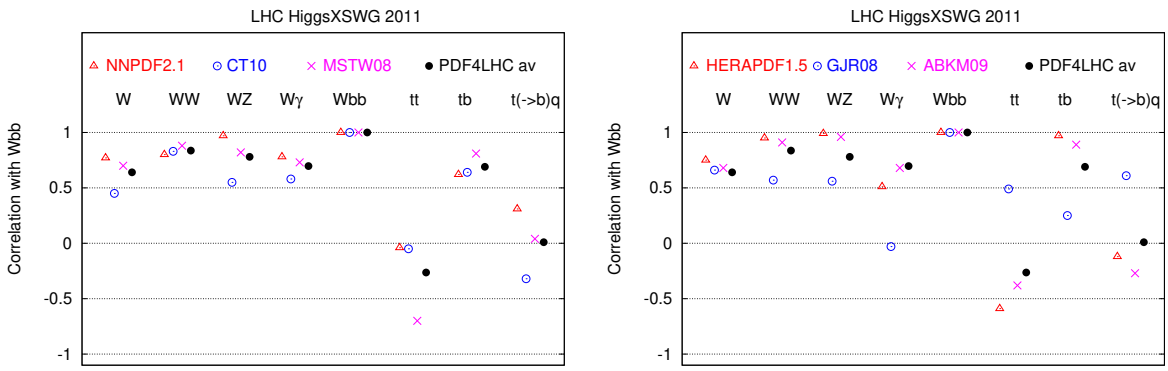

Fig. 10: The same as Figure 6 for $\mathrm{Wb\bar{b}}$ production.

and the correlations with quantities depending on high-x quarks and antiquarks, e.g., VBF and WW, is stronger. This is possibly related to the large high-x antiquark distribution in HERAPDF which contributes to $\mathrm{t\bar{t}H}$ but not ggH or very much to $\mathrm{t\bar{t}}$. GJR08 has a tendency to obtain more correlation between some gluon dominated processes, e.g., ggH and $\mathrm{t\bar{t}}$ and quark dominated processes, e.g., W and WZ, perhaps because the dynamical generation of PDFs couples the gluon and quark more strongly.

We can now also see the origin of the cases where the averages move two classes. For VBF–$\mathrm{W\gamma}$ at lower masses GJR08, ABKM09, and HERAPDF1.5 all lie lower than the (updated) PDF4LHC average, but not too different to CT10. For VBF–W at $M_{\mathrm{H}} = 500$ GeV, ABKM09, and GJR08 give a small anticorrelation, while others give a correlation, though it is only large in the case of MSTW2008. For $\mathrm{W\gamma}$–$\mathrm{t\bar{b}}$ the change is due to slightly lower correlations for GJR08. However, although the change is two

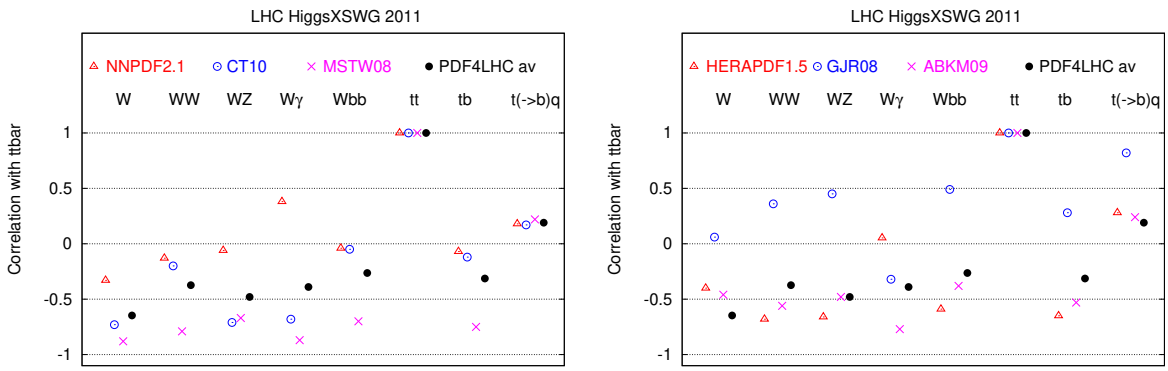

Fig. 11: The same as Figure 6 for $\mathrm{t\bar{t}}$ production.

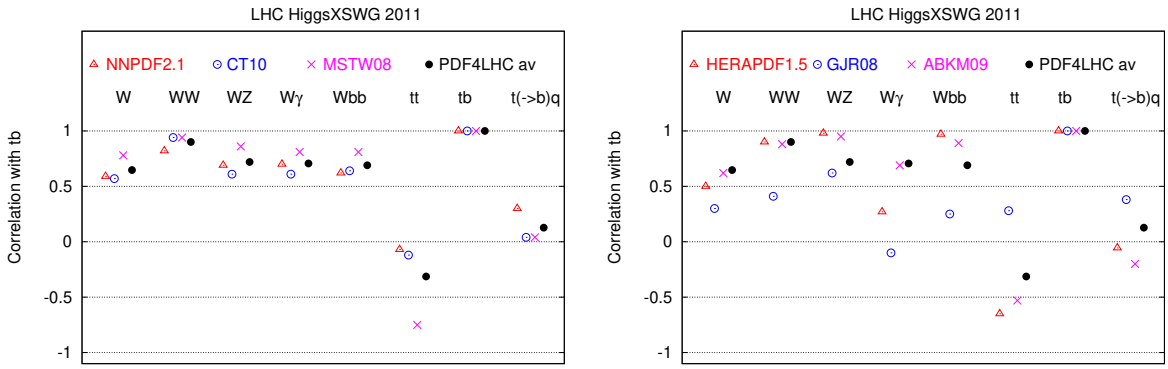

Fig. 12: The same as Figure 6 for $\mathrm{t\bar{b}}$ production.

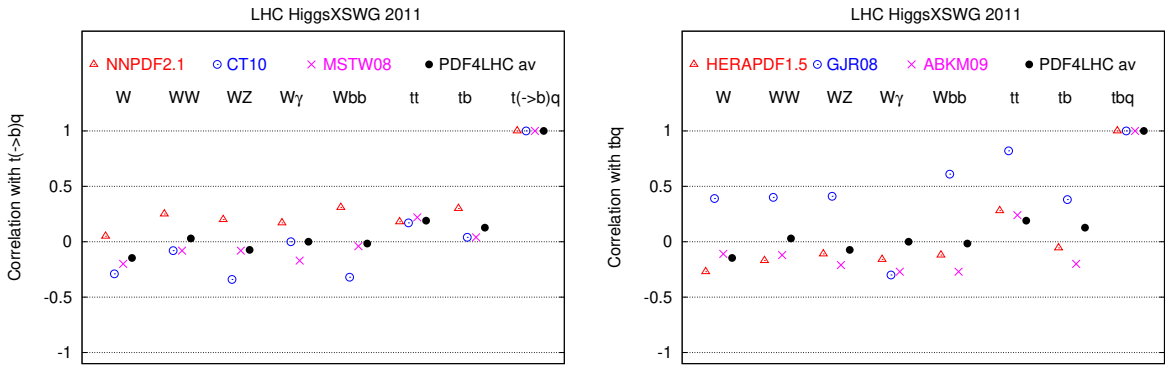

Fig. 13: The same as Figure 6 for t-channel $\mathrm{t}(\rightarrow \bar{\mathrm{b}})\mathrm{q}$ production.

classes, in practice it is barely more than 0.2. For WZ–$\mathrm{t\bar{t}H}$ at $M_{\mathrm{H}} = 120$ GeV both HERAPDF1.5 and GJR08 have a larger correlation. This increases with M_{H} for HERAPDF1.5 as noted, whereas GJR08 heads closer to the average, but the move at $M_{\mathrm{H}} = 120$ GeV is only marginally two classes, and is only one class for other masses. For $\mathrm{Wb\bar{b}}$–$\mathrm{t\bar{t}H}$ at $M_{\mathrm{H}} = 200$ GeV the situation is similar, and MSTW2008 gives easily the biggest pull in the direction of anticorrelation.

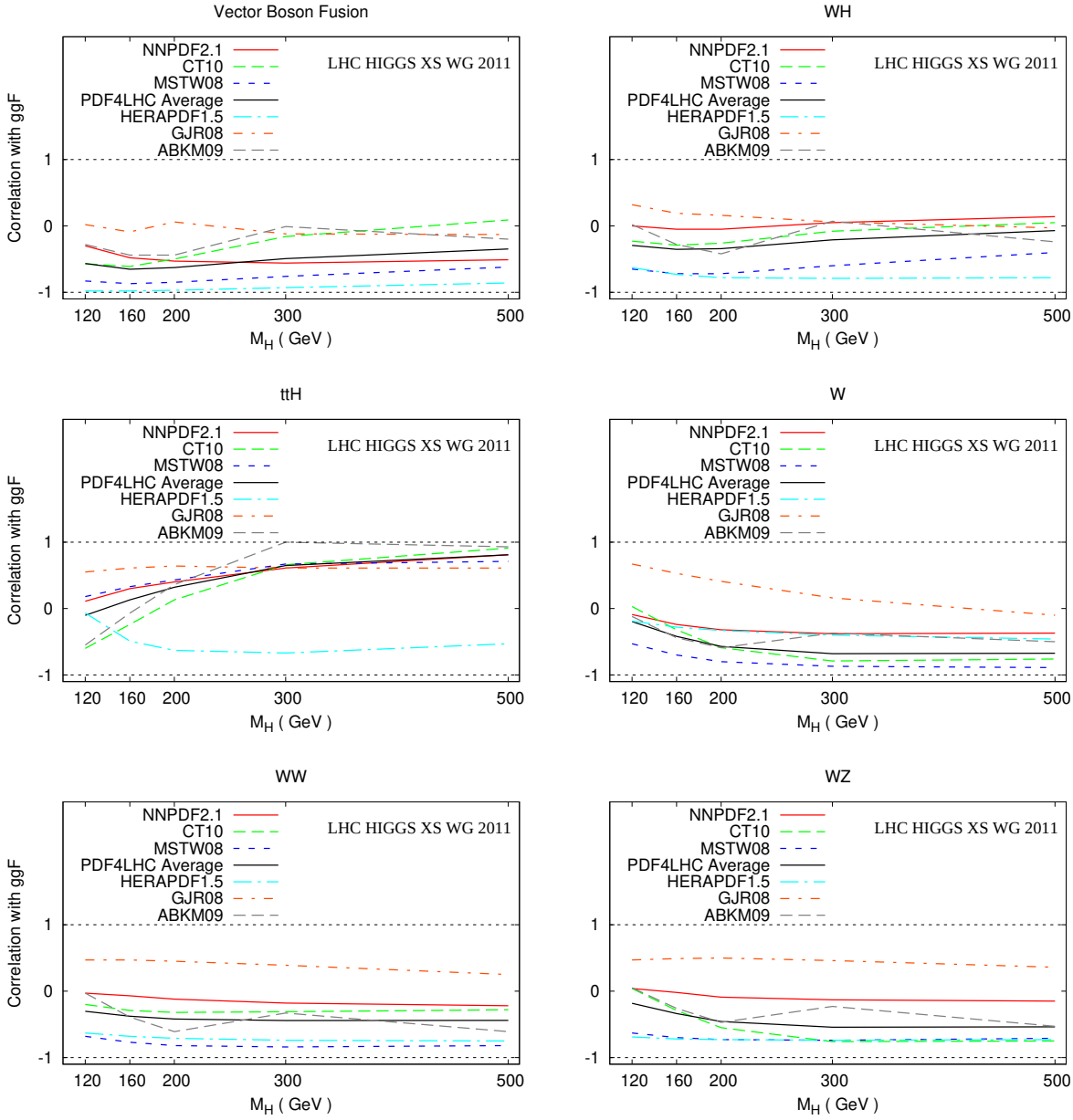

Fig. 14: Correlation between the gluon-fusion $\mathrm{gg} \to \mathrm{H}$ process and other signal and background processes as a function of M_{H}. We show the results for the individual PDF sets as well as the up-to-date PDF4LHC average.

3.2.2 Additional correlation studies

The inclusion of the α_{s} uncertainty on the correlations, compared to PDF only variation, was also studied for some PDF sets, e.g., MSTW2008 using the approximation that the PDF sets for the upper and lower α_{s} values [114] simply form another pair of orthogonal eigenvectors (show to be true in the quadratic approximation [115]). This increases the correlation between some processes, i.e., W production and Higgs via gluon fusion, because the former increases with α_{s} due to increased evolution of quarks while the latter increases due to direct dependence on α_{s}. Similarly for e.g., Higgs production via gluon fusion and $\mathrm{t\bar{t}}$ production since each depends directly on α_{s}. This may also contribute to some of the stronger correlations seen using GJR08 in some similar cases. In a handful of processes it reduces correlation, e.g., W and $\mathrm{Wb\bar{b}}$ since the latter has a much stronger α_{s} dependence. In most cases the change compared

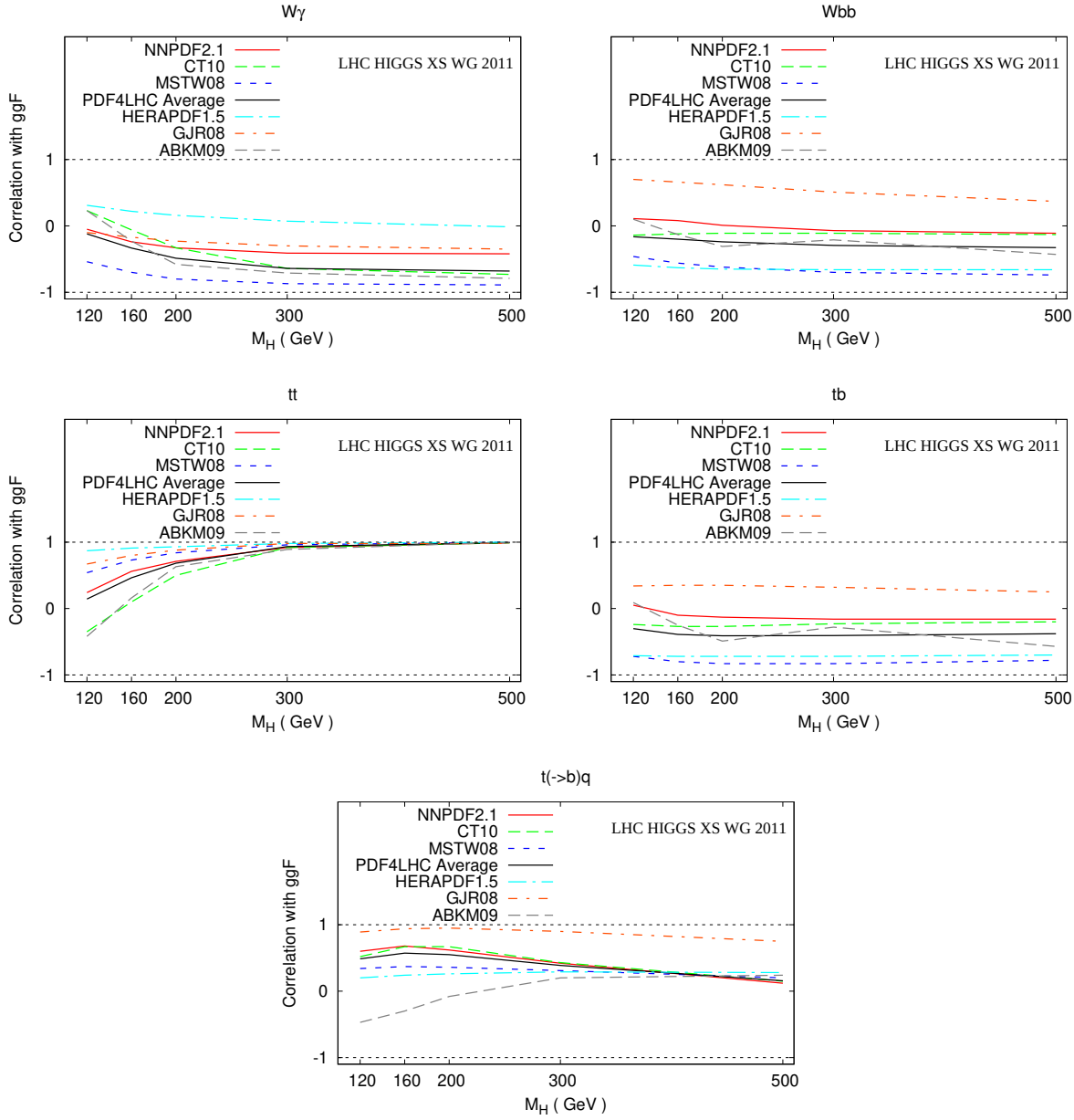

Fig. 15: Correlation between the gluon fusion $\mathrm{gg} \to \mathrm{H}$ process and other signal and background processes as a function of M_{H}. We show the results for the individual PDF sets as well as the up-to-date PDF4LHC average.

to PDF-only correlation for a given PDF sets small, and it is not an obvious contributing factor to the cases where the (updated) PDF4LHC average is noticeably different to the average using six sets, except possibly to $\mathrm{Wb\bar{b}}$–$\mathrm{t\bar{t}H}$ at $M_{\mathrm{H}} = 200$ GeV, where α_{s} does increase correlation.

A small number of correlations were also calculated at NNLO for MSTW2008 PDFs, i.e., W, Z and $\mathrm{gg} \to \mathrm{H}$ for the same range of M_{H}. The correlations when taking into account PDF uncertainty alone were almost identical to those at NLO, variations being less than 0.05. When α_{s} uncertainty was included the correlations changed a little more due to $\mathrm{gg} \to \mathrm{H}$ having more direct dependence on α_{s}, but this is a relatively minor effect. Certainly the results in Tables 10 and 11, though calculated at NLO, can be used with confidence at NNLO.

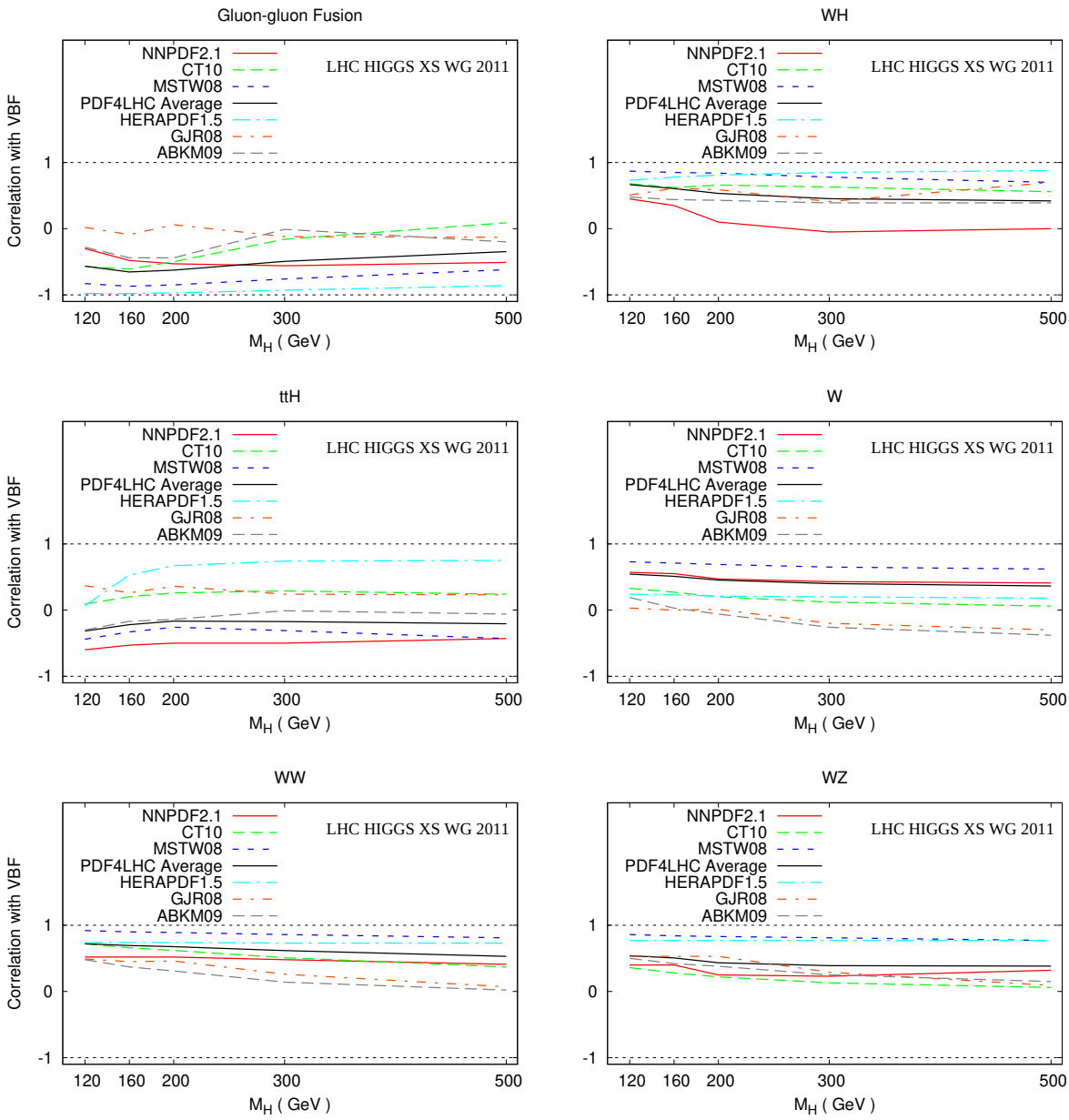

Fig. 16: The same as Figure 14 for the vector boson fusion process.

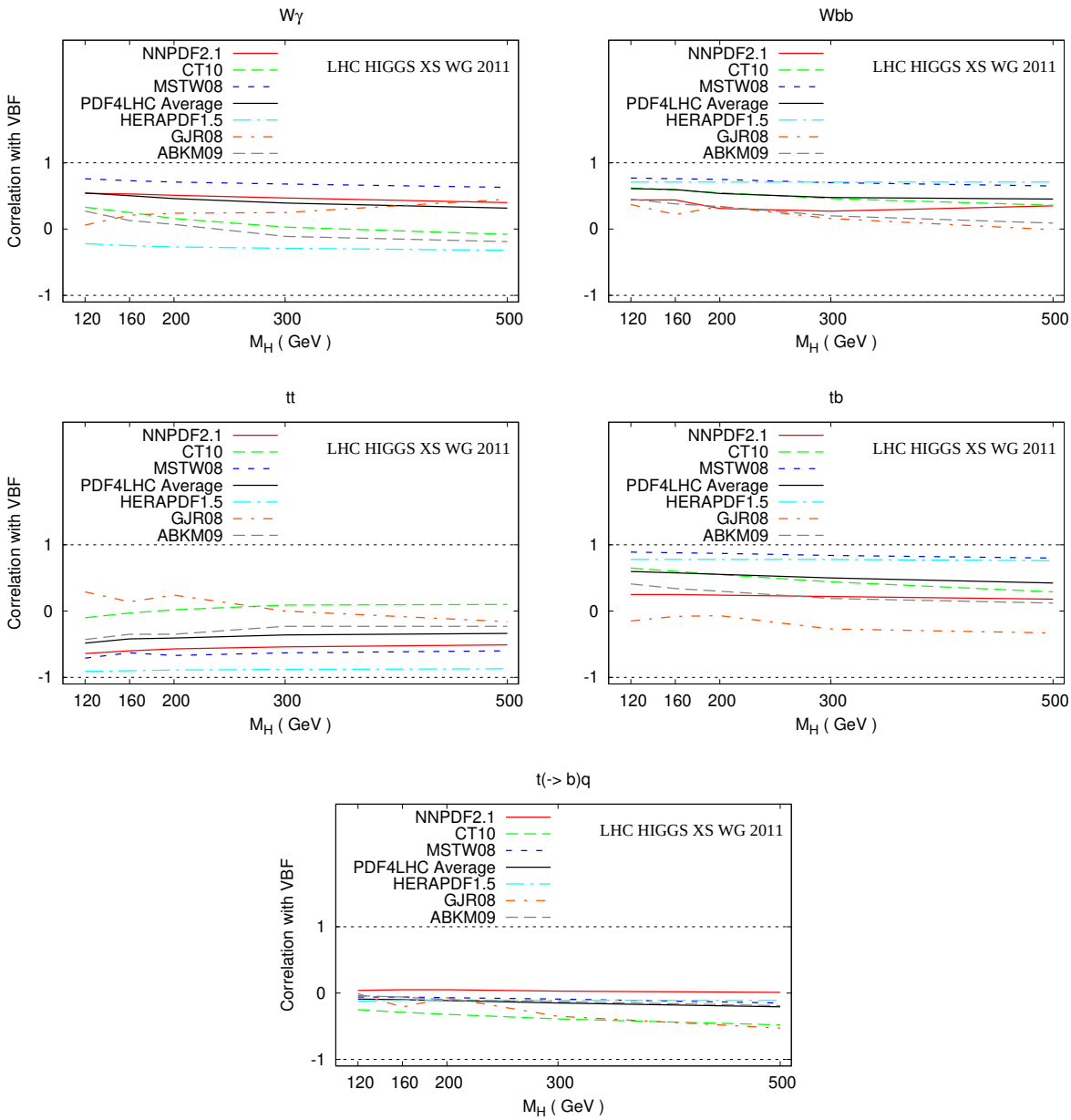

Fig. 17: The same as Figure 15 for the vector boson fusion process.

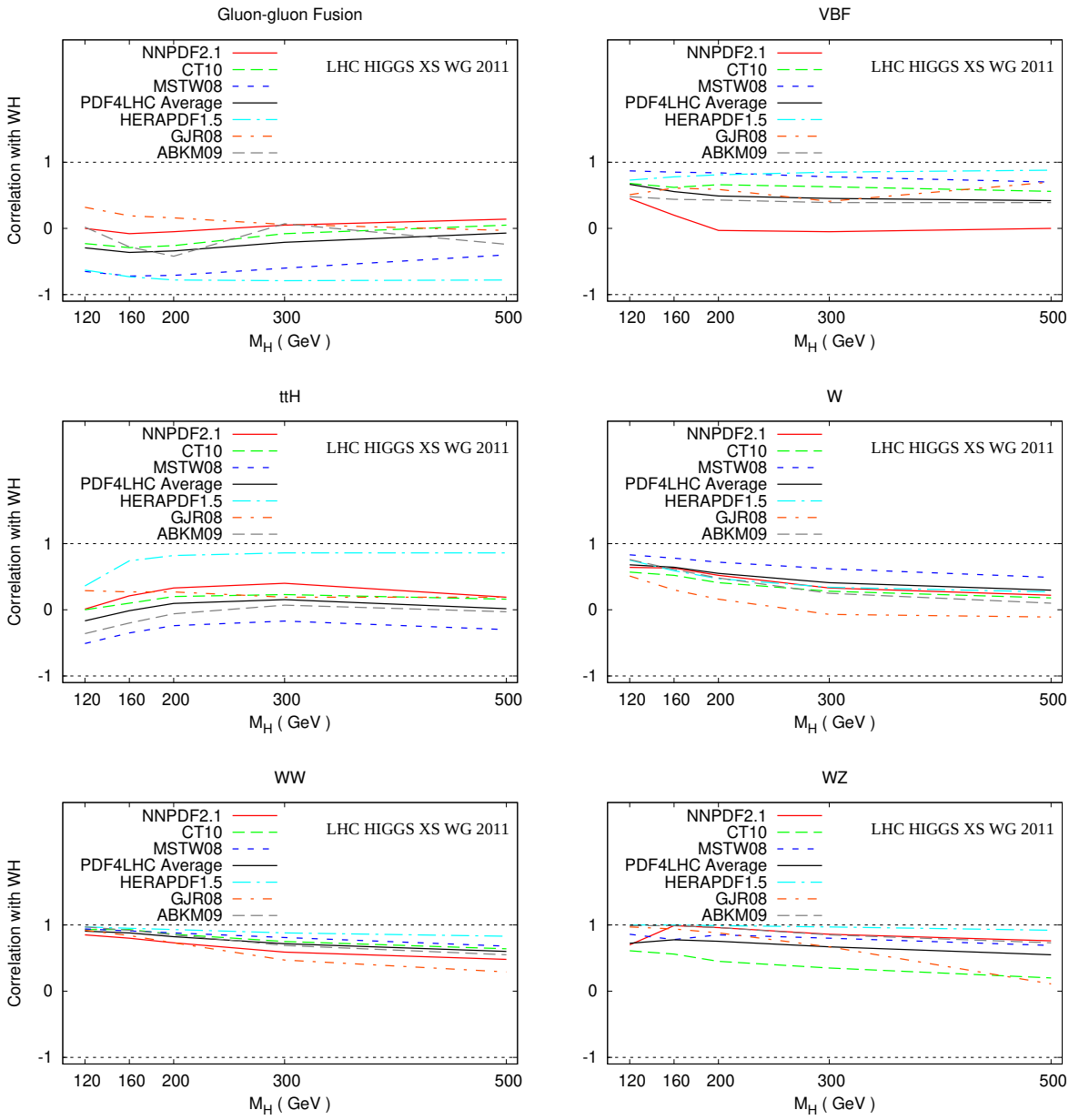

Fig. 18: The same as Figure 14 for the WH production process.

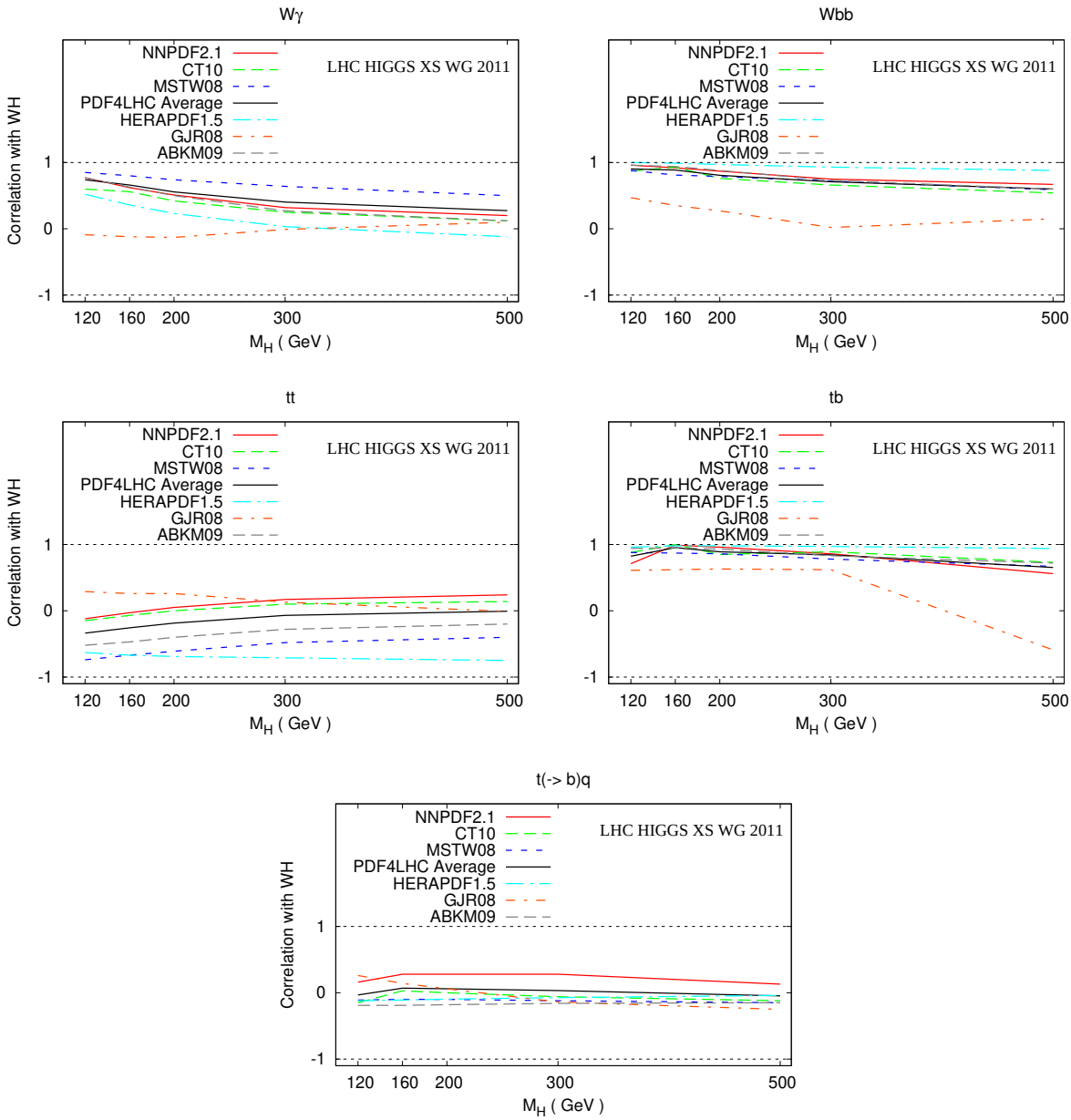

Fig. 19: The same as Figure 15 for the WH production process.

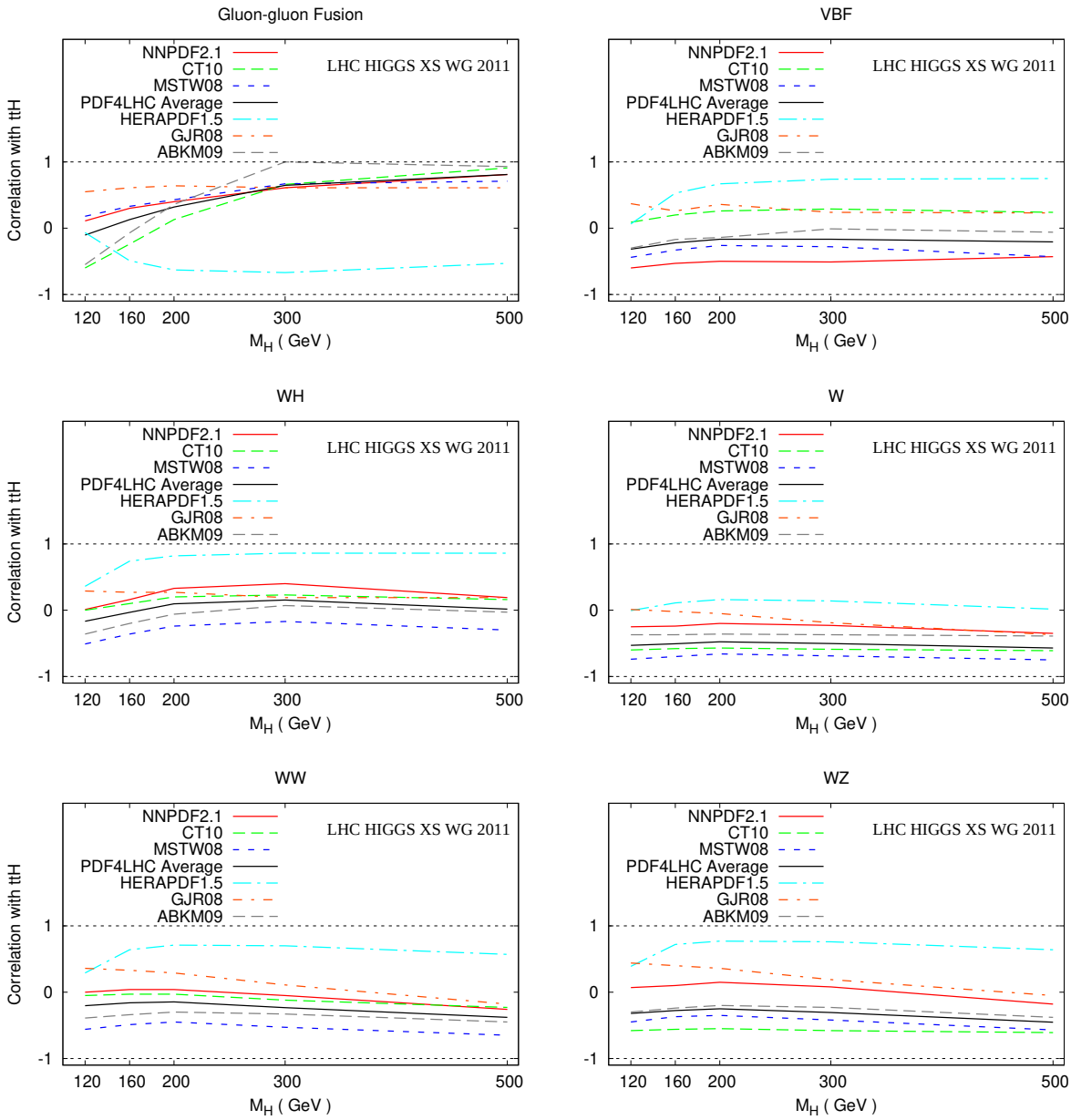

Fig. 20: The same as Figure 14 for the $t\bar{t}H$ production process.

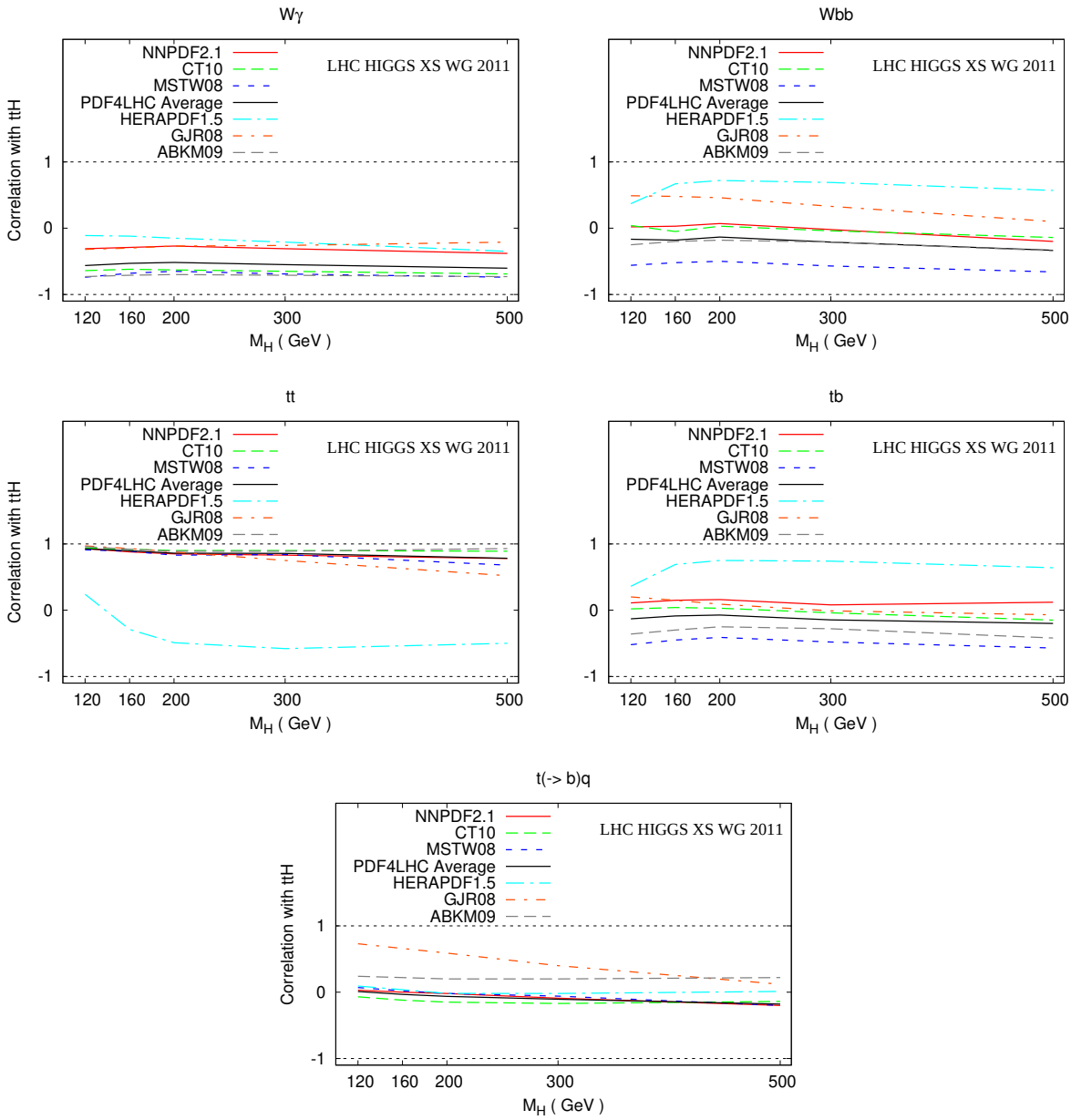

Fig. 21: The same as Figure 15 for the $t\bar{t}H$ production process.

4 NLO parton shower[7]

4.1 Introduction

Recently, Monte Carlo event generators have profited by a number of theoretical achievements that have significantly improved the capability of making accurate predictions and simulations of events taking place at high-energy colliders. A very short review of the state-of-the-art of the field has been given in the first volume of this Yellow Report [7], and we refer the reader there for the basic principles and the most important improvements with respect to a more standard parton-shower (PS) approach. We just recall the two main results: the possibility of consistently including exact next-to-leading order (NLO) corrections, i.e. to have NLO+PS generators [116–139] and the merging of parton-shower simulations and high-multiplicity tree-level matrix-element (ME) generators [140–150]. Moreover, in the last year, an impressive acceleration in achieving the full automatisation of NLO computations [151–155] as well as their interface to parton showers [156–159] has taken place. Thanks to such new techniques and their corresponding implementations, all the main Higgs-production channels (ggF,VBF,VH,ttH) at the LHC are now available in the context of NLO+PS [130, 132, 158, 160–162] together with some of the most important backgrounds [131, 163–170]. In this respect, it is certainly fair to state that state-of-the-art Higgs phenomenology at the LHC can now be performed at least at NLO+PS accuracy. This also implies that several important issues, such as those related to the estimation of uncertainties in NLO+PS simulations due, for instance, to scale uncertainties or different matching procedures, can be systematically studied for the first time. The aim of this section is to show how such studies can now be performed in the context of the current Higgs-boson searches. We stress that the results of our sample studies, which consider a light SM Higgs boson, can be easily extended to other Higgs mass ranges or to the search in scenarios with enhanced (or suppressed) couplings. In addition, in the case of a Higgs observation, such uncertainties would play a crucial role in the accurate determination of its properties.

In more detail, in this section we address the following topics:

- Uncertainties in NLO+PS generators. While in fixed-order computations there is considerable experience in using scale variation to estimate theoretical error, in the framework of NLO+PS generators this might not be sufficient. Suggestions for obtaining more realistic error bands will be given, and areas that will require further work will be identified. Uncertainties having to do with shower effects beyond the NLO level, hadronisation and underlying event (UE) will also be considered.
- Tuning of NLO+PS generators. In the case of Higgs production in gluon fusion, a next-to-next-to-leading-log (NNLL) matched to a next-to-next-to-leading-order (NNLO) calculation exists, and is implemented in the program HQT [171]. One can use the HQT results to improve the output of NLO+PS generators in several ways through reweighting the generated events, tuning the parameters of the NLO+PS generators or doing both things to achieve better agreement with HQT. Issues related to these procedures are discussed.
- Since the publication of the first volume of this Yellow Report [7], some improvements on existing generators have appeared. We present here these new developments.

The section is organised as follows. In Section 4.2 the POWHEG BOX and the MC@NLO Higgs-production generators are compared with the HQT prediction for the Higgs p_{T} spectrum. In Section 4.3 a study of uncertainties in $\mathrm{gg} \to \mathrm{H} \to \mathrm{WW}^{(*)}$ using SHERPA is presented. In Section 4.4 a study of systematic effects of NLO+PS tools in their implementation within the ATLAS and CMS event generation framework. In Section 4.5 we discuss issues related to the use of the HQT result to improve the NLO+PS programs. In particular, we provide recommendations on how to perform event reweighting, if needed, and how to set up the parameters of the NLO+PS generators to achieve better agreement with the HQT

[7] M. Felcini, F. Krauss, F. Maltoni, P. Nason and J. Yu. (eds.); J. Alwall, E. Bagnaschi, G. Degrassi, M. Grazzini, K. Hamilton, S. Höche, C. Jackson, H. Kim, Q. Li, F. Petriello, M. Schönherr, F. Siegert, P. Slavich, P. Torrielli and A. Vicini.

result. In Section 4.7, we present new generators for Higgs production in gluon fusion, including full top and bottom mass dependence, in the MADGRAPH and in the POWHEG BOX framework.

In Section 4.8, we present a new AMC@NLO feature that allows performing studies of scale and PDF dependences by reweighting the same set of events.

Finally, some controversial points yet to be resolved have emerged during the preparation of this report and are summarised in Section 4.9.

4.2 POWHEG BOX and MC@NLO comparison with HQT[8]

In general, there are several sources of uncertainties possibly affecting the NLO+PS results:

- Factorisation and renormalisation scale uncertainties. Normally, the NLO calculation underlying the NLO+PS generator has independent factorisation and renormalisation scales, and results are affected at the NNLO level if these scales are varied.
- Uncertainties related to the part of the real cross section that is treated with the shower algorithm.
- Uncertainties related to how the shower algorithm is implemented.
- Uncertainties related to the PDF's themselves and also whether the PDF's used in the shower algorithm are different from those used in the NLO calculation.
- Further uncertainties common to all shower generators, i.e. hadronisation, underlying event, etc.

We focus here on the first three items, which are by far the dominant ones. As a relevant and phenomenologically important observable, we consider the transverse-momentum distribution of the Higgs boson, in the process $\mathrm{gg} \to \mathrm{H}$. This observable is not a fully NLO one in the $\mathrm{gg} \to \mathrm{H} + X$ NLO cross-section calculation. For this reason it is very sensitive to both soft and hard effects and the NLO+PS results displays more marked differences with respect to the pure NLO calculation. The latter, in fact, is divergent for $p_{\mathrm{T}} \to 0$, with and infinite negative spike at $p_{\mathrm{T}} = 0$, representing the contribution of the virtual corrections. The NLO+PS approaches, instead, yield a positive cross section for all p_{T}, with the characteristic Sudakov peak at small p_{T}. Furthermore, this distribution can be computed (using the HQT program [171]) at a matched NNLL+NNLO accuracy, which can serve as a benchmark to characterise the output of the generators.

We begin by showing in Figure 22 the comparisons of MC@NLO + HERWIG and POWHEG + PYTHIA with HQT, with a choice of parameters that yields the best agreement, in shape, of the p_{T} distributions. This choice of parameters can be therefore considered the main outcome of this study, i.e. it embodies our recommendation for the settings of the two generators. The settings are as follows:

- MC@NLO should be run with the factorisation and renormalisation scale equal to M_{H}.
- POWHEG should be run with the h parameter equal to $M_{\mathrm{H}}/1.2$. For $M_{\mathrm{H}} = 120$ GeV, this setting is achieved introducing the line `hfact 100` in the `powheg.input` file.

In the figures, the uncertainty band of the MC@NLO+HERWIG and of POWHEG+PYTHIA, both compared to the HQT uncertainty band, are displayed. In the lower insert in the figure, the ratio of all results to the central value of HQT is also displayed. As stated above, MC@NLO+HERWIG is run with the central value of the renormalisation scale fixed to M_{H}, and POWHEG is run with the input line `hfact 100`. The red, solid curves represent the uncertainty band of the NLO+PS, while the dotted blue lines represent the band obtained with the HQT program. The reference scale is chosen equal to $M_{\mathrm{H}}/2$ in HQT, and the scale variations are performed in the same way as in the NLO+PS generators: once considers all variations of a factor of two above and below the central scale, with the restriction $0.5 < \mu_{\mathrm{R}}/\mu_{\mathrm{F}} < 2$. We have used the MSTW2008 NNLO central set for all curves. This is because HQT requires NNLO parton densities, and because we want to focus upon differences that have to do with the

[8] K. Hamilton, F. Maltoni, P. Nason and P. Torrielli.

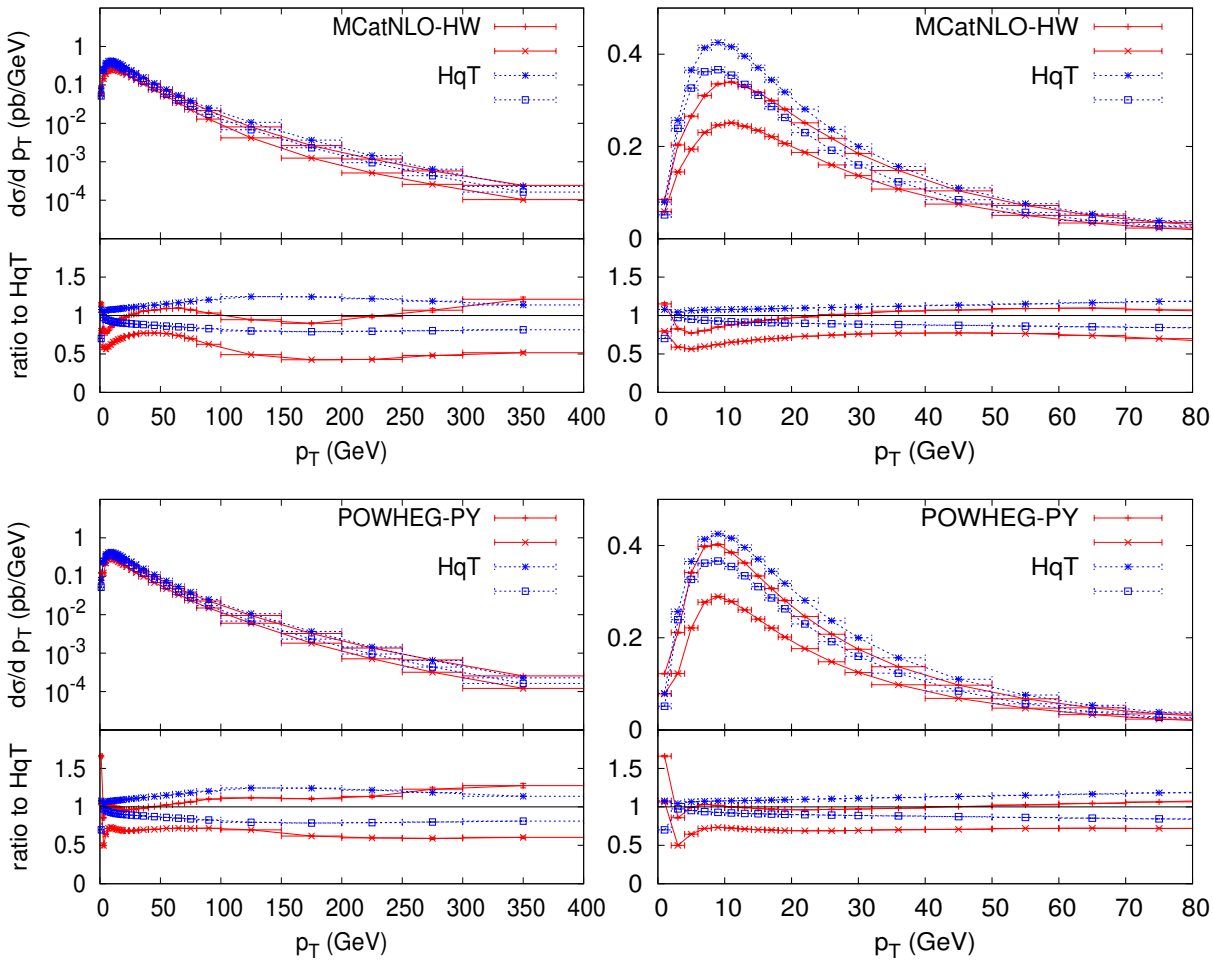

Fig. 22: Uncertainty bands for the transverse-momentum spectrum of the Higgs boson at LHC, 7 TeV, for a Higgs mass $M_{\rm H} = 120$ GeV. On the upper plots, the MC@NLO+HERWIG result obtained using the non-default value of the reference scale equal to $M_{\rm H}$. On the lower plots, the POWHEG+PYTHIA output, using the non-default $R^s + R^f$ separation. The uncertainty bands are obtained by changing $\mu_{\rm R}$ and $\mu_{\rm F}$ by a factor of two above and below the central value, taken equal to $M_{\rm H}$, with the restriction $0.5 < \mu_{\rm R}/\mu_{\rm F} < 2$.

calculation itself, rather than the PDF's. The HQT result has been obtained by running the program with full NNLL+NNLO accuracy, using the "switched" result. The resummation scale Q in HQT has been set to $M_{\rm H}/2$.

We notice that both programs are compatible in shape with the HQT prediction. We also notice that the error band of the two NLO+PS generators is relatively small at small $p_{\rm T}$ and becomes larger at larger $p_{\rm T}$. This should remind us that the NLO+PS prediction for the high $p_{\rm T}$ tail is in fact a tree-level-only prediction, since the production of a Higgs plus a light parton starts at order $\alpha_{\rm s}^3$, its scale variation is of order $\alpha_{\rm s}^4$, and its *relative* scale variation is of order $\alpha_{\rm s}^4/\alpha_{\rm s}^3$, i.e. of order $\alpha_{\rm s}$.[9] On the other hand the total integral of the curve, i.e. the total cross section (and in fact also the Higgs rapidity distribution, that is obtained by integrating over all transverse momenta) are given by a term of order $\alpha_{\rm s}^2$ plus a term of order $\alpha_{\rm s}^3$, and their scale variation is also of order $\alpha_{\rm s}^4$. Thus, their relative scale variation is of order $\alpha_{\rm s}^4/\alpha_{\rm s}^2$, i.e. $\alpha_{\rm s}^2$.

It is instructive to analyse the difference between MC@NLO and POWHEG at their default value of parameters. This is illustrated in Figure 23. The two programs are in reasonable agreement at

[9]Here we remind the reader that $\mu_{\rm F}^2 \frac{d}{d\mu_{\rm F}^2}\alpha_{\rm s}^3(\mu_{\rm R}) = -b_0 3\alpha_{\rm s}^4(\mu_{\rm R})$.

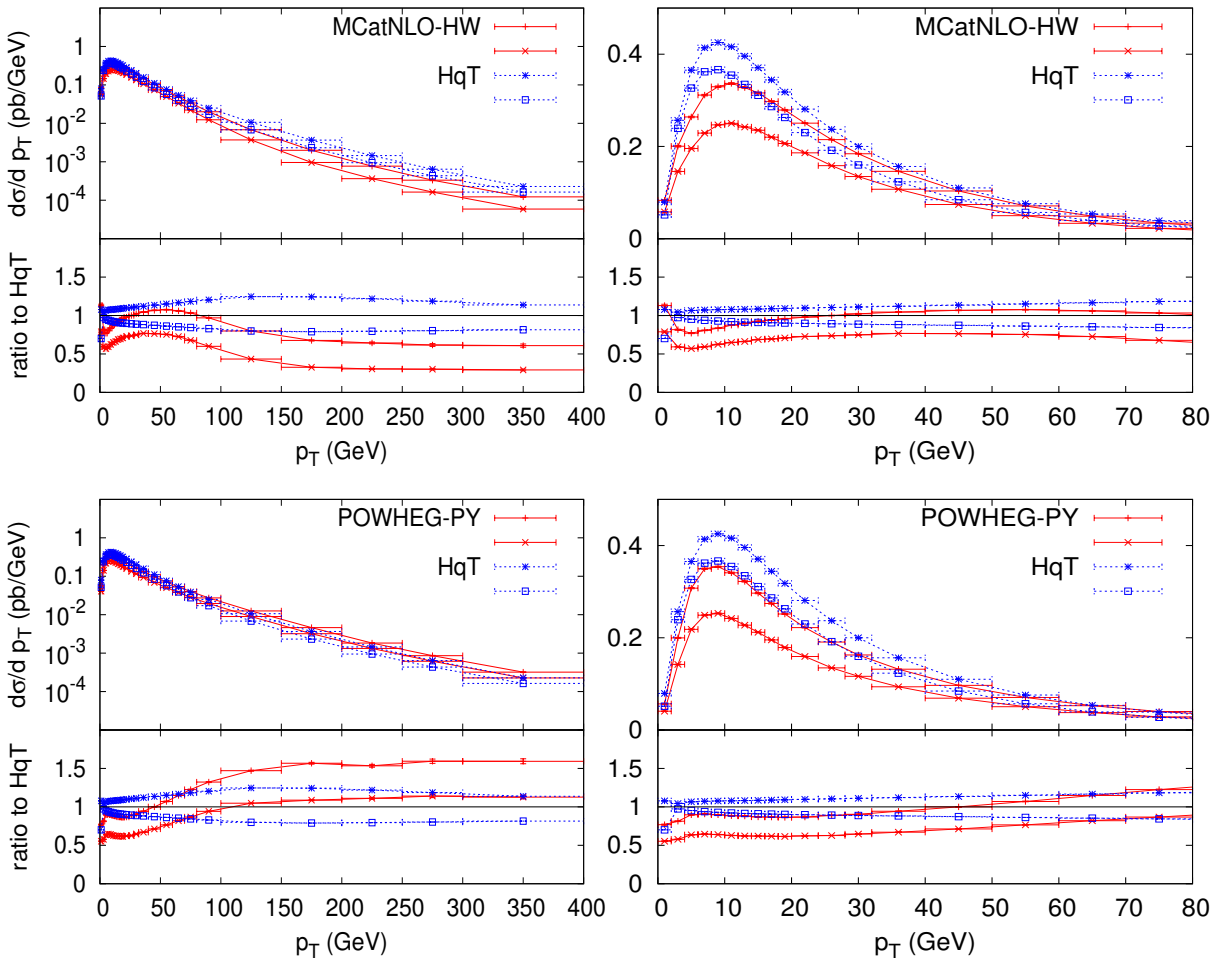

Fig. 23: The transverse-momentum spectrum of the Higgs in MC@NLO (upper) and in POWHEG+PYTHIA (lower) compared to the HQT result. In the lower insert, the same results normalised to the HQT central value are shown.

small transverse momentum, but display a large difference (about a factor of 3) in the high transverse momentum tail. This difference has two causes. One is the different scale choice in MC@NLO, where by default $\mu = m_{\rm T} = \sqrt{M_{\rm H}^2 + p_{\rm T}^2}$, where $p_{\rm T}$ is the transverse momentum of the Higgs. That accounts for a factor of $(\alpha_{\rm s}(m_{\rm T})/\alpha_{\rm s}(M_{\rm H}))^3$, which is about 1.6 for the last bin in the plots (compare the upper plots of Figure 22 with those of Figure 23). The remaining difference is due to the fact that in POWHEG, used with default parameters, the NLO K-factor multiplies the full transverse-momentum distribution. The POWHEG output is thus similar to what is obtained with NLO+PS generator, as already observed in the first volume of this Report.

This point deserves a more detailed explanation, which can be given along the lines of Ref. [132, 172]. We write below the differential cross section for the hardest emission in NLO+PS implementations (see the first volume of this report for details)

$$\mathrm{d}\sigma^{\rm NLO+PS} = \mathrm{d}\Phi_B \bar{B}^s(\Phi_B)\left[\Delta^s(p_\perp^{\rm min}) + \mathrm{d}\Phi_{R|B}\frac{R^s(\Phi_R)}{B(\Phi_B)}\Delta^s(p_{\rm T}(\Phi))\right] + \mathrm{d}\Phi_R R^f(\Phi_R), \qquad (11)$$

where

$$\bar{B}^s = B(\Phi_B) + \left[V(\Phi_B) + \int \mathrm{d}\Phi_{R|B} R^s(\Phi_{R|B})\right]. \qquad (12)$$

The sum $R^s + R^f$ yields the real cross section for $\mathrm{gg} \to \mathrm{Hg}$, plus the analogous terms for quark–gluon. Quark–antiquark annihilation is finite and therefore only contributes to R^f.

In MC@NLO, the R^s term is the shower approximation to the real cross section, and it depends upon the SMC that is being used in conjunction with it. In POWHEG, one has much freedom in choosing R^s, with the only constraint $R^s < R$, in order to avoid negative weights, and $R^s \to R$ in the small-transverse-momentum limit (in the sense that $R^s - R$ should be integrable in this region).

For the purpose of this review, we call $\mathbb{S}$ events (for shower) those generated by the first term on the r.h.s. of Eq. (11), i.e. those generated using the shower algorithm, and $\mathbb{F}$ (for finite) events those generated by the R^f term.[10] The scale dependence typically affects the $\bar{B}$ and the R^f terms in a different way. A scale variation in the square bracket on the r.h.s. of Eq. (11) is in practice never performed, since in MC@NLO this can only be achieved by changing the scale in the Monte Carlo event generator that is being used, and in POWHEG the most straightforward way to perform it (i.e. varying it naively by a constant factor) would spoil the NLL accuracy of the Sudakov form factor. We thus assume from now on that the scales in the square parenthesis are kept fixed. Scale variation will thus affect $\bar{B}^s$ and R^f.

We observe now that the shape of the transverse momentum of the hardest radiation in $\mathbb{S}$ events is not affected by scale variations, given that the square bracket on the r.h.s. of Eq. (11) is not affected by it, and that the factor $\bar{B}$ is p_{T} independent. From this, it immediately follows that the scale variation of the large-transverse-momentum tail of the spectrum is of relative order α_{s}^2, i.e. the same relative order of the inclusive cross section, rather than of relative order α_{s}, since $\bar{B}$ is a quantity integrated in the transverse momentum. Eq. (11), in the large-transverse-momentum tail, becomes

$$\mathrm{d}\sigma^{\mathrm{NLO+PS}} \approx \mathrm{d}\Phi_B \bar{B}^s(\Phi_B) \mathrm{d}\Phi_{R|B} \frac{R^s(\Phi_R)}{B(\Phi_B)} + \mathrm{d}\Phi_R R^f(\Phi_R). \tag{13}$$

From this equation we see that for large transverse momentum, the $\mathbb{S}$ event contribution to the cross section is enhanced by a factor $\bar{B}/B$, which is in essence the K-factor of the process. We wish to emphasize that this factor does not spoil the NLO accuracy of the result, since it affects the distribution by terms of higher order in α_{s}. Now, in POWHEG, in its default configuration, R^f is only given by the tiny contribution $\mathrm{q\overline{q}} \to \mathrm{Hg}$, which is non-singular, so that $\mathbb{S}$ events dominate the cross section. The whole transverse-momentum distribution is thus affected by the K-factor, yielding a result that is similar to what is obtained in ME+PS calculations, where the NLO K-factor is applied to the LO distributions. Notice also that changing the form of the central value of the scales again does not change the transverse-momentum distribution, that can only be affected by touching the scales in the Sudakov form factor.

A simple approach to give a realistic assessment of the uncertainties in POWHEG, is to also exploit the freedom in the separation $R = R^s + R^f$. Besides the default value $R^f = 0$, one can also perform the separation

$$R^s = \frac{h^2}{h^2 + p_{\mathrm{T}}^2} R\,, \qquad R^f = \frac{p_{\mathrm{T}}^2}{h^2 + p_{\mathrm{T}}^2} R\,. \tag{14}$$

In this way, $\mathbb{S}$ and $\mathbb{F}$ events are generated, with the former dominating the region $p_{\mathrm{T}} < h$ and the latter the region $p_{\mathrm{T}} > h$. Notice that by sending h to infinity one recovers the default behaviour. It is interesting to ask what happens if h is made vanishingly small. It is easy to guess that in this limit the POWHEG results will end up coinciding with the pure NLO result. The freedom in the choice of h, and also the freedom in changing the form of the separation in Eq. (14) can be exploited to explore further uncertainties in POWHEG. The Sudakov exponent changes by terms subleading in p_{T}^2, and so we can explore in this way uncertainties related to the shape of the Sudakov region. Furthermore, by suppressing R^s at large p_{T} the hard tail of the transverse-momentum distribution becomes more sensitive to the scale choice. The lower plots of Figure 22 displays the POWHEG result obtained using $h = M_{\mathrm{H}}/1.2$. Notice that in this way the large-transverse-momentum tail becomes very similar to the MC@NLO result. The

[10] In the MC@NLO language, these are called $\mathbb{S}$ and $\mathbb{H}$ events, where $\mathbb{S}$ stands for standard, and $\mathbb{H}$ for hard.

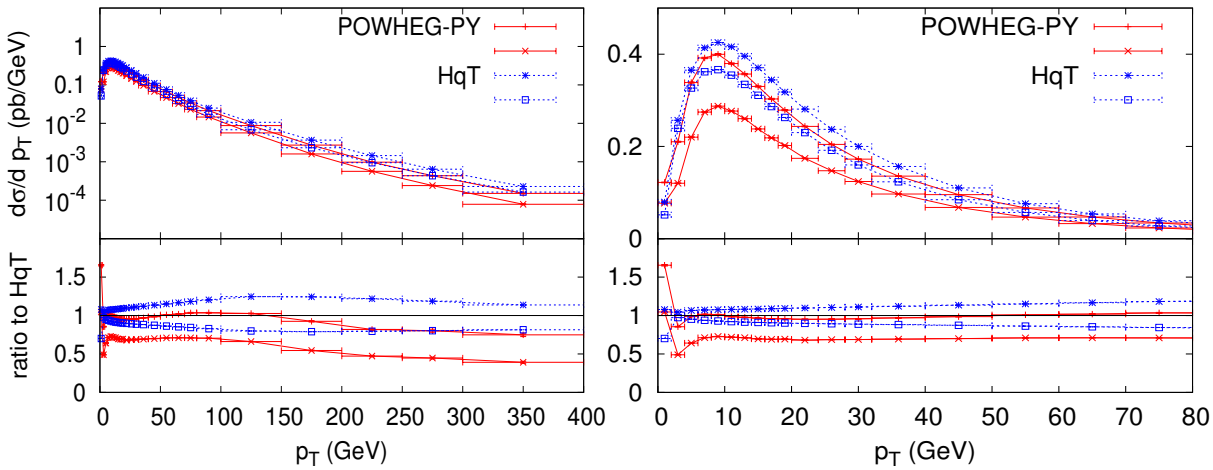

Fig. 24: The transverse-momentum spectrum of the Higgs in POWHEG+PYTHIA, using the separation of $\mathbb{S}$ and $\mathbb{F}$ events. The central scale is chosen equal to $\sqrt{p_{\rm T}^2 + M_{\rm H}^2}$.

shape of the distribution at smaller transverse momenta is also altered, and in better agreement with HQT. If $m_{\rm T}$ rather than $M_{\rm H}$ is chosen as reference value for the scale, we obtain the result of Figure 24, where we see also here a fall of the cross section at large transverse momentum.

The shape of the $p_{\rm T}$ distribution in MC@NLO+HERWIG is not much affected by the change of scale for $p_{\rm T} < 100$ GeV. This is due to the fact that this region is dominated by $\mathbb{S}$ events. It is interesting to ask whether this region is affected if one changes the underlying shower Monte Carlo generator. In MC@NLO, an interface to PYTHIA, using the virtuality-ordered shower, is also available [138]. The results are displayed in Figure 25. We observe the following. The large-transverse-momentum tails are consistent with the HERWIG version. We expect that since this region is dominated by $\mathbb{F}$ events. The shape of the Sudakov region has changed, showing a behaviour that is more consistent with the HQT central value, down to scales of about 30 GeV. Below this scale, we observe a 50% increase of the cross section as smaller $p_{\rm T}$ values are reached. It is clear from the figure that this feature is inherited from PYTHIA. In fact, the shape from the transverse-momentum spectrum in MC@NLO is inherited from the shower Monte Carlo. It is likely that the transverse-momentum-ordered PYTHIA may yield better agreement with the HQT result.

Summarizing, we find large uncertainties in both MC@NLO and POWHEG NLO+PS generators for Higgs production in gluon fusion. We have explored here uncertainties having to do with scale variation and to the separation of $\mathbb{S}$ and $\mathbb{F}$ events. If a higher accuracy result (namely HQT) was not available, the whole envelope of the uncertainties within each approach should be considered. These large uncertainties are all a direct consequence of the large NLO K-factor of the $\rm gg \to H$ process. In spite of this fact, we have seen that there are choices of scales and parameters that bring the NLO+PS results close in shape to the higher-accuracy calculation of the transverse-momentum spectrum provided by the HQT program. It is thus advisable to adopt these choices.

4.3 Uncertainties in $\rm gg \to H \to WW^{(*)}$[11]

In this section a wide variety of different physics effects and uncertainties related to key observables in the process $\rm gg \to H \to W^+W^- \to \mu^+ \nu_\mu e^- \overline{\nu}_e$ is presented; they include

– an appraisal of NLO matching methods, including a comparison with HNNLO [173] for some observables on the parton level;

[11] M. Grazzini, H. Hoeth, F. Krauss, F. Petriello, M. Schönherr and F. Siegert.

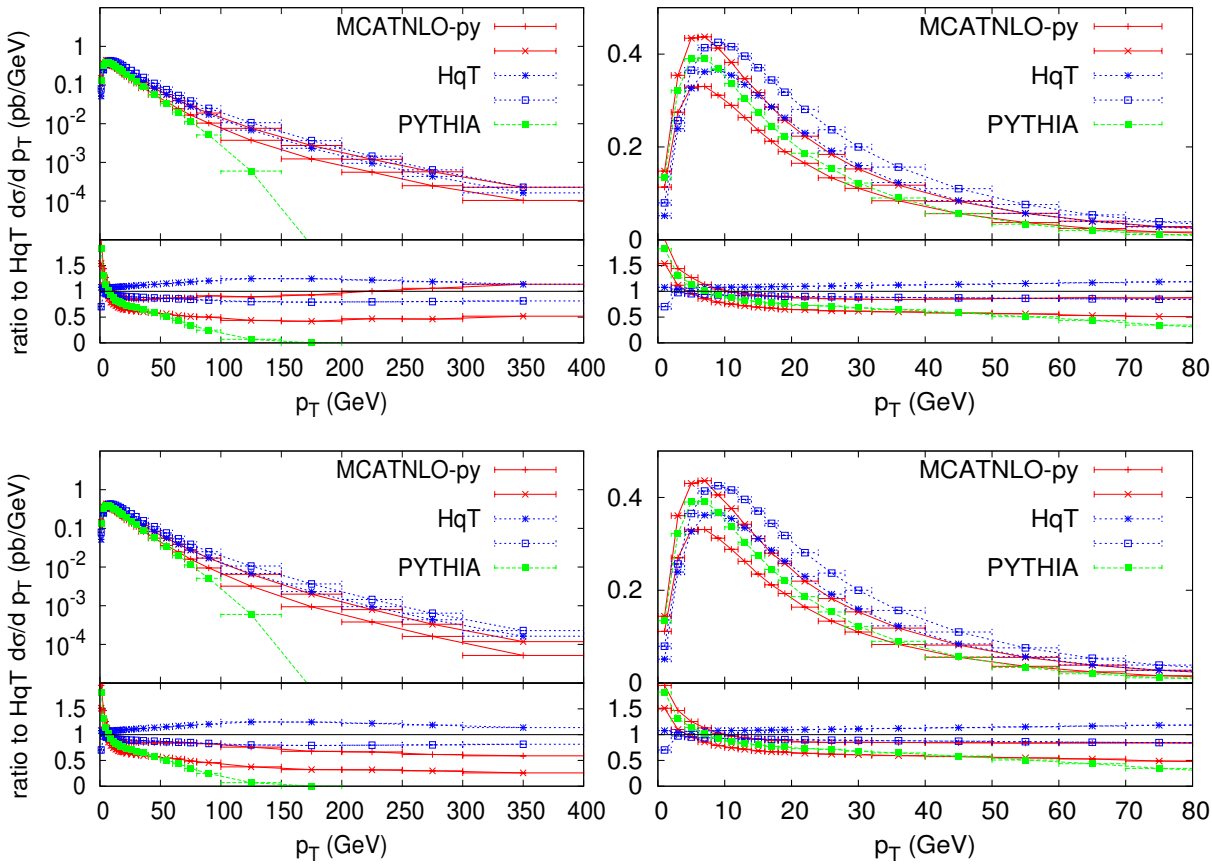

Fig. 25: The transverse-momentum spectrum of the Higgs in MC@NLO+PYTHIA. The central scale is chosen equal to $M_{\rm H}$ in the upper plot, and to $\sqrt{p_{\rm T}^2 + M_{\rm H}^2}$ in the lower plot. The bare PYTHIA result, normalised to the HQT central value total cross section, is also shown.

- perturbative uncertainties, like the impact of scale and PDF variations;
- the impact of parton showering and non-perturbative effects on parton-level results; and
- non-perturbative uncertainties, and in particular the impact of fragmentation variations and the effect of the underlying event and changes in its simulation.

4.3.1 Setup

In the following sections the SHERPA event generator [174] has been used in two modes: Matched samples have been produced according to the POWHEG [123, 126] and MC@NLO [116] methods, implemented as described in [157] and [159], respectively. In the following the corresponding samples will be denoted as SHERPA–POWHEG and SHERPA–MC@NLO, respectively. Unless stated otherwise, $M_{\rm H} = 160$ GeV and the following cuts have been applied to leptons ($\ell = {\rm e}, \mu$) and jets j:

- leptons: $p_{\rm T}^{(\ell)} > 15$ GeV and $|\eta^{(\ell)}| < 2.5$,
- jets (defined by the anti-$k_{\rm T}$ algorithm [175] with $R = 0.4$): $p_{\rm T}^{(j)} > 25$ GeV, $|\eta^{(j)}| < 4.5$.

By default, for purely perturbative studies, the central PDF from the MSTW2008 NLO set [107] has been used, while for those plots involving non-perturbative effects such as hadronisation and the underlying event, the central set of CT10 NLO [104] has been employed, since SHERPA has been tuned to jet data with this set. In both cases, the PDF set also fixes the strong coupling constant and its running behaviour in both matrix element and parton shower, and in the underlying event.

4.3.2 *Algorithmic dependence:* POWHEG *vs.* MC@NLO

Before embarking in this discussion, a number of points need to be stressed:

1. The findings presented here are very recent, and they are partially at odds with previous conclusions. So they should be understood as contributions to an ongoing discussion and hopefully trigger further work;
2. clearly the issue of scales and, in particular, of resummation scales tends to be tricky. By far and large, however, the community agrees that the correct choice of resummation scale Q is of the order of the factorisation scale, in the case at hand here, therefore $Q = \mathcal{O}(M_{\rm H})$ [12]. It is notoriously cumbersome to directly translate analytic resummation and scale choices there to parton-shower programs;
3. the version of the MC@NLO algorithm presented here differs in some aspects from the version implemented in the original MC@NLO program; there, typically the HERWIG parton shower is being used, guaranteeing an upper limitation in the resummed phase space given by the factorisation scale, and the FKS method [176] is used for the infrared subtraction on the matrix-element level, the difference is compensated by a suitable correction term. In contrast, here, SHERPA is used, where both the parton shower and the infrared subtraction rely on Catani–Seymour subtraction [177, 178], and the phase-space limitation in the resummation bit is varied through a suitable parameter [179] $\alpha \in [0,\ 1]$, with $\alpha = 1$ relating to no phase-space restriction. We will indicate the choice of α by a superscript. However, the results shown here should serve as an example only.

Starting with a comparison at the matrix-element level, consider Figure 26, where results from HNNLO are compared with an NLO calculation and the POWHEG and MC@NLO implementations in SHERPA where the parton shower has been stopped after the first emission. For the Higgs-boson transverse momentum we find that the HNNLO result is significantly softer than both the SHERPA–POWHEG and the SHERPA–MC@NLO $^{(\alpha=1)}$ sample – both have a significant shape distortion w.r.t. HNNLO over the full $p_{\rm T}({\rm H})$ range. In contrast the NLO and the SHERPA–MC@NLO $^{(\alpha=0.03)}$ result have a similar shape as HNNLO in the mid-$p_{\rm T}$ region, before developing a harder tail. The shape differences in the low-$p_{\rm T}$ region, essentially below $p_{\rm T}({\rm H})$ of about 20 GeV, can be attributed to resummation effects. The picture becomes even more interesting when considering jet rates at the matrix element level. Here, both the SHERPA–POWHEG and the SHERPA–MC@NLO $^{(\alpha=1)}$ sample have more 1 than 0-jet events, clearly at odds with the three other samples. Of course, switching on the parton shower will lead to a migration to higher jet bins, as discussed in the next paragraph. With this in mind, one could argue that the 1-jet rates in both the SHERPA–POWHEG and the SHERPA–MC@NLO $^{(\alpha=1)}$ sample seem to be in fair agreement with the *inclusive* 1-jet rate of HNNLO – this however does not resolve the difference in the 0-jet bin, and ultimately it nicely explains why these two samples produce a much harder radiation tail than HNNLO.

In Figure 27 now all plots are at the shower level. We can summarise the findings of this figure as follows: The SHERPA–POWHEG and SHERPA–MC@NLO $^{(\alpha=1)}$ results exhibit fairly identical trends for most observables, in particular, the Higgs-boson transverse momentum in various samples tends to be harder than the pure NLO result, HNNLO, or SHERPA–MC@NLO $^{(\alpha=0.03)}$. Comparing HNNLO with the NLO result and SHERPA–MC@NLO $^{(\alpha=0.03)}$ we find that in most cases the latter two agree fairly well with each other, while there are differences with respect to HNNLO. In the low-$p_{\rm T}$ region of the Higgs boson, the difference seems to be well described by a global K-factor of about $1.3s-1.5$, while HNNLO becomes softer in the high-$p_{\rm T}$ tail, leading to a sizable shape difference. One may suspect that this is due to a different description of configurations with two jets, where quantum interferences lead to non-trivial correlations of the outgoing particles in phase space, which, of course, are correctly accounted for in HNNLO, while the other results either do not include such configurations (the parton-level NLO curve) or rely on the spin-averaged and therefore correlation-blind parton shower to describe

[12] In HQT this scale by default is chosen to be $Q = M_{\rm H}/2$.

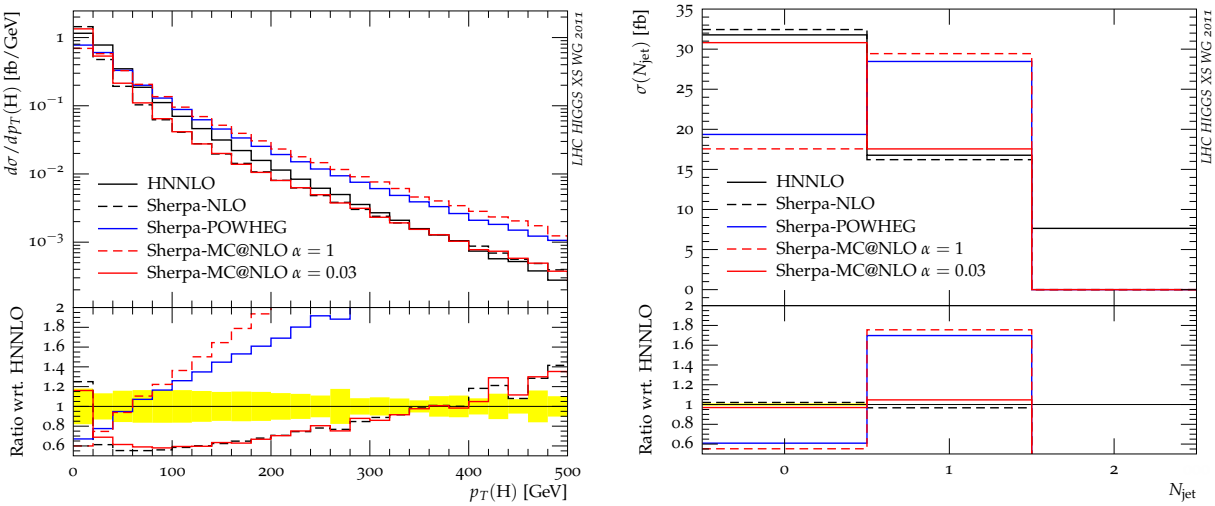

Fig. 26: The Higgs transverse momentum in all events (left) and the jet multiplicities (right) in $\mathrm{pp} \to \mathrm{H} \to \mathrm{e}^- \mu^+ \nu_\mu \bar{\nu}_\mathrm{e}$ production. Here different approaches are compared with each other: two fixed order parton-level calculations at NNLO (HNNLO, black solid) and NLO (black, dashed), and three matched results in the SHERPA implementations (SHERPA-POWHEG, blue and SHERPA-MC@NLO with $\alpha = 1$, red dashed and with $\alpha = 0.03$, red solid) truncated after the first emission. The yellow uncertainty band is given by the scale uncertainties of HNNLO.

them. This is also in agreement with findings in the jet multiplicities, where the SHERPA–MC@NLO $^{(\alpha=0.03)}$ and the NLO result agree with HNNLO in the 0-jet bin, while the SHERPA–POWHEG and SHERPA–MC@NLO $^{(\alpha=1)}$ result undershoot by about 30%, reflecting their larger QCD activity. For the 1- and 2-jet bins, however, their agreement with the HNNLO result improves and in fact, as already anticipated from the ME-level results, multiplying the SHERPA–POWHEG result with a global K-factor of about 1.5 would bring it to a very good agreement with HNNLO for this observable. In contrast the SHERPA–MC@NLO $^{(\alpha=0.03)}$ result undershoots HNNLO in the 1-jet bin by about 25% and in the 2-jet bin by about a factor of 4. Clearly here support from higher order tree-level matrix elements like in ME+PS or MENLOPS-type [136, 150] approaches would be helpful.

Where not stated otherwise, in the following sections, all curves relate to an NLO matching according to the SHERPA–MC@NLO prescription with $\alpha = 0.03$.

4.3.3 Perturbative uncertainties

The impact of scale variations on the Higgs transverse momentum in all events and in events with 0, 1, and 2 or more jets is exhibited in Figure 28, where a typical variation by factors of 2 and $1/2$ has been performed around the default scales $\mu_\mathrm{R} = \mu_\mathrm{F} = M_\mathrm{H}$. For the comparison with the fixed scale we find that distributions that essentially are of leading order accuracy, such as p_T distributions of the Higgs boson in the 1-jet region or the 1-jet cross section, the scale uncertainty is of the order of 40%, while for results in the resummation region of the parton shower, i.e., the 0-jet cross section or the Higgs-boson transverse momentum in the 0-jet bin, the uncertainties are smaller, at about 20%.

In contrast differences between the functional form of the scales choice are smaller, also exemplified in Figure 28, where the central value $\mu_\mathrm{F} = \mu_\mathrm{R} = M_\mathrm{H}/2$ has been compared with an alternative scale $\mu_\mathrm{F} = \mu_\mathrm{R} = m_\mathrm{T}^\mathrm{H}/2 = \sqrt{M_\mathrm{H}^2 + p_{T,\mathrm{H}}^2}/2$. It should be noted though that there the two powers of α_s related to the effective ggH vertex squared have been evaluated at a scale $\frac{1}{2} M_\mathrm{H}$. Anyway, with this in mind it is not surprising that differences only start to become sizable in the large-p_T regions of additional radiation, where they reach up to about 40%.

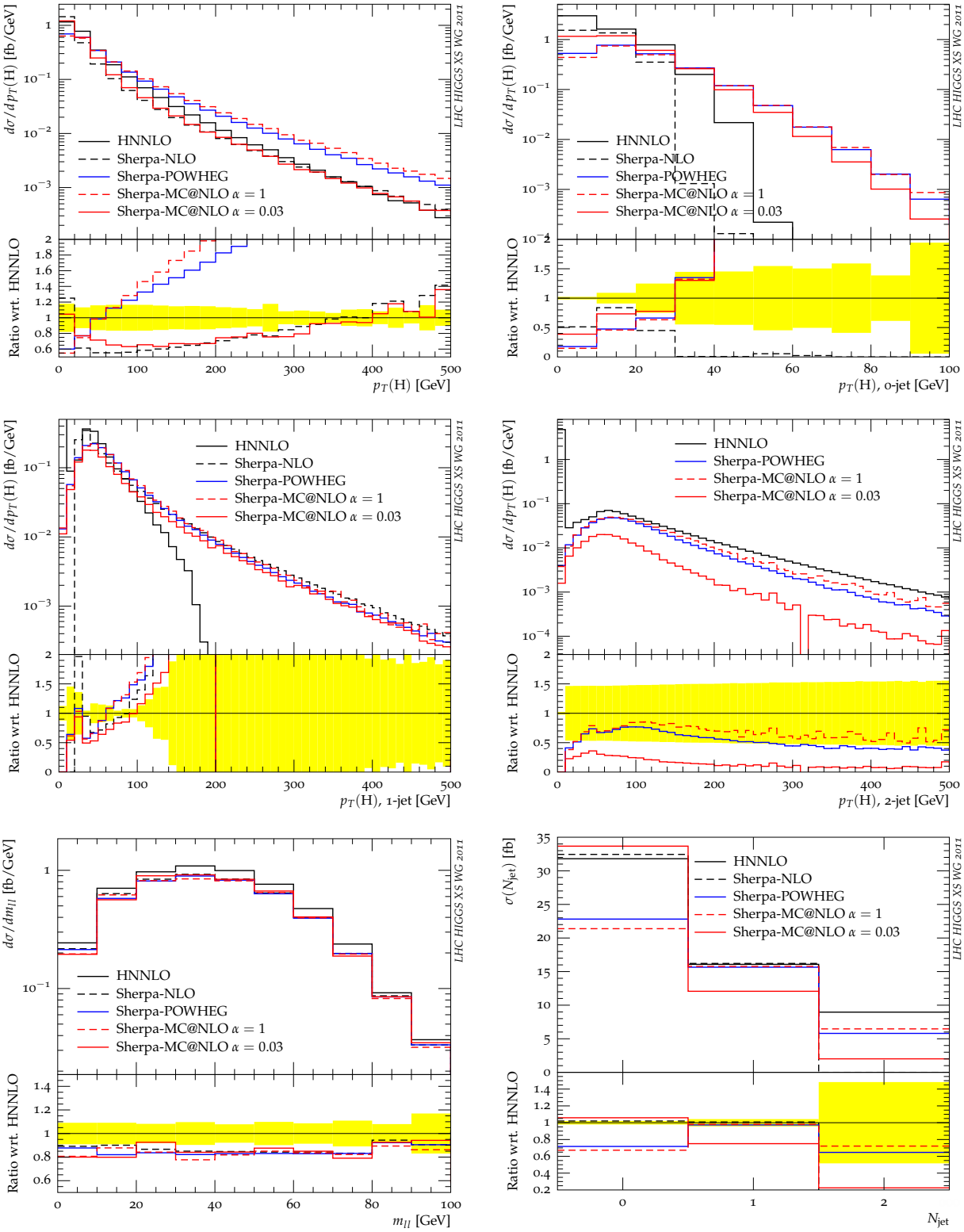

Fig. 27: The Higgs transverse momentum in all events, in events with 0, 1, and 2 and more jets, the invariant lepton mass, and the jet multiplicities in $pp \to H \to e^- \mu^+ \nu_\mu \bar{\nu}_e$ production. Here different approaches are compared with each other: two fixed-order parton-level calculations at NNLO (HNNLO, black solid) and NLO (black, dashed), and three matched results in the SHERPA implementations (SHERPA–POWHEG, blue and SHERPA–MC@NLO with $\alpha = 1$, red dashed and with $\alpha = 0.03$, red solid). The yellow uncertainty band is given by the scale uncertainties of HNNLO.

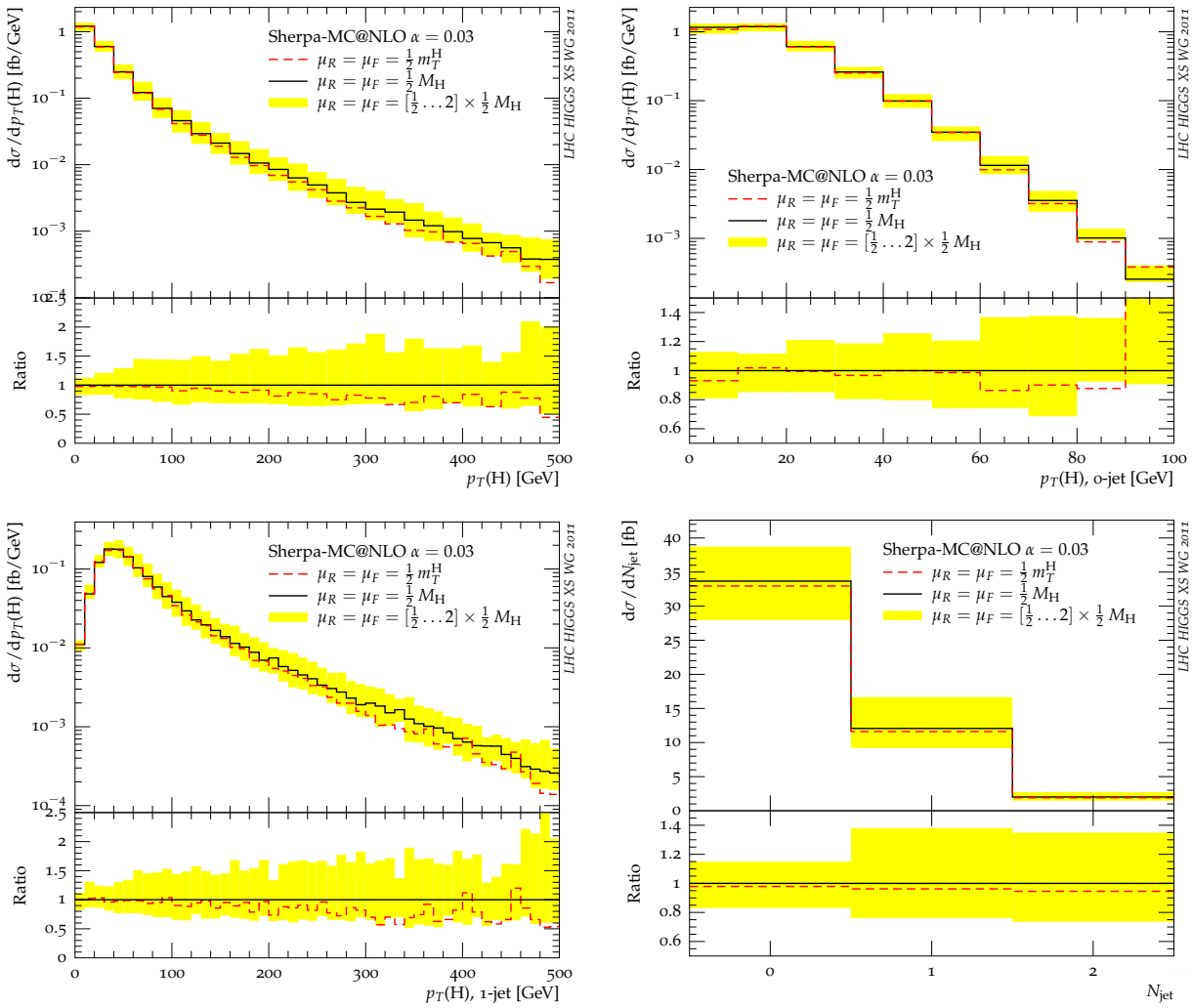

Fig. 28: The impact of scale variation by a factor of 2 and $1/2$ (yellow band) around the central scale $\mu_R = \mu_F = M_H/2$ (black solid line) and of a variation of the functional form of the scale to $\mu_R = \mu_F = \frac{1}{2} m_T^H$ (red dashed line) on the transverse momentum of the Higgs boson in all events, events with no and with one jet, and on jet multiplicities. All curves are obtained by an NLO matching according to the SHERPA–MC@NLO prescription with $\alpha = 0.03$.

Rather than performing a full PDF variation according to the recipe in Ref. [180], in Figure 29 results for MSTW2008 NLO, have been compared to those obtained with the central NLO set of CT10. By far and large, there is no sizable difference in any relevant shape. However, a difference of about 10% can be observed in the total normalisation, which can be traced back to the combined effect of minor differences in both the gluon PDF and the value of α_s.

4.3.4 Parton to hadron level

In Figure 30 the impact of adding parton showering, fragmentation, and the underlying event is exemplified for the same observables as in the figures before. In addition, the invariant lepton mass and the jet multiplicities are exhibited at the same stages of event generation. All curves are obtained by an NLO matching according to the SHERPA–MC@NLO prescription with $\alpha = 0.03$. In the following, the CT10 PDF was used to be able to use the corresponding tuning of the non-perturbative SHERPA parameters.

In general, the effect of parton showering is notable, resulting in a shift of the transverse momentum of the Higgs boson away from very low transverse momenta to values of about $20-80$ GeV with

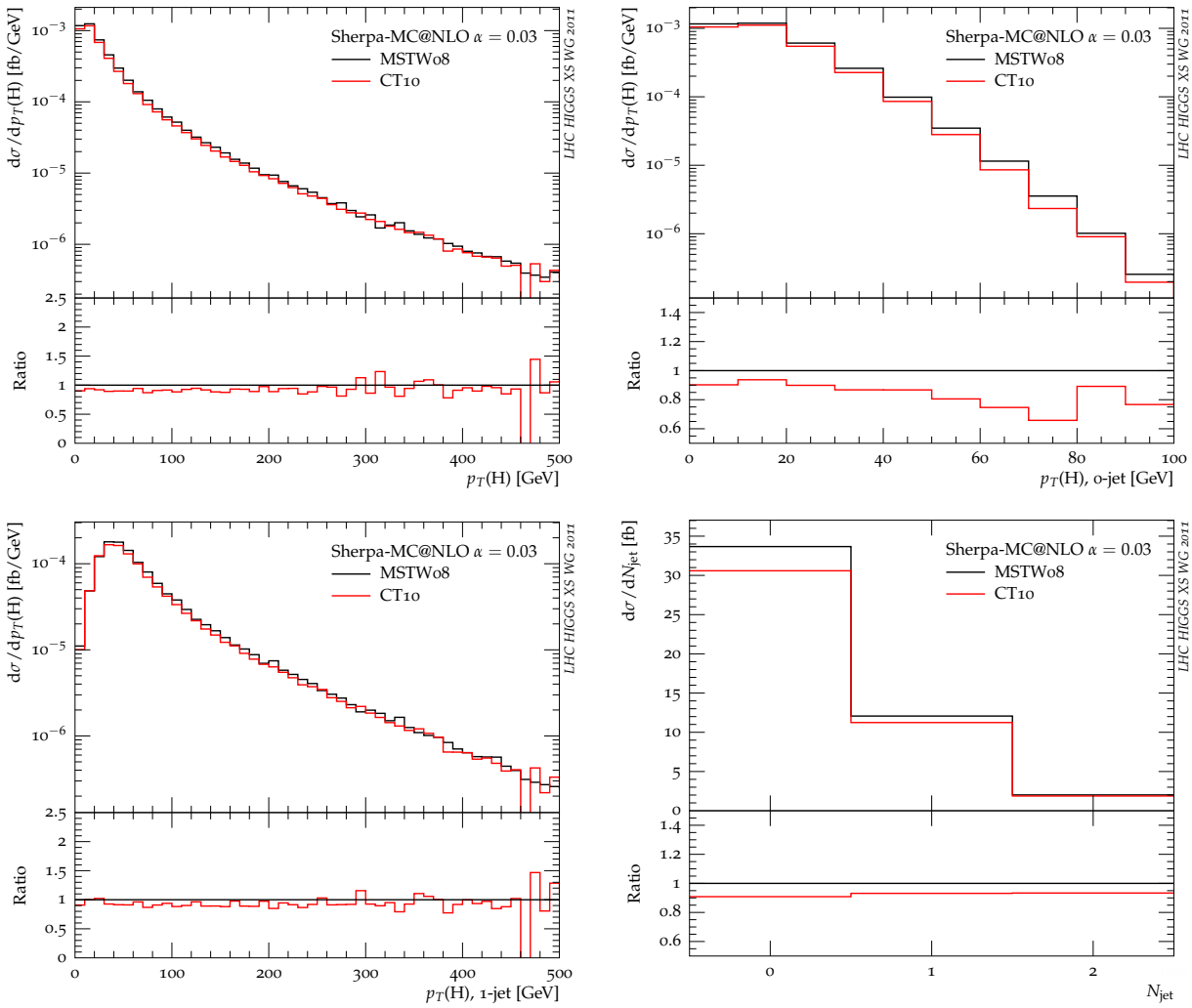

Fig. 29: The impact of different choices of PDFs – MSTW2008 NLO (black) and CT10 NLO (red) – for a $M_{\mathrm{H}} = 160$ GeV on the transverse momentum of the Higgs boson in all events, events with no and with one jet, and on jet multiplicities. All curves are obtained by an NLO matching according to the SHERPA-MC@NLO prescription with $\alpha = 0.03$.

deviations up to 10%. This effect is greatly amplified in the exclusive jet multiplicities, where the *exclusive* 1-jet bin on the parton level feeds down to higher jet multiplicities emerging in showering, leading to a reduction of about 50% in that bin (which are of course compensated by higher bins such that the net effect on the *inclusive* 1-jet bin is much smaller). A similar effect can be seen in the Higgs transverse momentum in the exclusive 0-jet bin, where additional radiation allows for larger transverse kicks of the Higgs boson without actually resulting in jets. In all cases, however, the additional impact of the underlying event is much smaller, with a maximal effect of about $15-20\%$ in the 2-jet multiplicity and in some regions of the Higgs transverse momentum.

4.3.5 Non-perturbative uncertainties

In the following, uncertainties due to non-perturbative effects have been estimated. Broadly speaking, two different physics reasons have been investigated, namely the impact of fragmentation, which has been assessed by switching from SHERPA's default cluster fragmentation [181] to the Lund string

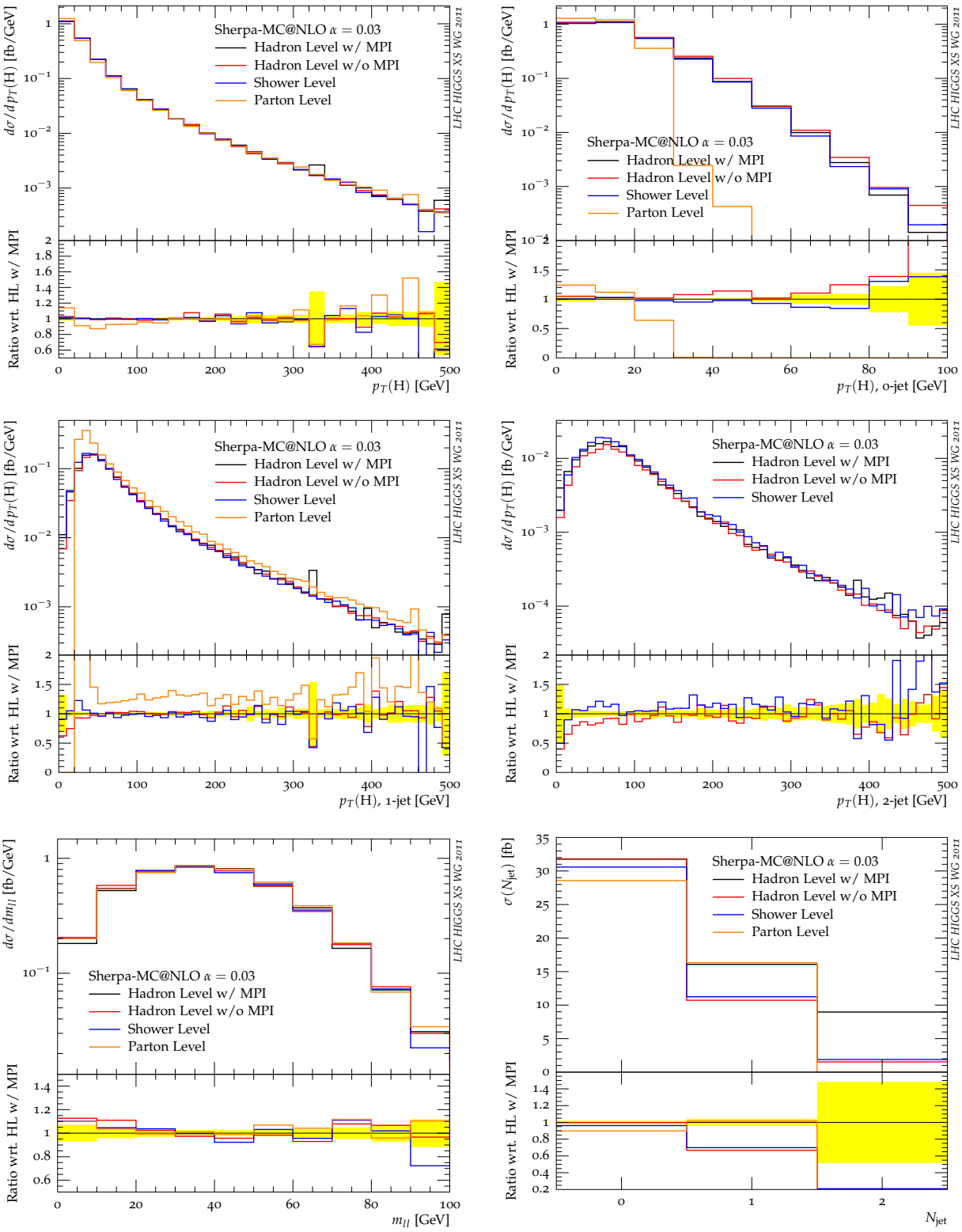

Fig. 30: The impact of going from the parton level (orange) over the parton shower level (red) to the hadron level without (blue) and with (black) the underlying event. The error band relates to the statistical fluctuations of the reference result – the full simulation. All curves are obtained by an NLO matching according to the SHERPA–MC@NLO prescription with $\alpha = 0.03$.

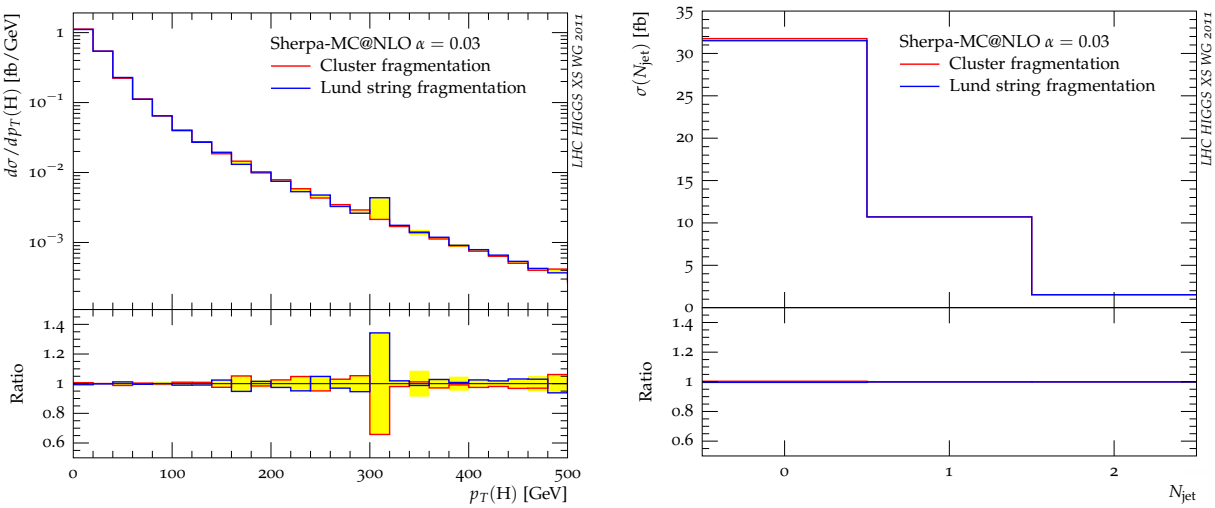

Fig. 31: The impact of different fragmentation models – cluster (black) and string (red) – for a $M_{\mathrm{H}} = 160$ GeV on the transverse momentum of the Higgs boson in all events, and on jet multiplicities. All curves are obtained by an NLO matching according to the SHERPA–MC@NLO prescription with $\alpha = 0.03$. The yellow band indicates a combination of statistical differences and the differences of the two fragmentation schemes.

fragmentation [182] encoded in PYTHIA6.4 [183] and suitably interfaced[13], and the impact of variations in the modelling of the underlying event. There SHERPA's model, which is based on [184], has been modified such that the transverse activity (the plateau region of N_{ch} in the transverse region) is increased/decreased by 10%.

We find that in all relevant observables the variation of the fragmentation model leads to differences which are consistent with statistical fluctuations in the different Monte Carlo samples. This is illustrated by the Higgs-boson transverse momentum and the jet multiplicities, displayed in Figure 31.

Similarly, differences due to the underlying event on the Higgs boson transverse momentum and various jet-related observables are fairly moderate and typically below 10%. This is especially true for jet multiplicities, where the 10% variation of the underlying event activity translates into differences of the order of $2-3\%$ only. However, it should be stressed here that the variation performed did not necessarily affect the hardness of the parton multiple scatterings, i.e., the amount of jet production in secondary parton scatters, but rather increased the number of comparably soft scatters, leading to an increased soft activity. In order to obtain a more meaningful handle on jet production due to multiple parton scattering dedicated analyses are mandatory in order to validate and improve the relatively naive model employed here.

[13] Both fragmentation schemes in the SHERPA framework have been tuned to the same LEP data, yielding a fairly similar quality in the description of data.

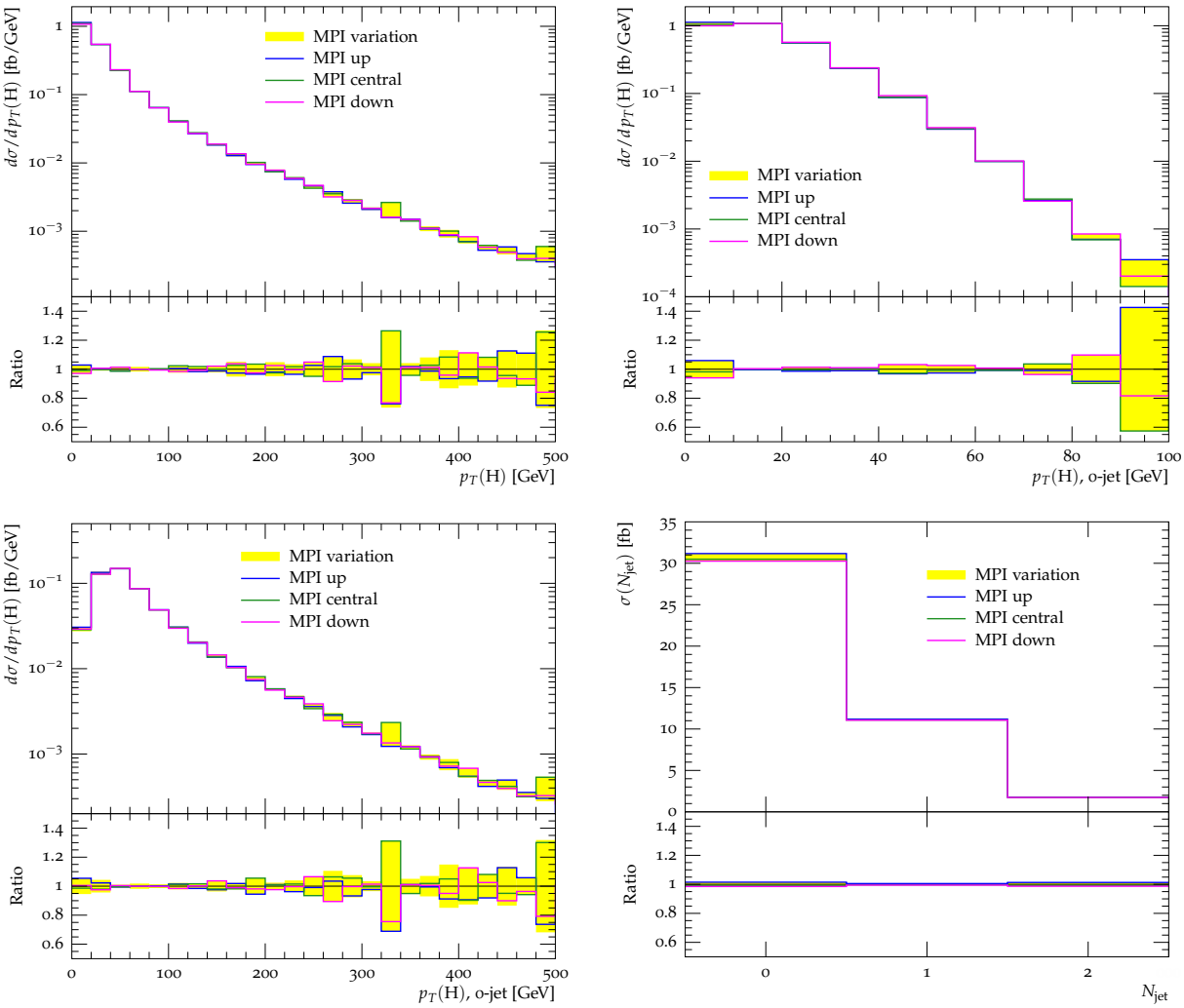

Fig. 32: Differences in the Higgs-boson transverse momentum in all events, in events with 0, 1, and in jet multiplicities due to variations in the modelling of the underlying event – central (black) vs. increased (blue) and suppressed (purple) activity – for a $M_{\mathrm{H}} = 160$ GeV. All curves are obtained by an NLO matching according to the SHERPA–MC@NLO prescription with $\alpha = 0.03$. The yellow band indicates the uncertainties related to the modelling of the underlying event.

4.4 Systematic studies of NLO MC tools in experimental implementations

In conjunction with systematic studies of theoretical tools, described in the previous sections, the NLO MC group has estimated the systematic uncertainties of the NLO MC tools in their implementation within the event-generation framework of the ATLAS and CMS experiments. This section describes the results of these studies performed both at the parton level, after hard scatterer parton showering, and after a fast detector simulation to account for detector effects.

The initial plans for the systematic uncertainty studies entail as follows:

- Higgs production process: gluon fusion, $\mathrm{gg} \to \mathrm{H}$;
- decay processes: $\mathrm{H} \to \mathrm{WW} \to \mathrm{l\nu l\nu}$ and $\mathrm{H} \to \mathrm{ZZ} \to 4\mathrm{l}$;
- MC tools: POWHEG BOX, MC@NLO, SHERPA, and HERWIG++;
- parton showering: PYTHIA and HERWIG;
- Higgs mass: 130 GeV and 170 GeV;
- PDF: MSTW, CT10, NNPDF, and CTEQ6.6;
- underlying events: Initial stage to switch off the UE in PYTHIA and switch off the soft UE in HERWIG to focus on matrix-element and parton-shower effects.

In the following sections, we describe the current studies with POWHEG interfaced with two different parton showering (PS) programs, PYTHIA or HERWIG, as implemented in ATLAS and CMS MC event generation.

4.4.1 NLO Monte Carlo tools and parameters

The study presented hereafter is based on the ATLAS implementation of POWHEG+PYTHIA and POWHEG+HERWIG. Two different Higgs mass values are considered: $M_{\mathrm{H}} = 170$ GeV and $M_{\mathrm{H}} = 130$ GeV, with 38 MeV and 4.9 MeV widths, respectively. The parton distribution function (PDF) CTEQ6.6 set is used for this study. All other parameters are kept at the default values implemented in POWHEG [172]. We present here the results for the $\mathrm{H} \to \mathrm{WW} \to \mathrm{l\nu l\nu}$ final state. This is one of the most relevant channels for discovery. A study for the other golden channel $\mathrm{H} \to \mathrm{ZZ} \to 4\mathrm{l}$ is in progress.

4.4.2 Comparisons of POWHEG+PYTHIA *or* POWHEG+HERWIG

The statistics of the $\mathrm{H} \to \mathrm{WW} \to \mathrm{l\nu l\nu}$ event samples consists of 22k events for POWHEG+PYTHIAand 50k event for POWHEG+HERWIG, for each Higgs mass values, $M_{\mathrm{H}} = 170$ GeV and 130 GeV. The event generator is interfaced to ATLAS fast detector simulation to include detector effects. This, however, along with the specific final-state selection scheme slowed down the event generation significantly, costing us about a week per sample. In order to expedite complicated systematic uncertainties, such as that of PDF, it would be desirable to improve the speed of specific selection schemes. The results presented in this section, however, are using the particle-level information without using the fast simulation to be comparable with studies carried out in other sections.

The comparisons of various Higgs kinematic quantities with POWHEG+PYTHIA and POWHEG+HERWIG showering have been investigated. Most the kinematic variables, such as Higgs mass, W transverse mass and the kinematic variables of the leptons from the decay show no appreciable differences between POWHEG+PYTHIA and POWHEG+HERWIG parton showering. Figure 33.(a) for $M_{\mathrm{H}} = 130$ GeV and Figure 34.(a) for $M_{\mathrm{H}} = 170$ GeV show good agreements between PYTHIA and HERWIG parton showering. The solid red circles in all plots represent the quantities from POWHEG+PYTHIA while the blue histograms represent those from POWHEG+HERWIG. The bin-by-bin ratio of POWHEG+HERWIG distributions with respect to POWHEG+PYTHIA distributions is shown in the lower plots, to compare the shapes of the distributions. However, as can be seen in Figure 33.(b) for $M_{\mathrm{H}} = 130$ GeV and Figure 34.(b) for $M_{\mathrm{H}} = 170$ GeV, a systematic difference between the

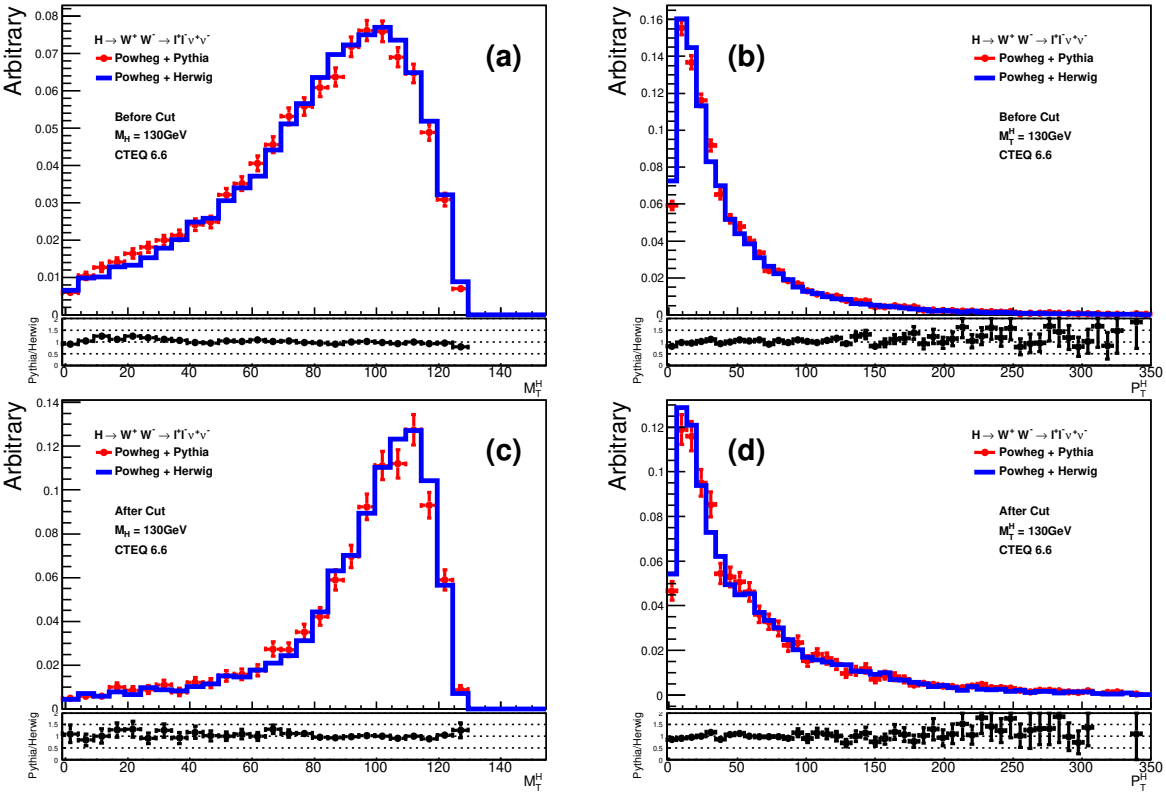

Fig. 33: (a) Higgs transverse mass without cuts, (b) Higgs transverse momentum without cuts, (c) Higgs transverse mass with cuts, and (d) Higgs transverse momentum with cuts for POWHEG+PYTHIA parton showering (red circles) and for POWHEG+HERWIG parton showering (blue histogram) for $M_{\rm H} = 130$ GeV. The plots below each of the histogram are the ratio of POWHEG+HERWIG with respect to POWHEG+PYTHIA.

two PS schemes is observed for this quantity. A systematic trend that the POWHEG+PYTHIA events display harder Higgs $p_{\rm T}$ distribution than for POWHEG+HERWIG can be seen clearly from the ratio plots, despite the fact that the statistical uncertainties increases as $p_{\rm T}$ grows. The linear fit to the ratio for Higgs $p_{\rm T}$ shows this trend with the value of the slope at $(9.1 \pm 2.6) \times 10^{-4}$ and $(6.2 \pm 1.6) \times 10^{-4}$ for $M_{\rm H} = 130$ GeV and $M_{\rm H} = 170$ GeV, respectively, demonstrating statistically significant systematic effect. The same trends have been observed in $p_{\rm T}$ of the $\rm W^+$ and $\rm W^-$ from the Higgs decay as well.

In order to investigate this effect further, we have looked into the $p_{\rm T}$ distributions of the jets, number of associated jets and jet efficiencies as a function of jet $p_{\rm T}$ cut values as shown in Figure 35 for $M_{\rm H} = 170$ GeV and $M_{\rm H} = 130$ GeV. It is shown that PYTHIA produces harder jet $p_{\rm T}$ distributions of the jets since their momentum must balance that of the Higgs.

4.4.3 Studies with experimental cuts

In order to ensure the relevance of these results for the experimental searches, the cuts applied in this study follow the recommendation from ATLAS $\rm H \to WW$ search group [185], as follows:

- exactly two leptons
- first leading lepton (l1) $p_{\rm T} > 25$ GeV, subleading lepton (l2) $p_{\rm T} > 15$ GeV;
- Two leptons have opposite charge $M_{\rm ll} > 15$ GeV;
- if l1,l2 have the different flavour, $M_{\rm ll} > 10$ GeV;
- if l1,l2 have the same flavours, apply a Z veto, $|M_{\rm ll} - M_{\rm Z}| > 15$ GeV;
- if l1,l2 has the same flavours $p_{\rm T}^{\rm ll} > 30$ GeV;

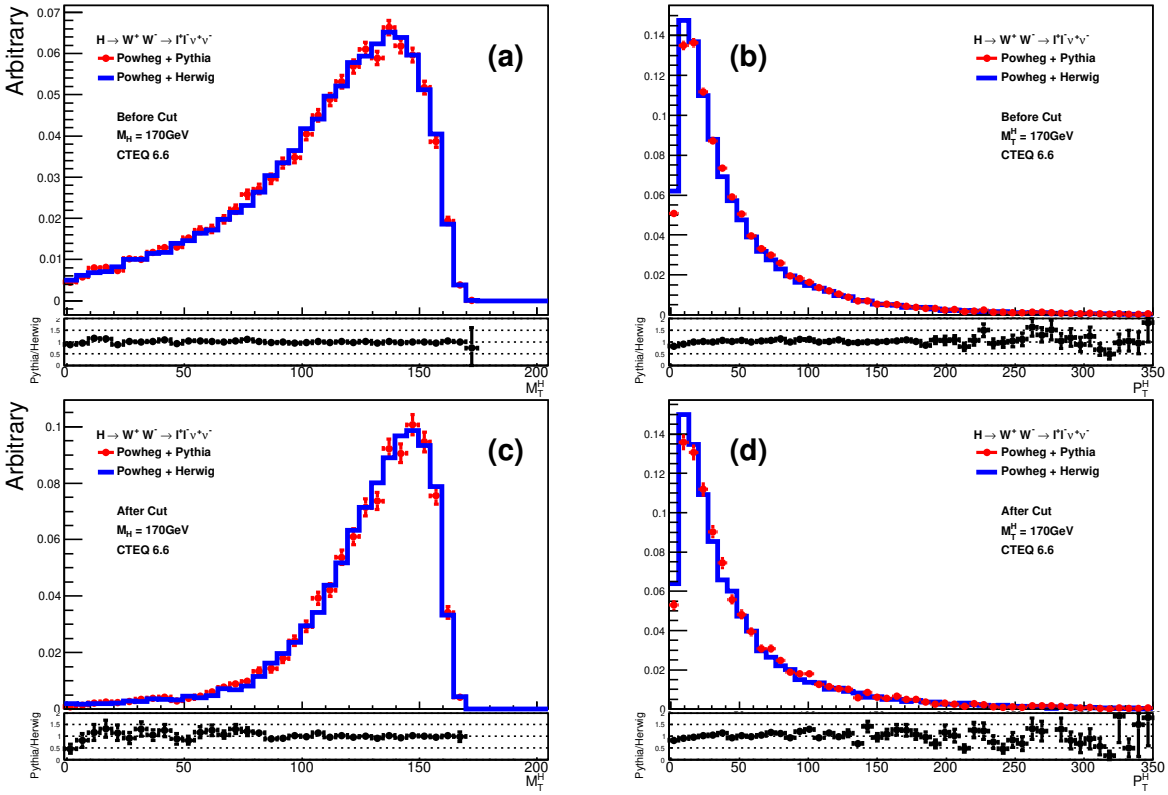

Fig. 34: (a) Higgs transverse mass without cuts, (b) Higgs transverse momentum without cuts, (c) Higgs transverse mass with cuts, and (d) Higgs transverse momentum with cuts for POWHEG+PYTHIA parton showering (red circles) and for POWHEG+HERWIG parton showering (blue histogram) for $M_{\rm H} = 170$ GeV. The plots below each of the histogram are the ratio of POWHEG+HERWIG with respect to POWHEG+PYTHIA.

- $M_{\rm ll} < 50$ GeV for $M_{\rm H} < 170$ GeV;
- $|\Delta\phi_{\rm ll}| < 1.3$ for $M_{\rm H} < 170$ GeV; $|\Delta\phi_{\rm ll}| < 1.8$ for 170 GeV $< M_{\rm H} <$ 220 GeV; no $|\Delta\phi_{\rm ll}|$ cut for $M_{\rm H} > 220$ GeV;
- $|\eta_{\rm ll}| < 1.3$ for $M_{\rm H} < 170$ GeV.

Figure 33.(c) and Figure 34.(c) show the reconstructed transverse mass of the Higgs from the final-state lepton and neutrino systems before and after the experimental selection cuts have been applied, for $M_{\rm H} = 130$ GeV and $M_{\rm H} = 170$ GeV, respectively. The comparison of the reconstructed transverse-mass distributions show no significant difference, before and after experimental cuts between the two PS schemes. Figure 33.(d) and Figure 34.(d) show the Higgs transverse momentum reconstructed from the final-state lepton and neutrino systems, before and after the experimental selection cuts have been applied, for $M_{\rm H} = 130$ GeV and $M_{\rm H} = 170$ GeV. The difference in these distributions between the two PS programs reflects the observation at parton level that POWHEG+PYTHIA displays harder Higgs $p_{\rm T}$ than that from POWHEG+HERWIG, while the statistical uncertainties at high $p_{\rm T}$ bins diminish.

4.4.4 Conclusions and future work

We have demonstrated that the systematic uncertainties resulting from interfacing POWHEG to PYTHIA and HERWIG programs are small in most of the quantities used for the search, independently of the selection cut values and of the Higgs-boson mass. On the other hand, the systematic uncertainties on Higgs and jets transverse momenta show sufficiently large differences between the two PS algorithms and therefore the associated systematic uncertainties cannot be ignored. A similar study is in progress

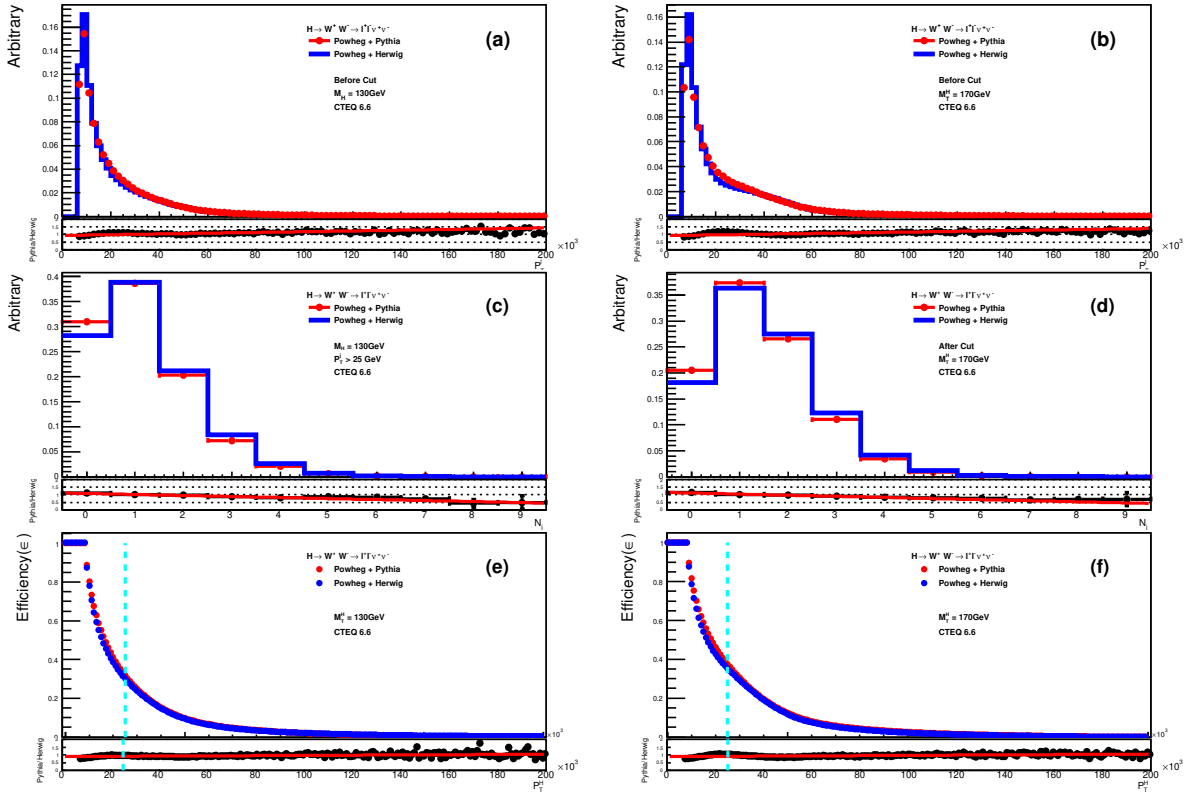

Fig. 35: p_{T} distributions of the jets from parton showering for (a) $M_{\mathrm{H}} = 130$ GeV and (b) $M_{\mathrm{H}} = 170$ GeV, number of associated jets with $p_{\mathrm{T}} > 25$ GeV for (c) $M_{\mathrm{H}} = 130$ GeV and (d) $M_{\mathrm{H}} = 170$ GeV, and jet efficiency as a function of jet p_{T} (e) $M_{\mathrm{H}} = 130$ GeV and (f) $M_{\mathrm{H}} = 130$ GeV. POWHEG+PYTHIA parton showering (red circles) and for POWHEG+HERWIG parton showering (blue histogram). The plots below each of the histogram are the ratio of POWHEG+HERWIG with respect to POWHEG+PYTHIA.

for the ZZ final state.

Thus, we conclude that the main difference between the two PS programs, interfaced to POWHEG, is observed in the Higgs transverse momentum, reflecting into the experimentally reconstructed transverse momentum of the leptons plus missing transverse energy system. However, this difference is found to be independent of the selection cuts and of the Higgs mass value within the two masses we have studied. Additional studies on higher Higgs masses would be needed to further confirm this conclusion.

Based on our experience with this study, we emphasize that it is necessary to improve the speed of the event generators in order to compute promptly the uncertainties associated to the PDF set choices, as well as to the description of the underlying event and pile-up effects. As it will be presented in the following, a first step in this direction has been undertaken by the AMC@NLO Monte Carlo which provides automatic evaluation of scale and PDF uncertainties by a simple reweighting procedure. Finally, further studies of fast simulation quantities will allow full assessment of the propagation of the theoretical uncertainties to the experimental quantities used for the search.

4.5 Guidelines for the use of HQT results to improve NLO+PS programs

In several parts of this report regarding specific Higgs signals, methods to reweight NLO+PS generators have been presented. In general, reweighting is not a straightforward and free-of-risk procedure, and reaching a final recommendation would require more studies. Here we summarise a few key points that should be kept in mind when setting up a reweighting procedure.

First of all, in general it is always recommended to rescale the total cross section of fully inclusive MC samples obtained via different techniques, LO+PS, NLO+PS, matching, and so on, to the best available prediction, at NNLO, fixed order, or resummed. For differential distributions a general strategy is, of course, not available, and reweighting should be considered case by case and observable by observable.

An observable that has a key role in the acceptance determination and therefore in exclusion limits is the transverse-momentum distribution of the Higgs. For this observable the best predictions are those provided by the HQT code. It is therefore natural to suggest to reweight all events from NLO+PS generators to the HQT distributions. Our recommendation, in this case, is to reweight at the level of showered events, *without* hadronisation and underlying event. This is especially important in the very-low-$p_{\rm T}$ region, where non-perturbative effects are sizeable. One must proceed in this way, since HQT does not include these non-perturbative effects. Thus, reweighting the full-hadron-level Monte Carlo output to HQT may lead to washing out small-transverse-momentum effects that are determined by hadronisation and the underlying events.

In the following discussion, we refer to the Higgs $p_{\rm T}$ spectrum obtained with the NLO+PS generator by switching off hadronisation and underlying event as the "shower distribution". The same distribution obtained with the full NLO+PS generator, including hadronisation and underlying event, as "hadron distribution". These definitions work for any NLO+PS scheme, MC@NLO, or POWHEG. In the POWHEG case, however, one can also compute the Higgs $p_{\rm T}$ using what is stored in the LHEF common block, before showering. We will call this "POWHEG-level distribution".

An appropriate reweighting strategy can be the following. First of all, one determines a reweighting function as the ratio of the HQT distribution to the shower distribution. When generating events, one should then apply the reweighting function evaluated at the transverse momentum of the Higgs, as determined at the end of the shower development, before hadronisation and underlying events are introduced. The event is then hadronised, and the underlying event is added. The $p_{\rm T}$ of the Higgs will be modified at this stage, especially at small $p_{\rm T}$. This procedure can only be applied if the shower-level output is available on an event-by-event basis. This may be the case of the fortran version of HERWIG, but it is not certainly the case of PYTHIA, with the underlying event characterised by multiparton interaction interleaved with the shower development.

An alternative reweighting procedure may be applied in the POWHEG case, where the Higgs transverse-momentum distribution is available also at the parton level, before the shower. It is usually observed that the effect of the shower on this distribution is quite mild. One then should determine a reweighting function to be applied as a function of the Higgs transverse momentum determined at the parton level, such that the transverse-momentum distribution of the Higgs after full shower (but before hadronisation) matches the one computed with HQT. It may be possible to achieve this by an iterative procedure: one takes the ratio of the shower spectrum over the parton-level spectrum as the initial reweighting function. One then generates events using this reweighting function, applied however to the Higgs transverse momentum at the parton level. This will lead to a residual mismatch of the shower spectrum with respect to the HQT spectrum, which can be used to multiplicatively correct the reweighting function. One keeps iterating the procedure, until convergence is reached. Events are then generated at the full hadron level, and reweighted on the basis of the transverse momentum at the POWHEG level.

No studies on the implementation of HQT reweighting according to the above guidelines have been performed for this report, and this topic requires further studies.

If the reweighting factor is nearly constant, the reweighting procedure is considerably simplified, since a nearly constant factor can be applied safely as a function of the Higgs $p_{\rm T}$ at the hadron level. We have noticed here that, with non-default value of parameters, POWHEG and MC@NLO approach better the HQT result. It is thus advisable to use this settings before attempting to reweight the distributions.

One simple reweighting option is to use the NLO+PS generators with the best settings discussed above, and reweight by a constant factor, to match the NNLO cross section. In this way, HQT is only

used to make a preferred choice of parameter settings in the NLO+PS generator. A conservative way to estimate the error band, in this case, would be to use the NLO+PS scale variation band, multiplied by the ratio of the NNLO cross section over the NLO+PS cross section evaluated at the central value of the scales.

The preferred settings are summarised as follows. In the MC@NLO case, we recommend to use the reference factorisation and renormalisation scale equal to $M_{\rm H}$ rather than $m_{\rm T}$. In POWHEG, we recommend using the R^s/R^f separation, with the `powheg.input` variable `hfact` set equal to $M_{\rm H}/1.2$. For the scale variation, we recommend to vary $\mu_{\rm R}$ and $\mu_{\rm F}$ independently by a factor of 2 above and below the reference scale, with the constraint $0.5 < \mu_{\rm R}/\mu_{\rm F} < 2$.

4.6 Guidelines to estimate non-perturbative uncertainties

In this section we propose a mechanism to evaluate the impact of non-perturbative uncertainties related to hadronisation and underlying event modelling. In the past, the former typically has been treated by comparing PYTHIA and HERWIG results, and analysing, bin by bin, the effect of the different fragmentation (i.e., parton showering) and hadronisation schemes. In contrast the latter often is dealt with by merely comparing a handful of different tunes of the same program, typically PYTHIA. Especially the latter seems to be a fairly unsystematic way, in particular when taking into account that various tunes rely on very different input data, and some of the traditional tunes still in use did not even include LHC results (and typically they therefore fail to describe them very well). We therefore propose the following scheme which essentially relies on systematic variations around a single tune, with a single PDF:

- In order to quantify hadronisation uncertainties within a model, use two different tune variations around the central one, defined by producing one charged particle more or less at LEP. The difference between different physics assumptions entering the hadronisation model (i.e., cluster vs. Lund string hadronisation), but tuned to the same data, still needs to be tested, of course, by running these models[14].
- For the model- and tune-intrinsic uncertainties of the underlying-event simulation we propose to systematically vary the activity, number of charged particles, and their summed transverse momentum, in the transverse region. There are basically two ways of doing it, one is by increasing or decreasing the respective plateaus by 10% (this has been done in the study here); alternatively, one could obtain tune variations which increase or decrease the "jettiness" of the underlying event. Effectively this amounts to changing the shape of the various activities in the transverse region.

While we appreciate that this way of obtaining systematic uncertainties is somewhat cumbersome at the moment, we would like to stress that with the advent of modern tuning tools such as Rivet-Professor [186], this is a perfectly straightforward and controlled procedure.

At this point it should also be noted that usually different PDFs lead to different tunes for the underlying event. Therefore, in order to obtain a meaningful estimate of uncertainties related to observables which are susceptible to the underlying event, it is important to also retune its modelling accordingly. Just changing the PDF but keeping the underlying event model parameters constant will typically lead to overestimated uncertainties. In a similar fashion, the impact of the strong coupling constant may lead to the necessity of a retune. This has recently been intensively discussed in Ref. [187], a similar discussion for the NLO+PS tools discussed here is still missing[15].

[14] In SHERPA this can be achieved even on top of the *same* parton showering by contrasting a native cluster hadronisation model with the Lund string of PYTHIA, made available through an interface. Of course, both models have been tuned to the same LEP data.

[15] In SHERPA this never was an issue, as the strong coupling used throughout the code is consistently given by the PDF.

4.7 Higgs production via gluon fusion: finite-mass effects[16]

Current implementations in NLO+PS codes of Higgs production process via gluon fusion [130, 132, 157, 188] are based on matrix elements evaluated in the Higgs effective theory (ET), i.e. in a theory where the heavy-quark loop(s) are shrunk to effective vertices. In several cases the user is given the possibility of rescaling the total cross section by a normalisation factor, defined as the ratio between the exact Born contribution where the full dependence on the top and bottom masses is kept into account and the Born contribution evaluated in the ET. While the ET is a very good approximation for light SM Higgs, fixed-order computations have shown that it fails for heavier Higgs masses, at large Higgs transverse momentum and for a BSM Higgs with enhanced couplings to b quarks.

Very recently, progress to include finite-mass effects has been achieved on two different fronts: matched predictions for Higgs production via heavy-quark loops in the SM and beyond have been obtained [189] and the NLO full-mass-dependent calculation has been implemented in POWHEG [190].

4.7.1 Higgs production via gluon fusion with loops via LO+PS merging

In Ref. [189] was presented the first fully exclusive simulation of gluon-fusion inclusive Higgs production based on the (leading-order) exact one-loop matrix elements for $\mathrm{H}+0,\,1,\,2$ partons, matched to PYTHIA parton showers using multiple merging schemes implemented in MADGRAPH 5 [191].

In order to take into account the full kinematic dependence of the heavy-quark loop in Higgs production, the full one-loop amplitudes for all possible subprocesses contributing to $\mathrm{H}+0,\,1,\,2$ partons have been calculated. To gain in speed and efficiency (the evaluation of multi-parton loop amplitudes is, in general, computationally quite expensive) a method has been devised to map the integrand in a quick (though approximate) way and to limit the evaluation of loops to a small number of points. Parton-level events for $\mathrm{H}+0,\,1,\,2$ partons are generated via MADGRAPH/MADEVENT in the ET, with scale choices optimised for the subsequent merging procedure. Before passing them to the PS program, events are reweighted by the ratio of full one-loop amplitudes over the ET ones, $r = |\mathcal{M}_{\mathrm{LOOP}}|^2/|\mathcal{M}_{\mathrm{ET}}|^2$. The reweighted parton-level events are unweighted, passed through PYTHIA and matched using the k_{T}-MLM or the shower-k_{T} scheme. Event samples are finally normalised to reference NNLO cross sections. The reweighting method does not make any approximation and with large enough statistics is exactly equivalent to the integration of the phase space of the full one-loop amplitudes.

Representative results for SM Higgs and a b-philic Higgs at the LHC at 7 TeV are shown in Figures 36–38. Jets are defined via the k_{T} algorithm with resolution parameter set to $D = 1$. Jets are required to satisfy $|\eta_j| < 4.5$ and $p_{\mathrm{T}}^j > 30$ GeV. For sake of simplicity, we adopt Yukawa couplings corresponding to the pole masses, i.e., for the top quark $m_{\mathrm{t}} = 173$ GeV and for the bottom-quark mass $m_{\mathrm{b}} = 4.6$ GeV. Other quark masses are neglected. Throughout our calculation, we adopt the CTEQ6L1 parton distribution functions (PDFs) [192] with the core process renormalisation and factorisation scales $\mu_{\mathrm{R}} = \mu_{\mathrm{F}} = M_{\mathrm{T}}^{\mathrm{H}} \equiv \sqrt{(p_{\mathrm{T}}^{\mathrm{H}})^2 + M_{\mathrm{H}}^2}$. For the merging performed in MADGRAPH/MADEVENT, the k_{T}-MLM scheme is chosen, with $Q_{\mathrm{min}}^{\mathrm{ME}} = 30$ GeV and $Q_{\mathrm{min}}^{\mathrm{jet}} = 50$ GeV.

In Figure 36 we show the Higgs p_{T} distribution for Standard Model Higgs gluon–gluon fusion production at the LHC with $M_{\mathrm{H}} = 140$ GeV in a range of p_{T} relevant for experimental analysis. We compare matched results in the ET theory and in the full theory (LOOP) with PYTHIA with $2 \to 2$ matrix element corrections. We also include the predictions from the analytic computation at NNLO+NNLL as obtained by HQT [193, 194]. The curves are all normalised to the NNLO+NNLL predictions. The three Monte Carlo based predictions agree very well in all the shown range of p_{T}, suggesting that for this observable, higher-multiplicity matrix-element corrections (starting from $2 \to 3$) and loop effects are not important. This is the case also for jet p_{T} distributions (not shown) in the same kinematical range.

In Figures 36–37, the Higgs and jet p_{T} distributions are shown for Standard Model Higgs gluon–

[16] J. Alwall, Q. Li and F. Maltoni.

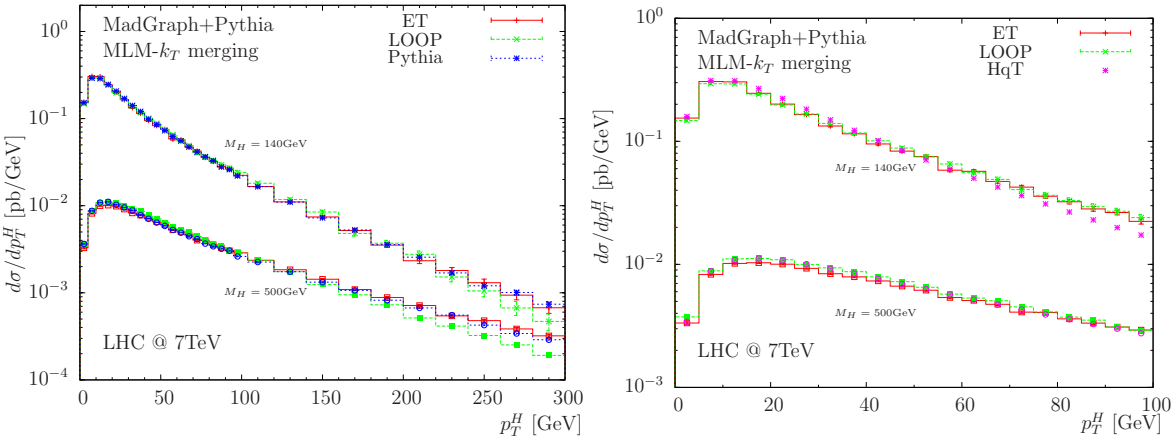

Fig. 36: SM Higgs $p_{\rm T}$ distributions for $M_{\rm H} = 140$ GeV and $M_{\rm H} = 500$ GeV in gluon-fusion production at 7 TeV LHC. In the upper plot results in the ET and with full loop dependence (LOOP) are compared over a large range of $p_{\rm T}$ values to the default PYTHIA implementation, which accounts for $2 \to 2$ matrix-element corrections. In the lower plot the low-$p_{\rm T}$ range is compared to the NNLO+NNLL results as obtained by HQT [193, 194]. Curves normalised to the NNLO total cross sections see Ref. [189].

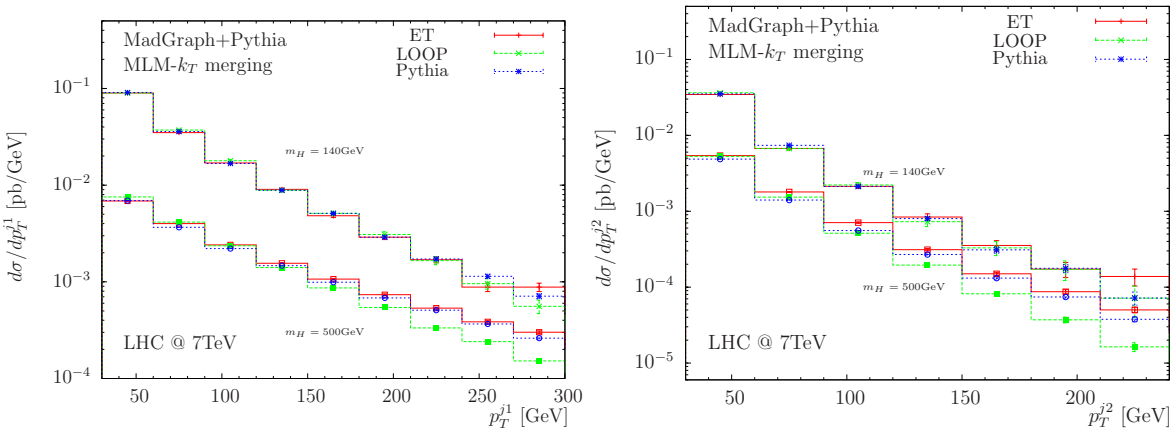

Fig. 37: Jet $p_{\rm T}$ distributions for associated jets in gluon-fusion production of $M_{\rm H} = 140$ GeV and $M_{\rm H} = 500$ GeV Higgs bosons at 7 TeV LHC. Plots from Ref. [189].

gluon fusion production at the 7 TeV LHC with $M_{\rm H} = 140$ and 500 GeV. Monte Carlo based results agree well with each other. As expected, loop effects show a softening of the Higgs $p_{\rm T}$, but only at quite high $p_{\rm T}$. We also see that the heavier the Higgs, the more important are the loop effects. This is expected, since the heavy Higgs boson can probe the internal structure of the top-quark loop already at small $p_{\rm T}$. The jet $p_{\rm T}$ distributions do confirm the overall picture and again indicate loop effects to become relevant only for rather high values of the $p_{\rm T}$. The agreement with the NNLO+NNLL predictions at small $p_{\rm T}$ for both Higgs masses it is quite remarkable. Key distributions, such as the $p_{\rm T}$ of the Higgs, do agree remarkably well with the best available predictions, for example NNLO+NNLL at small Higgs $p_{\rm T}$, and offer improved and easy-to-use predictions for other key observables such as the jet rates and distributions. In addition, for heavy Higgs masses and/or large $p_{\rm T}$, loop effects, even though marginal for phenomenology, can also be taken into account in the same approach, if needed.

In Figure 38, the $p_{\rm T}^{\rm H}$ distributions for gluon–gluon fusion production at the 7 TeV LHC of a b-philic Higgs with $M_{\rm H} = 140$ GeV are shown. For the sake of illustration, we define a simplified scenario where the Higgs coupling to the top quark is set to zero and study the Higgs and jet distributions relative to a "large-$\tan\beta$" scenario with bottom-quark loops dominating. Note that for simplicity we

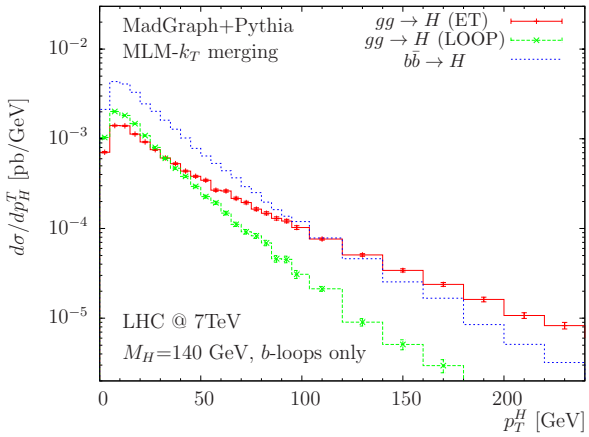

Fig. 38: b-philic Higgs p_{T} distribution a the Tevatron and the LHC with $M_{\mathrm{H}} = 140$ GeV. Results in the ET approximation (red curve) and with full loop dependence (green) are shown. Spectrum of Higgs produced via $\mathrm{b\bar{b}}$ fusion in the five-flavour scheme is also shown. All samples are matrix-element matched with up to two partons in the final state. Curves normalised to the corresponding NNLO total cross sections see Ref. [189].

keep the same normalisation as in the Standard Model, i.e., $y_{\mathrm{b}}/\sqrt{2} = m_{\mathrm{b}}/v$ with $m_{\mathrm{b}} = 4.6$ GeV, as the corresponding cross sections in enhanced scenarios can be easily obtained by rescaling. In the b-philic Higgs production, the particle running in the loop is nearly massless, and there is no region in M_{H} or p_{T} where an effective description is valid. This also means that a parton-shower generator alone has no possibility of correctly describing the effects of jet radiation, and genuine loop matrix elements plus a matched description are needed for achieving reliable simulations. For a b-philic Higgs the largest production cross section does not come from loop induced gluon fusion, but from tree-level $\mathrm{b\bar{b}}$ fusion. We have therefore included also this production mechanism in Figure 38. The corresponding histogram is obtained by merging tree-level matrix elements for $\mathrm{H} + 0, 1, 2$ partons (with a $\mathrm{hb\bar{b}}$ vertex) in the five-flavour scheme to the parton shower. This provides a complete and consistent event simulation of inclusive Higgs production in a b-philic (or large $\tan\beta$) scenario.

4.7.2 Finite-quark-mass effects in the gluon-fusion process in POWHEG[17]

Ref. [190] presented an upgraded version of the code that allows to compute the gluon-fusion cross section in the SM and in the MSSM. The SM simulation is based on matrix elements evaluated retaining the exact top and bottom mass dependence at NLO QCD and NLO EW. The MSSM simulation is based on matrix elements in which the exact dependence on the masses of quarks, squarks, and the Higgs boson has been retained in the LO amplitude, in the one-loop diagrams with real-parton emission and in the two-loop diagrams with quarks and gluons, whereas the approximation of vanishing Higgs mass has been employed in the two-loop diagrams involving superpartners. The leading NLO EW effects have also been included in the evaluation of the matrix elements. Results obtained with this new version of POWHEG are presented in the SM and in the MSSM sections of this Report.

The code provides a complete description of on-shell Higgs production, including NLO QCD corrections matched with a QCD parton shower and NLO EW corrections. In the examples discussed in Ref. [190], the combination POWHEG+PYTHIA has been considered. In the MSSM case, the relevant parameters of the MSSM Lagrangian can be passed to the code via a Susy Les Houches Accord spectrum file.

The code is available from the authors upon request. A release of the code that includes all the

[17] E. Bagnaschi, G. Degrassi, P. Slavich and A. Vicini.

Higgs decay channels is in preparation.

4.8 Scale and PDF uncertainties in MC@NLO

Computations of (differential) cross sections in hadron–hadron collisions are affected by uncertainties due to, from the one hand, the unperfected knowledge of parameters in the calculations, both perturbative and non-perturbative nature, and on the other hand due to truncation errors, i.e. to unknown higher-order terms in the perturbative expansion in $\alpha_{\rm s}$. Among all such uncertainties, scale and PDF ones do have a special status: their variations are typically associated with the purely theoretical uncertainty affecting observable predictions. It is customary to estimate the truncation uncertainty by using the dependence on renormalisation ($\mu_{\rm R}$) and factorisation ($\mu_{\rm F}$) scales. The reason is that such dependence also arises because the computation of the cross section is performed only to a given order, and therefore is thought to give an rough estimate of the possible impact of the unknown terms. PDF uncertainties, on the other hand, are evaluated following the directions of the various PDF groups (see Section 3) and it amounts to calculating the cross section multiple times on a well-definite ensemble of such functions. There is, however, something else that make such uncertainties special and particularly important in complex and therefore time expensive NLO computations: the bulk of the CPU cost of NLO computations can be rendered independent of scales and PDFs, as opposed to what happens in the case of other parameters, e.g. particle masses. Short-distance cross sections can be written as linear combinations of scale- and PDF-dependent terms, with coefficients independent of both scales and PDFs; it is thus possible to compute such coefficients once and for all, and to combine them at a later stage with different scales and PDFs at essentially zero cost from the CPU viewpoint. The crucial point is that this is not only the feature of the parton-level LO and NLO cross sections, but also of those performed in the context of MC@NLO. This implies that from the conceptual point of view the same procedure for determining scale and PDF uncertainties can be adopted in MC@NLO as in LO-based Monte Carlo simulation. This method is automatic, process independent, and being now implemented in AMCATNLO [168], it can provide scale and PDF uncertainties for an arbitrary process.

In practice parton-level events in the LHE format, soft and hard, are generated as usual through AMCATNLO for a central choice of scales and PDF. After that the weights corresponding to different PDF sets and arbitrary scale choices (that can be decided by the user) are determined and stored in ordered arrays associated to each event record. For any observable, obtained with events after showering and hadronisation and possibly detector simulation, one can fill a "central" histogram with the central weights and as many "variation" histograms corresponding to the other weights. This procedure very closely reproduces what is normally done for pure parton-level NLO computations and should be considered the equivalent one in the context of NLO+PS.

4.9 On-going debates and open issues

We summarise here an issue that has recently been reopened for discussion. Since this has only quite recently emerged, the present summary is a snapshot of the status of the discussion at the time of completion of this Report; we anticipate a rapid evolution in the following months.

The debate mainly concerns the origin of the large discrepancies between results for the large-transverse-momentum tail of the Higgs-boson $p_{\rm T}$ distribution obtained with MC@NLO and POWHEG methods, but it also addresses differences observed in the rapidity spectrum of the jet in Higgs production.

One view for an explanation of these discrepancies has been developed in Refs. [132, 172]. In the following, this explanation will be called the "K-factor effect" and it can be summarised as follows: NLO+PS generators produce two kinds of events that are merged in their output: $\mathbb{S}$ (for shower) and $\mathbb{F}$ (for finite) events. The real-emission cross section is decomposed into these two types of events. In the specific case of $\rm gg \to H$ the real emission cross section R is essentially given by the $\rm gg \to Hg$ cross section, and the $\rm gq$ and $\rm q\overline{q}$ channels can be neglected. This cross section is decomposed as follows:

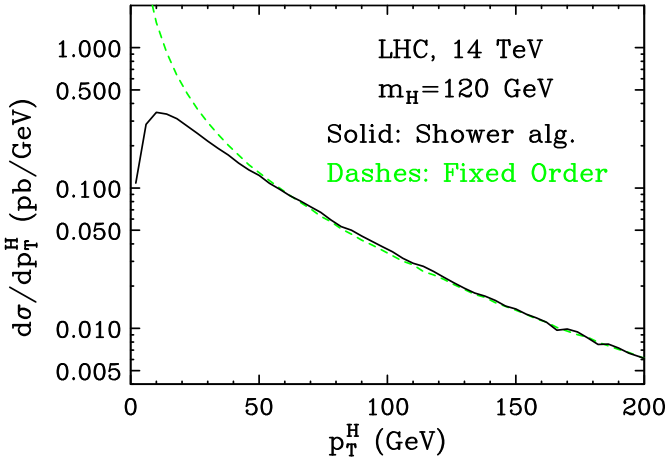

Fig. 39: Illustration of the difference in the Higgs $p_{\rm T}$ distribution computed at fixed order $\alpha_{\rm s}^3$ with respect to its generation using the shower algorithm.

$R = R^s + R^f$. While R^f has a finite integral, and thus yields a finite contribution to the real cross section, R^s is divergent, and its contribution is well defined only when suitably combined with the (also divergent) virtual cross section. The shower algorithm performs this combination, accounting only for leading logarithmic corrections (i.e. without including all NLO corrections.). The distribution of events generated from R^s using the shower algorithm is altered with respect to the fixed order one, as shown in Figure 39. The divergence at $p_{\rm T} \to 0$ of R^s is turned into a smooth, bell–shaped curve, characterizing the so–called Sudakov region. The basic shower algorithm is such that the integral of this distribution equals the Born cross section. In contrast, the R^f contribution can be generated with no particular problems, since it is finite.

When promoting the shower algorithm to the NLO level, one must make sure that the full output yields an NLO accurate cross section. A contribution to the NLO cross section comes from the R^f term, but also modifications of the R^s term are needed. These modifications induce a change in the transverse-momentum spectrum generated by the $\mathbb{S}$ events, that amounts roughly to an overall factor

$$K = \frac{\sigma^{(\rm NLO)} - \sigma^F}{\sigma^{(\rm LO)}}\,, \tag{15}$$

so that summing the $\mathbb{S}$ and $\mathbb{F}$ integrals of the transverse-momentum spectrum yields the total NLO cross section.

In MC@NLO, the R^s contribution corresponds to the shower Monte Carlo approximation to the real-emission cross section. In POWHEG, $R^s = R$ by default, although, as we have seen earlier, other choices are possible. According to Refs. [132, 172], it is the K-factor of Eq. (15) that determines the larger high $p_{\rm T}$ tail of the Higgs spectrum to be higher in POWHEG than in MC@NLO, since in the former $R^f = 0$, and K is in front of the whole distribution. On the other hand, in MC@NLO, the K-factor is only in front of the R^s contribution, that dominates the region of $p_{\rm T}$ below $M_{\rm H}$, while R^f dominates at large $p_{\rm T}$. Since the K-factor in Higgs production is particularly large, this effect is more evident here than in other processes.

We observe that the K-factor effect amounts to a correction of $\mathcal{O}(\alpha_{\rm s}^4)$ to the tail of the transverse-momentum distribution, which here is computed at order $\alpha_{\rm s}^3$. In the POWHEG BOX implementation of Higgs production, the partition $R = R^s + R^f$ can be tuned by setting an input parameter, h of Eq. (14), and thus the same large variation in the transverse-momentum tail can be observed within the POWHEG framework alone.

A discording view is expressed in Ref. [159], which we will refer to as “phase-space effect”. In this

recent publication, a new MC@NLO-inspired implementation in the SHERPA framework is introduced, with an R^s contribution that is a tunable function of one parameter, called α [179]. This parameter α controls the phase space available for radiation, such that $\alpha = 1$ corresponds to the full phase space available, and smaller values correspond to restricted phase spaces. It should be stressed here that this parameter does not directly translate into a scale with a clear relation to transverse momenta. By varying this parameter, not only the phase space available to the subtraction terms – the Catani–Seymour dipoles – but also the phase space available for $\mathbb{S}$ events in the parton shower can be varied. This is because in the SHERPA implementation, the same kernels are employed for both subtraction and showering, while in the original MC@NLO implementations this is not the case. There the phase space for soft events is directly obtained from the parton shower, and typically related to scales of the order of the factorisation scale. The variation in SHERPA, in contrast, does not exhibit this feature, which therefore ultimately results in large, unphysical variations in the tail of the transverse-momentum distribution within the SHERPA implementation of MC@NLO. However, this lead the authors of Ref. [159] to argue that the dominant mechanism of large deviations is not the K-factor, as claimed in Refs. [132, 172], but the additional phase space beyond the factorisation scale. According to the authors of Ref. [159], this phase-space effect manifests itself in a distortion of the Sudakov form factor, affecting $\mathbb{S}$ and, to a lesser extent, $\mathbb{F}$ events.

Phrasing it slightly differently, for $\alpha = 1$, the phase space for radiation in the $\mathbb{S}$ events allows the generation of transverse momenta up to the order of the available hadronic energy. This is also the case for the default POWHEG implementation without the additional dampening factor of Eq. (14). It can be argued that, in addition to the in-principle uncontrollable higher-order terms introduced at $\mathcal{O}(\alpha_{\rm s}^4)$ through the above discussed K-factor, also large $\log^2(S_{had}/p_{\rm T}^2)$ arise to *all* orders in perturbation theory – instead of terms like $\log^2(\mu_{\rm F}^2/p_{\rm T}^2)$ present in standard resummation implemented, e.g. in HQT[18]. It is argued that if the α parameter is set to values smaller than 1, a maximum $p_{\rm T}$ for $\mathbb{S}$ events, $p_{\rm T}^{\rm max}(\alpha)$, is introduced. Thus, the $\log^2(S_{\rm had}/p_{\rm T}^2)$ terms become in fact of order $\log^2(p_{\rm T}^{\rm max2}(\alpha)/p_{\rm T}^2)$. Values of α such that $p_{\rm T}^{\rm max}(\alpha)$ becomes of the order of the Higgs mass are thus justified, and yield differential cross sections that reproduce the NLO results for large $p_{\rm T}$ and that also get rid of the undesired effects in the rapidity distribution of the radiated jet in the SHERPA implementation of the MC@NLO algorithm. Too small values of α yield a transverse-momentum distribution that approaches the fixed order one, implying that a negative dip must arise at low $p_{\rm T}$ in the $p_{\rm T}$ distribution, in order for the total cross section to remain finite and independent of α.

Let us note in passing that in this framework, the notorious dip in the rapidity difference of Higgs boson and hardest jet can also be reproduced, for some values of α. The authors of Ref. [159] argue that this hints at the dip originating from unaccessible zones in the phase space for $\mathbb{S}$ events, which are not fully recovered by $\mathbb{F}$ events.

[18] Note that for LHC energies, the ratio $S_{had}/\mu_{\rm F}^2$ is of the same order of magnitude as $\mu_{\rm F}^2/\Lambda_{\rm QCD}^2$ (for $\mu_{\rm F} \sim 100$ GeV).

5 The gluon-fusion process[19]

In the first volume of this Handbook, the status of the inclusive cross section for Higgs production in gluon fusion was summarised [7]. Corrections arising from higher-order QCD, electroweak effects, as well as contributions beyond the commonly used effective-theory approximation were analysed. Uncertainties arising from missing terms in the perturbative expansion, as well as imprecise knowledge of parton distribution functions, were estimated to range from approximately 15% to 20%, with the precise value depending on the Higgs-boson mass.

Our goal in this second volume is to extend the previous study of the gluon-fusion mechanism to include differential cross sections. The motivation for such investigations is clear; experimental analyses must impose cuts on the final state in order to extract the signal from background. A precise determination of the corresponding signal acceptance is needed. Hopefully, it is computed to the same order in the perturbative expansion as the inclusive cross section. Possible large logarithms that can occur when cuts are imposed should be identified and controlled. In the case of Higgs production through gluon fusion, numerous tools exist to perform a precise theoretical calculation of the acceptance. The fully differential Higgs cross section to next-to-next-to-leading order (NNLO) in QCD is available in two parton-level Monte Carlo simulation codes, FEHiP [195, 196] and HNNLO [173, 197]. The Higgs transverse-momentum spectrum has been studied with next-to-leading order (NLO) accuracy [198–200], and supplemented with next-to-next-to-leading logarithmic (NNLL) resummation of small-p_{T} logarithms [193, 194, 201]. Other calculations and programs for studying Higgs production in the gluon-fusion channel are available, as discussed throughout this section. All of these results are actively used by the experimental community.

We aim in this section to discuss several issues that arise when studying differential results in the gluon-fusion channel which are relevant to LHC phenomenology. A short summary of the contents of this section is presented below.

- The amplitude for Higgs production through gluon fusion begins at one loop. An exact NNLO calculation of the cross section would therefore require a multi-scale, three-loop calculation. Instead, an effective-field-theory approach is utilised, which is valid for relatively light Higgs masses. The validity of this effective-theory approach has been extensively studied for the inclusive cross section, and was reviewed in the first volume of this Handbook [7]. However, the accuracy of the effective-theory approach must also be established for differential distributions. For example, finite-top-mass corrections of order $(p_{\mathrm{T}}^{\mathrm{H}}/m_{\mathrm{t}})^2$ can appear beyond the effective theory. It is also clear that bottom-quark mass effects on Higgs differential distributions cannot be accurately modeled within the effective theory. These issues are investigated in Section 5.1 of this report. A distortion of up to $\mathcal{O}(10\%)$ of the Higgs transverse-momentum spectrum is possible in the low-p_{T} region, due to the bottom effects in case of a light Higgs, while in the high-p_{T} region the finite top mass can induce an even larger modification of the shape of the distribution [190].
- The composition of the background to Higgs production in gluon fusion, followed by the decay $\mathrm{H} \to \mathrm{W}^+\mathrm{W}^-$, differs dramatically depending on how many jets are observed together with the Higgs in the final state. In the zero-jet bin, the dominant background comes from continuum production of $\mathrm{W}^+\mathrm{W}^-$. In the 1- and 2-jet bins, top-quark pair production becomes large. The optimisation of the experimental analysis therefore utilises a split into different jet-multiplicity bins. Such a split induces large logarithms associated with the ratio of the Higgs mass over the defining p_{T} of the jet. The most natural method of evaluating the theoretical uncertainty in the zero-jet bin, that of performing naive scale variations, leads to a smaller estimated uncertainty than the error on the inclusive cross section [173, 202–204]. This indicates a possible cancellation between logarithms of the p_{T} cut and the large corrections to the Higgs cross section, and a potential under-

[19] M. Grazzini, F. Petriello (eds.); E.A. Bagnaschi, A. Banfi, D. de Florian, G. Degrassi, G. Ferrera, G. P. Salam, P. Slavich, I. W. Stewart, F. Stoeckli, F. J. Tackmann, D. Tommasini, A. Vicini, W. J. Waalewijn and G. Zanderighi.

estimate of the theoretical uncertainty. An improved prescription for estimating the perturbative uncertainty in the exclusive jet bins is discussed in Section 5.2. Evidence is given that the cancellation suggested above does indeed occur, and that the uncertainty in the zero-jet bin is in fact nearly twice as large as the estimated error of the inclusive cross section. Further evidence for the accidental cancellation between large Sudakov logarithms and corrections to the total cross section is given in Section 5.3, where it is shown that different prescriptions for treating the uncontrolled $\mathcal{O}(\alpha_{\rm s}^3)$ corrections to the zero-jet event fraction lead to widely varying predictions at the LHC.

– A significant hindrance in our modeling of the cross section in exclusive jet bins is our inability to directly resum the large logarithms mentioned above. Instead, we must obtain insight into the all-orders structure of the jet-vetoed cross section using related observables. An example of such a quantity is the Higgs transverse-momentum spectrum. Through $\mathcal{O}(\alpha_{\rm s})$ it is identical to the jet-vetoed cross section, since at this order the Higgs can only recoil against a single parton whose $p_{\rm T}$ matches that of the Higgs. The large logarithms which arise when the Higgs transverse momentum becomes small can be resummed. Section 5.4 presents a resummed computation of the $p_{\rm T}$ spectrum at full NNLL accuracy matched to the NLO result valid at large $p_{\rm T}$, which is implemented in an updated version of the code HQT [194]. Although the large logarithmic terms that are resummed are not the same appearing in the jet-bin cross sections, a study of the uncertainties of the *shape* of the resummed $p_{\rm T}$ spectrum may help to quantify those uncertainties. Another variable used to gain insight into the effect of a jet veto is beam thrust, which is equivalent to a rapidity-weighted version of the standard variable $H_{\rm T}$. The resummation of beam thrust [205, 206], and the reweighting of the Monte Carlo program MC@NLO to the NNLL+NNLO prediction for beam thrust in order to gain insight into how well the jet-vetoed cross section is predicted by currently used programs, is described in Section 5.5.

Unlike the first volume of this report, no explicit numbers are given for use in experimental studies. The possible distributions of interest in the myriad studies performed at the LHC are too diverse to compile here. Our goal is to identify and discuss the relevant issues that arise, and to give prescriptions for their solution. We must also stress that such prescriptions are not set in stone, and are subject to change if theoretical advances occur. For example, if an exact NNLO calculation of the Higgs cross section with the full dependence on the quark masses becomes available, or the jet-vetoed Higgs cross section is directly resummed, these new results must be incorporated into the relevant experimental investigations.

5.1 Finite-quark-mass effects in the SM gluon-fusion process in POWHEG[20]

5.1.1 Introduction

The description of the gluon-fusion process can be approximated, in many cases, by an effective theory (ET) obtained by taking the limit of infinite mass for the top quark running in the lowest-order loop that couples the Higgs to the gluons, and neglecting all the other quark flavors. This limit greatly simplifies many calculations, reducing the number of loops that have to be considered by one. On the other hand it is important, when possible, to check whether the effect of an exact treatment of the quark contributions is significant compared to the actual size of the theoretical uncertainty.

The validity of the ET approach has been carefully analyzed for the total cross section. The latter receives very large NLO QCD corrections, which have been computed first in the ET [65, 207] and then retaining the exact dependence on the masses of the quarks that run in the loops [66, 208–211]. The NLO results computed in the ET and then rescaled by the exact leading-order (LO) result with full dependence on the top- and bottom-quark masses provide a description accurate at the few-per-cent level for $M_{\rm H} < 2\,m_{\rm t}$. The deviation for $2m_{\rm t} < M_{\rm H} < 1$ TeV does not exceed the 10% level. The NNLO QCD corrections to the total cross section are still large and have been computed in the ET [212–214]. The finite-top-mass effects at NNLO QCD have been studied in Refs. [215–218] and found to be small. The

[20] E.A. Bagnaschi, G. Degrassi, P. Slavich and A. Vicini.

resummation to all orders of soft-gluon radiation up to NNLL+NNLO has been studied in Ref. [219], within the ET, and including the exact dependence of the masses of the top and bottom quarks up to NLL+NLO in Refs. [7, 220]. The leading third-order (NNNLO) QCD terms have been discussed in the ET [221]. The role of electroweak (EW) corrections has been discussed in Refs. [24,26–29,222,223] and found to be, for a light Higgs, of the same order of magnitude as the QCD theoretical uncertainty. The impact of mixed QCD–EW corrections has been discussed in Ref. [224]. The residual uncertainty on the total cross section depends mainly on the uncomputed higher-order QCD effects and on the uncertainties that affect the parton distribution functions of the proton [7, 112, 180].

The Higgs differential distributions have been studied at NNLO QCD in the ET, first in the region in which the Higgs $p_{\rm T}$ is non-vanishing [198–200] [21], and then with proper treatment of the $p_{\rm T} = 0$ contribution [195–197]. The NLO QCD results including the exact dependence on the top and bottom-quark masses were first included in the code HIGLU based on Ref. [66]. More recently, the same calculation was repeated in Refs. [225–227]. The latter discussed at NLO QCD the role of the bottom quark, for light Higgs-boson masses. A description of the Higgs differential distributions, in the ET, including transverse-momentum resummation up to NNLL and matching to NLO and NNLO QCD results has been provided in Refs. [228, 229] and [201], respectively, and has been implemented in the code RESBOS. The Higgs transverse-momentum distribution, in the ET, including full NNLO QCD results and matched at NNLL QCD with the resummation of soft-gluon emissions, has been presented in Ref. [193] and is implemented in the code HQT. The latter allows for a quite accurate estimate of the perturbative uncertainty on this distribution, which turns out to be of the order of $\pm 10\%$ for light Higgs and for Higgs transverse momentum $p_{\rm T}^{\rm H} < 100$ GeV [194].

The shower Monte Carlo (SMC) codes matching NLO QCD results with QCD Parton Shower (PS) [116, 132] consider the gluon-fusion process only in the ET. Recently, a step towards the inclusion of the finite-quark-mass effects in PS was taken in Ref. [189], where parton-level events for Higgs production accompanied by zero, one, or two partons are generated with matrix elements obtained in the ET and then, before being passed to the PS, they are re-weighted by the ratio of the full one-loop amplitudes over the ET ones. This procedure is equivalent to generating events directly with the full one-loop amplitudes, yet it is much faster.

In Ref. [190] the implementation in the POWHEG framework [123, 126, 156] of the NLO QCD matrix elements for the gluon fusion, including the exact dependence on the top- and bottom-quark masses, has been presented. We discuss here the effect of the exact treatment of the quark masses on the Higgs transverse-momentum distribution, comparing the results of the old POWHEG release, obtained in the ET, with those of this new implementation [190]. In particular, we consider here the matching of POWHEG with the PYTHIA [183] PS.

5.1.2 Quark mass effects in the POWHEG *framework*

In this section we briefly discuss the implementation of the gluon-fusion Higgs production process in the POWHEG BOX framework, following closely Ref. [132]. We fix the notation keeping the discussion at a general level, and refer to Ref. [190] for a detailed description and for the explicit expressions of the matrix elements. The generation of the hardest emission is done in POWHEG according to the following formula:

$$\begin{aligned} d\sigma &= \bar{B}(\bar{\Phi}_1)\, d\bar{\Phi}_1 \left\{ \Delta\left(\bar{\Phi}_1, p_{\rm T}^{\rm min}\right) + \Delta\left(\bar{\Phi}_1, p_{\rm T}\right) \frac{R\left(\bar{\Phi}_1, \Phi_{\rm rad}\right)}{B\left(\bar{\Phi}_1\right)} d\Phi_{\rm rad} \right\} \\ &+ \sum_q R_{q\bar{q}}\left(\bar{\Phi}_1, \Phi_{\rm rad}\right) d\bar{\Phi}_1 d\Phi_{\rm rad} \,. \end{aligned} \tag{16}$$

[21] These computations provide an NLO QCD calculation of the Higgs $p_{\rm T}$ spectrum.

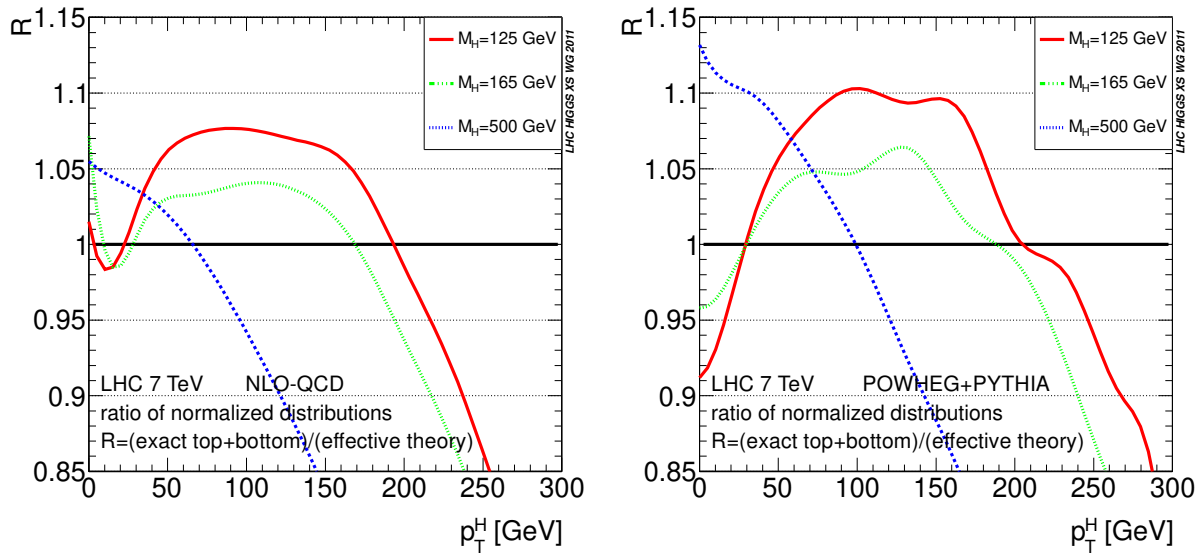

Fig. 40: Ratio, for different values of the SM Higgs-boson mass, of the normalised Higgs transverse-momentum distribution computed with exact top- and bottom-mass dependence over the one obtained in the ET. Left: ratio of the NLO QCD predictions. Right: ratio of the POWHEG+PYTHIA predictions.

In the equation above the variables $\bar{\Phi}_1 \equiv (M^2, Y)$ denote the invariant mass squared and the rapidity of the Higgs boson, which describe the kinematics of the Born (i.e., lowest-order) process $\mathrm{gg} \to \phi$. The variables Φ_{rad} describe the kinematics of the additional final-state parton in the real emission processes. The factor $\bar{B}(\bar{\Phi}_1)$ in Eq. (16) is related to the total cross section computed at NLO in QCD. It contains the value of the differential cross section, including real and virtual radiative corrections, for a given configuration of the Born final-state variables, integrated over the radiation variables. The integral of this quantity on $d\bar{\Phi}_1$, without acceptance cuts, yields the total cross section and is responsible for the correct NLO QCD normalisation of the result. The terms within curly brackets in Eq. (16) describe the real emission spectrum of an extra parton: the first term is the probability of not emitting any parton with transverse momentum larger than a cutoff $p_{\mathrm{T}}^{\mathrm{min}}$, while the second term is the probability of not emitting any parton with transverse momentum larger than a given value p_{T} times the probability of emitting a parton with transverse momentum equal to p_{T}. The sum of the two terms fully describes the probability of having either zero or one additional parton in the final state. The probability of non-emission of a parton with transverse momentum k_{T} larger than p_{T} is obtained using the POWHEG Sudakov form factor

$$\Delta(\bar{\Phi}_1, p_{\mathrm{T}}) = \exp\left\{ -\int d\Phi_{\mathrm{rad}} \frac{R(\bar{\Phi}_1, \Phi_{\mathrm{rad}})}{B(\bar{\Phi}_1)} \theta(k_{\mathrm{T}} - p_{\mathrm{T}}) \right\} , \tag{17}$$

where the Born squared matrix element is indicated by $B(\bar{\Phi}_1)$ and the squared matrix element for the real emission of an additional parton can be written, considering the subprocesses $\mathrm{gg} \to \phi\mathrm{g}$ and $\mathrm{gq} \to \phi\mathrm{q}$, as

$$R(\bar{\Phi}_1, \Phi_{\mathrm{rad}}) = R_{\mathrm{gq}}(\bar{\Phi}_1, \Phi_{\mathrm{rad}}) + \sum_{\mathrm{q}} \left[R_{\mathrm{gq}}(\bar{\Phi}_1, \Phi_{\mathrm{rad}}) + R_{\mathrm{qg}}(\bar{\Phi}_1, \Phi_{\mathrm{rad}}) \right] . \tag{18}$$

Finally, the last term in Eq. (16) describes the effect of the $\mathrm{q}\bar{\mathrm{q}} \to \phi\mathrm{g}$ channel, which has been kept apart in the generation of the first hard emission, because it does not factorise into the Born cross section times an emission factor.

The NLO QCD matrix elements used in this implementation have been computed in Refs. [210, 211]. We compared the numerical results for the distributions with those of the code FEHIPRO [208], finding good agreement. We also checked that, in the case of a light Higgs and considering only the top

contribution, the ET provides a very good approximation of the exact result for small values of the Higgs transverse momentum $p_{\rm T}^{\rm H}$, and only when $p_{\rm T}^{\rm H} > m_{\rm t}$ does a significant discrepancy appear, due to the fact that the internal structure of the top-quark loop is resolved.

In order to appreciate the importance of the exact treatment of the quark masses, we compare in Figure 40 the normalised distributions computed with the exact top- and bottom-mass dependence with the corresponding distributions obtained in the ET. The normalised distributions are defined dividing each distribution by the corresponding total cross section, and allow a comparison of the shape of the distributions. In the left panel of Figure 40 we plot the ratio of the normalised $p_{\rm T}^{\rm H}$ distributions (exact over ET) computed using the real radiation matrix elements that enter in the NLO QCD calculation, for different values of the Higgs mass ($M_{\rm H} = 125,\ 165,\ 500$ GeV). The plot shows that, for a light Higgs, the bottom-quark contribution induces positive $\mathcal{O}(10\%)$ corrections in the intermediate $p_{\rm T}^{\rm H}$ range. On the other hand, for a heavy Higgs, the bottom-quark contribution is negligible, while the exact treatment of the top-quark contribution tends to enhance the distribution at small $p_{\rm T}^{\rm H}$ and significantly reduce it at large $p_{\rm T}^{\rm H}$ (where in any case the cross section is small).

The matching of the NLO QCD results with a QCD PS is obtained by using the basic POWHEG formula, Eq. (16), for the first hard emission, and then by vetoing in the PS any emission with a virtuality larger than the one of the first emission. The use of the exact matrix elements in Eq. (16), and in particular in the POWHEG Sudakov form factor, Eq. (17), has an important impact on the $p_{\rm T}^{\rm H}$ distribution when compared with the distribution obtained in the ET. Indeed, one should observe that the POWHEG Sudakov form factor is a process-dependent quantity. For a given transverse momentum $p_{\rm T}$, in the exponent we find the integral of the ratio of the full squared matrix elements R/B over all the transverse momenta $k_{\rm T}$ larger than $p_{\rm T}$.

The results of the matching of POWHEG with the PYTHIA PS are illustrated in the right plot of Figure 40, where we show the ratio of the normalised $p_{\rm T}^{\rm H}$ distribution computed with exact top- and bottom-mass dependence over the corresponding distribution computed in the ET, for the same values of $M_{\rm H}$ as in the left plot. We shall first discuss the case of a light Higgs boson, with $M_{\rm H} = 125$ GeV. For small $p_{\rm T}^{\rm H}$, the Sudakov form factor with exact top- and bottom-quark mass dependence $\Delta({\rm t+b, exact})$ is smaller than the corresponding factor $\Delta({\rm t}, \infty)$ with only top in the ET, because we have that $R({\rm t+b, exact})/B({\rm t+b, exact}) > R({\rm t}, \infty)/B({\rm t}, \infty)$. The inequality holds for two reasons: $i)$ the $p_{\rm T}^{\rm H}$ distribution is proportional to the squared real matrix element R and, for $p_{\rm T}^{\rm H} < 200$ GeV, $R({\rm t+b, exact}) > R({\rm t}, \infty)$, as has been discussed in Refs. [190, 225, 227]; $ii)$ the bottom quark reduces the LO cross section, with respect to the case with only the top quark in the ET [66]. Thus, for small $p_{\rm T}^{\rm H}$ the Sudakov form factor suppresses the $p_{\rm T}^{\rm H}$ distribution by almost 10% with respect to the results obtained in the ET. Since the emission probability is also proportional to the ratio R/B, as can be read from Eq. (16), starting from $p_{\rm T}^{\rm H} \simeq 30$ GeV this factor prevails over the Sudakov factor, and the distribution with exact dependence on the quark masses becomes larger than the one in the ET by slightly more than 10% – as already observed at NLO QCD in the left plot. We remark that the effects due to the exact treatment of the masses of the top and bottom quarks $i)$ are of the same order of magnitude as the QCD perturbative theoretical uncertainty estimated with HQT and $ii)$ have a non-trivial shape for different values of $p_{\rm T}^{\rm H}$. If added to the HQT prediction, these effects would modify in a non-trivial way the prediction of the central value of the distribution.

A different behaviour is found in the case of a heavy Higgs boson, with $M_{\rm H} = 500$ GeV, because the bottom quark plays a negligible role. At NLO QCD only the top-quark mass effects are relevant, at large $p_{\rm T}^{\rm H}$, yielding a negative correction. In turn, the Sudakov form factor, evaluated for small $p_{\rm T}^{\rm H}$, is larger than in the ET (in fact $R({\rm t+b, exact})/B({\rm t+b, exact}) < R({\rm t}, \infty)/B({\rm t}, \infty)$), yielding what we would call a Sudakov enhancement. Also in this case, starting from $p_{\rm T}^{\rm H} \simeq 70$ GeV the effect of the emission probability factor R/B prevails over the effect of the Sudakov form factor, leading to negative corrections with respect to the ET case.

5.1.3 Summary

An improved release of the code for Higgs-boson production in gluon fusion in the POWHEG framework has been prepared [190], including the complete NLO QCD matrix elements with exact dependence on the top- and bottom-quark masses. This code allows a full simulation of the process, matching the NLO results with the SMC PYTHIA.

The quark-mass effects on the total cross section and on the Higgs rapidity distribution are at the level of a few per cent. On the other hand, the bottom-quark contribution is especially relevant in the study of the transverse-momentum distribution of a light Higgs boson. Indeed, the bottom contribution enhances the real emission amplitude with respect to the result obtained in the ET. The outcome is a non-trivial distortion of the shape of the Higgs transverse-momentum distribution, at the level of $\mathcal{O}(10\%)$ of the result obtained in the ET. These effects are comparable to the present estimates of the perturbative QCD theoretical uncertainty (see Section 5.4).

5.2 Perturbative uncertainties in exclusive jet bins[22]

5.2.1 Overview

In this section we discuss the evaluation of perturbative theory uncertainties in predictions for exclusive jet cross sections, which have a particular number of jets in the final state. This is relevant for measurements where the data are divided into exclusive jet bins, and is usually done when the background composition strongly depends on the number of jets, or when the overall sensitivity can be increased by optimizing the analysis for the individual jet bins. The primary example is the $\mathrm{H} \to \mathrm{WW}$ analysis, which is performed separately in exclusive 0-jet, 1-jet, and 2-jet channels. Other examples are vector-boson fusion analyses, which are typically performed in the exclusive 2-jet channel, boosted $\mathrm{H} \to \mathrm{b\bar{b}}$ analyses that include a veto on additional jets, as well as $\mathrm{H} \to \tau\tau$ and $\mathrm{H} \to \gamma\gamma$ which benefit from improved sensitivity when the Higgs recoils against a jet. When the measurements are performed in exclusive jet bins, the perturbative uncertainties in the theoretical predictions must also be evaluated separately for each individual jet bin [203]. When combining channels with different jet multiplicities, the correlations between the theoretical uncertainties can be significant and must be taken into account [204]. We will use the notation σ_N for an *exclusive* N-jet cross section (with exactly N jets), and the notation $\sigma_{\geq N}$ for an *inclusive* N-jet cross section (with N or more jets). Three possible methods for evaluating the uncertainties in exclusive jet cross sections are:

A) "Direct Exclusive Scale Variation". Here the uncertainties are evaluated by directly varying the renormalisation and factorisation scales in the fixed-order predictions for each exclusive jet cross section σ_N. The results are taken as 100% correlated, such that when adding the exclusive jet cross sections one recovers the scale variation in the total cross section.

B) "Combined Inclusive Scale Variation", as proposed in Ref. [204]. Here, the perturbative uncertainties in the inclusive N-jet cross sections, $\sigma_{\geq N}$, are treated as the primary uncertainties that can be evaluated by scale variations in fixed-order perturbation theory. These uncertainties are treated as uncorrelated for different N. The exclusive N-jet cross sections are obtained using $\sigma_N = \sigma_{\geq N} - \sigma_{\geq N+1}$. The uncertainties and correlations follow from standard error propagation, including the appropriate anticorrelations between σ_N and $\sigma_{N\pm1}$ related to the division into jet bins.

C) "Uncertainties from Resummation with Reweighting." Resummed calculations for exclusive jet cross sections can provide uncertainty estimates that allow one to simultaneously include both types of correlated and anticorrelated uncertainties as in methods A and B. The magnitude of the uncertainties may also be reduced from the resummation of large logarithms.

[22] I. W. Stewart and F. J. Tackmann.

Method B avoids a potential underestimate of the uncertainties in individual jet bins due to strong cancellations that can potentially take place in method A. An explicit demonstration that different treatments of the uncontrolled higher-order $\mathcal{O}(\alpha_s^3)$ terms in method A can lead to very different LHC predictions is given in Section 5.3. Method B produces realistic perturbative uncertainties for exclusive jet cross sections when using fixed-order predictions for various processes. It is the main topic of this section, which follows Ref. [204]. In method C one can utilise higher-order resummed predictions for the exclusive jet cross sections, which allow one to obtain improved central values and further refined uncertainty estimates. This is discussed in Section 5.5. The uncertainties from method B are more consistent with the information one gains about jet-binning effects from using resummation.

For method B the theoretical motivation from the basic structure of the perturbative series is outlined in Section 5.2.2. An implementation for the example of the 0-jet and 1-jet bins is given in Section 5.2.3. If theory predictions are required for irreducible backgrounds in jet bins, then the same method should be used to evaluate the perturbative uncertainties, for e.g., in the case of $\mathrm{H} \to \mathrm{WW}$, the $\mathrm{q\bar{q}} \to \mathrm{WW}$ and $\mathrm{gg} \to \mathrm{WW}$ direct production channels.

Note that here we are only discussing the theoretical uncertainties due to unknown higher-order perturbative corrections, which are commonly estimated using scale variation. Parametric uncertainties, such as PDF and α_s uncertainties, must be treated appropriately as common sources for all investigated channels.

5.2.2 Theoretical motivation

To start, we consider the simplest example of dividing the total cross section, σ_{total}, into an *exclusive* 0-jet bin, $\sigma_0(p^{\mathrm{cut}})$, and the remaining *inclusive* (≥ 1)-jet bin, $\sigma_{\geq 1}(p^{\mathrm{cut}})$,

$$\sigma_{\mathrm{total}} = \int_0^{p^{\mathrm{cut}}} dp\, \frac{d\sigma}{dp} + \int_{p^{\mathrm{cut}}} dp\, \frac{d\sigma}{dp} \equiv \sigma_0(p^{\mathrm{cut}}) + \sigma_{\geq 1}(p^{\mathrm{cut}})\,. \tag{19}$$

Here p denotes the kinematic variable which is used to divide up the cross section into jet bins. A typical example is $p \equiv p_{\mathrm{T}}^{\mathrm{jet}}$, defined by the largest p_{T} of any jet in the event, such that $\sigma_0(p_{\mathrm{T}}^{\mathrm{cut}})$ only contains events with jets having $p_{\mathrm{T}} < p_{\mathrm{T}}^{\mathrm{cut}}$, and $\sigma_{\geq 1}(p_{\mathrm{T}}^{\mathrm{cut}})$ contains events with at least one jet with $p_{\mathrm{T}} > p_{\mathrm{T}}^{\mathrm{cut}}$. The definition of σ_0 may also include dependence on rapidity, such as only considering jets within the rapidity range $|\eta^{\mathrm{jet}}| < \eta^{\mathrm{cut}}$.

The phase-space restriction defining σ_0 changes its perturbative structure compared to that of σ_{total} and in general gives rise to an additional perturbative uncertainty which we denote by Δ_{cut}. This can be thought of as an uncertainty related to large logarithms of p^{cut}, or more generally as an uncertainty associated to computing a less inclusive cross section, which is theoretically more challenging. In Eq. (19) both σ_0 and $\sigma_{\geq 1}$ depend on the phase-space cut, p^{cut}, and by construction this dependence cancels in $\sigma_0 + \sigma_{\geq 1}$. Hence, the additional uncertainty Δ_{cut} induced by p^{cut} must be 100% anticorrelated between $\sigma_0(p^{\mathrm{cut}})$ and $\sigma_{\geq 1}(p^{\mathrm{cut}})$, such that it cancels in their sum. For example, using a covariance matrix to model the uncertainties and correlations, the contribution of Δ_{cut} to the covariance matrix for $\{\sigma_0, \sigma_{\geq 1}\}$ must be of the form

$$C_{\mathrm{cut}} = \begin{pmatrix} \Delta_{\mathrm{cut}}^2 & -\Delta_{\mathrm{cut}}^2 \\ -\Delta_{\mathrm{cut}}^2 & \Delta_{\mathrm{cut}}^2 \end{pmatrix}\,. \tag{20}$$

The questions then are: (1) How can we estimate Δ_{cut} in a simple way, and (2) how is the perturbative uncertainty Δ_{total} of σ_{total} related to the uncertainties of σ_0 and $\sigma_{\geq 1}$? To answer these questions, we discuss the perturbative structure of the cross sections in more detail.

By restricting the cross section to the 0-jet region, one restricts the collinear initial-state radiation from the colliding hard partons as well as the overall soft radiation in the event. This restriction on additional emissions leads to the appearance of Sudakov double logarithms of the form $L^2 = \ln^2(p^{\mathrm{cut}}/Q)$ at

each order in perturbation theory, where Q is the hard scale of the process. For Higgs production from gluon fusion, $Q = M_{\rm H}$, and the leading double logarithms appearing at $\mathcal{O}(\alpha_{\rm s})$ are

$$\sigma_0(p_{\rm T}^{\rm cut}) = \sigma_B\Big(1 - \frac{3\alpha_{\rm s}}{\pi}\, 2\ln^2\frac{p_{\rm T}^{\rm cut}}{M_{\rm H}} + \cdots\Big)\,, \tag{21}$$

where σ_B is the Born (tree-level) cross section.

The total cross section only depends on the hard scale Q, which means by choosing the scale $\mu \simeq Q$, the fixed-order expansion does not contain large logarithms and has the structure[23]

$$\sigma_{\rm total} \simeq \sigma_B\big[1 + \alpha_{\rm s} + \alpha_{\rm s}^2 + \mathcal{O}(\alpha_{\rm s}^3)\big]\,. \tag{22}$$

As usual, varying the scale in $\alpha_{\rm s}$ (and the PDFs) one obtains an estimate of the size of the missing higher-order terms in this series, corresponding to $\Delta_{\rm total}$.

The inclusive 1-jet cross section has the perturbative structure

$$\sigma_{\geq 1}(p^{\rm cut}) \simeq \sigma_B\big[\alpha_{\rm s}(L^2 + L + 1) + \alpha_{\rm s}^2(L^4 + L^3 + L^2 + L + 1) + \mathcal{O}(\alpha_{\rm s}^3 L^6)\big]\,, \tag{23}$$

where the logarithms $L = \ln(p^{\rm cut}/Q)$. For $p^{\rm cut} \ll Q$ these logarithms can get large enough to overcome the $\alpha_{\rm s}$ suppression. In the limit $\alpha_{\rm s}L^2 \simeq 1$, the fixed-order perturbative expansion breaks down and the logarithmic terms must be resummed to all orders in $\alpha_{\rm s}$ to obtain a meaningful result. For typical experimental values of $p^{\rm cut}$ fixed-order perturbation theory can still be considered, but the logarithms cause large corrections at each order and dominate the series. This means varying the scale in $\alpha_{\rm s}$ in Eq. (23) tracks the size of the large logarithms and therefore allows one to get an estimate of the size of missing higher-order terms caused by $p^{\rm cut}$, which corresponds to the uncertainty $\Delta_{\rm cut}$. Therefore, we can approximate $\Delta_{\rm cut} = \Delta_{\geq 1}$, where $\Delta_{\geq 1}$ is obtained from the scale variation for $\sigma_{\geq 1}$.

The exclusive 0-jet cross section is equal to the difference between Eqs. (22) and (23), and so has the schematic structure

$$\begin{aligned}\sigma_0(p^{\rm cut}) &= \sigma_{\rm total} - \sigma_{\geq 1}(p^{\rm cut})\\ &\simeq \sigma_B\Big\{\big[1 + \alpha_{\rm s} + \alpha_{\rm s}^2 + \mathcal{O}(\alpha_{\rm s}^3)\big] - \big[\alpha_{\rm s}(L^2 + L + 1) + \alpha_{\rm s}^2(L^4 + L^3 + L^2 + L + 1) + \mathcal{O}(\alpha_{\rm s}^3 L^6)\big]\Big\}\,.\end{aligned} \tag{24}$$

In this difference, the large positive corrections in $\sigma_{\rm total}$ partly cancel against the large negative logarithmic corrections in $\sigma_{\geq 1}$. For example, at $\mathcal{O}(\alpha_{\rm s})$ there is a value of L for which the $\alpha_{\rm s}$ terms in Eq. (24) cancel exactly. At this $p^{\rm cut}$ the NLO 0-jet cross section has vanishing scale dependence and is equal to the LO cross section, $\sigma_0(p^{\rm cut}) = \sigma_B$. Due to this cancellation, a standard use of scale variation in $\sigma_0(p^{\rm cut})$ does not actually probe the size of the large logarithms, and thus is not suitable to estimate $\Delta_{\rm cut}$. This issue impacts the uncertainties in the experimentally relevant region for $p^{\rm cut}$.

For example, for $\rm gg \to H$ (with $\sqrt{s} = 7$ TeV, $M_{\rm H} = 165$ GeV, $\mu_{\rm F} = \mu_{\rm R} = M_{\rm H}/2$), one finds [173, 195–197]

$$\begin{aligned}\sigma_{\rm total} &= (3.32\,{\rm pb})\big[1 + 9.5\,\alpha_{\rm s} + 35\,\alpha_{\rm s}^2 + \mathcal{O}(\alpha_{\rm s}^3)\big]\,,\\ \sigma_{\geq 1}\big(p_{\rm T}^{\rm jet} > 30\ {\rm GeV}, |\eta^{\rm jet}| < 3.0\big) &= (3.32\,{\rm pb})\big[4.7\,\alpha_{\rm s} + 26\,\alpha_{\rm s}^2 + \mathcal{O}(\alpha_{\rm s}^3)\big]\,.\end{aligned} \tag{25}$$

In $\sigma_{\rm total}$ one can see the impact of the well-known large K factors. (Using instead $\mu_{\rm F} = \mu_{\rm R} = M_{\rm H}$ the $\alpha_{\rm s}$ and $\alpha_{\rm s}^2$ coefficients in $\sigma_{\rm total}$ increase to 11 and 65.) In $\sigma_{\geq 1}$, one can see the impact of the large

[23] These expressions for the perturbative series are schematic. The convolution with the parton distribution functions (PDFs) and μ-dependent logarithms enter in the coefficients of the series, which are not displayed. (The single logarithms related to the PDF evolution are not the logarithms we are most interested in discussing.)

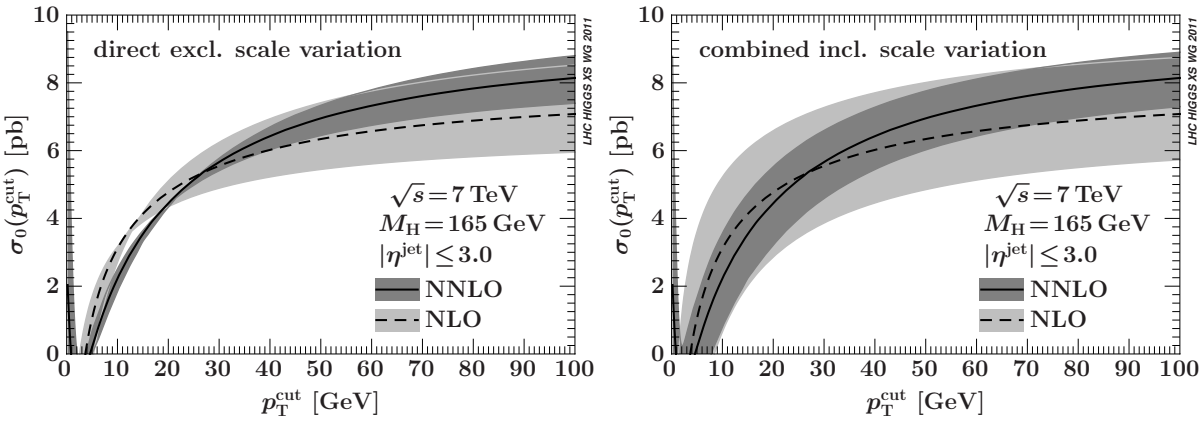

Fig. 41: Fixed-order perturbative uncertainties for $\mathrm{gg} \to \mathrm{H} + 0$ jets at NLO and NNLO. On the left, the uncertainties are obtained from the direct exclusive scale variation in $\sigma_0(p_\mathrm{T}^\mathrm{cut})$ between $\mu = M_\mathrm{H}/4$ and $\mu = M_\mathrm{H}$ (method A). On the right, the uncertainties are obtained by independently evaluating the inclusive scale uncertainties in σ_total and $\sigma_{\geq 1}(p^\mathrm{cut})$ and combining them in quadrature (method B). The plots are taken from Ref. [204].

logarithms on the perturbative series. Taking their difference to get σ_0, one observes a sizeable numerical cancellation between the two series at each order in α_s.

Since Δ_cut and Δ_total are by definition uncorrelated, by associating $\Delta_\mathrm{cut} = \Delta_{\geq 1}$ we are effectively treating the perturbative series for σ_total and $\sigma_{\geq 1}$ as independent with uncorrelated perturbative uncertainties. That is, considering $\{\sigma_\mathrm{total}, \sigma_{\geq 1}\}$, the covariance matrix is diagonal,

$$\begin{pmatrix} \Delta_\mathrm{total}^2 & 0 \\ 0 & \Delta_{\geq 1}^2 \end{pmatrix} , \tag{26}$$

where Δ_total and $\Delta_{\geq 1}$ are evaluated by separate scale variations in the fixed-order predictions for σ_total and $\sigma_{\geq 1}$. This is consistent, since for small p^cut the two series have very different structures. In particular, there is no reason to believe that the same cancellations in σ_0 will persist at every order in perturbation theory at a given p^cut. It follows that the perturbative uncertainty in $\sigma_0 = \sigma_\mathrm{total} - \sigma_{\geq 1}$ is given by $\Delta_\mathrm{total}^2 + \Delta_{\geq 1}^2$, and the resulting covariance matrix for $\{\sigma_0, \sigma_{\geq 1}\}$ is

$$C = \begin{pmatrix} \Delta_{\geq 1}^2 + \Delta_\mathrm{total}^2 & -\Delta_{\geq 1}^2 \\ -\Delta_{\geq 1}^2 & \Delta_{\geq 1}^2 \end{pmatrix} . \tag{27}$$

The $\Delta_{\geq 1}$ contributions here are equivalent to Eq. (20) with $\Delta_\mathrm{cut} = \Delta_{\geq 1}$. Note also that all of Δ_total occurs in the uncertainty for σ_0. This is reasonable from the point of view that σ_0 starts at the same order in α_s as σ_total and contains the same leading virtual corrections.

The limit $\Delta_\mathrm{cut} = \Delta_{\geq 1}$ that Eq. (27) is based on is of course not exact. However, the preceding arguments show that it is a more reasonable starting point than using a common scale variation for the different jet bins as in method A, since the latter does not account for the additional p^cut induced uncertainties. These two methods of evaluating the perturbative uncertainties are contrasted in Figure 41 for $\mathrm{gg} \to \mathrm{H} + 0$ jets at NLO (light gray) and NNLO (dark gray) as a function of $p_\mathrm{T}^\mathrm{cut}$ (using $\mu = M_\mathrm{H}/2$ for the central scale choice). The left panel shows the uncertainties from method A obtained from a direct scale variation by a factor of two in $\sigma_0(p_\mathrm{T}^\mathrm{cut})$. For small values of $p_\mathrm{T}^\mathrm{cut}$ the cancellations that take place in $\sigma_0(p^\mathrm{cut})$ cause the error bands to shrink and eventually vanish at $p_\mathrm{T}^\mathrm{cut} \simeq 25$ GeV, where there is an almost exact cancellation between the two series in Eq. (24). In contrast, in the right panel the uncertainties are obtained using the above method B by combining the independent inclusive uncertainties to obtain the exclusive uncertainty, $\Delta_0^2 = \Delta_\mathrm{total}^2 + \Delta_{\geq 1}^2$. For large values of $p_\mathrm{T}^\mathrm{cut}$ this reproduces the direct exclusive scale variation, since $\sigma_{\geq 1}(p^\mathrm{cut})$ becomes small. On the other hand, for

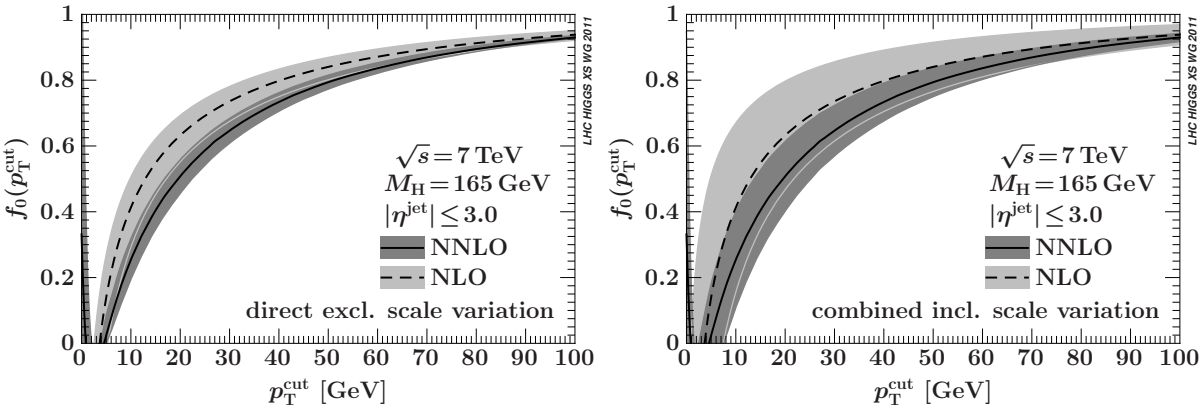

Fig. 42: Same as Figure 41 but for the 0-jet fraction $f_0(p_{\rm T}^{\rm cut}) = \sigma_0(p_{\rm T}^{\rm cut})/\sigma_{\rm total}$.

small values of $p_{\rm T}^{\rm cut}$ the uncertainties estimated in this way are more realistic, because they explicitly estimate the uncertainties due to the large logarithmic corrections. The features of this plot are quite generic. In particular, the same pattern of uncertainties is observed for the Tevatron, when using $\mu = M_{\rm H}$ as our central scale (with $\mu = 2M_{\rm H}$ and $\mu = M_{\rm H}/2$ for the range of scale variation), whether or not we only look at jets at central rapidities, or when considering the exclusive 1-jet cross section. We also note that using independent variations for $\mu_{\rm F}$ and $\mu_{\rm R}$ does not change this picture, in particular the $\mu_{\rm F}$ variation for fixed $\mu_{\rm R}$ is quite small. In Figure 42 we again compare the two methods, but now for the event fraction $f_0(p_{\rm T}^{\rm cut}) = \sigma_0(p_{\rm T}^{\rm cut})/\sigma_{\rm total}$. At large $p_{\rm T}^{\rm cut}$ the curves approach unity, and the uncertainty asymptotically vanishes. At small $p_{\rm T}^{\rm cut}$ the uncertainties in f_0 are quite small with method A. In method B the uncertainties are more realistic, and there is now a significant overlap between the bands at NLO and NNLO.

The generalisation of the above discussion to more jets and several jet bins is straightforward. For the N-jet bin we replace $\sigma_{\rm total} \to \sigma_{\geq N}$, $\sigma_0 \to \sigma_N$, and $\sigma_{\geq 1} \to \sigma_{\geq N+1}$, and take the appropriate σ_B. If the perturbative series for $\sigma_{\geq N}$ exhibits large $\alpha_{\rm s}$ corrections due to its logarithmic series or otherwise, then the presence of a different series of large logarithms in $\sigma_{\geq N+1}$ will again lead to cancellations when we consider the difference $\sigma_N = \sigma_{\geq N} - \sigma_{\geq N+1}$. Hence, $\Delta_{\geq N+1}$ will again give a better estimate for the extra $\Delta_{\rm cut}$ type uncertainty that arises from separating $\sigma_{\geq N}$ into σ_N and $\sigma_{\geq N+1}$. Plots for the 1-jet bin for Higgs production from gluon fusion can be found in Ref. [204].

5.2.3 Example implementation for $H + 0$ Jet and $H + 1$ jet channels

To illustrate the implications for a concrete example we consider the 0-jet and 1-jet bins together with the remaining (≥ 2)-jet bin. By construction only neighboring jet bins are correlated, so the generalisation to more jet bins is not any more complicated. We denote the total inclusive cross section by $\sigma_{\rm total}$, and the inclusive 1-jet and 2-jet cross sections by $\sigma_{\geq 1}$ and $\sigma_{\geq 2}$. Their respective absolute uncertainties are $\Delta_{\rm total}$, $\Delta_{\geq 1}$, $\Delta_{\geq 2}$, and their relative uncertainties are given by $\delta_i = \Delta_i/\sigma_i$. The exclusive 0-jet cross section, σ_0, and 1-jet cross section, σ_1, satisfy the relations

$$\sigma_0 = \sigma_{\rm total} - \sigma_{\geq 1}\,, \qquad \sigma_1 = \sigma_{\geq 1} - \sigma_{\geq 2}\,, \qquad \sigma_{\rm total} = \sigma_0 + \sigma_1 + \sigma_{\geq 2}\,. \tag{28}$$

Experimentally it is convenient to work with the exclusive 0-jet and 1-jet fractions defined as

$$f_0 = \frac{\sigma_0}{\sigma_{\rm total}}\,, \qquad f_1 = \frac{\sigma_1}{\sigma_{\rm total}}\,. \tag{29}$$

Treating the inclusive uncertainties $\Delta_{\rm total}$, $\Delta_{\geq 1}$, $\Delta_{\geq 2}$ as uncorrelated, the covariance matrix for

the three quantities $\{\sigma_{\rm total}, \sigma_0, \sigma_1\}$ is given by

$$C = \begin{pmatrix} \Delta^2_{\rm total} & \Delta^2_{\rm total} & 0 \\ \Delta^2_{\rm total} & \Delta^2_{\rm total} + \Delta^2_{\geq 1} & -\Delta^2_{\geq 1} \\ 0 & -\Delta^2_{\geq 1} & \Delta^2_{\geq 1} + \Delta^2_{\geq 2} \end{pmatrix} . \tag{30}$$

The relative uncertainties and correlations for σ_0 and σ_1 directly follow from Eq. (30). Writing them in terms of the relative quantities f_i and δ_i, one gets

$$\begin{aligned}
\delta(\sigma_0)^2 &= \frac{1}{f_0^2}\,\delta^2_{\rm total} + \Big(\frac{1}{f_0} - 1\Big)^2 \delta^2_{\geq 1}\,, \\
\delta(\sigma_1)^2 &= \Big(\frac{1-f_0}{f_1}\Big)^2 \delta^2_{\geq 1} + \Big(\frac{1-f_0}{f_1} - 1\Big)^2 \delta^2_{\geq 2}\,, \\
\rho(\sigma_0, \sigma_{\rm total}) &= \left[1 + \frac{\delta^2_{\geq 1}}{\delta^2_{\rm total}}(1-f_0)^2\right]^{-1/2}, \\
\rho(\sigma_1, \sigma_{\rm total}) &= 0\,, \\
\rho(\sigma_0, \sigma_1) &= -\left[1 + \frac{\delta^2_{\rm total}}{\delta^2_{\geq 1}}\,\frac{1}{(1-f_0)^2}\right]^{-1/2} \left[1 + \frac{\delta^2_{\geq 2}}{\delta^2_{\geq 1}}\Big(1 - \frac{f_1}{1-f_0}\Big)^2\right]^{-1/2} .
\end{aligned} \tag{31}$$

Alternatively, we can use $\{\sigma_{\rm total}, f_0, f_1\}$ as the three independent quantities. Their relative uncertainties and correlations following from Eq. (30) are then

$$\begin{aligned}
\delta(f_0)^2 &= \Big(\frac{1}{f_0} - 1\Big)^2 (\delta^2_{\rm total} + \delta^2_{\geq 1})\,, \\
\delta(f_1)^2 &= \delta^2_{\rm total} + \Big(\frac{1-f_0}{f_1}\Big)^2 \delta^2_{\geq 1} + \Big(\frac{1-f_0}{f_1} - 1\Big)^2 \delta^2_{\geq 2}\,, \\
\rho(f_0, \sigma_{\rm total}) &= \left[1 + \frac{\delta^2_{\geq 1}}{\delta^2_{\rm total}}\right]^{-1/2}, \\
\rho(f_1, \sigma_{\rm total}) &= -\frac{\delta_{\rm total}}{\delta(f_1)}\,, \\
\rho(f_0, f_1) &= -\left(1 + \frac{1-f_0}{f_1}\frac{\delta^2_{\geq 1}}{\delta^2_{\rm total}}\right)\Big(\frac{1}{f_0} - 1\Big)\frac{\delta^2_{\rm total}}{\delta(f_0)\delta(f_1)}\,.
\end{aligned} \tag{32}$$

The basic steps of the analysis are the same irrespective of the statistical model:

1. Independently evaluate the inclusive perturbative uncertainties $\delta_{\rm total}$, $\delta_{\geq 1}$, $\delta_{\geq 2}$ by appropriate scale variations in the available fixed-order calculations.
2. Consider the δ_i uncorrelated and use Eqs. (28) or (29) to propagate them into the uncertainties of $\sigma_{0,1}$ or $f_{0,1}$.

For example, when using log-likelihoods, the independent uncertainties $\delta_{\rm total}$, $\delta_{\geq 1}$, $\delta_{\geq 2}$ are implemented via three independent nuisance parameters.

In Step 1, $\delta_{\rm total}$ can be taken from the NNLO perturbative uncertainty in the first Yellow Report [7], while $\delta_{\geq 1}$ is evaluated at relative NLO and $\delta_{\geq 2}$ at relative LO using any of HNNLO [173, 197], FEHiP [195, 196], or MCFM [230]. For the central scales $\mu_{\rm F} = \mu_{\rm R} = M_{\rm H}/2$ should be used to be consistent with $\sigma_{\rm total}$ from Ref. [7]. Numerically $\sigma_{\geq 1}$ also exhibits better convergence with this choice for the central scale. Note that $\sigma_{\geq 2}$ is defined by inverting the cut on the second jet in σ_1 and is not independent of $\{\sigma_{\rm total}, \sigma_0, \sigma_1\}$. Its per-cent uncertainty $\delta_{\geq 2}$ naturally enters because of the theory correlation model and for this purpose it should be taken at LO. Also note that $\sigma_{\geq 2}$ is different from the 2-jet bin, σ_2.

If σ_2 is included one extends the matrix by an extra row/column, and uses as input that the uncertainties in $\sigma_{\rm total}$, $\sigma_{\geq 1}$, $\sigma_{\geq 2}$, $\sigma_{\geq 3}$ are independent.

When σ_2 is used in the analysis with additional vector-boson fusion cuts, one can determine the uncertainties with the appropriate $\sigma_{\geq 2}$ at NLO and $\sigma_{\geq 3}$ at LO from MCFM [230]. To combine the σ_2 with additional vector-boson-fusion cuts with the 0-jet and 1-jet gluon-fusion bins, one treats the VBF uncertainty as uncorrelated with those from gluon fusion, and assigns a 100% correlation between the perturbative uncertainties of the two different gluon-fusion $\sigma_{\geq 2}$s that appear in these computations.

Step 2 above also requires values for f_0 and f_1 as input. In the experimental analyses, the central values for f_0 and f_1 effectively come from a full Monte Carlo simulation. By only using relative quantities, the different overall normalisations in the fixed-order calculation and the Monte Carlo drop out. However, the values for f_0 and f_1 obtained from the fixed-order calculation can still be quite different from those in the Monte Carlo, because the fixed-order results incorporate NNLO $\alpha_{\rm s}$ corrections, while the Monte Carlo includes some resummation as well as detector effects. A priori the values for $f_{0,1}$ obtained either way could be used as input for the uncertainty calculation in Step 2. One can cross check that the two choices lead to similar results for the final uncertainties.

It is useful to illustrate this with a numerical example corresponding to Figure 41, for which we take $p_{\rm T}^{\rm cut} = 30$ GeV and $\eta^{\rm cut} = 3.0$. For $M_{\rm H} = 165$ GeV, we have $\sigma_{\rm total} = (8.76 \pm 0.80)$ pb, $\sigma_{\geq 1} = (3.10 \pm 0.61)$ pb, and $\sigma_{\geq 2} = (0.73 \pm 0.42)$ pb, corresponding to the relative uncertainties $\delta_{\rm total} = 9.1\%$, $\delta_{\geq 1} = 19.9\%$, and $\delta_{\geq 2} = 57\%$. Using these as inputs in Eq. (31) we find for the exclusive jet cross sections $\delta(\sigma_0) = 18\%$, $\delta(\sigma_1) = 31\%$ with correlations coefficients $\rho(\sigma_0, \sigma_{\rm total}) = 0.79$, $\rho(\sigma_1, \sigma_{\rm total}) = 0$, and $\rho(\sigma_0, \sigma_1) = -0.50$. We see that σ_0 and σ_1 have a substantial negative correlation because of the jet bin boundary they share. For the exclusive jet fractions using Eq. (32) we obtain $\delta(f_0) = 12\%$ and $\delta(f_1) = 33\%$ with correlations $\rho(f_0, \sigma_{\rm total}) = 0.42$, $\rho(f_1, \sigma_{\rm total}) = -0.28$, and $\rho(f_0, f_1) = -0.84$. The presence of $\sigma_{\rm total}$ in the denominator of the f_i's yields a nonzero anticorrelation for f_1 and $\sigma_{\rm total}$, and a decreased correlation for f_0 and $\sigma_{\rm total}$ compared to σ_0 and $\sigma_{\rm total}$. In contrast to these results, in method A one considers the direct scale variation in the exclusive $\sigma_{0,1}$ as in the left panel of Figure 41. Due to the cancellations between the perturbative series, this approach leads to unrealistically small uncertainties (with the above inputs $\delta(\sigma_0) = 3.2\%$ and $\delta(\sigma_1) = 8.3\%$), which is reflected in the pinching of the bands in the left plot in Figure 41.

As a final remark, we note that strictly speaking, it is somewhat inconsistent to use the relative uncertainties for $f_{0,1}$ from fixed order and apply them to the Monte Carlo predictions for $f_{0,1}$. A more sophisticated treatment would be to first correct the measurements for detector effects to truth-level using Monte Carlo. In the second step, the corrected measurements of σ_0 and σ_1 (with truth-level cuts) can be directly compared to the available calculations, taking into account the theoretical uncertainties as described above. This also automatically makes a clean separation between experimental and theoretical uncertainties. Given the importance and impact of the jet selection cuts, this is very desirable. It would both strengthen the robustness of the extracted experimental limits and validate the theoretical description of the jet selection.

5.3 Perturbative uncertainties in jet-veto efficiencies[24]

In this section we continue our discussion of perturbative uncertainties in predictions for exclusive cross sections, concentrating on the 0-jet cross section, corresponding to having a Higgs and no jets with a transverse momentum above a given $p_{\rm T}^{\rm cut}$.

We examine here the question of the theoretical uncertainty in the prediction of the jet-veto efficiency. In particular, we consider the ambiguity that arises in its calculation from a ratio of two cross sections that are both known at next-to-next-to-leading order (NNLO).

In the following, $\sigma_0(p_{\rm T}^{\rm cut})$ will denote the 0-jet cross section as a function of the jet-transverse-

[24] A. Banfi, G. P. Salam and G. Zanderighi.

momentum threshold $p_{\rm T}^{\rm cut}$, whilst $\sigma_{\rm total}$ will denote the Higgs total cross section, without any jet veto. It is also useful to consider the ratio of these cross sections, $f_0(p_{\rm T}^{\rm cut}) = \sigma_0(p_{\rm T}^{\rm cut})/\sigma_{\rm total}$, which is commonly referred to as the jet-veto efficiency, or the 0-jet fraction as in Section 5.2. Knowledge of this efficiency, and its uncertainty, is important in interpreting measured limits on the Higgs cross section in the 0-jet bin as a limit on the total Higgs production cross section.

Both $\sigma_0(p_{\rm T}^{\rm cut})$ and $\sigma_{\rm total}$ have a fixed-order perturbative expansion of the form

$$\sigma_0(p_{\rm T}^{\rm cut}) = \sigma_0^{(0)}(p_{\rm T}^{\rm cut}) + \sigma_0^{(1)}(p_{\rm T}^{\rm cut}) + \sigma_0^{(2)}(p_{\rm T}^{\rm cut}) + \dots\,, \tag{33a}$$

$$\sigma_{\rm total} = \sigma^{(0)} + \sigma^{(1)} + \sigma^{(2)} + \dots\,, \tag{33b}$$

where the superscript i denotes the fact that the given contribution to the cross section is proportional to $\alpha_{\rm s}^i$ relative to the Born cross section (of order $\alpha_{\rm s}^2$ in the present case). Since no jets are present at the Born level we have $\sigma_0^{(0)}(p_{\rm T}^{\rm cut}) \equiv \sigma^{(0)}$.

The state-of-the-art of fixed-order QCD predictions is NNLO, i.e. the calculation of $\sigma_0(p_{\rm T}^{\rm cut})$ and $\sigma_{\rm total}$ with tools like FEHiP [196] and HNNLO [173].

There is little ambiguity in the definition of the fixed-order results for the total and jet-vetoed cross sections, with the only freedom being, as usual, in the choice of the renormalisation and the factorisation scale. However, given the expressions of σ_0 and $\sigma_{\rm total}$ at a given perturbative order, there is some additional freedom in the way one computes the jet-veto efficiency. For instance, at NNLO the efficiency can be defined as

$$f_0^{(a)}(p_{\rm T}^{\rm cut}) \equiv \frac{\sigma_0^{(0)}(p_{\rm T}^{\rm cut}) + \sigma_0^{(1)}(p_{\rm T}^{\rm cut}) + \sigma_0^{(2)}(p_{\rm T}^{\rm cut})}{\sigma^{(0)} + \sigma^{(1)} + \sigma^{(2)}}\,. \tag{34}$$

This option is the most widely used and may appear at first sight to be the most natural, insofar as one keeps as many terms as possible both in the numerator and denominator. It corresponds to method A of evaluating the uncertainty in the fraction of events in the 0-jet bin defined in Section 5.2.1.

However, other prescriptions are possible. For instance, since the zeroth-order term of $f_0(p_{\rm T}^{\rm cut})$ is equal to 1, one can argue that it is really only $1 - f_0(p_{\rm T}^{\rm cut})$ that has a non-trivial perturbative series, given by the ratio of the inclusive 1-jet cross section above $p_{\rm T}^{\rm cut}$, $\sigma_{\text{1-jet}}^{\rm NLO}(p_{\rm T}^{\rm cut})$, to the total cross section, where

$$\sigma_{\text{1-jet}}^{\rm NLO}(p_{\rm T}^{\rm cut}) = \sigma^{(1)} + \sigma^{(2)} - \left(\sigma_0^{(1)}(p_{\rm T}^{\rm cut}) + \sigma_0^{(2)}(p_{\rm T}^{\rm cut})\right)\,. \tag{35}$$

Insofar as the 1-jet cross section is known only to NLO, in taking the ratio to the total cross section one should also use NLO for the latter, so that an alternative prescription reads

$$f_0^{(b)}(p_{\rm T}^{\rm cut}) = 1 - \frac{\sigma_{\text{1-jet}}^{\rm NLO}(p_{\rm T}^{\rm cut})}{\sigma^{(0)} + \sigma^{(1)}}\,. \tag{36}$$

Finally, another motivated expression for the jet-veto efficiency is just the fixed-order expansion up to $\mathcal{O}(\alpha_{\rm s}^2)$ of Eq. (34), which can be expressed in terms of the LO and NLO inclusive jet cross sections above $p_{\rm T}^{\rm cut}$ as follows

$$f_0^{(c)}(p_{\rm T}^{\rm cut}) = 1 - \frac{\sigma_{\text{1-jet}}^{\rm NLO}(p_{\rm T}^{\rm cut})}{\sigma^{(0)}} + \frac{\sigma^{(1)}}{(\sigma^{(0)})^2}\sigma_{\text{1-jet}}^{\rm LO}(p_{\rm T}^{\rm cut})\,. \tag{37}$$

Prescriptions (a), (b), and (c) differ by terms of relative order $\alpha_{\rm s}^3$ with respect to the Born level, i.e. NNNLO. Therefore, the size of the differences between them is a way to estimate the associated theoretical uncertainty that goes beyond the usual variation of scales.

Let us see how these three prescriptions fare in practice in the case of interest, namely Higgs production at the LHC with 7 TeV centre-of-mass energy. We use MSTW2008NNLO parton distribution functions [107] (even for LO and NLO predictions) with $\alpha_{\rm s}(M_{\rm Z}) = 0.11707$ and three-loop running. Furthermore, we use the large-$m_{\rm t}$ approximation. We choose a Higgs mass of 145 GeV, and default

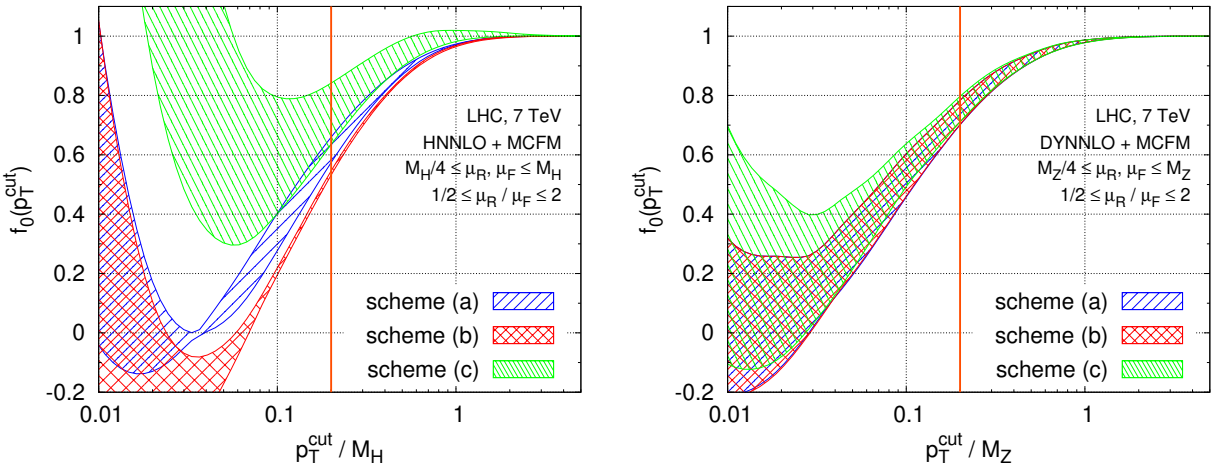

Fig. 43: Jet-veto efficiency for Higgs (left) and Z-boson production (right) using three different prescriptions for the NNLO expansion, see Eqs. (34), (36), (37). The bands are obtained by varying renormalisation and factorisation scales independently around the central value $M_{\rm H}/2$ ($M_{\rm Z}/2$) by a factor of two up and down (with the constraint $\frac{1}{2} < \mu_{\rm R}/\mu_{\rm F} < 2$). NNLO predictions are obtained by suitably combining the total cross sections obtained with HNNLO [173] (DYNNLO [231]) with the 1-jet cross section $\sigma_{\text{1-jet}}(p_{\rm T}^{\rm cut})$ computed with MCFM [232].

renormalisation and factorisation scales of $M_{\rm H}/2$. We cluster partons into jets using the anti-$k_{\rm T}$ jet algorithm [175] with $R = 0.5$, which is the default jet definition for CMS. Switching to $R = 0.4$, as used by ATLAS, has a negligible impact relative to the size of the uncertainties. We include jets up to infinite rapidity, but have checked that the effect of a rapidity cut of $4.5/5$, corresponding to the ATLAS/CMS acceptances, is also much smaller than other uncertainties discussed here.

The corresponding results for the jet-veto efficiencies over a wide range of values of $p_{\rm T}^{\rm cut}/M_{\rm H}$ are shown in Figure 43 (left). Each of the three prescriptions Eqs. (34), (36), (37) is presented together with an associated uncertainty band corresponding to an independent variation of renormalisation and factorisation scales $M_{\rm H}/4 < \mu_{\rm R}, \mu_{\rm F} < M_{\rm H}$ (with the constraint $\frac{1}{2} < \mu_{\rm R}/\mu_{\rm F} < 2$). The solid red vertical line corresponds to a reference jet veto of $0.2 M_{\rm H} \sim 29$ GeV, which is in the ballpark of the value used by ATLAS and CMS to split the cross section in 0-, 1-, and 2-jet bins (25 GeV and 30 GeV, respectively). Several features can be observed: firstly, the three schemes lead to substantially different predictions for the jet-veto efficiency, spanning a range from about 0.50 to 0.85 at the reference jet-veto value. Furthermore, the uncertainty bands from the different schemes barely overlap, indicating that scale uncertainties alone are a poor indicator of true uncertainties here. Finally the uncertainty bands' widths are themselves quite different from one scheme to the next.

The above features are all caused by the poor convergence of the perturbative series. In particular, it seems that two classes of effects are at play here. Firstly, for $p_{\rm T}^{\rm cut} \ll M_{\rm H}$, there are large Sudakov logarithms $\alpha_{\rm s}^n \ln^{2n}(p_{\rm T}^{\rm cut}/M_{\rm H})$. These are the terms responsible for the drop in veto efficiency at low $p_{\rm T}^{\rm cut}$ and the lack of a resummation of these terms to all orders is responsible for the unphysical increase in veto efficiency seen at very low $p_{\rm T}^{\rm cut}$ (resummations of related observables are discussed in Ref. [194, 206]). The second class of effects stems from the fact that the total cross section has a very large NLO/LO K-factor, ~ 2, with substantial corrections also at NNLO (see Table 12). The jet-veto efficiency is closely connected to the 1-jet rate, for which the NNLO corrections are not currently known. It is conceivable that they could be as large, in relative terms, as the NNLO corrections to the total cross section and our different schemes for calculating the perturbative efficiency effectively take that uncertainty into account.

The reader may wonder whether it is really possible to attribute the differences between schemes to the poor convergence of the total cross section. One cross-check of this statement is to examine the jet-veto efficiency for Z-boson production, where, with a central scale choice $\mu = M_{\rm Z}/2$, NLO corrections

	LO	NLO	NNLO
H [pb]	$3.94^{+1.01}_{-0.73}$	$8.53^{+1.86}_{-1.34}$	$10.5^{+0.8}_{-1.0}$
Z [nb]	$22.84^{+2.07}_{-2.40}$	$28.6^{+0.8}_{-1.2}$	$28.6^{+0.4}_{-0.4}$

Table 12: Cross sections for Higgs and Z-boson production in 7 TeV p p collisions, at various orders in perturbation theory. The central value corresponds to the default scale $\mu_{\rm R} = \mu_{\rm F} = M_{\rm H}/2$ ($M_{\rm Z}/2$), the error denotes the scale variation when $\mu_{\rm R}$ and $\mu_{\rm F}$ are varied independently by a factor two around the central value, with the constraint $\frac{1}{2} < \mu_{\rm R}/\mu_{\rm F} < 2$.

to the total cross section are about 25%, and the NNLO ones are a couple of per cent (see Table 12). The results for the jet-veto efficiency are shown in Figure 43 (right). While overall uncertainties remain non-negligible (presumably due to large Sudakov logarithms), the three expansion schemes do indeed give almost identical results for $p_{\rm T}^{\rm cut}/M_{\rm Z} = 0.2$. This supports our interpretation that the poor total-cross-section convergence is a culprit in causing the differences between the three schemes in the Higgs case.

To conclude, in determining the jet-veto efficiency for Higgs production, one should be aware that fixed-order predictions depend significantly on the precise form of the perturbative expansion used to calculate the efficiency, Eqs. (34), (36), or (37). This uncertainty is not reflected in the scale dependence of the predictions, which is likely due to the accidental cancellations between physically unrelated large Sudakov effects and large total-cross-section corrections that are discussed in Section 5.2 and Ref. [204].

5.4 The Higgs $p_{\rm T}$ spectrum and its uncertainties[25]

5.4.1 Introduction

In this section we focus on the transverse-momentum ($p_{\rm T}$) spectrum of the SM Higgs boson. This observable is of direct importance in the experimental search. A good knowledge of the $p_{\rm T}$ spectrum can help to define strategies to improve the statistical significance. When studying the $p_{\rm T}$ distribution of the Higgs boson in QCD perturbation theory it is convenient to distinguish two regions of transverse momenta. In the large-$p_{\rm T}$ region ($p_{\rm T} \sim M_{\rm H}$), where the transverse momentum is of the order of the Higgs-boson mass $M_{\rm H}$, perturbative QCD calculations based on the truncation of the perturbative series at a fixed order in $\alpha_{\rm s}$ are theoretically justified. In this region, the $p_{\rm T}$ spectrum is known up to leading order (LO) [233] with the full dependence of the masses of the top and bottom quarks, and up to the next-to-leading order (NLO) [198–200] in the large-$m_{\rm t}$ limit.

In the small-$p_{\rm T}$ region ($p_{\rm T} \ll M_{\rm H}$), where the bulk of the events is produced, the convergence of the fixed-order expansion is spoiled by the presence of large logarithmic terms, $\alpha_{\rm s}^n \ln^m(M_{\rm H}^2/p_{\rm T}^2)$. To obtain reliable predictions, these logarithmically-enhanced terms have to be systematically resummed to all perturbative orders [193, 234–244]. It is then important to consistently match the resummed and fixed-order calculations at intermediate values of $p_{\rm T}$, in order to obtain accurate QCD predictions for the entire range of transverse momenta.

The resummation of the logarithmically enhanced terms is effectively (approximately) performed by standard Monte Carlo event generators. In particular, MC@NLO [116] and POWEG [123] combine soft-gluon resummation through the parton shower with the LO result valid at large $p_{\rm T}$, thus achieving a result with formal NLO accuracy.

The numerical program HQT [193] implements soft-gluon resummation up to NNLL accuracy [245] combined with fixed-order perturbation theory up to NLO in the large-$p_{\rm T}$ region [200]. The program is used by the Tevatron and LHC experimental collaborations to reweight the $p_{\rm T}$ spectrum of the Monte Carlo event generators used in the analysis and is thus of direct relevance in the Higgs-boson

[25] D. de Florian, G.Ferrera, M.Grazzini and D.Tommasini.

search.

The program HQT is based on the transverse-momentum resummation formalism described in Refs. [193, 243, 244], which is valid for a generic process in which a high-mass system of non strongly-interacting particles is produced in hadron–hadron collisions.

The phenomenological analysis presented in Ref. [193] has been recently extended in Ref. [194]. In particular, the exact values of the NNLO hard-collinear coefficients $\mathcal{H}_N^{\mathrm{H}(2)}$ Refs. [197, 246] and of the NNLL coefficient $A^{(3)}$ [247] have been implemented. The ensuing calculation of the p_{T} spectrum is implemented in the updated version of the numerical code HQT, which can be downloaded from Ref. [171].

5.4.2 Transverse-momentum resummation

In this section we briefly recall the main points of the transverse-momentum resummation approach proposed in Refs. [193, 243, 244], in the case of a Higgs boson H produced by gluon fusion. As recently pointed out in Ref. [244], the gluon fusion p_{T}-resummation formula has a structure different from the resummation formula for $\mathrm{q\overline{q}}$ annihilation. The difference originates from the collinear correlations that are a specific feature of the perturbative evolution of colliding hadrons into gluon partonic initial states. These gluon collinear correlations produce, in the small-p_{T} region, coherent spin correlations between the helicity states of the initial-state gluons and definite azimuthal-angle correlations between the final-states particles of the observed high-mass system. Both these kinds of correlations have no analogue for $\mathrm{q\overline{q}}$ annihilation processes in the small-p_{T} region. In the case of Higgs-boson production, H being a scalar particle, the azimuthal correlations vanish and only gluon spin correlations are present [244].

We consider the inclusive hard-scattering process

$$\mathrm{p}(p_1) + \mathrm{p}(p_2) \;\rightarrow\; \mathrm{H}(M_{\mathrm{H}}, p_{\mathrm{T}}) + X, \tag{38}$$

where the protons with momenta p_1 and p_2 collide to produce the Higgs boson H of mass M_{H} and transverse momentum p_{T}, and X is an arbitrary and undetected final state.

According to the QCD factorisation theorem the corresponding transverse-momentum differential cross section $d\sigma_{\mathrm{H}}/dp_{\mathrm{T}}^2$ can be written as

$$\frac{d\sigma_{\mathrm{H}}}{dp_{\mathrm{T}}^2}(p_{\mathrm{T}}, M_{\mathrm{H}}, s) = \sum_{a,b} \int_0^1 dx_1 dx_2\, f_{a/h_1}(x_1, \mu_{\mathrm{F}}^2)\, f_{b/h_2}(x_2, \mu_{\mathrm{F}}^2)\, \frac{d\hat{\sigma}_{H,ab}}{dp_{\mathrm{T}}^2}(p_{\mathrm{T}}, M_{\mathrm{H}}, \hat{s}; \alpha_{\mathrm{s}}(\mu_{\mathrm{R}}^2), \mu_{\mathrm{R}}^2, \mu_{\mathrm{F}}^2)\ , \tag{39}$$

where $f_{a/h}(x, \mu_{\mathrm{F}}^2)$ ($a = q, \bar{q}, g$) are the parton densities of the colliding hadron h at the factorisation scale μ_{F}, $d\hat{\sigma}_{H,ab}/dp_{\mathrm{T}}^2$ are the perturbative QCD partonic cross sections, s ($\hat{s} = x_1 x_2 s$) is the square of the hadronic (partonic) centre-of-mass energy, and μ_{R} is the renormalisation scale.

In the region where $p_{\mathrm{T}} \sim M_{\mathrm{H}}$, the QCD perturbative series is controlled by a small expansion parameter, $\alpha_{\mathrm{s}}(M_{\mathrm{H}})$, and fixed-order calculations are theoretically justified. In this region, the QCD radiative corrections are known up to NLO [198–200]. In the small-p_{T} region ($p_{\mathrm{T}} \ll M_{\mathrm{H}}$), the convergence of the fixed-order perturbative expansion is hampered by the presence of large logarithmic terms, $\alpha_{\mathrm{s}}^n \ln^m(M_{\mathrm{H}}^2/p_{\mathrm{T}}^2)$ (with $1 \leq m \leq 2n-1$). To obtain reliable predictions these terms have to be resummed to all orders.

The resummation is addressed at the level of the partonic cross section, which is decomposed as

$$\frac{d\hat{\sigma}_{\mathrm{H},ab}}{dp_{\mathrm{T}}^2} = \frac{d\hat{\sigma}_{\mathrm{H},ab}^{(\mathrm{res.})}}{dp_{\mathrm{T}}^2} + \frac{d\hat{\sigma}_{\mathrm{H},ab}^{(\mathrm{fin.})}}{dp_{\mathrm{T}}^2}\ . \tag{40}$$

The first term on the right-hand side includes all the logarithmically-enhanced contributions, at small p_{T}, and has to be evaluated to all orders in α_{s}. The second term is free of such contributions and can thus

be computed at fixed order in the perturbative expansion. To correctly take into account the kinematic constraint of transverse-momentum conservation, the resummation program has to be carried out in the impact parameter space b. Using the Bessel transformation between the conjugate variables $p_{\rm T}$ and b, the resummed component $d\hat{\sigma}^{(\rm res.)}_{{\rm H},ac}$ can be expressed as

$$\frac{d\hat{\sigma}^{(\rm res.)}_{{\rm H},ac}}{dp_{\rm T}^2}(p_{\rm T}, M_{\rm H}, \hat{s}; \alpha_{\rm s}(\mu_{\rm R}^2), \mu_{\rm R}^2, \mu_{\rm F}^2) = \int_0^\infty db\, \frac{b}{2}\, J_0(bp_{\rm T})\, \mathcal{W}^{\rm H}_{ac}(b, M_{\rm H}, \hat{s}; \alpha_{\rm s}(\mu_{\rm R}^2), \mu_{\rm R}^2, \mu_{\rm F}^2)\ , \tag{41}$$

where $J_0(x)$ is the 0th-order Bessel function. The resummation structure of $\mathcal{W}^{\rm H}_{ac}$ can be organised in exponential form considering the Mellin N-moments $\mathcal{W}^{\rm H}_N$ of $\mathcal{W}^{\rm H}$ with respect to the variable $z = M_{\rm H}^2/\hat{s}$ at fixed $M_{\rm H}$ [26],

$$\begin{aligned}\mathcal{W}^{\rm H}_N(b, M_{\rm H}; \alpha_{\rm s}(\mu_{\rm R}^2), \mu_{\rm R}^2, \mu_{\rm F}^2) &= \mathcal{H}^{\rm H}_N\left(M_{\rm H}, \alpha_{\rm s}(\mu_{\rm R}^2); M_{\rm H}^2/\mu_{\rm R}^2, M_{\rm H}^2/\mu_{\rm F}^2, M_{\rm H}^2/Q^2\right)\\ &\quad\times \exp\{\mathcal{G}_N(\alpha_{\rm s}(\mu_{\rm R}^2), L; M_{\rm H}^2/\mu_{\rm R}^2, M_{\rm H}^2/Q^2)\}\ ,\end{aligned} \tag{42}$$

were we have defined the logarithmic expansion parameter $L \equiv \ln(Q^2b^2/b_0^2)$, and $b_0 = 2e^{-\gamma_E}$ ($\gamma_E = 0.5772...$ is the Euler number).

The scale $Q \sim M_{\rm H}$, appearing in the right-hand side of Eq. (42), named resummation scale [193], parameterises the arbitrariness in the resummation procedure. The form factor $\exp\{\mathcal{G}_N\}$ is *universal* and contains all the terms $\alpha_{\rm s}^n L^m$ with $1 \le m \le 2n$, that are logarithmically divergent as $b \to \infty$ (or, equivalently, $p_{\rm T} \to 0$). The exponent $\mathcal{G}_N$ can be systematically expanded as

$$\begin{aligned}\mathcal{G}_N(\alpha_{\rm s}, L; M_{\rm H}^2/\mu_{\rm R}^2, M_{\rm H}^2/Q^2) &= L\, g^{(1)}(\alpha_{\rm s}L) + g_N^{(2)}(\alpha_{\rm s}L; M_{\rm H}^2/\mu_{\rm R}^2, M_{\rm H}^2/Q^2)\\ &\quad+ \frac{\alpha_{\rm s}}{\pi} g_N^{(3)}(\alpha_{\rm s}L; M_{\rm H}^2/\mu_{\rm R}^2, M_{\rm H}^2/Q^2) + \mathcal{O}(\alpha_{\rm s}^n L^{n-2})\end{aligned} \tag{43}$$

where the term $L\, g^{(1)}$ resums the leading logarithmic (LL) contributions $\alpha_{\rm s}^n L^{n+1}$, the function $g_N^{(2)}$ includes the NLL contributions $\alpha_{\rm s}^n L^n$ [242], $g_N^{(3)}$ controls the NNLL terms $\alpha_{\rm s}^n L^{n-1}$ [245, 247], and so forth. The explicit form of the functions $g^{(1)}$, $g_N^{(2)}$, and $g_N^{(3)}$ can be found in Ref. [193].

The *process-dependent* function $\mathcal{H}^{\rm H}_N$ does not depend on the impact parameter b and includes all the perturbative terms that behave as constants as $b \to \infty$. It can thus be expanded in powers of $\alpha_{\rm s} = \alpha_{\rm s}(\mu_{\rm R}^2)$:

$$\begin{aligned}\mathcal{H}^{\rm H}_N(M_{\rm H}, \alpha_{\rm s}; M_{\rm H}^2/\mu_{\rm R}^2, M_{\rm H}^2/\mu_{\rm F}^2, M_{\rm H}^2/Q^2) &= \sigma^{(0)}_{\rm H}(\alpha_{\rm s}, M_{\rm H})\Big[1 + \frac{\alpha_{\rm s}}{\pi}\, \mathcal{H}^{{\rm H},(1)}_N(M_{\rm H}^2/\mu_{\rm F}^2, M_{\rm H}^2/Q^2)\\ &\quad+ \left(\frac{\alpha_{\rm s}}{\pi}\right)^2 \mathcal{H}^{{\rm H},(2)}_N(M_{\rm H}^2/\mu_{\rm R}^2, M_{\rm H}^2/\mu_{\rm F}^2, M_{\rm H}^2/Q^2) + \mathcal{O}(\alpha_{\rm s}^3)\Big]\ ,\end{aligned} \tag{44}$$

where $\sigma^{(0)}_{\rm H}(\alpha_{\rm s}, M_{\rm H})$ is the partonic cross section at the Born level. The first order $\mathcal{H}^{{\rm H},(1)}_N$ [248] and the second order $\mathcal{H}^{{\rm H},(2)}_N$ [197, 246] coefficients in Eq. (44), for the case of Higgs-boson production in the large-$m_{\rm t}$ approximation, are known.

To reduce the impact of unjustified higher-order contributions in the large-$p_{\rm T}$ region, the logarithmic variable L in Eq. (42), which diverges for $b \to 0$, is actually replaced by $\widetilde{L} \equiv \ln\left(Q^2b^2/b_0^2 + 1\right)$ [193, 249]. The variables L and $\widetilde{L}$ are equivalent when $Qb \gg 1$ (i.e. at small values of $p_{\rm T}$), but they lead to a different behaviour of the form factor at small values of b. An important consequence of this replacement is that, after inclusion of the finite component, we exactly recover the fixed-order perturbative value of the total cross section upon integration of the $p_{\rm T}$ distribution over $p_{\rm T}$.

[26] For the sake of simplicity the resummation formulae is written only for the specific case of the diagonal terms in the flavour space. In general, the exponential is replaced by an exponential matrix with respect to the partonic indices (a detailed discussion of the general case can be found in Ref. [193]).

The finite component of the transverse-momentum cross section $d\sigma_{\rm H}^{(\rm fin.)}$ (see Eq. (40)) does not contain large logarithmic terms in the small-$p_{\rm T}$ region, it can thus be evaluated by truncation of the perturbative series at a given fixed order.

In summary, to carry out the resummation at NLL+LO accuracy, we need the inclusion of the functions $g^{(1)}$, $g_N^{(2)}$, $\mathcal{H}_N^{\rm H,(1)}$, in Eqs. (43,44), together with the evaluation of the finite component at LO; the addition of the functions $g_N^{(3)}$ and $\mathcal{H}_N^{\rm H,(2)}$, together with the finite component at NLO (i.e. at relative $\mathcal{O}(\alpha_{\rm s}^2)$) leads to the NNLL+NLO accuracy. We point out that our best theoretical prediction (NNLL+NLO) includes the *full* NNLO perturbative contribution in the small-$p_{\rm T}$ region plus the NLO correction at large $p_{\rm T}$. In particular, the NNLO result for the total cross section is exactly recovered upon integration over $p_{\rm T}$ of the differential cross section $d\sigma_{\rm H}/dp_{\rm T}$ at NNLL+NLO accuracy.

Finally we recall that the resummed form factor $\exp\{\mathcal{G}_N(\alpha_{\rm s}(\mu_{\rm R}^2),\widetilde{L})\}$ has a singular behaviour, related to the presence of the Landau pole in the QCD running coupling, at the values of b where $\alpha_{\rm s}(\mu_{\rm R}^2)\widetilde{L} > \pi/\beta_0$ (β_0 is the first-order coefficient of the QCD β function). To perform the inverse Bessel transformation with respect to the impact parameter b a prescription is thus necessary. We follow the regularisation prescription of Refs. [250,251]: the singularity is avoided by deforming the integration contour in the complex b space.

5.4.3 Results

The results we are going to present are obtained with an updated version of the numerical code HQT [171]. The new version of this code was improved with respect to the one used in Ref. [193]. The main differences regard the implementation of the exact value of the second-order coefficients $\mathcal{H}_N^{\rm H,(2)}$ computed in Ref. [197] and the use of the recently derived value of the coefficient $A^{(3)}$ [247], which contributes to NNLL accuracy (the results in Ref. [193] were obtained by using the $A^{(3)}$ value from threshold resummation [252]). Detailed results for the $p_{\rm T}$ spectrum at the Tevatron and the LHC are presented in Ref. [194]. Here we focus on the uncertainties of the $p_{\rm T}$ spectrum at the LHC.

The calculation is performed strictly in the large-$m_{\rm t}$ approximation. Effects beyond this approximation were discussed in Section 5.1.

The hadronic $p_{\rm T}$ cross section at NNLL+NLO accuracy is computed by using NNLO parton distributions functions (PDFs) with $\alpha_{\rm s}(\mu_{\rm R}^2)$ evaluated at 3-loop order. We use the MSTW2008 parton densities unless otherwise stated.

As discussed in Section 5.4.2, the resummed calculation depends on the factorisation and renormalisation scales and on the resummation scale Q. Our convention to compute factorisation and renormalisation scale uncertainties is to consider independent variations of $\mu_{\rm F}$ and $\mu_{\rm R}$ by a factor of two around the central values $\mu_{\rm F} = \mu_{\rm R} = M_{\rm H}$ (i.e. we consider the range $M_{\rm H}/2 < \{\mu_{\rm F},\mu_{\rm R}\} < 2\,M_{\rm H}$), with the constraint $0.5 < \mu_{\rm F}/\mu_{\rm R} < 2$. Similarly, we follow Ref. [193] and choose $Q = M_{\rm H}/2$ as central value of the resummation scale, considering scale variations in the range $M_{\rm H}/4 < Q < M_{\rm H}$.

We focus on the uncertainties on the *normalised* $p_{\rm T}$ spectrum (i.e., $1/\sigma \times d\sigma/dp_{\rm T}$). As mentioned in Section 5.4.1, the typical procedure of the experimental collaborations is to use the information on the total cross section [7] to rescale the best theoretical predictions of Monte Carlo event generators, whereas the NNLL+NLO result for the spectrum, obtained with the public program HQT, is used to reweight the transverse-momentum spectrum of the Higgs boson in the simulation. Such a procedure implies that the important information provided by the resummed NNLL+NLO spectrum is not its integral, i.e. the total cross section, but its *shape*. The sources of uncertainties on the shape of the spectrum are essentially the same as for the inclusive cross section: the uncertainty from missing higher-order contributions, estimated through scale variations, PDF uncertainties, and the uncertainty from the use of the large-$m_{\rm t}$ approximation, which is discussed in Section 5.1. One additional uncertainty in the $p_{\rm T}$ spectrum that needs be considered comes from non-perturbative (NP) effects.

It is known that the transverse-momentum distribution is affected by NP effects, which become important as $p_{\rm T}$ becomes small. A customary way of modelling these effects is to introduce an NP transverse-momentum smearing of the distribution. In the case of resummed calculations in impact-parameter space, the NP smearing is implemented by multiplying the b-space perturbative form factor by an NP form factor. The parameters controlling this NP form factor are typically obtained through a comparison to data. Since the Higgs boson has not been discovered yet, the way to fix the NP form factor is somewhat arbitrary. Here we follow the procedure adopted in Refs. [193, 194], and we multiply the resummed form factor in Eq. (41) by a gaussian smearing $S_{NP} = \exp\{-gb^2\}$, where the parameter g is taken in the range ($g = 1.67{-}5.64$ GeV^2) suggested by the study of Ref. [253]. The above procedure can give us some insight on the quantitative impact of these NP effects on the Higgs-boson spectrum.

In Figure 44 (left panels) we compare the NNLL+NLO shape uncertainty as coming from scale variations (solid lines) to the NP effects (dashed lines) for $M_{\rm H} = 120$ GeV and $M_{\rm H} = 165$ GeV. Scale variations are performed as follows: we independently vary $\mu_{\rm F}, \mu_{\rm R}$ and Q in the ranges $M_{\rm H}/2 < \{\mu_{\rm F}, \mu_{\rm R}\} < 2M_{\rm H}$ and $M_{\rm H}/4 < Q < M_{\rm H}$, with the constraints $0.5 < \mu_{\rm F}/\mu_{\rm R} < 2$ and $0.5 < Q/\mu_{\rm R} < 2$. The bands are obtained in practice by normalizing each spectrum to unity, and computing the relative difference with respect to the central normalised prediction obtained with the MSTW2008 NNLO set (with $g = 0$). In other words, studying uncertainties on the normalised distribution allows us to assess the true uncertainty in the shape of the resummed $p_{\rm T}$ spectrum.

We see that, both for $M_{\rm H} = 120$ GeV and for $M_{\rm H} = 165$ GeV, the scale uncertainty ranges from about $\pm 4\%$ at $p_{\rm T} \sim 10$ GeV to $\pm 5\%$ at $p_{\rm T} \sim 70$ GeV. As $p_{\rm T}$ increases, the scale uncertainty rapidly increases. This should not be considered as particularly worrying, since for large transverse momenta, the resummed result looses predictivity, and should be replaced by the standard fixed-order result. The impact of NP effects ranges from about 10% to 20% in the very small-$p_{\rm T}$ region ($p_{\rm T} \lesssim 10$ GeV), is about $3{-}4\%$ for $p_{\rm T} \sim 20$ GeV, and quickly decreases as $p_{\rm T}$ increases. We conclude that the uncertainty from unknown NP effects is smaller than the scale uncertainty, and is comparable to the latter only in the very-small-$p_{\rm T}$ region.

The impact of PDF uncertainties at 68% CL on the shape of the $p_{\rm T}$ spectrum is studied in Figures 44 (right panels). By evaluating PDF uncertainties with MSTW2008 NNLO PDFs we see that the uncertainty is at the $\pm(1{-}2)\%$ level. The use of different PDF sets affects not only the absolute value of the NNLO cross section (see, e.g., Ref. [254]), but also the shape of the $p_{\rm T}$ spectrum. The predictions obtained with NNPDF 2.1 PDFs are in good agreement with those obtained with the MSTW2008 set, and the uncertainty bands overlap over a wide range of transverse momenta, both for $M_{\rm H} = 120$ GeV and $M_{\rm H} = 165$ GeV. On the contrary, the prediction obtained with the ABKM09 NNLO set is softer, and the uncertainty band does not overlap with the MSTW2008 band. This behaviour is not completely unexpected: when the Higgs boson is produced at large transverse momenta, larger values of Bjorken x are probed, where the ABKM gluon is smaller than MSTW2008 one. The JR09 band shows a good compatibility with the MSTW2008 result where the uncertainty is, however, rather large.

5.5 Monte Carlo and resummation for exclusive jet bins[27]

5.5.1 Overview

In this section we discuss the use of predictions for exclusive jet cross sections that involve resummation for the jet-veto logarithms, $\ln(p^{\rm cut}/M_{\rm H})$, induced by the jet cut parameter $p^{\rm cut}$ shown in Eq. (19) of Section 5.2. It is common practice to account for the $p^{\rm cut}$ dependence in exclusive $H{+}0$ jet cross sections using Monte Carlo programs such as PYTHIA, MC@NLO, or POWHEG, which include a resummation of at least the leading logarithms (LL). One may also improve the accuracy of spectrum predictions by reweighting the Monte Carlo to resummed predictions for the Higgs q_T spectrum (see Section 5.4), which starts to differ from the jet-veto spectrum at $\mathcal{O}(\alpha_{\rm s}^2)$. The question then remains how to assess theoretical

[27] I. W. Stewart, F. Stöckli, F. J. Tackmann and W. J. Waalewijn.

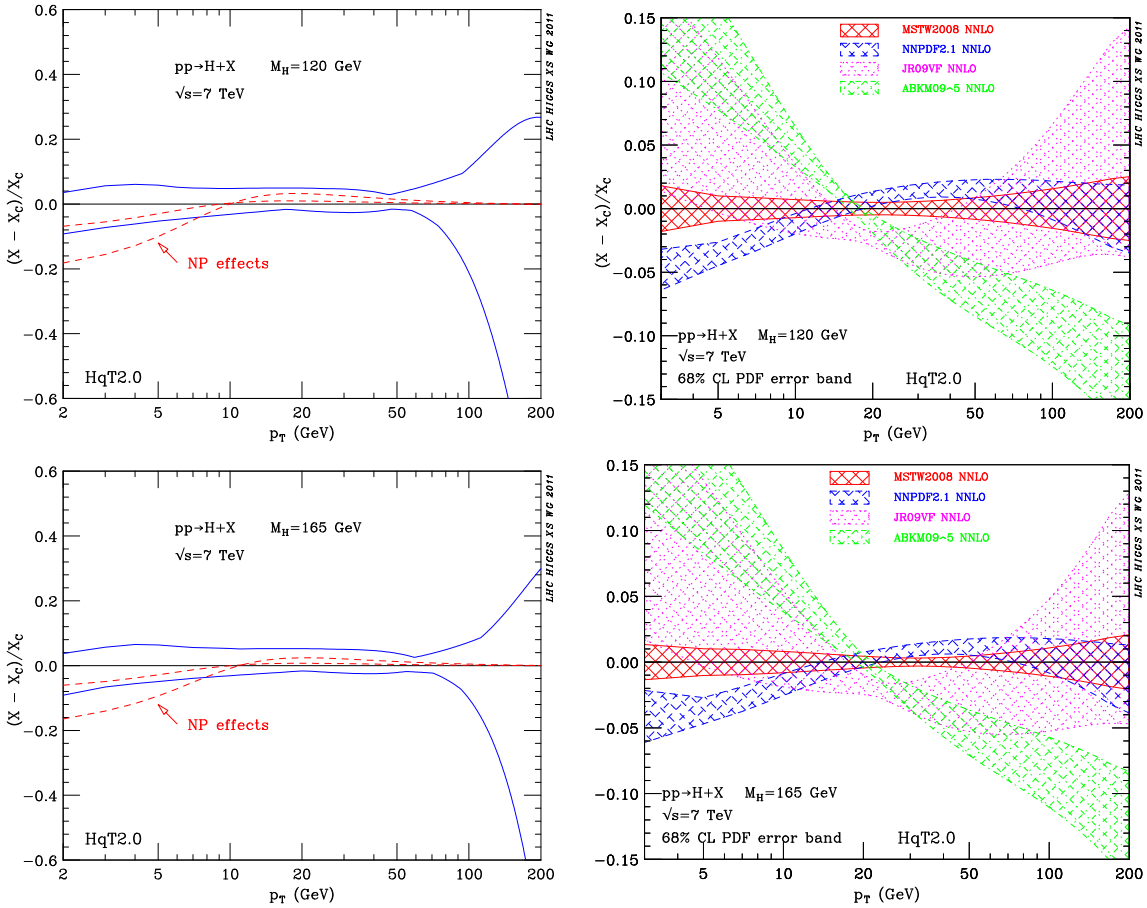

Fig. 44: Uncertainties in the shape of the $p_{\rm T}$ spectrum: scale uncertanties compared with NP effects (left panels); PDF uncertainties (right panels).

uncertainties, and three methods (A, B, and C) were outlined in Section 5.2.

In this section we consider assessing the perturbative uncertainties when using resummed predictions for variables $p^{\rm cut}$ that implement a jet veto, corresponding to method C. An advantage of using these resummed predictions with method C is that they contain perturbation theory scale parameters which allow for an evaluation of two components of the theory error, one which is 100% correlated with the total cross section (as in method A), and one related to the presence of the jet-bin cut which is anti-correlated between neighboring jet bins (as in method B). Our discussion of the correlation matrix obtained from method C follows Ref. [204].

We consider two choices for the jet-veto variable, the standard $p_{\rm T}^{\rm jet}$ variable with a rapidity cut $|\eta| < \eta^{\rm cut}$ (using anti-k_T with $R = 0.5$), and the beam thrust variable [205], which is a rapidity-weighted H_T, defined as

$$\mathcal{T}_{\rm cm} = \sum_k |\vec{p}_{Tk}| e^{-|\eta_k|} = \sum_k (E_k - |p_k^z|)\,. \tag{45}$$

The sum here is over all objects in the final state except the Higgs decay products, and can in principle be considered over particles, topo-clusters, or jets with a small R parameter. We make use of resummed predictions for $H + 0$ jets from gluon fusion at next-to-next-to-leading logarithmic order with NNLO fixed-order precision (NNLL+NNLO) from Ref. [206]. The resulting cross section $\sigma_0(\mathcal{T}_{\rm cm}^{\rm cut})$ has the jet veto implemented by a cut $\mathcal{T}_{\rm cm} < \mathcal{T}_{\rm cm}^{\rm cut}$. This cross section contains a resummation of large logarithms at two orders beyond standard LL parton-shower programs, and also includes the correct NNLO corrections

for $\sigma_0(\mathcal{T}_{\rm cm}^{\rm cut})$ for any cut.

A similar resummation for the case of $p_{\rm T}^{\rm jet}$ is not available. Instead, we use MC@NLO and reweight it to the resummed predictions in $\mathcal{T}_{\rm cm}$ including uncertainties and then use the reweighted Monte Carlo sample to obtain cross-section predictions for the standard jet veto, $\sigma_0(p_{\rm T}^{\rm cut})$. We will refer to this as the reweighted NNLL+NNLO result. Since the Monte Carlo here is only used to provide a transfer matrix between $\mathcal{T}_{\rm cm}$ and $p_{\rm T}^{\rm jet}$, and both variables implement a jet veto, one expects that most of the improvements from the higher-order resummation are preserved by the reweighting. However, we caution that this is not equivalent to a complete NNLL+NNLO result for the $p_{\rm T}^{\rm cut}$ spectrum, since the reweighting may not fully capture effects associated with the choice of jet algorithm and other effects that enter at this order for $p_{\rm T}^{\rm cut}$. The dependence on the Monte Carlo transfer matrix also introduces an additional uncertainty, which should be studied and is not included in our numerical results below. (We have checked that varying the fixed-order scale in MC@NLO between $\mu = M_{\rm H}/4$ and $\mu = 2M_{\rm H}$ has a very small effect on the reweighted results.) The transfer matrix is obtained at the parton level, without hadronisation or underlying event, since we are reweighting a partonic NNLL+NNLO calculation. In all our results we consistently use MSTW2008 NNLO PDFs.

In Section 5.5.2 we discuss the determination of perturbative uncertainties in the resummed calculations (method C), and compare them with those at NNLO obtained from a direct exclusive scale variation (method A) and from combined inclusive scale variation (method B) for both $\sigma_0(p_{\rm T}^{\rm cut})$ and $\sigma_0(\mathcal{T}_{\rm cm}^{\rm cut})$. In Section 5.5.3 we compare the predictions for the 0-jet bin event fraction at different levels of resummation, comparing results from NNLO, MC@NLO, and the (reweighted) NNLL+NNLO analytic results.

5.5.2 Uncertainties and correlations from resummation

The resummed H + 0-jet cross section predictions of Ref. [206] follow from a factorisation theorem for the 0-jet cross section [205], $\sigma_0(\mathcal{T}_{\rm cm}^{\rm cut}) = H\,\mathcal{I}_{gi}\,\mathcal{I}_{gj} \otimes S f_i f_j$, where H contains hard virtual effects, the $\mathcal{I}$s and S describe the veto-restricted collinear and soft radiation, and the fs are standard parton distributions. Fixed-order perturbation theory is carried out at three scales, a hard scale $\mu_H^2 \sim M_{\rm H}^2$ in H, and beam and soft scales $\mu_B^2 \sim M_{\rm H}\mathcal{T}_{\rm cm}^{\rm cut}$ and $\mu_S^2 \sim (\mathcal{T}_{\rm cm}^{\rm cut})^2$ for $\mathcal{I}$ and S, and are then connected by NNLL renormalisation group evolution that sums the jet-veto logarithms, which are encoded in ratios of these scales. The perturbative uncertainties can be assessed by considering two sources: i) an overall scale variation that simultaneously varies $\{\mu_H, \mu_B, \mu_S\}$ up and down by a factor of two which we denote by Δ_{H0}, and ii) individual variations of μ_B or μ_S that each hold the other two scales fixed [206], whose envelope we denote by the uncertainty Δ_{SB}. Here Δ_{H0} is dominated by the same sources of uncertainty as the total cross section $\sigma_{\rm total}$, and hence should be considered 100% correlated with its uncertainty $\Delta_{\rm total}$. The uncertainty Δ_{SB} is only present due to the jet bin cut, and hence gives the $\Delta_{\rm cut}$ uncertainty discussed in Section 5.2 that is anti-correlated between neighboring jet bins.

If we simultaneously consider the cross sections $\{\sigma_0, \sigma_{\geq 1}\}$ then the full correlation matrix with method C is

$$C = \begin{pmatrix} \Delta_{SB}^2 & -\Delta_{SB}^2 \\ -\Delta_{SB}^2 & \Delta_{SB}^2 \end{pmatrix} + \begin{pmatrix} \Delta_{H0}^2 & \Delta_{H0}\,\Delta_{H\geq 1} \\ \Delta_{H0}\,\Delta_{H\geq 1} & \Delta_{H\geq 1}^2 \end{pmatrix}, \tag{46}$$

where $\Delta_{H\geq 1} = \Delta_{\rm total} - \Delta_{H0}$ encodes the 100% correlated component of the uncertainty for the (≥ 1)-jet inclusive cross section. Computing the uncertainty in $\sigma_{\rm total}$ gives back $\Delta_{\rm total}$. Eq. (46) can be compared to the corresponding correlation matrix from method A, which would correspond to taking $\Delta_{SB} \to 0$ and obtaining the analog of Δ_{H0} by up/down scale variation without resummation ($\mu_H = \mu_B = \mu_S$). It can also be compared to method B, which would correspond to taking $\Delta_{SB} \to \Delta_{\geq 1}$ and $\Delta_{H\geq 1} \to 0$, such that $\Delta_{H0} \to \Delta_{\rm total}$. Using method C captures both of the types of uncertainty that appear in methods A and B. Note that the numerical dominance of Δ_{SB}^2 over $\Delta_{H0}\Delta_{H\geq 1}$ in the 0-jet region is another way to justify the preference for using method B when given a choice between methods

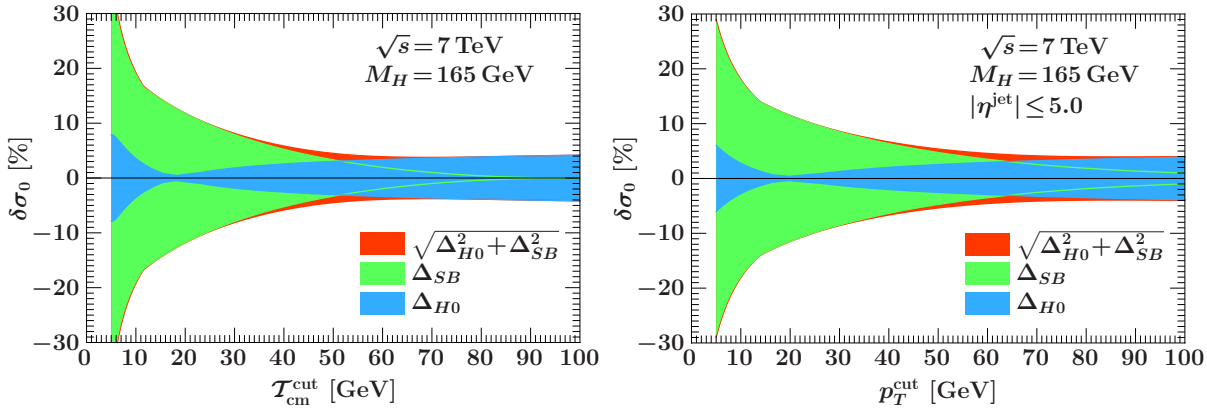

Fig. 45: Relative uncertainties for the 0-jet bin cross section from resummation at NNLL+NNLO for beam thrust $\mathcal{T}_{\rm cm}$ on the left and $p_{\rm T}^{\rm jet}$ on the right.

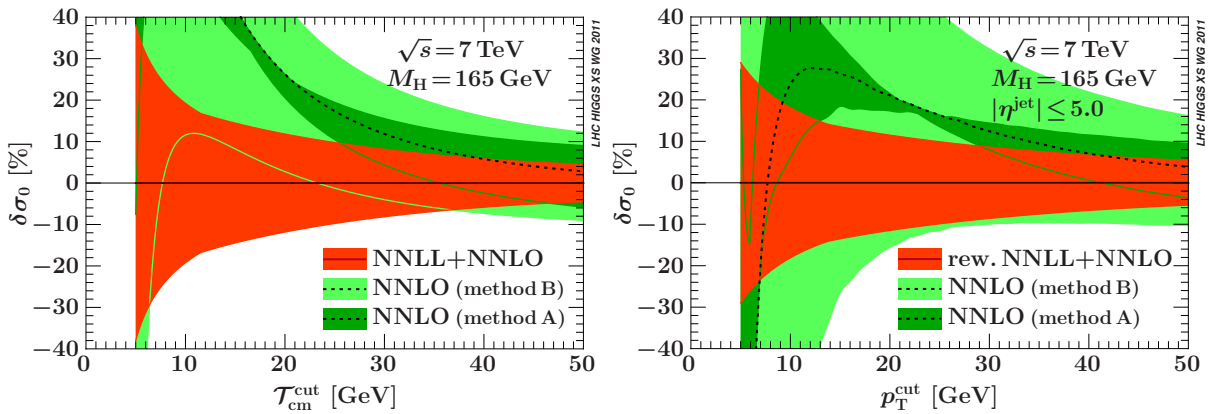

Fig. 46: Comparison of uncertainties for the 0-jet bin cross section for beam thrust $\mathcal{T}_{\rm cm}$ on the left and $p_{\rm T}^{\rm jet}$ on the right. Results are shown at NNLO using methods A and B (direct exclusive scale variation and combined inclusive scale variation as discussed in Section 5.2), and for the NNLL+NNLO resummed result (method C). All curves are normalised relative to the NNLL+NNLO central value.

A and B. For example, for $p_{\rm T}^{\rm cut} = 30$ GeV and $|\eta^{\rm jet}| < 5.0$ we have $\Delta_{SB}^2 = 0.17$ and $\Delta_{H0}\Delta_{H\geq 1} = 0.02$. From Eq. (46) it is straightforward to derive the uncertainties and correlations in method C when considering the 0-jet event fraction, $\{\sigma_{\rm total}, f_0\}$, in place of the jet cross sections. We will discuss results for $f_0(p_{\rm T}^{\rm cut})$ and $f_0(\mathcal{T}_{\rm cm}^{\rm cut})$ in Section 5.5.3 below.

In Figure 45 we show the uncertainties Δ_{SB} (light green) and Δ_{H0} (medium blue) as a function of the jet-veto variable, as well as the combined uncertainty adding these components in quadrature (dark orange). From the figure we see that the μ_{H0} dominates at large values where the veto is turned off and we approach the total cross section, and that the jet-cut uncertainty Δ_{SB} dominates for the small cut values that are typical of experimental analyses with Higgs jet bins. The same pattern is observed in the left panel which directly uses the NNLL+NNLO predictions for $\mathcal{T}_{\rm cm}^{\rm cut}$, and the right panel which shows the result from reweighting these predictions to $p_{\rm T}^{\rm cut}$ as explained above.

A comparison of the uncertainties for the 0-jet bin cross section from methods A (medium green), B (light green), and C (dark orange) is shown in Figure 46, where the results are normalised to the highest-order result to better show the relative differences and uncertainties. The NNLO uncertainties in methods A and B are computed in the manner discussed in Section 5.2. The uncertainties in method C are the combined uncertainties from resummation given by $\sqrt{\Delta_{H0}^2 + \Delta_{SB}^2}$ in Figure 45. In the left panel

	method A	method B	method C
$\delta\sigma_0(p_{\rm T}^{\rm cut})$	3%	19%	9%
$\delta\sigma_{\geq 1}(p_{\rm T}^{\rm cut})$	19%	19%	14%
$\rho(\sigma_{\rm total}, \sigma_0)$	1	0.78	0.15
$\rho(\sigma_{\rm total}, \sigma_{\geq 1})$	1	0	0.65
$\rho(\sigma_0, \sigma_{\geq 1})$	1	-0.63	-0.65
$\delta f_0(p_{\rm T}^{\rm cut})$	6%	13%	9%
$\delta f_{\geq 1}(p_{\rm T}^{\rm cut})$	10%	21%	11%
$\rho(\sigma_{\rm total}, f_0)$	-1	0.43	-0.38
$\rho(\sigma_{\rm total}, f_{\geq 1})$	1	-0.43	0.38

Table 13: Example of relative uncertainties δ and correlations ρ obtained for the LHC at 7 $\rm TeV$ for $p_{\rm T}^{\rm cut} = 30\,{\rm GeV}$ and $|\eta^{\rm jet}| < 5.0$. (Method A is shown for illustration only and should not be used for the reasons discussed in Section 5.2.)

we use $\mathcal{T}_{\rm cm}^{\rm cut}$ as jet-veto variable and full results for the NNLO and NNLL+NNLO cross sections, while in the right panel we use $p_{\rm T}^{\rm cut}$ as jet-veto variable with the full NNLO and the reweighted NNLL+NNLO results. One observes that the resummation of the large jet-veto logarithms lowers the cross section in both cases. For cut values $\gtrsim 25$ GeV the relative uncertainties in the resummed result and the reduction in the resummed central value compared to NNLO are similar for both jet-veto variables. One can also see that the NNLO uncertainties from method B are more consistent with the higher-order NNLL+NNLO-resummed results than those in method A.

From Figure 46 we observe that the uncertainties in method C including resummation (dark orange bands) are reduced by about a factor of two compared to those in method B (light green bands). Since the 0-jet bin plays a crucial role in the $\rm H \to WW$ channel for Higgs searches, and these improvements will also be reflected in uncertainties for the 1-jet bin, the improved theoretical precision obtained with method C has the potential to be quite important.

To appreciate the effects of the different methods on the correlation matrix we consider as an example the results for $p_{\rm T}^{\rm cut} = 30$ GeV and $|\eta^{\rm jet}| < 5.0$. The inclusive cross sections are $\sigma_{\rm total} = (8.76 \pm 0.80)\,{\rm pb}$ at NNLO, and $\sigma_{\geq 1} = (3.10 \pm 0.61)\,{\rm pb}$ at NLO. The relative uncertainties and correlations at these cuts for the three methods are shown in Table 13. The numbers for the cross sections are also translated into the equivalent results for the event fractions, $f_0(p_{\rm T}^{\rm cut}) = \sigma_0(p_{\rm T}^{\rm cut})/\sigma_{\rm total}$ and $f_{\geq 1}(p_{\rm T}^{\rm cut}) = \sigma_{\geq 1}(p_{\rm T}^{\rm cut})/\sigma_{\rm total}$. Note that method A should not be used for the reasons discussed in detail in Section 5.2, which are related to the lack of a contribution analogous to Δ_{SB} in this method, and the resulting very small and underestimated $\delta\sigma_0$. In methods B and C we see, as expected, that σ_0 and $\sigma_{\geq 1}$ have a substantial anti-correlation due to the jet-bin boundary they share.

In Section 5.2, method B was discussed for $\{\sigma_{\rm total}, \sigma_0, \sigma_1\}$, where we also account for the jet-bin boundary between σ_1 and $\sigma_{\geq 2}$. The method C results discussed here so far are relevant for the jet-bin boundary between σ_0 and $\sigma_{\geq 1}$. To also separate $\sigma_{\geq 1}$ into a 1-jet bin σ_1 and a $\sigma_{\geq 2}$ one can simply use method B for this boundary by treating $\Delta_{\geq 2}$ as uncorrelated with the total uncertainty $\Delta_{\geq 1}$ from method C. Once it becomes available one can also use a resummed prediction with uncertainties for this boundary with method C.

5.5.3 Comparison of NNLO, MC@NLO, and resummation at NNLL+NNLO

In this section we compare the results for the 0-jet event fraction f_0 from different theoretical methods including various levels of logarithmic resummation. We use the event fraction for this comparison since it is the quantity used in experimental analyses and what is typically provided by the Monte Carlo. We compare three different results using both $p_{\rm T}^{\rm jet}$ and beam thrust as jet-veto variables:

1. Fixed-order perturbation theory at NNLO without resummation, where the uncertainties are evaluated using method B.
2. MC@NLO, which includes the LL (and partial NLL) resummation provided by the parton shower. For the uncertainties we use the relative NNLO uncertainties evaluated using method B.
3. Resummation at NNLL+NNLO, with the uncertainties provided by the resummation (method C). For beam thrust we directly compare to the full result at this order. For $p_{\mathrm{T}}^{\mathrm{jet}}$ we use the resummed beam-thrust result reweighted to $p_{\mathrm{T}}^{\mathrm{jet}}$ using Monte Carlo as explained at the beginning of this section.

The comparison for $f_0(\mathcal{T}_{\mathrm{cm}}^{\mathrm{cut}})$ is shown in Figure 47 and for $f_0(p_{\mathrm{T}}^{\mathrm{jet}})$ in Figure 48. The left panels in each case show the 0-jet event fractions, and the right panels normalise these same results to the highest-order curve to illustrate the relative differences and uncertainties. Since the parton shower includes the resummation of the leading logarithms, we expect the MC@NLO results to show a behavior similar to the NNLL-resummed result, which is indeed the case. For both variables, the MC@NLO central value is near the upper edge of the NNLL+NNLO uncertainty band (dark orange band). From Figure 48 we see that the uncertainties assigned to the MC@NLO results via method B (light blue band) include the NNLL+NNLO central value for $f_0(p_{\mathrm{T}}^{\mathrm{cut}})$.[28] We also see that the uncertainties for $f_0(p_{\mathrm{T}}^{\mathrm{cut}})$ in method C are reduced by roughly a factor of two compared to MC@NLO with method B. This is the analog of the observation that we made for $\sigma_0(p_{\mathrm{T}}^{\mathrm{cut}})$ in Figure 46 when comparing NNLO method B and method C uncertainties.

From the δf_0 plots in Figure 47 and Figure 48 we observe that the impact of the resummation on the NNLL+NNLO central value compared to the NNLO central value without resummation is similar for both jet-veto variables for cut values $\gtrsim 25$ GeV. In this region the MC@NLO central value lies closer to the NNLO than the NNLL+NNLO for both variables. However, it is hard to draw conclusions on the impact of resummation by only comparing MC@NLO and NNLO since they each contain a different set of higher-order corrections beyond NLO. For smaller cut values $\lesssim 25$ GeV, the two variables start to behave differently, and the NNLL+NNLO resummation has a larger impact relative to NNLO when cutting on $\mathcal{T}_{\mathrm{cm}}$ than when cutting on $p_{\mathrm{T}}^{\mathrm{cut}}$.

To understand these features in more detail one has to take into account two different effects arising from the two ways in which these jet-veto variables differ. First, the objects are weighted differently according to their rapidity in the two jet-veto variables. For $\mathcal{T}_{\mathrm{cm}}$ the particles are weighted by $e^{-|\eta|}$, while for $p_{\mathrm{T}}^{\mathrm{jet}}$ no weighting in η takes place. Second, the way in which the cut restriction is applied to the objects in the final state is different. By cutting on $\mathcal{T}_{\mathrm{cm}}$, the restriction is applied to the sum over all objects (either particles or jets) in the final state, while by cutting on the leading $p_{\mathrm{T}}^{\mathrm{jet}}$ the restriction is applied to the maximum value of all objects (after an initial grouping into jets with small radius). To disentangle these two effects we consider two additional jet-veto variables: H_T which inclusively sums over all object $|p_{\mathrm{T}}|$s in the same way as $\mathcal{T}_{\mathrm{cm}}$ does, but without the rapidity weighting, and also $\mathcal{T}_{\mathrm{jet}}$, the largest individual beam thrust of any jet, which has the same object treatment as $p_{\mathrm{T}}^{\mathrm{jet}}$, but with the beam-thrust rapidity weighting. The effect of the different rapidity weighting already appears in the LL series for the jet veto, i.e., at $\mathcal{O}(\alpha_{\mathrm{s}})$ the coefficient of the leading double logarithm is a factor of two larger for $p_{\mathrm{T}}^{\mathrm{cut}}$ than for $\mathcal{T}_{\mathrm{cm}}^{\mathrm{cut}}$, $\sigma_0(p_{\mathrm{T}}^{\mathrm{cut}}) \propto 1 - 6\alpha_{\mathrm{s}}/\pi \ln^2(p_{\mathrm{T}}^{\mathrm{cut}}/M_{\mathrm{H}}) + \ldots$ versus $\sigma_0(\mathcal{T}_{\mathrm{cm}}^{\mathrm{cut}}) \propto 1 - 3\alpha_{\mathrm{s}}/\pi \ln^2(\mathcal{T}_{\mathrm{cm}}^{\mathrm{cut}}/M_{\mathrm{H}}) + \ldots$. In contrast, the LL series is the same for H_T and $p_{\mathrm{T}}^{\mathrm{jet}}$, and for $\mathcal{T}_{\mathrm{cm}}$ and $\mathcal{T}_{\mathrm{jet}}$. The larger logarithms for $p_{\mathrm{T}}^{\mathrm{cut}}$ than $\mathcal{T}_{\mathrm{cm}}^{\mathrm{cut}}$ are reflected by the fact that $\sigma_0(p_{\mathrm{T}}^{\mathrm{cut}})$ is noticeably smaller than $\sigma_0(\mathcal{T}_{\mathrm{cm}}^{\mathrm{cut}})$ at equal cut values. For the same type of object restriction the effect of the resummation follows the pattern expected from the leading logarithms: The resummation has a larger impact for $p_{\mathrm{T}}^{\mathrm{jet}}$ than $\mathcal{T}_{\mathrm{jet}}$, and also for H_T than $\mathcal{T}_{\mathrm{cm}}$. On the other hand, a cut on the (scalar) sum of objects is always a stronger restriction than the

[28] The blue uncertainty bands for the MC@NLO curves are cut off at very small cut values only because the NNLO cross section diverges there and so its relative uncertainties are no longer meaningful. This happens for cut values well below the region of experimental interest.

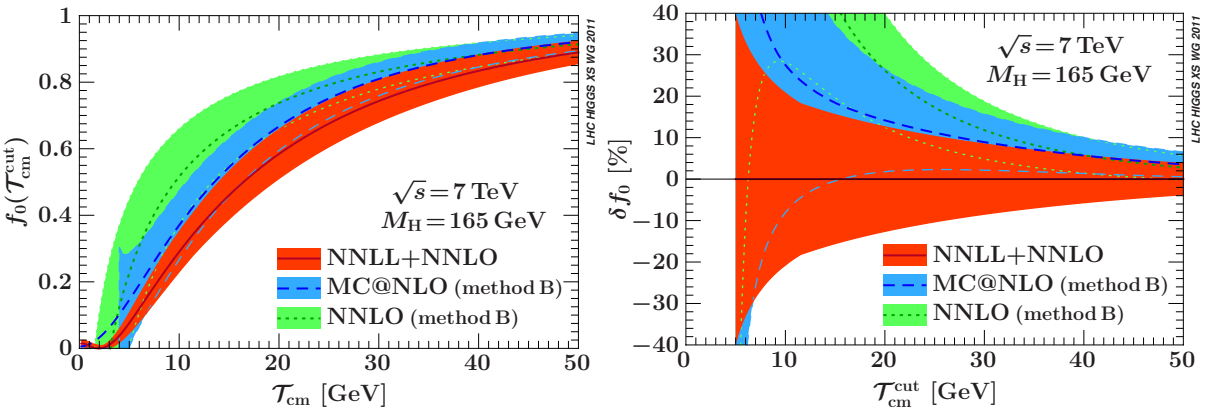

Fig. 47: Comparison of the 0-jet fraction for different levels of resummation using beam thrust as the jet-veto variable. Results are shown at NNLO (using method B uncertainties), MC@NLO (using the relative NNLO uncertainty from method B), and for the analytic NNLL+NNLO resummed result.

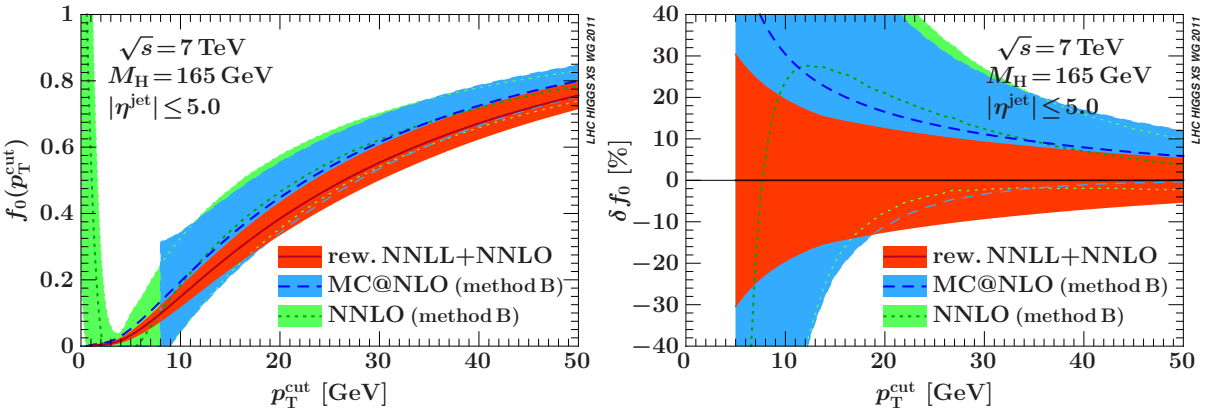

Fig. 48: Comparison of the 0-jet fraction for different levels of resummation using $p_{\rm T}^{\rm jet}$ with $|\eta^{\rm jet}| < 5.0$ as the jet-veto variable. Results are shown at NNLO (using method B uncertainties), MC@NLO (using the relative NNLO uncertainty from method B), and for the reweighted NNLL+NNLO resummed result.

same cut on the maximum value of all objects, since the former restricts wide-angle radiation more. As a result the resummation has more impact on $\mathcal{T}_{\rm cm}$ than on $\mathcal{T}_{\rm jet}$, and also on H_T than on $p_{\rm T}^{\rm jet}$. From what we observe in Figure 47 and Figure 48, these two competing effects appear to approximately balance each other for $p_{\rm T}^{\rm jet}$ and $\mathcal{T}_{\rm cm}$ for cut values $\gtrsim 25$ GeV.

To summarise, our results provide an important validation of using method B with relative uncertainties obtained at NNLO and applying these to the event fractions obtained from NLO Monte Carlos. While we have only compared to MC@NLO, we expect the same to be true for POWHEG as well. By reweighting the Monte Carlo to the NNLL+NNLO result the uncertainties in the predictions can be further reduced to those obtained from the higher-order resummation using method C, and this provides an important avenue for improving the analysis beyond method B. It would also be very useful to investigate experimentally the viability of using $\mathcal{T}_{\rm jet}$ as the jet-veto variable, by only summing over the jet (or jets) with the largest individual beam thrust, as this would combine the advantages of a jet-based variable with the theoretical control provided by the beam-thrust resummation.

6 VBF production mode[29]

The production of a Standard Model Higgs boson in association with two hard jets in the forward and backward regions of the detector, frequently quoted as the "vector-boson fusion" (VBF) channel, is a cornerstone in the Higgs-boson search both in the ATLAS [255] and CMS [256] experiments at the LHC. Higgs-boson production in the VBF channel also plays an important role in the determination of Higgs-boson couplings at the LHC (see e.g. Ref. [13]).

The production of a Higgs boson + 2 jets receives two contributions at hadron colliders. The first type, where the Higgs boson couples to a weak boson that links two quark lines, is dominated by t- and u-channel-like diagrams and represents the genuine VBF channel. The hard jet pairs have a strong tendency to be forward–backward directed in contrast to other jet-production mechanisms, offering a good background suppression. The second type of diagrams are actually a contribution to WH and ZH production, with the $\mathrm{W/Z}$ decaying into a pair of jets.

In the previous report [7], state-of-the-art predictions and error estimates for the total cross sections for $\mathrm{pp} \to \mathrm{H}{+}2\,\mathrm{jets}$ have been compiled. These were based on an (approximate) NNLO calculation [257] of the total VBF cross section based on the structure-function approach and on calculations of the electroweak (EW) corrections by the Monte Carlo programs HAWK [258–260] and VBFNLO [261, 262]. The EW corrections were simply included as a multiplicative correction factor to the NNLO QCD prediction.

In this contribution we consider predictions for cross sections with cuts and distributions. This is particularly interesting for VBF, as cuts on the tagging jets are used to suppress events from Higgs + 2 jet production via gluon fusion and other backgrounds and to enhance the VBF signal. Since no NNLO calculation for VBF exists so far for differential distributions or cross sections with cuts, we use NLO codes. We also provide results for NLO QCD corrections + parton shower, as generated using the POWHEG [123] method and implemented in the POWHEG BOX code [156].

6.1 Theoretical framework

The results presented in Section 6.3 have been obtained with the Monte Carlo programs HAWK and VBFNLO, which include both QCD and EW NLO corrections, and with POWHEG, a method to interface QCD NLO calculations with parton showers. Some details on these codes are given in the following.

6.1.1 HAWK

The Monte Carlo event generator HAWK [258–260] has already been described in Ref. [7]. Since then, it has been extended to the processes $\mathrm{pp} \to \mathrm{WH} \to \nu_l\, l\, \mathrm{H}$ and $\mathrm{pp} \to \mathrm{ZH} \to l^- l^+ \mathrm{H}/\nu_l \bar{\nu}_l \mathrm{H}$ [263] (see Section 7.1). Here we summarise its most important features for the VBF channel. HAWK includes the complete NLO QCD and EW corrections and all weak-boson fusion and quark–antiquark annihilation diagrams, i.e. t-channel and u-channel diagrams with VBF-like vector-boson exchange and s-channel Higgs-strahlung diagrams with hadronic weak-boson decay, as well as all interferences.

For the results presented below, s-channel contributions and interferences have been switched off in order to allow for a direct comparison with the results of the other codes. The contributions from s-channels and interferences are below 1% once VBF cuts are applied. While HAWK allows for the inclusion of contributions of b-quark parton distribution functions (PDFs) and final-state b quarks at LO, these contributions have been switched off as well. With VBF cuts, they can amount to about 2%. Also contributions from photon-induced processes, which are part of the real EW corrections and at the level of $1{-}2\%$, have not been included, since photon PDFs are not supported by the PDF sets used. HAWK allows for an on-shell Higgs boson or for an off-shell Higgs boson (with optional decay into a pair of

[29] A. Denner, S. Farrington, C. Hackstein, C. Oleari, D. Rebuzzi (eds.); S. Dittmaier, A. Mück, S. Palmer and W. Quayle.

gauge singlets). For the virtuality of the off-shell Higgs boson the usual Breit–Wigner distribution

$$\frac{1}{\pi}\frac{M_{\mathrm{H}}\,\Gamma_{\mathrm{H}}}{\left(M^2-M_{\mathrm{H}}^2\right)^2+(M_{\mathrm{H}}\,\Gamma_{\mathrm{H}})^2} \tag{47}$$

is used. This form results from the gauge-invariant expansion about the complex Higgs-boson pole and is properly normalised. As any other parametrisation, it becomes unreliable for large Higgs-boson masses, where the Higgs-boson width gets large and contributions far from the pole become sizeable.

6.1.2 VBFNLO

VBFNLO [264, 265] is a parton-level Monte Carlo event generator that can be used to simulate vector-boson fusion, double and triple vector-boson production in hadronic collisions at next-to-leading order in the strong coupling constant, as well as Higgs-boson plus two jet production via gluon fusion at the one-loop level. For Higgs-boson production via VBF, both the NLO QCD and electroweak corrections to the t-channel can be included [262, 266] in the Standard Model and the (complex) MSSM[30], and the NLO QCD corrections are included for anomalous couplings between the Higgs and a pair of vector bosons.

VBFNLO can also simulate the Higgs decays $\mathrm{H} \to \gamma\gamma, \mu^+\mu^-, \tau^+\tau^-, \mathrm{b}\overline{\mathrm{b}}$ in the narrow-width approximation, either taking the appropriate branching ratios from an input SLHA file or calculating them internally at LO. The Higgs-boson decays $\mathrm{H} \to \mathrm{W}^+\mathrm{W}^- \to \mathrm{l}^+\nu_{\mathrm{l}}\mathrm{l}^-\overline{\nu}_{\mathrm{l}}$ and $\mathrm{H} \to \mathrm{ZZ} \to \mathrm{l}^+\mathrm{l}^-\mathrm{l}^+\mathrm{l}^-, \mathrm{l}^+\mathrm{l}^-\nu_{\mathrm{l}}\overline{\nu_{\mathrm{l}}}$ are calculated using a Breit–Wigner distribution for the Higgs boson and the full LO matrix element for the $\mathrm{H} \to 4f$ decay.

For the results presented here, a modified version of VBFNLO was used that simulated a Higgs-boson decay with a branching ratio of 1 and a Breit–Wigner distribution (47) for the virtuality of the off-shell Higgs boson.

6.1.3 POWHEG

The POWHEG method is a prescription for interfacing NLO calculations with parton-shower generators, like HERWIG and PYTHIA. It was first presented in Ref. [123] and was described in great detail in Ref. [126]. In Ref. [160], Higgs-boson production in VBF has been implemented in the framework of the POWHEG BOX [156], a computer framework that implements in practice the theoretical construction of Ref. [126].

All the details of the implementation can be found in Ref. [160]. Here we briefly recall that, in the calculation of the partonic matrix elements, all partons have been treated as massless. This gives rise to a different treatment of quark flavours for diagrams where a Z boson or a W boson is exchanged in the t-channel. In fact, for all Z-exchange contributions, the b-quark is included as an initial and/or final-state massless parton. For the (dominant) W-exchange contributions, no initial b-quark has been considered, since it would have produced mostly a t quark in the final state, which would have been misleadingly treated as massless. The Cabibbo–Kobayashi–Maskawa (CKM) matrix V_{CKM} has been taken as

$$V_{\mathrm{CKM}} = \begin{array}{c} \\ \mathrm{u} \\ \mathrm{c} \\ \mathrm{t} \end{array} \begin{array}{c} \begin{array}{ccc} \mathrm{d} & \mathrm{s} & \mathrm{b} \end{array} \\ \begin{pmatrix} 0.9748 & 0.2225 & 0.0036 \\ 0.2225 & 0.9740 & 0.041 \\ 0.009 & 0.0405 & 0.9992 \end{pmatrix} \end{array}. \tag{48}$$

We point out that, as long as no final-state hadronic flavour is tagged, this is practically equivalent to the result obtained using the identity matrix, due to unitarity.

[30] For more details see Section 12.3.4.

The Higgs-boson virtuality M^2 has been generated distributed according to

$$\frac{1}{\pi}\frac{M^2\,\Gamma_{\rm H}/M_{\rm H}}{\left(M^2-M_{\rm H}^2\right)^2+(M^2\,\Gamma_{\rm H}/M_{\rm H})^2}\,, \tag{49}$$

with fixed decay width $\Gamma_{\rm H}$.

As a final remark, we recall that the renormalisation $\mu_{\rm R}$ and factorisation $\mu_{\rm F}$ scales have been taken equal to the transverse momentum of the radiated parton, during the generation of radiation, as the POWHEG method requires. The transverse momentum of the radiated parton is taken, in the case of initial-state radiation, as exactly equal to the transverse momentum of the parton with respect to the beam axis. For final-state radiation one takes instead

$$p_{\rm T}^2 = 2E^2(1-\cos\theta), \tag{50}$$

where E is the energy of the radiated parton and θ the angle it forms with respect to the final-state parton that has emitted it, both taken in the partonic centre-of-mass frame. The scales used in the calculation of the POWHEG $\bar{B}$ function (i.e. the function that is used to generate the underlying Born variables to which the POWHEG BOX attaches the radiation ones) are instead the ones defined in the forthcoming Eq. (54).

6.2 VBF parameters and cuts

The numerical results presented in Section 6.3 have been computed using the values of the EW parameters given in Appendix A of Ref. [7]. The electromagnetic coupling is fixed in the G_F scheme, to be

$$\alpha_{G_F} = \sqrt{2}G_F M_{\rm W}^2(1-M_{\rm W}^2/M_{\rm Z}^2)/\pi = 1/132.4528\ldots. \tag{51}$$

The weak mixing angle is defined in the on-shell scheme,

$$\sin^2\theta_{\rm w} = 1 - M_{\rm W}^2/M_{\rm Z}^2 = 0.222645\ldots\,. \tag{52}$$

We consider the following set of Higgs-boson masses and corresponding total widths, as reported in Refs. [7, 14]:

$M_{\rm H}$ [GeV]	120	150	200	250	500	600
$\Gamma_{\rm H}$ [GeV]	0.00348	0.0173	1.43	4.04	68.0	123

(53)

The renormalisation and factorisation scales are set equal to the W-boson mass,

$$\mu_{\rm R} = \mu_{\rm F} = M_{\rm W}. \tag{54}$$

In the calculation of the NLO differential cross sections, we have used the MSTW2008 [107] and CTEQ6.6 [103] PDFs.

Jets are constructed according to the anti-$k_{\rm T}$ algorithm, with the rapidity–azimuthal separation $\Delta R = 0.5$, using the default recombination scheme (E scheme). Jets are subject to the following cuts

$$p_{{\rm T}j} > 20\ {\rm GeV}, \qquad |y_j| < 4.5\,, \tag{55}$$

where y_j denotes the rapidity of the (massive) jet. Jets are ordered according to their $p_{\rm T}$ in decreasing progression. The jet with highest $p_{\rm T}$ is called leading jet, the one with next highest $p_{\rm T}$ subleading jet, and both are the tagging jets. Only events with at least two jets are kept. They must satisfy the additional constraints

$$|y_{j_1} - y_{j_2}| > 4\,, \qquad m_{jj} > 600\ {\rm GeV}. \tag{56}$$

The Higgs boson is generated off shell, according to Eqs. (47) or (49), and there are no cuts applied to its decay products.

For the calculation of EW corrections, real photons are recombined with jets according to the same anti-$k_{\rm T}$ algorithm as used for jet recombination.

6.3 Results

In the following we present a few results for the LHC at 7 TeV calculated with HAWK, VBFNLO, and POWHEG, for the Higgs-boson masses listed in Eq. (53).

6.3.1 Total cross sections with VBF cuts

We have calculated the cross section for VBF at NLO within the cuts given in Section 6.2 using the MSTW2008NLO and CTEQ6.6 PDF sets with and without EW corrections. The results are shown in Tables 14 and 16 including the statistical errors of the Monte Carlo integration. The results of HAWK and VBFNLO without EW corrections agree within 1%. For the results with EW corrections there is a slight discrepancy between HAWK and VBFNLO at the level of $1-1.3\%$ for small Higgs-boson masses. For heavy Higgs-boson masses the difference increases because of leading two-loop heavy-Higgs corrections that are included in HAWK but not in VBFNLO. These corrections contribute about 3% and 2% for $M_{\rm H} = 600$ GeV and 500 GeV, respectively. The EW corrections calculated with HAWK amount to -8% for small Higgs-boson masses, decrease, and change sign with increasing Higgs-boson mass and reach $+2.4\%$ for $M_{\rm H} = 600$ GeV. We also show the scale uncertainties obtained with HAWK by varying the factorisation and renormalisation scales in the range $M_{\rm W}/2 < \mu < 2M_{\rm W}$[31] and the PDF uncertainties obtained from the corresponding 90% C.L. error PDFs according to the CTEQ prescription with symmetric errors [103]. We give these uncertainties only for the cross section with EW corrections as they are practically the same without EW corrections. Both the PDF uncertainties and the scale uncertainties are larger than for the total cross section without cuts (c.f. Ref. [7]). Note that we do not include the uncertainties from varying $\alpha_{\rm s}$ in the PDFs as these are small (below 1%) and thus negligible compared to the PDF uncertainties [267].

Tables 15 and 17 show the corresponding results obtained with POWHEG at pure NLO QCD and with PYTHIA or HERWIG parton showers. The NLO results in the second columns can be directly compared with the NLO results without EW corrections of Tables 14 and 16. While POWHEG and HAWK/VBFNLO agree within integration errors for small Higgs-boson masses the results differ by 13% and 25% for $M_{\rm H} = 500$ GeV and $M_{\rm H} = 600$ GeV. We checked that this difference is due to the different Breit–Wigner distributions, (47) and (49), used in the codes, in the treatment of the unstable Higgs boson. This difference should be viewed as an estimate of the theoretical uncertainty of the present calculations based on Breit–Wigner distributions. The proper treatment of a heavy Higgs boson is described in Section 15, but has not yet been implemented for VBF. Inclusion of the parton showers reduces the cross sections by $5\%-7\%$ with a larger effect for small Higgs-boson masses, because more events are cut away after showering. The results for PYTHIA and HERWIG parton showers are in good agreement.

6.3.2 Differential distributions

In this section we present some results for differential distributions for the setup defined in Section 6.2 and MSTW2008NLO PDFs. For each distribution we show the NLO results from HAWK with (blue solid) and without (green dash-dotted) EW corrections, the results of VBFNLO with EW corrections (black long-dashed) and the NLO QCD results from POWHEG (red short-dashed). Each plot contains results for $M_{\rm H} = 120$ GeV (upper set of curves) and for $M_{\rm H} = 600$ GeV (lower set of curves). In addition we show the relative EW corrections obtained from HAWK. These are insensitive to PDFs and could be taken into account in any QCD-based prediction for the respective distributions (based on the cuts of Section 6.2) via reweighting. The data files of the histograms are provided at the TWiki page of the VBF working group[32].

[31] More precisely, we calculated the cross sections for the 5 scale combinations $\{\mu_{\rm R}, \mu_{\rm F}\} = \{M_{\rm W}, M_{\rm W}\}$, $\{M_{\rm W}/2, M_{\rm W}\}$, $\{M_{\rm W}, M_{\rm W}/2\}$, $\{2M_{\rm W}, M_{\rm W}\}$, and $\{M_{\rm W}, 2M_{\rm W}\}$, and took the maximum and the minimum of the results as the upper and lower bound of the variation.

[32] https://twiki.cern.ch/twiki/bin/view/LHCPhysics/VBF

Table 14: Higgs-boson NLO cross sections at 7 TeV with VBF cuts and CTEQ6.6 PDF set with and without EW corrections, relative EW corrections and theoretical uncertainties from PDF and scale variations.

	w/ EW corr		w/o EW corr		EW corr	uncert.	
$M_{\rm H}$ [GeV]	HAWK [fb]	VBFNLO [fb]	HAWK [fb]	VBFNLO [fb]	HAWK [%]	PDF [%]	scale [%]
120	261.18 ± 0.43	258.27 ± 0.41	283.91 ± 0.42	282.80 ± 0.19	-8.0 ± 0.2	± 3.5	$+0.5 - 0.5$
150	218.40 ± 0.36	216.84 ± 0.40	236.75 ± 0.35	236.68 ± 0.14	-7.8 ± 0.2	± 3.5	$+1.0 - 0.5$
200	165.22 ± 0.24	163.50 ± 0.24	176.46 ± 0.24	176.89 ± 0.10	-6.4 ± 0.2	± 3.6	$+0.6 - 0.6$
250	123.81 ± 0.17	122.67 ± 0.17	133.13 ± 0.16	133.15 ± 0.07	-7.0 ± 0.2	± 3.8	$+0.6 - 0.5$
500	38.10 ± 0.07	37.31 ± 0.08	38.38 ± 0.07	38.41 ± 0.02	-0.7 ± 0.3	± 4.3	$+0.4 - 0.4$
600	26.34 ± 0.12	25.46 ± 0.07	25.70 ± 0.11	25.55 ± 0.01	2.5 ± 0.7	± 4.4	$+0.7 - 0.6$

Table 15: POWHEG Higgs-boson NLO QCD cross sections at 7 TeV with VBF cuts and CTEQ6.6 PDF set: fixed NLO results, POWHEG showered by PYTHIA (PY) and by HERWIG (HW).

$M_{\rm H}$ [GeV]	POWHEG NLO [fb]	POWHEG + PY [fb]	POWHEG + HW [fb]
120	282.87 ± 0.75	262.96 ± 0.99	262.04 ± 0.99
150	237.30 ± 0.57	221.54 ± 0.79	219.95 ± 0.79
200	177.05 ± 0.38	164.55 ± 0.55	163.83 ± 0.55
250	132.93 ± 0.26	124.19 ± 0.40	123.65 ± 0.40
500	34.04 ± 0.07	31.92 ± 0.09	31.78 ± 0.10
600	20.56 ± 0.03	19.47 ± 0.06	19.30 ± 0.06

Table 16: Higgs-boson NLO cross sections at 7 TeV with VBF cuts and MSTW2008NLO PDF set with and without EW corrections, relative EW corrections and theoretical uncertainties from PDF and scale variations.

	w/ EW corr		w/o EW corr		EW corr	uncert.	
$M_{\rm H}$ [GeV]	HAWK [fb]	VBFNLO [fb]	HAWK [fb]	VBFNLO [fb]	HAWK [%]	PDF [%]	scale [%]
120	259.74 ± 0.69	256.69 ± 0.83	282.17 ± 0.68	281.37 ± 0.22	-8.0 ± 0.2	± 5.0	$+0.6 - 0.5$
150	217.58 ± 0.37	215.46 ± 0.33	235.73 ± 0.36	235.46 ± 0.15	-7.7 ± 0.2	± 5.1	$+0.5 - 0.5$
200	164.18 ± 0.24	162.10 ± 0.26	175.29 ± 0.23	175.23 ± 0.15	-6.3 ± 0.2	± 5.0	$+0.5 - 0.5$
250	122.73 ± 0.20	120.96 ± 0.61	131.90 ± 0.19	131.86 ± 0.07	-7.0 ± 0.2	± 5.2	$+0.5 - 0.7$
500	37.26 ± 0.09	36.57 ± 0.10	37.57 ± 0.10	37.61 ± 0.02	-0.8 ± 0.2	± 5.2	$+0.7 - 0.4$
600	25.71 ± 0.08	24.83 ± 0.06	25.21 ± 0.08	25.01 ± 0.02	2.0 ± 0.2	± 5.1	$+0.4 - 0.7$

Table 17: POWHEG Higgs-boson NLO QCD cross sections at 7 TeV with VBF cuts and MSTW2008NLO PDF set: fixed NLO results, POWHEG showered by PYTHIA (PY) and by HERWIG (HW).

$M_{\rm H}$ [GeV]	POWHEG NLO [fb]	POWHEG + PY [fb]	POWHEG + HW [fb]
120	281.97 ± 0.76	262.23 ± 0.99	260.44 ± 1.00
150	235.29 ± 0.67	218.24 ± 0.79	216.70 ± 0.79
200	175.38 ± 0.42	162.80 ± 0.55	161.45 ± 0.55
250	131.57 ± 0.26	123.21 ± 0.40	122.62 ± 0.40
500	33.21 ± 0.06	31.03 ± 0.09	30.85 ± 0.09
600	20.03 ± 0.03	18.74 ± 0.05	18.67 ± 0.06

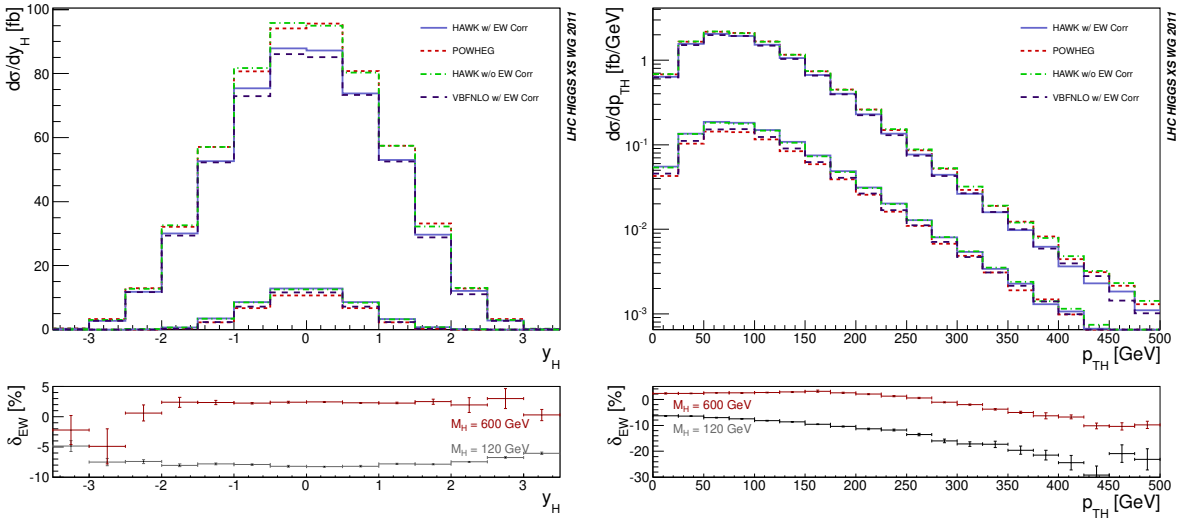

Fig. 49: Higgs-boson rapidity (left) and transverse momentum (right). The top plots show the comparison between HAWK (with and without EW corrections), POWHEG at NLO QCD and VBFNLO (with EW corrections) for $M_{\rm H} = 120$ GeV (upper set of curves) and $M_{\rm H} = 600$ GeV (lower set of curves) for MSTW2008NLO PDF set. The bottom plots display the percentage EW corrections, for each of the two mass points.

Figure 49 displays the rapidity $y_{\rm H}$ and the transverse momentum $p_{\rm TH}$ of the Higgs boson. While the difference in normalisation between POWHEG and HAWK for the high Higgs-boson mass has been explained for the total cross section, the shapes of the distributions agree well between the different codes. While EW corrections are flat for the rapidity distribution, the EW corrections increase with increasing $p_{\rm TH}$.

For the distributions in the transverse momentum of the leading and subleading jets, $p_{{\rm T}j_1}$ and $p_{{\rm T}j_2}$, shown in Figure 50 and of the di-jet invariant mass m_{jj}, presented on the left-hand side of Figure 51 similar remarks are applicable. The shapes of the different distributions agree well between the different codes. The EW corrections reduce the cross section more and more with increasing energy scale, a generic behaviour of EW corrections that can be attributed to weak Sudakov logarithms. EW corrections range from a few to -20%. The distribution in the azimuthal-angle separation between the two tagging jets ϕ_{jj} is shown on the right-hand side of Figure 51. In particular, for the light Higgs boson, the electroweak corrections distort the distribution at the level of several per cent.

6.3.3 POWHEG *differential distributions*

In this section, we present a few results obtained by POWHEG interfaced to HERWIG and PYTHIA, in the configuration described in Section 6.2 and for a Higgs-boson mass of 120 GeV. These results have been generated using the MSTW2008 PDF set. They depend only very slightly on the value of the Higgs-boson mass and on the PDF set used, so similar conclusions can be drawn using NNPDF2.0 and CTEQ6.6. All results are correct at NLO in QCD. No EW corrections are included. We have generated 0.5M events with the POWHEG BOX. We have run PYTHIA with the Perugia 0 tuning and HERWIG in its default configuration, with intrinsic $p_{\rm T}$-spreading of 2.5 GeV.

In Figure 52 we plot the invariant mass of the two tagging jets, m_{jj}, and the absolute value of the distance in rapidity of the two tagging jets, $|y_{j_1} - y_{j_2}|$. In all distributions presented in this section the solid blue lines represent the NLO result, and the green and the red curves the results of POWHEG interfaced to HERWIG and PYTHIA, respectively. The effect of the cuts on the showered results produces a reduction of the total cross section that appears manifest in the two distributions shown. There is an agreement between the two showered results, slightly below the NLO curves. This behaviour

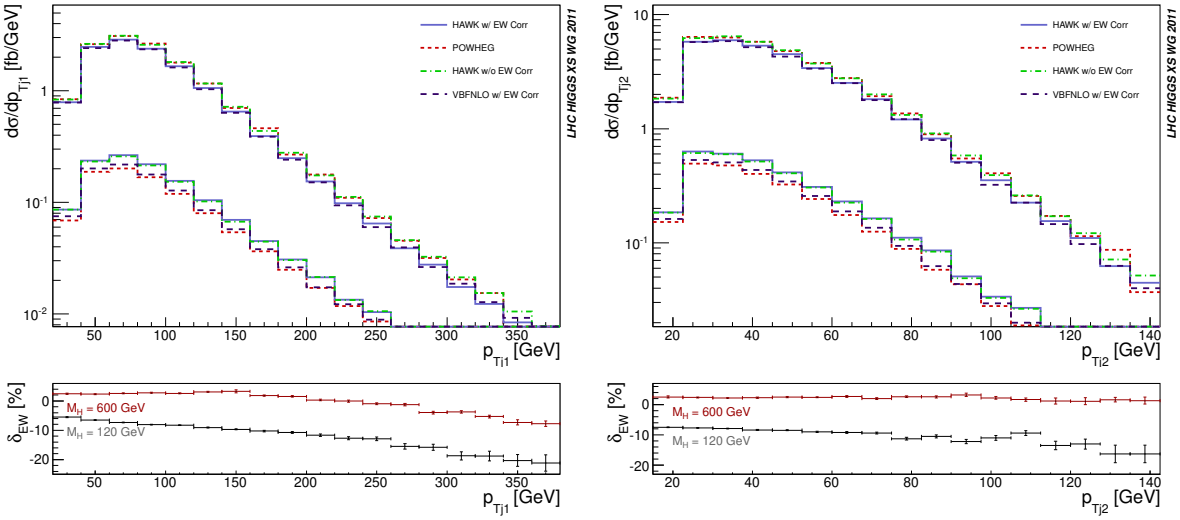

Fig. 50: Transverse momentum of the leading (left) and sub-leading jet (right). The top plots show the comparison between HAWK (with and without EW corrections), POWHEG at NLO QCD and VBFNLO (with EW corrections) for $M_{\rm H} = 120$ GeV (upper set of curves) and $M_{\rm H} = 600$ GeV (lower set of curves) for MSTW2008NLO PDF set. The bottom plots display the percentage EW corrections, for each of the two mass points.

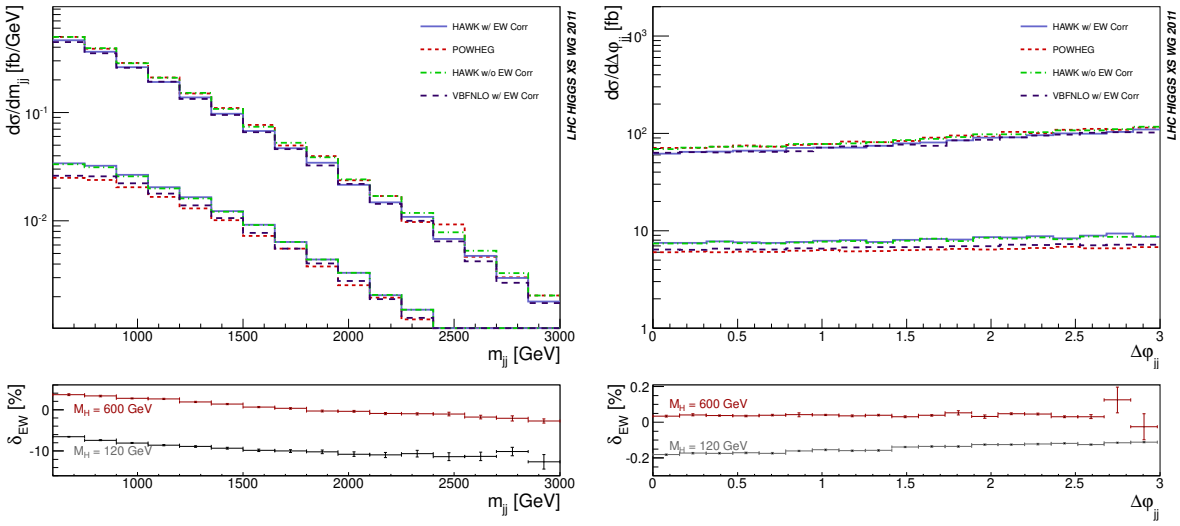

Fig. 51: Di-jet invariant mass (left) and azimuthal separation between the two tagging jets (right). The top plots show the comparison between HAWK (with and without EW corrections), POWHEG QCD and VBFNLO (with EW corrections) for $M_{\rm H} = 120$ GeV (upper set of curves) and $M_{\rm H} = 600$ GeV (lower set of curves) for MSTW2008NLO PDF set. The bottom plots display the percentage EW corrections for each of the two mass points.

is generic for several physical distributions.

Larger disagreements between the NLO QCD and showered results and between the two showering programs can be seen in Figure 53. On the left-hand side of this figure, we have plotted the rapidity distribution of the third hardest jet (the one with highest $p_{\rm T}$ after the two tagging jets). The distributions obtained using POWHEG interfaced to HERWIG and PYTHIA are very similar, but show that fewer events pass the cuts with respect to the unshowered NLO result. Nevertheless, they confirm the behaviour that the third jet tends to be emitted in the vicinity of either of the tagging jets. We recall here that, strictly speaking, this is a LO distribution, since the third jet in the NLO calculation comes only

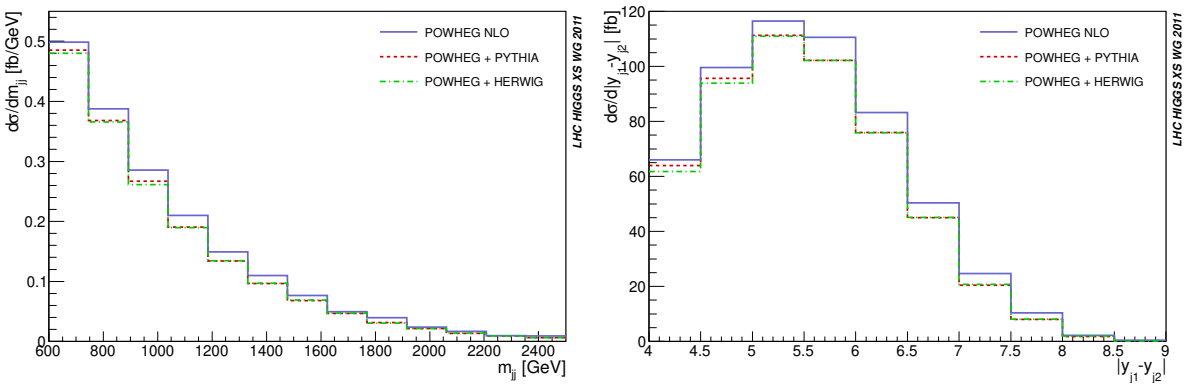

Fig. 52: Invariant mass of the two tagging jets, m_{jj}, (left) and absolute value of the distance in rapidity of the two tagging jets, $|y_{j_1} - y_{j_2}|$, (right). We show the comparison among NLO QCD and the POWHEG interfaced to HERWIG and PYTHIA results.

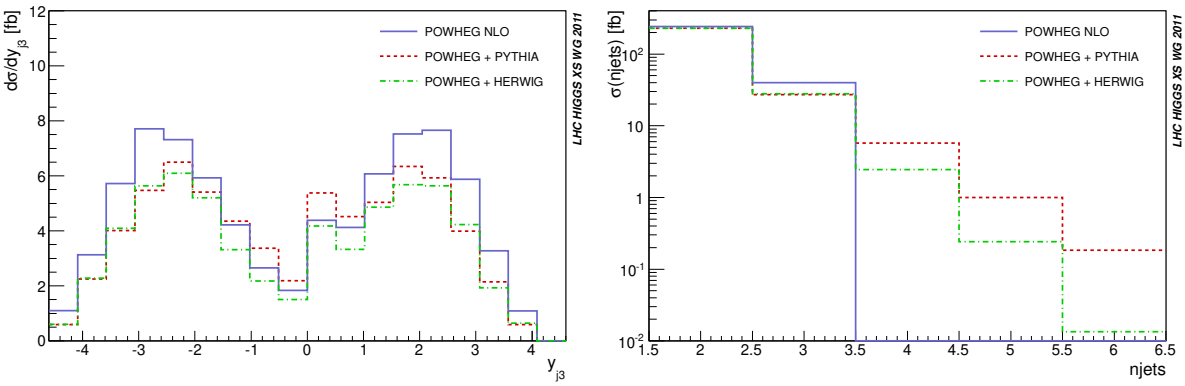

Fig. 53: Rapidity distribution of the third hardest jet, y_{j_3} (left) and exclusive jet-multiplicity (right). We show the comparison among NLO QCD and the POWHEG interfaced to HERWIG and PYTHIA results.

from the real-emission contributions.

We turn now to quantities that are more sensitive to the collinear and soft physics of the shower. The jet activity is one such quantity. In order to quantify it, we plot the exclusive jet-multiplicity distribution for jets that pass the cuts of Eq. (55) in the right-hand plot of Figure 53. The first two tagging jets and the third jet are well represented by the NLO cross section, which obviously cannot contribute to events with more than three jets. From the 4th jet on, the showers of HERWIG and PYTHIA produce sizable differences (note the log scale of the plot), the jets from PYTHIA being harder and/or more central than those from the HERWIG shower.

Striking differences between the NLO QCD results and POWHEG can be seen in the relative transverse momentum of all the particles clustered inside one of the two tagging jets $p_{\mathrm{T}}^{\mathrm{rel},j}$. This quantity brings information on the "shape" of the jet. It is defined as follows:

- For each jet we perform a longitudinal boost to a frame where the jet has zero rapidity.
- In this frame, we compute the quantity

$$p_{\mathrm{T}}^{\mathrm{rel},j} = \sum_{i \in j} \frac{|\vec{k}^i \times \vec{p}^j|}{|\vec{p}^j|}\,, \tag{57}$$

where k^i are the momenta of the particles that belong to the jet with momentum p^j.

This quantity is thus the sum of the absolute values of the transverse momenta, taken with respect to the

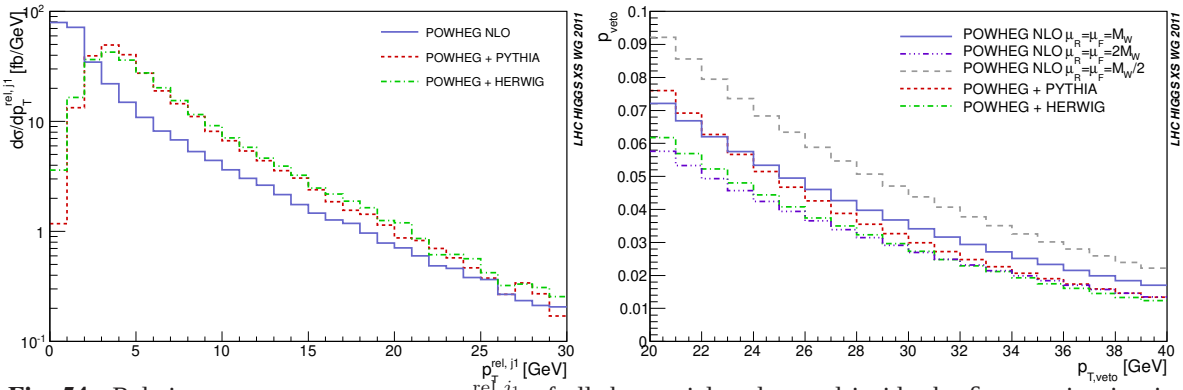

Fig. 54: Relative transverse momentum $p_{\mathrm{T}}^{\mathrm{rel},j_1}$ of all the particles clustered inside the first tagging jet, in the reference frame where the jet has zero rapidity, defined according to Eq. (57) (left) and probability of finding a veto jet defined as in Eq. (59) as a function of $p_{\mathrm{T,veto}}$ (right). We show the comparison among NLO QCD and the POWHEG interfaced to HERWIG and PYTHIA results. In addition, on the right plot, we show the NLO QCD results obtained with $\mu_{\mathrm{R}} = \mu_{\mathrm{F}} = M_{\mathrm{W}}/2$ and $\mu_{\mathrm{R}} = \mu_{\mathrm{F}} = 2M_{\mathrm{W}}$.

jet axis, of the particles inside the jet, in the frame specified above. In the left-hand side of Figure 54 we have plotted the relative transverse momentum with respect to the first tagging jet, $p_{\mathrm{T}}^{\mathrm{rel},j_1}$. While the black NLO curve is diverging as $p_{\mathrm{T}}^{\mathrm{rel},j_1}$ approaches zero, the Sudakov form factors damp this region in the POWHEG results.

As a last comparison, we have studied the probability of finding veto jets, i.e. jets that fall within the rapidity interval of the two tagging jets,

$$\min\left(y_{j_1}, y_{j_2}\right) < y_j < \max\left(y_{j_1}, y_{j_2}\right). \tag{58}$$

In fact, for the central-jet-veto proposal, events are discarded if any additional jet with a transverse momentum above a minimal value, $p_{\mathrm{T,veto}}$, is found between the tagging jets. The probability, P_{veto}, of finding a veto jet is defined as

$$P_{\mathrm{veto}} = \frac{1}{\sigma_2^{\mathrm{NLO}}} \int_{p_{\mathrm{T,veto}}}^{\infty} dp_{\mathrm{T}}^{j,\mathrm{veto}} \frac{d\sigma}{dp_{\mathrm{T}}^{j,\mathrm{veto}}}\,, \tag{59}$$

where $p_{\mathrm{T}}^{j,\mathrm{veto}}$ is the transverse momentum of the hardest veto jet, and σ_2^{NLO} is the total cross section (within VBF cuts) for $\mathrm{H}jj$ production at NLO [33]. In the right-hand plot of Figure 54 we have plotted the NLO QCD and POWHEG interfaced to HERWIG and PYTHIA predictions. For $M_{\mathrm{H}} = 120$ GeV, we have $\sigma_2^{\mathrm{NLO}} = 282$ fb, with the settings described in Section 6.2. In addition to the NLO curve obtained with $\mu_{\mathrm{R}} = \mu_{\mathrm{F}} = M_{\mathrm{W}}$, we have added the NLO results computed with $\mu_{\mathrm{R}} = \mu_{\mathrm{F}} = M_{\mathrm{W}}/2$ (upper dashed line) and $\mu_{\mathrm{R}} = \mu_{\mathrm{F}} = 2M_{\mathrm{W}}$ (lower dash-dotted line) that show that the POWHEG curves are consistent with the LO band obtained with a change of the renormalisation and factorisation scale by a factor of two and that the distance between POWHEG+PYTHIA and POWHEG+HERWIG is comparable with the scale uncertainty of the LO result.

6.3.4 Efficiency of VBF cuts

The efficiency $\epsilon^{\{\mu_{\mathrm{R}},\mu_{\mathrm{F}}\}}$ of the VBF selection cuts is defined as $\epsilon^{\{\mu_{\mathrm{R}},\mu_{\mathrm{F}}\}} = \sigma_{\mathrm{cuts}}^{\{\mu_{\mathrm{R}},\mu_{\mathrm{F}}\}}/\sigma_{\mathrm{inc}}^{\{\mu_{\mathrm{R}},\mu_{\mathrm{F}}\}}$, where σ_{cuts} is the cross section after all the forward jet tagging described above and an additional jet-veto cut $p_{\mathrm{T,veto}}$, and σ_{inc} is the inclusive cross section before cuts, both computed with the renormalisation and factorisation scales set to μ_{R} and μ_{F}, respectively. The uncertainty on this ratio is of particular interest to

[33] Strictly speaking, P_{veto} is a LO quantity, since it receives contributions only from the real-emission diagrams.

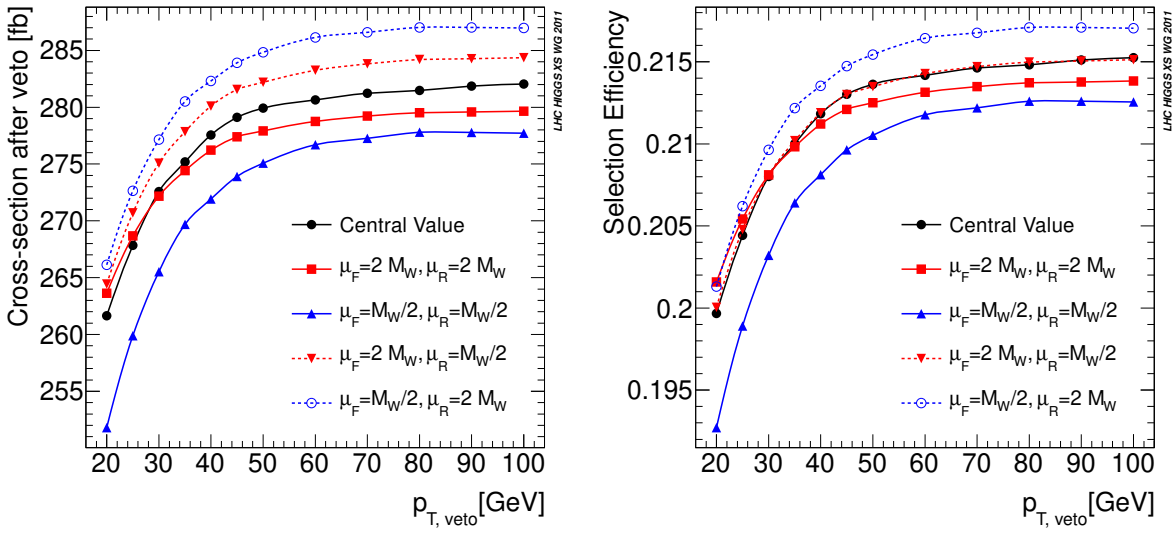

Fig. 55: The NLO QCD cross section for $M_{\rm H} = 120$ GeV after all cuts as a function of $p_{\rm T,veto}$ (left) and the efficiency of the forward jet tagging and central-jet-veto cuts as a function of $p_{\rm T,veto}$ (right). Results obtained with VBFNLO.

Table 18: NLO QCD cross sections and efficiencies from VBFNLO for the full VBF selection including the jet veto cut of 20 GeV and the corresponding relative uncertainties from the QCD scale and PDFs.

$M_{\rm H}$	Cross section			Efficiency		
[GeV]	[fb]	[%]	[%]	[%]	[%]	[%]
120	261.64	±3.76	±4.91	0.200	±3.485	±1.468
150	218.69	±3.59	±4.66	0.221	±3.376	±1.196
200	163.34	±3.92	±4.66	0.252	±3.829	±1.490
250	123.06	±4.16	±5.11	0.279	±4.145	±1.493
500	33.55	±4.37	±5.43	0.365	±4.766	±1.227
600	20.82	±4.44	±5.58	0.384	±4.958	±1.002

experimental studies since the theoretical prediction of the efficiency is used to translate the experimental upper bound on the yield after cuts to a more useful limit on the inclusive signal cross section.

Figure 55 shows the cross section after cuts (left) and the efficiency of the selection cuts (right) as functions of $p_{\rm T,veto}$ for $M_{\rm H} = 120$ GeV. The values are calculated using VBFNLO, at NLO QCD and with the MSTW2008 PDF set. To evaluate scale uncertainties, the inclusive cross section and the exclusive cross sections after cuts are recomputed with four altered choices of the renormalisation and factorisation scales: $\{\mu_{\rm R}, \mu_{\rm F}\} = \{M_{\rm W}/2,\ M_{\rm W}/2\}$, $\{2M_{\rm W},\ 2M_{\rm W}\}$, $\{2M_{\rm W},\ M_{\rm W}/2\}$, and $\{M_{\rm W}/2,\ 2M_{\rm W}\}$. The cross section and efficiency curves with these altered scale choices are shown as the red and blue solid and dashed curves in Figure 55. The scale uncertainty on the selection efficiency for a given choice of $p_{\rm T,veto}$ is taken as the largest deviation of the predicted efficiency obtained using any of these altered scale choices from the result obtained from the central-value scale choice $\{\mu_{\rm R}, \mu_{\rm F}\} = \{M_{\rm W},\ M_{\rm W}\}$. PDF uncertainties are estimated using the MSTW2008 90% C.L. error PDF sets according to the CTEQ prescription with symmetric errors [103].

Table 18 shows the central value as well as the relative scale and PDF uncertainties for the cross section after cuts and the selection efficiency, for several values of the Higgs-boson mass and for a jet-veto cut of 20 GeV. For the cross sections, the scale uncertainties are at the level of $\sim 4\%$, while the

PDF uncertainties are closer to 5%. For the efficiencies, the scale uncertainties are also close to 4%, but the PDF uncertainties are generally smaller, around 1%.

7 WH/ZH production mode[34]

7.1 Theoretical developments

In the previous report [7] state-of-the-art predictions and error estimates for the total cross sections for $\mathrm{pp} \to \mathrm{WH/ZH}$ have been compiled, based on (approximate) next-to-next-to-leading-order (NNLO) QCD and next-to-leading-order (NLO) electroweak (EW) corrections. In more detail, the QCD corrections ($\sim 30\%$) comprise Drell–Yan-like contributions [268], which respect factorisation according to $\mathrm{pp} \to \mathrm{V}^* \to \mathrm{VH}$ and represent the dominant parts, and a smaller remainder, which contributes beyond NLO. The NLO EW corrections to the total cross sections were evaluated as in Ref. [269] and turn out to be about $-(5-10)\%$. In the report [7] the Drell–Yan-like NNLO QCD predictions are dressed with the NLO EW corrections in fully factorised form as suggested in Ref. [270], i.e. the EW corrections simply enter as multiplicative correction factor, which is rather insensitive to QCD scale and parton distribution function (PDF) uncertainties. For ZH production the one-loop-induced subprocess $\mathrm{gg} \to \mathrm{ZH}$, which is part of the non-Drell–Yan-like NNLO QCD corrections, was taken into account as well. For the LHC with a centre-of-mass (CM) energy of $7(14)$ TeV the QCD scale uncertainties were assessed to be about 1% and $1-2(3-4)\%$ for WH and ZH production, respectively, while uncertainties of the PDFs turn out to be about $3-4\%$.

After the completion of the report [7] theoretical progress has been made in various directions:

- On the QCD side, the Drell–Yan-like NNLO corrections to WH production are available now [271] including the full kinematical information of the process and leptonic W decays.
- For total cross sections the non-Drell–Yan-like remainder at NNLO QCD (apart from the previously known $\mathrm{gg} \to \mathrm{ZH}$ subprocess) has been calculated recently [272]; in particular, this includes contributions with a top-quark induced gluon–Higgs coupling. As previously assumed, these effects are at the per-cent level. They typically increase towards larger Higgs masses and scattering energies, reaching about $2.5\%(3\%)$ for ZH production at 7 TeV$(14$ TeV$)$. Since these Yukawa-induced terms arise for the first time at $\mathcal{O}(\alpha_\mathrm{s}^2)$, they also increase the perturbative uncertainty which, however, still remains below the error from the PDFs.
- On the EW side, the NLO corrections have been generalised to the more complex processes $\mathrm{pp} \to \mathrm{WH} \to \nu_\mathrm{l}\mathrm{lH}$ and $\mathrm{pp} \to \mathrm{ZH} \to \mathrm{l}^-\mathrm{l}^+\mathrm{H}/\nu_\mathrm{l}\bar{\nu}_\mathrm{l}\mathrm{H}$ including the W/Z decays, also fully supporting differential observables [263]; these results are available as part of the HAWK Monte Carlo program [260], which was originally designed for the description of Higgs production via vector-boson fusion including NLO QCD and EW corrections [258].

The following numerical results on differential quantities are, thus, obtained as follows:

- WH production: The fully differential (Drell–Yan-like) NNLO QCD prediction of Ref. [271] is reweighted with the relative EW correction factor calculated with HAWK, analogously to the previously used procedure for the total cross section. The reweighting is done bin by bin for each distribution.
- ZH production: Here the complete prediction is obtained with HAWK including NLO QCD and EW corrections, employing the factorisation of relative EW corrections as well.

7.2 Numerical results

For the numerical results in this section, we have used the following setup. The renormalisation and factorisation scales have been identified and set to

$$\mu_\mathrm{R} = \mu_\mathrm{F} = M_\mathrm{H} + M_\mathrm{V}, \tag{60}$$

[34] S. Dittmaier, R.V. Harlander, J. Olsen, G. Piacquadio (eds.); A. Denner, G. Ferrera, M. Grazzini, S. Kallweit, A. Mück and F. Tramontano.

where M_{V} is the W/Z-boson mass for WH/ZH production. We have employed the MSTW2008 PDF sets at NNLO for WH production and the PDF4LHC prescription to calculate the cross section for ZH production at NLO. The relative EW corrections have been calculated using the central NLO MSTW2008 PDF, but hardly depend on the PDF and scale choice. We use the G_F scheme to fix the electromagnetic coupling α and use the values of α_{s} associated to the given PDF set. For the QCD predictions to WH production, we employ the full CKM matrix which enters via global factors multiplying the different partonic channels. For all the HAWK predictions, we neglect mixing of the first two generations with the third generation. In the EW loop corrections, the CKM matrix is set to unity, since quark mixing is negligible there. For ZH production, bottom quarks in the initial state are only included in LO within HAWK because of their small impact on the cross sections.

Both the NNLO QCD prediction as well as the HAWK predictions are obtained for off-shell vector bosons. The vector-boson width can be viewed as a free parameter of the calculation, and we have chosen $\Gamma_{\mathrm{W}} = 2.08872$ GeV and Γ_{Z} from the default input. The NNLO QCD calculation [271] predicts the integrated W-boson production cross section in the presence of the cuts defined below, so that it had to be multiplied by the branching ratio $\mathrm{BR}_{\mathrm{W}\to\mathrm{l}\nu_{\mathrm{l}}}$ for a specific leptonic final state. Because the EW radiative corrections to the BR are included in the EW corrections from HAWK, the partial W width has to be used at Born level in the QCD-improved cross section, i.e. $\mathrm{BR}_{\mathrm{W}\to\mathrm{l}\nu_{\mathrm{l}}} = \Gamma^{\mathrm{Born}}_{\mathrm{W}\to\mathrm{l}\nu_{\mathrm{l}}}/\Gamma_{\mathrm{W}}$, where $\Gamma^{\mathrm{Born}}_{\mathrm{W}\to\mathrm{l}\nu_{\mathrm{l}}} = G_F M_{\mathrm{W}}^3/(6\sqrt{2}\pi)$. Using any different input value for $\Gamma^{\mathrm{new}}_{\mathrm{W}}$, all results are thus, up to negligible corrections, changed by the ratio $\Gamma_{\mathrm{W}}/\Gamma^{\mathrm{new}}_{\mathrm{W}}$. In the HAWK prediction, the branching ratios for the different leptonic channels are implicitly included by calculating the full matrix elements. However, up to negligible corrections the same scaling holds if another numerical value for the input width was used. In particular, the relative EW corrections hardly depend on Γ_{W}.

All results are given for a specific leptonic decay mode, e.g. for $\mathrm{He^+e^-}$ or $\mathrm{H\mu^+\mu^-}$ production, and are not summed over lepton generations. While for charged leptons the results depend on the prescription for lepton–photon recombination (see below), the results for invisible Z decays, of course, do not depend on the neutrino flavour and can be trivially obtained by multiplying the $\mathrm{H}\nu_{\mathrm{l}}\bar{\nu}_{\mathrm{l}}$ results by three.

In the calculation of EW corrections, we alternatively apply two versions of handling photons that become collinear to outgoing charged leptons. The first option is to assume perfect isolation between charged leptons and photons, an assumption that is at least approximately fulfilled for (bare) muons. The second option performs a recombination of photons and nearly collinear charged leptons and, thus, mimics the inclusive treatment of electrons within electromagnetic showers in the detector. Specifically, a photon γ and a lepton l are recombined for $R_{\mathrm{l}\gamma} < 0.1$, where $R_{\mathrm{l}\gamma} = \sqrt{(y_{\mathrm{l}} - y_\gamma)^2 + \phi^2_{\mathrm{l}\gamma}}$ is the usual separation variable in the $y-\phi$-plane with y denoting the rapidity and $\phi_{\mathrm{l}\gamma}$ the angle between l and γ in the plane perpendicular to the beams. If l and γ are recombined, we simply add their four-momenta and treat the resulting object as quasi-lepton. If more than one charged lepton is present in the final state, the possible recombination is performed with the lepton delivering the smaller value of $R_{\mathrm{l}\gamma}$. The corresponding EW corrections are labeled δ^{bare} and δ^{rec}, respectively.

After employing the recombination procedure we apply the following cuts on the charged leptons,

$$p_{\mathrm{T,l}} > 20 \text{ GeV}, \quad |y_{\mathrm{l}}| < 2.5, \tag{61}$$

where $p_{\mathrm{T,l}}$ is the transverse momentum of the lepton l. For channels with at least one neutrino in the final state we require a missing transverse momentum

$$p_{\mathrm{T,miss}} > 25 \text{ GeV}, \tag{62}$$

which is defined as the total transverse momentum of the neutrinos in the event. In addition, we apply the cuts

$$p_{\mathrm{T,H}} > 200 \text{ GeV}, \quad p_{\mathrm{T,W/Z}} > 190 \text{ GeV} \tag{63}$$

on the transverse momentum of the Higgs and the weak gauge bosons, respectively. The corresponding selection of events with boosted Higgs bosons is improving the signal-to-background ratio in the context of employing the measurement of the jet substructure in $\mathrm{H} \to \mathrm{b\bar{b}}$ decays leading to a single fat jet. The need for background suppression calls for (almost) identical cuts on the transverse momentum of the vector bosons and the Higgs boson. However, symmetric cuts induce large radiative corrections in fixed-order calculations in the corresponding p_{T} distributions near the cut. Since the Higgs boson and the vector boson are back-to-back at LO, any initial-state radiation will either decrease $p_{\mathrm{T,H}}$ or $p_{\mathrm{T,W/Z}}$ and the event may not pass the cut anymore. Hence, the differential cross section near the cut is sensitive to almost collinear and/or rather soft initial-state radiation. By choosing the above (slightly asymmetric) cuts this large sensitivity to higher-order corrections can be removed for the important $p_{\mathrm{T,H}}$-distribution. Of course, since the LO distribution for $p_{\mathrm{T,W/Z}}$ is vanishing for $p_{\mathrm{T,W/Z}} < 200$ GeV due to the $p_{\mathrm{T,H}}$ cut, the higher-order corrections to the $p_{\mathrm{T,W/Z}}$ distributions are still large in this region.

In the following plots, we show several relative corrections and the absolute cross-section predictions based on factorisation for QCD and EW corrections,

$$\sigma = \sigma^{\mathrm{QCD}} \times (1 + \delta_{\mathrm{EW}}^{\mathrm{rec}}) + \sigma_{\gamma}\,, \tag{64}$$

where σ^{QCD} is the best QCD prediction at hand, $\delta_{\mathrm{EW}}^{\mathrm{rec}}$ is the relative EW correction with recombination and σ_{γ} is the cross section due to photon-induced processes which are at the level of 1% and estimated employing the MRSTQED2004 PDF set for the photon. In detail, we discuss the distributions in $p_{\mathrm{T,H}}$, $p_{\mathrm{T,V}}$, $p_{\mathrm{T,l}}$, and y_{H}. More detailed results can be found in Ref. [263].

Figure 56 shows the distributions for the two WH production channels $\mathrm{Hl^{+}\nu}$ and $\mathrm{Hl^{-}\bar{\nu}}$ and for the ZH production channels $\mathrm{Hl^{+}l^{-}}$ and $\mathrm{H\nu\bar{\nu}}$. The respective EW corrections are depicted in Figure 57 for the two different treatments of radiated photons, but the difference between the two versions, which amounts to $1{-}3\%$, is small. The bulk of the EW corrections, which are typically in the range of $-(10{-}15)\%$, is thus of pure weak origin. In all p_{T} distributions the EW corrections show a tendency to grow more and more negative for larger p_{T}, signalling the onset of the typical logarithmic high-energy behaviour (weak Sudakov logarithms). The rapidity distributions receive rather flat EW corrections, which resemble the ones to the respective integrated cross sections. Note that the latter are significantly larger in size than the ones quoted in Ref. [7] for the total cross sections, mainly due to the influence of the p_{T} cuts on the Higgs and gauge bosons, which enforce the dominance of larger scales in the process. This can be clearly seen upon comparing the results with the ones shown in Figure 58, where only the basic cuts are applied, but not Eq. (63). For the basic cuts, the EW corrections are globally smaller in size by about 5%, but otherwise show the same qualitative features.

The relative EW corrections shown here could be taken into account in any QCD-based prediction for the respective distributions (based on the quoted cuts) via reweighting. For this purpose the data files of the histograms are available at the TWiki page of the WH/ZH working group[35]. The small photon-induced contributions, which are included in our best prediction and at the level of 1% for WH production and negligible for ZH production, are also available and could be simply added.

For definiteness, in Table 19, we show the integrated results corresponding to the cuts in the boosted setup.

Finally, we estimate the uncertainties resulting from the remaining spurious QCD scale dependences, missing higher-order contributions, and uncertainties in the PDFs:

– We estimate the scale uncertainties upon varying the renormalisation and factorisation scales independently by a factor of two around our default scale choice. At NNLO for WH production, the integrated cross section for the boosted Higgs analysis varies by $\Delta_{\mathrm{scale}} = 2\%$. In the considered distributions, the variation of the scales only affects the overall normalisation. Only in the $p_{\mathrm{T,W/Z}}$

[35] https://twiki.cern.ch/twiki/bin/view/LHCPhysics/WHZH

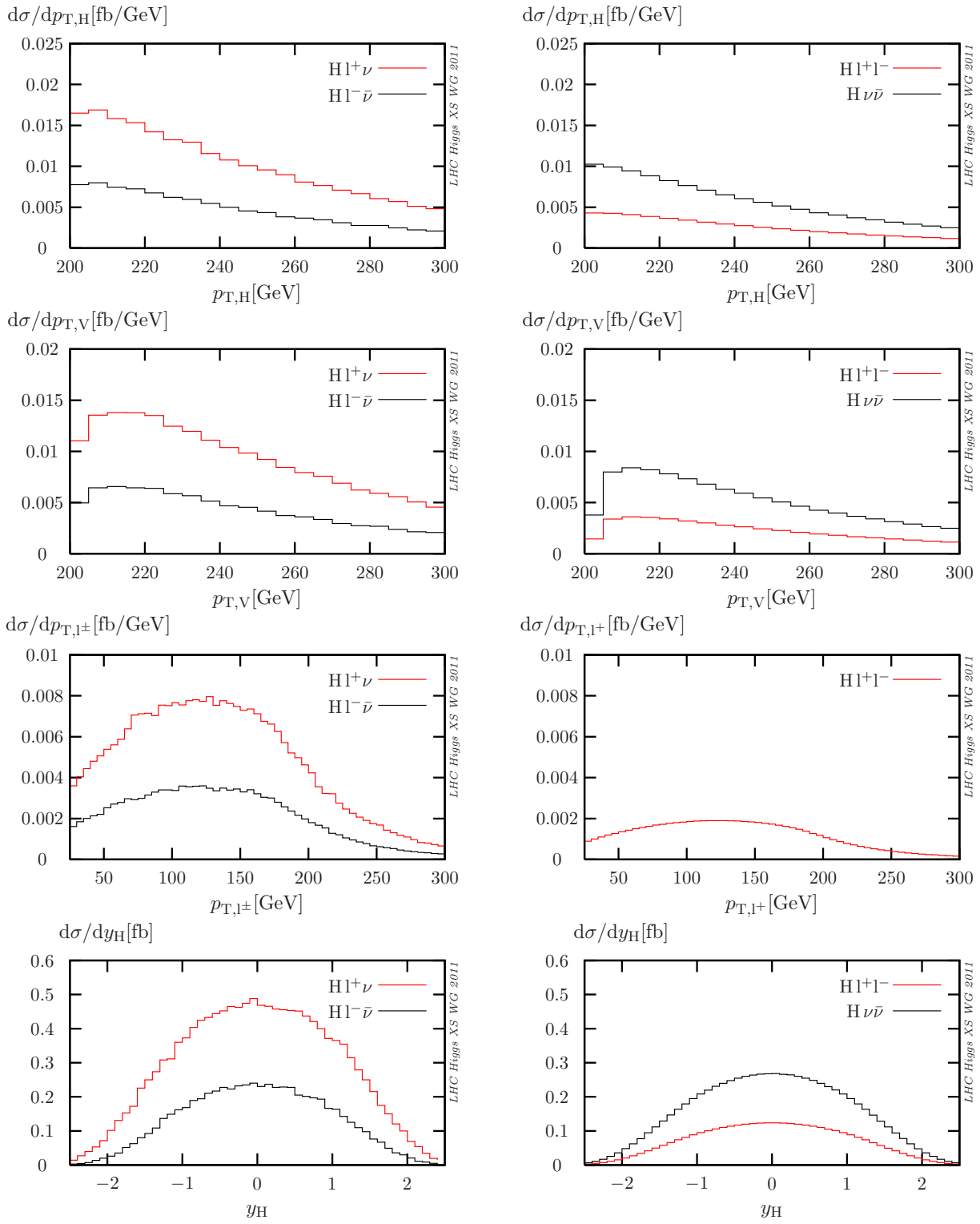

Fig. 56: Predictions for the $p_{\mathrm{T,H}}$, $p_{\mathrm{T,V}}$, $p_{\mathrm{T,l}}$, and y_{H} distributions (top to bottom) for Higgs strahlung off W bosons (left) and Z bosons (right) for boosted Higgs bosons at the 7 TeV LHC for $M_{\mathrm{H}} = 120$ GeV.

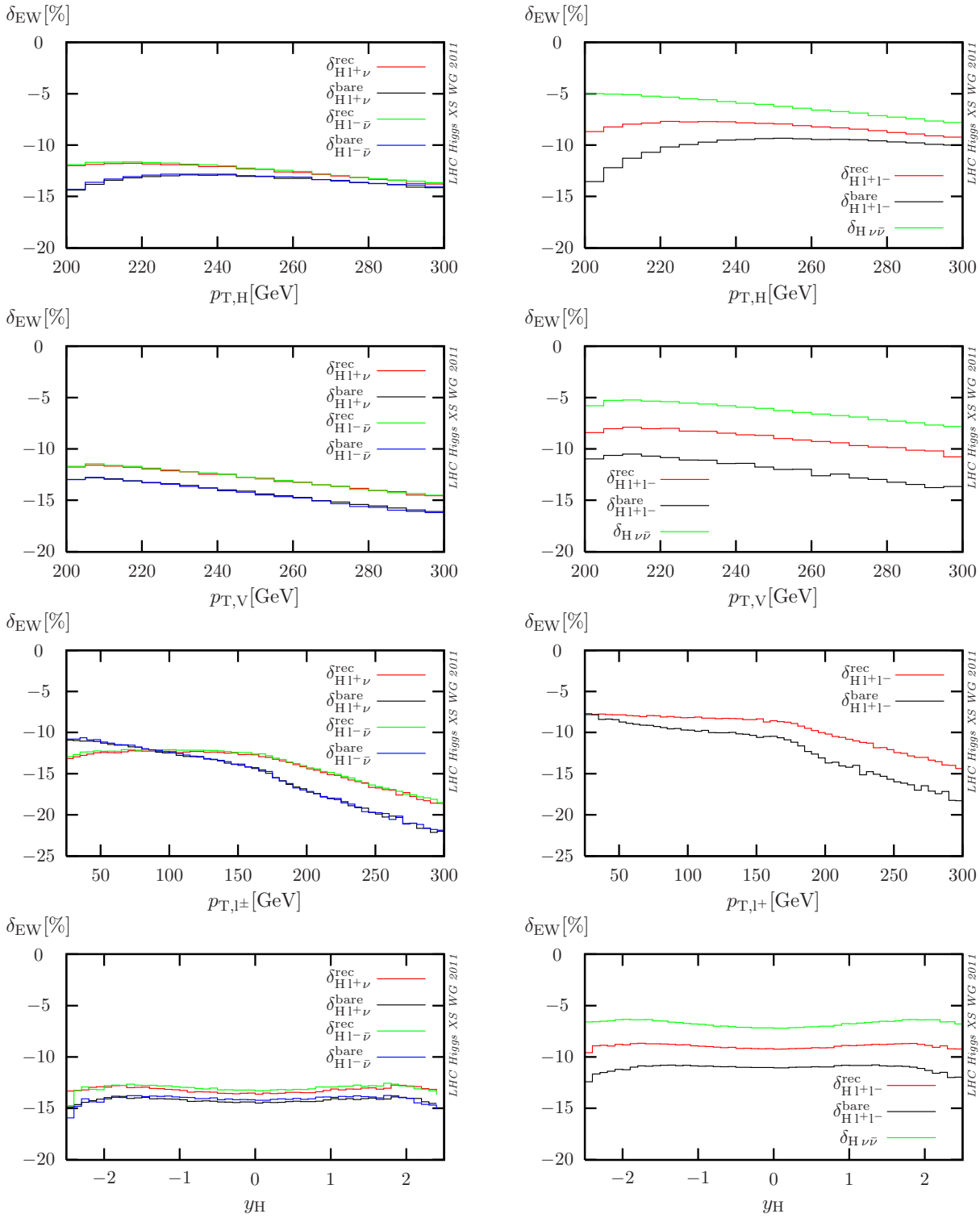

Fig. 57: Relative EW corrections for the $p_{\rm T,H}$, $p_{\rm T,V}$, $p_{\rm T,l}$, and $y_{\rm H}$ distributions (top to bottom) for Higgs strahlung off W bosons (left) and Z bosons (right) for boosted Higgs bosons at the 7 TeV LHC for $M_{\rm H} = 120$ GeV.

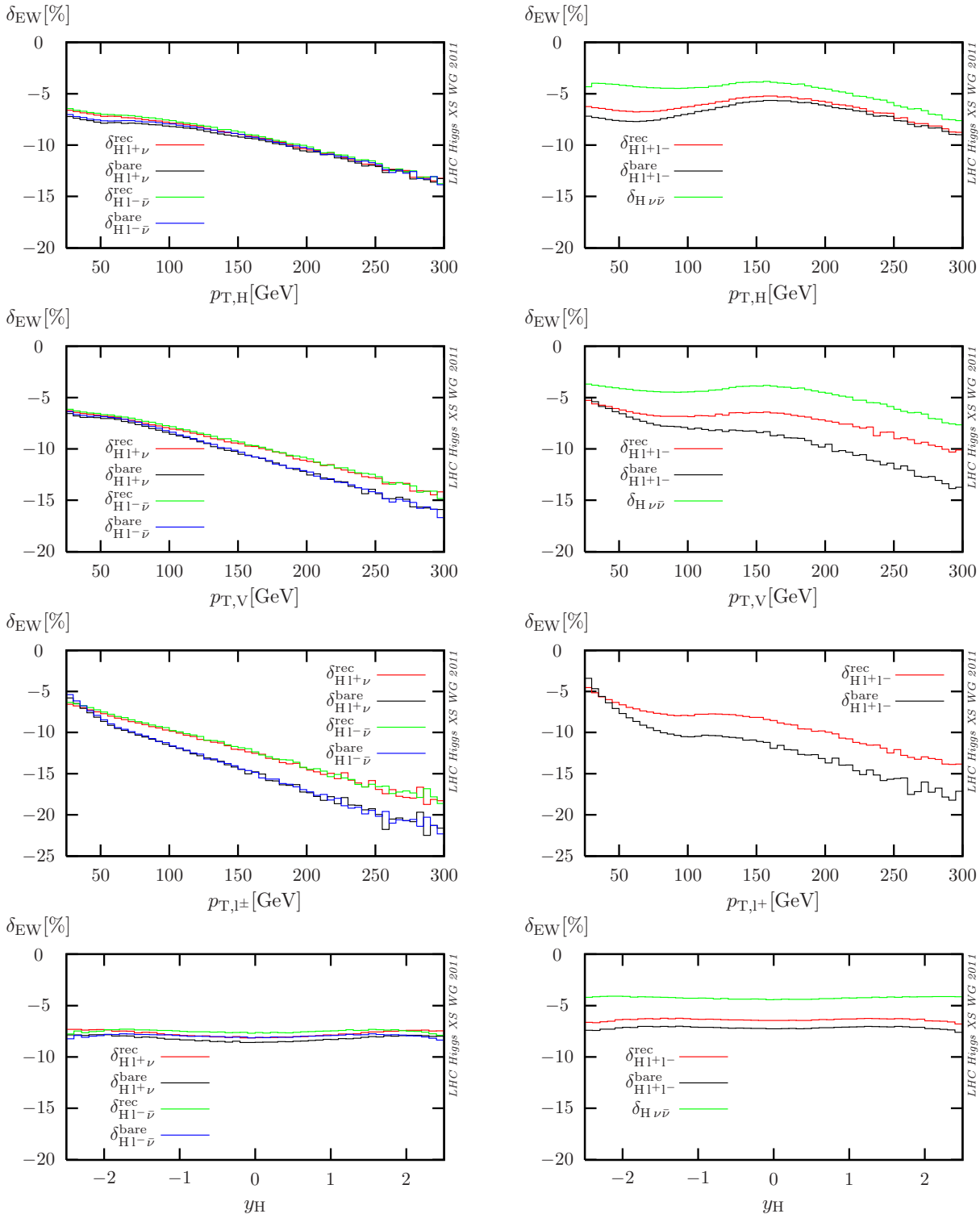

Fig. 58: Relative EW corrections for the $p_{\rm T,H}$, $p_{\rm T,V}$, $p_{\rm T,l}$, and $y_{\rm H}$ distributions (top to bottom) for Higgs strahlung off W bosons (left) and Z bosons (right) for the basic cuts at the 7 TeV LHC for $M_{\rm H} = 120$ GeV.

channel	$\mathrm{Hl^+\nu_l} + X$	$\mathrm{Hl^-\bar{\nu}_l} + X$	$\mathrm{Hl^+l^-} + X$	$\mathrm{H\nu_l\bar{\nu}_l} + X$
σ/ fb	$1.384(4)$	$0.617(2)$	$0.3467(1)$	$0.7482(1)$
$\delta_{\mathrm{EW}}^{\mathrm{bare}}/\%$	-14.3	-14.0	-11.0	-6.9
$\delta_{\mathrm{EW}}^{\mathrm{rec}}/\%$	-13.3	-13.1	-9.0	-6.9
σ_γ/ fb	0.020	0.010	0.0002	0.0000
$\Delta_{\mathrm{PDF}}/\%$	±5	±5	±5	±5
$\Delta_{\mathrm{scale}}/\%$	±2	±2	±2	±2
$\Delta_{\mathrm{HO}}/\%$	±1	±1	±7	±7

Table 19: Integrated cross sections, EW corrections, and estimates $\Delta_{\mathrm{PDF/scale}}$ for the PDF and scale uncertainties for the different Higgs-strahlung channels in the boosted setup for the LHC at 7 TeV for $M_{\mathrm{H}} = 120$ GeV.

distribution near 200 GeV, also the scale variation indicates that higher-order corrections are large, as discussed above. Here, scale variation leads to an error estimate of a few 10% at NLO. For ZH production at NLO, the scale variation even leads to an error estimate slightly below 2%.

– Both for WH and ZH production, starting at NNLO new types of higher-order QCD contributions arise that are not reflected by scale variations at (N)NLO. Specifically, this comprises the gluon-induced contribution to ZH production (not taken into account in our NLO prediction here), which is known to be sizable, and the top-loop-induced NNLO contributions to WH and ZH production, which have been computed recently at the inclusive level [272]. The corresponding uncertainty $\Delta_{\mathrm{HO}} = 7(1)\%$ for ZH (WH) production, which we estimate from the known size of those effects on the total cross sections, is also shown in Table 19. The relatively large uncertainty for ZH production will be reduced once the NNLO QCD corrections are known at the differential level as well.

– Concerning PDF uncertainties, as stated above, all central values for WH correspond to the central MSTW2008 prediction at NNLO. At 68% confidence level (C.L.), the MSTW error sets indicate a PDF error slightly below 2%. In distributions again only the overall normalisation is affected, and the distributions are not distorted (not shown in the plots). According to the PDF4LHC prescription, we rescale the NNLO uncertainty from MSTW by the additional spread observed at NLO (which is a factor of ~ 2.5) when including the CT10 (rescaled to 68% C.L.) and NNPDF 2.1 at 68% C.L. in the error estimate. While for $\mathrm{W^+H}$ production the error band is symmetric, the actual error for $\mathrm{W^-H}$ production covers the region from -8% to $+2\%$. For ZH production, we follow the NLO prescription and use the midpoint of the above PDF sets as the central value. The resulting PDF error also amounts to about $\pm5\%$. For the p_{T} distributions, individual PDF sets again only lead to differences in the overall normalisation. Only in the rapidity distribution of the Higgs boson, the shape of the distribution is distorted at the level of a few per cent.

8 ttH Process[36]

The process of Higgs radiation off top quarks $\mathrm{q\bar{q}/gg} \to \mathrm{Ht\bar{t}}$ becomes particularly relevant for Higgs searches at the LHC in the light-Higgs-mass region below ~ 130 GeV. Given the recent Higgs-boson exclusion limits provided by the Tevatron and LHC experiments, and given the indirect constraints provided by the electroweak precision fits [273], the light-Higgs-boson mass region will play a crucial role in confirming or excluding the Higgs mechanism of electroweak symmetry breaking as minimally implemented in the Standard Model. Indeed, it will be hard for the LHC running at $\sqrt{s} = 7$ TeV to exclude the light-Higgs-boson mass region with enough statistical significance and more in depth studies will be necessary in order to extract more information from the available data. In this context, a careful study of $\mathrm{t\bar{t}H}$ production will become important. Finally, if a light scalar is discovered, the measurement of the $\mathrm{t\bar{t}H}$ production rate can provide relevant information on the top–Higgs Yukawa coupling.

The full next-to-leading-order (NLO) QCD corrections to $\mathrm{t\bar{t}H}$ production have been calculated [274–277] resulting in a moderate increase of the total cross section at the LHC by at most $\sim 20\%$, depending on the value of M_{H} and on the PDF set used. More importantly, the QCD NLO corrections reduce the residual scale dependence of the inclusive cross section from $\mathcal{O}(50\%)$ to a level of $\mathcal{O}(10\%)$, when the renormalisation and factorisation scales are varied by a factor of 2 above and below a conventional central scale choice (the NLO studies in the literature use $\mu_0 = m_{\mathrm{t}} + M_{\mathrm{H}}/2$), and clearly show their importance in obtaining a more stable and reliable theoretical prediction.

Using the NLO codes developed by the authors of Refs. [274–277], in a previous report [7] we studied the inclusive $\mathrm{t\bar{t}H}$ production at both $\sqrt{s} = 7$ TeV and 14 TeV and we provided a breakdown of the estimated theoretical error from renormalisation- and factorisation-scale dependence, from α_{s}, and from the choice of parton distribution functions (PDFs). The total theoretical errors were also estimated combining the uncertainties from scale dependence, α_{s} dependence, and PDF dependence according to the recommendation of the LHC Higgs Cross Section Working Group [7]. For low Higgs-boson masses, the theoretical errors typically amount to $10-15\%$ of the corresponding cross sections.

In this second report we move towards exclusive studies and address the problem of evaluating the impact of QCD corrections and the corresponding residual theoretical uncertainty in the presence of kinematic constraints and selection cuts that realistically model the experimental measurement. We focus on three main studies: 1) a study of the theoretical uncertainty from scale dependence, α_{s}, and PDFs on some significant differential distributions for the on-shell parton-level process $\mathrm{pp} \to \mathrm{t\bar{t}H}$ calculated at NLO in QCD (see Section 8.1); 2) a study of the effects of interfacing the NLO parton-level calculations with parton-shower Monte Carlo programs, namely PYTHIA and HERWIG, including a comparison between the MC@NLO and POWHEG BOX frameworks, recently applied to the case of $\mathrm{t\bar{t}H}$ and $\mathrm{t\bar{t}A}$ production in Ref. [158] and Ref. [162], respectively (see Section 8.2); 3) a study of the background process $\mathrm{pp} \to \mathrm{t\bar{t}b\bar{b}}$ based on the NLO QCD results presented in Refs. [278–282], including a comparison between signal and background ($\mathrm{pp} \to \mathrm{t\bar{t}b\bar{b}}$) at the parton level, based on the study presented in Ref. [282] (see Section 8.3).

8.1 NLO distributions for $\mathrm{t\bar{t}H}$ associated production

In this section we study the theoretical error on NLO QCD distributions for $\mathrm{t\bar{t}H}$ on-shell production at a centre-of-mass (CM) energy of 7 TeV. Input parameters are chosen following the Higgs Cross Section Working Group recommendation [7].

We focus on the case of a Higgs boson with $M_{\mathrm{H}} = 120$ GeV and study the dependence of the differential cross sections listed above from the renormalisation and factorisation scale, from α_{s}, and from the PDFs. We vary the renormalisation and factorisation scales together by a factor of 2 around a central value $\mu_{\mathrm{R}} = \mu_{\mathrm{F}} = \mu_0 = m_{\mathrm{t}} + M_{\mathrm{H}}/2$. For the α_{s} and PDFs uncertainties, we present in this

[36] L. Reina, M. Spira (eds.); S. Dawson, R. Frederix, M. V. Garzelli, A. Kardos, C. G. Papadopoulos, Z. Trócsányi and D. Wackeroth.

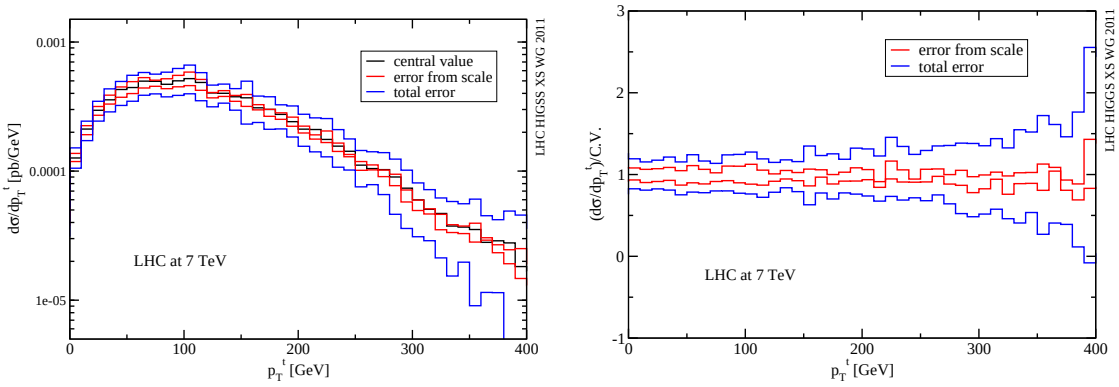

Fig. 59: Theoretical uncertainty on top(antitop)-quark transverse-momentum ($p_{\rm T}^{\rm t}$) distribution: the l.h.s. shows the actual distributions, the r.h.s. the spread around the central value in per cent. A detailed explanation of the red and blue bands is given in the text.

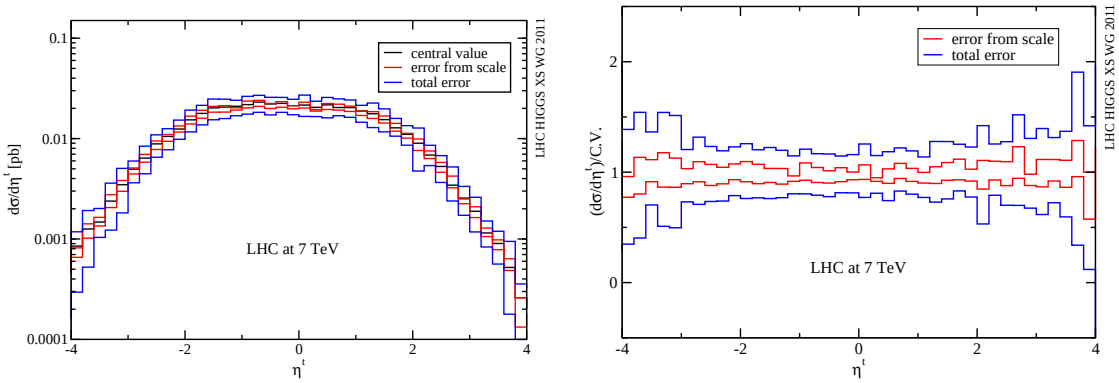

Fig. 60: Theoretical uncertainty on top(antitop)-quark pseudorapidity ($\eta^{\rm t}$) distribution: the l.h.s. shows the actual distributions, the r.h.s. the spread around the central value in per cent. A detailed explanation of the red and blue bands is given in the text.

report results obtained by varying $\alpha_{\rm s}$ and the choice of PDFs within the CTEQ6.6 [192] set, according to the CTEQ6.6 recommendation. A complete study including also the MSTW2008 [107, 114] and NNPDF2.1 [283] sets of PDFs will be updated on the $\rm t\bar{t}H$ TWiki page as soon as available. Since we consider a single set of PDFs (CTEQ6.6), we show more conservative 90% C.L. errors. Together with the inclusive results presented in Ref. [7], which included a comparison between CTEQ6.6, MSTW2008, and NNPDF2.0 [96], the current study should provide a good guidance to estimate the theoretical uncertainty on the differential distributions for the on-shell $\rm t\bar{t}H$ production.

In this section we consider distributions in transverse momentum ($p_{\rm T}$) and pseudorapidity (η) of the top/antitop quarks and of the Higgs boson, and in the $R(\rm t,\bar{t})$, $R(\rm t,H)$, $R(\bar{\rm t},\rm H)$ variables, where R is the distance in the (ϕ,η) plane.

In Figures 59-62 we present results for the differential cross sections in the $p_{\rm T}$ and η of both t ($\bar{\rm t}$ would be equivalent) and H, while in Figures 63 and 64 we present results for differential cross sections in $R(\rm t,\bar{t})$, $R(\rm t,H)$, and $R(\bar{\rm t},\rm H)$. In the figures, the left-hand-side (l.h.s) plot shows the actual distributions, while the right-hand-side (r.h.s) plot gives the spread around the central value in per cent. More specifically, in the l.h.s. part of each plot we show a central distribution obtained for $\mu_{\rm R}=\mu_{\rm F}=\mu_0$ (black histogram), a differential band that represents the variation of the distribution when $\mu_{\rm R}=\mu_{\rm F}$ is varied from $\mu_0/2$ to $2\mu_0$ (delimited by the upper and lower red histograms), and a differential band

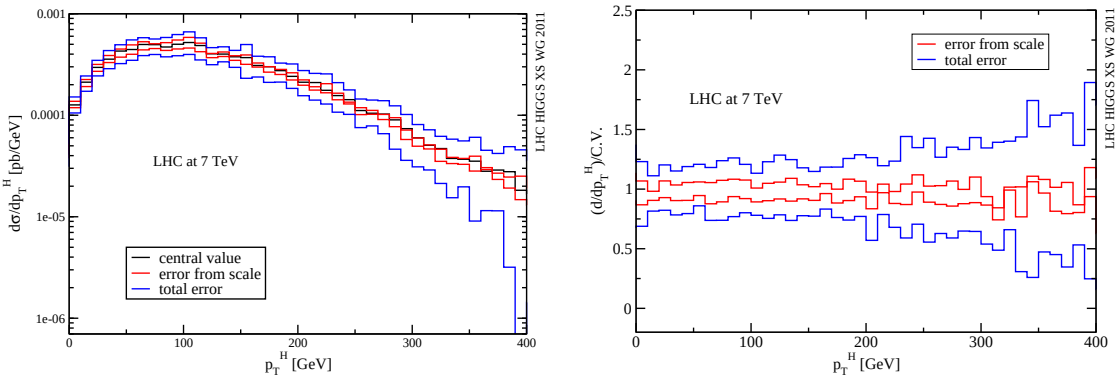

Fig. 61: Theoretical uncertainty on Higgs-boson transverse momentum ($p_{\mathrm{T}}^{\mathrm{H}}$) distribution: the l.h.s. shows the actual distributions, the r.h.s. the spread around the central value in per cent. A detailed explanation of the red and blue bands is given in the text.

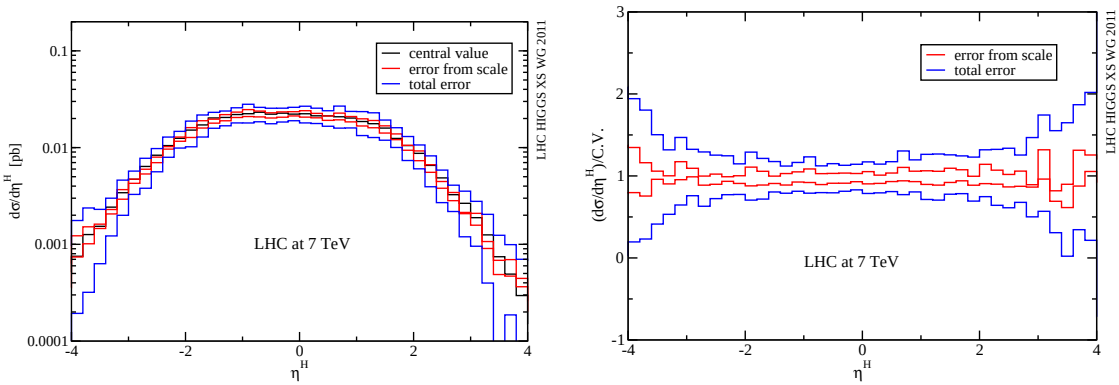

Fig. 62: Theoretical uncertainty on Higgs-boson pseudorapidity (η^{H}) distribution: the l.h.s. shows the actual distributions, the r.h.s. the spread around the central value in per cent. A detailed explanation of the red and blue bands is given in the text.

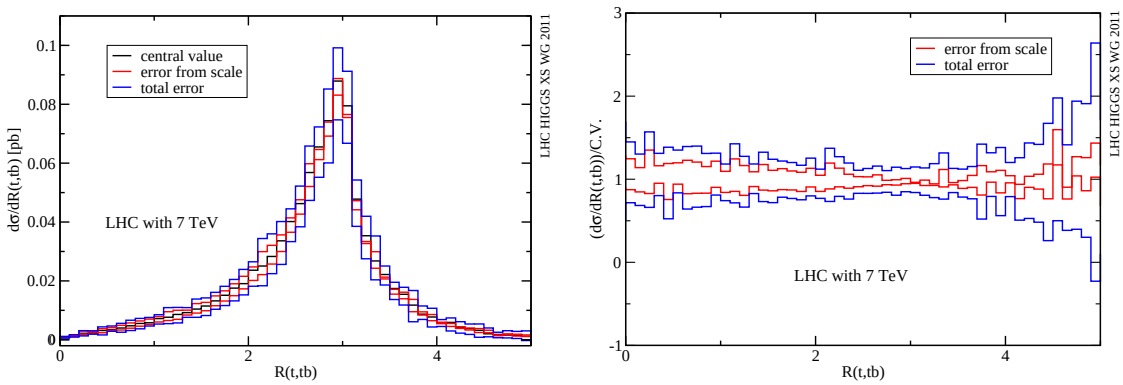

Fig. 63: Theoretical uncertainty on the top-antitop quark (η, ϕ) distance ($R(\mathrm{t}, \bar{\mathrm{t}})$) distribution: the l.h.s. shows the actual distributions, the r.h.s. the spread around the central value in per cent. A detailed explanation of the red and blue bands is given in the text.

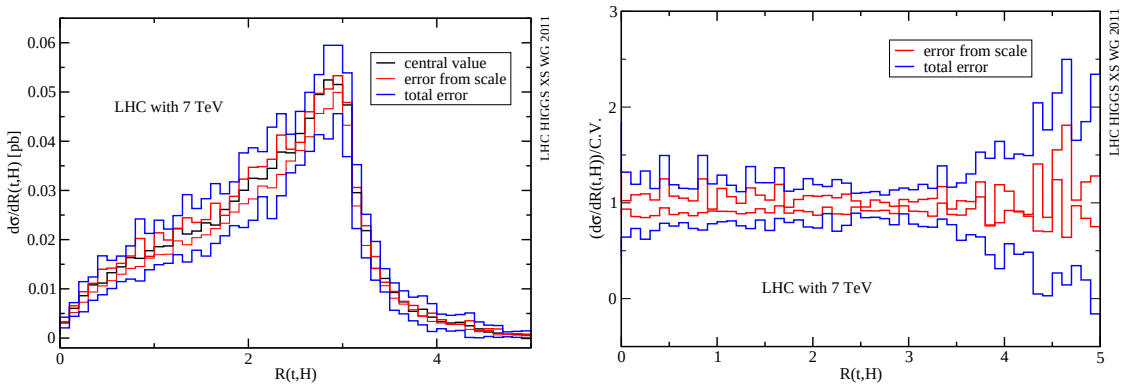

Fig. 64: Theoretical uncertainty on top-Higgs (η, ϕ) distance $(R(\mathrm{t}, \mathrm{H}))$ distribution in the no-cut configuration: the l.h.s. shows the actual distributions, the r.h.s. the spread around the central value in per cent. A detailed explanation of the red and blue bands is given in the text.

that represents the variation of the distribution when also the uncertainty from α_s and PDFs is added (delimited by the upper and lower blue histograms). Therefore the red band represents an estimate of the theoretical uncertainty from residual scale dependence, while the blue band represents an estimate of the total theoretical error, at NLO in QCD. The theoretical errors from α_s and PDF have been determined consistently within the CTEQ6.6 package and combined in quadratures, before adding the result linearly to the error from scale dependence, bin by bin. On the other hand, in the r.h.s. part of each plot we illustrate the error and to this purpose we just plot the ratio of the histograms that delimit the scale dependence and (α_s+PDF) uncertainty differential bands to the corresponding central value, i.e. the ratio of the red and blue histograms to the black one, bin by bin.

All distributions show interesting common features. We notice that towards the end points of each plot, statistical fluctuations obscure the main behaviour of the distributions and our estimates become unreliable. The problem can be easily addressed if needed by using higher statistics. All over the statistically significant range of each plot we see that different kinematic regions bear different errors, and are more or less sensitive to the residual theoretical uncertainties. In general, the residual scale dependence ranges between 10% and 20%, while the total error, including the α_s+PDF residual uncertainty (90% C.L.), ranges between 20% and 50%.

We point out that more-in-depth-studies would benefit from the inclusion of the $\mathrm{t\bar{t}H}$ final-state decays, which has recently become available via the interface with parton-shower Monte Carlo programs (PYTHIA and HERWIG), as discussed in Section 8.2, and we therefore recommend for future studies that a full study of the theoretical uncertainty be done in such context. Indeed, all the results presented in Section 8.2 already include a study of the PDF error obtained using the MSTW2008 set of PDFs.

8.2 Interface of NLO $\mathrm{t\bar{t}H}$ and $\mathrm{t\bar{t}A}$ calculations with parton-shower Monte Carlo programs

Recently, $\mathrm{t\bar{t}H}$ production at LHC has been studied by aMC@NLO [158] and POWHEL [162], two state-of-the-art independent frameworks, which allow to combine, through a proper NLO matching procedure, the computation of hard-scattering processes at NLO accuracy in QCD, to a parton-shower evolution (resumming at least the leading logarithmic soft and collinear divergences at all orders in perturbation theory) down to the hadronisation energy scale.

POWHEL is based on codes included in the HELAC-NLO package [153, 284], used for the computation of all matrix elements provided as input to the POWHEG BOX [156] program, which adopts the FKS subtraction scheme [176] to factor out the IR singularities in phase-space integrations and implements the POWHEG matching scheme [123, 126]. The aMC@NLO code, on the other hand, is

built upon the MadFKS [151] framework which also uses the FKS subtraction scheme. The MADLOOP code [152] is used to generate the virtual corrections. To match the results to the parton shower, the MC@NLO method has been employed [116].

So far, both codes have been used for phenomenological studies at the hadron level of several different processes interesting for Tevatron and LHC physics [158, 162, 166, 168–170, 285, 286]. This is the first time their results are compared in full detail, fixing a common scheme agreed upon by their developers for the study of $\mathrm{t\bar{t}H}$ production at LHC. The setup, the set of cuts adopted for the comparison, as well as the definition of the considered observables, is presented in the following.

We consider two Higgs scenarios:

1. Standard Model Higgs boson;
2. pseudo-scalar Higgs boson.

For both scenarios the Higgs-boson mass was set to $M_{\mathrm{H}} = 120$ GeV and standard Yukawa couplings were assumed. The top mass was assumed to be $m_{\mathrm{t}} = 172.5$ GeV. A dynamical scale, defined as $(M_{\mathrm{T,t}}\ M_{\mathrm{T,\bar{t}}}\ M_{\mathrm{T,H}})^{1/3}$, where $M_{\mathrm{T},i}$ is the transverse mass $\sqrt{M_i^2 + p_{\mathrm{T},i}^2}$, was used in the generation of the events at $\sqrt{s} = 7$ TeV. The factorisation and the renormalisation scales were set equal. The NLO MSTW2008 PDF set with 5 active flavours was used, together with the corresponding α_{s} and 68% C.L. uncertainty set. Particle decay, shower, hadronisation, and hadron decay effects have been simulated by means of the latest fortran version of the HERWIG code [287, 288], HERWIG 6.5.20. The Higgs boson was forced to decay in the $\mathrm{b\bar{b}}$ channel with a branching ratio equal to one, π^0 and $\mu^{\pm}$ were set stable to simplify the analyses, whereas all other particles and hadrons (including B-hadrons) were assumed to be stable or to decay according to the default implementation of the shower MC. Multiparticle interaction effects were neglected. Jets were reconstructed through the anti-k_{T} clustering algorithm [175], as implemented in FastJet 3.0.0, with a recombination radius parameter R fixed to 0.5.

The following four sets of cuts were adopted:

Set 0) No cut (inclusive analysis);

set 1) $p_{\mathrm{T,H}} > 200$ GeV, computed after showering and before H decay (boosted analysis);

Set 2) (i) $E^{\mathrm{j}}_{\mathrm{T,min}} = 25$ GeV and (ii) $|\eta^{\mathrm{j}}| < 2.5$ for all jets (otherwise the jet is discarded), (iii) $\#\mathrm{jets} > 4$ for each event (hadronic-cut analysis) ;

Set 3) besides including cuts in set 2), (iv) we focused on the di-leptonic channel, asking for at least one l^+ and one l^- with (v) $E^{\mathrm{l}^{\pm}}_{\mathrm{T,min}} = 20$ GeV and (vi) $|\eta^{\mathrm{l}^{\pm}}| < 2.5$, whereas the transverse missing energy of the event was constrained to be (vii) $\not{E}_{\mathrm{T,min}} > 30$ GeV. Charged leptons not satisfying both cut (v) and cut (vi) were discarded in all events (all-cut analysis).

We have studied a set of ~ 20 observables[37] for both different scenarios (SM and pseudo-scalar Higgs) and found similar results by POWHEL and aMC@NLO simulations. In the following, we restrict ourselves to a representative set of distributions. Results for scenario 1, i.e. the scalar Higgs boson, are presented in Figures 65–68, whereas results for scenario 2, i.e. the pseudo-scalar Higgs, are included in Figures 69 and 70. In the upper part of each plot, the predictions of both POWHEL and aMC@NLO interfaced to HERWIG are shown (by blue dashed and black solid lines, respectively). The lower part of each plot is furthermore divided into two regions. In the top region we exhibit the scale and PDF uncertainties computed by aMC@NLO using the procedure outlined in Ref. [168], while in the bottom region the ratio of the predictions obtained by POWHEL and aMC@NLO is presented (i.e. the ratio of the curves in the main plot), as well as the ratio of the results of POWHEL interfaced to PYTHIA and to HERWIG. The scale dependence is obtained by the independent variation of factorisation and

[37] We can share a complete and detailed list of results with other working groups who wish to perform the same analysis and make comparisons.

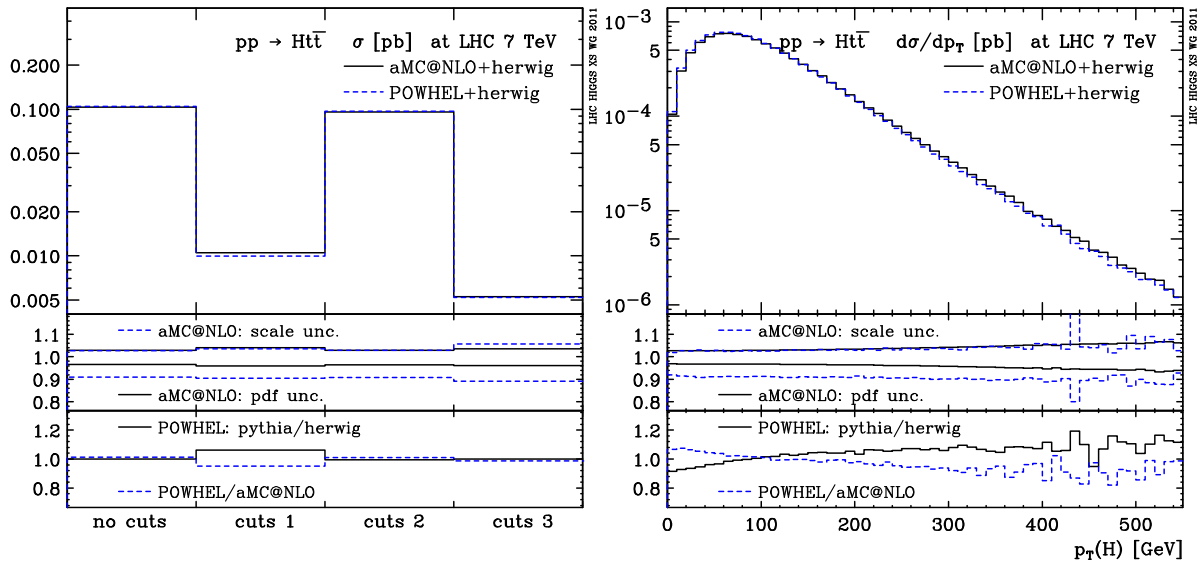

Fig. 65: Total rates for scalar-Higgs-boson production after the different cuts defined in the text (*left*) and transverse momentum of the Higgs boson (*right*) in the no-cut configuration. In the upper inset the scale and PDF uncertainties computed by aMC@NLO interfaced to HERWIG are shown. The lower inset displays the ratio of POWHEL over aMC@NLO and the ratio between the results computed by interfacing POWHEL to PYTHIA and HERWIG. See text for more details.

renormalisation scales around the default value μ_0 in the range $[\mu_0/2, 2\mu_0]$, with the restriction that $1/2 < \mu_R/\mu_F < 2$; the PDF uncertainty is obtained by running the 40 MSTW 68% C.L. sets and combining them using the Hessian method. As for PYTHIA, the last Fortran version available in the web, PYTHIA 6.4.25, has been adopted, in the Perugia 2011 tune configuration [289], one of the most updated leading-order tunes that takes into account recent LHC experimental data, providing a p_T-ordered shower (in the absence of a tune specifically designed for NLO matched computations). Furthermore, t, H, and gauge-boson masses, and total decay widths in PYTHIA have been constrained to the same values as in HERWIG, and the H forced to decay into $\mathrm{b\bar{b}}$ in all events.

Let us describe the features of the figures in more detail. In the left panel of Figure 65, the predictions for the total rates after the various cuts described above are given. For both the POWHEG as well as the MC@NLO method the total rates before applying cuts are given by the fixed-order NLO results and are in agreement. The rates after the cuts defined by sets 2) and 3) turned out to be, as well, very similar in the two approaches. On the other hand, there is a 5% difference between the total rate obtained by POWHEL interfaced to HERWIG and the other predictions (POWHEL interfaced to PYTHIA and aMC@NLO interfaced to HERWIG) just in case of the boosted-Higgs scenario, identified by the set 1) of cuts, where only events with a Higgs boson with a transverse momentum of at least 200 GeV are kept in the analysis. The origin of this difference can be understood from the plot on the right-hand side of Figure 65: the transverse momentum of the Higgs boson as computed by POWHEL + HERWIG turns out to be slightly softer in comparison to the other two predictions. The uncertainty coming from scale variations is of the order of $+5\%, -10\%$, and becomes slightly larger when the cuts of set 3) (all-cut analysis) are applied. The uncertainties from the PDFs are smaller, $\pm 5\%$.

In the plot on the left-hand side of Figure 66 the total transverse momentum of the $\mathrm{t\bar{t}H}$ system is shown. This observable is expected to be very sensitive to the matching procedure used and, in the low-p_T region, very sensitive to the parton shower. It turns out that the predictions obtained by aMC@NLO and POWHEL are in agreement within expectations, differences being below 10%, except in the very soft region, where the differences indeed increase. Like before, both the aMC@NLO + HERWIG and the POWHEL + PYTHIA predictions are marginally harder than the POWHEL + HERWIG ones. The

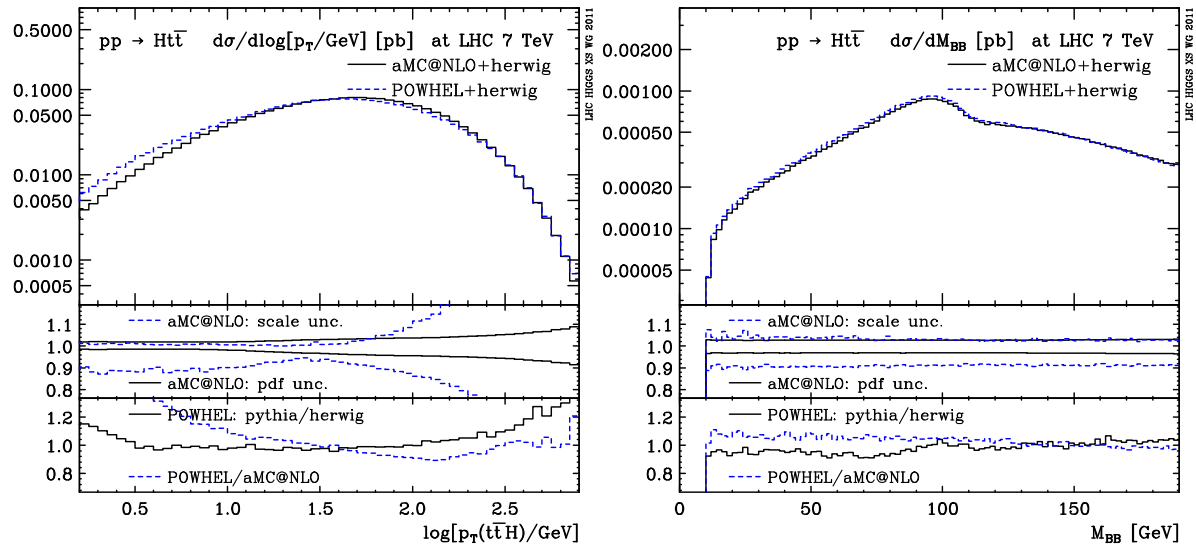

Fig. 66: Transverse momentum of the Higgs–top–antitop system (*left*) and invariant mass of the two hardest lowest-lying B hadrons (*right*). The different regions of the plots are defined as in Figure 65. See text for more details.

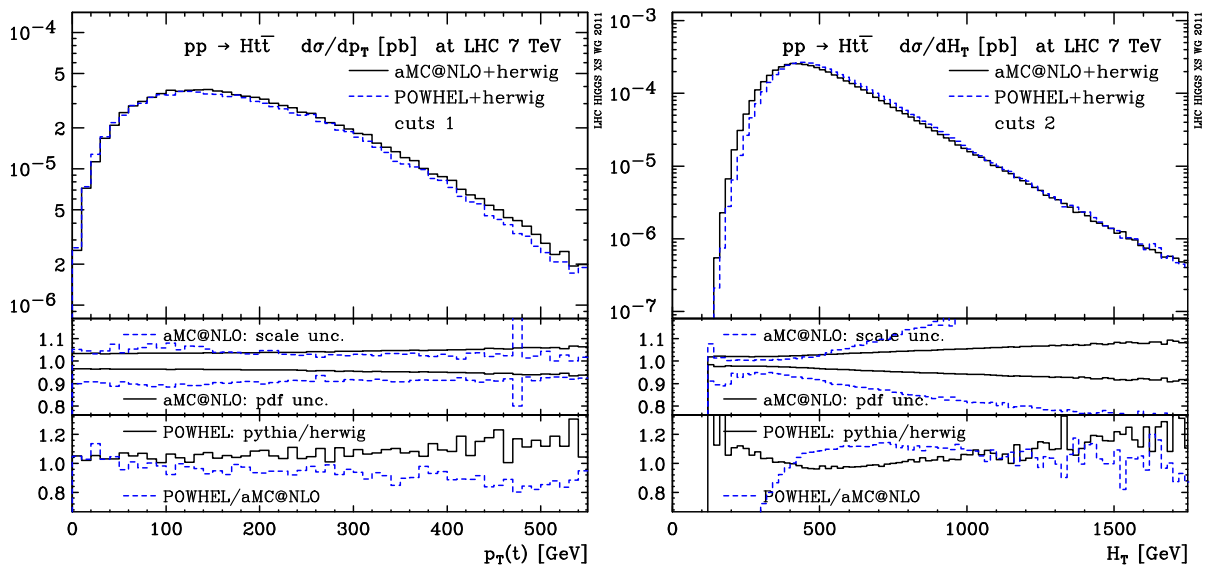

Fig. 67: Transverse momentum of the top quark in the boosted-Higgs scenario (*left*) and scalar sum of transverse energies (*right*) under the cuts of set 2). The different regions of the plots are defined as in Fig. 65. See text for more details.

uncertainties coming from scale variations are small in the low-$p_{\rm T}$ region, where this observable has NLO accuracy, while in the large-$p_{\rm T}$ region, i.e. $p_{\rm T} > 100$ GeV, the uncertainty grows and shows the usual large dependence typical of a LO observable. Note that, even though in the low-$p_{\rm T}$ region this observable is accurate up to NLO, the results are very sensitive to large logarithms that are resummed by the parton shower. Therefore, the scale dependence can not be considered at all an accurate estimate of the total uncertainties. In the plot on the right-hand side of Figure 66, the invariant mass of the two hardest lowest-lying B hadrons is shown. Like before, POWHEL + HERWIG results are slightly softer than the other two predictions, however differences amount to less than 10% in the whole range spanned by this observable and are within the uncertainties coming from scale dependence and the PDF error sets.

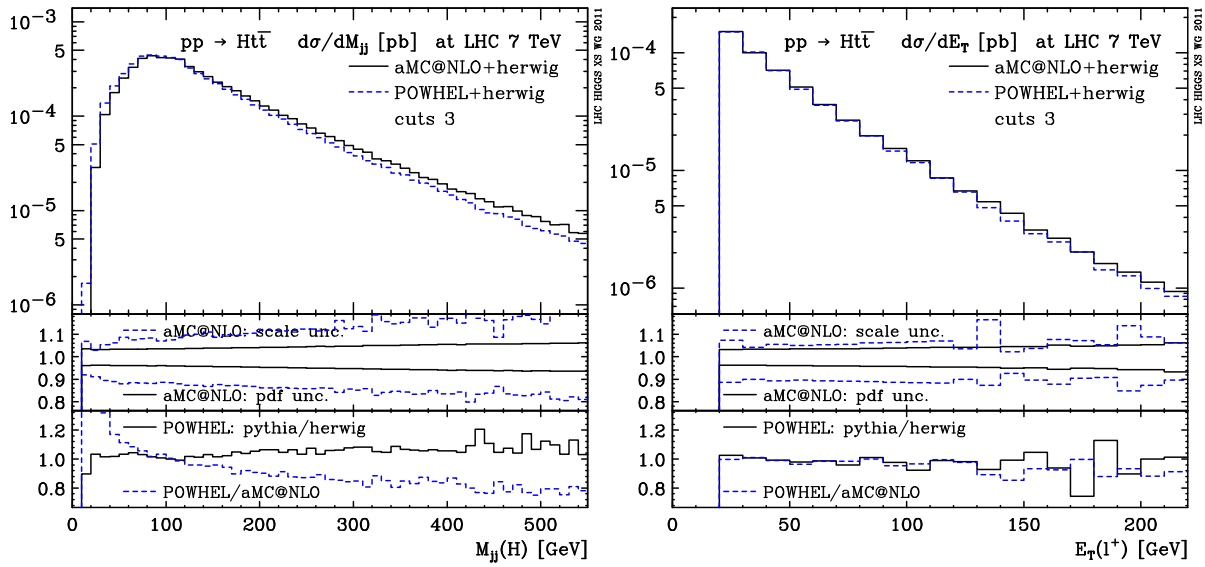

Fig. 68: Invariant mass of all jet pairs passing the cuts of set 3) (*left*) and transverse energy of the hardest positively-charged lepton (*right*). The different regions of the plots are defined as in Fig. 65. See text for more details.

As was already noted above and can be observed from the plot on the left-hand side of Figure 65, the POWHEL + HERWIG predictions are 5% smaller than the aMC@NLO + HERWIG and POWHEL + PYTHIA ones. This is again related to the fact that the POWHEL + HERWIG results are slightly softer than the other two. When looking into the boosted-Higgs scenario (set 1) of cuts) (see above), the same features are visible in the plot of the transverse momentum of the top quark, shown on the left-hand side of Figure 67. In the plot on the right-hand side of Figure 67, on the other hand, the $H_{\rm T}$ distribution is displayed for events passing the set of cuts 2), i.e. at least 4 central jets with a minimum transverse energy of 25 GeV. This observable was defined as the scalar sum of transverse energies $H_{\rm T}$=$\sum_j E_{{\rm T},j}$ + $\sum_l E_{{\rm T},l}$ + $\not{E}_{\rm T}$, where j runs over all jets passing the cuts, l runs over all charged leptons and $\not{E}_{\rm T}$ is the missing transverse energy. For this observable the differences between aMC@NLO and POWHEL turned out to be larger, aMC@NLO being slightly softer this time.

One of the complications of extracting a Higgs signal using the $\rm t\bar{t}H$ channel is the combinatorial background: there are many jets in the signal process and assigning the correct ones to the Higgs decay is a non-trivial task. For example, if one naively takes all events with two oppositely charged leptons and at least 4 jets, i.e. the set 3) of cuts (see above), and plots the invariant mass of all jet pairs satisfying the cuts, there is hardly any peak visible at the Higgs mass, $M_{\rm H} = 120$ GeV, as can be seen in the plot on the left-hand side of Figure 68. This is one of the challenges of finding a $\rm t\bar{t}H$ signal.

As a final comparison between aMC@NLO and POWHEL for the scalar Higgs (scenario 1), we show on the right-hand side of Figure 68 the transverse energy of the hardest positively-charged lepton after the cuts of set 3). Results are in good agreement and no differences are visible within statistical fluctuations.

The total rates for the pseudo-scalar Higgs boson, scenario 2, are presented in the plot on the left-hand side of Figure 69. Rates without cuts and set 2) and 3) of cuts, are about a third of the corresponding ones relative to scalar Higgs-boson production, see Figure 65. For the boosted-Higgs scenario the difference is much smaller, with rates for pseudo-scalar Higgs production only about 25% smaller than the rates for the scalar Higgs. The origin of this effect is that a pseudo-scalar Higgs boson is in general more boosted, as can clearly be seen by comparing the plot on the right-hand side of Figure 69 with the one on the right-hand side of Figure 65. Therefore, a boosted-Higgs search following the guidelines of Ref. [290], will work equally well for a pseudo-scalar boson [158]. The scale and PDF uncertainties are

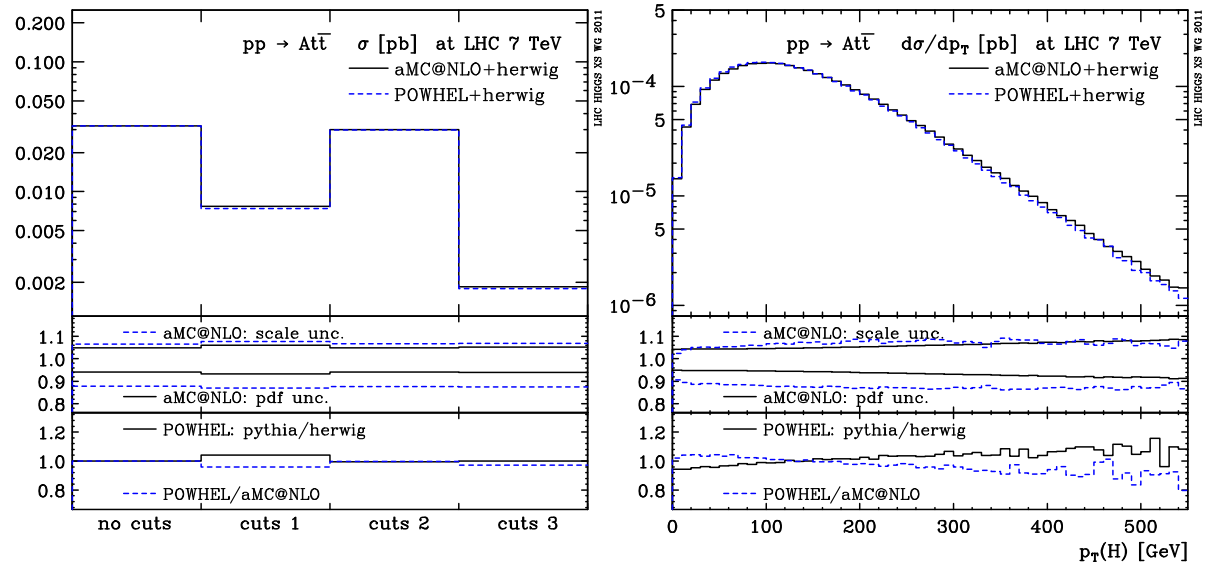

Fig. 69: Total rates for pseudo-scalar Higgs boson production after the different cuts defined in the text (*left*) and transverse momentum of the pseudo-scalar Higgs boson (*right*) in the no-cut configuration. The different regions of the plots are defined as in Fig. 65. See text for more details.

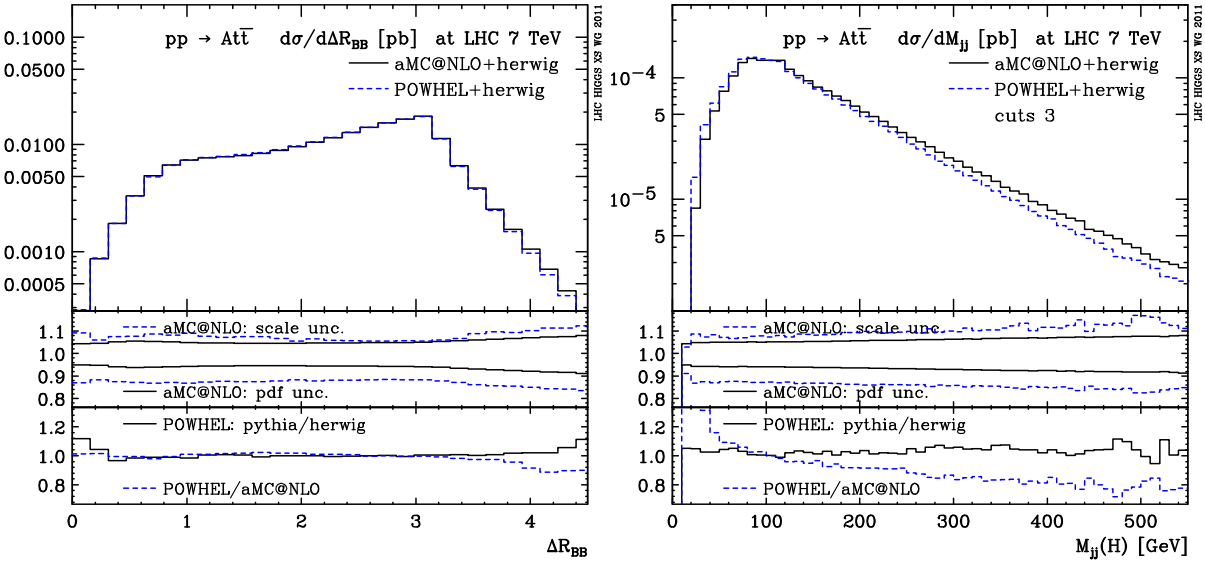

Fig. 70: Separation in pseudo-rapidity and azimuthal angle of the two hardest lowest-lying B hadrons in the events (no-cut analysis) (*left*) and invariant mass of all jet pairs passing the set 3) of cuts (*right*). The different regions of the plots are defined as in Fig. 65. See text for more details.

slightly larger in the case of the pseudo-scalar, being $+7\%, -13\%$ and $\pm 6\%$ respectively. The differences among the three predictions obtained by aMC@NLO and POWHEL interfaced to HERWIG and POWHEL interfaced to PYTHIA are smaller compared to scalar Higgs-boson predictions, even though, in general, POWHEL + HERWIG results are still slightly softer than the ones obtained by the other two frameworks.

Finally, in the plot on the left-hand side of Figure 70 the separation for the two hardest lowest-lying B hadrons in pseudo-rapidity and azimuthal angle, $\Delta R_{B_1 B_2} = \sqrt{(\Delta\eta_{B_1 B_2})^2 + (\Delta\phi_{B_1 B_2})^2}$ is presented. Results for aMC@NLO and POWHEL are in excellent agreement, well below 3% over almost the entire range. For large separations the difference increase towards 10% or so. As expected, for large separation

also the scale dependence increases. In the plot on the right-hand side of Figure 70 the invariant mass of all jet pairs defined for events passing the cuts of set 3) (see above) is shown. Like for the scalar case, there is hardly any Higgs signal visible over the continuous background coming from jet pairs that do not correspond to the Higgs-boson decay (and are instead produced as a consequence of top and antitop decays). We point out that all three predictions are the same for the peak around the Higgs mass on Figures 66 (left) and 68 (right), making the predictions particularly robust in this most important region.

We conclude that we are confident that the predictions for $\mathrm{t\bar{t}H}$ and $\mathrm{t\bar{t}A}$ production are under good theoretical control. The differences between aMC@NLO and POWHEL interfaced to HERWIG and POWHEL interfaced to PYTHIA are, in general, below 10% in those regions not completely dominated by parton-shower effects. In general, POWHEL + HERWIG gives slightly softer predictions than the other two frameworks. Reaching this level of agreement between the results obtained by different frameworks has required several interactions among us, since many different details in the independent setup of the codes and in the precise definition of the observables can produce sizable differences.[38]

8.3 The $\mathrm{pp} \to \mathrm{t\bar{t}b\bar{b}}$ background

In the low-Higgs-boson-mass region, where a SM Higgs boson mainly decays to $\mathrm{b\bar{b}}$, QCD $\mathrm{t\bar{t}b\bar{b}}$ and $\mathrm{t\bar{t}}jj$ production represent the most important backgrounds. The selection strategies proposed so far by ATLAS and CMS are based on the full reconstruction of the $\mathrm{t\bar{t}b\bar{b}}$ signature, starting from a final state with four b jets and additional light jets. Upon reconstruction of the top quarks, two b quarks are identified as originating from the top-quark decays, while the remaining two b quarks represent a Higgs candidate, to be identified via the invariant-mass reconstruction of the $\mathrm{b\bar{b}}$ pair. Simulations indicate that the presence of other b and light jets in the final state greatly affects the correct identification of the $\mathrm{b\bar{b}}$ pair from the Higgs decay therefore diluting the signal to background ratio. More recently, the idea of searching for a highly-boosted Higgs boson (producing a *fat* jet containing the $\mathrm{b\bar{b}}$ decay products) has been proposed to enhance the signal to background ratio.

Whether $\mathrm{t\bar{t}H}$ will provide a discovery channel very much depends on how well we can study the characteristics of the $\mathrm{t\bar{t}b\bar{b}}$ and $\mathrm{t\bar{t}}jj$ backgrounds and find ways to efficiently discriminate them from the signal. Requiring three b tags would strongly suppress the $\mathrm{t\bar{t}}jj$ contamination, and would leave $\mathrm{t\bar{t}b\bar{b}}$ as the dominant background.

The NLO QCD corrections to the $\mathrm{t\bar{t}b\bar{b}}$ production background have been calculated [278–282] and discussed for the LHC at the CM energy of 14 TeV. The corrections enhance and stabilise the cross section. Traditionally the simulations of $\mathrm{t\bar{t}b\bar{b}}$ were based on a LO cross section and used $\mu_{\mathrm{R}} = \mu_{\mathrm{F}} = m_{\mathrm{t}} + m_{\mathrm{b\bar{b}}}/2$ as the central renormalisation and factorisation scales. NLO studies have shown that this scale choice does not provide an adequate description of the QCD dynamics of $\mathrm{t\bar{t}b\bar{b}}$, since this process is a multiscale process that involves scales much below $m_{\mathrm{t}} + m_{\mathrm{b\bar{b}}}/2$. The theoretical stability of the cross section is greatly improved by choosing a dynamical scale like $\mu_{\mathrm{R}}^2 = \mu_{\mathrm{F}}^2 = m_{\mathrm{t}}\sqrt{p_{\mathrm{Tb}}p_{\mathrm{T\bar{b}}}}$. In this case, the NLO corrections increase the background cross section within the signal region by about $20-30\%$ [278–280]. Most importantly, the scale dependence is significantly reduced to a level significantly below 30%. Examples of p_{T} distributions for the hardest and softest b jets are given in Figure 71, where the unboosted ($m_{\mathrm{b\bar{b}}} > 100$ GeV) and boosted ($p_{\mathrm{T,b\bar{b}}} > 200$ GeV) regimes are compared.

In addition a comparison between the signal process $\mathrm{pp} \to \mathrm{t\bar{t}H} \to \mathrm{t\bar{t}b\bar{b}}$ and the $\mathrm{t\bar{t}b\bar{b}}$ background has been obtained in the narrow-width approximation [282]. In Figure 72, a few histograms, namely the invariant mass, the transverse momentum, the rapidity of the two-b-jet system, as well as the transverse momentum of the single b-jet are shown. In all figures the red solid line refers to the NLO QCD background, the blue dotted line to the LO QCD background, while the green dash-dotted and cyan dashed

[38] The codes and/or the event files ready to-be-showered are available in the POWHEL and aMC@NLO websites, `http://grid.kfki.hu/twiki/bin/view/DbTheory/TthProd` and `http://amcatnlo.cern.ch`, respectively.

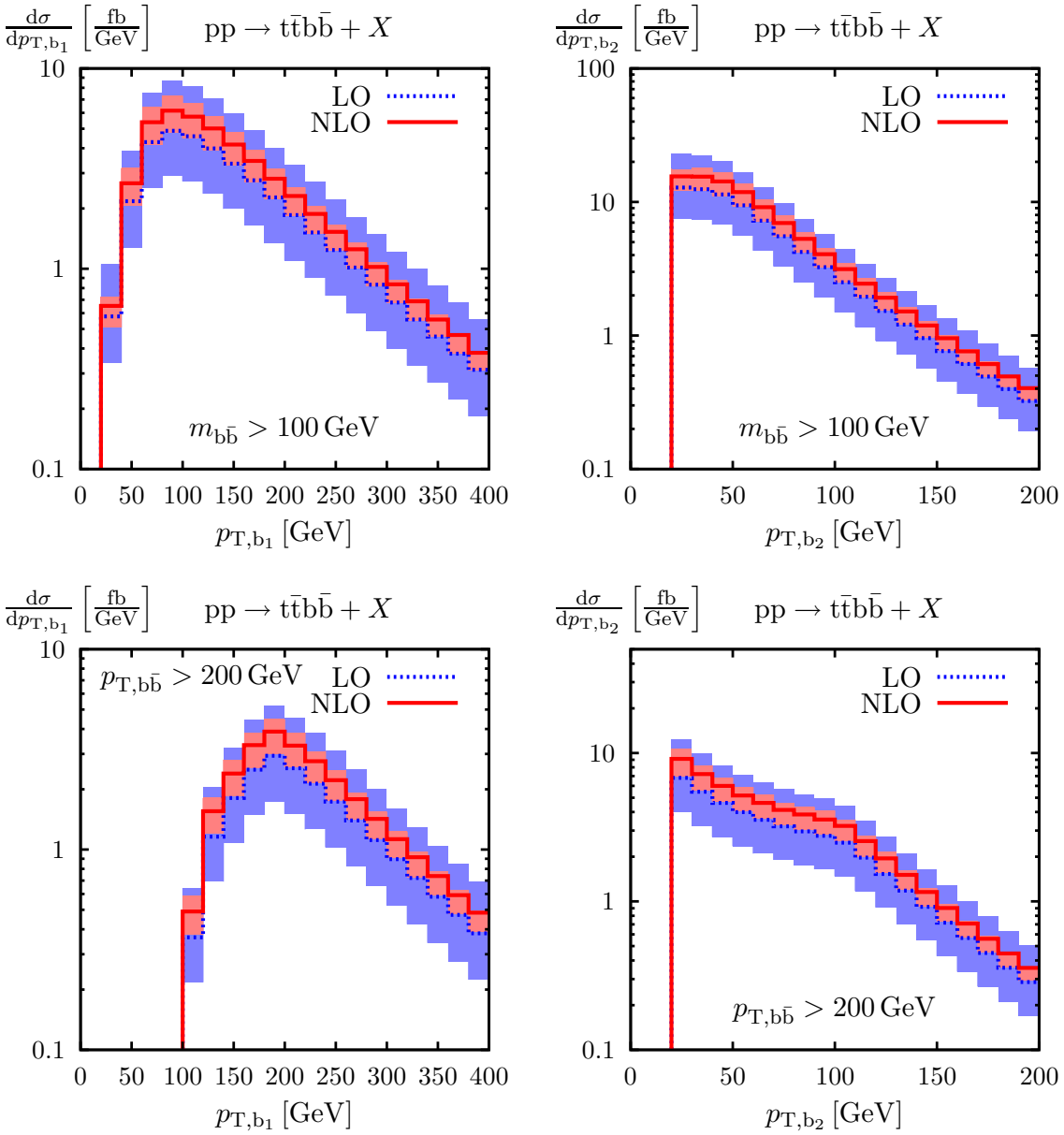

Fig. 71: Transverse momentum of the harder (p_{T,b_1}) and softer (p_{T,b_2}) b jets at 14 TeV CM energy: absolute LO and NLO prediction for the unboosted ($m_{b\bar{b}} > 100$ GeV, upper plots) and boosted regimes ($p_{T,b\bar{b}} > 200$ GeV, lower plots). The uncertainty bands correspond to a factor two scale variation. From Ref. [280].

line to the NLO and LO signal, respectively. Apart from the invariant mass of the $b\bar{b}$ system and the p_T spectrum of the b quark, the shapes look very similar for signal and background.

This makes it possible to study the signal and background processes including the final-state Higgs decay into $b\bar{b}$ with cuts at the same time at NLO. However, it should be noted that the final-state top decays have not been included at NLO so that a full NLO signal and background analysis including all experimental cuts is not possible so far. The top-quark decays are expected to affect the final-state distributions more than the Higgs decays into $b\bar{b}$ pairs. The next natural step will then be to interface the NLO calculation of $t\bar{t}b\bar{b}$ production with PYTHIA and HERWIG. This will provide the ultimate tool to study both signal and background in the presence of both decays of the Higgs boson and of the top/antitop pair.

Finally, we note that the NLO QCD corrections to $pp \to t\bar{t}jj$ have been calculated as well [291,

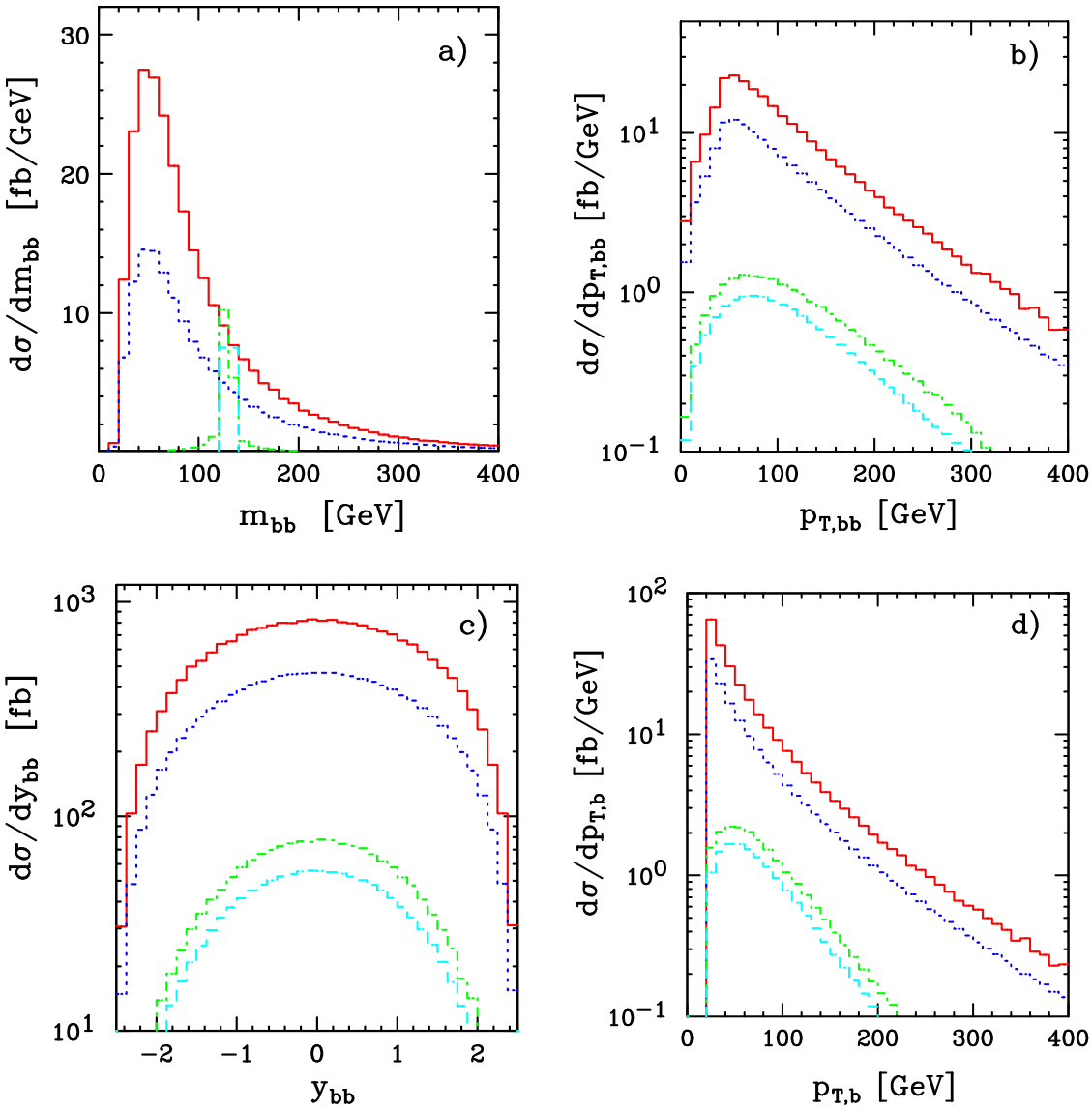

Fig. 72: Distribution of the invariant mass $m_{\mathrm{b\bar{b}}}$ of the bottom-anti-bottom pair (a), distribution in the transverse momentum $p_{\mathrm{T_{b\bar{b}}}}$ of the bottom-anti-bottom pair (b), distribution in the rapidity $y_{\mathrm{b\bar{b}}}$ of the bottom–anti-bottom pair (c), and distribution in the transverse momentum $p_{\mathrm{T,b}}$ of the bottom quark (d) for $\mathrm{pp} \to \mathrm{t\bar{t}H} \to \mathrm{t\bar{t}b\bar{b}} + X$ and $\mathrm{pp} \to \mathrm{t\bar{t}b\bar{b}} + X$ at the LHC for the CM energy of 14 TeV. The red solid line refers to the NLO QCD background, the blue dotted line to the LO QCD background, while the green dash-dotted and cyan dashed line to the NLO and LO signal, respectively. From Ref. [282].

292], however, in the boosted-Higgs analysis the major background to the $\mathrm{t\bar{t}H}$ signal is due to $\mathrm{t\bar{t}b\bar{b}}$ production [290].

9 $\gamma\gamma$ decay mode[39]

9.1 Introduction

Despite its relatively low branching fraction and considerable reducible and irreducible backgrounds from SM QCD processes, the $\gamma\gamma$ decay mode benefits from a clean signature, provided that a sufficiently high-resolution electromagnetic calorimeter is used. The mode $\mathrm{H} \to \gamma\gamma$ is generally considered to be the principal discovery channel at the LHC for a Higgs boson having a mass between 100 GeV and 150 GeV. Furthermore, given the recent combined results from the ATLAS and CMS collaborations from analyses corresponding to up to 2.3 fb^{-1} of integrated luminosity excluding with 95% confidence a Standard Model Higgs boson in the range 141 GeV $< M_{\mathrm{H}} < 476$ GeV, the $\gamma\gamma$ decay mode is the channel whose sensitive range remains at this writing the least constrained. The corresponding individual ATLAS [293, 294] and CMS [295] results have also been made public.

9.2 Sets of acceptance criteria used

Three sets of acceptance criteria, shown in Table 20, have been used for the studies presented in this section. Two of them ('ATLAS', 'CMS') are based on acceptance criteria of the ATLAS and CMS $\mathrm{H} \to \gamma\gamma$ searches; the third ('Loose') corresponds roughly to typical acceptance criteria used in the measurement of Standard Model prompt photon processes which constitute backgrounds to these searches.

Table 20: The three sets of acceptance criteria used for studies in this section.

	'CMS'	'ATLAS'	'Loose'
$E_{\mathrm{T}\gamma 1}$[GeV]	> 40	> 40	> 20 or 23
$E_{\mathrm{T}\gamma 2}$[GeV]	> 30	> 25	> 20
$\lvert\eta_\gamma\rvert$	< 2.5	< 2.37	< 2.5
Excluded $\lvert\eta_\gamma\rvert$	$[1.4442, 1.566]$	$[1.37, 1.52]$	
$M_{\gamma\gamma}$[GeV]	$[100, 160]$	$[100, 160]$	> 80

For the studies concerning background processes in the Standard Model, parton-level isolation requirements have been imposed, requiring a maximum transverse hadronic energy of 5 GeV within a solid cone of radius $\Delta R = \sqrt{\Delta\eta^2 + \Delta\phi^2} = 0.4$ or 0.3 as noted.

9.3 Signal modelling and differential K-factors

9.3.1 Reweighting of the p_{T} spectrum for the gluon-fusion production process

The effect of reweighting the Higgs-boson p_{T} spectrum given by the NLO program POWHEG (with parton-shower simulation, hadronisation, and underlying event from PYTHIA 6.4) to that given by the inclusive NNLL program HQT [194] has been evaluated for the $\gamma\gamma$ final state. Figure 73 shows the distribution of relative HQT/POWHEG event weights as a function of Higgs-boson p_{T} for $M_{\mathrm{H}} = 120$ GeV; the distribution is fit with a 4th-degree polynomial function for $p_{\mathrm{T}} < M_{\mathrm{H}}$ and a constant function for $p_{\mathrm{T}} > M_{\mathrm{H}}$. The fitted functions for four Higgs-boson masses relevant to the $\mathrm{H} \to \gamma\gamma$ search are also shown; there is a slight to moderate dependence on the Higgs-boson mass.

It is important to evaluate the impact of the p_{T}-reweighting on other observables susceptible to be used in the $\mathrm{H} \to \gamma\gamma$ search. Figure 74 shows the distributions, after application of the 'CMS' acceptance criteria, of the kinematical observables $\Delta\phi^{\gamma\gamma}$, the difference in azimuthal angle between the two photons, $\eta^{\gamma\gamma}$, the pseudo-rapidity of the diphoton system, and $\cos\theta^*$, the cosine of the angle between one of the photons and the beamline in the centre-of-mass frame of the Higgs boson, before and after the HQT reweighting, for $M_{\mathrm{H}} = 120$ GeV. The p_{T}-reweighting has a significant effect on both the $\Delta\phi^{\gamma\gamma}$ and

[39] S. Gascon-Shotkin, M. Kado (eds.); N. Chanon, L. Cieri, G. Davies, D. D'Enterria, D. de Florian, S. Ganjour, J. -Ph. Guillet, C. -M. Kuo, N. Lorenzo,E. Pilon and J. Schaarschmidt.

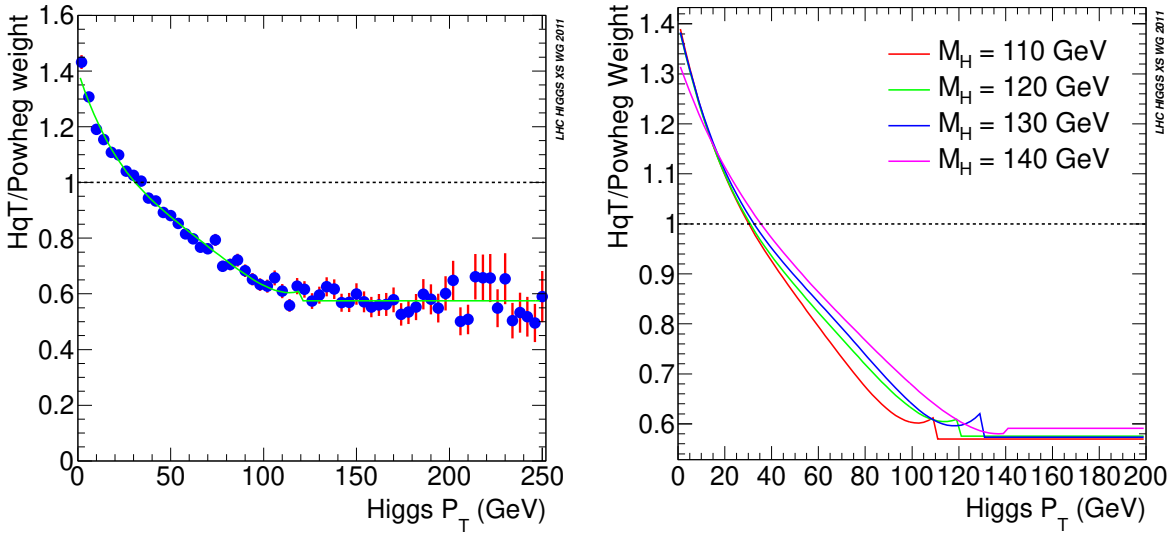

Fig. 73: (Left) Distribution of relative HQT/POWHEG event weights as a function of Higgs-boson p_{T} for $M_{\mathrm{H}} = 120\,\mathrm{GeV}$ with fit superposed. (Right) Fitted event weight functions for $M_{\mathrm{H}} = 110, 120, 130, 140\,\mathrm{GeV}$ as a function of Higgs-boson p_{T}.

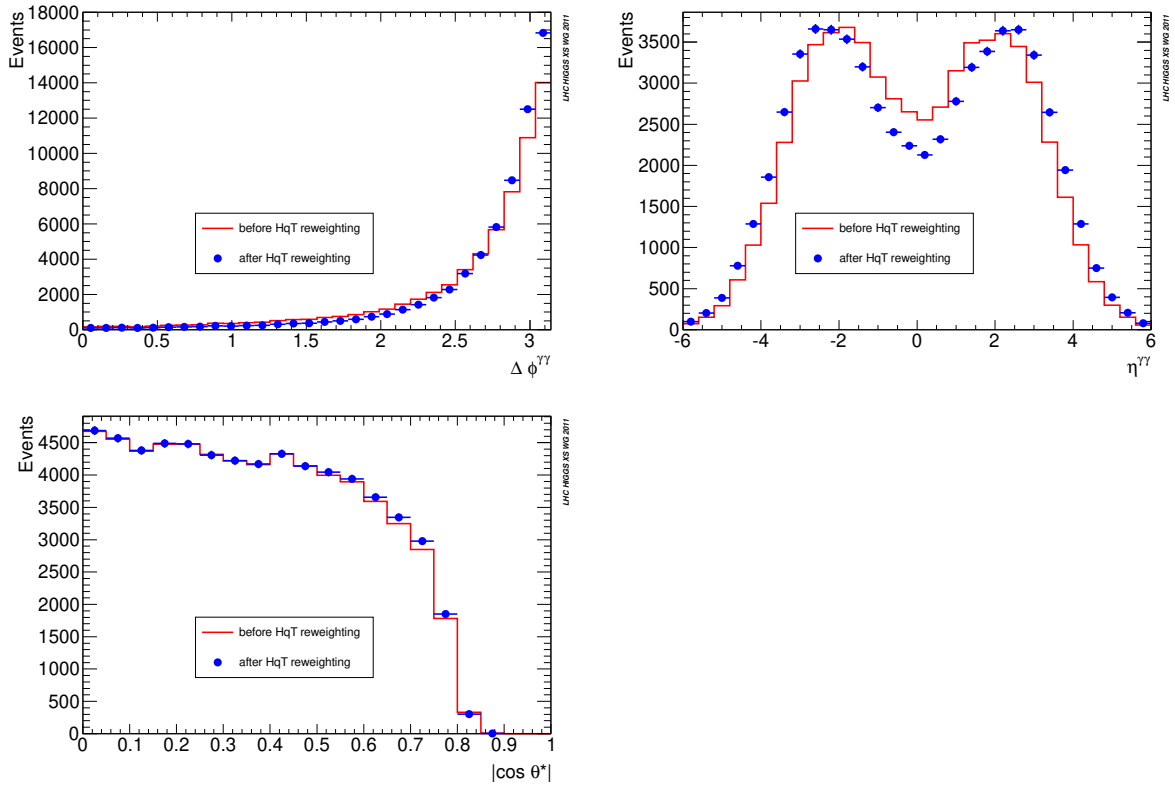

Fig. 74: Distributions of kinematical observables potentially important for the $\mathrm{H} \to \gamma\gamma$ search, for $M_{\mathrm{H}} = 120\,\mathrm{GeV}$, after application of 'CMS' acceptance criteria, before (red histogram) and after (blue dots) reweighting of the Higgs-boson p_{T} spectrum to that of HQT. Top left: $\Delta\phi^{\gamma\gamma}$; top right: $\eta^{\gamma\gamma}$; bottom: $\cos\theta^*$.

Table 21: Average values of the destructive interference factor δ as a function of Higgs-boson mass, for the 'ATLAS' acceptance criteria.

$M_{\rm H}$[GeV]	100	105	110	115	120	125	130	135	140	145	150
δ[%]	-3.16	-2.83	-2.59	-2.42	-2.31	-2.28	-2.36	-2.54	-2.87	-3.40	-4.33

$\eta^{\gamma\gamma}$ distributions; the $\Delta\phi^{\gamma\gamma}$ distribution is shifted to higher values, corresponding to the two photons being more back to back, and that of $\eta^{\gamma\gamma}$ is shifted away from small rapidity values towards the forward–backward zones. However, the $\cos\theta^*$ distribution is only slightly affected, with a small enhancement around $\cos\theta^* = 0.7$ and a corresponding small deficiency at the highest values. This has important implications for the treatment of the signal–background interference, which will be discussed below.

9.3.2 Doubly-differential K-factors for the gluon-fusion production process

To propagate higher-order effects to kinematical distributions produced by POWHEG [127], one can also perform a 2D reweighting with a K-factor $K(q_{\rm T,H}, Y_{\rm H})$ where $q_{\rm T,H}$ is the transverse momentum of the Higgs boson and $Y_{\rm H}$ its rapidity [296]. In the following we describe such a 2D reweighting procedure using HNNLO [197] and POWHEG [297]. This study should be repeated with HQT in place of HNNLO.

The K-factors $K(q_{\rm T,H}, Y_{\rm H})$ are computed by applying the 'Loose' kinematical criteria with $E_{\rm T,\gamma 1} > 20$ GeV and $E_{\rm T,\gamma 2} > 20$ GeV. An isolation criterion $\sum E_{\rm T} < 5$ GeV in a cone $\Delta R < 0.3$ around the photons is applied at parton level in HNNLO, while $\sum E_{\rm T} < 7$ GeV is used at generator level in POWHEG. The K-factors have been computed by bins of 4 GeV in $q_{\rm T,H}$ and 0.25 in $Y_{\rm H}$. Since the lowest $q_{\rm T,H}$ bins give a divergent cross section at fixed order, they have been merged in order to yield a constant K-factor in the range $0 < q_{\rm T,H} < 20$ GeV (the reweighted POWHEG spectrum profits therefore from a leading-log shape resulting from the PYTHIA parton shower in this range). Contiguous bins in the $(q_{\rm T,H}, Y_{\rm H})$ plane are then merged together to smooth out statistical fluctuations (they could also be fitted with smooth functions). The K-factors thus obtained by this procedure for the Higgs-boson masses $M_{\rm H} = 110, 120, 130, 140$ GeV are given in Appendix C (Table C.1). The differential cross-section distributions for HNNLO, POWHEG, and POWHEG after the application of the K-factors are shown in Figure 75. The need for such K-factors in the low-$q_{\rm T,H}$, central $Y_{\rm H}$ region is noticeable.

As expected, the use of the 2D K-factors is found to accurately reproduce the transverse momentum and the rapidity of the Higgs boson (see Figure 75) to within 5%. It also accurately reproduces angular variables such as $\cos\theta^*$ to the same level of precision.

9.3.3 Gluon-fusion signal and background interference

The $\gamma\gamma$ decay channel is affected by destructive interference between the Higgs-boson gluon-fusion production process and the Standard Model continuum $\rm gg \to \gamma\gamma$ 'box' process, which constitutes an irreducible background. This interference has been calculated at the two-loop level by Dixon and Siu [298], and the interference factor δ can be obtained as a function of the angle θ^*, where θ^* is the angle between one of the photons and the beamline in the centre-of-mass frame of the Higgs boson, the distribution of which is subject to experimental acceptance criteria, and y is the photon rapidity:

$$\theta^* = \arccos\Big(\tanh\frac{y(\gamma_1) - y(\gamma_2)}{2}\Big). \tag{65}$$

Average values of δ are shown in Table 21, where the values of θ^* have been obtained subject to the 'ATLAS' acceptance criteria defined at the beginning of this section. These are at the level of a few per cent, reaching a minimum of 2.28% for $M_{\rm H} = 125$ GeV and increasing to 3.16% and 4.33%, respectively, for $M_{\rm H} = 100$ GeV and $M_{\rm H} = 150$ GeV. However, for very low values of θ^*, δ can reach

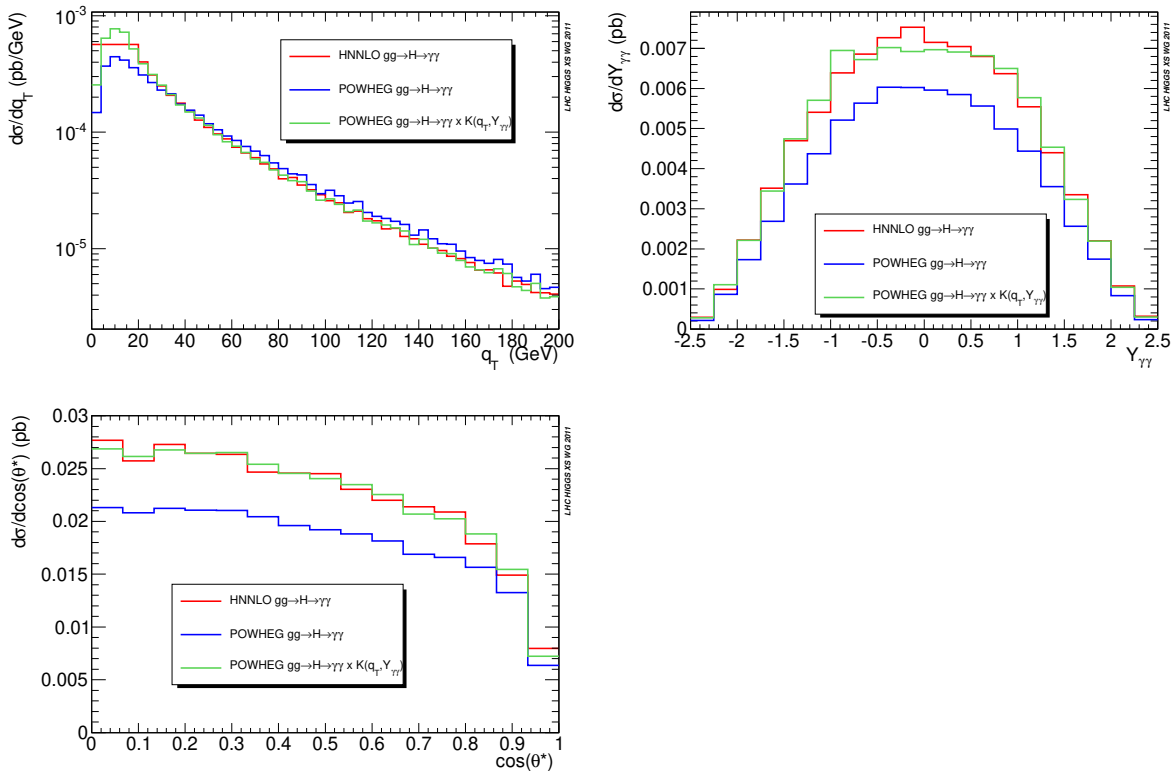

Fig. 75: Differential cross sections of the $\mathrm{gg} \to \mathrm{H} \to \gamma\gamma$ process for $M_{\mathrm{H}} = 120$ GeV: Higgs-boson transverse momentum (top left), Higgs-boson rapidity (top right), and $\cos\theta^*$ (bottom) for HNNLO, POWHEG, and POWHEG reweighted with $K(q_{\mathrm{T,H}}, Y_{\mathrm{H}})$.

far higher values, as much as 15% or more. Figure 76 shows, for the 'ATLAS' acceptance criteria and $M_{\mathrm{H}} = 120$ GeV, the distribution of δ values and δ as a function of θ^*.

At the beginning of this section it was shown that the $\cos\theta^*$ distribution was relatively insensitive to the p_{T}-reweighting. This means that it probably does not matter which (the p_{T}-reweighting or the interference correction) is performed first. It has been suggested [299] that the two steps should be performed in both orders, and the difference, for example in the two distributions of the cumulative event weights, should be taken as a theoretical systematic uncertainty.

In addition, the calculation performed in Ref. [298] takes only virtual QCD corrections into account, and the scattering angle used is that of the beam axis. To check the stability of the result for those cases where the diphoton system sizeably differs from the framework used for the calculation, the interference term is recomputed for signal events with a transverse momentum of the Higgs boson in excess of 20 GeV. The overall variation of the term is of the order of 10%. This systematic uncertainty on the $O(3\%)$ correction to the $\sigma \times$ BR can be neglected when considering the QCD scale, PDF, and α_s systematic uncertainties on the overall signal normalisation.

9.4 Background extraction and modelling

9.4.1 Background modelling biases and systematic uncertainties

The search for the Higgs boson in the diphoton channel relies, for both ATLAS [293,294] and CMS [295], on analytic models of the background shape. The scope of these models is to have a reasonable fit of the background diphoton invariant-mass distribution in the data to allow an accurate estimate of the background in the signal region from the side bands. Various models were investigated, a single or

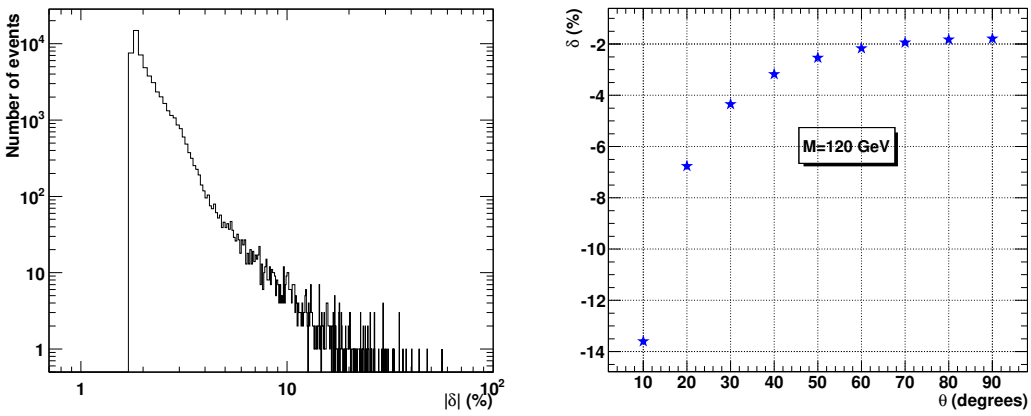

Fig. 76: Absolute value of the destructive interference factor δ (left) and its value as a function of θ^*, for $M_{\rm H} = 120$ GeV using the 'ATLAS' acceptance criteria.

double exponential parametrisation or polynomial shapes. These models and in particular the simple exponential function are of course not adequate to model the background over any diphoton invariant-mass range, but are a good approximation in small ranges. Assessing the ability of the functional form to model correctly the background over a given mass range should be determined from large Monte Carlo simulation samples of irreducible and reducible backgrounds and checked in the data.

To quantify the potential bias of a given functional form the difference between the fitted function to large Monte Carlo samples and its shape in a narrow mass window can be used, or a signal-plus-background model can be fitted, and the average number of signal events fitted will give an estimate of the bias. Preliminary studies of this type using the DIPHOX [300] and RESBOS [301–305] simulations have been carried out [293,294] showing that a simple exponential function or a second order polynomial when fitted over a mass range of 100 GeV to 160 GeV can introduce sizable biases, of the order of $10-20\%$ of a Standard Model signal. Such bias can be reduced either by using a higher-order polynomial as was done by CMS [295] or reducing the fitting mass range. In both cases the cost of reducing a potential bias is a reduction in the statistical precision of the determination of the background. The choice of optimal functional form, the constraints on its parameters, and the fitting range can be studied using the available Monte Carlo programs. Checks can also be made using the data, but it should be noted that their result can be biased both by statistical fluctuations in the search region and the potential presence of a signal. Such checks were carried out in ATLAS [293, 294] using a double exponential model fitted to the data to generate an ensemble of pseudo-experiments which were then fitted using a simple exponential. This check showed a fair agreement between the possible bias measured in the Monte Carlo and that measured from the two parametrisations.

In ATLAS [293,294], to account for a potential bias in the statistical treatment of the results of this channel, a fraction of the signal fitted is allowed to be assigned to a bias in the background modeling.

Detailed Monte Carlo based studies are necessary to accurately estimate the potential bias arising from a given choice of parametrisation of the background in the diphoton channel. Although such bias can be accounted for in the statistical treatment of the analysis results, it is preferable to keep it small relative to the expected number of signal events. Checks on the data are also important to further confirm the choice of background model. Depending on the kinematic requirements chosen in ATLAS and CMS, the background modeling systematic uncertainty could be correlated between experiments.

9.4.2 Status of background calculations

The irreducible background to the H $\to \gamma\gamma$ search is composed of prompt photon pairs from the quark–antiquark annihilation, gluon-fusion, and gluon–(anti)quark scattering processes. One or both photons come either directly from the hard process or from parton fragmentation, in which a cascade of successive collinear splittings yields a radiated photon. The contributions from the so-called 'direct' components have been calculated at NLO and implemented in the programs DIPHOX [300], GAMMA2MC [306], and MCFM [232]. In addition, DIPHOX contains a complete implementation at NLO of single- and double-fragmentation contributions. The calculation implemented in the RESBOS [301–305] program has NNLL resummation accuracy and an effective treatment of LO single fragmentation.

The direct contribution from the gluon-fusion channel, known as the 'box' contribution, is technically at NNLO at lowest order, and has been calculated [307], in addition to many of the higher-order corrections at N^{3}LO, and implemented in GAMMA2MC and RESBOS. These corrections are quantitatively of equal importance as the direct contributions, due to the significant gluon luminosity at the LHC.

Experimental measurements of differential prompt diphoton pair cross sections at both the Tevatron [308,309] and at the LHC [310,311] have exhibited largely satisfactory agreement with the ensemble of theoretical predictions. The exception has been in the so-called 'collinear' regime, corresponding to low values of $\Delta\phi^{\gamma\gamma}$ and $M^{\gamma\gamma}$, high values of $\cos\theta^*$, and the characteristic 'shoulder' in the p_{T} spectrum of the diphoton system. These disagreements were thought to be due to the absence of NNLO contributions in the theoretical predictions from either the direct or fragmentation components.

Recently, a fully-differential calculation of the direct components at NNLO using the q_{T} subtraction formalism [197] has been performed and implemented in the parton-level program 2GAMMANNLO [312]. Contributions from fragmentation are not included and are formally eliminated by the application of the so-called smooth cone isolation criterion due to Frixione et al. [313]: For a cone of radius $r = \sqrt{\Delta\eta^2 + \Delta\phi^2} < R$ around a photon with transverse momentum p_{T}^{γ}, the total amount of partonic transverse energy E_{T} must be less than $E_{\mathrm{T}}^{\max}(r)$, where

$$E_{\mathrm{T}}^{\max}(r) = \epsilon_\gamma p_{\mathrm{T}}^{\gamma}\Big(\frac{1-\cos r}{1-\cos R}\Big)^n. \tag{66}$$

In the above definition ϵ_γ and n are parameters, with $0 < \epsilon_\gamma < 1$. Figure 77 shows the differential cross section $d\sigma/d\Delta\phi_{\gamma\gamma}$ as predicted by 2GAMMANNLO at both NNLO and NLO (but excluding the higher-order 'box' diagram corrections), compared to a recent measurement by the CMS collaboration [311] at $\sqrt{s} = 7$ TeV, with acceptance criteria closely following the 'Loose' selection defined at the beginning of this section. There is satisfactory agreement between this preliminary theoretical prediction and the CMS data, indicating that the addition of the direct NNLO contributions alone may correct much of the disagreement, modulo the fact that the CMS analysis used simple hollow cone isolation requirements and not the Frixione criterion.

Figure 78 shows the same differential distribution $d\sigma/d\Delta\phi_{\gamma\gamma}$ predicted by 2GAMMANNLO at both NNLO and NLO, this time for the 'ATLAS' and 'CMS' acceptance criteria defined at the beginning of this section.

9.4.3 Doubly-differential K-factors

Although the ATLAS and CMS H $\to \gamma\gamma$ analyses estimate the background directly from data, it is nevertheless useful to benefit from the best possible background estimate from Monte Carlo simulations. Furthermore, this is needed for meaningful data/Monte Carlo comparisons as well as to train classifiers in multivariate analyses. For these purposes, we propose in this section a differential reweighting of parton-shower events to NLO calculations. This has been achieved by using parton-shower events obtained with $\gamma\gamma$+jets samples generated with MADGRAPH [314] (which contains the Born diagram and up to two

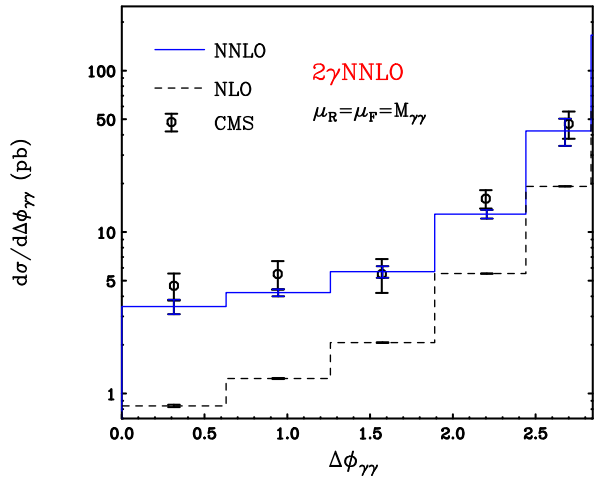

Fig. 77: Differential diphoton cross section as a function of $\Delta\phi_{\gamma\gamma}$ at NNLO (blue) and at NLO (dotted black) calculated with a preliminary result from the 2GAMMANNLO program, superimposed on results from CMS data (points) from 2010 [311].

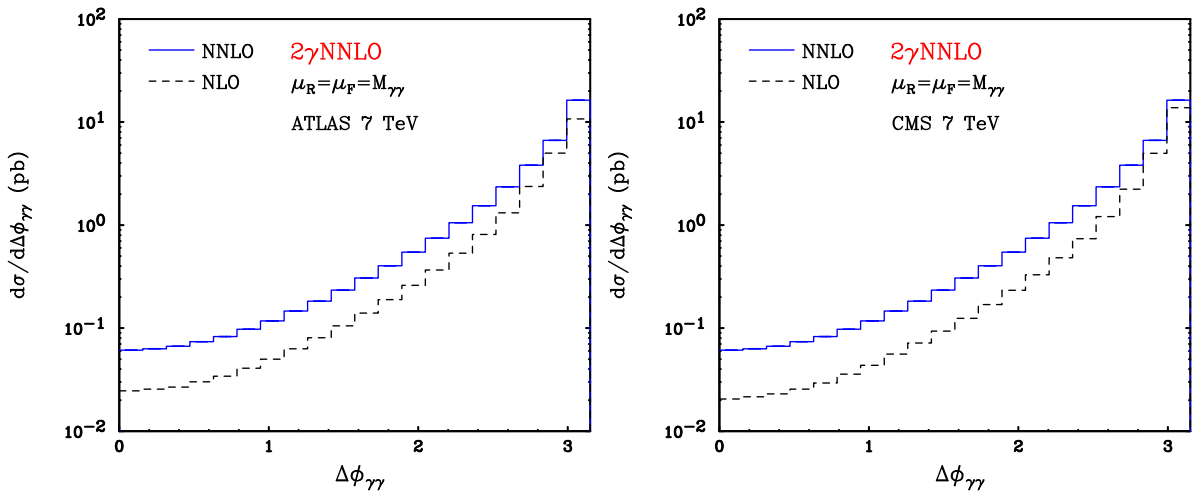

Fig. 78: Differential diphoton cross section as a function of $\Delta\phi_{\gamma\gamma}$ at NNLO (blue) and at NLO (dotted black) calculated with a preliminary result from the 2GAMMANNLO program, for the 'ATLAS' (left) and 'CMS' (right) acceptance criteria.

supplementary hard jets) hadronised with PYTHIA [315], and lowest-order box events generated with PYTHIA. Events have been reweighted to NLO with DIPHOX [300] (NLO Born and single- and double-fragmentation contributions) and GAMMA2MC [306] (NLO box contributions). It should be noted that the MADGRAPH γγ+jets process includes the fragmentation contribution at the matrix-element level as a bremsstrahlung contribution, while DIPHOX includes the full treatment of the fragmentation function at NLO. This study should be repeated with 2GAMMANNLO.

In order to reproduce most of the kinematic features of the NLO processes, it has been found that it is sufficient to perform a 2D reweighting with a K-factor $K(q_{\mathrm{T},\gamma\gamma}, M_{\gamma\gamma})$, where $q_{\mathrm{T},\gamma\gamma}$ is the transverse momentum of the diphoton system and $M_{\gamma\gamma}$ its invariant mass [297]. The K-factors $K(q_{\mathrm{T},\gamma\gamma}, M_{\gamma\gamma})$ are computed by applying the 'Loose' kinematical cuts with $E_{\mathrm{T},\gamma 1} > 20$ GeV and $E_{\mathrm{T},\gamma 2} > 20$ GeV. An isolation criterion $\sum E_{\mathrm{T}} < 5$ GeV in a cone $\Delta R < 0.3$ around the photons is applied at parton level and $\sum E_{\mathrm{T}} < 7$ GeV at generator level. The K-factors have been computed for bins of 4 GeV in $q_{\mathrm{T},\gamma\gamma}$

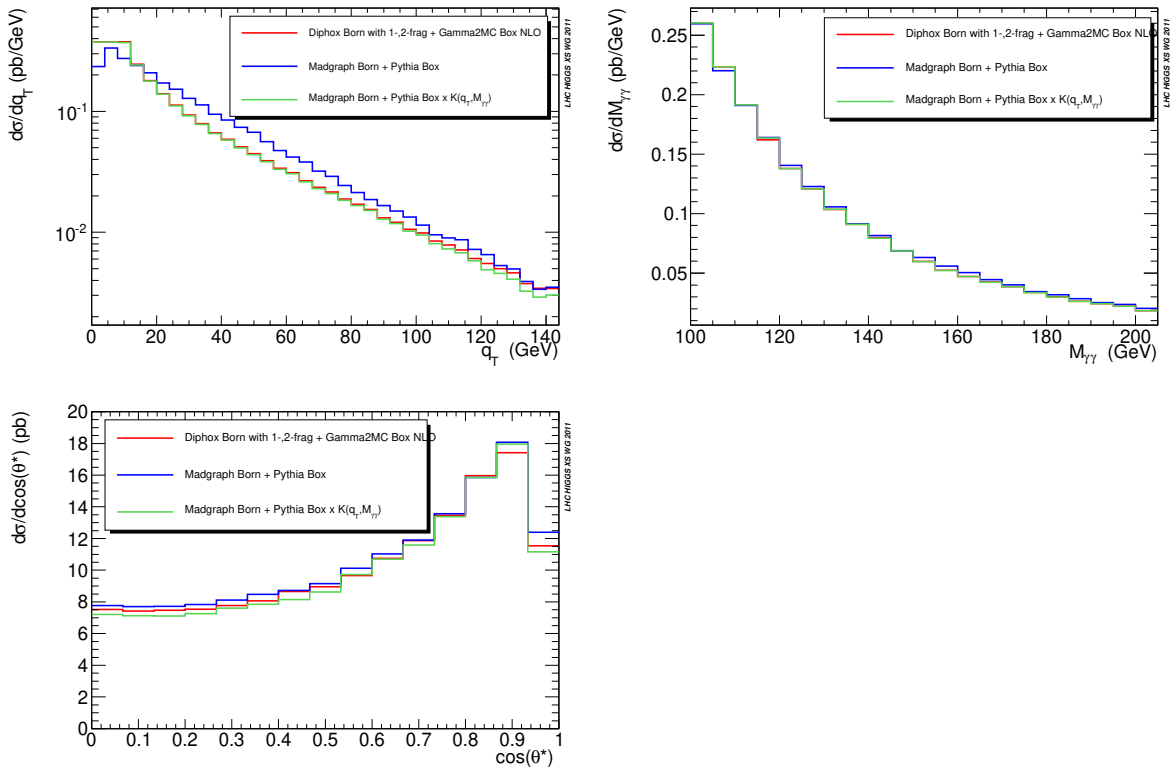

Fig. 79: Differential cross sections for diphoton production from the sum of the quark–antiquark annihilation, gluon-fusion, and gluon–(anti)quark scattering processes: Diphoton transverse momentum (top left), diphoton invariant mass (top right), and $\cos\theta^*$ (bottom) for a combination of DIPHOX and GAMMA2MC, a combination of MADGRAPH and PYTHIA, and the latter combination reweighted with $K(M_{\gamma\gamma}, q_{\mathrm{T,H}})$.

and 5 GeV in $M_{\gamma\gamma}$. Contiguous bins in the ($q_{\mathrm{T},\gamma\gamma}$, $M_{\gamma\gamma}$) plane are then merged together to smooth out statistical fluctuations (they could be alternatively fitted with smooth functions). The K-factors obtained by this procedure are shown in Appendix C (Table C.5). The differential cross-section distributions for a combination of DIPHOX and GAMMA2MC, and a combination of MADGRAPH and PYTHIA after the application of the K-factors are shown in Figure 79. It is interesting to note that the supplementary hard jets in the MADGRAPH γγ+jets samples allows the population of the high-$q_{\mathrm{T},\gamma\gamma}$ and high-$M_{\gamma\gamma}$ regions, which would have been forbidden by the LO kinematics of the PYTHIA Born samples had they been used.

As expected, the 2D K-factors are found to accurately reproduce the transverse momentum and the invariant-mass spectra of the diphoton system (see Figure 79) in the region where the $\mathrm{H} \to \gamma\gamma$ searches are performed ($M_{\gamma\gamma} > 100$ GeV). They also accurately reproduce angular variables such as $\cos\theta^*$.

10 WW* decay mode[40]

10.1 Introduction

For Higgs-boson masses $M_{\mathrm{H}} \gtrsim 135\,\mathrm{GeV}$, the Higgs boson decays mainly into a WW^* pair. The W's decay mainly hadronically, but this decay topology is experimentally difficult to exploit due to the high cross section of multi-jet processes in pp collisions. If one of the W's decays to $\mathrm{l}\nu$, where l indicates an electron or muon, and the other to two quarks, the background from $\mathrm{pp} \to \mathrm{W} + \text{jets}$ with $\mathrm{W} \to \mathrm{l}\nu$, becomes dominant. For high values of the Higgs mass, a strong cut on the neutrino transverse momentum (measured as missing energy, $E_{\mathrm{T}}^{\mathrm{miss}}$, in the detector) can be used to reject the $\mathrm{W} + \text{jets}$ background. For low values of the Higgs mass only the fully leptonic decay channel of the W's ($\mathrm{WW} \to \mathrm{l}\nu\mathrm{l}\nu$) can be used for Higgs search with high sensitivity.

The main background in this channel is $\mathrm{pp} \to \mathrm{t}\bar{\mathrm{t}} \to \mathrm{WbWb} \to \mathrm{l}\nu\mathrm{l}\nu\mathrm{bb}$. This background is characterised by the presence of high missing E_{T} from the two neutrinos and high jet multiplicity from the b quarks.

In order to maximise the sensitivity, the analysis is performed in jet categories, that means the whole sample is divided in 0, 1, and > 1 jets subsamples. The use of jet categories is common to other channels like $\mathrm{H} \to \gamma\gamma$ and $\mathrm{H} \to \tau\tau$. In the first two subsections we will discuss the concrete implementation of the jet categorisation in the $\mathrm{H} \to \mathrm{WW}$ analysis. The follwoing sections discuss the treatment of the irreducible SM WW background.

10.2 Jet bin categorisation and uncertainties

The main Higgs production process at LHC is gluon fusion $\mathrm{gg} \to \mathrm{H}$ whose inclusive cross section is known at NNLO QCD + NLO EW + higher-order improvements [7], with uncertainties from residual QCD scale dependences and from PDF errors of $6-10\%$ and $8-10\%$ for the LHC at 7 TeV centre-of-mass energy. The $\mathrm{gg} \to \mathrm{H}$ process is characterised by large contributions from extra gluon emission. The amount of extra jets produced in the process has been computed using the POWHEG MC program interfaced to PYTHIA for the showering with the following results: 44% of the events have more than one jet and 13% have more than two jets. The jet algorithm used is the anti-k_{T} with a cone $\Delta R = 0.4$, and a cut on the transverse momentum of the jet of 25 GeV and a pseudorapidity cut of 4.5 are imposed. The CTEQ6.6 NLO PDF set has been used for the computation. Scale uncertainties on the exclusive jet cross sections result to be smaller than the scale uncertainty on the inclusive cross sections. This points to several studies, also reported in this report, showing that the conventional scale uncertainty variation underestimate the exclusive jet bin uncertainty. In order to compute more realistic uncertainties a procedure has been set up that furnishes more reasonable values. As described in the following, it consists in evaluating the scale uncertainty on the inclusive multi-jet cross sections, $\sigma_{\geq 0}$, $\sigma_{\geq 1}$, and $\sigma_{\geq 2}$, and propagating them uncorrelated to the exclusive jet bins. These uncertainties produce large correlations among several channels. In the WW case, three different channels are analysed: $\mathrm{e}^+\mathrm{e}^-$, $\mathrm{e}^\pm\mu^\pm$, and $\mu^+\mu^-$. The jet bin uncertainties have to be considered fully correlated among them.

Analysis selection criteria for the several channels are different, and the scale uncertainties on the inclusive jet cross section can be different according to the several selections that are considered. In order to decouple the largest contribution to the jet counting from the specific analysis criteria the signal yield in a given jet bin is defined as follows,

$$N_{0j} = \sigma_{\geq 0} f_0 A_0, \quad N_{1j} = \sigma_{\geq 0} f_1 A_1, \quad N_{2j} = \sigma_{\geq 0} f_2 A_2, \tag{67}$$

where f_0, f_1 and f_2 are defined as

$$f_0 = \frac{\sigma_{\geq 0} - \sigma_{\geq 1}}{\sigma_{\geq 0}}, \quad f_1 = \frac{\sigma_{\geq 1} - \sigma_{\geq 2}}{\sigma_{\geq 0}}, \quad f_2 = \frac{\sigma_{\geq 2}}{\sigma_{\geq 0}}. \tag{68}$$

[40] S. Diglio, B. Di Micco, R. Di Nardo, A. Farilla, B. Mellado and F. Petrucci (eds.).

Table 22: Common cuts for the $\mathrm{H} \to \mathrm{WW}^*$ analysis for the evaluation of jet bin uncertainties on the signal yield. The p_{Tl1}, p_{Tl2} are the cuts on the lepton p_{T}, $E_{\mathrm{T}}^{\mathrm{miss}}$ is the total p_{T} of the neutrinos, m_{ll} is the invariant mass of the two leptons, and p_{Tjetcut} is the cut imposed on the jet p_{T} for the jet counting.

$p_{\mathrm{Tl1}}, p_{\mathrm{Tl2}} > 20$ GeV , $\lvert\eta_1\rvert, \lvert\eta_2\rvert < 2.5$
$E_{\mathrm{T}}^{\mathrm{miss}} > 30$ GeV
$m_{\mathrm{ll}} > 12$ GeV
$p_{\mathrm{Tjetcut}} < 30$ GeV with $\lvert\eta\rvert < 3$ and using anti-k_{T} algorithm with cone size 0.5

Table 23: Inclusive jet uncertainties used for exclusive jet bin uncertainties estimation.

$\Delta\sigma_{\geq 0}$	$\Delta\sigma_{\geq 1}$	$\Delta\sigma_{\geq 2}$
10%	20%	70%

Table 24: Analysis cuts used in the $\mathrm{H} \to \mathrm{WW}^* \to \mathrm{l\nu l\nu}$ analysis in the ATLAS experiment, the $p_{\mathrm{T}}^{\mathrm{ll}}$ variable is the sum of the p_{T}'s of the two letpons, the $\mathrm{Z}_{\tau\tau}$ veto is a veto applied to the invariant mass of the $\tau\tau$ system reconstructed in the collinear approximation (the neutrino from τ decay is supposed to fly in the same direction of the charged lepton) of $\lvert m_{\tau\tau} - M_{\mathrm{Z}}\rvert > 15$ GeV.

$M_{\mathrm{H}} < 200$ GeV	$M_{\mathrm{H}} > 200$ GeV
$E_{\mathrm{T}}^{\mathrm{missrel}} > 40$ GeV	$E_{\mathrm{T}}^{\mathrm{missrel}} > 40$ GeV
$m_{\mathrm{ll}} < 50$ GeV	$m_{\mathrm{ll}} < 150$ GeV
$\Delta\phi_{\mathrm{ll}} < 1.8$	no $\Delta\phi_{\mathrm{ll}}$ cut
$\lvert m_{\mathrm{ll}} - M_{\mathrm{Z}}\rvert > 15$ GeV	$\lvert m_{\mathrm{ll}} - M_{\mathrm{Z}}\rvert > 15$ GeV
0-jet: $p_{\mathrm{T}}^{\mathrm{ll}} > 30$ GeV	
1-jet: $p_{\mathrm{T}}^{\mathrm{l1}} + p_{\mathrm{T}}^{\mathrm{l2}} + E_{\mathrm{T}}^{\mathrm{miss}} + p_{\mathrm{T}}^{\mathrm{jet}} < 30$ GeV	
$\mathrm{Z}_{\tau\tau}$ veto	

The central values of f_0, f_1, and f_2 are computed using the POWHEG MC after the reweighting of the Higgs p_{T} to HQT 2.0 and the full reconstruction chain of each experiment, while for the purpose of error propagation they are evaluated using HNNLO. In order to properly correlate the uncertainties among several measurements and between the ATLAS and CMS collaborations, a common set of cuts has been defined in order to compute the uncertainties on the $\sigma_{\geq n\mathrm{jets}}$ and the f_i values used in the error propagation. The cuts are shown in Table 22.

The scale uncertainties on $\sigma_{\geq 0}$, $\sigma_{\geq 1}$, and $\sigma_{\geq 2}$ have been computed using HNNLO and are shown in Table 23, the renormalisation and factorisation scales were varied by a factor two up and down in order to get the error. The errors shown are the maximum variation obtained in the Higgs mass range $130 < M_{\mathrm{H}} < 300$ GeV.

The A_i coefficients are the acceptances specific for each analysis, they are the acceptances due to the further cuts applied in addition to the cuts shown in Table 22. The scale uncertainty on A_i has been evaluated studying the fractional variation of events passing all analysis cuts over the event passing the selection in Table 22. The effects observed are small and have been evaluated only for the $\mu\mu$ channel and two Higgs mass points. The cuts used by the ATLAS collaboration for the 0-jet and 1-jet analysis are shown in Table 24. The analysis is divided in a low mass analysis, applied for $M_{\mathrm{H}} < 200$ GeV, and an high-mass analysis for $M_{\mathrm{H}} > 200$ GeV. The two analyses differ in the treatment of the WW background; details are described in Section 10.4.

The fractional variation of the A_0 and A_1 varying the normalisation and factorisation scale at $\mu_{\mathrm{R}} = \mu_{\mathrm{F}} = 2M_{\mathrm{H}}$ and $\mu_{\mathrm{R}} = \mu_{\mathrm{F}} = 1/2M_{\mathrm{H}}$ with respect to the central value of $\mu_{\mathrm{R}} = \mu_{\mathrm{F}} = M_{\mathrm{H}}$ are shown in Table 25 both for the low-mass and the high-mass analyses. The uncertainties obtained are

Table 25: Acceptance variation for the 0 and 1-jet analysis for two Higgs mass points. The acceptance are evaluated for the low-mass analysis for $M_{\rm H} = 130$ GeV and the high-mass analysis for $M_{\rm H} = 200$ GeV.

		$M_{\rm H} = 130$ GeV	$M_{\rm H} = 200$ GeV
A_0	$\mu_{\rm R} = \mu_{\rm F} = 2M_{\rm H}$	-1 per mil	$+3\%$
A_0	$\mu_{\rm R} = \mu_{\rm F} = M_{\rm H}/2$	$+5$ per mil	-1.3%
A_1	$\mu_{\rm R} = \mu_{\rm F} = 2M_{\rm H}$	-6 per mil	$+4\%$
A_1	$\mu_{\rm R} = \mu_{\rm F} = M_{\rm H}/2$	$+4\%$	$+3\%$

much smaller than the scale uncertainties on the inclusive jet cross sections.

10.3 Discussion about the 2-jet bin

The error on the 2-jet inclusive bin has been computed using the HNNLO program. It predicts a quite large error on the 2-jet cross section because the 2-jet bin is computed at LO. The inlcusive 2-jet cross section $\sigma_{\geq 2}$ is about 30% of the inclusive 1-jet cross section $\sigma_{\geq 1}$. With further cuts that are usually used in the 2-jet channel this can reach very small values. Typically the 2-jet bin is used in vector-boson fusion (VBF) and VH analyses where the analyses are tuned to maximise the cross sections in the VBF and HV channels. Recently an NLO calculation of the $\rm gg \rightarrow H + 2$ jets process became available and implemented in MCFM. The scale uncertainties of these results are smaller than the uncertainty from HNNLO that computes the $\rm H + 2$ jets cross section at LO. In order to use the smaller error from MCFM we need to compare the cross section computed with MCFM with the respective cross section computed with the POWHEG Monte Carlo after the reweighting to HQT 2.0. In fact the signal yield is computed using the POWHEG MC that evaluates the 2-jet cross section only through the parton shower. It is therefore important to compare the central value of the 2-jet cross section from POWHEG with Higgs $p_{\rm T}$ reweighting and with the MCFM v6.0 computation. The comparison is performed applying the following cuts,

$$p_{\rm T}^{\rm l1} > 20 \text{ GeV}, \quad p_{\rm T}^{\rm l2} > 10 \text{ GeV}, \quad |\eta_{\rm l1}| < 2.5, \quad |\eta_{\rm l2}| < 2.5, \tag{69}$$

and at least two anti-$k_{\rm T}$ jets with $p_{\rm T} > 25$ GeV with a cone $\Delta R = 0.4$. The computation has been performed using the CTEQ6.6 PDF set and the renormalisation and factorisation scales fixed at the value of the Higgs mass. The total POWHEG cross section has been normalised at the NNLO value. The results are shown in Table 26 and plotted in Figure 80.

Renormalisation and factorisation scale variations from $M_{\rm H}/4$ to 2 $M_{\rm H}$ have been evaluated and tabulated in Table 27. The scale uncertainty is computed by taking the maximum spread in the cross section obtained spanning the values $M_{\rm H}/2 < \mu_{\rm R}, \mu_{\rm F} < 2M_{\rm H}$ but keeping $1/2 < \mu_{\rm R}/\mu_{\rm F} < 2$. The obtained uncertainties are summarised in Table 28.

10.4 Backgrounds

The main backgrounds to the $\rm H \rightarrow WW$ channel are the top background, the Drell–Yan process $\rm pp \rightarrow Z/\gamma^* +$ jets with $\rm Z/\gamma^* \rightarrow l^+l^-$, the $\rm pp \rightarrow W +$ jets, with $\rm W \rightarrow l\nu$, with a fake lepton from the jets, and the irreducible $\rm pp \rightarrow W^+W^-$ background. The reducible backgrounds are estimated with data-driven technique slightly different between the two collaborations. The treatment of the irreducible WW background is mainly affected by theoretical uncertainties and will be discussed in the following.

For a relatively light Higgs, the W bosons in the $\rm WW^*$ pair produced in the Higgs decay have opposite spin orientations, since the Higgs has spin zero. In the weak decay of the W, due to the $V - A$ nature of the interaction, the positively charged lepton is preferably emitted in the direction of the $\rm W^+$ spin and the negative letpon in the opposite direction of the W^- spin. Therefore the two charged leptons are emitted close to each other, and their di-lepton invariant mass $m_{\rm ll}$ is small. This feature is used in the

Table 26: Comparison between the POWHEG and MCFM 2 jet inclusive cross section, the error shown are the statistical errors, the ratio of the two cross sections doesn't exceed 11% in the whole M_{H} range.

M_{H} [GeV]	MCFM [fb]	POWHEG [fb]	Ratio: POWHEG/MCFM
130	4.09 ± 0.05	3.89 ± 0.05	0.95 ± 0.02
135	5.41 ± 0.09	5.13 ± 0.06	0.95 ± 0.02
140	6.67 ± 0.07	6.22 ± 0.08	0.93 ± 0.01
145	8.20 ± 0.18	7.55 ± 0.09	0.92 ± 0.02
150	9.02 ± 0.14	8.66 ± 0.10	0.96 ± 0.02
155	9.67 ± 0.09	9.57 ± 0.11	0.99 ± 0.01
160	10.55 ± 0.07	10.80 ± 0.12	1.02 ± 0.01
165	10.88 ± 0.20	11.29 ± 0.16	1.04 ± 0.02
170	10.67 ± 0.13	10.54 ± 0.11	0.99 ± 0.02
175	9.86 ± 0.10	10.09 ± 0.11	1.02 ± 0.01
180	9.41 ± 0.08	9.69 ± 0.10	1.03 ± 0.01
185	8.31 ± 0.09	8.32 ± 0.09	1.00 ± 0.01
190	7.43 ± 0.05	7.40 ± 0.08	1.00 ± 0.01
195	6.82 ± 0.06	6.97 ± 0.07	1.02 ± 0.01
200	6.72 ± 0.07	6.51 ± 0.07	0.97 ± 0.01
220	5.26 ± 0.05	5.70 ± 0.09	1.08 ± 0.02
240	4.97 ± 0.04	5.17 ± 0.12	1.04 ± 0.02
260	4.41 ± 0.02	4.80 ± 0.07	1.09 ± 0.01
280	4.07 ± 0.04	4.29 ± 0.10	1.05 ± 0.02
300	3.77 ± 0.02	4.18 ± 0.06	1.11 ± 0.02

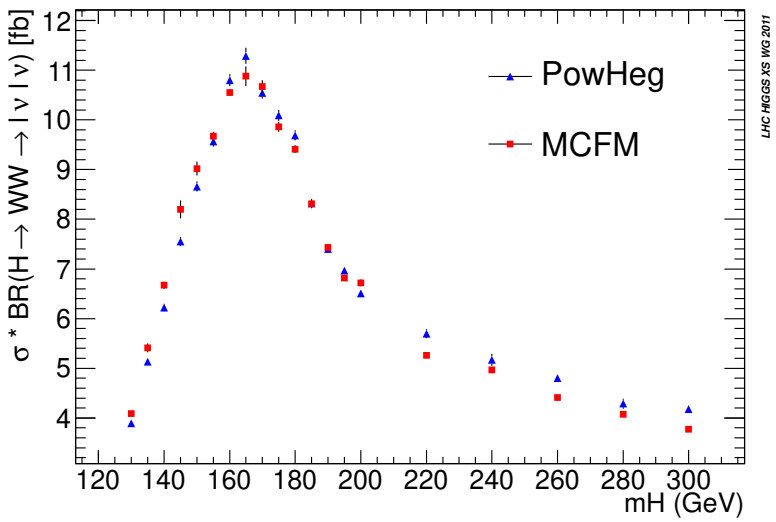

Fig. 80: The $\mathrm{pp} \to \mathrm{H} + 2$ jets cross section evaluated using typical charged leptons and jets selection cuts of the $\mathrm{WW} + 2$ jets analysis.

Table 27: The $\mathrm{gg} \to \mathrm{H} + 2$ jets cross section evaluated for different scale choices.

M_{H} [GeV]	$\xi_{\mathrm{R}} = \mu_{\mathrm{R}}/M_{\mathrm{H}}$	$\xi_{\mathrm{F}} = \mu_{\mathrm{F}}/M_{\mathrm{H}}$	σ [fb]
	0.25	0.25	5.17 ± 0.64
	0.25	0.5	4.60 ± 0.24
	0.5	0.25	4.88 ± 0.11
	0.5	0.5	5.14 ± 0.14
	0.5	1	4.98 ± 0.08
130	1	0.5	4.42 ± 0.05
	1	1	4.17 ± 0.06
	1	2	4.13 ± 0.05
	2	1	3.41 ± 0.03
	2	2	3.34 ± 0.05
	0.25	0.25	6.47 ± 0.36
	0.25	0.5	12.46 ± 0.38
	0.5	0.25	13.27 ± 0.32
	0.5	0.5	13.03 ± 0.30
	0.5	1	12.24 ± 0.36
160	1	0.5	10.77 ± 0.12
	1	1	10.52 ± 0.13
	1	2	10.28 ± 0.07
	2	1	8.43 ± 0.09
	2	2	8.35 ± 0.07
	0.25	0.25	6.43 ± 0.15
	0.25	0.5	6.96 ± 0.11
	0.5	0.25	6.84 ± 0.11
	0.5	0.5	6.70 ± 0.13
	0.5	1	6.66 ± 0.14
220	1	0.5	5.85 ± 0.06
	1	1	5.56 ± 0.06
	1	2	5.33 ± 0.04
	2	1	4.48 ± 0.03
	2	2	4.59 ± 0.06

Table 28: Scale uncertainties on the $\mathrm{gg} \to \mathrm{H} + 2$ jets cross section evaluated using the MCFM program.

M_{H} [GeV]	scale uncertainties
130	23%
160	24%
220	20%

low-mass analysis to define a signal-free control region through the cut $m_{\mathrm{ll}} > 80$ GeV. The event yield of the WW^* background is computed in the control region and extrapolated to the signal region. The WW yield in the signal region is therefore

$$N_{\mathrm{S.R.}}^{\mathrm{WW0j}} = \alpha_{\mathrm{0j}} N_{\mathrm{C.R.}}^{\mathrm{WW0j}}, \quad N_{\mathrm{S.R.}}^{\mathrm{WW1j}} = \alpha_{\mathrm{1j}} N_{\mathrm{C.R.}}^{\mathrm{WW1j}}. \tag{70}$$

The value of α is affected both by theoretical and experimental errors. Because α is defined using only leptonic quantities, the experimental error is negligible and the theoretical error is carefully evaluated in Section 10.5.

For $M_{\mathrm{H}} > 200$ GeV it is not possible to define a signal-free control region, therefore the WW

Table 29: Definition of the signal and control regions.

M_{H} [GeV]	$110 - 200$
ATLAS	$\Delta\phi_{\mathrm{ll}} < 1.8$
S.R.	$m_{\mathrm{ll}} < 50$ GeV
ATLAS	$m_{\mathrm{ll}} > M_{\mathrm{Z}} + 15$ GeV$(\mathrm{ee}, \mu\mu)$
C.R.	$m_{\mathrm{ll}} > 80$ GeV$(\mathrm{e}\mu)$

yield needs to be determined directly from the theoretical expectation. In Section 10.7.1 we discuss the evaluation of the jet bin uncertainties on the expected WW^* yield.

10.5 Theoretical uncertainties on the extrapolation parameters α for the 0j and 1j analyses

The WW background is estimated for $M_{\mathrm{H}} < 200$ GeV using event counts in a well defined control region (C.R. in the following). The control region is defined using cuts on m_{ll} and $\Delta\phi_{\mathrm{ll}}$ variables. In Table 29 we show the cuts used by the ATLAS collaborations to define the signal and the WW C.R. for the different channels.

The amount of WW background in signal region is determined from the control region through the parameter α defined by

$$\alpha_{\mathrm{WW}} = N^{\mathrm{WW}}_{\mathrm{S.R.}} / N^{\mathrm{WW}}_{\mathrm{C.R.}}, \tag{71}$$

where α is evaluated independently for the 0-jet and 1-jet bin. The Standard Model WW^* yield is obtained using the MC@NLO Monte Carlo program interfaced to HERWIG for parton showering. MC@NLO computes the $\mathrm{pp} \to \mathrm{WW}^* \to \mathrm{l\nu l\nu}$ at NLO including off-shell contributions. Spin correlations for off-shell W's are not treated at matrix-element (ME) level and a correction is provided after the generation step to take into account the spin correlation with some approximation. Furthermore MC@NLO does not implement all electroweak diagrams contributing to the $\mathrm{pp} \to \mathrm{l\nu l\nu}$ process. In particular, "singly-resonant" processes are missing in the calculation. A singly-resonant diagram is, e.g. a diagram where at least a lepton neutrino pair is not connected to the same W decay vertex. The full ME calculation for the spin correlation and the inclusion of all singly-resonant diagrams is implemented in the MCFM v6.0 parton level Monte Carlo generator. In order to take into account uncertainties in the modelling of the WW background, the MC@NLO and MCFM v6.0 output have been compared. The comparison has been performed summing up the contribution of all jet bins in order to integrate out effects from the simulation of the jet multiplicity, which are not well modelled by parton-level Monte Carlo programs. The CTEQ6.6 PDF error set has been used in the comparison and it has been used inclusively in the number of jets. In Figures 81, 82, 83, and 84 we show the comparison between MCFM v6.0 and MC@NLO on several variables. The transverse mass m_{T} is defined by

$$m_{\mathrm{T}} = \sqrt{(E^{\mathrm{ll}}_{\mathrm{T}} + E^{\mathrm{miss}}_{\mathrm{T}})^2 - (\vec{p}^{\,\mathrm{ll}}_{T} + \vec{p}^{\,\mathrm{miss}}_{\mathrm{T}})^2}, \tag{72}$$

where $E^{\mathrm{ll}}_{\mathrm{T}} = \sqrt{(\vec{p}^{\,\mathrm{ll}}_{\mathrm{T}})^2 + m^2_{\mathrm{ll}}}$, $|\vec{p}^{\,\mathrm{miss}}_{\mathrm{T}}| = E^{\mathrm{miss}}_{\mathrm{T}}$, and $\vec{p}^{\,\mathrm{ll}}_{T}$ is the transverse momentum of the di-lepton system.

Small difference between the two calculations are visible in all variables, the $m_{\,ll}$ variable that is used to define the WW C.R. is in very good agreement. The effect of these discrepancies on the α parameter has been evaluated to be:

$$\frac{\alpha(\mathrm{MC@NLO})}{\alpha(\mathrm{MCFM})} = 0.980 \pm 0.015, \tag{73}$$

where the error is due to the MC statistics, a conservative error of 3.5% is used in the analysis.

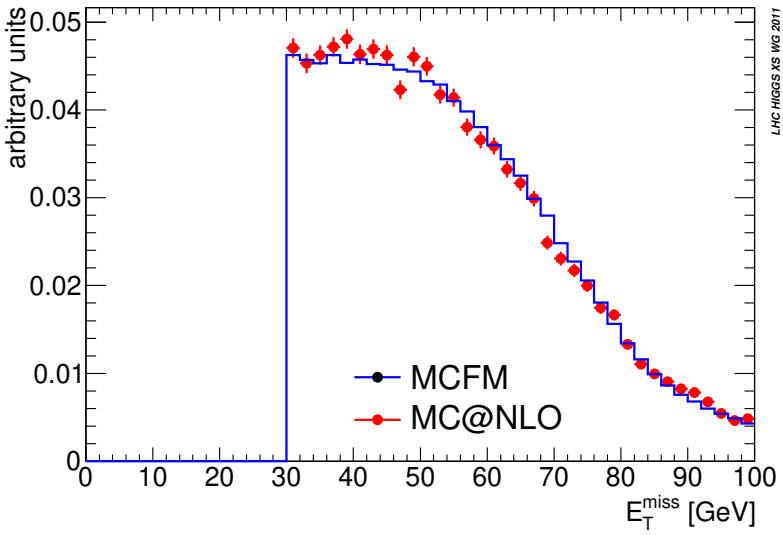

Fig. 81: Comparison between MCFM v6.0 and MC@NLO: The shape of the missing-E_{T} distribution is shown for events passing the charged-lepton and missing-E_{T} cuts.

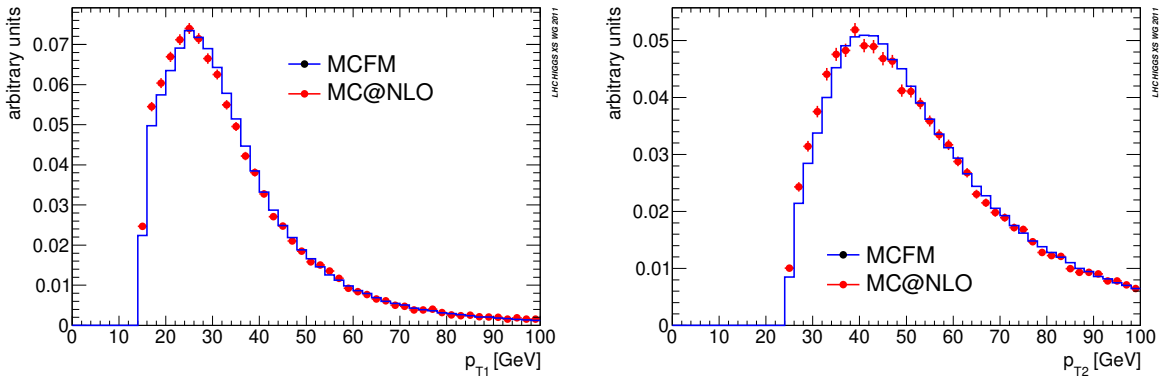

Fig. 82: Comparison between MCFM v6.0 and MC@NLO: the shapes of the p_{T} of the softer charged lepton (left) and of the hardest charged lepton (right) are shown for events passing the charged-lepton and missing-E_{T} cuts.

Further uncertainties on the α parameters are obtained using different PDF sets in the simulation of the WW^* background. In particular, the α values have been computed with the CTEQ6.6 error set and computing the error according the recommended procedure, the values obtained using the central PDFs of MSTW2008 and NNPDF2.1 has also been computed. The results obtained are shown in Table 30.

Higher-order corrections can affect the p_{T} distribution of the WW^* pair and the α values. Their effect has been estimated by changing the renormalisation (μ_{R}) and the factorisation (μ_{F}) scales in MC@NLO. The renormalisation scales are defined as $\mu_{\mathrm{R}} = \xi_{\mathrm{R}}\mu_0$ and $\mu_{\mathrm{F}} = \xi_{\mathrm{F}}\mu_0$ where μ_0 is a dynamic scale defined as

$$\mu_0 = \frac{\sqrt{p_{\mathrm{TW1}}^2 + M_{\mathrm{W1}}^2} + \sqrt{p_{\mathrm{TW2}}^2 + M_{\mathrm{W2}}^2}}{2}. \tag{74}$$

The nominal scale is obtained with $\xi_{\mathrm{R}} = \xi_{\mathrm{F}} = 1$ while the scale uncertainty is obtained by varying ξ_{R} and ξ_{F} in the range $1/2{-}2$ while keeping $\xi_{\mathrm{R}}/\xi_{\mathrm{F}}$ in between $1/2$ and 2; the maximum spread is taken as

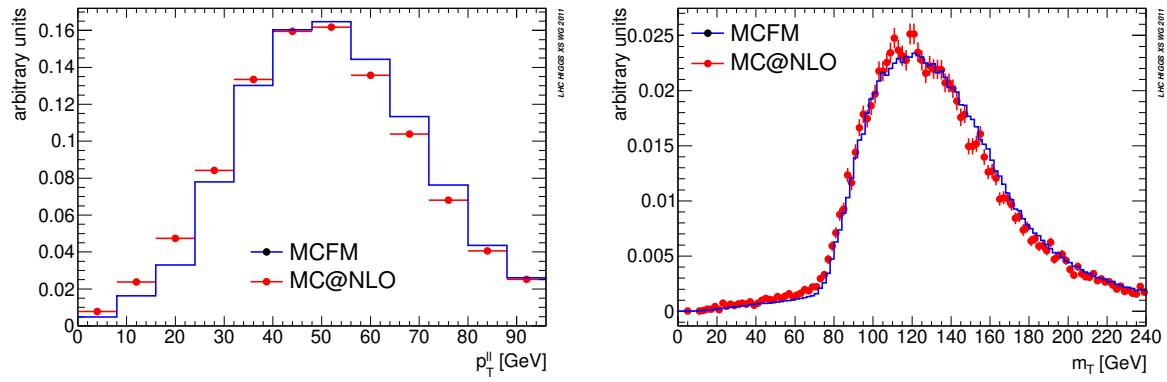

Fig. 83: Comparison between MCFM v6.0 and MC@NLO: the shapes of the p_{T} of the charged letpon system (left) and the transverse mass of the event (right), are shown, the definition of the transverse mass variable is given in the text.

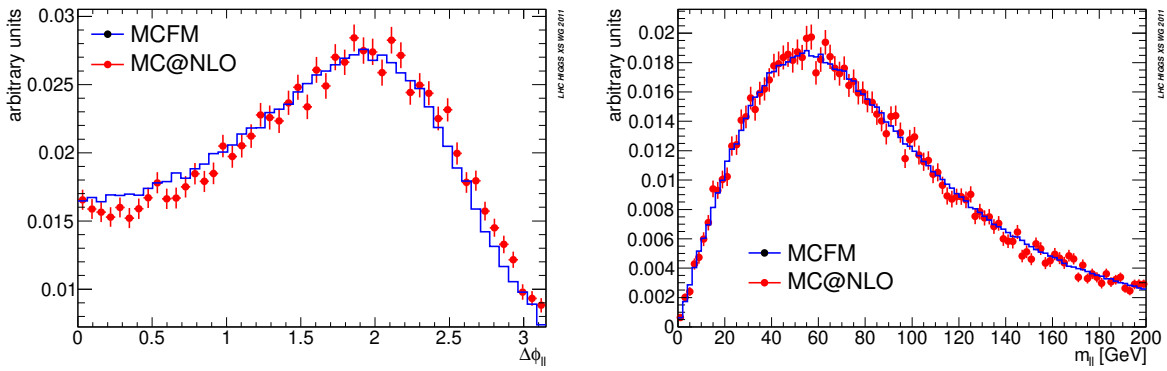

Fig. 84: Comparison between MCFM v6.0 and MC@NLO shapes of the angle between the two leptons in the transverse plane $\Delta\phi_{\mathrm{ll}}$ (left) and the invariant mass of the di-lepton system m_{ll} (right). The two variables are used for the definition of the signal and the WW^* control regions.

Table 30: The α parameters computed using different PDF sets and spread obtained spanning on the CTEQ6.6 error set.

	CTEQ 6.6 error set	MSTW2008	NNPDF2.1
$\alpha_{\mathrm{WW}}^{0\mathrm{j}}$	2.5%	$+0.1$ per mil	$+2.7\%$
$\alpha_{\mathrm{WW}}^{1\mathrm{j}}$	2.6%	-7 per mil	$+1.2\%$

scale uncertainties. The uncertainties obtained are shown in Table 31 where we summarise also the PDF and modelling uncertainties. The correlation between the α parameters of the 0-jet and 1-jet analysis is also evaluated in the calculation and they are found to be fully correlated.

10.6 Contribution from the gg $\rightarrow$ WW process

MC@NLO MC computes the process $\mathrm{pp} \rightarrow \mathrm{WW}^*$ at NLO. Up to NLO only, processes initiated by two incoming quarks contribute to the amplitude of the process. At the LHC the process $\mathrm{gg} \rightarrow \mathrm{WW}$ can deliver a non-negligible contribution. It is therefore important to estimate the gg contribution at the LHC. This contribution could be further enhanced by the analysis cuts that mainly select the Higgs topology that is induced by a gg process. At low mass the gg contribution is again normalised through the

Table 31: Scale and PDF uncertainties on WW extrapolation parameters α for the NLO $\mathrm{qq}, \mathrm{qg} \to \mathrm{WW}$ process, the errors are found to be fully correlated between the 0-jet and 1-jet bin.

	scale	PDFs	modelling
$\alpha^{0\mathrm{j}}_{\mathrm{WW}}$	2.5%	3.7%	3.5%
$\alpha^{1\mathrm{j}}_{\mathrm{WW}}$	4%	2.9%	$3.5\ \%$
$\alpha^{0\mathrm{j}}_{\mathrm{WW}}, \alpha^{1\mathrm{j}}_{\mathrm{WW}}$ correlation		1	

Table 32: Pdf uncertainties on WW extrapolation parameters α for the $\mathrm{gg} \to \mathrm{WW}$ process.

	CTEQ 6.6 error set	MSTW 2008	NNPDF2.1	MSTW LO	MSTW NNLO
$\alpha^{0\mathrm{j}}_{\mathrm{WW}}$	2.6%	-4per mil	-4 per mil	$+3.6\%$	-0.6 per mil
$\alpha^{1\mathrm{j}}_{\mathrm{WW}}$	2.8%	-2 per mil	< 1 per mil	$+3.6\%$	$+0.4$ per mil

Table 33: Scale and PDF uncertainties on WW extrapolation parameters α for the $\mathrm{gg} \to \mathrm{WW}$ process.

	scale	PDFs
$\alpha^{0\mathrm{j}}_{\mathrm{WW}}$	6%	4.4%
$\alpha^{1\mathrm{j}}_{\mathrm{WW}}$	9%	4.6%

control region, so that only the uncertainties on the α parameters are relevant for the analysis. The PDF uncertainty has been evaluated by the band spanned by the CTEQ6.6 PDF error set and comparing the central value with those from the MSTW2008 and NNPDF2.1 sets. Moreover, because the $\mathrm{gg} \to \mathrm{WW}$ lowest-order cross section is proportional to α_{s}^2 there are ambiguities on the set of PDF's that has to be used to evaluate the cross section. Therefore we include in the PDF uncertainty the values obtained using LO, NLO, and NNLO PDF sets. The MSTW family of PDF's has been used for this estimate. The results are shown in Table 32.

The scale uncertainites have been evaluated by varying independently by a factor four the renormalisation and factorisation scales with respect to the nominal value $\mu_0 = M_{\mathrm{W}}$ while keeping the ratio between $1/2$ and 2. The results are shown in Table 33 together with the overall PDF uncertainty.

The values shown in Table 33 have to be applied only to the $\mathrm{gg} \to \mathrm{WW}$ component of the WW background, the incidence of the $\mathrm{gg} \to \mathrm{WW}$ contribution in the signal region is anyway small given the low $\mathrm{gg} \to \mathrm{WW}$ cross section. The yield of the $\mathrm{gg} \to \mathrm{WW}$ is 5% of the total WW background in the 0-jet channel and 7% in the 1-jet channel.

10.7 WW background estimate for the high-mass selection

10.7.1 Jet-bin cross sections

For high values of M_{H}, namely $M_{\mathrm{H}} > 200$ GeV, the statistics in the WW control region becomes quite small, and the control region gets contaminated by a significant signal fraction. In this region a direct evaluation of the WW yield in the signal region is recommended. The WW yield in jet bins is treated in the same way and can be written as follows,

$$N^{\mathrm{WW}}_{0\mathrm{j}} = \sigma_{\geq 0} f_0 A_0, \quad N^{\mathrm{WW}}_{1\mathrm{j}} = \sigma_{\geq 0} f_1 A_1, \tag{75}$$

with f_0 and f_1 defined as

$$f_0 = \frac{\sigma_{\geq 0} - \sigma_{\geq 1}}{\sigma_{\geq 0}}, \quad f_1 = \frac{\sigma_{\geq 1} - \sigma_{\geq 2}}{\sigma_{\geq 0}}. \tag{76}$$

The cross sections are computed for jets with $p_{\mathrm{T}} > 25$ GeV and $|\eta| < 4.5$ for the ATLAS experiment. The inclusive-cross-section uncertainty is evaluated using MC@NLO, applying the scale

Table 34: Inclusive multi-jet cross sections computed with MC@NLO and their scale variation. The values shown are obtained for a single lepton combination. CTEQ6.6 PDFs are used in the computation.

$\sigma_{\geq 0}$ [fb]	$\Delta\sigma_{\geq 0}$ [%]	$\sigma_{\geq 1}$ [fb]	$\Delta\sigma_{\geq 1}$ [%]	$\sigma_{\geq 2}$ [fb]	$\Delta\sigma_{\geq 2}$ [%]	$\sigma_{\geq 3}$ [fb]	$\Delta\sigma_{\geq 3}$
532	3.3	159	6.5	41	8.7	9	11

Table 35: Multi-jet cross section ratios compared between MC@NLO and ALPGEN.

	MC@NLO	ALPGEN
$\sigma_{\geq 2}/\sigma_{\geq 1}$	0.256	0.360
$\sigma_{\geq 3}/\sigma_{\geq 2}$	0.057	0.112

Table 36: Uncertainties on the inclusive jet cross sections due to scale and modelling for jet $p_{\mathrm{T}} > 25$ GeV and $|\eta| < 4.5$.

$\Delta\sigma_{\geq 0}$ [%]	$\Delta\sigma_{\geq 1}$ [%]	$\Delta\sigma_{\geq 2}$ [%]	$\Delta\sigma_{\geq 3}$ [%]
3	6	42	100

variation prescription as above. The values of the inclusive cross section obtained and their uncertainties are shown in Table 34; they have been evaluated for a single lepton combination.

MC@NLO simulates the $\mathrm{pp} \to \mathrm{WW} + 2$ jets process through the NLO $\mathrm{pp} \to \mathrm{WW}^* \to \mathrm{l\nu l\nu}$ plus parton shower. This means that no ME computation for the $\mathrm{pp} \to \mathrm{WW} + 2$ jets is implemented in the generator. In order to take into account mismodelling of the parton-shower MC we compare the ratio $\sigma_{\geq 2}/\sigma_{\geq 1}$ and $\sigma_{\geq 3}/\sigma_{\geq 2}$ between MC@NLO and ALPGEN which computes WW production cross section up to three jets. The two W's are simulated on shell by ALPGEN, and spin correlations are not included. Moreover, only tree-level diagrams are computed by ALPGEN; therefore the comparison is performed only for jet multiplicity higher than one where ALPGEN provides a ME computation for the jet yield. The comparison is shown in Table 35. The discrepancy between the two generators on these ratios is added in quadrature to the scale variation for the 2-jets and the 3-jets inclusive cross section.

The inclusive multi-jet uncertainties due to scale and modelling are summarised in Table 36.

10.7.2 Theoretical errors on acceptances

In addition to the scale uncertainties on the jet fractions, f_i, we need to evaluate also the scale uncertainties on the acceptances A_i as defined in Eq. 75. These include scale variation effects with all other cuts except for the jet counting. In order to decouple the jet-bin scale uncertainty from other uncertainties, the acceptance needs to be evaluated in a given jet bin. This is done in MC@NLO by requiring a jet-exclusive bin at the beginning of the selection and then evaluating the ratio

$$N_{\text{cuts and jet bin}}/N_{\text{jet bin}}. \tag{77}$$

The maximum relative spread of this ratio is used as the fractional acceptance scale uncertainty. In ATLAS the following cuts are applied in both 0-jet and 1-jet bins for $M_{\mathrm{H}} > 220$ GeV and the ee and $\mu\mu$ channels: $p_{T1} > 25$ GeV, $p_{T2} > 15$ GeV, $|\eta| < 2.5$, $E_{\mathrm{T}}^{\mathrm{miss}} > 40$ GeV, $\Delta\phi_{\mathrm{ll}} < 2.6$, $m_{\mathrm{ll}} < 140$ GeV && $|m_{\mathrm{ll}} - M_{\mathrm{Z}}| > 15$ GeV, while in the 0-jet channel $|p_{\mathrm{Tl1}} + p_{\mathrm{Tl2}}| > 30$ GeV and in the 1-jet channel $|p_{\mathrm{Tl1}} + p_{\mathrm{Tl2}} + p_{\mathrm{Tjet}} + E_{\mathrm{T}}^{\mathrm{miss}}| < 30$ GeV cuts are added. The scale uncertainty is 5% in the 0-jet bin and 2% in the 1-jet bin.

In case LO MC are used to compute the acceptance in the analysis, the LO–MC@NLO discrepancy on the given acceptance value has to be added to the scale variation value.

10.8 PDF errors

PDF errors are much smaller than scale uncertainties and are less linked to the jet activity associated to the WW production. Also correlations between jet bins can be neglected. Therefore in evaluating PDF uncertainties we directly compute the product $f_i A_i$, which is the relative variation in the event yield in the signal region, by varying PDFs within the CTEQ6.6 error set and comparing the central values to the ones obtained with MSTW2008 and NNPDF2.1. The uncertainty obtained is 2% for both 0-jet and 1-jet bins.

11 ZZ* decay mode[41]

11.1 Introduction

The ZZ decay mode of the Standard Model (SM) Higgs boson has a lower branching fraction than the WW decay over the full range of the Higgs mass hypotheses inspected; nevertheless the final state with four leptons (electrons and muons) from the ZZ decay is very clean and almost background free so it is considered to be the main discovery channel at the LHC. The four-lepton channel is also the most precise final state to reconstruct the mass peak of the Higgs boson thanks to the high resolution of the lepton momentum reconstruction with the ATLAS and the CMS detectors.

Both ATLAS and CMS collaborations performed prospective studies in the past and published also results about the direct searches for the Higgs boson in ZZ to four-lepton final state, after collecting data in 2010 and 2011 for about 5 fb^{-1} of integrated luminosity. Detailed descriptions of the reference analyses concerning four-lepton final state are provided in Refs. [316, 317].

Complementary final states with two leptons and two jets, two leptons and two neutrinos, two leptons and two taus have been also inspected; they are mostly relevant for a Higgs-boson mass above the ZZ doubly-resonant peak where the contribution from reducible and irreducible background processes can be significantly reduced. Detailed descriptions of the reference analyses concerning those final states are provided in Refs. [318–322]. The focus of this section is on the evaluation of the impact of some theoretical issues on the predictions and on the results for the analyses previously mentioned, and on the estimation of the most important source of background (the production of ZZ) and its related uncertainties.

11.2 The H $\rightarrow$ ZZ signal process

The simulation of the production and the decay of the Higgs boson in the ZZ final state has been done by using several Monte Carlo generator programs, both in ATLAS and in CMS collaborations. The predictions of different programs in terms of cross-section values and distributions for the most important observables have been compared and are reported in this section.

The Standard Model input parameters as specified in the Appendix of Ref. [7] have been used. The following set of PDF's, CT10, NNPDF2.0 and MSTW2008, have been considered to estimate the central value of the geometrical acceptance and the uncertainty on it originating from the PDF parametrisation; the PDF4LHC prescription of Ref. [101] has been followed. In order to estimate the QCD scale uncertainty on the acceptance the CT10 PDF has been used as central value and the QCD scale is varied following the prescription of Ref. [7].

11.2.1 Leading-order and next-to-leading-order generators

The multi-purpose generator program PYTHIA version 6.4 [183] and the generator program POWHEG BOX [156] have been used for the current Higgs simulation by ATLAS and CMS collaborations; PYTHIA is a leading-order (LO) generator while POWHEG BOX [156] implements calculations at the next-to-leading order (NLO).

Events with Higgs bosons produced via gluon fusion and vector-boson fusion mechanisms, and decaying into ZZ to four-lepton final state are generated by both the programs; if M_{Z_1} is the di-lepton combination from Z decay that gives the invariant mass closest to the Z-boson nominal mass and M_{Z_2} is the other $\mathrm{Z}^{(*)}$, the distributions of the transverse momentum and Higgs mass for a Higgs boson with mass $M_{\mathrm{H}} = 150$ GeV are compared in Figure 85 after applying the following cuts defining the acceptance of the selection: $M_{\mathrm{Z}_1} > 50$ GeV, $M_{\mathrm{Z}_2} > 12$ GeV and $p_{\mathrm{T}} > 5$ GeV, $|\eta| < 2.5$ for all the leptons. For the vector-boson fusion topology the predictions are different at low transverse momentum over the full

[41] N. De Filippis, S. Paganis (eds.), S. Bolognesi, T. Cheng, R. K. Ellis, M.D. Jorgensen, N. Kauer, M. Kovac, C. Mariotti, P. Nason, T.C. Petersen, J. Price and I. Puljak.

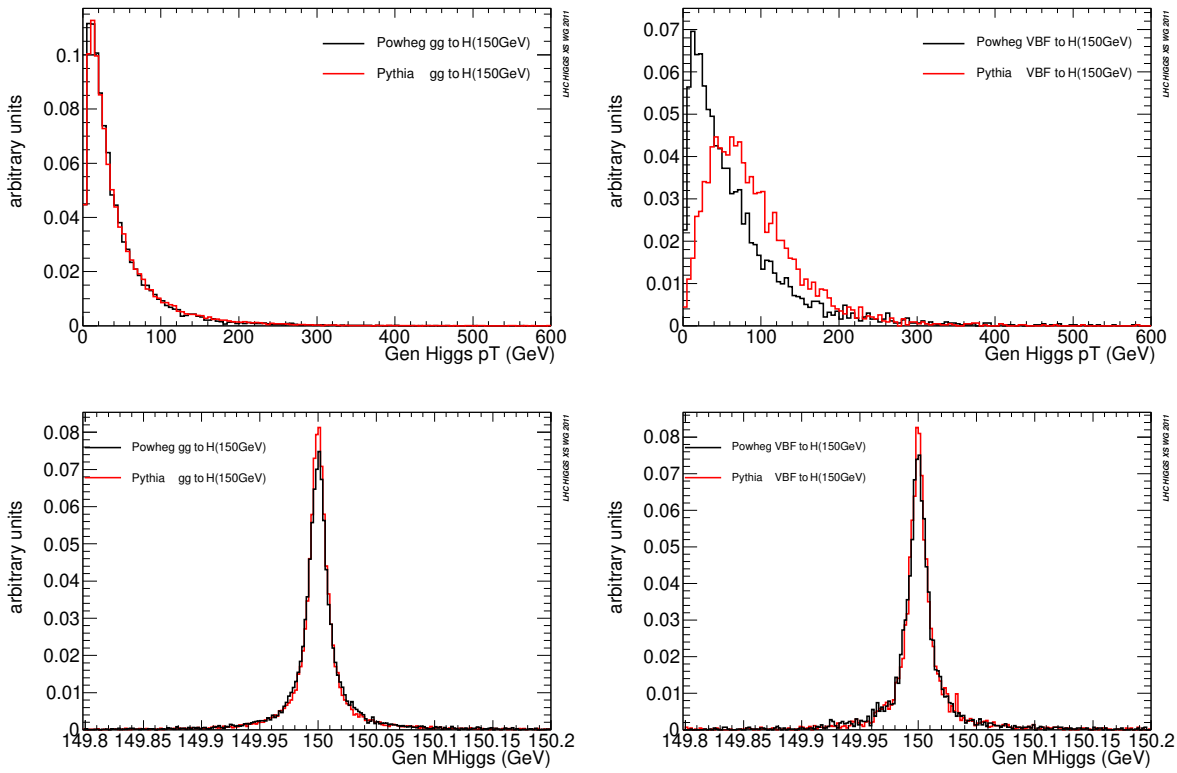

Fig. 85: Higgs-boson transverse momentum and mass spectrum derived with PYTHIA (LO) and POWHEG (NLO) generators for the four-lepton final state from the decay of the Higgs boson with mass $M_{\mathrm{H}} = 150$ GeV, asking $M_{\mathrm{Z}_1} > 50$ GeV, $M_{\mathrm{Z}_2} > 12$ GeV and $p_{\mathrm{T}} > 5$ GeV, $|\eta| < 2.5$. Plots are normalised to the same area.

Higgs-boson mass range inspected; in the case of gluon–gluon fusion production, differences become relevant for very large M_{H} where anyway the MC's are using an approximation of the Higgs-boson lineshape that can be substantially different from the predicted one, as discussed in Section 15.

11.2.2 Theoretical uncertainties

The PDF4LHC prescription is used to estimate the uncertainty on the acceptance for signal events related to the PDF+α_{s} choice. The results are quoted as the envelope containing all variations for the three sets of PDFs: CT10, MSTW2008, NNPDF.

Concerning the four-lepton analysis the correction factor on the acceptance with respect to the central value and the final parametrisation is reported in Figure 86 as a function of the Higgs mass. A 2% mass-independent error to account for these uncertainties is derived and can be assumed as a conservative estimate over the full mass range.

The uncertainty on the acceptance and the total Higgs cross section uncertainties from PDF+α_{s} have to be considered uncorrelated; the level of correlation between the acceptance and cross section for $M_{\mathrm{H}} = 120$ GeV and 400 GeV is shown in Figure 87; there is a very little correlation for the low Higgs boson mass while a negative correlation seems to develop for very high mass.

11.2.3 Higher-order-corrected Higgs-boson transverse-momentum spectrum

The total inclusive cross sections for Higgs-boson production have been computed at NNLO+NNLL [7, 28, 66, 207, 212–214, 219, 220, 224]. The differential cross section for the transverse momentum is expected to differ with respect to the one predicted at lower perturbative order; the Higgs-boson transverse-

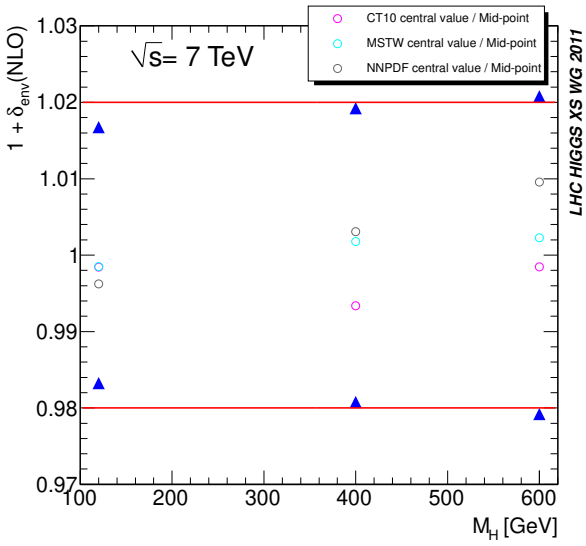

Fig. 86: The difference between the central value of the acceptance for four-lepton events and the acceptance computed with plus and minus $1\,\sigma$ of the total PDF+$\alpha_{\rm s}$ variation (blue markers), following the PDF4LHC prescription; the circles markers correspond to the ratio between central value of CT10, MSTW, and NNPDF and the middle value of the envelope.

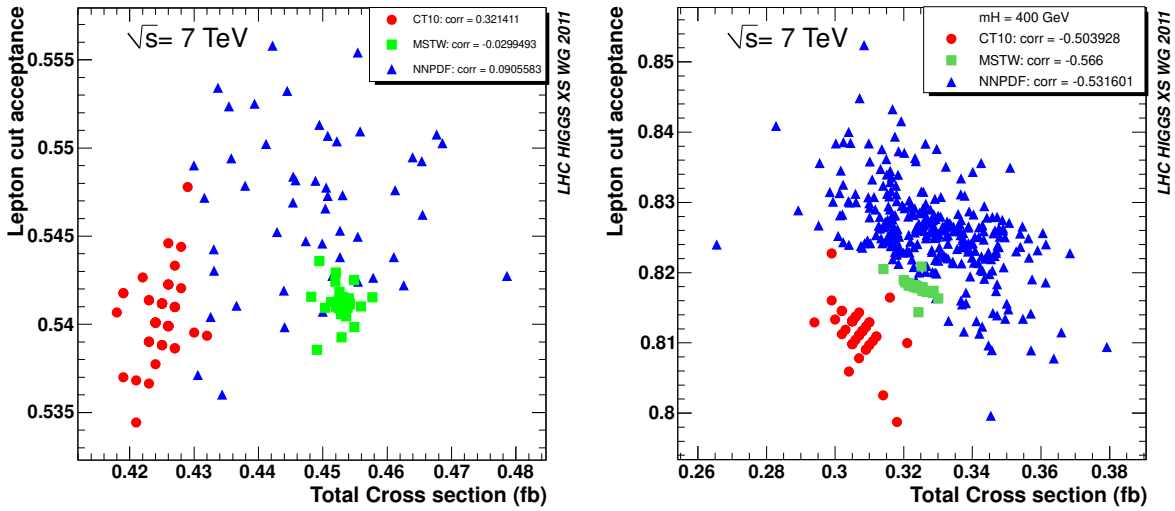

Fig. 87: Scatter plots of the signal four-lepton acceptance as a function of the total cross section for signal events with $M_{\rm H} = 120$ GeV (left) and $M_{\rm H} = 400$ GeV (right), for different PDF sets. The three PDF sets are shown in different colours/symbols.

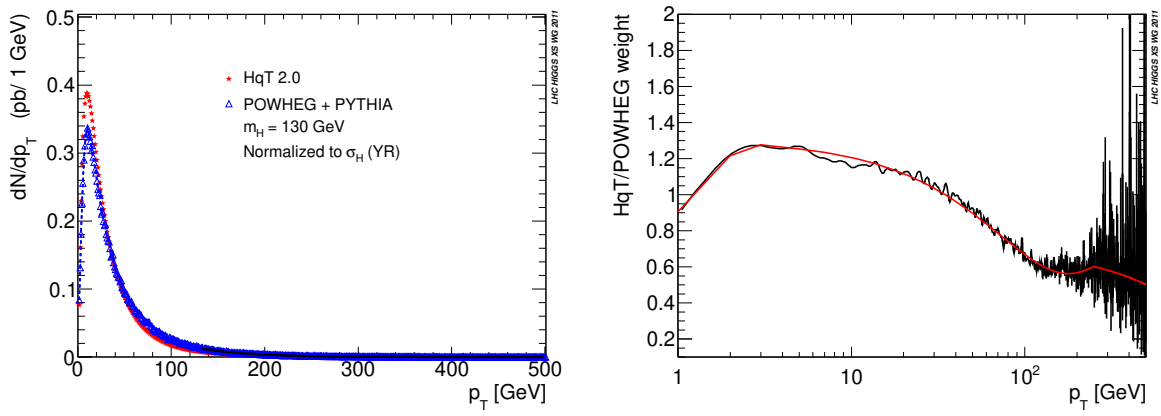

Fig. 88: (Left) p_{T} spectrum of the SM Higgs boson of mass $M_{\mathrm{H}} = 130$ GeV produced via gluon-gluon fusion as obtained by using the POWHEG generator (and PYTHIA for parton shower, hadronisation and underlying event) and HQT tool. (Right) the ratio HQT vs POWHEG as a function of the Higgs-boson p_{T}.

momentum distribution has been computed using the technique of resummation of the large logarithmic contributions appearing at transverse momenta much smaller than the Higgs-boson mass [194].

In this section the predictions of the tool implementing this calculation at NNLL, namely HQT [194], are compared with those from the NLO generator program POWHEG BOX. The way to compare the tools is described in Section 4.2. The comparison requires the simulation with POWHEG generator of the Higgs production and the usage of parton-shower algorithm. An alternative way that could be inspected is to compute the weight function $f(p_{\mathrm{T}})$ to be applied for each simulated event, with p_{T} being the Higgs p_{T} at the POWHEG level (i.e. before showering) such that the p_{T} of the Higgs after showering (but without underlying event and hadronisation) agrees with HQT. In this section the p_{T} distributions from POWHEG, after simulating the parton shower, the hadronisation, and the underlying event with PYTHIA 6.4 program, are compared with HQT.

The transverse-momentum (p_{T}) distribution of the Higgs boson produced via gluon fusion is reported in Figure 88 (left) as obtained by using the POWHEG generator and the HQT tool; the two distributions are normalised to the gluon-fusion cross section reported in YR1 [7]. The p_{T} is significantly affected over the full range and for low Higgs-boson masses ($M_{\mathrm{H}} < 150$ GeV); HQT gives a larger differential cross section at low p_{T} ($p_{\mathrm{T}} < 15$ GeV) with respect to POWHEG (up to 40% increment), while at large p_{T} the opposite behaviour is observed. The ratio between the p_{T} distributions for each p_{T} bin can be used as a weight for the POWHEG spectrum that has been used for the current $\mathrm{H} \to \mathrm{ZZ}$ analyses in CMS and ATLAS. The ratio (or weight) is reported in Figure 88 (right) and the best fit curve is overimposed to the histogram. A table with the weights for several Higgs-boson masses and p_{T} bins is reported in the Appendix B (Table B.1).

The differences in the Higgs-boson p_{T} spectrum affects also the M_{Z_1}, M_{Z_2}, and four-lepton p_{T} and η distributions, thus the number of accepted events in the detector. The impact of the reweighting of POWHEG events on the acceptance of the four-lepton analysis has been evaluated. The ratio between the acceptance values for POWHEG events with four-electrons, four-muons, and two-electrons + two-muons final state from $\mathrm{H} \to \mathrm{ZZ}$ decay, when turning on/off the reweighting with HQT, are shown in Figure 89 as a function of M_{H}. The impact of the reweighting on the acceptance amount to $1{-}2\%$ at most at low Higgs-boson masses and to at most 1% at $M_{\mathrm{H}} > 250$ GeV.

All the previous results are estimated with the CT10 PDF [107] set and the input values from Ref. [7].

The predictions of the POWHEG generator at NLO reweighted with and without HQT are com-

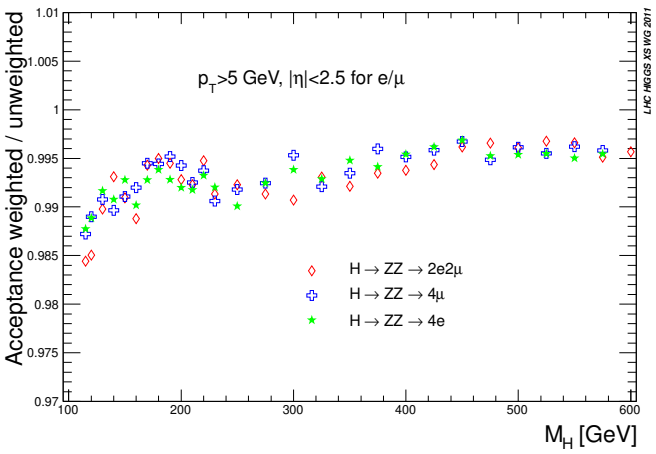

Fig. 89: Ratio between the acceptance values for POWHEG events with four electrons, four muons, and two electrons and two muons final state from $\mathrm{H} \to \mathrm{ZZ}$ decay, when turning on/off the reweighting with HQT.

pared with the predictions from HNNLO [323] at NNLO in Figures 90 and 91.

The predictions of POWHEG are also reported after Higgs-boson p_{T} reweighting using HQT [194] in the low-p_{T} region and HNNLO in the high-p_{T} region, as discussed previously and reported in Table B.1. As expected, the Higgs-boson p_{T} is softer in HNNLO than HQT in the low-p_{T} region and the effect is more pronounced in the high-Higgs-boson-mass case (the high-p_{T} tail matches instead with the reweighted POWHEG, by construction). It is interesting to notice that, while at low mass the p_{T} of the leptons has the same behaviour as the Higgs-boson p_{T} (i.e., softer for HNNLO), at high mass HNNLO predicts a stronger p_{T} for the leptons. The mass distribution of the Z with larger mass has larger tails in HNNLO, while the opposite is true for the subleading Z mass. It is worth noticing that the Higgs-boson p_{T} reweighting in POWHEG does not affect the Z invariant-mass distributions. Finally the rapidity of the Higgs boson is less central in HNNLO and the same holds for the lepton pseudorapidity, but the difference goes to zero at high mass.

11.3 The ZZ background process

The understanding of the background processes from the theoretical and the experimental sides is mandatory to be able to perform a search for new physics.

The main goal of this section is to compare the predictions from different generators for the ZZ process (in particular for the four-lepton final state). The production of two Z bosons represents the irreducible background for the direct searches for the Higgs boson in the $\mathrm{H} \to \mathrm{ZZ}$ channels at LHC.

The Standard Model input parameters as specified in the Appendix of Ref. [7] have been used. The PDF's used are: CT10, NNPDF2.0, and MSTW2008. The central value of the cross section and the uncertainty originating from the PDF are estimated following the PDF4LHC prescription. In order to estimate the QCD scale uncertainty the CT10 PDF has been used as central value and the QCD scale is varied following the prescription of Ref. [7].

Differential distributions and theoretical uncertainties are calculated for a few sets of cuts:

- Cut 1: $M_{\mathrm{Z}_1} > 12$ GeV and $M_{\mathrm{Z}_2} > 12$ GeV,
- Cut 2: $M_{\mathrm{Z}_1} > 50$ GeV, $M_{\mathrm{Z}_2} > 12$ GeV, $p_{\mathrm{T}}(\mathrm{l}) > 5$ GeV, and $|\eta(\mathrm{l})| < 2.5$,
- Cut 3: $60 < M_{\mathrm{Z}_1} < 120$ GeV and $60 < M_{\mathrm{Z}_2} < 120$ GeV.

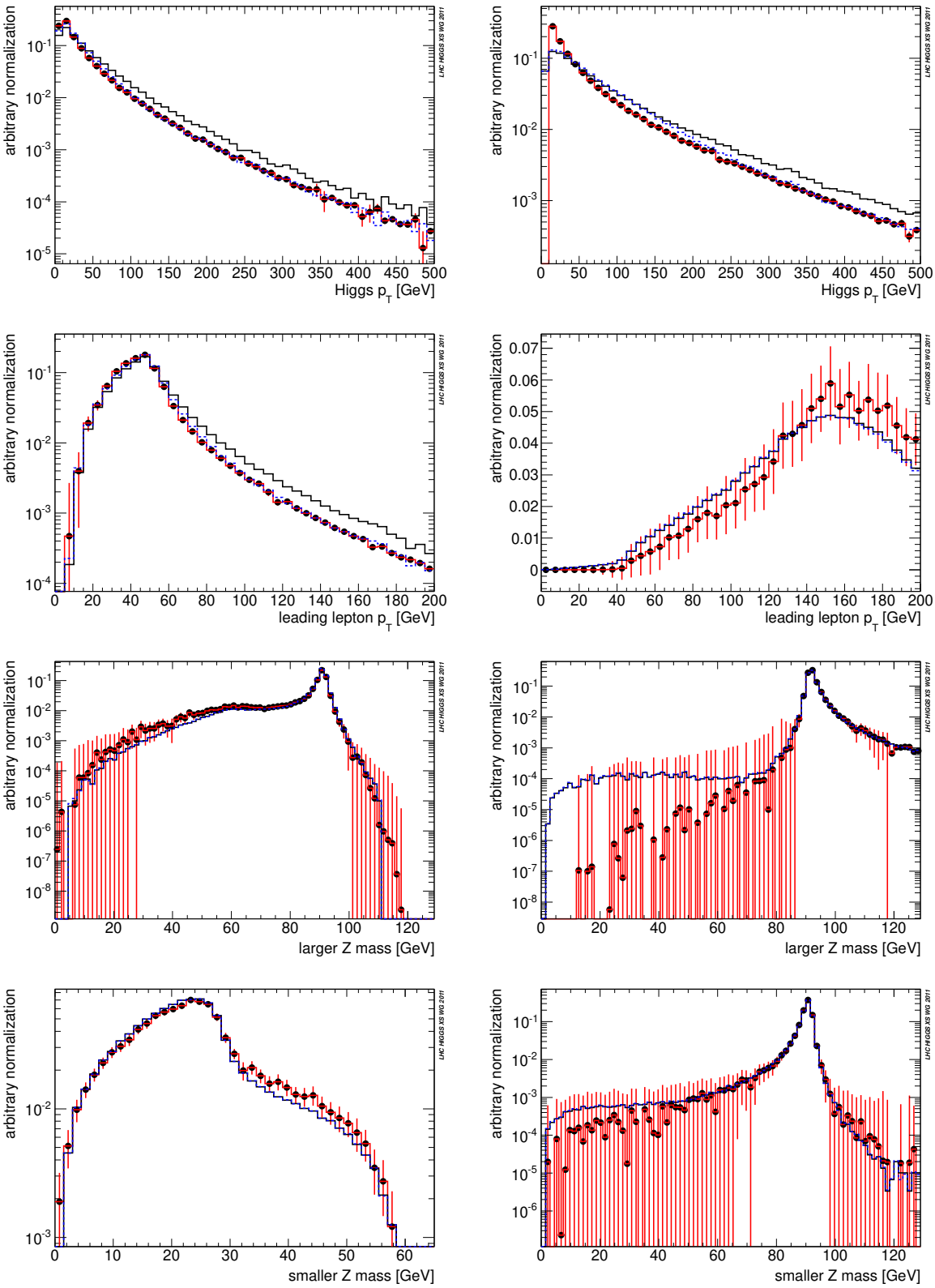

Fig. 90: Differential distributions (in arbitrary units) at 7 TeV for Higgs-boson masses 200 GeV (left) and 500 GeV (right) for three different Monte Carlo generators: POWHEG (black), HNNLO (red), POWHEG reweighted with HQT and HNNLO (blue).

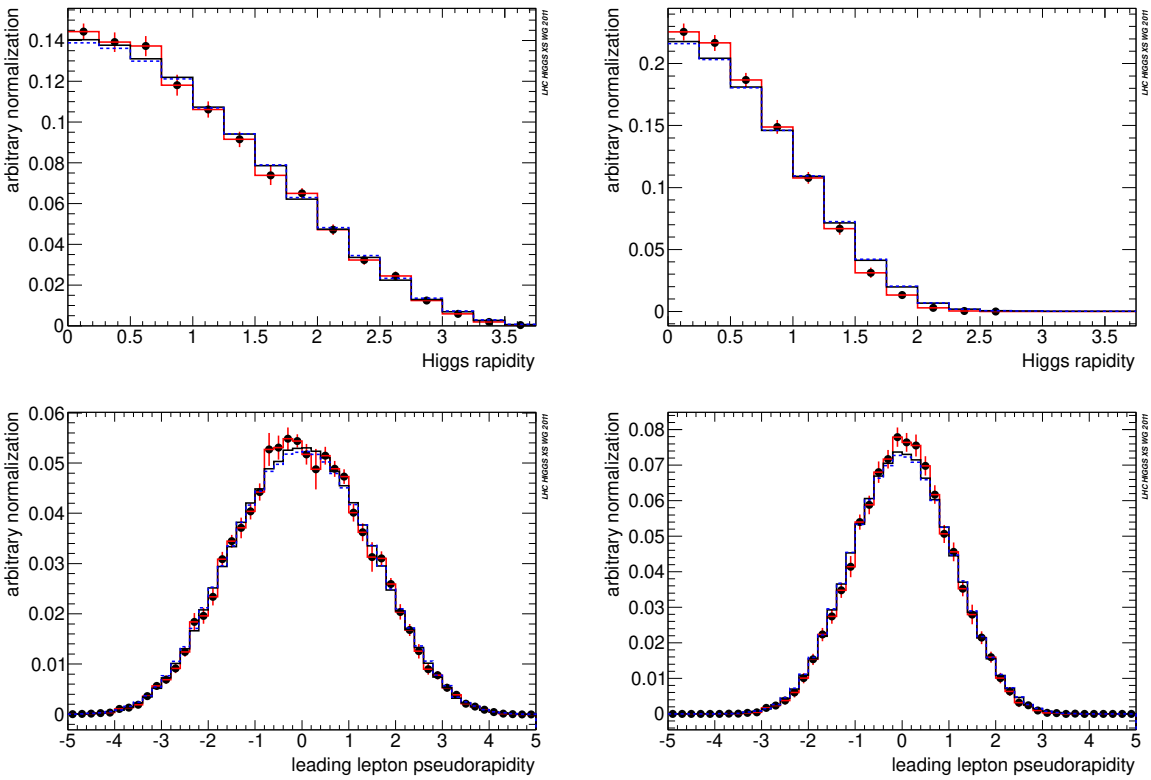

Fig. 91: Differential distributions (in arbitrary units) at 7 TeV for Higgs-boson masses 200 GeV (left) and 500 GeV (right) for three different Monte Carlo generators: POWHEG (black), HNNLO (red), POWHEG reweighted with HQT and HNNLO (blue).

11.3.1 $q\bar{q} \to ZZ$ *generators*

11.3.1.1 MCFM *predictions*

The MCFM program [232, 324, 325] v6.1 computes the cross section at LO and NLO for the process $q\bar{q} \to l\bar{l}l'\bar{l}'$ mediated by the exchange of the two bosons Z, γ^* and their interference, for the doubly-resonant (or t-channel) and singly-resonant (or s-channel) diagrams, and for the process $gg \to l\bar{l}l'\bar{l}'$.

Figure 92 (left) shows the four-lepton invariant-mass distribution obtained with MCFM at LO for ZZ production, including or not the singly-resonant (or s-channel) contribution. The prediction without the singly-resonant contribution is obtained with MCFM v5.8. The "Cut 1" selection is applied, i.e. $m_{ll} > 12$ GeV.

At LO the cross section as a function of $m_{2e2\mu}$ for the process $q\bar{q} \to ZZ \to 2e2\mu$ is shown in Figure 92 (right) and for three different set of cuts. The black line corresponds to the "Cut 1" selection, i.e. $m_{ll} > 12$ GeV, that is the minimal cut requested in the analyses to subtract the contribution to heavy-flavour resonances decaying into leptons. The blue line is obtained taking into account the acceptance of the detectors, thus asking the leptons to have $p_T > 5$ GeV and $\eta < 2.5$ ("Cut 2" selection). The red line is the differential cross section for the production of two Z bosons, both on shell, i.e. asking for 60 GeV $< m_{ll} <$ 120 GeV ("Cut 3" selection).

Figure 93 (left) shows the cross section at NLO for the full process $pp \to ZZ^{(*)} \to 2e2\mu$ and the gg contribution separately in the inset, as a function of the invariant mass of the 4 leptons. The peak at 91 GeV is dominated by the contribution of the singly-resonant (or s-channel) diagrams, while for $m_{4l} > 120$ GeV the doubly-resonant diagrams (or t-channel) are essentially the only contribution.

In Figure 93 (right) the cross section for $m_{2e2\mu}$ from MCFM v6.1 is shown for three different sets

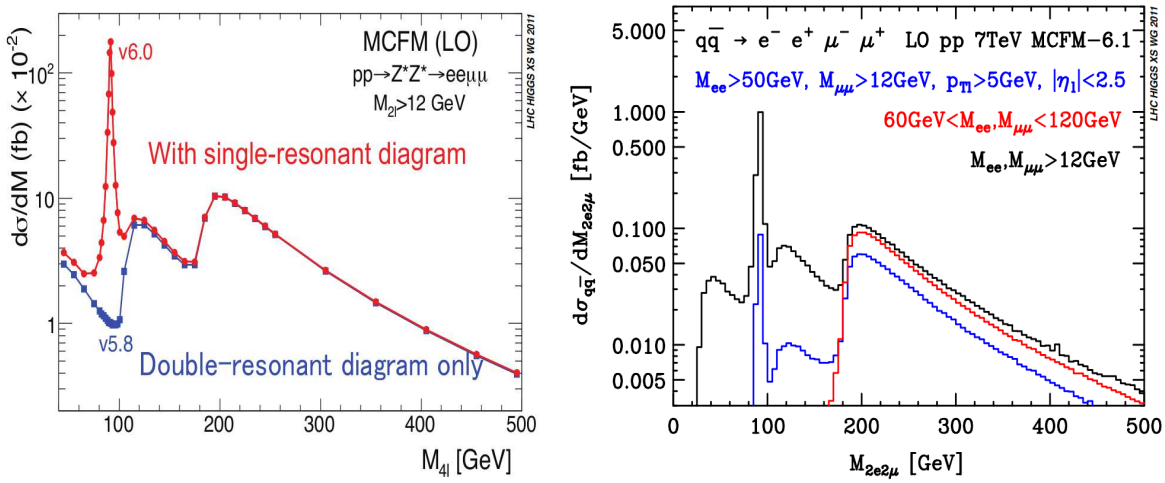

Fig. 92: (left) The cross sections for $q\overline{q} \to ZZ^{(*)} \to 2e2\mu$ as a function of $m_{2e2\mu}$ at 7 TeV from MCFM for the full calculation and without the singly-resonant contribution; (right) LO cross sections for $q\overline{q} \to ZZ^{(*)} \to 2e2\mu$ as a function of $m_{2e2\mu}$ at 7 TeV from MCFM at LO.

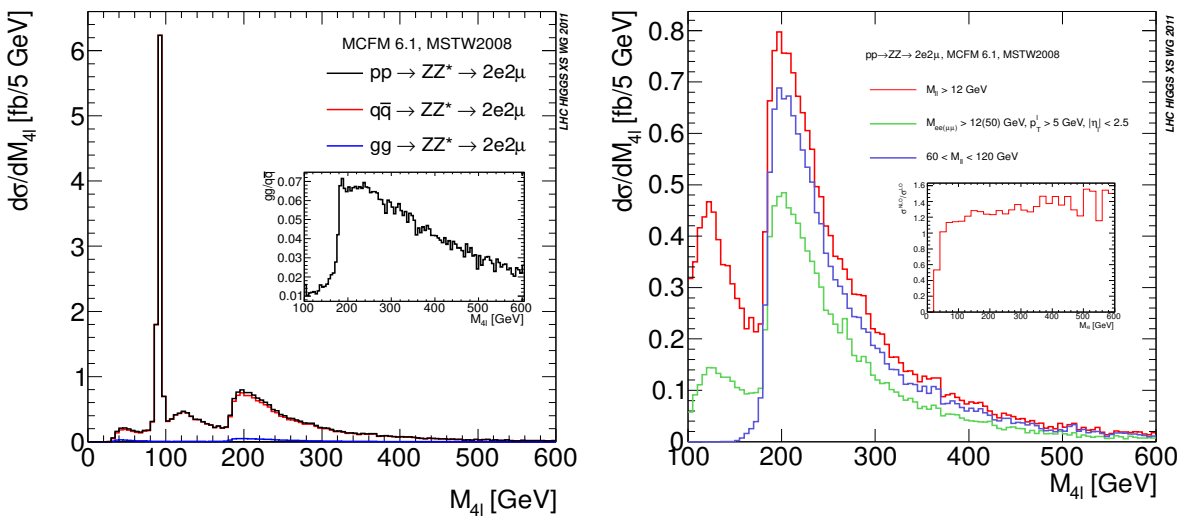

Fig. 93: (Left) The cross sections for $ZZ^{(*)}$ production as a function of $m_{2e2\mu}$ at 7 TeV from MCFM at NLO; (right) cross sections for $ZZ^{(*)}$ production as a function of $m_{2e2\mu}$ at 7 TeV from MCFM at NLO for three different sets of cuts as described in the text.

of cuts for the doubly-resonant region only. In the inset the ratio "k" of the NLO and LO predictions is plotted for the "Cut 1" selection. The "k"-factor depends on m_{4l} and increases to about 20% at high masses.

11.3.1.2 POWHEG *predictions*

In POWHEG BOX [156] a new implementation of the vector-boson pair production process at NLO has been provided [167]. The Z/γ^* interference as well as singly-resonant contributions are properly included. Interference terms arising from identical leptons in the final state are considered.

In Figure 94 the four-lepton-invariant-mass distributions for the final state $2e2\mu$ are shown for POWHEG, using two different PDF sets (MSTW and CT10), and compared with MCFM v6.1. The

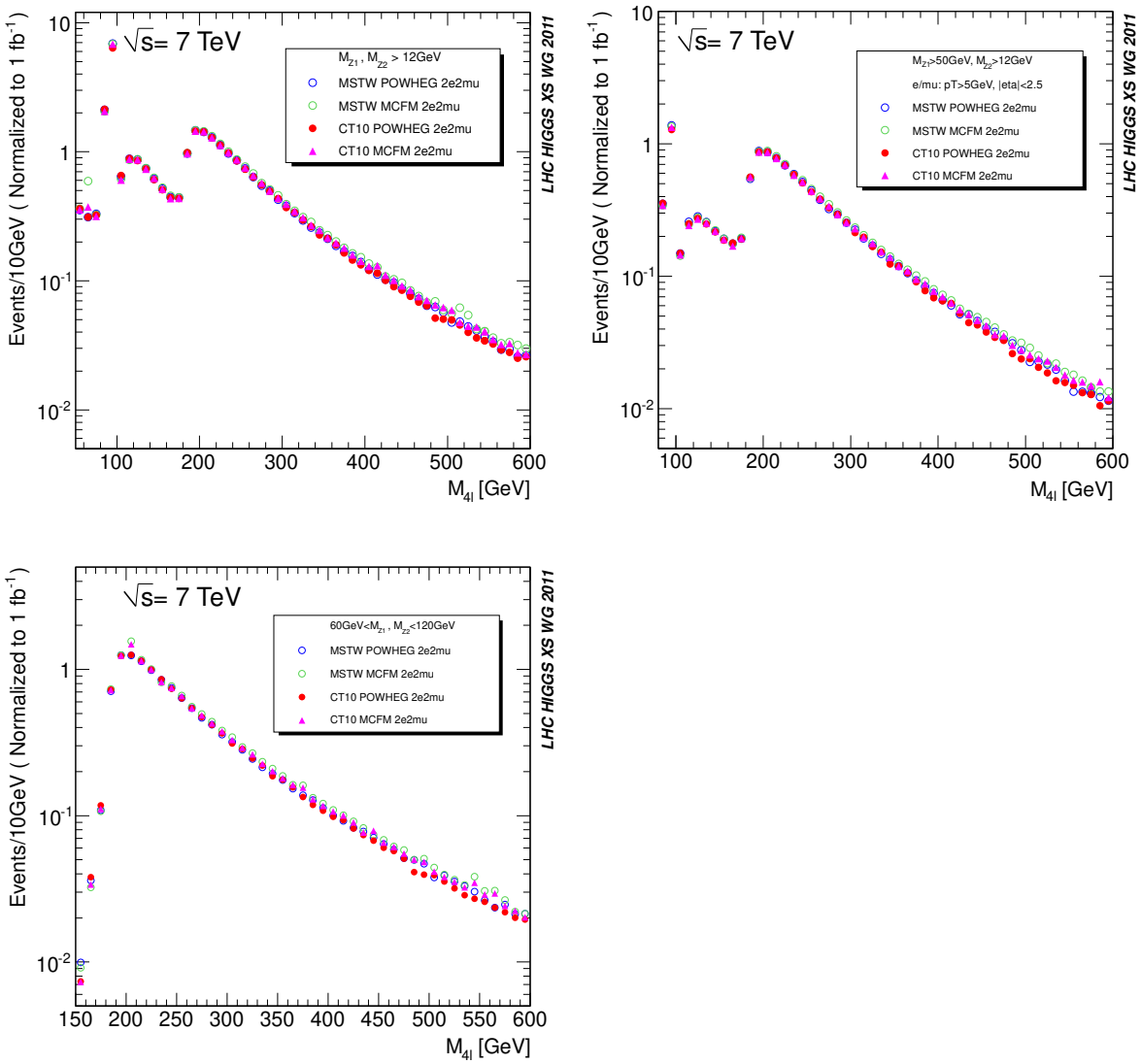

Fig. 94: $ZZ \to 2e2\mu$ invariant-mass distributions at 7 TeV with POWHEG and MCFM v6.1. Two different PDF sets are used. The top-left plot is obtained applying only $m_{2l} > 12$ GeV; the top-right plot asking $M_{Z_1} > 50$ GeV, $M_{Z_2} > 12$ GeV, $p_T(l) > 5$ GeV, $|\eta(l)| < 2.5$, and the bottom plot asking $60 < M_{Z_1} < 120$ GeV and $60 < M_{Z_2} < 120$ GeV.

plot on the top-left is obtained asking $m_{ll} > 12$ GeV, i.e. the "Cut 1". The plot on the top-right is asking the second sets of cuts, "Cut 2". The one on the bottom is for "Cut 3" selection, i.e. the two Z bosons in the vicinity of their mass shells. The two programs show a very good agreement. The difference due to the different PDF sets is discussed in Section 11.3.4.

In Figure 95 the m_{4l} distribution is shown for the $2e2\mu$ and $4e$ final states in order to see the effect of the interference between identical leptons. The two top figures are obtained with the "Cut 1" selection, the middle ones with "Cut 2" selection, and the bottom ones with "Cut 3" selection. The total cross section increases by about 4% because of the interference. The effects of using two different PDF sets is also seen.

A full comparison has been also performed between the predictions of both POWHEG at NLO and PYTHIA at LO. This is shown in Figure 96 where the distributions are normalised to the the corresponding cross sections. The differences come from the lack of the singly-resonant contribution in

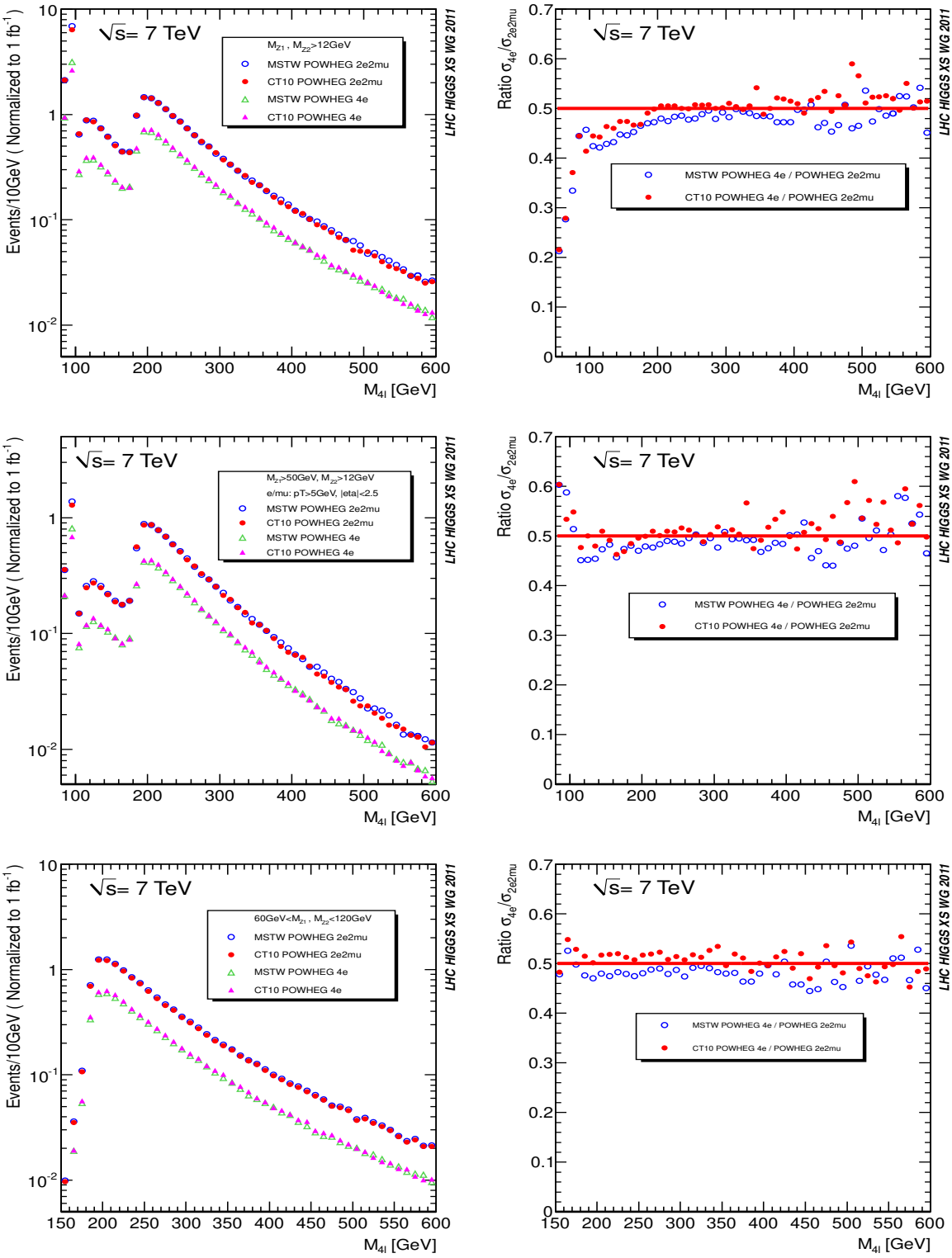

Fig. 95: ZZ $\rightarrow$ 2e2μ and ZZ $\rightarrow$ 4e invariant-mass distributions and their ratio at 7 TeV with POWHEG. Two different PDF sets are used. The upper plots are obtained applying only $m_{2l} > 12$ GeV, the middle plots applying $M_{Z_1} > 50$ GeV, $M_{Z_2} > 12$ GeV, $p_T(l) > 5$ GeV, $|\eta(l)| < 2.5$, and the bottom plots applying $60 < M_{Z_1} < 120$ GeV and $60 < M_{Z_2} < 120$ GeV.

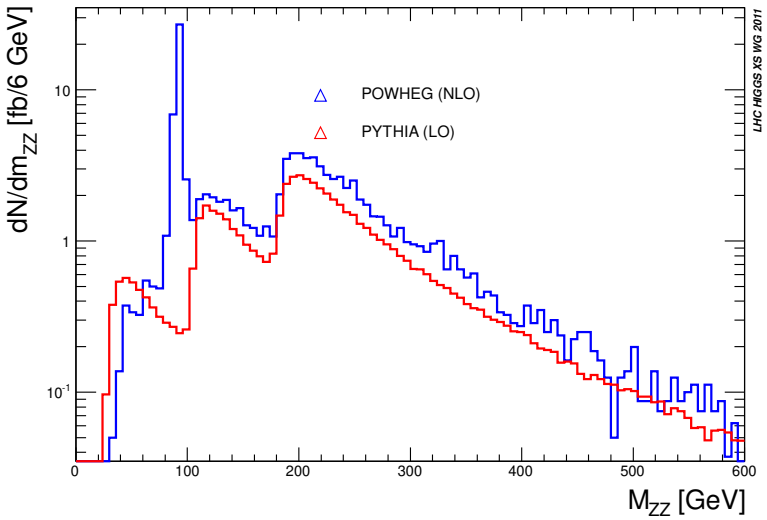

Fig. 96: $\mathrm{ZZ} \to 4\mu$ invariant-mass distributions at 7 TeV as derived by PYTHIA and POWHEG

PYTHIA and the LO calculations for the doubly-resonant contribution.

11.3.2 $\mathrm{gg} \to$ ZZ *generators*

The gluon-induced ZZ background, although technically of NNLO compared to the lowest-order Z-pair production, can amount to a substantial fraction of the total irreducible background. We take into account these diagrams, but a full NNLO calculation for the process $\mathrm{q\overline{q}} \to \mathrm{ZZ}$ is not available. The contributions of the gg diagrams are included in MCFM v6.1 and the dedicated tool GG2ZZ [326], which computes the $\mathrm{gg} \to \mathrm{ZZ}$ at LO, which is of order α_s^2, compared to α_s^0 for the LO $\mathrm{q\overline{q}} \to \mathrm{ZZ}$.

The two programs provide the functionality to compute the cross section after applying a cut on the minimally generated invariant mass of the same-flavour lepton pairs (which can be interpreted as the Z/γ^* invariant mass), ${m_\mathrm{ll}}^\mathrm{min} = 12$ GeV.

11.3.3 $\mathrm{gg} \to$ ZZ*: Comparison of* GG2ZZ *and* MCFM

In this section, a comparison of results for the $\mathrm{gg} \to \mathrm{Z}(\gamma^*)\mathrm{Z}(\gamma^*) \to \mathrm{l\bar{l}l'\bar{l}'}$ (l = charged lepton) continuum background calculated at LO with GG2ZZ and MCFM is presented.[42] The MCFM calculation of the gg subprocess is described in Ref. [325]. MCFM also includes a NLO calculation of the $\mathrm{q\overline{q}}$ subprocess [324, 325]. For GG2ZZ, first results have been presented in Ref. [326]. GG2ZZ employs the same calculational techniques as GG2WW [328, 329]. Because of the Furry and (generalised) Landau–Yang theorems, all graphs with $\mathrm{gg}V$ triangle quark loop (including those with s-channel Z propagator) vanish. The MCFM calculation exploits that the top quark decouples in good approximation. The t contribution to the quark loop is therefore neglected. The b contribution is included in the massless limit. In GG2ZZ, the b and t contributions are included with finite masses.

Parton-level cross sections and M_ZZ distributions for pp collisions at $\sqrt{s} = 7$ TeV are compared for the three sets of cuts "Cut 1", "Cut 2" and "Cut 3". In addition, a $p_\mathrm{T}(\mathrm{Z}) > 0.05$ GeV cut is applied to prevent that numerical instabilities spoil the amplitude evaluation. This technical cut reduces the cross sections by at most 0.05%. Results are given for a single lepton flavour combination, e.g. $\mathrm{l} = \mathrm{e}^-, \mathrm{l}' = \mu^-$. Lepton masses are neglected. The input-parameter set of Ref. [7], App. A, is used

[42] Off-shell results for the same-flavour process $\mathrm{gg} \to \mathrm{ZZ} \to \mathrm{l\bar{l}l\bar{l}}$ have been presented in Ref. [327].

Table 37: Cross sections in fb for $\mathrm{gg} \to \mathrm{Z}(\gamma^*)\mathrm{Z}(\gamma^*) \to \mathrm{l}\bar{\mathrm{l}}\mathrm{l}'\bar{\mathrm{l}}'$ in pp collisions at $\sqrt{s} = 7$ TeV and a single lepton flavour combination calculated at LO with GG2ZZ-2.0 and MCFM-6.1. Three cut sets are applied: $M_{\mathrm{Z}_1} > 12$ GeV, $M_{\mathrm{Z}_2} > 12$ GeV (Cut 1); $M_{\mathrm{Z}_1} > 50$ GeV, $M_{\mathrm{Z}_2} > 12$ GeV, $p_{\mathrm{T}}(\mathrm{l}) > 5$ GeV, $|\eta(\mathrm{l})| < 2.5$ (Cut 2); 60 GeV $< M_{\mathrm{Z}_1} < 120$ GeV, 60 GeV $< M_{\mathrm{Z}_2} < 120$ GeV (Cut 3).

	$\sigma(\mathrm{gg} \to \mathrm{Z}(\gamma^*)\mathrm{Z}(\gamma^*) \to \mathrm{l}\bar{\mathrm{l}}\mathrm{l}'\bar{\mathrm{l}}')$ [fb], pp, $\sqrt{s} = 7$ TeV		
	GG2ZZ-2.0	MCFM-6.1	$\sigma_{\mathrm{MCFM}}/\sigma_{\mathrm{GG2ZZ}}$
Cut 1	$1.157(2)$	$1.168(2)$	$1.010(2)$
Cut 2	$0.6317(4)$	$0.6293(4)$	$0.9962(8)$
Cut 3	$0.8328(3)$	$0.8343(3)$	$1.0019(5)$

Table 38: Effects of finite b and t masses for the cross section of $\mathrm{gg} \to \mathrm{Z}(\gamma^*)\mathrm{Z}(\gamma^*) \to \mathrm{l}\bar{\mathrm{l}}\mathrm{l}'\bar{\mathrm{l}}'$ when cut set "Cut 1" is applied. Other details as in Table 37.

Cut 1: $M_{\mathrm{Z}_1} > 12$ GeV, $M_{\mathrm{Z}_2} > 12$ GeV	σ [fb]	$\sigma_{\mathrm{MCFM}}/\sigma_{\mathrm{GG2ZZ}}$
GG2ZZ-2.0 ($m_{\mathrm{t}} = 172.5$ GeV, $m_{\mathrm{b}} = 4.75$ GeV)	$1.157(2)$	$1.010(2)$
MCFM-6.1 (5 massless quark flavours)	1.168(2)	—
GG2ZZ-2.0 ($m_{\mathrm{t}} = 10^5$ GeV, $m_{\mathrm{b}} = 10^{-4}$ GeV)	$1.1677(8)$	$1.001(2)$

with NLO Γ_{Z} and G_μ scheme. The renormalisation and factorisation scales are set to M_{Z}. The PDF set MSTW2008 NNLO with 3-loop running for $\alpha_{\mathrm{s}}(\mu^2)$ and $\alpha_{\mathrm{s}}(M_{\mathrm{Z}}^2) = 0.11707$ is used. The fixed-width prescription is used for Z propagators.

For cut sets "Cut 1", "Cut 2" and "Cut 3", results calculated with GG2ZZ and MCFM are shown in Table 37 (cross section) and Figure 97 (left, M_{ZZ} distribution). The cross sections agree up to 1% or better. Nevertheless, the residual deviations are significant relative to the MC integration errors. The M_{ZZ} distributions agree, except in the vicinity of the peaks at 50 and 200 GeV. In these invariant-mass regions, MCFM's differential cross section is slightly larger than GG2ZZ's. Table 38 and Figure 97 (right) demonstrate that the observed deviations are consistent with differences of the calculations in GG2ZZ and MCFM as discussed above. In the limit $m_{\mathrm{b}} \to 0$ and $m_{\mathrm{t}} \to \infty$, GG2ZZ's results are expected to agree with MCFM's results within MC integration errors. In Table 38 and Figure 97 (right), this is confirmed for cut set "Cut 1". Note that for cut sets "Cut 1" and "Cut 3" the finite-mass effects decrease the cross section, while for cut set "Cut 2" the cross section is increased (see Table 37).[43]

11.3.4 Theoretical uncertainties

PDF+α_{s} and QCD scale uncertainties for $\mathrm{pp} \to \mathrm{ZZ} \to 2\mathrm{e}2\mu$ at NLO and $\mathrm{gg} \to \mathrm{ZZ} \to 2\mathrm{e}2\mu$ are evaluated using MCFM version 6.1. The following cuts are applied to the leptons: $m_{\mathrm{ee}} > 12$ GeV , $m_{\mu\mu} > 12$ GeV, electrons' $p_{\mathrm{T}} > 7$ GeV and $|\eta| < 2.5$, and muons' $p_{\mathrm{T}} > 5$ GeV and $|\eta| < 2.4$. No cuts on the minimal ΔR-distance between jets and lepton, and lepton and lepton pairs are applied. The cross section is calculated inclusively for the number of jets found.

For the estimation of the PDF+α_{s} systematic errors, the PDF4LHC prescription [101] is applied. The upper and lower edges of the envelope are computed with the three PDF sets: CT10 [104],

[43]For cut set "Cut 2", one obtains $0.6297(4)$ fb with GG2ZZ-2.0 and $m_{\mathrm{t}} = 10^5$ GeV, $m_{\mathrm{b}} = 10^{-4}$ GeV, which agrees with MCFM-6.1's result.

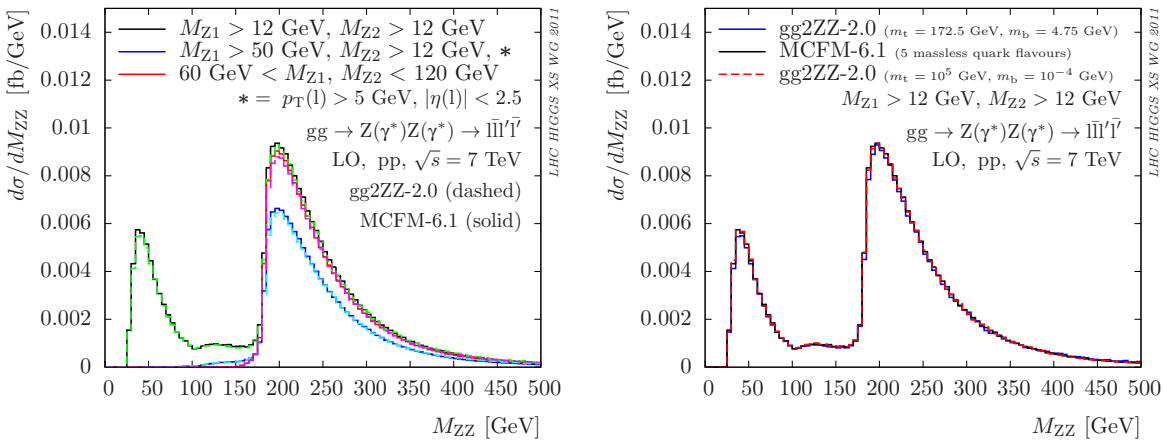

Fig. 97: (left) M_{ZZ} distributions for $gg \to Z(\gamma^*)Z(\gamma^*) \to l\bar{l}l'\bar{l}'$ calculated with MCFM-6.1 (Cut 1: black, Cut 2: blue, Cut 3: red) and GG2ZZ-2.0 (Cut 1: green dashed, Cut 2: cyan dashed, Cut 3: magenta dashed), other details as in Table 37; (right) effects of finite b and t masses for the M_{ZZ} distribution of $gg \to Z(\gamma^*)Z(\gamma^*) \to l\bar{l}l'\bar{l}'$ when cut set Cut 1 is applied, other details as in Table 37.

MSTW2008 [107], NNPDF [95], which can be parametrised as follow:

$$\text{ZZ @ NLO:} \qquad \kappa(m_{4l}) = 1 + 0.0035\sqrt{m_{4l}/\text{GeV} - 30}, \tag{78}$$

$$gg \to \text{ZZ:} \qquad \kappa(m_{4l}) = 1 + 0.0066\sqrt{m_{4l}/\text{GeV} - 10}. \tag{79}$$

In Figure 98 the difference between the central value of the cross section and the cross section computed with plus and minus 1σ of the total PDF+α_s variation, following the PDF4LHC prescription, is shown with the filled triangle marker for $q\bar{q} \to ZZ^{(*)} \to 2e2\mu$ (left) and for $gg \to ZZ^{(*)} \to 2e2\mu$ (right) as a function of $m_{2e2\mu}$ at 7 TeV from MCFM. The red line is the parametrisation from Eq. (78) and Eq. (79). The difference between the central value of the cross section and the cross section computed with the 3 different PDF sets (CT10, MSTW, and NNPDF) varying them by plus and minus 1 σ for $q\bar{q} \to ZZ^{(*)} \to 2e2\mu$ (left) and for $gg \to ZZ^{(*)} \to 2e2\mu$ (right) are also

For the estimation of QCD scale systematic errors, we calculate variations in the differential cross section $d\sigma/dm_{4l}$ as the renormalisation and factorisation scales are changed by a factor of two up and down from their default value $\mu_R = \mu_F = M_Z$. The dependence of the systematic QCD scale errors on the four-lepton invariant mass can be parametrised as follows:

$$\text{ZZ @ NLO:} \qquad \kappa(m_{4l}) = 1.00 + 0.01\sqrt{(m_{4l}/\text{GeV} - 20)/13}, \tag{80}$$

$$gg \to \text{ZZ:} \qquad \kappa(m_{4l}) = 1.04 + 0.10\sqrt{(m_{4l}/\text{GeV} + 40)/40}. \tag{81}$$

In Figure 99 the cross section for $q\bar{q} \to ZZ^{(*)} \to 2e2\mu$ (left) and for $gg \to ZZ^{(*)} \to 2e2\mu$ (right) is shown as a function of $m_{2e2\mu}$ at 7 TeV from MCFM computed with the CT10 PDF and varying the QCD scale by a factor of two. In Figure 100 the ratio of the cross section computed at the different scale and the cross section computed at the central value of the QCD scale (i.e. at M_Z) is shown as a function of the four-lepton invariant mass. The red lines are the parametrisation from Eq. (80) and Eq. (81) .

11.3.5 Summary

In Table 39 a summary of cross sections for ZZ production (both quark annihilation and gluon fusion) is presented for the three sets of cuts, with uncertainties calculated following the PDF4LHC prescription.

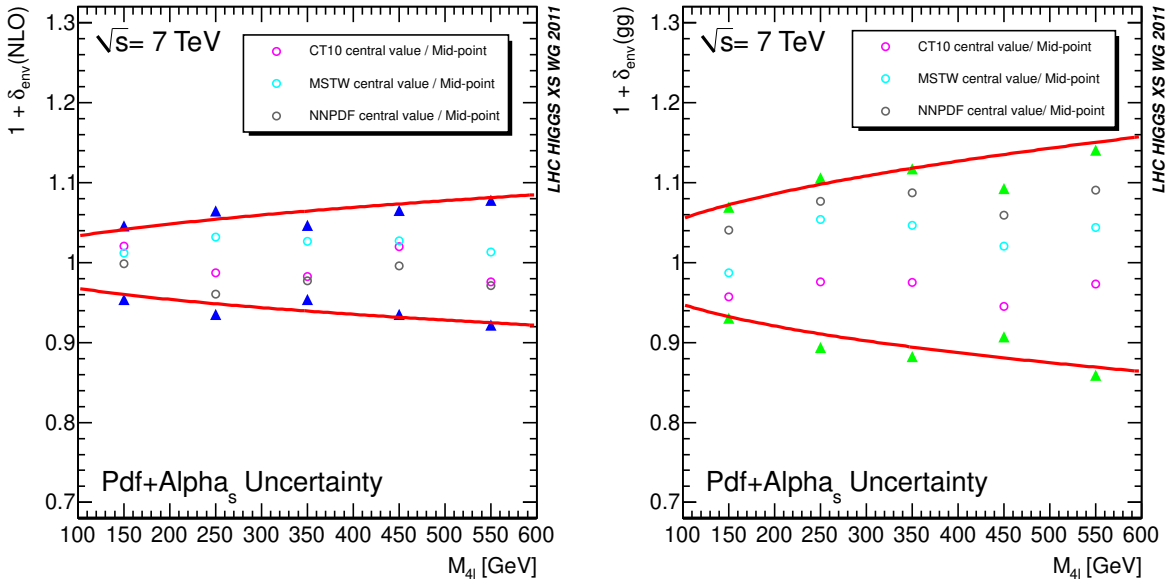

Fig. 98: The difference between the central value of the cross section and the cross section computed with 3 different PDF sets and the total PDF+α_s variation (blue markers) varying them by plus and minus 1σ for $q\overline{q} \to ZZ^{(*)} \to 2e2\mu$ (left) and for $gg \to ZZ^{(*)} \to 2e2\mu$ (right) as a function of $m_{2e2\mu}$ at 7 TeV from MCFM.

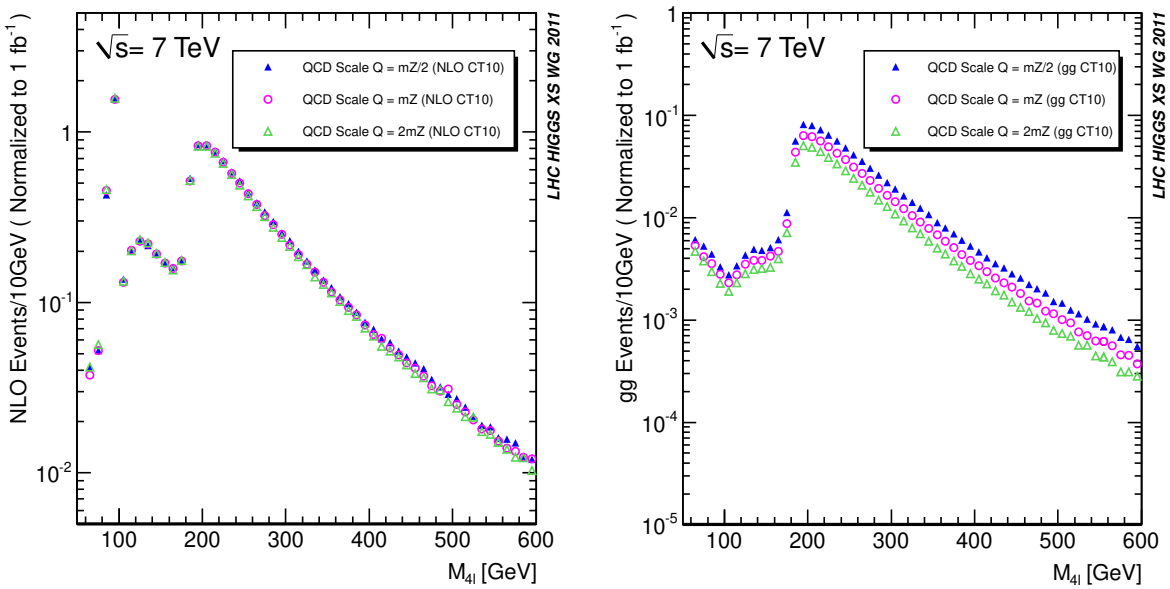

Fig. 99: The cross section for $q\overline{q} \to ZZ^{(*)} \to 2e2\mu$ (left) and for $gg \to ZZ^{(*)} \to 2e2\mu$ (right) as a function of $m_{2e2\mu}$ at 7 TeV from MCFM computed with the CT10 PDF and varying the QCD scale by a factor of two.

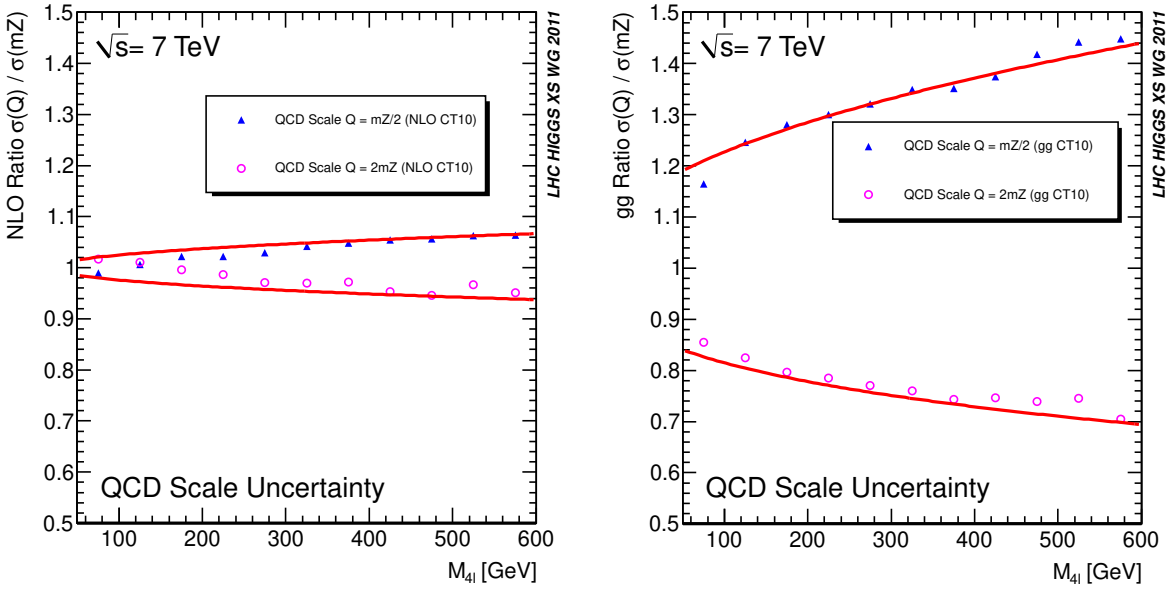

Fig. 100: The ratio of the cross sections computed at different scales and the cross section computed at central value of the QCD scale for $q\overline{q} \to ZZ^{(*)} \to 2e2\mu$ (left) and $gg \to ZZ^{(*)} \to 2e2\mu$ (right) as a function of $m_{2e2\mu}$ at 7 TeV from MCFM. The red line is the parametrisation described in the text

Table 39: Cross sections in fb with uncertainties for $pp \to Z(\gamma^*)Z(\gamma^*) \to l\bar{l}l'\bar{l}'$ in pp collisions at $\sqrt{s} = 7$ TeV calculated at NLO with MCFM-6.1. Three cut sets are applied: $M_{Z_1} > 12$ GeV, $M_{Z_2} > 12$ GeV(Cut 1); $M_{Z_1} > 50$ GeV, $M_{Z_2} > 12$ GeV, $p_T(l) > 5$ GeV, $|\eta(l)| < 2.5$ (Cut 2); 60 GeV $< M_{Z_1} < 120$ GeV, 60 GeV $< M_{Z_2} < 120$ GeV(Cut 3).

	σ [fb]	PDF+α_s [%]	QCD Scale [%]	Total [%]
Cut 1	15.962	3.53	2.10	5.63
Cut 2	5.306	3.44	4.23	7.68
Cut 3	6.965	2.95	3.87	6.82

In Table 40 calculations are extended for single-Z production and the ratio of ZZ to Z, which can be used for normalisation of ZZ production with data, with detailed breakdown of uncertainties.

11.4 Angular distributions in H $\to$ ZZ decays

The angular distributions of final decay products from the Higgs-boson decays are strictly related to the scalar nature of the Standard Model Higgs boson. The angular distributions may be eventually used to separate H $\to$ ZZ events from regular SM di-boson events, and will in the end serve to verify if any Higgs signature is indeed from a scalar boson. The MC program generators used for the H $\to$ ZZ process are PYTHIA and POWHEG (for which gluon fusion and vector-boson fusion are separated), while PYTHIA is used for the SM di-boson production. The study presented in this section has been made with simulated Higgs events with mass of 120 GeV.

Table 40: Cross sections in fb for $\mathrm{pp} \to \mathrm{Z}(\gamma^*)\mathrm{Z}(\gamma^*) \to 4\mathrm{e}$ or 4μ, $\mathrm{Z} \to 2\mathrm{e}$ or 2μ and their ratios in pp collisions at $\sqrt{s} = 7$ TeV calculated at NLO with MCFM-6.1. For ZZ cross sections calculations the following cuts are applied: $M_{\mathrm{Z}_1} > 50$ GeV, $M_{\mathrm{Z}_2} > 12$ GeV, $p_{\mathrm{T}}(\mathrm{l}) > 5$ GeV, $|\eta(\mathrm{l})| < 2.5$ (Cut 2). The set of cuts for Z cross sections calculations is: $M_{\mathrm{Z}} > 40$ GeV, $p_{\mathrm{T}}(\mathrm{l1}) > 20$ GeV, $p_{\mathrm{T}}(\mathrm{l2}) > 10$ GeV, $|\eta(\mathrm{l})| < 2.5$

PDF	$\sigma(\mathrm{ZZ} \to 4\mathrm{e}/4\mu)$ [fb]	$\sigma(\mathrm{Z} \to 2\mathrm{e}/2\mu)$ [10^5 fb]	$\sigma(\mathrm{ZZ})/\sigma(\mathrm{Z})$ [10^{-6}]
		PDF+α_{s}	
CT10	$5.235 \pm 2.13\%$	$5.478 \pm 2.37\%$	$9.556 \pm 1.52\%$
MSTW2008	$5.408 \pm 1.50\%$	$5.494 \pm 1.70\%$	$9.844 \pm 0.90\%$
NNPDF2.0	$5.290 \pm 1.50\%$	$5.259 \pm 1.60\%$	$10.06 \pm 0.80\%$
Envelope	$5.306 \pm 3.44\%$	$5.392 \pm 4.02\%$	$9.776 \pm 3.73\%$
		QCD	
$\mu = M_{\mathrm{Z}}/2$	$+4.23\%$	-0.90%	$+5.17\%$
$\mu = 2M_{\mathrm{Z}}$	-3.26%	$+1.20\%$	-4.41%
$\lvert\max\rvert$	4.23%	1.20%	5.17%
Total	$5.306 \pm 7.68\%$	$5.392 \pm 5.22\%$	$9.776 \pm 8.90\%$

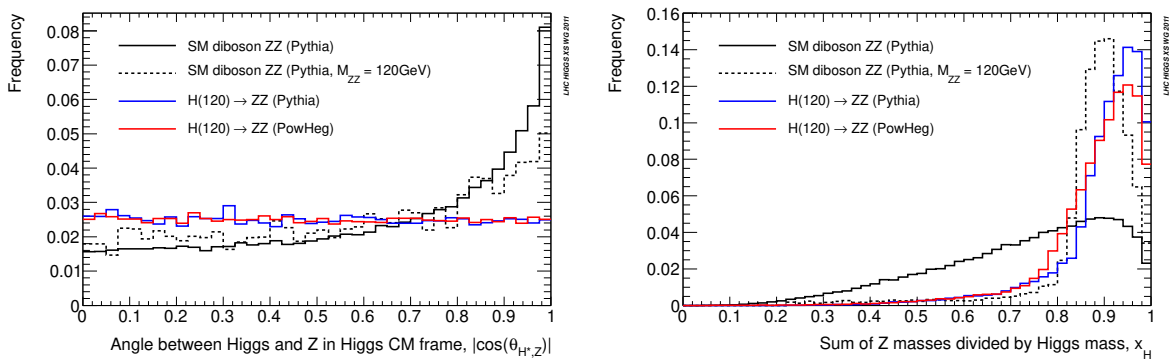

Fig. 101: (a) Distribution of $\cos(\theta^*_{\mathrm{H,Z}})$ for Higgs events with $M_{\mathrm{H}} = 120$ GeV and ZZ di-boson events. (b) Distribution of x_{H} (the sum of the Z masses divided by the Higgs mass) for the same samples.

11.4.1 Comparison and cross check of angular distributions

The primary angular distribution to consider is the angle between the Higgs boson[44] direction and a Z in the rest frame of the Higgs, $\theta^*_{\mathrm{H,Z}}$; since the SM Higgs boson is a scalar, $\cos(\theta^*_{\mathrm{H,Z}})$ it has to be a uniform distribution. While the dominant production process for the Higgs is gluon fusion, $\mathrm{q\overline{q}}$ dominates SM di-boson ZZ production. As a consequence of this, the SM di-boson ZZ system is created in a spin state different from the one of the Higgs, and so here $\cos(\theta^*_{\mathrm{H,Z}})$ is not expected to be uniform. The $\cos(\theta^*_{\mathrm{H,Z}})$ distribution for $\mathrm{H} \to \mathrm{ZZ}$ (both for PYTHIA and POWHEG) as well as for SM di-boson ZZ production is shown in Figure 101a; the distribution is indeed uniform in case of the Higgs for both generators, while it is not uniform for the SM di-boson ZZ case. In the same figure the distribution obtained when the ZZ invariant mass is required to be around 120 GeV (which diminishes the separation) is also shown.

Another independent variable sensitive to the spin of the ZZ system, is the sum of the Z masses divided by the Higgs-boson mass, x_{H} (quantity related to the p_{T} of the Z's in the Higgs-boson rest frame); that variable is expected to be larger for Higgs events than for SM di-boson ZZ events, but in both cases close to unity, due to the lacking phase space, as shown in Figure 101b. Some difference has been found between PYTHIA and POWHEG, as PYTHIA generally yields a larger value of x_{H}.

[44]For simplicity we refer to the ZZ system as the Higgs, even if no Higgs is involved.

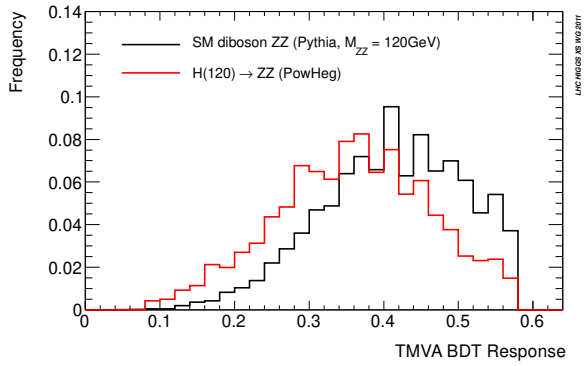

Fig. 102: Separation between $\mathrm{H} \rightarrow \mathrm{ZZ}$ and SM di-boson ZZ using five angular variables combined in a Boosted Decision Tree (BDT).

11.4.2 Separating $\mathbf{H} \rightarrow \mathbf{ZZ}$ *from* ZZ *using angular variables*

In addition to the above two observables, several other variables are also sensitive to the spin of the ZZ system; the rapidity of that system, y_{H}, and the angle between the Z and the leptons in the Z rest frame, $\theta^*_{\mathrm{Z,l-}}$ are different, yielding five variables in total. Nevertheless most of the variables tend to give less separation once a fiducial selection based on acceptance ($p_{\mathrm{T}}(\mathrm{l}) > 7$ GeV, $\eta(\mathrm{l}) < 2.5$) is applied.

The final separation between $\mathrm{H} \rightarrow \mathrm{ZZ}$ and SM di-boson ZZ derived by combining the angular variables in a neural net (Boosted decision tree, BDT), can be found in Figure 102; the separation is quite poor, and so not much further separation can be gained from considering the angular variables.

12 Neutral-Higgs-boson production in the MSSM[45]

12.1 The MSSM Higgs sector: general features

Within the Minimal Supersymmetric Standard Model (MSSM) the Higgs-boson sector contains, contrary to the SM, two scalar doublets, accommodating five physical Higgs bosons [330–337]. These are, at lowest order, the light and heavy CP-even h and H, the CP-odd A, and the charged Higgs bosons $\mathrm{H}^{\pm}$. At the tree level the MSSM Higgs sector can be expressed in terms of the SM gauge couplings and two further input parameters, conventionally chosen as $\tan\beta \equiv v_2/v_1$, the ratio of the two vacuum expectation values, and either M_{A} or $M_{\mathrm{H}^{\pm}}$. Consequently, all other masses and mixing angles can be predicted. However, the Higgs sector of the MSSM is affected by large higher-order corrections, which have to be taken into account for reliable phenomenological predictions. The higher-order corrections arise in particular due to the large top Yukawa coupling, leading to large loop contributions from the top and stop sector to the Higgs masses and couplings. Similarly, for large values of $\tan\beta$ effects from the bottom/sbottom sector can also be large. In particular, the relation between the bottom-quark mass and the bottom Yukawa coupling receives $\tan\beta$-enhanced contributions entering via Δ_{b} [90–93, 338–342]. These corrections are non-vanishing even in the limit of asymptotically large values of the SUSY mass parameters. For the light Higgs boson these corrections vanish if the Higgs-boson mass scale, M_{A} or $M_{\mathrm{H}^{\pm}}$ also goes to large values. An analogous contribution, although in general smaller, exists for the τ lepton. The MSSM Higgs sector is CP conserving at lowest order. However, CP-violating effects can enter via the potentially large loop corrections. In this case all three neutral Higgs bosons mix with each other. As in Ref. [7] we will focus here on the CP-conserving case and use M_{A} as input parameter.

In a large part of the MSSM parameter space the couplings of the light CP-even Higgs boson to SM gauge bosons and fermions become SM like. This decoupling limit is reached for $M_{\mathrm{A}} \gg M_{\mathrm{Z}}$, however in practice it is already realised for $M_{\mathrm{A}} \gtrsim 2M_{\mathrm{Z}}$. Consequently, in this parameter region the light CP-even Higgs boson of the MSSM resembles the Higgs boson of the SM. Results for the light CP-even Higgs-boson production cross sections and decay branching ratios approach the corresponding SM values, provided that the additional SUSY mass scales are too high to affect the Higgs production and decay.

However, in general the Higgs phenomenology in the MSSM can differ very significantly from the SM case. Depending on M_{A} and the SUSY mass scales, the relevant couplings entering production and decay processes of a MSSM Higgs boson can be very different from the corresponding couplings in the SM case. Consequently, the lower bound on the Higgs mass in the SM from the searches at LEP cannot be applied directly to the MSSM case [343, 344]; much lighter Higgs masses are possible in the MSSM without being in conflict with the present search limits. Furthermore, the presence of more than one Higgs boson in the spectrum can give rise to overlapping signals in the Higgs searches, in particular in parameter regions where the Higgs-boson widths are large or the experimental resolution does not allow for a separation of the individual Higgs mass peaks.

Due to the enlarged spectrum in the MSSM, further production and decay processes are possible compared to the SM case. In particular, MSSM Higgs bosons can be produced in association with or in decays of SUSY particles, and decays of MSSM Higgs bosons into SUSY particles, if kinematically allowed, can have a large impact on the Higgs branching ratios. In certain parts of the parameter space decays of heavy MSSM Higgs bosons into lighter Higgs can also become important. These decays could potentially yield valuable information on the Higgs self-couplings. However, in the following we will mainly focus on SM-type Higgs production processes at the LHC. In particular, we will investigate Higgs production in gluon fusion, weak-boson fusion and in association with bottom quarks. Corresponding results for the total cross sections were discussed in Ref. [7].

Due to the large number of free parameters in the MSSM, it is customary to interpret searches

[45] M. Spira, M. Vazquez Acosta, M. Warsinsky, G. Weiglein (eds.); E.A. Bagnaschi, M. Cutajar, G. Degrassi, R. Harlander, S. Heinemeyer, M. Krämer, A. Nikitenko, S. Palmer, M. Schumacher, P. Slavich, A. Vicini, T. Vickey and M. Wiesemann.

for the Higgs bosons in terms of benchmark scenarios where the lowest-order input parameters $\tan\beta$ and $M_{\rm A}$ (or $M_{\rm H^\pm}$) are varied, while the other SUSY parameters entering via radiative corrections are set to certain benchmark values. In the following we will focus, in particular, on the $m_{\rm h}^{\rm max}$ benchmark scenario [10]. Within the on-shell scheme it is defined as[46]

$$M_{\rm SUSY} = 1\ \text{TeV},\ X_{\rm t} = 2M_{\rm SUSY},\ \mu = 200\ \text{GeV},\ M_{\tilde{\rm g}} = 800\ \text{GeV},\ M_2 = 200\ \text{GeV},\ A_{\rm b} = A_{\rm t}, \quad (82)$$

where $M_{\rm SUSY}$ denotes the common soft-SUSY-breaking squark mass of the third generation, $X_{\rm t} = A_{\rm t} - \mu/\tan\beta$ the stop mixing parameter, $A_{\rm t}$ and $A_{\rm b}$ the stop and sbottom trilinear couplings, respectively, μ the Higgsino mass parameter, $M_{\tilde{\rm g}}$ the gluino mass, and M_2 the SU(2)-gaugino mass parameter. Adding to the results of Ref. [7] for the total inclusive cross sections within the $m_{\rm h}^{\rm max}$ benchmark scenario we will present the inclusive results for the no-mixing scenario in this chapter, too. The no-mixing benchmark scenario is defined as [10]

$$M_{\rm SUSY} = 2\ \text{TeV},\ X_{\rm t} = 0,\ \mu = 200\ \text{GeV},\ M_{\tilde{\rm g}} = 1.6\ \text{TeV},\ M_2 = 200\ \text{GeV},\ A_{\rm b} = A_{\rm t}\ . \quad (83)$$

While in the SM the Higgs-boson mass is a free input parameter, in the MSSM all masses, mixings, and couplings can be calculated in terms of the other model parameters. Consequently, calculations of Higgs production and decay processes in the MSSM require, as a first step, the evaluation of the Higgs-boson masses and mixing contributions in terms of $M_{\rm A}$, $\tan\beta$, and all other relevant SUSY parameters that enter via radiative corrections. Furthermore, the mixing between the different (neutral) Higgs bosons must be taken into account in order to ensure the correct on-shell properties of the Higgs fields appearing in the S-matrix elements of production or decay processes. To perform this kind of evaluations in terms of the MSSM input parameters, several codes exist. Two codes use electroweak scale parameters as input, FeynHiggs [77–80] and CPsuperH [81, 82], while other codes can also work with GUT scale input, SoftSusy [345], Spheno [346, 347], and SuSpect [348]. While certain differences in the implemented calculations exist, all of the above codes incorporate higher-order corrections in the MSSM Higgs sector up to the two-loop level. FeynHiggs was chosen for the corresponding calculations in Ref. [7], and following these previous evaluations, we use FeynHiggs to calculate the Higgs-boson masses and effective couplings in the MSSM here as well (where we deviate from this, it will be clearly indicated). A brief comparison of FeynHiggs and CPsuperH and the respective differences in the $m_{\rm h}^{\rm max}$ and no-mixing benchmarks can be found in Ref. [7], while a comparison between FeynHiggs and the three codes SoftSusy, Spheno, and SuSpect can be found in Ref. [349]. The masses, mixings, and couplings obtained in this way can be passed via the SUSY Les Houches Accord [83, 84] to other codes for further evaluation.

12.2 Status of inclusive calculations

12.2.1 Summary of existing calculations and implementations

Gluon fusion

Gluon fusion has been studied in great detail in the framework of the SM. In fact, the requirement of higher-order corrections to this process has been one of the most powerful driving forces for the development of new theoretical concepts and techniques. The theory prediction currently used by the experimental collaborations includes the full NLO QCD corrections [66, 208, 210, 350] as well as NNLO QCD corrections in the limit of heavy top quarks [212–214], resummation of soft-collinear logarithms through NNLL in the limit of heavy top quarks [219], full electroweak NLO contributions [24, 28], and an estimate of the mixed QCD/EW terms [224].

[46] It should be noted that while $M_{\rm SUSY}$ formally is common for all three generations of scalar quarks, the only relevant ones are the third generation squarks. Consequently, limits obtained at the LHC on first and second generation squarks do not play a relevant role for this scenario.

For the MSSM, however, the corrections to the gluon-fusion process have been treated much less rigorously until recently. Not even through $\mathcal{O}(\alpha_s^3)$, i.e., NLO QCD, has there been a prediction that takes into account all strongly interacting SUSY particles.

Schematically, the amplitude for Higgs production through gluon fusion can be written as

$$\mathcal{A}(\mathrm{gg} \to \mathrm{h}) = \sum_{\mathrm{q}\in\{\mathrm{t,b}\}} \left(a_{\mathrm{q}}^{(0)} + a_{\tilde{q}}^{(0)} + a_{\mathrm{q}}^{(1)} + a_{\tilde{q}}^{(1)} + a_{\tilde{\mathrm{q}}\tilde{\mathrm{g}}}^{(1)} \right) . \tag{84}$$

The superscripts (0) and (1) denote one- and two-loop contributions, respectively. The term $a_{\mathrm{q}}^{(0,1)}$ comprises contributions from Feynman diagrams with only the quark q and gluons running in loops. Similarly, $a_{\tilde{q}}^{(0,1)}$ contains only squarks $\tilde{\mathrm{q}}$ and gluons, while $a_{\tilde{\mathrm{q}}\tilde{\mathrm{g}}}^{(1)}$ is due to diagrams containing quarks q, squarks $\tilde{\mathrm{q}}$, and gluinos simultaneously.

Of course, also the real radiation of quarks and gluons has to be taken into account: $\mathrm{gg} \to \mathrm{hg}$, $\mathrm{qg} \to \mathrm{hq}$, and $\mathrm{q}\overline{\mathrm{q}} \to \mathrm{hg}$. They are either quark- or squark-loop mediated, but no mixed quark/squark (or gluino) terms occur at NLO.

The LO result, $\sum_{\mathrm{q}}(a_{\mathrm{q}}^{(0)} + a_{\tilde{\mathrm{q}}}^{(0)})$, has been known since a long time in analytic form. Also the real radiation can be (and has been) evaluated quite straightforwardly using standard techniques, see e.g., Refs. [66, 94, 211].

The pure quark terms $a_{\mathrm{q}}^{(0)} + a_{\mathrm{q}}^{(1)}$ correspond to the NLO SM contribution. The first result that was valid for a general quark to Higgs mass ratio was presented in Ref. [350, 351] in the form of one-dimensional integrals. Meanwhile, more compact expressions in terms of analytic functions have been found [208–210].

These general results justified with hindsight the use of the heavy-top limit for the gluon-fusion process within the Standard Model [65,207]: it approximates the exact QCD correction factor $\sigma^{\mathrm{NLO}}/\sigma^{\mathrm{LO}}$ to within $2{-}3\%$ for $M_{\mathrm{h}} < 2m_{\mathrm{t}}$ [352, 353]. The question whether this observation carries over to NNLO has been answered by comparing the asymptotic expansion of the total cross section in terms of $1/m_{\mathrm{t}}$ to the usually adopted expression

$$\sigma_{\text{eff}} = \left(\frac{\sigma^{\mathrm{NNLO}}}{\sigma^{\mathrm{LO}}} \right)_{m_{\mathrm{t}}\to\infty} \sigma^{\mathrm{LO}}(m_{\mathrm{t}}) . \tag{85}$$

They agree at the sub-per-cent level [215, 217, 218, 354, 355]. It is thus fair to say that the SM-like top-quark induced terms are known through NNLO, while the bottom quark terms are known through NLO.

Technically, the squark-induced terms are very similar to the quark-induced ones. Consequently, results for general squark masses are known also in this case through NLO [94, 208, 210]. In order to arrive at a consistent result within the MSSM, also mixed quark/squark/gluino contributions need to be taken into account, however.

For the top sector, this has been done by constructing an effective Lagrangian where all SUSY particles and the top quark are integrated out [356–358]. The SUSY effects are then reduced to the calculation of the proper Wilson coefficient, while the actual process diagrams are identical to the ones in the heavy-top limit in the SM case. The genuine SUSY QCD corrections in this limit turned out to be of moderate size.

For the bottom sector, this approach is no longer applicable in a straightforward way, because the bottom quark cannot be assumed heavy. The problem are the mixed bottom/sbottom/gluino diagrams. A numerical result for general masses has been presented in Refs. [359, 360]. A more compact expression can be obtained through asymptotic expansions in the limit $m_{\tilde{\mathrm{b}}}, m_{\tilde{\mathrm{g}}} \gg M_{\mathrm{H}}, m_{\mathrm{b}}$, as applied in Refs. [361, 362].

In Ref. [362], all contributions of strongly interacting particles in the MSSM have been combined in a single program GGHBSUSY. This includes (i) the exact real radiation contributions due to quark and squark loops for both the top and the bottom sector; (ii) the exact two-loop virtual terms due to top- and bottom-quark loops; (iii) the squark-loop and mixed quark/squark/gluino-induced terms in the limit $M_{\tilde{g}} = M_{\tilde{q}_1} = M_{\tilde{q}_2} \gg \{M_H, m_t, m_b\}$. Needless to say that this includes also all the interference terms.

The program GGHBSUSY links FEYNHIGGS which provides the on-shell values of the input parameters.

b-quark associated production

The inclusive total cross section for bottom-quark associated Higgs-boson production, denoted[47] $pp/p\bar{p} \to (b\bar{b})H + X$, can be calculated in two different schemes. As the mass of the bottom-quark is large compared to the QCD scale, $m_b \gg \Lambda_{QCD}$, bottom-quark production is a perturbative process and can be calculated order by order. Thus, in a four-flavour scheme (4FS), where one does not consider b-quarks as partons in the proton, the lowest-order QCD production processes are gluon–gluon fusion and quark–antiquark annihilation, $gg \to b\bar{b}H$ and $q\bar{q} \to b\bar{b}H$, respectively. However, the inclusive cross section for $gg \to (b\bar{b})H$ develops logarithms of the form $\ln(\mu_F/m_b)$, which arise from the splitting of gluons into nearly collinear $b\bar{b}$ pairs. The large factorisation scale $\mu_F \approx M_H/4$ corresponds to the upper limit of the collinear region up to which factorisation is valid [363–365]. For Higgs-boson masses $M_H \gg 4m_b$, the logarithms become large and spoil the convergence of the perturbative series. The $\ln(\mu_F/m_b)$ terms can be summed to all orders in perturbation theory by introducing bottom parton densities. This defines the so-called five-flavour scheme (5FS). The use of bottom distribution functions is based on the approximation that the outgoing b-quarks are at small transverse momentum. In this scheme, the LO process for the inclusive $(b\bar{b})H$ cross section is bottom fusion, $b\bar{b} \to H$.

If all orders in perturbation theory were taken into account, the four- and five-flavour schemes would be identical, but the way of ordering the perturbative expansion is different. At any finite order, the two schemes include different parts of the all-order result, and the cross section predictions do thus not match exactly. While this leads to an ambiguity in the way the cross section is calculated, it also offers an opportunity to test the importance of various higher-order terms and the reliability of the theoretical prediction. The 4FS calculation is available at NLO [366, 367], while the 5FS cross section has been calculated at NNLO accuracy [368]. Electroweak corrections to the 5FS process have been found to be small [369] and will not be considered in the numerical results presented here, except for the effective MSSM couplings used for dressing the predictions obtained within the SM.

Total cross sections

Within the m_h^{max} scenario the Higgs-boson production cross sections develop a significant dependence on the μ parameter. The ratios of the total cross sections for different μ values and the predictions for $\mu = 200$ GeV are shown in Fig. 103 for two values of $\tan\beta = 5, 30$. While for moderate values of $\tan\beta$ the effect of the μ variation between -400 GeV and 800 GeV is less than $10-15\%$, larger effects up to a factor of about 2 arise for large values of $\tan\beta$. These effects emerge dominantly due to the μ dependence of the Δ_b corrections to the bottom Yukawa couplings. While the results for the associated Higgs-boson production with bottom quarks are valid up to NNLO, the corresponding results for the gluon-fusion process rely on the approximation that the genuine SUSY QCD corrections are dominated by the same Δ_b corrections to the bottom Yukawa couplings which, however, up to now has not yet been confirmed by explicit calculations of these corrections. In Fig. 104 the central predictions for the gluon-fusion processes $gg \to h, H, A$ and neutral Higgs radiation off bottom quarks within the 5FS are shown as a function of the corresponding Higgs mass within the no-mixing scenario for two values of

[47] The notation $(b\bar{b})H$ is meant to indicate that the $b\bar{b}$ pair is not required as part of the signature in this process, so that its final-state momenta must be integrated over the full phase space.

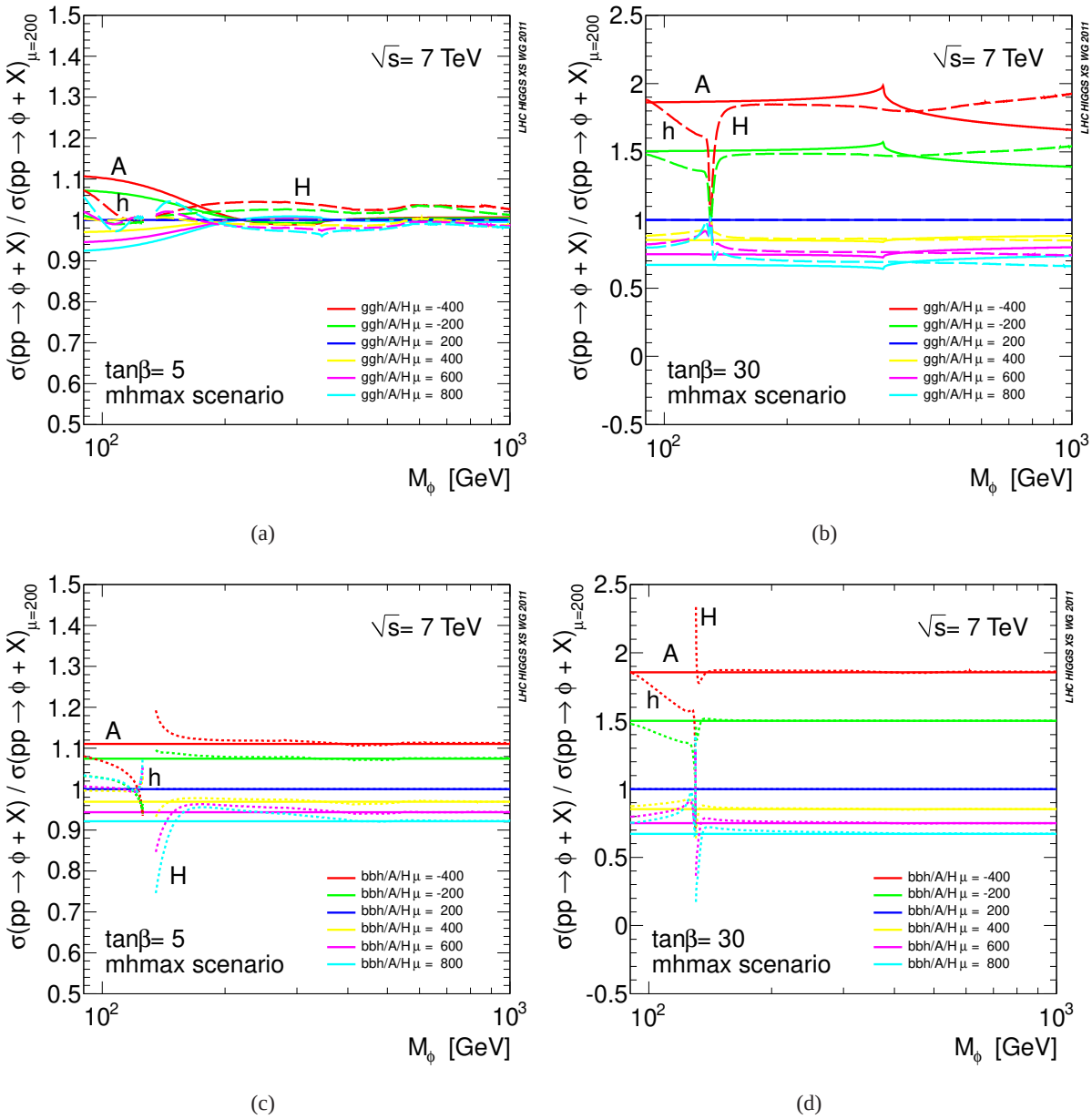

Fig. 103: Ratios of the total MSSM production cross sections via gluon fusion and Higgs radiation off bottom quarks within the 5FS for $\sqrt{s} = 7$ TeV using NNLO and NLO MSTW2008 PDFs [107,114] for the $m_{\rm h}^{\rm max}$ scenario with different μ values relative to the central prediction with $\mu = 200$ GeV; (a) gluon fusion for $\tan\beta = 5$, (b) gluon fusion for $\tan\beta = 30$, (c) Higgs radiation off bottom quarks for $\tan\beta = 5$, (d) Higgs radiation off bottom quarks for $\tan\beta = 30$.

$\tan\beta = 5, 30$. It is clearly visible that Higgs-boson radiation off bottom quarks plays the dominant role for $\tan\beta = 30$ while for $\tan\beta = 5$ the gluon fusion is either dominant or competitive.

The results for the total cross sections have been obtained from the grids generated by GGH@NNLO and HIGLU for the gluon-fusion process and BBH@NNLO for $\rm b\overline{b} \to \phi$ and rescaling the corresponding Yukawa couplings by the MSSM factors calculated with FEYNHIGGS.

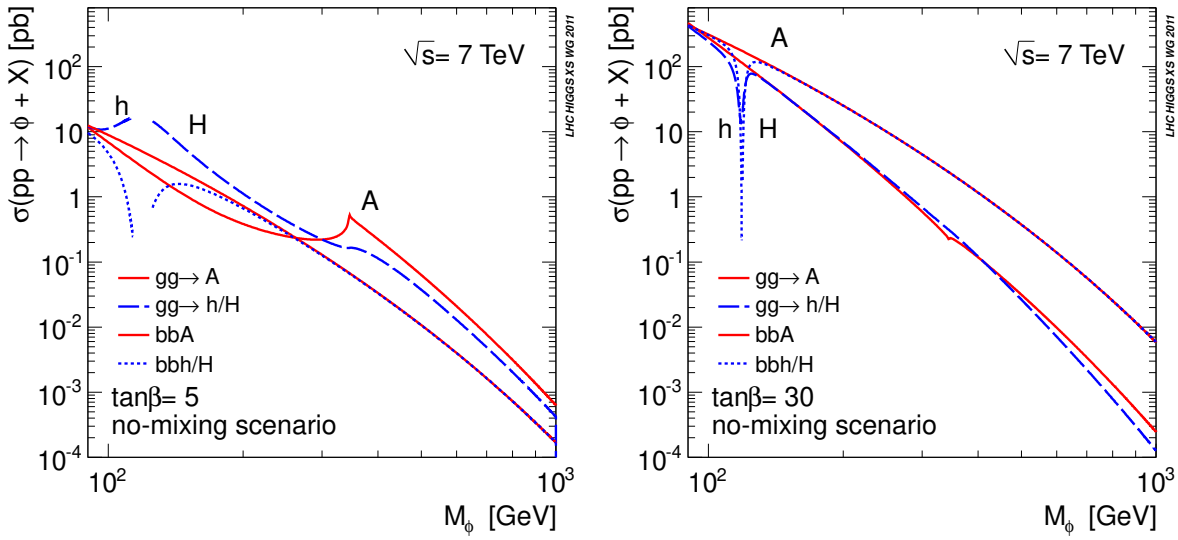

(a) (b)

Fig. 104: Central predictions for the total MSSM production cross sections via gluon fusion and Higgs radiation off bottom quarks within the 5FS for $\sqrt{s} = 7$ TeV using NNLO and NLO MSTW2008 PDFs [107, 114] for the no-mixing scenario; (a) $\tan\beta = 5$, (b) $\tan\beta = 30$.

12.2.2 Santander matching

A simple and pragmatic formula for the combination of the four- and five-flavour scheme calculations of bottom-quark associated Higgs-boson production has been suggested in Ref. [370]. The matching formula originated from discussions among the authors of Ref. [370] at the *Higgs Days at Santander 2009* and is therefore dubbed "Santander matching". We shall briefly describe the matching scheme and provide matched predictions for the inclusive cross section $\mathrm{pp} \to (\mathrm{b\overline{b}})\mathrm{H} + X$ at the LHC operating at a centre-of-mass energy of 7 TeV within the Standard Model for illustrative purposes.

The 4FS and 5FS calculations provide the unique description of the cross section in the asymptotic limits $M_\mathrm{H}/m_\mathrm{b} \to 1$ and $M_\mathrm{H}/m_\mathrm{b} \to \infty$, respectively. For phenomenologically relevant Higgs-boson masses away from these asymptotic regions both schemes are applicable and include different types of higher-order contributions. The matching suggested in Ref. [370] interpolates between the asymptotic limits of very light and very heavy Higgs bosons.

A comparison of the 4FS and 5FS calculations reveals that both are in numerical agreement for moderate Higgs-boson masses (see Fig. 23 of Ref. [7]). Once larger Higgs-boson masses are considered, the effect of the collinear logarithms $\ln(M_\mathrm{H}/m_\mathrm{b})$ becomes more and more important and the two approaches begin to differ. The two approaches are combined in such a way that they are given variable weight, depending on the value of the Higgs-boson mass. The difference between the two approaches is formally logarithmic. Therefore, the dependence of their relative importance on the Higgs-boson mass should be controlled by a logarithmic term. The coefficients are determined such that

(a) the 5FS gets 100% weight in the limit $M_\mathrm{H}/m_\mathrm{b} \to \infty$;

(b) the 4FS gets 100% weight in the limit where the logarithms are "small". There is obviously quite some arbitrariness in this statement. In Ref. [370] it is assumed that "small" means $\ln(M_\mathrm{H}/m_\mathrm{b}) = 2$. The consequence of this particular choice is that the 4FS and the 5FS both get the same weight for Higgs-boson masses around 100 GeV, consistent with the observed agreement between the 4FS and the 5FS in this region.[48]

[48]Note that one should use the *pole mass* for m_b here rather than the running mass, since it is really the dynamical mass that

This leads to the following formula

$$\sigma^{\text{matched}} = \frac{\sigma^{\text{4FS}} + w\,\sigma^{\text{5FS}}}{1+w}\,, \tag{86}$$

with the weight w defined as

$$w = \ln\frac{M_{\rm H}}{m_{\rm b}} - 2\,, \tag{87}$$

and σ^{4FS} and σ^{5FS} denote the total inclusive cross section in the 4FS and the 5FS, respectively. For $m_{\rm b} = 4.75$ GeV and specific values of $M_{\rm H}$, this leads to

$$\begin{aligned}
\sigma^{\text{matched}}\big|_{M_{\rm H}=100\,\text{GeV}} &= 0.49\,\sigma^{\text{4FS}} + 0.51\,\sigma^{\text{5FS}}\,,\\
\sigma^{\text{matched}}\big|_{M_{\rm H}=200\,\text{GeV}} &= 0.36\,\sigma^{\text{4FS}} + 0.64\,\sigma^{\text{5FS}}\,,\\
\sigma^{\text{matched}}\big|_{M_{\rm H}=300\,\text{GeV}} &= 0.31\,\sigma^{\text{4FS}} + 0.69\,\sigma^{\text{5FS}}\,,\\
\sigma^{\text{matched}}\big|_{M_{\rm H}=400\,\text{GeV}} &= 0.29\,\sigma^{\text{4FS}} + 0.71\,\sigma^{\text{5FS}}\,,\\
\sigma^{\text{matched}}\big|_{M_{\rm H}=500\,\text{GeV}} &= 0.27\,\sigma^{\text{4FS}} + 0.73\,\sigma^{\text{5FS}}\,.
\end{aligned} \tag{88}$$

A graphical representation of the weight factor w is shown in Fig. 105 (a).

The theoretical uncertainties in the 4FS and the 5FS calculations should be added linearly, using the weights w defined in Eq. (87). This ensures that the combined error is always larger than the minimum of the two individual errors. Neglecting correlations and assuming equality of the uncertainties in the 4FS and 5FS calculations would imply that the matched uncertainty is reduced by a factor of $w/(1+w)$ with respect to the common individual uncertainties. This seems unreasonable. In the approach adopted in Ref. [370] the matched uncertainty would be equal to the individual ones in this case. On the other hand, taking the envelope of the 4FS and 5FS error bands seems overly conservative.

The estimates of the theoretical uncertainties in the 4FS and the 5FS calculations are obtained through $\mu_{\rm F}$, $\mu_{\rm R}$, PDF, and $\alpha_{\rm s}$ variation as described in Ref. [7]. They can be quite asymmetric, which is why the combination should be done separately for the upper and the lower uncertainty limits:

$$\Delta\sigma_{\pm} = \frac{\Delta\sigma_{\pm}^{\text{4FS}} + w\,\Delta\sigma_{\pm}^{\text{5FS}}}{1+w}\,, \tag{89}$$

where $\Delta\sigma_{\pm}^{\text{4FS}}$ and $\Delta\sigma_{\pm}^{\text{5FS}}$ are the upper/lower uncertainty limits of the 4FS and the 5FS, respectively.

We shall now discuss the numerical implications of the Santander matching and provide matched predictions for the inclusive cross section $\mathrm{pp} \to (\mathrm{b\overline{b}})\mathrm{H} + X$ at the LHC operating at a centre-of-mass energy of 7 TeV. The individual numerical results for the 4FS and 5FS calculations have been obtained in the context of the *LHC Higgs Cross Section Working Group* with input parameters as described in Ref. [7]. Note that the cross section predictions presented below correspond to Standard Model bottom Yukawa couplings and a bottom-quark mass of $m_{\rm b} = 4.75$ GeV. SUSY effects can be taken into account by simply rescaling the bottom Yukawa coupling to the proper value [369, 371].

Fig. 105 (b) shows the central values for the 4FS and the 5FS cross section, as well as the matched result, as a function of the Higgs-boson mass. The ratio of the central 4FS and the 5FS predictions to the matched result is displayed in Fig. 106 (b) (central dashed and dotted line): for $M_{\rm H} = 100$ GeV, the 4FS and the 5FS contribute with approximately the same weight to the matched cross section, with

rules the re-summed logarithms.

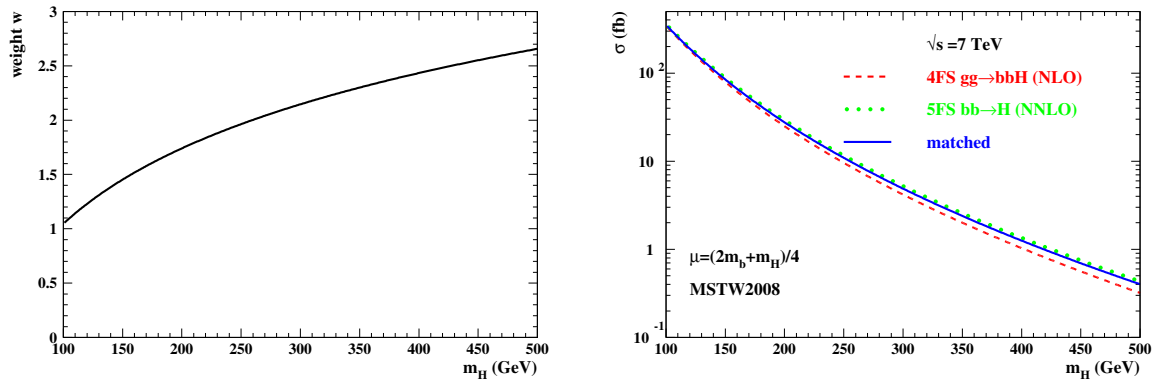

(a) (b)

Fig. 105: (a) Weight factor w, Eq. (87), as a function of the Higgs-boson mass $M_{\rm H}$. The bottom-quark pole mass has been set to $m_{\rm b} = 4.75$ GeV. (b) Central values for the total inclusive cross section in the 4FS (red, dashed), the 5FS (green, dotted), and for the Santander-matched cross section (blue, solid). Here and in the following we use the MSTW2008 PDF set [107] (NLO for the 4FS, NNLO for the 5FS).

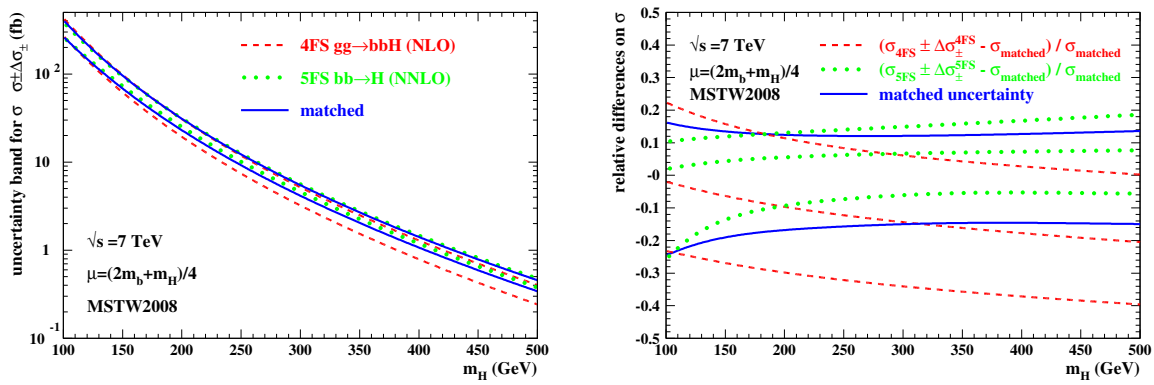

(a) (b)

Fig. 106: (a) Theory uncertainty bands for the total inclusive cross section in the 4FS (red, dashed), the 5FS (green, dotted), and for the Santander-matched cross section (blue, solid). (b) Uncertainty bands and central values, relative to the central value of the Santander-matched result (same line coding as panel (a)).

deviations between the individual 4FS and the 5FS predictions and the matched one of less than 5%. With increasing Higgs-boson mass, the 4FS result deviates more and more from the matched cross section due to its decreasing weight. At $M_{\rm H} = 500$ GeV, it agrees to less than 20% with the matched result, while the 5FS is still within 8% of the latter.

The corresponding theory error estimates are shown in Figure 106. The absolute numbers are displayed in panel (a), while in panel (b) they are shown relative to the central value of the matched result. Up to $M_{\rm H} \approx 300$ GeV, the combined uncertainty band covers the central values of both the 4FS and the 5FS. For larger Higgs-boson masses, the 4FS central value is slightly outside this band.

12.3 Status of differential cross sections

12.3.1 Dressing SM predictions with effective couplings

In making predictions for Higgs-boson production (or decay) processes in the MSSM one has to face the fact that certain types of higher-order corrections have only been calculated in the SM case up to now, while their counterpart for the case of the MSSM is not yet available. One the one hand, starting from dedicated MSSM calculations for Higgs cross sections or decay widths treats higher-order corrections of SM type and SUSY type on the same footing. On the other hand, this approach may be lacking the known to be relevant (or at least the most up to date) SM-type corrections. Consequently, it can be advantageous to start from SM-type processes including all the known higher-order corrections, and to dress suitable SM-calculation building blocks with appropriate MSSM coupling factors (effective couplings). At the same time, for internal consistency, the MSSM predictions for Higgs-boson masses etc. have to be used. While for the results for the MSSM Higgs production in gluon fusion we discuss below the results of genuine MSSM calculations, for MSSM Higgs production in association with bottom quarks the SM predictions are dressed with appropriate effective couplings in the MSSM. For the weak-boson fusion channel we discuss the genuine MSSM result and compare it to that that of the effective coupling approach. A similar comparison for the other Higgs production channels will be investigated in a later stage.

12.3.2 Implementation of Higgs production via gluon fusion in the MSSM in POWHEG

The gluon-fusion mechanism, $\mathrm{gg} \to \phi \;\; (\phi = \mathrm{h}, \mathrm{H}, \mathrm{A})$, is one of the most important processes for the production of the neutral Higgs bosons of the MSSM. An overview about the existing calculations is given in Section 12.2.1.

The aim is to obtain results for Higgs-boson kinematic distributions, but going beyond the approximation of restricting to the quark-loop contributions (dressed with appropriate MSSM couplings). The results are obtained by combining all the available NLO QCD information, i.e., including the superpartner contributions, with the description of initial-state multiple-gluon emission via a QCD parton shower (PS) Monte Carlo. The analysis relies on the POWHEG method [123, 126], which allows to systematically merge NLO calculations with vetoed PS, avoiding double counting and preserving the NLO accuracy in the total cross section. The merging procedure can be implemented using a computer code framework called the POWHEG BOX [156], which allows to build an event generator that always assigns a positive weight to the hardest event. The POWHEG implementation of the gluon-fusion Higgs production process in the SM was reported in Ref. [132] (see also Ref. [130]) and subsequent modifications to include the finite-quark-mass effects were presented elsewhere [190].

We briefly summarise what is included in our POWHEG implementation of $\mathrm{gg} \to \mathrm{h}, \mathrm{H}$ in the MSSM (with more details in Ref. [190]). For the contributions of diagrams with real-parton emission, as well as for the leading-order (LO) virtual contributions, we use one-loop matrix elements with exact dependence on the quark, squark, and Higgs masses from Ref. [211]. Concerning the NLO QCD virtual contributions involving squarks, we use the results of Ref. [358] for the stop contributions, obtained in the approximation of vanishing Higgs mass, and the results of Ref. [361] for the sbottom contributions, obtained via an asymptotic expansion in the large supersymmetric masses that is valid up to and including terms of $\mathcal{O}(m_\mathrm{b}^2/m_\phi^2)$, $\mathcal{O}(m_\mathrm{b}/M_\mathrm{SUSY})$, and $\mathcal{O}(M_\mathrm{Z}^2/M_\mathrm{SUSY}^2)$, with M_SUSY a generic superparticle mass. For the remaining NLO QCD contributions, arising from the two-loop diagrams with quarks and gluons, we use the exact results of Ref. [210]. The two-loop electroweak corrections, for which a complete calculation in the MSSM is not available, are included in an approximate way by properly rescaling the SM light-quark contributions given in Refs. [24,223]. This approximation is motivated by the observation that, in the SM, the light-quark contributions make up the dominant part of the electroweak corrections when the Higgs mass is below the threshold for top-pair production.

As discussed above, it is necessary to compute the entire spectrum of masses and couplings of the

model in a consistent way, starting from a given set of input parameters. In our numerical analysis, we use the code SOFTSUSY [345] to compute the MSSM spectrum and the couplings of the Higgs bosons to quarks and squarks starting from a set of running parameters expressed in the $\overline{\mathrm{DR}}$ renormalisation scheme. However, it is in principle possible to interface the code with other spectrum calculators (such as, e.g.,, FEYNHIGGS) that adopt different choices of renormalisation conditions for the input parameters.

For illustrative purposes we present numerical results for the production of the lightest CP-even Higgs boson, h, at the LHC with centre-of-mass energy of 7 TeV, in a representative region of the MSSM parameter space. Events are generated with the described implementation of POWHEG, then matched with the PYTHIA PS [183]. We compute the total inclusive cross section for light Higgs production in gluon fusion, as well as the transverse-momentum distribution for a light Higgs boson produced in association with a jet, and we compare them with the corresponding quantities computed for a SM Higgs boson with the same mass.

The relevant MSSM Lagrangian parameters are chosen as:

$$m_Q = m_U = m_D = 500 \text{ GeV}, \;\; X_\mathrm{t} = 1250 \text{ GeV}, \;\; M_3 = 2\,M_2 = 4\,M_1 = 400 \text{ GeV}, \;\; |\mu| = 200 \text{ GeV}, \tag{90}$$

where m_Q, m_U and m_D are the soft-SUSY-breaking mass terms for stop and sbottom squarks, $X_\mathrm{t} \equiv A_\mathrm{t} - \mu \cot\beta$ is the left–right mixing term in the stop mass matrix (where A_t is the soft-SUSY-breaking Higgs–squark coupling and μ is the higgsino mass parameter in the superpotential), and M_i (for $i = 1, 2, 3$) are the soft-SUSY-breaking gaugino masses. We consider the input parameters in Eq. (90) as expressed in the $\overline{\mathrm{DR}}$ renormalisation scheme, at a reference scale $Q = 500$ GeV. The choice of X_t/m_Q resembles the choice in the $m_\mathrm{h}^\mathrm{max}$ scenario. We recall that, in our conventions, the $\tan\beta$-dependent corrections to the relation between the bottom mass and the bottom Yukawa coupling [90–93, 338–342] enhance the Higgs couplings to bottom and sbottoms for $\mu < 0$ and suppress them for $\mu > 0$.

We perform a scan on the parameters that determine the Higgs-boson masses and mixing at tree level, M_A and $\tan\beta$, varying them in the ranges 90 GeV $< M_\mathrm{A} < 200$ GeV and $2 < \tan\beta < 50$. For each value of $\tan\beta$ we derive A_t from the condition on X_t, then we fix the corresponding Higgs–sbottom coupling as $A_\mathrm{b} = A_\mathrm{t}$. For each point in the parameter space, we use SOFTSUSY to compute the physical (i.e.,, radiatively corrected) Higgs-boson masses M_h and M_H, and the effective mixing angle α that diagonalises the radiatively-corrected mass matrix in the CP-even Higgs sector. We obtain from SOFTSUSY also the MSSM running quark masses $m_\mathrm{t}(Q)$ and $m_\mathrm{b}(Q)$, expressed in the $\overline{\mathrm{DR}}$ scheme at the scale $Q = 500$ GeV. The running quark masses are used both in the calculation of the running stop and sbottom masses and mixing angles, and in the calculation of the top and bottom contributions to the form factors for Higgs-boson production (the latter are computed using the $\overline{\mathrm{DR}}$ results presented in Refs. [358, 361]).

In Figure 107 we plot the ratio of the cross section for the production of the lightest scalar h in the MSSM over the cross section for the production of a SM Higgs boson with the same mass. For a consistent comparison, we adopt the $\overline{\mathrm{DR}}$ scheme in both the MSSM and the SM calculations. The plot on the left is obtained with $\mu > 0$, while the plot on the right is obtained with $\mu < 0$. In order to interpret the plots, it is useful to recall that for small values of M_A it is the heaviest scalar H that has SM-like couplings to fermions, while the coupling of h to top (bottom) quarks is suppressed (enhanced) by $\tan\beta$. In the lower-left region of the plots, with small M_A and moderate $\tan\beta$, the enhancement of the bottom contribution does not compensate for the suppression of the top contribution, and the MSSM cross section is smaller than the corresponding SM cross section. On the other hand, for sufficiently large $\tan\beta$ (in the lower-right region of the plots) the enhancement of the bottom contribution prevails, and the MSSM cross section becomes larger than the corresponding SM cross section. For $\mu < 0$ the coupling of h to bottom quarks is further enhanced by the $\tan\beta$-dependent threshold corrections, and the ratio between the MSSM and SM predictions can significantly exceed a factor of ten. We also note that for sufficiently large M_A, i.e., when the couplings of h to quarks approach their SM values, the MSSM cross section is smaller than the SM cross section.

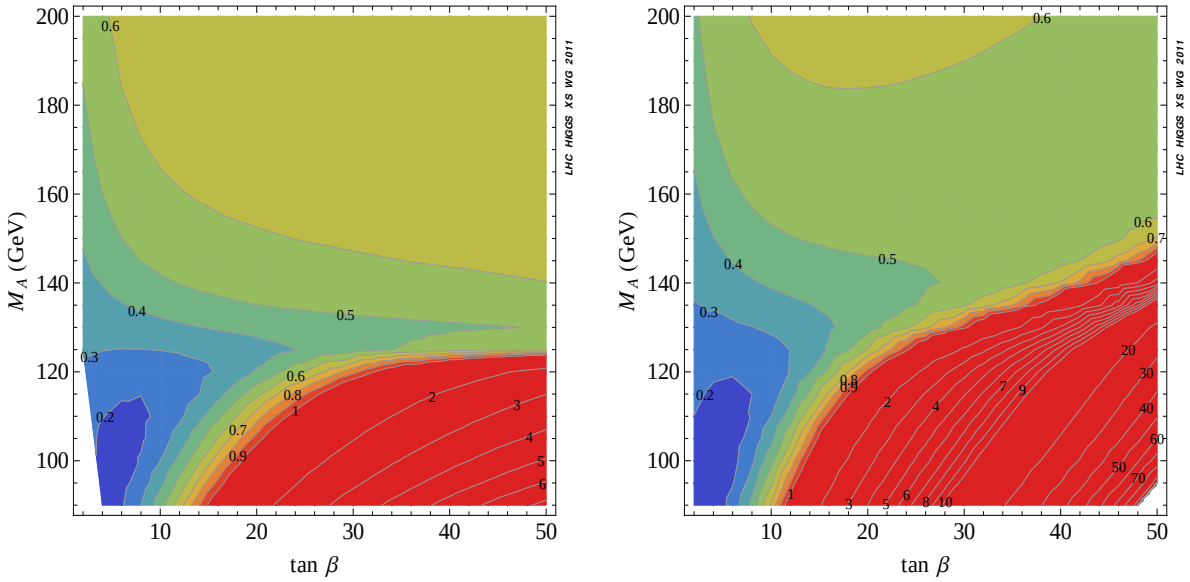

Fig. 107: Ratio of the total cross section for h production in the MSSM over the cross section for the production of a SM Higgs boson with the same mass. The plot on the left is for $\mu > 0$ while the plot on the right is for $\mu < 0$.

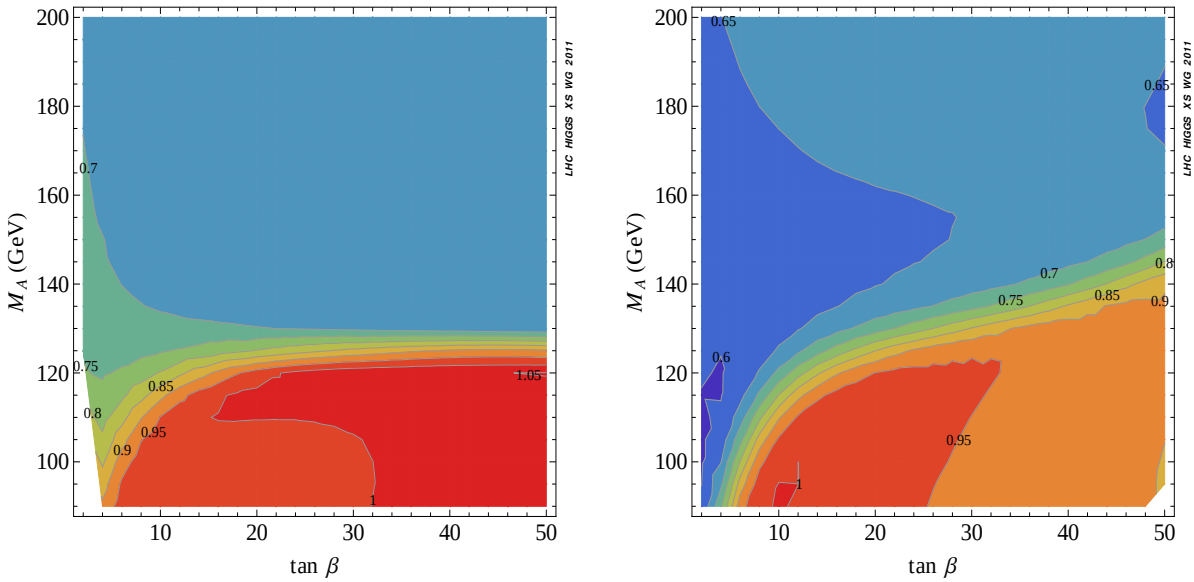

Fig. 108: Ratio of the full cross section for h production in the MSSM over the approximated cross section computed with only quarks running in the loops. The plot on the left is for $\mu > 0$ while the plot on the right is for $\mu < 0$.

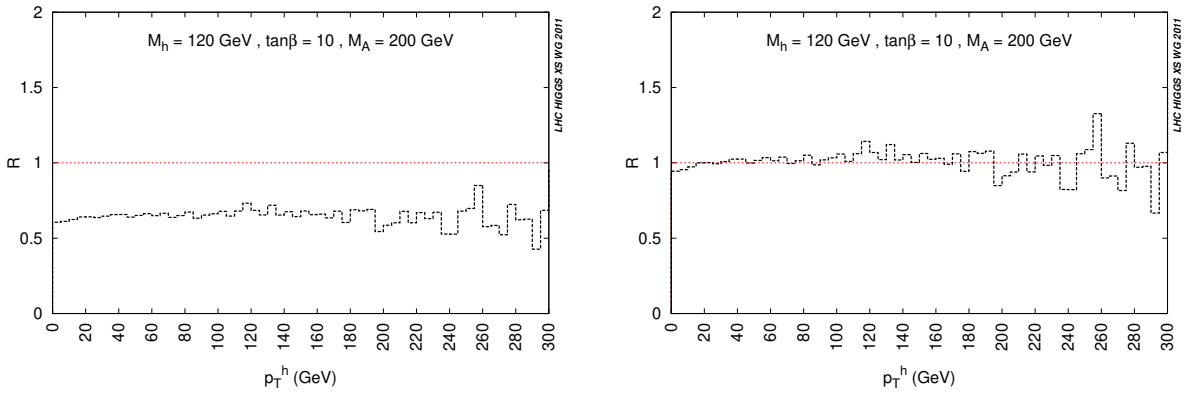

Fig. 109: Left: ratio of the transverse-momentum distribution of the lightest scalar h in the MSSM over the transverse-momentum distribution of a SM Higgs boson with the same mass. Right: ratio of the corresponding shapes.

To assess the genuine effect of the squark contributions (as opposed to the effect of the modifications in the Higgs–quark couplings), we plot in Figure 108 the ratio of the full MSSM cross section for the production of the lightest scalar h over the approximated MSSM cross section computed with only quarks running in the loops. As in Figure 107, the plot on the left is obtained with $\mu > 0$, while the plot on the right is obtained with $\mu < 0$. We observe that, in most of the considered region of the MSSM parameter space, the squark contributions reduce the total cross section. We identify three regions: $i)$ for sufficiently large $\tan\beta$ and sufficiently small M_{A} the squark contribution is modest, ranging between -10% and $+5\%$; this region roughly coincides with the one in which the total MSSM cross section is dominated by the $\tan\beta$-enhanced bottom-quark contribution, and is larger than the SM cross section; $ii)$ a transition region, where the corrections rapidly become as large as -30%; this region coincides with the one in which the SM and MSSM cross sections are similar to each other; $iii)$ for sufficiently large M_{A} the squark correction is almost constant, ranging between -40% and -30%; this region coincides with the one in which the MSSM cross section is smaller than the corresponding SM cross section.

We now discuss the distribution of the transverse momentum $p_{\mathrm{T}}^{\mathrm{h}}$ of a light scalar h produced in association with a jet, considering two distinct scenarios. First, we take a point in the MSSM parameter space ($M_{\mathrm{A}} = 200$ GeV, $\tan\beta = 10$ and $\mu > 0$) in which the coupling of h to the bottom quark is not particularly enhanced with respect to the SM value, so that the bottom contribution to the cross section is not particularly relevant. Because a light Higgs boson cannot resolve the top and squark vertices, unless we consider very large transverse momentum, we expect the form of the $p_{\mathrm{T}}^{\mathrm{h}}$ distribution to be very similar to the one for a SM Higgs boson of equal mass, the two distributions just differing by a scaling factor related to the total cross section. This is illustrated in the left plot of Figure 109, where we show the ratio of the transverse-momentum distribution for h over the distribution for a SM Higgs boson of equal mass. In the right plot of Figure 109 we show the ratio of the corresponding shapes, i.e., the distributions normalised to the corresponding cross sections. This ratio, as expected, is close to one in most of the $p_{\mathrm{T}}^{\mathrm{h}}$ range.

We then consider the opposite situation, namely when the coupling of h to the bottom quark is significantly enhanced. In this situation two tree-level channels, i.e., $\mathrm{b\bar{b}} \to \mathrm{gh}$ and $\mathrm{bg} \to \mathrm{bh}$, can also contribute to the production mechanism and influence the shape of the $p_{\mathrm{T}}^{\mathrm{h}}$ distribution [372, 373]. Leaving a study of the effects of those additional channels to a future analysis, we will now illustrate how the kinematic distribution of the Higgs boson can help discriminate between the SM and the MSSM. To this purpose, we focus on three points in the $(M_{\mathrm{A}}, \tan\beta)$ plane characterised by the fact that the total cross section for h production agrees, within 5%, with the cross section for the production of a SM Higgs

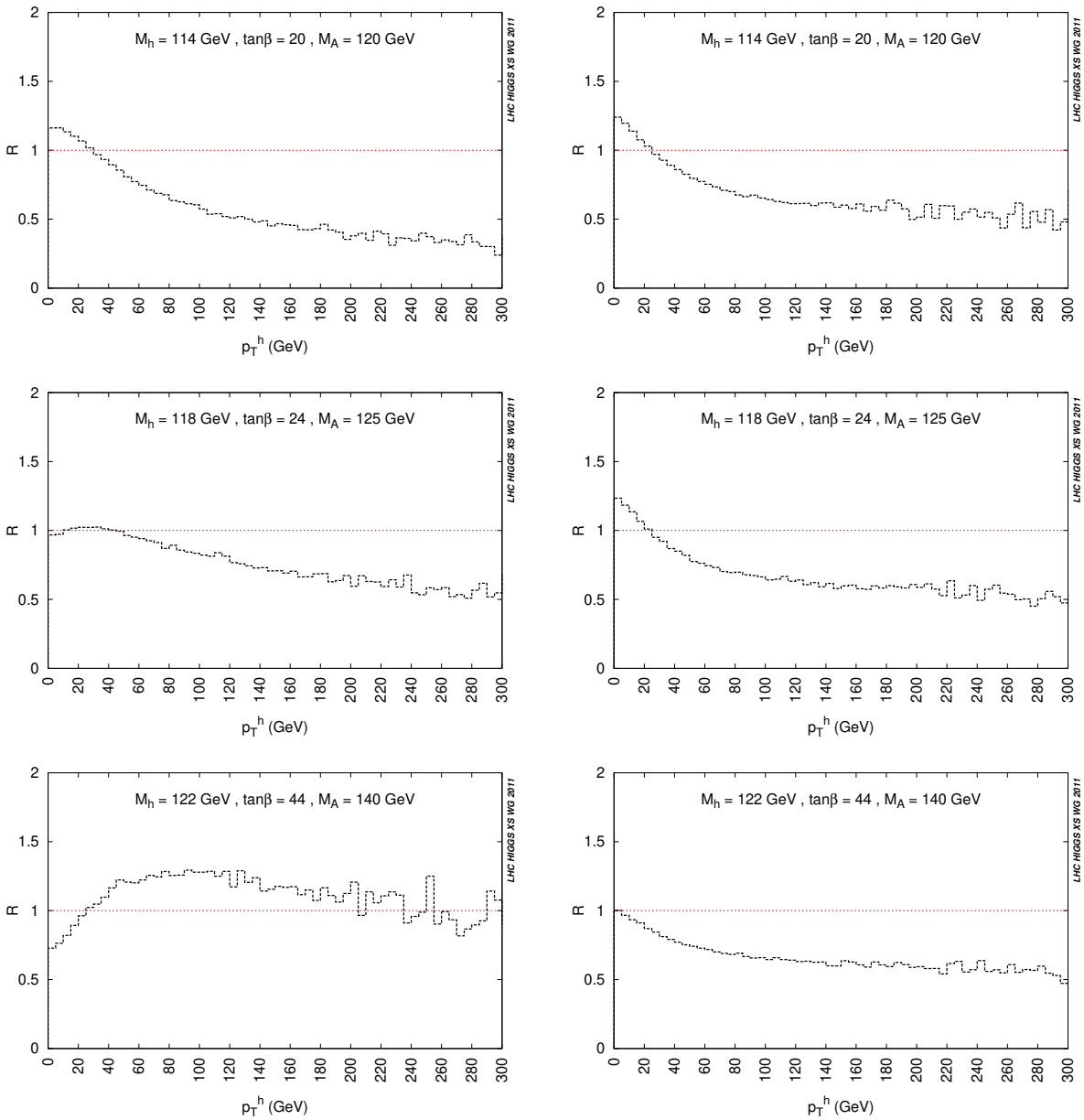

Fig. 110: Left plots: ratio of the transverse momentum-distribution for the lightest scalar h in the MSSM over the distribution for a SM Higgs with the same mass. Right plots: ratio of the transverse-momentum distribution for h in the MSSM over the approximate distribution computed with only quarks running in the loops. The plots are obtained with $\mu < 0$, and with three different choices of M_{A} and $\tan\beta$ for which the MSSM and SM predictions for the total cross section agree within 5%.

boson of equal mass. Thus, we are considering points around the curve labeled "1" in Figure 107 (we set $\mu < 0$, as in the right plot of that figure). In the left panels of Figure 110 we show the ratio of the transverse-momentum distribution for h over the distribution for a SM Higgs boson of equal mass. We see that, because of the enhancement of the bottom-quark contribution, the shape of the transverse momentum distribution in the MSSM can differ significantly from the SM case. Indeed, the region at small $p_{\mathrm{T}}^{\mathrm{h}}$ can receive an enhancement (at moderate $\tan\beta$) compared with the SM result, but also a significant suppression (at large $\tan\beta$). The tail at large $p_{\mathrm{T}}^{\mathrm{h}}$ can receive a suppression down to a factor 4 (at moderate $\tan\beta$), but can also almost coincide with the SM result (at large $\tan\beta$).

In the right panels of Figure 110, for the same points in the $(M_{\mathrm{A}}, \tan\beta)$ plane as in the left panels, we show the ratio of the $p_{\mathrm{T}}^{\mathrm{h}}$ distribution over the approximate distribution computed with only quarks running in the loops. Even though the light Higgs boson cannot resolve the squark loops, we see that the squark contributions affect the shape of the $p_{\mathrm{T}}^{\mathrm{h}}$ distribution, because of the interference with the bottom contribution. In particular, we observe that the squark contributions may yield an enhancement of the distribution at small $p_{\mathrm{T}}^{\mathrm{h}}$, and in all cases they yield a negative correction for $p_{\mathrm{T}}^{\mathrm{h}} > 20$ GeV. The negative correction becomes quite flat, at about -40%, for $p_{\mathrm{T}}^{\mathrm{h}} > 100$ GeV.

12.3.3 Difference in kinematic acceptance between SM and MSSM production of $\mathrm{gg} \to \mathrm{H} \to \tau\tau$

Current LHC MSSM $\mathrm{H} \to \tau\tau$ analyses [374, 375] use the Standard Model generation of $\mathrm{gg} \to \mathrm{H}$ events with the infinite-top-mass approximation as implemented in PYTHIA [183] (used by CMS) or POWHEG [156] (used by ATLAS). Both ATLAS and CMS collaborations have presented analyses in the $m_{\mathrm{h}}^{\max}$ scenario [10] as given in Eq. (82). At large values of $\tan\beta$ in the $m_{\mathrm{h}}^{\max}$ scenario $\mathrm{gg} \to \mathrm{H}$ production proceeds predominantly via a bottom-quark loop producing a softer $p_{\mathrm{T}}^{\mathrm{H}}$ spectrum than that predicted in the Standard Model production dominated by the top loop [189, 376],[49] as discussed in the previous section. As a result, the kinematic acceptance of $\mathrm{gg} \to \mathrm{H} \to \tau\tau$ events may be overestimated in the current LHC analyses. To determine the size of this effect, the PYTHIA generated $p_{\mathrm{T}}^{\mathrm{H}}$ spectrum is re-weighted to match the shape predicted when considering only the b-loop contribution to the $\mathrm{gg} \to \mathrm{H}$ process [189]. The acceptance of $\mathrm{H} \to \tau\tau$ events in the $\mathrm{e}+\tau$-jet final state in the CMS detector is then estimated before and after re-weighting the events.

Samples of $\mathrm{gg} \to \mathrm{H} \to \tau\tau$ events with $M_{\mathrm{H}} = 140$ GeV and $M_{\mathrm{H}} = 400$ GeV are generated with PYTHIA using the infinite-top-mass approximation, and the τ leptons are decayed with TAUOLA. Using the $p_{\mathrm{T}}^{\mathrm{H}}$ spectra obtained with b loops only [189], the generated events are assigned weights $w_i = N_i^{\mathrm{b-loop}}/N_i^{\mathrm{Pythia}}$ in i bins of $p_{\mathrm{T}}^{\mathrm{H}}$ where N_i^{Pythia} and $N_i^{\mathrm{b-loop}}$ are the normalised event rates expected from PYTHIA and with only b-loop contribution, respectively. Events with $p_{\mathrm{T}}^{\mathrm{H}} < 240$ GeV and $p_{\mathrm{T}}^{\mathrm{H}} < 300$ GeV are considered for $M_{\mathrm{H}} = 140$ GeV and $M_{\mathrm{H}} = 400$ GeV, respectively. Figure 111 shows the generated $p_{\mathrm{T}}^{\mathrm{H}}$ distributions for the two mass points before and after applying the event weights.

Figure 112 shows the generated p_{T} distributions of the visible τ decay products: electrons and τ-jets (τ_{h}). The electrons and τ-jets are required to pass kinematic selections at the generator level corresponding to the kinematic selections of the CMS $\mathrm{H} \to \tau\tau$ analysis [374]. The electron is required to have $p_{\mathrm{T}} > 20$ GeV and $|\eta| < 2.1$, and the τ_{h} is required to have $p_{\mathrm{T}} > 20$ GeV and $|\eta| < 2.3$. Events containing a $\mathrm{e}+\tau_{\mathrm{h}}$ pair separated by $\Delta R > 0.5$ are selected. The acceptance, defined as the ratio of selected to generated events, is calculated before and after applying the reweighting procedure and shown in Table 41.

It is found that in current analyses, the acceptance for the MSSM $\mathrm{gg} \to \mathrm{H} \to \tau\tau$ process with only b loops is smaller than for the SM $\mathrm{gg} \to \mathrm{H} \to \tau\tau$ process by approximately 3% for $M_{\mathrm{H}} = 140$ GeV, and consistent with the SM process for $M_{\mathrm{H}} = 400$ GeV. The small size of the effect is due to the relatively

[49] For $\tan\beta > 12$ and $M_{\mathrm{A}} = 140$ GeV in the $m_{\mathrm{h}}^{\max}$ scenario the cross section of $\mathrm{gg} \to \phi$ ($\phi = \mathrm{h}, \mathrm{H}, \mathrm{A}$) production through only b loops [377] is less than 10% different from the full MSSM $\mathrm{gg} \to \phi$ production cross section [7].

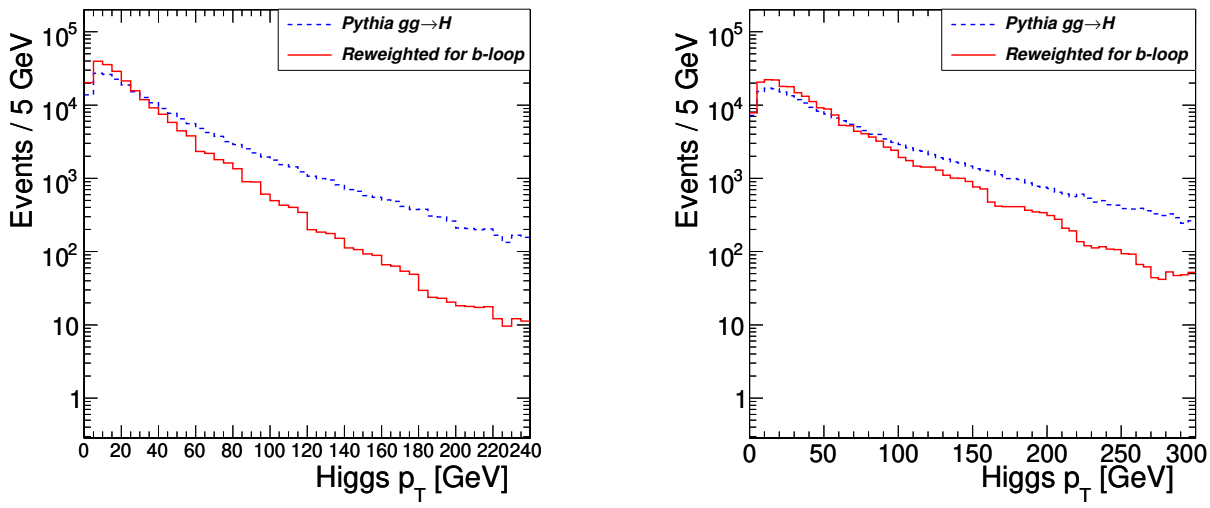

Fig. 111: Generated $p_{\mathrm{T}}^{\mathrm{H}}$ distributions for $M_{\mathrm{H}} = 140$ GeV (left) and $M_{\mathrm{H}} = 400$ GeV (right) for the $\mathrm{gg} \to \mathrm{H}$ process generated with PYTHIA (dashed) and after re-weighting (solid) to correct for $\mathrm{gg} \to \mathrm{H}$ production dominated by the b-loop contribution.

Table 41: The $\mathrm{e}+\tau_{\mathrm{h}}$ acceptances before and after re-weighting to correct for b-loop contribution.

M_{H} [GeV]	Acceptance PYTHIA $\mathrm{gg} \to \mathrm{H}$	Acceptance re-weighted for b-loop	Correction factor
140	0.072 ± 0.001	0.070 ± 0.001	0.97 ± 0.01
400	0.149 ± 0.001	0.152 ± 0.001	1.02 ± 0.02

low p_{T} thresholds on the visible τ decay products used in the current analyses.

12.3.4 Higher-order MSSM corrections for Higgs production in vector-boson fusion

12.3.4.1 VBFNLO

Higgs production via (weak) vector-boson fusion (VBF) is an important SM production channel at the LHC [11, 12, 378]. In the MSSM, it is expected that at least one Higgs boson will have a significant coupling to the weak bosons, meaning VBF should be an important production channel in the MSSM as well. Since the latest release, VBFNLO [264, 265] has provided the ability to study production of the three neutral Higgs bosons h, H, and A via vector-boson fusion in the MSSM with real or complex parameters[50].

The MSSM implementation makes use of the anomalous Higgs couplings previously available in VBFNLO. These use the most general structure of the coupling between a scalar particle and a pair of gauge bosons, which can be written as [266]

$$T^{\mu\nu}(q_1, q_2) \quad = \quad a_1(q_1, q_2) g^{\mu\nu} + a_2(q_1, q_2) \left[(q_1 q_2)\, g^{\mu\nu} - q_1^{\mu} q_2^{\nu} \right] + a_3(q_1, q_2) \epsilon^{\mu\nu\rho\sigma} q_{1\rho} q_{2\sigma}, \quad (91)$$

where $a_{1,2,3}$ are Lorentz-invariant formfactors and $q_{1,2}$ are the momenta of the gauge bosons. Production of the MSSM Higgs bosons is implemented in VBFNLO by altering the value of the formfactor a_1 (which at tree level is the only non-zero formfactor). The MSSM parameters can be specified either via a SLHA file or, if VBFNLO is linked to FEYNHIGGS [77–80], by the user.

[50] At Born level in the MSSM with real parameters, the CP-odd Higgs boson A is not produced.

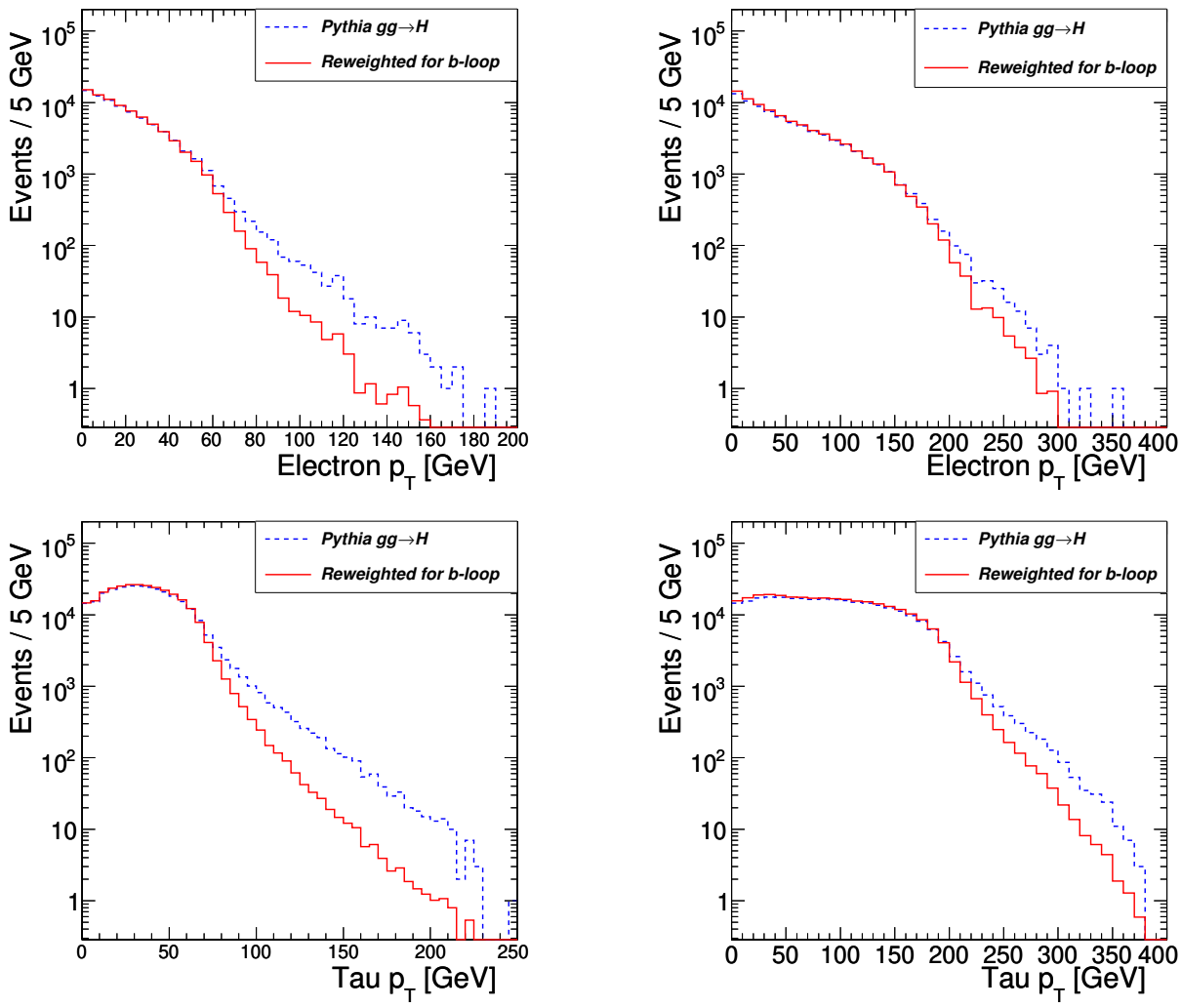

Fig. 112: Generated $p_{\mathrm{T}}^{\mathrm{e}}$ and p_{T}^{τ} distributions for $M_{\mathrm{H}} = 140$ GeV (left) and $M_{\mathrm{H}} = 400$ GeV (right) for the $\mathrm{gg} \to \mathrm{H}$ process generated with PYTHIA (dashed) and after re-weighting (solid) to correct for $\mathrm{gg} \to \mathrm{H}$ production dominated by the b-loop contribution.

12.3.4.2 Higgs mixing

Mixing between the neutral Higgs bosons can be very significant numerically,[51] and needs to be taken into account in order to produce phenomenologically relevant results. There is some flexibility, however, in the manner in which this mixing is included in the VBF process, and VBFNLO provides several options. These are implemented by altering the formfactors of Eq. (91) appropriately, and are as follows:

1. Wave-function normalisation factors (the Z-factors as defined in Ref. [80]) are used which ensure the correct on-shell properties of the produced Higgs boson. These wave-function normalisation factors incorporate the potentially numerically large and process-independent Higgs propagator corrections. For this option, it is recommended that FEYNHIGGS is used, which calculates the necessary Z-factors including all one-loop corrections as well as the dominant two-loop corrections in the MSSM with complex parameters.[52] Since the higher-order Higgs propagator corrections are

[51] In the MSSM with real parameters, mixing occurs between the two neutral CP-even Higgs bosons, h and H, and if complex parameters are allowed, mixing between all three neutral Higgs bosons, h, H, and A must be considered.

[52] If a SLHA file is used as input and this option is chosen, VBFNLO can calculate the Z-factors if linked to LOOP-

contained in the Z-factors, the mixing angle α needs to be evaluated at lowest order.

2. Since the Higgs mixing contributions are universal and appear in the same way in higher-order diagrams as well, it seems natural to apply them in a factorised way such that they multiply both the tree-level and the loop-level contributions. Compared to the case where the Z-factors are only applied at the tree level, this option can have a significant numerical effect in rather extreme regions of the MSSM parameter space, especially when CP-violating effects are considered. In the $m_{\mathrm{h}}^{\max}$ scenario, however, including mixing at loop-level as well as at tree level has very little effect, even in the non-decoupling regime.
3. If the momentum dependence of the Z-factors and CP-violating effects are neglected, the contribution of the Z-factors reduces to a correction to the Higgs mixing angle, resulting in an effective mixing angle, α_{eff} (numerical values for α_{eff} can either be taken from the SLHA file, or from FEYNHIGGS). It should be noted, however, that this simple approximation is not sufficient to ensure the correct on-shell properties of the produced Higgs boson.
4. The Higgs mixing can be treated like an additional counterterm that is added at NLO.

Various Higgs decays are included in VBFNLO: $\mathrm{H} \to \gamma\gamma$, $\mathrm{H} \to \mu^+\mu^-$, $\mathrm{H} \to \tau^+\tau^-$, $\mathrm{H} \to \mathrm{b}\bar{\mathrm{b}}$, $\mathrm{H} \to \mathrm{W}^+\mathrm{W}^- \to \mathrm{l}^+\nu_{\mathrm{l}}\mathrm{l}^-\bar{\nu}_{\mathrm{l}}$, $\mathrm{H} \to \mathrm{ZZ} \to \mathrm{l}^+\mathrm{l}^-\nu_{\mathrm{l}}\bar{\nu}_{\mathrm{l}}$ and $\mathrm{H} \to \mathrm{ZZ} \to \mathrm{l}^+\mathrm{l}^-\mathrm{l}^+\mathrm{l}^-$. When working in the MSSM, the branching ratios and widths needed can either be read from the SLHA file or taken from the FEYNHIGGS output.

12.3.4.3 Electroweak corrections to VBF in the MSSM

In the SM, the electroweak corrections to VBF have been found to be as important numerically as the NLO QCD corrections $\mathcal{O}(-5\%)$ in the mass range $100-200$ GeV [258, 259, 262]. In the MSSM, these corrections [262, 381, 382] are also potentially important and should be considered for phenomenologically relevant studies. In the decoupling region of the MSSM parameter space, these corrections tend to be – as expected – very similar to those in the SM for the light scalar Higgs boson. In other areas of parameter space, however, the electroweak corrections can differ significantly between the SM and the MSSM.

The complete SM-type and dominant SUSY NLO electroweak corrections to vector-boson fusion have been incorporated into the program VBFNLO, as described in Ref. [262], supplementing the already existing SM NLO QCD corrections. In the SM, the full electroweak corrections to the t-channel VBF process are included. In the MSSM all SM-type boxes and pentagons, together with all MSSM corrections to the vertex and self energy type diagrams are incorporated. For the Higgs-boson vertex and self-energy corrections this has been done using an effective HVV vertex, with formfactors as in Eq. (91), and an effective qqV coupling is used to include the loop corrections to that vertex. To include the box and pentagon diagrams, on the other hand, the full $2 \to 3$ matrix element has been calculated. An on-shell renormalisation scheme has been used, ensuring that the renormalised mass parameters of the Higgs and gauge bosons correspond to the physical masses.

The remaining SUSY electroweak corrections – i.e., the chargino and neutralino boxes and pentagons – are sub-dominant in the investigated $m_{\mathrm{h}}^{\max}$ scenario [381, 382]. Due to this, and the large CPU time needed to calculate these corrections, they are not yet included in VBFNLO. The SUSY QCD corrections were investigated in Refs. [16, 381–383] and found to be small.

VBFNLO offers several options for the parametrisation of the electromagnetic coupling. The choice of parametrisation has a significant effect on the relative size of the electroweak corrections, as the charge renormalisation constant, δZ_{e}, must be altered to suit the LO coupling.

TOOLS [379, 380], but only in the MSSM with real parameters, and only to one-loop level.

12.3.4.4 VBF parameters and cuts

The numerical results presented here were produced using VBFNLO to simulate VBF production of the light CP-even Higgs boson and have been evaluated in the $m_{\rm h}^{\rm max}$ scenario as described in Eq. (82).

FEYNHIGGS-2.7.4 is used to calculate the MSSM parameters – in particular the Higgs boson masses, mixing, and widths. Matching the setup of the investigation of the vector-boson-fusion channel in the SM, described in Section 6.2, the electroweak parameters used here are as given in Appendix A of Ref. [7], the electromagnetic coupling is defined via the Fermi constant $G_{\rm F}$, and the renormalisation and factorisations scales are set to $M_{\rm W}$. The anti-k_T algorithm is used to construct the jets, and the cuts used are also as in Section 6.2:

$$\Delta R = 0.5, \quad p_{\rm T_j} > 20 \text{ GeV}, \quad |y_j| < 4.5, \quad |y_{j_1} - y_{j_2}| > 4, \quad m_{jj} > 600 \text{ GeV}. \tag{92}$$

The Higgs boson is generated on-shell.

For each parameter point the cross sections and distributions have been calculated twice – once in the MSSM, including NLO QCD and all MSSM electroweak corrections except for the SUSY boxes and pentagons (i.e., those containing charginos and neutralinos), and once in the SM with a Higgs mass equal to that in the MSSM, including the complete SM QCD and electroweak corrections. The SM cross section can then be rescaled by a SUSY factor, in order to assess the impact of the SUSY-type corrections. Two SUSY factors have been investigated, S_Z and S_α, which can be expressed as follows,

$$\begin{aligned} S_Z &= |Z_{\rm hh} \sin(\beta - \alpha_{\rm tree}) + Z_{\rm hH} \cos(\beta - \alpha_{\rm tree})|^2, \\ S_\alpha &= \sin^2(\beta - \alpha_{\rm eff}). \end{aligned} \tag{93}$$

Here S_Z is an effective coupling that is composed from the full wave-function-normalisation factors that ensure the correct on-shell properties of the produced Higgs boson, see the description in Section 12.3.4.2. S_α, on the other hand, is an approximate effective coupling arising from S_Z in the limit where the momentum dependence of the Z-factors is neglected. For the full result within the MSSM, the wave-function normalisation factors are used without further approximations.

12.3.4.5 Total cross sections

Table 42 shows the NLO cross sections (together with the statistical errors from the Monte Carlo integration) in the MSSM and for the rescaled SM with the MSTW2008NLO PDF set[53]. As expected, in the decoupling regime (i.e., for large values of $M_{\rm A}$), the rescaling of the SM works well, giving adjusted cross sections within 2% of the true MSSM value. The rescaling is worst for high values of $\tan\beta$ and low values of $M_{\rm A}$, in the non-decoupling regime, where there is a factor of more than 3 difference between the rescaled SM cross sections and the true MSSM cross section, implying that the SUSY corrections at this point in parameter space are significant. It should be noted, however, that in this region of parameter space the leading-order cross section is extremely small. The seemingly large corrections are directly related to the fact that the cross section itself is heavily suppressed in this region. They therefore do not endanger the reliability of the theoretical prediction for Higgs-boson production in weak-boson fusion where it is phenomenologically relevant. In parameter regions where the leading-order cross section is heavily suppressed, one in general has to take into account also the squared one-loop contribution, which may be of comparable size as the product of the one-loop amplitude with the tree-level contribution. For the scenario under consideration, there is not a large difference between the two rescaling factors described in Eq. (93); S_Z performs slightly better in the more extreme regions of the scenario (i.e., large $\tan\beta$, small $M_{\rm A}$), whereas S_α (accidentally) provides a better description in the decoupling region.

[53]The simulation has also been run using the CTEQ6.6 PDF set, and very similar features were found. It should be noted that both PDF sets are in principle not sufficient for processes where NLO electroweak corrections are incorporated, since the PDF sets do not involve any QED contributions. However, the QED effects are expected to be small on the one hand and on the other hand we intend to show the basic higher-order corrections in this section, the size of which will not depend on the choice of the PDFs significantly.

Table 42: Higgs NLO cross sections at 7 TeV with VBF cuts and the MSTW2008NLO PDF set, for the $m_{\rm h}^{\rm max}$ scenario in the MSSM and for the corresponding SM cross section rescaled by the SUSY factors S_α and S_Z, as defined in Eq. (93).

$\tan\beta$	$M_{\rm A}$ [GeV]	NLO, MSSM [fb]	NLO, SM$\times S_\alpha$ [fb]	NLO, SM$\times S_Z$ [fb]
	100	148.261 $\pm$ 0.381	152.605 $\pm$ 0.298	153.425 $\pm$ 0.299
3	200	249.060 $\pm$ 2.123	250.880 $\pm$ 1.548	252.419 $\pm$ 1.558
	500	253.411 $\pm$ 0.813	255.963 $\pm$ 0.698	257.394 $\pm$ 0.701
	100	13.059 $\pm$ 0.052	16.108 $\pm$ 0.024	16.066 $\pm$ 0.024
15	200	236.179 $\pm$ 1.399	237.359 $\pm$ 1.392	238.746 $\pm$ 1.400
	500	235.097 $\pm$ 2.989	239.307 $\pm$ 0.899	240.668 $\pm$ 0.904
	100	0.544 $\pm$ 0.003	1.835 $\pm$ 0.007	1.806 $\pm$ 0.007
50	200	237.742 $\pm$ 0.438	238.196 $\pm$ 0.597	239.551 $\pm$ 0.600
	500	236.179 $\pm$ 1.266	236.496 $\pm$ 2.518	237.832 $\pm$ 2.532

In the SM, the electroweak corrections are of the order -8%. In the MSSM, the electroweak corrections in the decoupling regime are slightly larger than this, by approximately $0.5-1\%$, and in the non-decoupling regime the electroweak corrections become much larger – reaching more than – 70% for $\tan\beta = 50$ and $M_{\rm A} = 100$ GeV (as explained above, this large correction is related to the fact that the leading-order cross section is heavily suppressed in this parameter region).

12.3.4.6 Differential distributions

A number of differential distributions were generated for the parameter points above. Here, we examine a selection of them for the two 'extreme' points

$$\tan\beta = 3, M_{\rm A} = 500 \text{ GeV},$$
$$\tan\beta = 50, M_{\rm A} = 100 \text{ GeV}.$$

Each plot compares the leading-order result in the MSSM (solid black) with the NLO MSSM value (dotted green) and the SM NLO result rescaled by the SUSY factors S_α (pink dash-dotted) and S_Z (red short-dashed) using the MSTW2008NLO PDF set.

Figure 113 shows the azimuthal-angle distribution, ϕ_{jj} between the two tagging jets. This distribution is of special interest in VBF studies, as it provides an opportunity to study the structure of the HVV coupling. As with the total cross sections, for the low-$\tan\beta$, high-$M_{\rm A}$ case, the rescaling procedure works reasonably well. For the extreme case of high-$\tan\beta$ and low-$M_{\rm A}$ (shown on the right-hand side of Figure 113), where the cross section is heavily suppressed, a simple rescaling of the SM cross section would not be sufficient to accurately describe the MSSM result. It should be noted, however, that even in this extreme case the shapes of the distributions are very similar at LO and NLO, in both the SM and the MSSM, which means that the higher-order corrections do not significantly alter the structure of the HVV coupling.

Figure 114 presents the differential distribution of the transverse momentum of the leading jet (i.e., the jet with the highest $p_{\rm T}$). As with the azimuthal-angle distribution, the SM rescaling is seen to work well in the decoupling regime (left plot), but not in the non-decoupling regime (right plot), where the relative effect of the MSSM electroweak corrections is much larger than in the SM, while the cross section itself is heavily suppressed. The shape, however, of the distribution remains essentially unchanged. The NLO corrections (and in particular the EW contribution) cause an increasing reduction to the cross section at higher energy scales, as noted in Section 6.3.2. This feature is enhanced in the MSSM.

The Higgs transverse-momentum ($p_{\rm T,H}$) and rapidity ($y_{\rm H}$) differential distributions are shown in Figure 115, which shows the same general behaviour of the SM–MSSM comparison as the previous

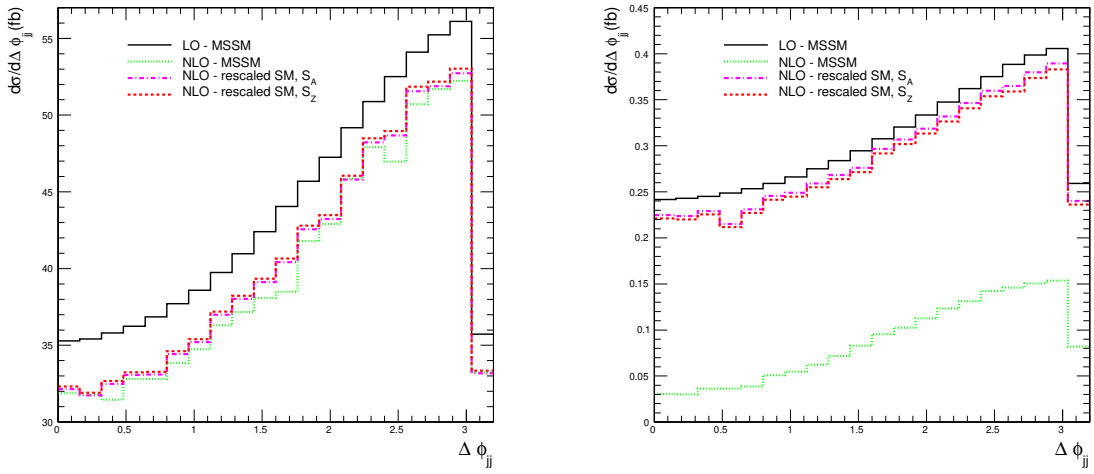

(a) (b)

Fig. 113: Azimuthal-angle distributions for $\tan\beta = 3$, $M_{\rm A} = 500$ GeV (left plot) and $\tan\beta = 50$, $M_{\rm A} = 100$ GeV (right plot), comparing the MSSM results with the rescaled SM values with the MSTW2008NLO PDF set.

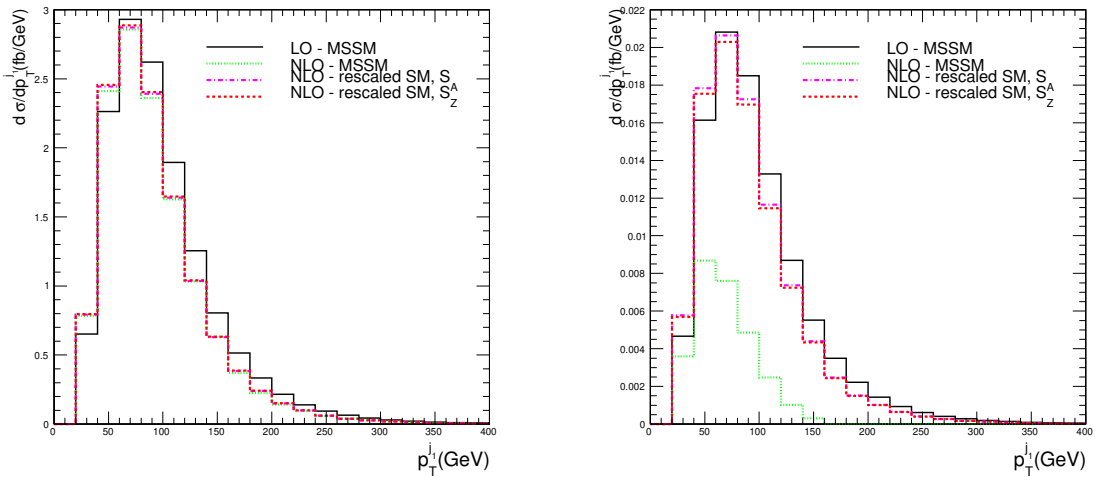

(a) (b)

Fig. 114: Transverse momentum of the leading jet for $\tan\beta = 3$, $M_{\rm A} = 500$ GeV (left plot) and $\tan\beta = 50$, $M_{\rm A} = 100$ GeV (right plot), comparing the MSSM results with the rescaled SM values with the MSTW2008NLO PDF set.

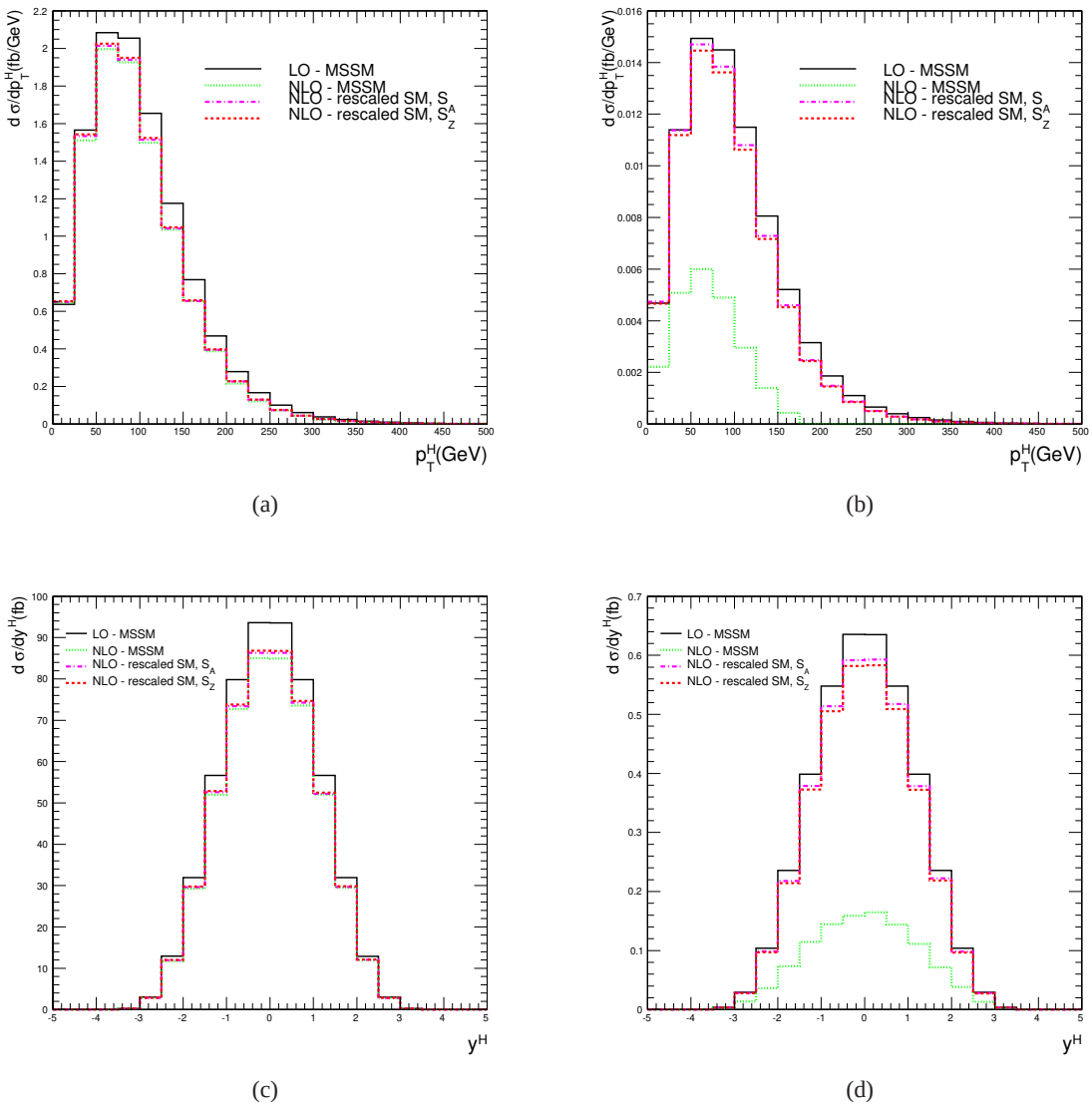

Fig. 115: Distribution of Higgs transverse momentum (upper plots) and rapidity (lower plots) for $\tan\beta = 3$, $M_{\rm A} = 500$ GeV (left plots) and $\tan\beta = 50$, $M_{\rm A} = 100$ GeV (right plots), comparing the MSSM results with the rescaled SM values with the MSTW2008NLO PDF set.

plots. The NLO corrections are much larger for the non-decoupling parameter point (right-hand plots), resulting in poorer rescaling behaviour in the region where the cross section itself is very small, but the shape of the distributions is relatively unaffected. As with the distribution of the transverse momentum of the leading jet, $p_{\rm T,j1}$, the magnitude of the NLO corrections increases with $p_{\rm T}$, and increases at a greater rate in the MSSM with $\tan\beta = 50$, $M_{\rm A} = 100$ GeV than in the corresponding rescaled SM results. The NLO corrections to the Higgs rapidity distribution are relatively constant as a function of the Higgs boson's rapidity. For high $\tan\beta$ and low $M_{\rm A}$ a certain effect on the shape is visible, but once again this behaviour appears in a parameter region where the cross section itself is very small.

12.3.5 MSSM NLO corrections for Higgs radiation from bottom quarks in the 5FS

Apart from the total inclusive cross section for Higgs production at the LHC, it is important to have predictions for (a) kinematical distributions of the Higgs boson and associated jets, and (b) the fraction

of events with zero, one, or more jets. In supersymmetric theories the associated production of a Higgs boson with bottom quarks is the dominant process in a large parameter region of the MSSM (see, e.g., Ref. [7]). The proper theory description of this process has been a subject of discussion for quite some time. The result is a rather satisfactory reconciliation of the two possible approaches, the so-called four- and five-flavor scheme (4FS and 5FS), which led to the "Santander-matching" procedure, see above.

Higher-order corrections in the 5FS are usually easier to calculate than in the 4FS, because one deals with a $2 \to 1$ rather than a $2 \to 3$ process at LO. However, since the 5FS works in the collinear approximation of the outgoing bottom quarks, effects from large transverse momenta of the bottom quarks are taken into account only at higher orders in this approach. In fact, NNLO plays a special role in the 5FS, which becomes obvious by noticing that it is the first order where the 5FS contains the LO Feynman diagram of the 4FS [368]. Hence only then the 5FS includes two outgoing bottom quarks at large transverse momentum.

With the total inclusive cross section under good theoretical control, it is natural to study more differential quantities. Being a $2 \to 1$ process, kinematical distributions in the 5FS are trivial at LO, just like in gluon fusion: the p_{T} of the Higgs boson vanishes, and the rapidity distribution is given by the boost of the partonic relative to the hadronic system.

Non-trivial distributions require a jet in the final state. The p_{T} and y distributions of the Higgs boson in the process $b\bar{b} \to \phi$+jet were studied at NLO in Ref. [384] (here and in what follows, $\phi \in \{\mathrm{h}, \mathrm{H}, \mathrm{A}\}$). Combining these results with the NNLO inclusive total cross section [368], one may obtain NNLO results with kinematical cuts.

As mentioned above, particularly interesting for experimental analyses is the decomposition of the events into $\phi + n$-jet bins. The case $n = 0$ can be obtained at NNLO by calculating the case $n \geq 1$ at NLO level, and subtracting it from the total inclusive cross section [385, 386]. For consistency, however, both ingredients should be evaluated using NNLO PDFs and running of α_{s}. This is indicated by the superscript NLO′ in the following equation:

$$\sigma_{\text{jet-veto}}^{\text{NNLO}} \equiv \sigma_{\text{0-jet}}^{\text{NNLO}} = \sigma_{\text{tot}}^{\text{NNLO}} - \sigma_{\geq\text{1-jet}}^{\text{NLO}'} \,. \tag{94}$$

Note that this equation is understood without any flavor requirements on the outgoing jet.

As an exemplary case, we consider results for the jet parameters (anti-k_{T} [175])

$$R = 0.4, \qquad p_{\mathrm{T}}^{\text{jet}} > 20 \text{ GeV}, \qquad |\eta^{\text{jet}}| < 4.8. \tag{95}$$

Fig. 116 shows the contributions of the NNLO jet-vetoed ($\phi + 0$-jet) and the NLO inclusive ϕ+jet rate to the NNLO total cross section in the $m_{\mathrm{h}}^{\max}$ scenario for two different values of $\tan\beta$. The corresponding numbers are given in Tables 43 and 44. Note, however, that the sum of the $\phi + n$-jet cross sections does not add up exactly to the total rate, because they are evaluated at different perturbative orders, and therefore with different sets of PDFs and α_{s} evolution. These numbers have been derived from the SM results of Ref. [386], reweighted by the MSSM bottom Yukawa coupling with the help of `FeynHiggs`.

Fig. 117 displays the relative perturbative error estimates, obtained by varying the renormalisation scale μ_{R} by a factor of two around $\mu_0 = M_\phi/4$ while keeping the factorisation scale μ_{F} fixed at μ_0, and then doing the same with μ_{F} and μ_{R} interchanged. The PDF+α_{s} uncertainties are those from MSTW2008 [107]. The full error estimate was obtained by quadratically adding the perturbative to the PDF+α_{s} error estimate. Note that these plots are the same as in the SM; the precise numerical values can therefore be taken from Ref. [386].

The 5FS has also been used in order to evaluate associated $\phi + \mathrm{b}$ production through NLO [387], which is contained in the recent ϕ+jet calculation [386]. Updated numbers can be obtained quite easily with the help of the program `MCFM` [232]. Here, however, we use the program described in Ref. [386]. Employing again the NNLO result for the total inclusive cross section, one may evaluate the b-vetoed

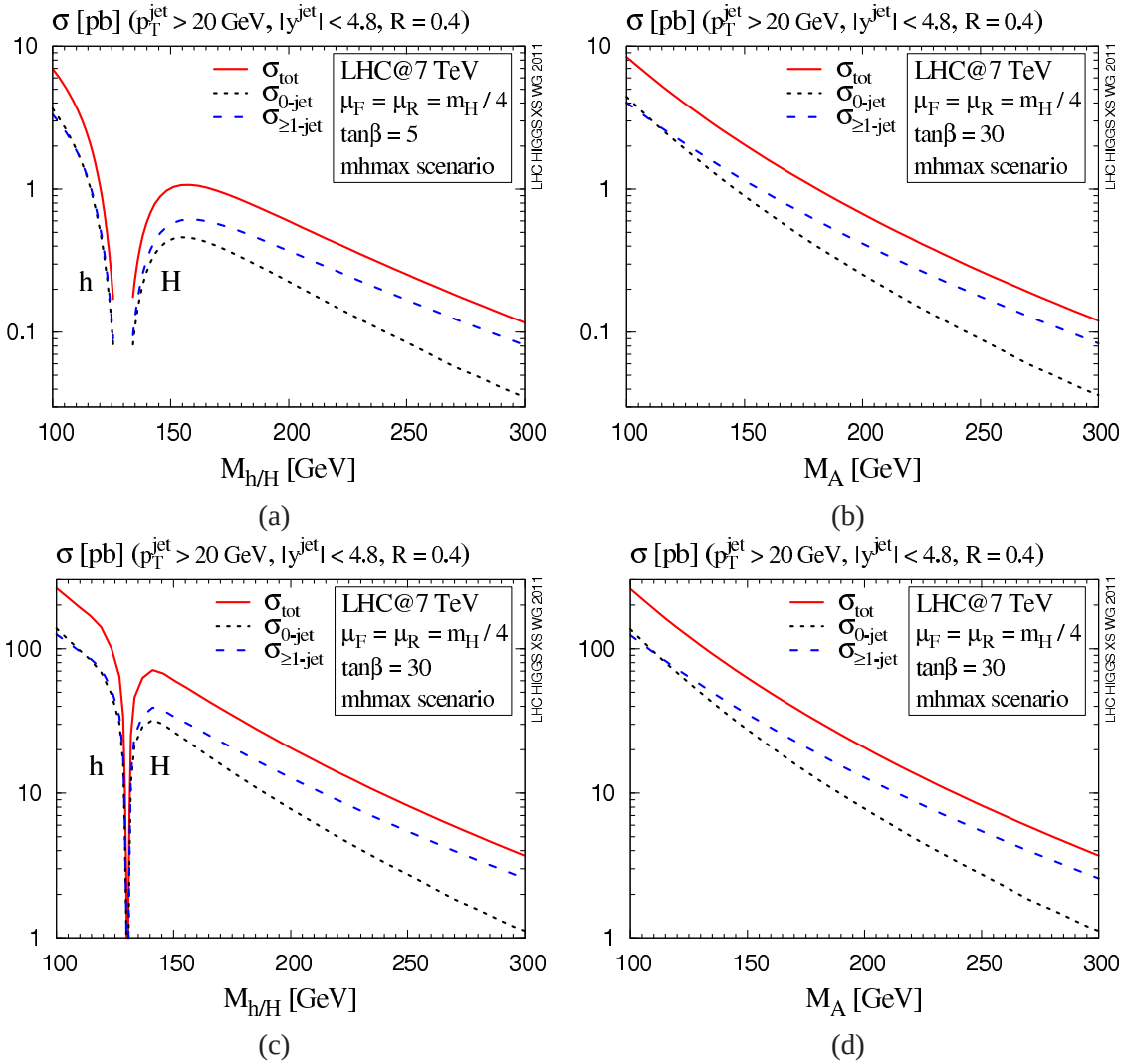

Fig. 116: Total inclusive (solid/red) and Higgs plus n-jet cross section for $n = 0$ (dashed/blue) and $n \geq 1$ (dotted/black) in the $m_{\rm h}^{\rm max}$ scenario for (a,b) $\tan\beta = 5$ and (c,d) $\tan\beta = 30$. Left and right column correspond to the CP-even and the CP-odd Higgs bosons, respectively.

cross section through NNLO, along the lines of Eq. (94):

$$\sigma^{\rm NNLO}_{\text{b-jet veto}} \equiv \sigma^{\rm NNLO}_{\rm 0b} = \sigma^{\rm NNLO}_{\rm tot} - \sigma^{\rm NLO'}_{\geq \rm 1b\text{-jet}} \,. \tag{96}$$

It should be recalled, however, that this quantity does not take into account the finite b-jet efficiency $\epsilon_{\rm b}$. This distinguishes it from the Higgs cross section with zero b-tags $\sigma_{\rm 0b\text{-tag}}$, which can be obtained by combining $\sigma_{\rm 0b}$ with the rate for having one or two b quarks in the final state, i.e., $\sigma_{\rm 1b}$ and $\sigma_{\rm 2b}$ [386]:

$$\sigma^{\rm NNLO}_{\rm 0b\text{-tag}} = \sigma^{\rm NNLO}_{\rm 0b} + (1-\epsilon_{\rm b})\sigma^{\rm NLO}_{\rm 1b} + (1-\epsilon_{\rm b})^2\sigma^{\rm LO}_{\rm 2b}. \tag{97}$$

In this case, we set the jet parameters to

$$R = 0.4, \qquad p_{\rm T}^b > 20\,{\rm GeV}, \qquad |\eta^b| < 2.5. \tag{98}$$

The $\phi + 0$b-, 1b-, and 2b-contributions are shown, together with the total cross section, in Fig. 118, for the same parameters as in Fig. 116. The numbers were again produced with the help of the results from Ref. [386], reweighted by the corresponding MSSM Yukawa coupling.

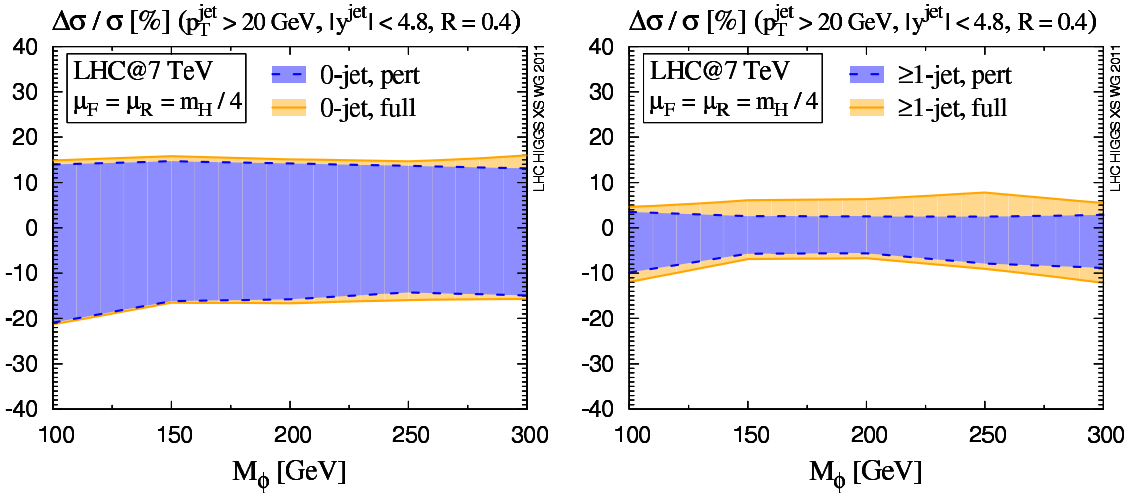

(a) (b)

Fig. 117: Relative perturbative and full error estimates for (a) the jet-vetoed cross section and (b) the inclusive ϕ+jet cross section. The full error estimate is obtained by adding the perturbative and the PDF+α_s-error quadratically.

12.3.6 Comparison of b-jet acceptance and kinematic distributions in $\mathrm{b\overline{b}} \to \mathrm{H}$ *production between* PYTHIA *and high-order calculations*

At large values of tanβ and M_A the $\mathrm{b\overline{b}} \to \phi$ process dominates the production of the MSSM neutral Higgs bosons [388]. The most recent SUSY $\phi \to \tau\tau$ analysis in CMS [389] uses a combination of two analyses: with at least one b-tagged jet and with zero b-tagged jets. For the event generation of $\mathrm{pp} \to \mathrm{b\overline{b}h}$ process the PYTHIA Monte Carlo (process 186) is used. The comparison of PYTHIA with the 4FS calculations is shown in the earlier paper [390] for the p_T distribution of b-jets where good agreement at the level of 10% is found. In this note we compare acceptance efficiency for b-jets, p_T, and η distributions for b-jets and Higgs bosons as given by PYTHIA with the high-order calculations in the 5FS described in Ref. [386] and Section 12.3.5. The jets have been reconstructed from the final-state partons using the anti-k_T algorithm [175] with parameter R=0.5. The jet is defined as a b-jet if at least one b quark is present in the list of the jet constituents. The kinematic acceptance cuts for b-jets used were the same as in the CMS analysis [389]: $p_T > 20$ GeV, $|\eta| < 2.4$. Table 45 and Table 46 show the fraction of b-jets within the acceptance obtained from the high order calculations (second column) and from PYTHIA generator (5-th column) for $M_H = 140$ GeV and 400 GeV. The errors of the theoretical calculations due to the scale variation and PDF are shown in the third and fourth columns of Table 45 and Table 46. The total theoretical cross section for the Standard Model $\mathrm{b\overline{b}} \to \mathrm{H}$ process for $M_H = 140$ GeV is 108.85 pb and for $M_H = 400$ GeV it is 1.29 pb.

Good agreement between PYTHIA and the high order calculations in the 5FS is found for the fractions of zero b-jets and at least one b-jet in the acceptance. The fraction of two b-jets predicted by the 5FS calculations is lower than given by PYTHIA, but agrees within the theoretical errors.

We compare the differential distributions p_T and rapidity (y) of the leading p_T b-jet within the acceptance between PYTHIA and the NLO predictions. Figure 119 shows the distributions of y^b normalised on unity for $M_H = 140$ GeV (left) and $M_H = 400$ GeV (right). One can see the difference between PYTHIA and the NLO curves especially for the heavy Higgs boson. Figure 120 shows the distributions of p_T^b normalised on unity for $M_H = 140$ GeV (left) and $M_H = 400$ GeV (right). There is good agreement between PYTHIA and the NLO predictions.

We also compare the p_T and rapidity distributions of the Higgs boson with at least one b-jet in the

Table 43: Numerical values for the total cross section $\sigma_{\text{tot}}^{\text{NNLO}}$, the $\phi + 0$-jet rate $\sigma_{\text{0-jet}}^{\text{NNLO}}$, and the inclusive ϕ+jet rate $\sigma_{\geq\text{1-jet}}^{\text{NLO}}$ for the $m_{\text{h}}^{\max}$ scenario for $\tan\beta = 5$ ($\phi \in \{\text{h}, \text{H}, \text{A}\}$).

LHC @ 7 TeV, $\lvert y^{\text{jet}}\rvert < 4.8$, $p_{\text{T}}^{\text{jet}} > 20$ GeV, $R = 0.4$; $m_{\text{h}}^{\max}(\tan\beta = 5)$									
M_{A}	$\sigma_{\text{tot}}^{\text{NNLO}}$ [pb]			$\sigma_{\text{0-jet}}^{\text{NNLO}}$ [pb]			$\sigma_{\geq\text{1-jet}}^{\text{NLO}}$ [pb]		
[GeV]	A	h	H	A	h	H	A	h	H
100	8.42	9.84	0.392	4.43	5.38	0.180	4.03	4.59	0.214
110	6.12	7.10	0.574	3.09	3.74	0.261	3.05	3.40	0.315
120	4.54	5.05	0.788	2.22	2.59	0.353	2.35	2.47	0.436
130	3.43	3.54	0.974	1.62	1.78	0.429	1.83	1.77	0.545
140	2.63	2.48	1.07	1.19	1.23	0.461	1.44	1.26	0.606
150	2.04	1.78	1.06	0.894	0.878	0.446	1.14	0.913	0.611
160	1.60	1.33	0.974	0.681	0.652	0.400	0.924	0.686	0.573
170	1.27	1.03	0.861	0.522	0.505	0.344	0.749	0.536	0.516
180	1.02	0.836	0.744	0.406	0.407	0.291	0.613	0.434	0.453
190	0.825	0.698	0.635	0.320	0.339	0.242	0.503	0.364	0.392
200	0.673	0.599	0.539	0.254	0.290	0.201	0.417	0.313	0.337
210	0.552	0.526	0.457	0.203	0.254	0.165	0.348	0.275	0.290
220	0.457	0.470	0.387	0.163	0.227	0.136	0.292	0.246	0.249
230	0.380	0.427	0.328	0.133	0.206	0.113	0.246	0.224	0.213
240	0.318	0.393	0.278	0.108	0.190	0.0942	0.208	0.206	0.184
250	0.267	0.366	0.237	0.0894	0.176	0.0785	0.178	0.192	0.158
260	0.226	0.343	0.203	0.0735	0.165	0.0649	0.152	0.180	0.136
270	0.192	0.324	0.173	0.0600	0.156	0.0541	0.130	0.170	0.118
280	0.163	0.308	0.149	0.0509	0.148	0.0461	0.112	0.162	0.102
290	0.140	0.294	0.129	0.0426	0.142	0.0388	0.0967	0.155	0.0891
300	0.120	0.283	0.111	0.0363	0.136	0.0338	0.0836	0.149	0.0774

acceptance.

Table 44: Same as Table 43, but for $\tan\beta = 30$.

LHC @ 7 TeV, $\lvert y^{\rm jet}\rvert < 4.8$, $p_{\rm T}^{\rm jet} > 20$ GeV, $R = 0.4$; $m_{\rm h}^{\rm max}(\tan\beta = 30)$									
$M_{\rm A}$	$\sigma_{\rm tot}^{\rm NNLO}$ [pb]			$\sigma_{\rm 0\text{-}jet}^{\rm NNLO}$ [pb]			$\sigma_{\geq 1\text{-jet}}^{\rm NLO}$ [pb]		
[GeV]	A	h	H	A	h	H	A	h	H
100	259	265	0.776	136	140	0.365	124	127	0.415
110	188	195	1.93	94.9	98.4	0.906	93.8	97.0	1.03
120	140	141	7.19	68.2	68.9	3.38	72.3	72.7	3.85
130	105	64.2	46.0	49.7	30.6	21.4	56.3	34.0	24.8
140	80.8	11.1	71.2	36.6	5.25	32.2	44.3	5.92	39.2
150	62.7	3.83	59.8	27.5	1.81	26.2	35.2	2.04	33.6
160	49.3	2.03	48.0	20.9	0.955	20.4	28.4	1.08	27.7
170	39.1	1.32	38.4	16.1	0.621	15.8	23.0	0.702	22.6
180	31.4	0.961	30.9	12.5	0.453	12.3	18.9	0.513	18.6
190	25.4	0.756	25.1	9.86	0.356	9.74	15.5	0.404	15.3
200	20.7	0.625	20.5	7.81	0.295	7.74	12.8	0.334	12.7
210	17.0	0.535	16.9	6.26	0.252	6.20	10.7	0.286	10.6
220	14.0	0.471	13.9	5.01	0.222	4.97	8.98	0.252	8.92
230	11.7	0.423	11.6	4.08	0.200	4.05	7.56	0.226	7.51
240	9.77	0.386	9.71	3.33	0.182	3.31	6.41	0.206	6.37
250	8.22	0.357	8.17	2.75	0.168	2.73	5.46	0.191	5.43
260	6.95	0.334	6.91	2.26	0.157	2.25	4.66	0.178	4.64
270	5.90	0.315	5.87	1.85	0.148	1.84	3.99	0.168	3.97
280	5.03	0.299	5.00	1.57	0.141	1.56	3.44	0.160	3.43
290	4.30	0.286	4.28	1.31	0.135	1.30	2.97	0.153	2.96
300	3.70	0.274	3.68	1.12	0.129	1.11	2.57	0.146	2.56

Table 45: The fraction of b-jets within the acceptance obtained from the high-order calculations in the 5FS (second column) and from PYTHIA generator (5-th column) for $M_{\rm H} = 140$ GeV. The errors of the theoretical calculations due to the scale variation and PDF in % are shown in third and fourth columns

final state i	$\sigma_i^{\rm th}/\sigma_{\rm tot}^{\rm th}$	scale error(%)	PDF error (%)	PYTHIA $\rm pp \to b\bar{b}h$
0 b-jet	0.6381	-14.4 +8.8	-4.6 +3.6	0.621
one b-jet	0.3286	-6.9 +4.4	-3.2 +5.0	0.322
two b-jets	0.0417	-33.1 +59.0	-3.0 +2.3	0.057

Table 46: The fraction of b-jets within the acceptance obtained from the high order calculations in the 5FS (second column) and from PYTHIA generator (5-th column) for $M_{\rm H} = 400$ GeV. The errors of the theoretical calculations due to the scale variation and PDF are shown in third and fourth columns

final state i	$\sigma_i^{\rm th}/\sigma_{\rm tot}^{\rm th}$	scale error (%)	PDF error (%)	PYTHIA $\rm pp \to b\bar{b}h$
0 b-jet	0.519	-7.2 +8.9	-6.7 +7.6	0.511
one b-jet	0.426	-8.9 +5.8	-6.4 +6.4	0.387
two b-jets	0.063	-28.4 +45.5	-4.5 +4.4	0.102

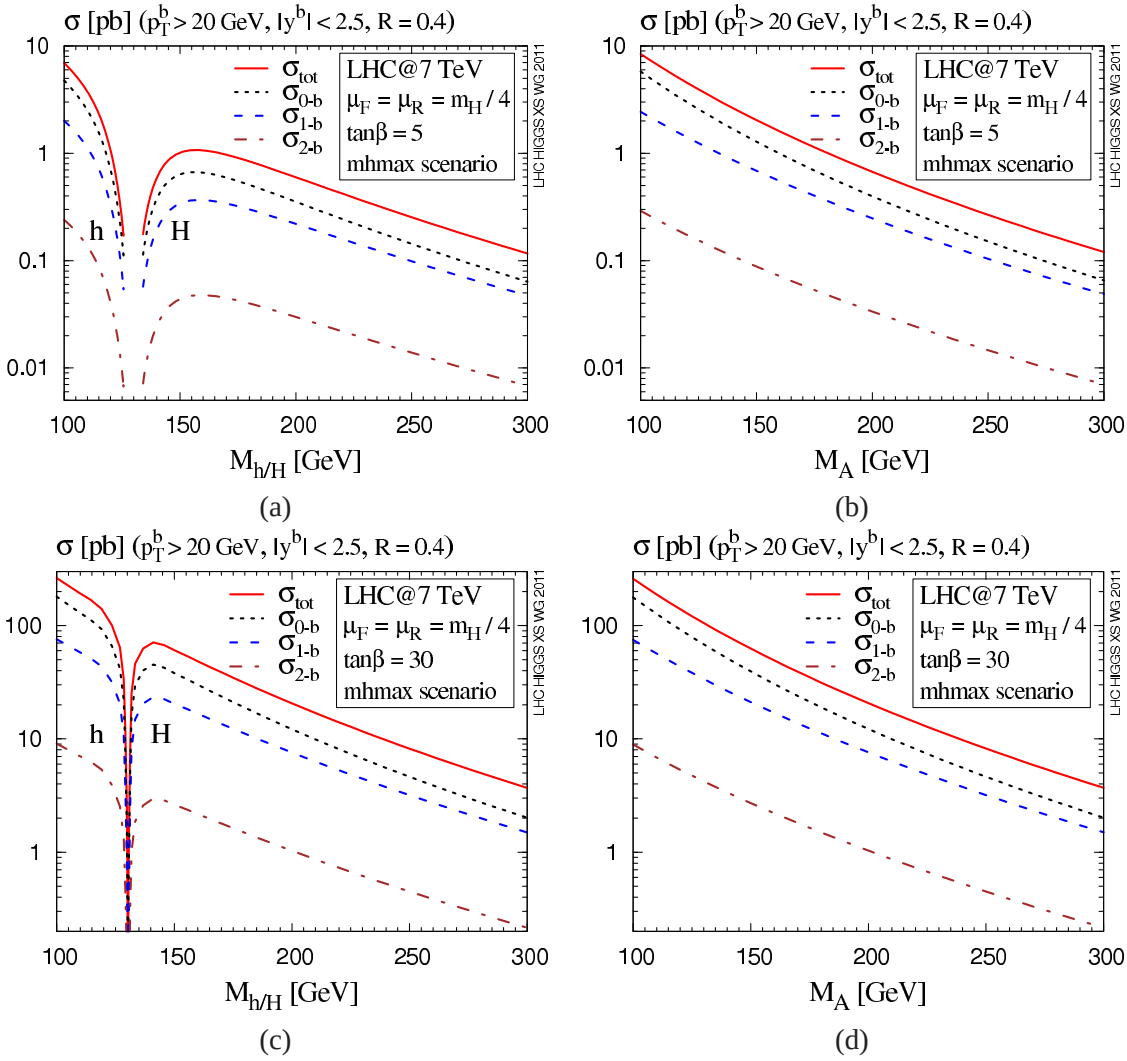

Fig. 118: Total inclusive (solid/red) and Higgs plus nb-jet cross section for $n = 0$ (dashed/blue), $n = 1$ (dotted/black), and $n = 2$ (dash-dotted/brown) in the $m_{\rm h}^{\rm max}$ scenario for (a,b) $\tan\beta = 5$ and (c,d) $\tan\beta = 30$. Left and right column correspond to the CP-even and the CP-odd Higgs bosons, respectively.

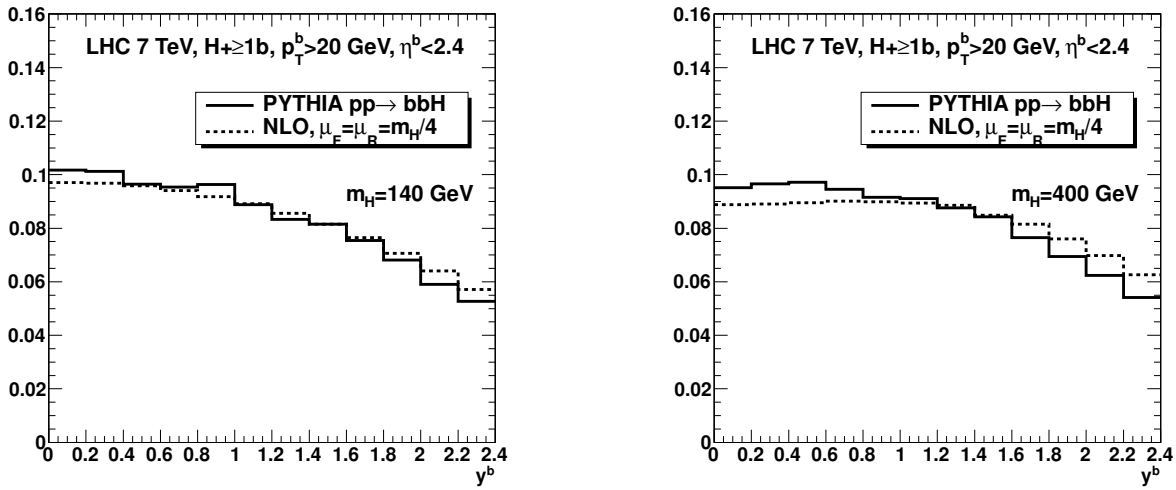

Fig. 119: The rapidity distributions of the leading p_{T} b-jet normalised on unity for $M_{\mathrm{H}} = 140$ GeV (left) and $M_{\mathrm{H}} = 400$ GeV (right) obtained with PYTHIA (solid lines) and with NLO calculations (dashed lines).

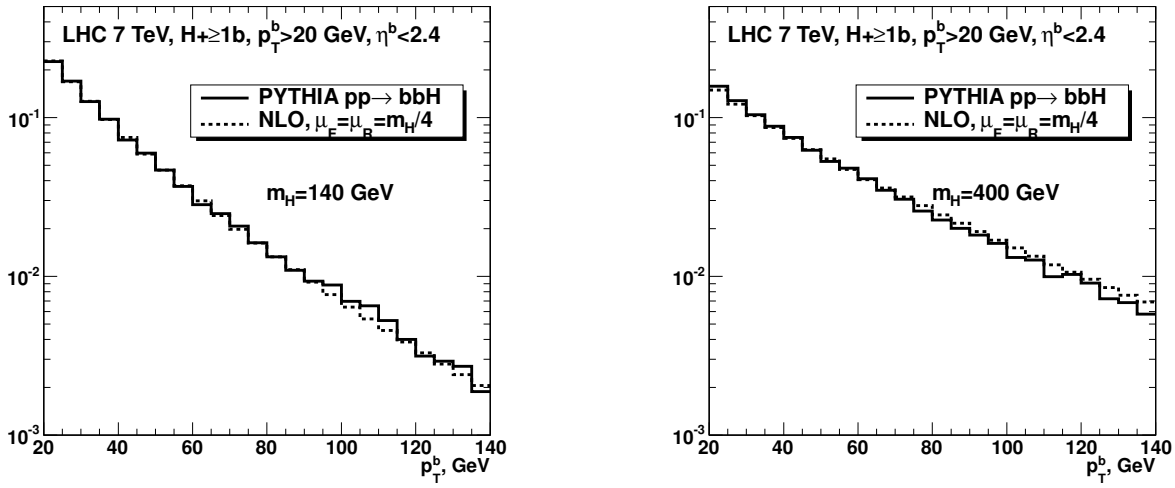

Fig. 120: The p_{T} distributions of the leading p_{T} b-jet normalised on unity for $M_{\mathrm{H}} = 140$ GeV (left) and $M_{\mathrm{H}} = 400$ GeV (right) obtained with PYTHIA (solid lines) and with NLO calculations (dashed lines).

13 Charged-Higgs-boson production and decay[54]

Many extensions of the Standard Model, in particular supersymmetric theories, require two Higgs doublets leading to five physical scalar Higgs bosons, including two (mass-degenerate) charged particles $\mathrm{H}^{\pm}$. The discovery of a charged Higgs boson would provide unambiguous evidence for an extended Higgs sector beyond the Standard Model. Searches at LEP have set a limit $M_{\mathrm{H}^{\pm}} > 79.3$ GeV on the mass of a charged Higgs boson in a general two-Higgs-doublet model [391]. One usually distinguishes a "light charged Higgs", $M_{\mathrm{H}^{\pm}} < m_{\mathrm{t}}$, and a "heavy charged Higgs", $M_{\mathrm{H}^{\pm}} > m_{\mathrm{t}}$. Within the MSSM, the charged Higgs boson mass is constrained by the pseudoscalar Higgs mass and the W-boson mass through $M^2_{\mathrm{H}^{\pm}} = M^2_{\mathrm{A}} + M^2_{\mathrm{W}}$ at tree level, with only moderate higher-order corrections [80, 392–394]. A mass limit on the MSSM charged Higgs boson can thus be derived from the limit on the pseudoscalar Higgs boson, $M_{\mathrm{A}} > 93.4$ GeV [344], resulting in $M_{\mathrm{H}^{\pm}} \gtrsim 120$ GeV. At the Tevatron, searches for light charged Higgs bosons in top-quark decays $\mathrm{t} \to \mathrm{bH}^{\pm}$ [395, 396] have placed some constraints on the MSSM parameter space, but do not provide any further generic bounds on $M_{\mathrm{H}^{\pm}}$.

There are two main mechanisms for charged Higgs boson production at the LHC:

$$\begin{array}{lll} \text{top-quark decay:} & \mathrm{t} \to \mathrm{bH}^{\pm}+\mathrm{X} & \text{if } M_{\mathrm{H}^{\pm}} \lesssim m_{\mathrm{t}}\,, \\ \text{associated production:} & \mathrm{pp} \to \mathrm{tbH}^{\pm}+\mathrm{X} & \text{if } M_{\mathrm{H}^{\pm}} \gtrsim m_{\mathrm{t}}\,. \end{array}$$

The first process is dominant for the light charged Higgs, while the second process dominates for a heavy charged Higgs boson. Alternative production mechanisms like quark–antiquark annihilation $\mathrm{q}\bar{\mathrm{q}}' \to \mathrm{H}^{\pm}$ and $\mathrm{H}^{\pm} + \mathrm{jet}$ production [397], associated $\mathrm{H}^{\pm}\mathrm{W}^{\mp}$ production [398], or Higgs pair production [399–401] have suppressed rates, and it is not yet clear whether a signal could be established in any of those channels. Some of the above production processes may, however, be enhanced in models with non-minimal flavour violation. As the cross section for light-charged-Higgs-boson production are significantly higher than for heavy charged Higgs bosons, early searches at the LHC and also this section focuses mainly on those. All results shown below are for the $m_{\mathrm{h}}^{\max}$ scenario of the MSSM.

13.1 Light charged Higgs boson

To estimate the cross section for events with charged Higgs bosons in top-quark pair production, the following ingredients are needed: The top-quark pair production cross section, the branching ratio BR($\mathrm{t} \to \mathrm{bH}^{+}$) and the light-charged-Higgs-boson decay branching ratios. Complete scans of the $(M_{\mathrm{H}^{\pm}}, \tan\beta)$ plane for $\sqrt{s} = 7$ TeV are available in electronic format [55].

13.1.1 Top-quark pair production cross section

The $\mathrm{t}\bar{\mathrm{t}}$ production cross section at $\sqrt{s} = 7$ TeV is predicted to be 165^{+4}_{-9}(scale)$^{+7}_{-7}$(PDF) pb by approximate NNLO calculations [402, 403] recommended by the ATLAS Top Working Group [404]. The scale uncertainty is obtained as the "envelope" from a variation of the renormalisation scale μ_{R} and the factorisation scale μ_{F} from 0.5 to 2 times m_{t} (with $0.5 < \mu_{\mathrm{F}}/\mu_{\mathrm{R}} < 2$). The PDF uncertainty, obtained using MSTW2008 [107], is taken at the 68% C.L.; the two uncertainties should be added linearly.

13.1.2 Top-quark decays via a charged Higgs boson

The decay width calculation of the top quark to a light charged Higgs boson is compared for two different programs, FeynHiggs, version 2.8.5 [77–80], and HDECAY, version 4.43 [17, 405]. The $m_{\mathrm{h}}^{\max}$ benchmark scenario is used [10], which (in the on-shell scheme) is defined in Eq. (82). We slightly deviate from the original definition and use $M_{\mathrm{H}^{\pm}}$ instead of M_{A} as input parameter. Furthermore, also the μ

[54] M. Flechl, S. Heinemeyer, M. Krämer, S. Lehti (eds.); M. Hauru, M. Spira and M. Ubiali.

[55] `https://twiki.cern.ch/twiki/bin/view/LHCPhysics/MSSMCharged`

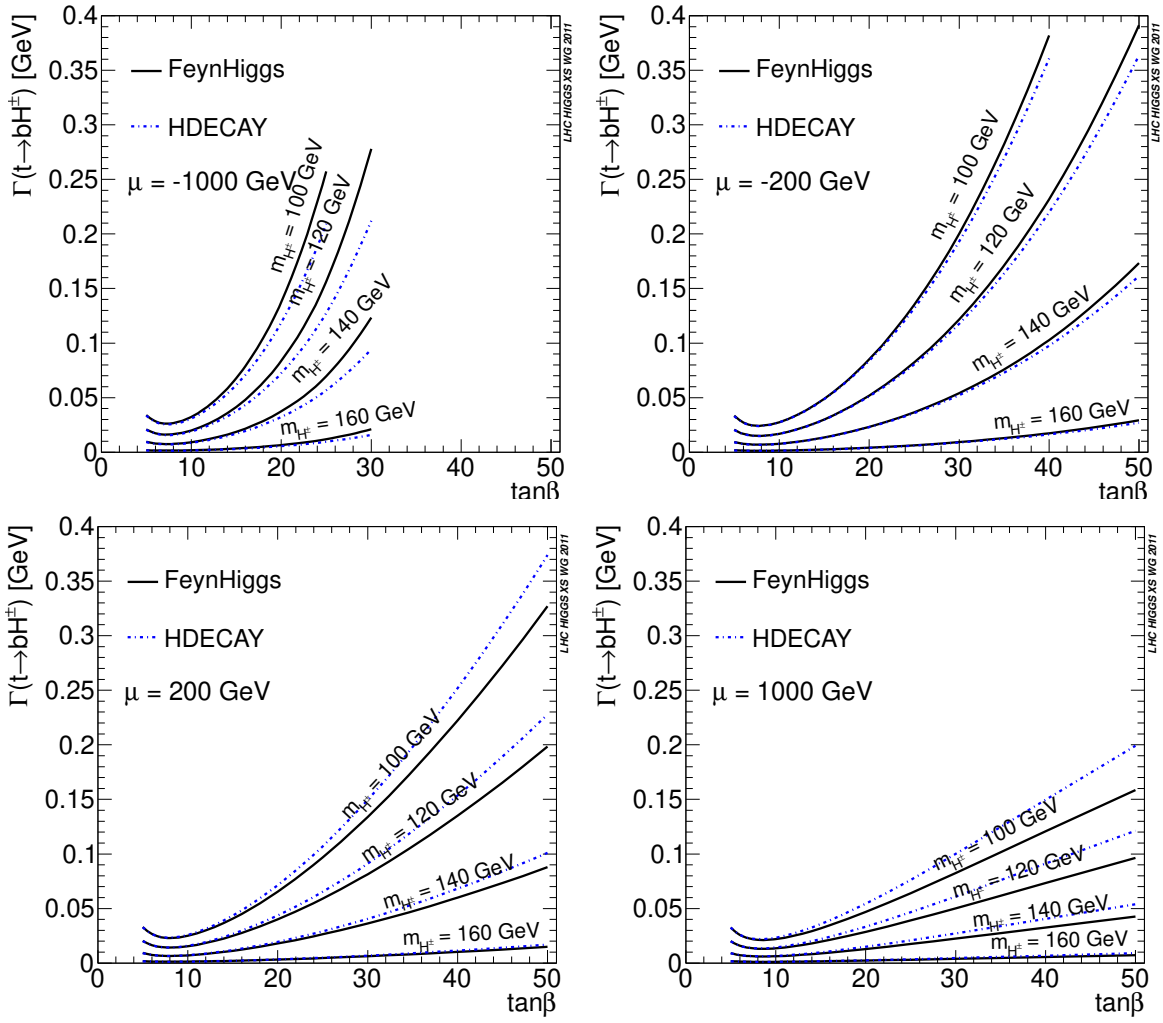

Fig. 121: The decay width $\Gamma(\mathrm{t} \to \mathrm{bH}^{\pm})$ calculated with FEYNHIGGS and HDECAY as a function of $\tan\beta$ for different values of μ and $M_{\mathrm{H}^{\pm}}$.

parameter is varied with values $\pm 1000, \pm 200$ GeV [406]. The Standard Model parameters are taken as given in Ref. [7], Appendix A.

The FEYNHIGGS calculation is based on the evaluation of $\Gamma(\mathrm{t} \to \mathrm{W}^{+}\mathrm{b})$ and $\Gamma(\mathrm{t} \to \mathrm{H}^{+}\mathrm{b})$. The former is calculated at NLO according to Ref. [407]. The decay to the charged Higgs boson and the bottom quark uses $m_{\mathrm{t}}(m_{\mathrm{t}})$ and $m_{\mathrm{b}}(m_{\mathrm{t}})$ in the Yukawa coupling, where the latter receives the additional correction factor $1/(1 + \Delta_{\mathrm{b}})$. The numerical results presented here are based on the evaluation of Δ_{b} in Ref. [408]. Furthermore additional QCD corrections taken from Ref. [342] are included, see also Ref. [409].

The HDECAY calculation is based on the evaluation of $\Gamma(\mathrm{t} \to \mathrm{W}^{+}\mathrm{b})$ and $\Gamma(\mathrm{t} \to \mathrm{H}^{+}\mathrm{b})$. The decays were evaluated including the full NLO QCD corrections (including bottom mass effects) [407] (and references therein). The top and (kinematical) bottom masses are taken as the pole masses while the bottom mass of the Yukawa coupling is taken as running $\overline{\mathrm{MS}}$ mass at the scale of the top mass. SUSY QCD and electroweak corrections are approximated via Δ_{b} based on Refs. [90–93, 338–342].

FEYNHIGGS has been run with the selected set of parameters. The FEYNHIGGS output is then used to set the values for the HDECAY input parameters. The main result from the comparison is shown in Figures 121 and 122. The decay width $\Gamma(\mathrm{t} \to \mathrm{W}^{+}\mathrm{b})$ calculated by both programs agrees very well,

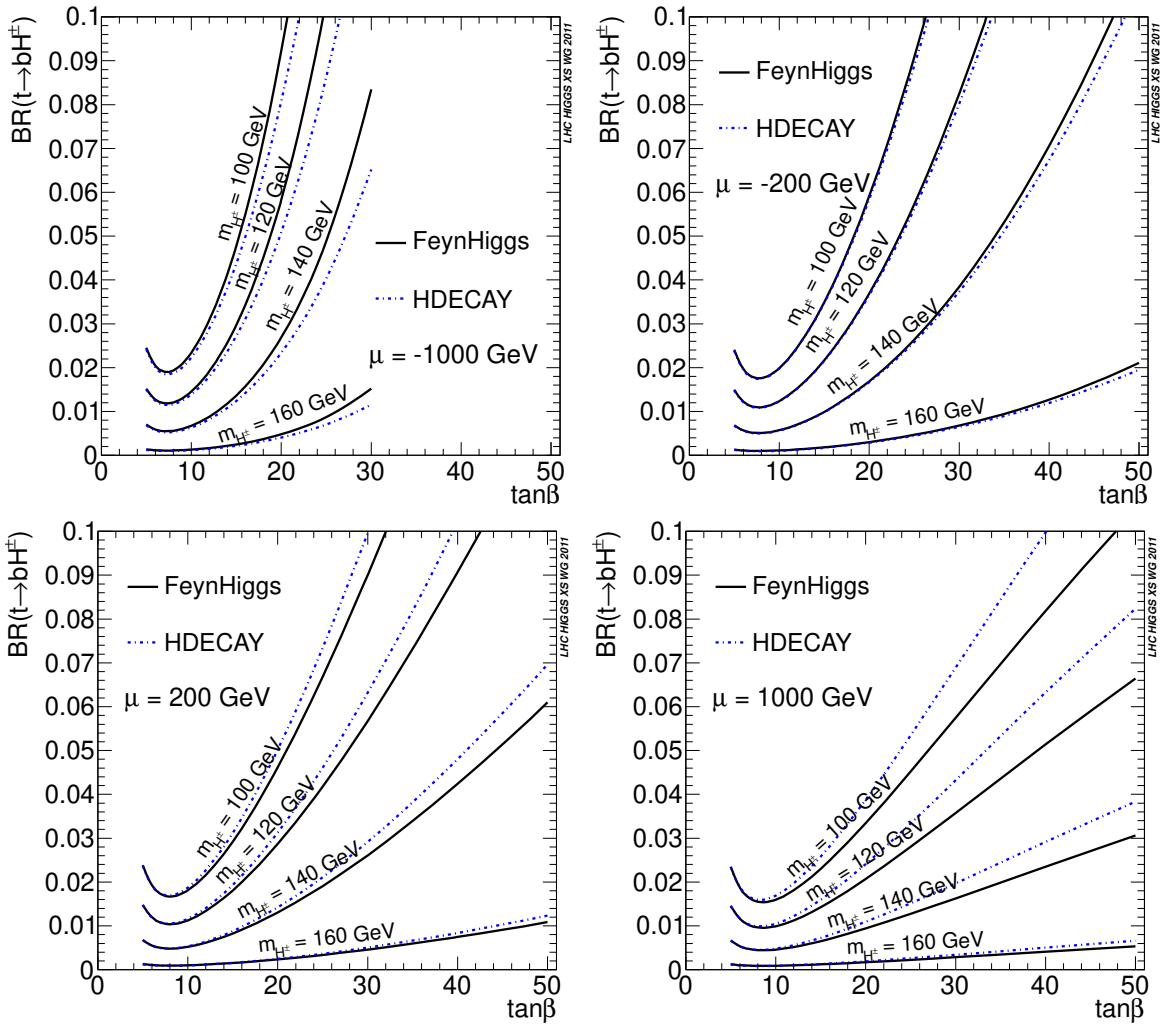

Fig. 122: The branching fraction $\mathrm{BR}(\mathrm{t} \to \mathrm{bH}^{\pm})$ calculated with FEYNHIGGS and HDECAY as a function of $\tan\beta$ for different values of μ and $M_{\mathrm{H}^{\pm}}$.

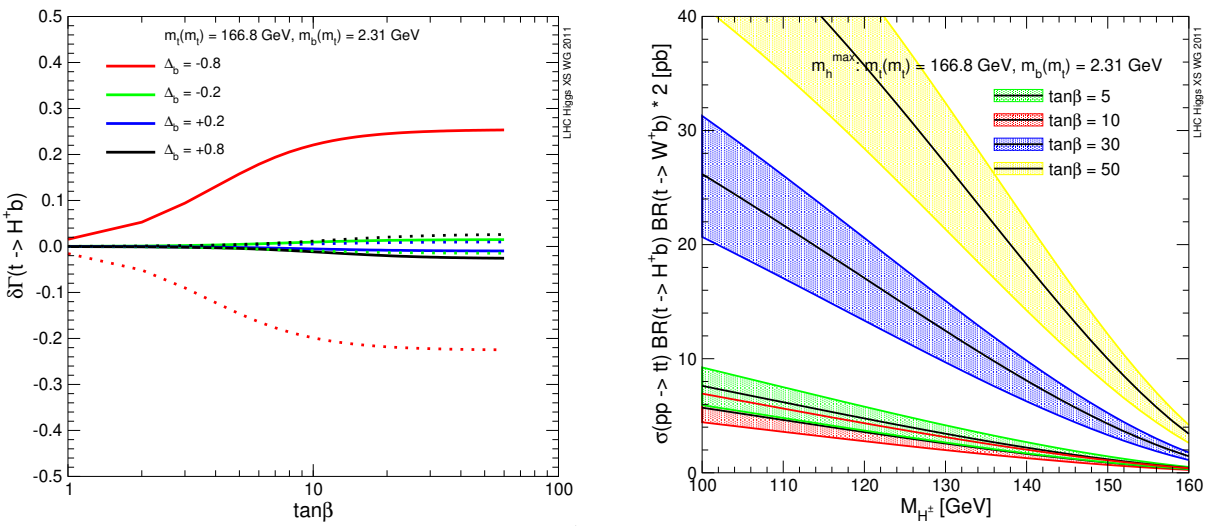

Fig. 123: Left: Relative uncertainty in $\Gamma(\mathrm{t} \to \mathrm{bH}^{\pm})$ assuming a 3% residual uncertainty in Δ_{b}. Right: $\sigma_{\mathrm{tt}} \cdot \mathrm{BR}(\mathrm{t} \to \mathrm{bH}^{\pm}) \cdot \mathrm{BR}(\mathrm{t} \to \mathrm{bW}^{\pm}) \cdot 2$ including scale and PDF uncertainties, uncertainties for missing electroweak and QCD corrections, and Δ_{b}-induced uncertainties.

the difference being only of the order of 0.2%. The difference in $\Gamma(\mathrm{t} \to \mathrm{H}^+\mathrm{b})$ varies from negligible (0.1%) to a maximum of about 9%, the largest difference being at high values of $\tan\beta$. The source of the differences is thought to come from differences in the Δ_b evaluation, largest at high values of $\tan\beta$, or from two-loop corrections to Δ_b. A similarly good agreement is observed for the corresponding branching ratio.

Figure 123 (left) shows the relative uncertainty of the total decay width $\Gamma(\mathrm{t} \to \mathrm{H}^+\mathrm{b})$, assuming a residual uncertainty of the Δ_b corrections of 3% (which is reached after the inclusion of the leading two-loop contributions to Δ_b [91–93]). Combining the calculations on $\mathrm{t\bar{t}}$ production and decay, the cross section for the process $\mathrm{pp} \to \mathrm{t\bar{t}} \to \mathrm{WbH^\pm b}$ can be predicted. The result for $\sigma_{\mathrm{tt}} \cdot \mathrm{BR}(\mathrm{t} \to \mathrm{bH^\pm}) \cdot \mathrm{BR}(\mathrm{t} \to \mathrm{bW^\pm}) \cdot 2$ at $\sqrt{s} = 7$ TeV is shown in Figure 123 (right), together with the dominating systematic uncertainties: PDF and scale uncertainties on the $\mathrm{t\bar{t}}$ cross section, 5% for missing one-loop electroweak diagrams, 2% for missing two-loop QCD diagrams, and Δ_b-induced uncertainties. The theory uncertainties are added linearly to the (quadratically) combined experimental uncertainties.

13.1.3 Light-charged-Higgs-boson decay

In the $m_\mathrm{h}^\mathrm{max}$ scenario of the MSSM, the $\mathrm{BR}(\mathrm{H}^\pm \to \tau\nu) \approx 1$ for all parameter values is still allowed by the LEP experiments [391]. (Only for very large values of $M_{\mathrm{H}^\pm}$ the off-shell decay to tb can reach a level of up to 10%.) The uncertainty on this assumption is less than 1% and thus negligible compared to other uncertainties.

The charged-Higgs-boson decay widths calculated with FEYNHIGGS and HDECAY in $m_\mathrm{h}^\mathrm{max}$ benchmark scenario are compared in the same manner as described in Section 13.1.2. The total decay width of the charged Higgs boson is shown in Figure 124. The decay channels $\mathrm{H}^\pm \to \tau\nu_\tau$, $\mathrm{H}^\pm \to \mathrm{AW}$, $\mathrm{H}^\pm \to \mathrm{cs}$, $\mathrm{H}^\pm \to \mathrm{HW}$, $\mathrm{H}^\pm \to \mu\nu_\mu$, and $\mathrm{H}^\pm \to \mathrm{tb}$ available in both programs are studied. For $\mathrm{H}^\pm \to \tau\nu_\tau$, FEYNHIGGS includes the Higgs propagator corrections up to the two-loop level. Concerning the latter, in HDECAY these corrections are included in the approximation of vanishing external momentum. On the other hand, it includes the full NLO QCD corrections to charged-Higgs decays into quarks, which are incorporated in FEYNHIGGS only in the approximation of a heavy charged Higgs boson. The experimentally most interesting decay channel $\mathrm{H}^\pm \to \tau\nu_\tau$ showed a good agreement, with HDECAY consistently predicting a 3.5% larger decay width than FEYNHIGGS, due to the differences described above. The result is shown in Figure 125. A good agreement is also found in the $\mathrm{H}^\pm \to \mu\nu_\mu$ channel, again with HDECAY predicting consistently a $\sim 3.5\%$ larger decay width than FEYNHIGGS. In the $\mathrm{H}^\pm \to \mathrm{cs}$ channel a notable discrepancy of $7-19\%$ is found. The result of the comparison in the $\mathrm{H}^\pm \to \mathrm{cs}$ channel is shown in Figure 126. The differences in $\mathrm{H}^\pm \to \mathrm{cs}$ may be attributed to the QCD corrections implemented in FEYNHIGGS, which are valid only in the limit of large charged-Higgs masses (in comparison to the quark masses), whereas in HDECAY they are more complete. This channel can only play a significant role for very low values of $\tan\beta$ and is numerically negligible within the $m_\mathrm{h}^\mathrm{max}$ scenario.

13.2 Heavy charged Higgs boson

For heavy charged Higgs bosons, $M_{\mathrm{H}^\pm} \gtrsim m_\mathrm{t}$, associated production $\mathrm{pp} \to \mathrm{tbH^\pm}+\mathrm{X}$ is the dominant production mode. Two different formalisms can be employed to calculate the cross section for associated $\mathrm{tbH^\pm}$ production. In the four-flavour scheme (4FS) with no b quarks in the initial state, the lowest-order QCD production processes are gluon–gluon fusion and quark–antiquark annihilation, $\mathrm{gg} \to \mathrm{tbH^\pm}$ and $\mathrm{q\bar{q}} \to \mathrm{tbH^\pm}$, respectively. Potentially large logarithms $\propto \ln(\mu_\mathrm{F}/m_\mathrm{b})$, which arise from the splitting of incoming gluons into nearly collinear $\mathrm{b\bar{b}}$ pairs, can be summed to all orders in perturbation theory by introducing bottom parton densities. This defines the five-flavour scheme (5FS) [410]. The use of bottom distribution functions is based on the approximation that the outgoing b quark is at small transverse momentum and massless, and the virtual b quark is quasi on shell. In this scheme, the leading-order

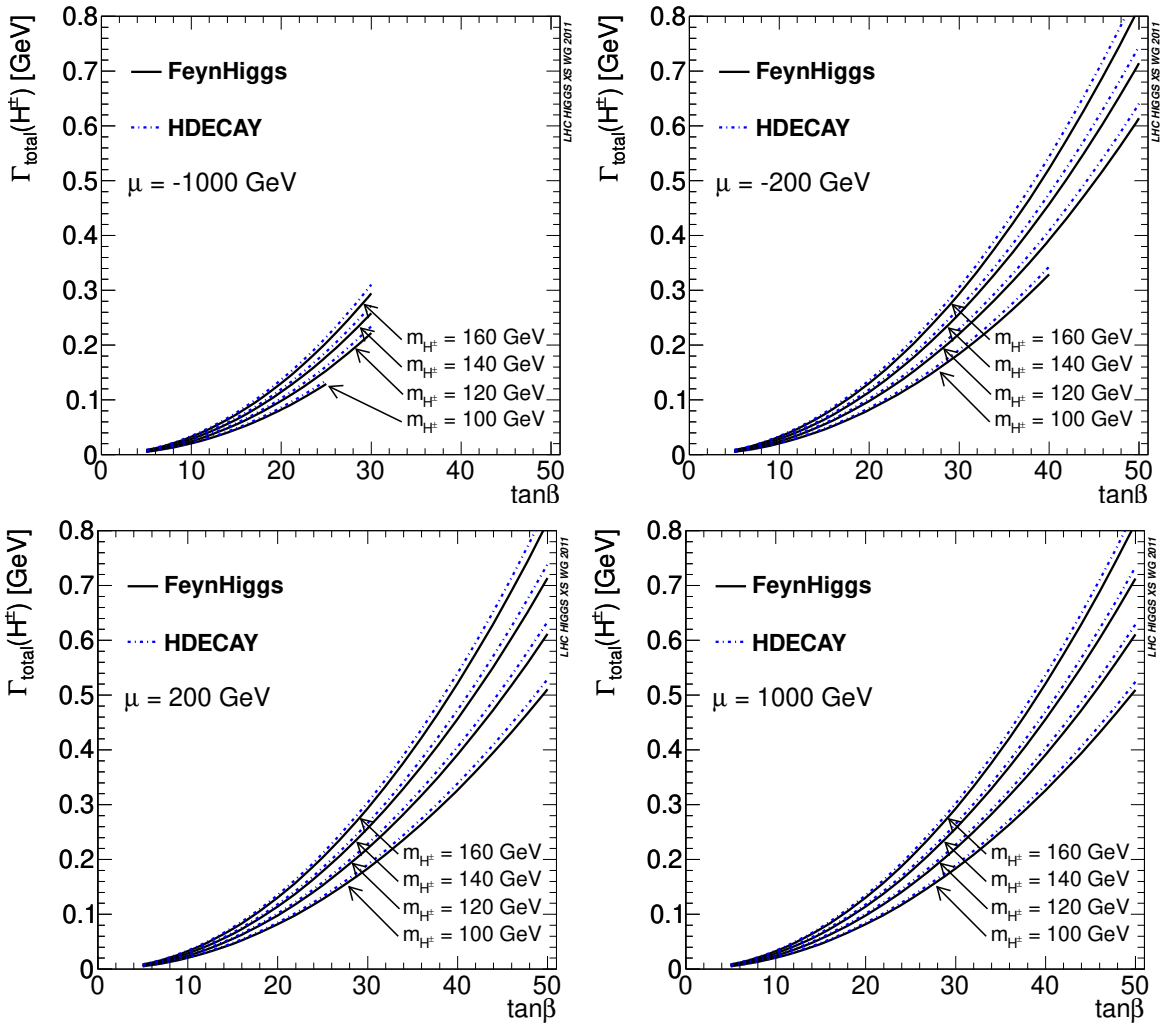

Fig. 124: The decay width of $\mathrm{H}^{\pm}$ calculated with FEYNHIGGS and HDECAY as a function of $\tan\beta$ for different values of μ and $M_{\mathrm{H}^{\pm}}$.

(LO) process for the inclusive $\mathrm{tbH}^{\pm}$ cross section is gluon–bottom fusion, $\mathrm{gb} \to \mathrm{tH}^{\pm}$. The next-to-leading order (NLO) cross section in the 5FS includes $\mathcal{O}(\alpha_{\mathrm{s}})$ corrections to $\mathrm{gb} \to \mathrm{tH}^{\pm}$ and the tree-level processes $\mathrm{gg} \to \mathrm{tbH}^{\pm}$ and $\mathrm{q\bar{q}} \to \mathrm{tbH}^{\pm}$. To all orders in perturbation theory the four- and five-flavour schemes are identical, but the way of ordering the perturbative expansion is different, and the results do not match exactly at finite order. For the inclusive production of neutral Higgs bosons with bottom quarks, $\mathrm{pp} \to \mathrm{b\bar{b}H{+}X}$, the four- and five-flavour scheme calculations numerically agree within their respective uncertainties, once higher-order QCD corrections are taken into account [366, 411–413], see Section 12 of this Report.

There has been considerable progress recently in improving the cross-section predictions for the associated production of charged Higgs bosons with heavy quarks by calculating NLO SUSY QCD and electroweak corrections in the four- and five-flavour schemes [364, 414–420], and the matching of the NLO five-flavour scheme calculation with parton showers [421].

13.2.1 Santander matching

A simple and pragmatic formula for the combination of the four- and five-flavour scheme calculations of bottom-quark associated Higgs-boson production has been suggested in Ref. [370]. The matching

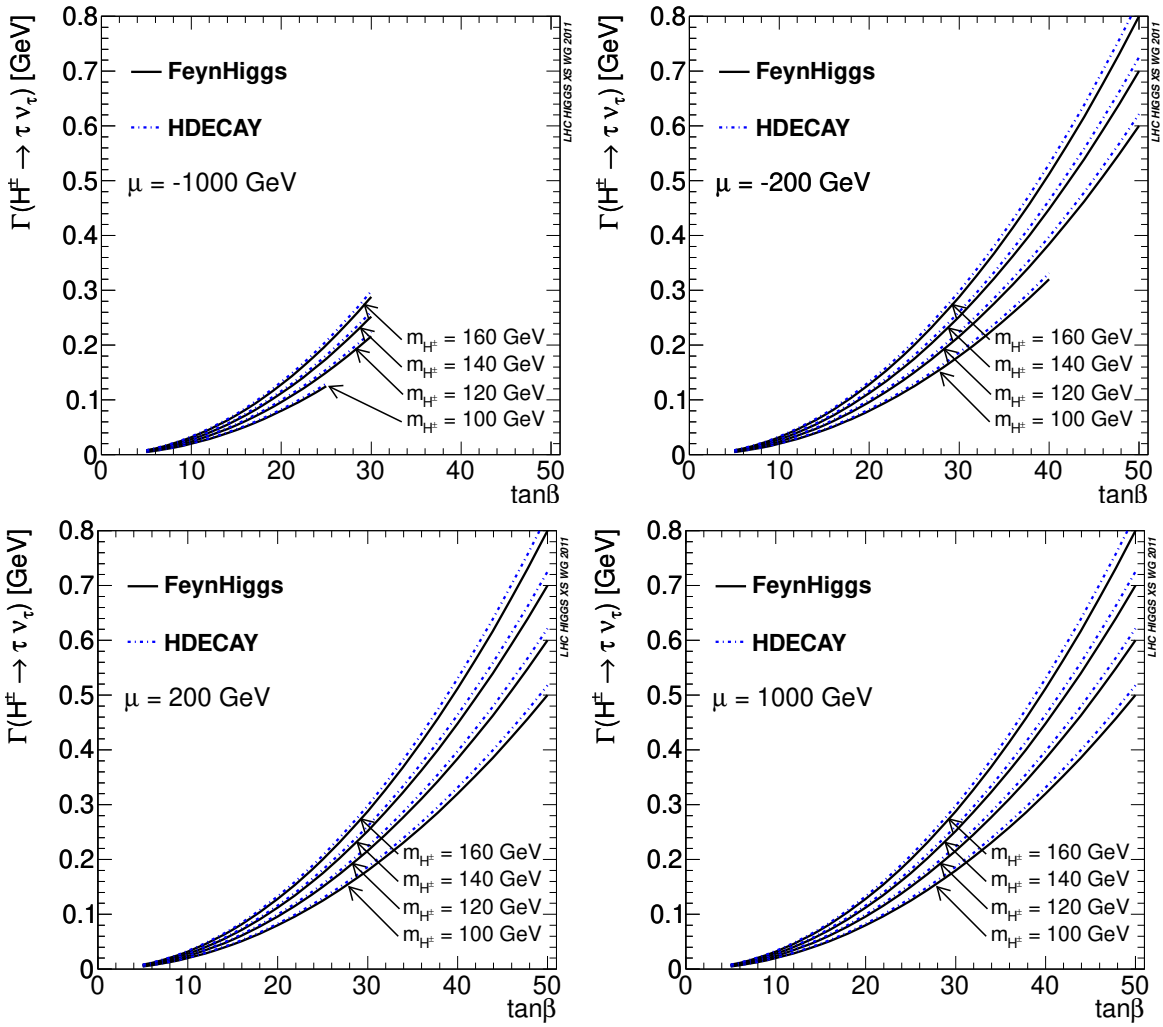

Fig. 125: The decay width $\Gamma(\mathrm{H}^{\pm} \to \tau\nu_{\tau})$ calculated with FEYNHIGGS and HDECAY as a function of $\tan\beta$ for different values of μ and $M_{\mathrm{H}^{\pm}}$.

formula originated from discussions among the authors of Ref. [370] at the *Higgs Days at Santander 2009* and is therefore dubbed "Santander matching". The matching scheme has been described in some detail in Section 12.2.2. Here we shall very briefly summarise the main features of the scheme and provide matched predictions for the inclusive cross section $\mathrm{pp} \to \mathrm{tbH}^{\pm}+\mathrm{X}$ at the LHC operating at a centre-of-mass energy of 7 TeV.

The 4FS and 5FS calculations provide the unique description of the cross section in the asymptotic limits $M_{\mathrm{H}}/m_{\mathrm{b}} \to 1$ and $M_{\mathrm{H}}/m_{\mathrm{b}} \to \infty$, respectively (here and in the following M_{H} denotes a generic Higgs boson mass). The two approaches are combined in such a way that they are given variable weight, depending on the value of the Higgs-boson mass. The difference between the two approaches is formally logarithmic. Therefore, the dependence of their relative importance on the Higgs-boson mass should be controlled by a logarithmic term. This leads to the following formula [370]:

$$\sigma^{\text{matched}} = \frac{\sigma^{\text{4FS}} + w\,\sigma^{\text{5FS}}}{1+w}\,, \tag{99}$$

with the weight w defined as

$$w = \ln\frac{M_{\mathrm{H}}}{m_{\mathrm{b}}} - 2\,, \tag{100}$$

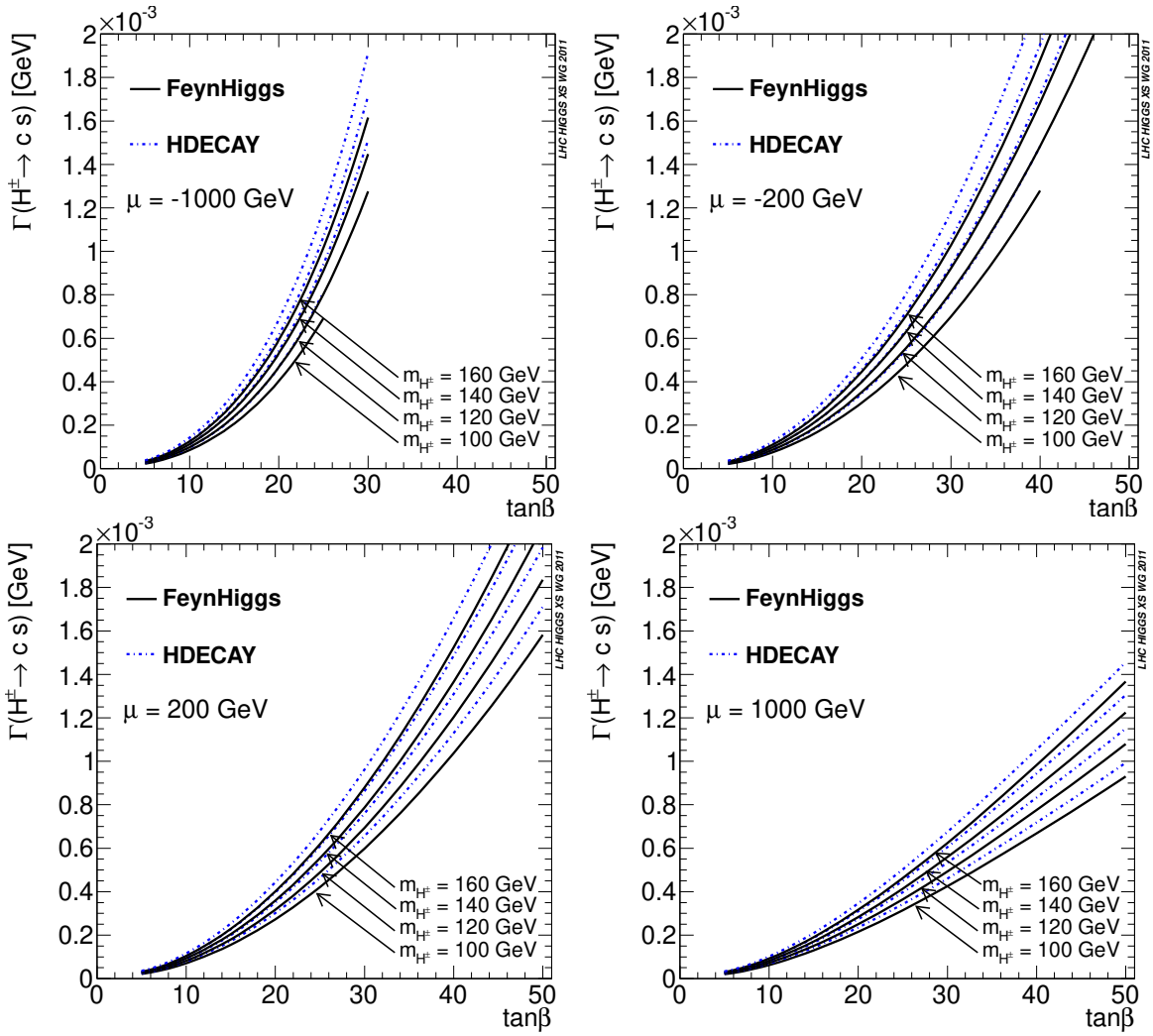

Fig. 126: The decay width $\Gamma(\mathrm{H}^{\pm} \to \mathrm{cs})$ calculated with FEYNHIGGS and HDECAY as a function of $\tan\beta$ for different values of μ and $M_{\mathrm{H}^{\pm}}$. A discrepancy of $7-19\%$ is observed.

and σ^{4FS} and σ^{5FS} denote the total inclusive cross section in the 4FS and the 5FS, respectively. For $m_{\mathrm{b}} = 4.75$ GeV the weight factor increases from $w \approx 1.75$ at $M_{\mathrm{H}} = 200$ GeV to $w \approx 2.65$ at $M_{\mathrm{H}} = 500$ GeV.

The theoretical uncertainties in the 4FS and the 5FS calculations should be added linearly, using the weights w defined in Eq. (100). This ensures that the combined error is always larger than the minimum of the two individual errors, see the discussion in Ref. [370]. As the uncertainties can be asymmetric, the combination should be done separately for the upper and the lower uncertainty limits:

$$\Delta\sigma_{\pm} = \frac{\Delta\sigma_{\pm}^{\mathrm{4FS}} + w\,\Delta\sigma_{\pm}^{\mathrm{5FS}}}{1+w}\,, \tag{101}$$

where $\Delta\sigma_{\pm}^{\mathrm{4FS}}$ and $\Delta\sigma_{\pm}^{\mathrm{5FS}}$ are the upper/lower uncertainty limits of the 4FS and the 5FS, respectively.

We shall now discuss the numerical implications of the Santander matching and provide matched predictions for the inclusive cross section $\mathrm{pp} \to \mathrm{tbH}^{\pm}+\mathrm{X}$ at the LHC operating at a centre-of-mass energy of 7 TeV. The individual numerical results for the 4FS and 5FS calculations have been obtained with input parameters as described in Ref. [7]. Note that the cross-section predictions presented below correspond to NLO QCD results for the production of heavy charged Higgs bosons in a two-Higgs-

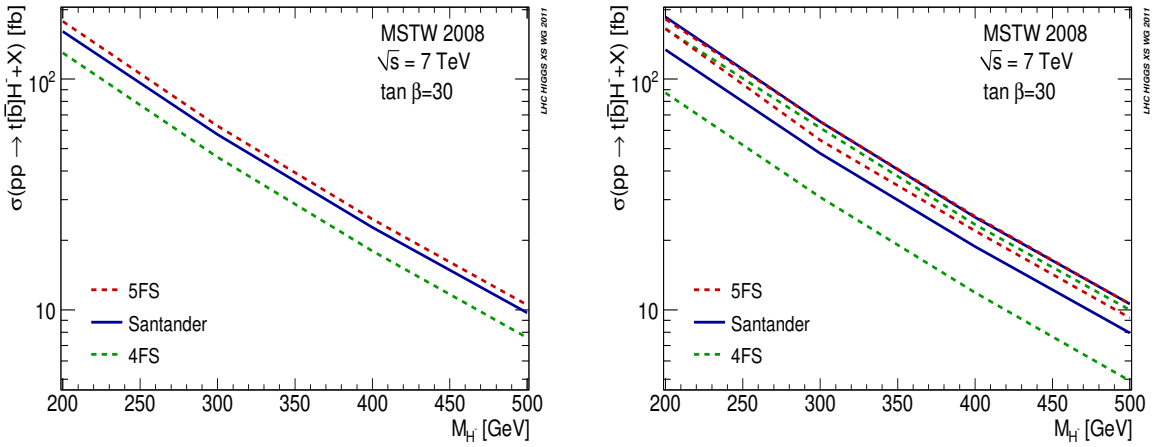

(a) (b)

Fig. 127: (a) Central values for the total inclusive cross section in the 5FS (red, dashed), the 4FS (green, dashed), and for the matched cross section (blue, solid). Here and in the following we use the MSTW2008 PDF set [107]. (b) Theory uncertainty bands for the total inclusive cross section in the 5FS (red, dashed), the 4FS (green, dashed), and for the matched cross section (blue, solid).

doublet model. SUSY effects can be taken into account by rescaling the bottom Yukawa coupling to the proper value [369, 371].

Let us briefly discuss the choice of renormalisation and factorisation scales and the estimate of the theory uncertainty in the 4FS and 5FS NLO calculations as presented in Ref. [7]. In the 4FS both scales have been set to $\mu = (m_{\rm t} + m_{\rm b} + M_{\rm H^-})/3$ as the default choice. The NLO scale uncertainty has been estimated from the variation of the scales by a factor of three about the central scale, see also the discussion in Ref. [422]. The residual NLO scale uncertainty in the 4FS is then approximately $\pm 30\%$. In the 5FS calculation the central scale has been set to $\mu = (m_{\rm t} + M_{\rm H^-})/4$ (see Ref. [416]). A small residual NLO scale uncertainty of less then about 10% is found when varying the scales by a factor three about the central scale. We note that the scale uncertainty of the NLO 5FS calculation is surprisingly small, and that the scale dependence of the NLO cross section is monotonically rising when the scale is decreased. Furthermore, the choice of the factorisation scale in the 5FS calculations is intricate and may depend both on the kinematics of the process and on the Higgs-boson mass, see e.g., Refs. [363,423,424]. Thus, a proper estimate of the theory uncertainty of the 5FS calculation may require further investigation.

For the results presented below, however, we simply adopt the 4FS and 5FS cross section and theory uncertainty predictions as presented in Ref. [7]. As no estimate of the PDF error of the 5FS calculation has been given, we only consider the renormalisation and factorisation scale uncertainty.

Figure 127 (a) shows the central values for the 4FS and the 5FS cross section, as well as the matched result, as a function of the Higgs-boson mass. The corresponding theory error estimates are shown in Figure 127 (b). Taking the scale uncertainty into account, the 4FS and 5FS cross sections at NLO are consistent, even though the predictions in the 5FS at our choice of the central scales are larger than those of the 4FS by approximately 30%, almost independently of the Higgs-boson mass. Qualitatively similar results have been obtained from a comparison of 4FS and 5FS NLO calculations for single-top production at the LHC [425]. We note that the lower end of the error band of the matched calculation approximately coincides with the central prediction of the 4FS, while the upper end of the band is very close to the upper band of the 5FS scale error.

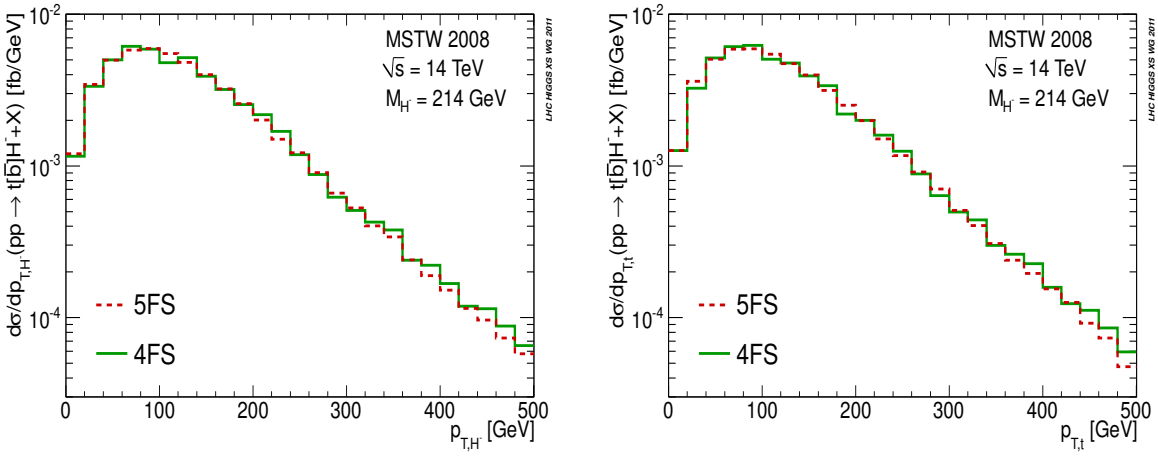

(a) (b)

Fig. 128: Normalised transverse-momentum distributions of the Higgs boson (a) and the top quark (b) for $\mathrm{pp} \to \mathrm{t\bar{b}H^-} + X$ at the LHC (14 TeV). Shown are results in the 4FS (NLO) and 5FS (NLO plus parton shower).

13.2.2 Differential distributions

Let us now turn to the transverse-momentum distributions of the final-state particles. To illustrate the impact of the higher-order QCD corrections on the shape of the distributions and to analyse the difference between the 4FS and 5FS calculations, we discuss results for the LHC operating at 14 TeV energy, as presented in Refs. [7, 421]. In both calculations, the distributions have been evaluated for the default scale choice $\mu = (m_\mathrm{t} + m_\mathrm{b} + M_{\mathrm{H}^-})/3$ and $\mu = (m_\mathrm{t} + M_{\mathrm{H}^-})/4$, respectively.

We first discuss the transverse-momentum distribution of the top and Higgs particles. As shown in Refs. [7, 421], the impact of higher-order corrections, including the parton shower, is small for the top and Higgs p_T. In Figure 128 (a) and (b) we compare the NLO (4FS) and NLO + parton-shower (5FS) results for the transverse-momentum distribution of the top and Higgs, respectively. Note that we have normalised both distribution to one. It is evident from the comparison shown in Figure 128 that the shapes of the Higgs and top transverse-momentum distribution in the 4FS and 5FS agree very well.

The bottom p_T distribution is described with different accuracy in the 4FS and 5FS calculations. While in the 4FS the kinematics of the process is treated exactly already at LO, the 5FS is based on the approximation that the bottom quark is produced at small transverse momentum. In the 5FS a finite bottom p_T is thus only generated at NLO through the parton process $\mathrm{gg} \to \mathrm{tbH}^\pm$, which is the LO process of the 4FS. We thus focus on the transverse-momentum distribution of the bottom quark as described within the 4FS and compare the predictions at LO and at NLO in Figure 129, see Ref. [422]. The bottom-quark p_T distribution, which extends to $p_{\mathrm{T,b}} \gg m_\mathrm{b}$, is significantly softened at NLO. The large impact on the $p_{\mathrm{T,b}}$ distribution is due to collinear gluon radiation off bottom quarks that is enhanced by a factor $\alpha_\mathrm{s} \ln(m_\mathrm{b}/p_{\mathrm{T,b}})$. The enhancement should be significantly reduced if the bottom quarks are reconstructed from jets, since the application of a jet algorithm treats the bottom–gluon system inclusively in the collinear cone, so that the logarithmic enhancement cancels out.

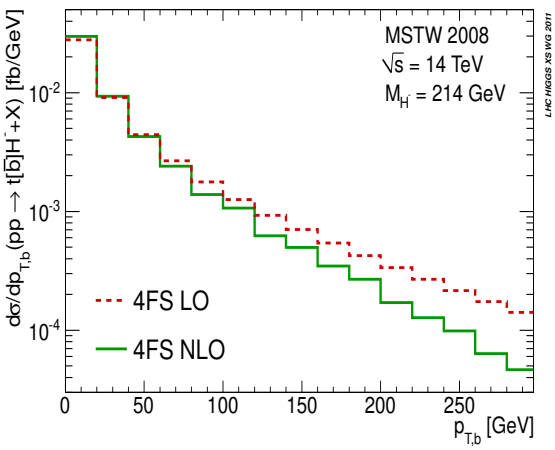

Fig. 129: Transverse-momentum distributions of the bottom quark in the 4FS for $\mathrm{pp} \to \mathrm{t\bar{b}H^-} + X$ at the LHC (14 TeV). Shown are results at LO and NLO.

14 Predictions for Higgs production and decay with a 4th SM-like fermion generation[56]

14.1 General setup

We study the extension of the SM that includes a 4th generation of heavy fermions, consisting of an up- and a down-type quark $(\mathrm{t}', \mathrm{b}')$, a charged lepton (l'), and a massive neutrino (ν_{l}'). The 4th-generation fermions all have identical gauge couplings as their SM copies and equivalent Yukawa couplings proportional to their masses, but do not mix with the other three SM generations. The masses of the hypothetical new fermions in this study are

$$\begin{aligned} m_{\mathrm{b}'} &= m_{\mathrm{l}'} = m_{\nu_{\mathrm{l}}'} = 600\ \text{GeV}, \\ m_{\mathrm{t}'} &= m_{\mathrm{b}'} + \left[1 + \frac{1}{5}\ln\left(\frac{M_{\mathrm{H}}}{115\ \text{GeV}}\right)\right] 50\ \text{GeV}, \end{aligned} \tag{102}$$

where the relation among them is used to escape current exclusion limits from electroweak (EW) precision data (see Refs. [426, 427]). In the following we call the Standard Model with 3 generations "SM3" and the Standard Model with a 4th generation of fermions "SM4". Owing to screening (see Section 14.2), leading-order (LO) or next-to-leading-order (NLO) QCD predictions typically depend only weakly on the precise values of masses of the heavy fermions. This is completely different for NLO EW corrections, which are enhanced by powers of the masses of the heavy fermions and induce a strong dependence of the results on these masses.

Part of the results shown in the following have already been anticipated in Ref. [428].

14.2 Higgs production via gluon fusion

So far, the experimental analysis has concentrated on models with ultra-heavy 4th-generation fermions, excluding the possibility that the Higgs boson decays to heavy neutrinos. Furthermore, the 2-loop EW corrections have been included under the assumption that they are dominated by light fermions. At the moment the experimental strategy consists in computing the cross-section ratio $R = \sigma(\mathrm{SM4})/\sigma(\mathrm{SM3})$ with HIGLU [405] while NLO EW radiative corrections are switched off.

In this section we concentrate on full 2-loop EW corrections to Higgs-boson production (through gg-fusion) at LHC in SM4 and refer to the work of Refs. [66, 429] for the inclusion of QCD corrections. The naive expectation is that light fermions dominate the low-Higgs-boson-mass regime and, therefore, EW corrections can be well approximated by the ones [28, 29] in SM3. It is worth noting that the leading behaviour of the EW corrections for high values of masses in the 4th generation has been known for a long time [430, 431] (see also Ref. [432]) showing an enhancement of radiative corrections.

To avoid misunderstandings we define the following terminology: for a given amplitude A, in the limit $m_{\mathrm{f}} \to \infty$ we distinguish *decoupling* for $A \sim 1/m_{\mathrm{f}}^2$ (or higher negative powers), *screening* for $A \to$ constant (or $A \sim \ln m_{\mathrm{f}}^2$), and *enhancement* for $A \sim m_{\mathrm{f}}^2$ (or higher positive powers). To discuss decoupling we need few definitions: SM3 is the usual SM with one $\mathrm{t}-\mathrm{b}$ doublet; SM4 is the extension of SM3 with a new family of heavy fermions, $\mathrm{t}'-\mathrm{b}'$ and $\mathrm{l}'-\nu_{\mathrm{l}}'$. All relevant formulae for the asymptotic limit can be found in Refs. [430, 431]. Considering only EW corrections, the amplitude for gg-fusion reads[57]

$$\begin{aligned} A_{\mathrm{SM3}} &= A_{\mathrm{t}}^{\text{1-loop}} + A_3^{\mathrm{NLO}}, \quad A_3^{\mathrm{NLO}} = A_{\mathrm{t}}^{\text{2-loop}} + \delta_{\mathrm{t}}^{\mathrm{FR}}\, A_{\mathrm{t}}^{\text{1-loop}}, \\ A_{\mathrm{SM4}} &= A_Q^{\text{1-loop}} + A_4^{\mathrm{NLO}}, \quad A_4^{\mathrm{NLO}} = A_Q^{\text{2-loop}} + \delta_{Q+L}^{\mathrm{FR}}\, A_Q^{\text{1-loop}}, \end{aligned} \tag{103}$$

where

$$A_Q = A_{\mathrm{t}+\mathrm{t}'+\mathrm{b}'}, \qquad \delta_{Q+L}^{\mathrm{FR}} = \delta_{\mathrm{t}+\mathrm{t}'+\mathrm{b}'+\mathrm{l}'+\nu_{\mathrm{l}}'}^{\mathrm{FR}}\,. \tag{104}$$

[56] A. Denner, S. Dittmaier, A. Mück, G. Passarino, M. Spira, C. Sturm, S. Uccirati and M.M. Weber.

[57] Here we neglect the contributions of bottom-quark loops which amount to up to about 3% within SM4 and $5-10\%$ in SM3. The bottom-quark contributions are, however, included in our numerical results for the gluon-fusion cross section.

In Eq.(103) $\delta^{\rm FR}$ gives the contribution from finite renormalisation, including Higgs-boson wave-function renormalisation (see Sect. 3.4 of Ref. [29] for technical details).

First we recall the standard argument for the asymptotic behaviour in LO $\rm gg$-fusion, extendible to NLO and next-to-next-to-leading (NNLO) QCD corrections [66], and give a simple argument to prove enhancement at NLO EW level.

Any Feynman diagram contributing to the Higgs–gluon–gluon vertex has dimension one and involves the Yukawa coupling (proportional to $m_{\rm f}/M_{\rm W}$) of the fermion f circulating in the loop. Naively this suggests an asymptotic scaling of the amplitude proportional to $m_{\rm f}^2$ for large $m_{\rm f}$, i.e. enhancement. However, the total $\rm Hgg$ amplitude must be proportional to $T_{\mu\nu} = p_1 \cdot p_2\, \delta_{\mu\nu} - p_{2\mu} p_{1\nu}$ (where $p_{1,2}$ are the two gluon momenta) because of gauge invariance, and T has dimension two. Thus, the scaling of the whole amplitude for large $m_{\rm f}$ is reduced by two powers in $m_{\rm f}$, leading to a constant limit, i.e. screening, if there is exactly one Yukawa coupling. The part of the diagram that is not proportional to T cancels in the total amplitude because of gauge invariance (all higher powers of $m_{\rm f}$ will go away, and this explains the presence of huge cancellations in the total amplitude). At LO there is only one Yukawa coupling as in NLO and NNLO QCD where one adds only gluon lines, so there is screening. At EW NLO there are diagrams with three Yukawa couplings, therefore giving the net $m_{\rm f}^2$ behaviour predicted in Ref. [430], so there is enhancement and at the 2-loop level it goes at most with $m_{\rm f}^2$. We define

$$\sigma_{\rm SM3}\,({\rm gg} \to {\rm H}) = \sigma_{\rm SM3}^{\rm LO}\,({\rm gg} \to {\rm H})\,\left(1 + \delta_{\rm EW}^{(3)}\right), \quad \sigma_{\rm SM4}\,({\rm gg} \to {\rm H}) = \sigma_{\rm SM4}^{\rm LO}\,({\rm gg} \to {\rm H})\,\left(1 + \delta_{\rm EW}^{(4)}\right). \tag{105}$$

Analysing the results of Refs. [430, 431], valid for a light Higgs boson, one can see that in SM3 there is enhancement in the quark sector for $m_{\rm t} \gg m_{\rm b}$ ($\delta_{\rm EW}^{(3)} \sim G_F m_{\rm t}^2$, where G_F is the Fermi coupling constant). The full calculation of Ref. [28] shows that the physical value for the top-quark mass is not large enough to make this quadratic behaviour relevant with respect to the contribution from light fermions. From Ref. [430] we can also understand that a hypothetical SM3 with degenerate ${\rm t}-{\rm b}$ ($m_{\rm t} = m_{\rm b} = m_{\rm q}$) would generate an enhancement in the small-Higgs-mass region with the opposite sign ($\delta_{\rm EW}^{(3)} \sim -G_F m_{\rm q}^2$). Moving to SM4, Eq. (62) of Ref. [431] shows that the enhanced terms coming from finite renormalisation exactly cancel the similar contribution from 2-loop diagrams for $m_{\rm t'} = m_{\rm b'}$, so that for mass-degenerate ${\rm t'}-{\rm b'}$ (and $m_{\rm t} \gg m_{\rm b}$) we observe screening in the 4th-generation quark sector. This accidental cancellation follows from the 3 of colour $\rm SU(3)$ and from the fact that we have 3 heavy quarks contributing to LO almost with the same rate (no enhancement at LO). However, the same is not true for ${\rm l'}-{\rm \nu_l'}$ (there are no 2-loop diagrams with leptons in $\rm gg$-fusion), so we observe enhancement in the leptonic sector of SM4, which actually dominates the behaviour at small values of $M_{\rm H}$. To summarise the asymptotics at NLO EW:

- SM3 with heavy–light quark doublet ($m_{\rm t} \gg m_{\rm b}$): (positive) enhancement;
- SM3 with a hypothetical heavy–heavy (mass-degenerate, $m_{\rm t} = m_{\rm b}$) quark doublet: (negative) enhancement;
- SM4 with heavy–light or heavy–heavy (mass-degenerate) quark doublets in the 4th generation (and $m_{\rm t} \gg m_{\rm b}$): enhancement in heavy–light, screening in heavy–heavy;
- SM4 including heavy–heavy ${\rm l'}-{\rm \nu_l'}$ doublet: enhancement.

We have verified that our (complete) results confirm the asymptotic estimates of Refs. [430, 431].

In order to prove that light-fermion dominance in SM3 below 300 GeV is a numerical accident due to the fact that the top quark is not heavy enough, we have computed $\delta_{\rm EW}^{(3)}$ for a top quark of 800 GeV at $M_{\rm H} = 100$ GeV and found top-quark dominance. A similar effect of the top quark is also present in SM4; if, for instance, we fix all heavy-fermion masses $m_{\rm f'}$ to 600 GeV, we find $\delta_{\rm EW}^{(4)} = 12.1\%(29.1\%)$ at $m_{\rm t} = 172.5$ GeV$(600$ GeV$)$.

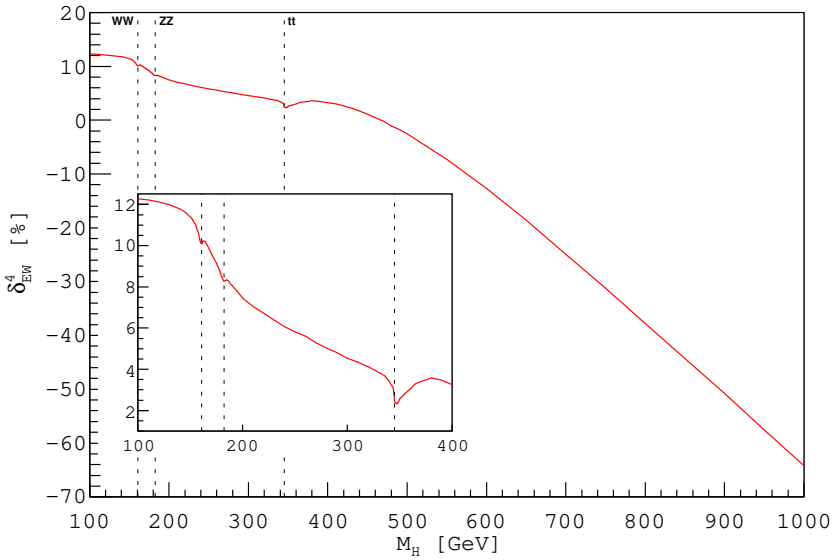

Fig. 130: Relative corrections in SM4 ($t'-b'$ and $l'-\nu_l{}'$ doublets) due to 2-loop EW corrections to $gg \to H$. The masses of the 4th-generation fermions are chosen according to Eq. (102). In the inset a blow-up of the small-M_H region is shown.

Moving to SM4, the LO gg-fusion cross section for a light Higgs boson is about nine times the one of SM3, because three instead of one heavy fermions propagate in the loop [433]. If one assumes that also NLO SM4 is dominated by light-fermion corrections, i.e., that EW corrections are the same for SM3 and SM4, one expects $\delta^{(4)}_{EW} \approx \delta^{(3)}_{EW}/3$ for very heavy fermions. According to Ref. [431] this would be true provided that no heavy leptons are included.

Our complete result (see Ref. [434]) is shown in Figure 130 where the $t'-b'$ and the $l'-\nu_l{}'$ doublets are included. Numbers for the relative EW corrections are listed in Table 47. Electroweak NLO corrections due to the 4th generation are positive and large for a light Higgs boson, positive but relatively small around the $t\bar{t}$ threshold, and start to become negative around 450 GeV. Increasing further the value of the Higgs-boson mass, the NLO effects tend to become huge and negative ($\delta^{(4)}_{EW} < -100\%$) showing minima around the heavy-quark thresholds. Above those thresholds $\delta^{(4)}_{EW}$ starts to grow again and becomes positive around $M_H = 1750$ GeV (not shown).

Having computed the EW corrections $\delta^{(4)}_{EW}$ we should discuss some aspects of their inclusion in the production cross section $\sigma\,(gg \to H + X)$, i.e. their interplay with QCD corrections and the remaining theoretical uncertainty. The most accepted choice is given by

$$\sigma^F = \sigma^{LO}\left(1 + \delta_{QCD}\right)\left(1 + \delta_{EW}\right), \tag{106}$$

which assumes complete factorisation of QCD and EW corrections. The latter is based on the work of Ref. [224] where it is shown that, at zero Higgs momentum, exact factorisation is violated but with a negligible numerical impact; the result of Ref. [224] can be understood in terms of soft-gluon dominance.

The residual part beyond the soft-gluon-dominated part contributes up to $5-10\%$ to the total inclusive cross section (for Higgs masses up to 1 TeV). Thus, with EW corrections we are talking about non-factorizable effects which are at most 5% in SM4.

EW corrections become -100% just before the heavy-quark thresholds making the use of the perturbative approach questionable. At EW NNLO there are diagrams with five Yukawa couplings; according to our argument on decoupling the enhancement at 3 loops goes as the 4th power of the heavy-fermion mass, unless some accidental screening occurs. Here we have no solid argument to estimate the

Table 47: NLO EW corrections to $\mathrm{gg} \to \mathrm{H} + X$ cross sections in SM4 for the low-mass region: $\delta_{\mathrm{EW}}^{(4)} \pm \Delta$, where Δ is the numerical integration error.

M_{H} [GeV]	$\delta_{\mathrm{EW}}^{(4)}$ [%]	Δ [%]	M_{H} [GeV]	$\delta_{\mathrm{EW}}^{(4)}$ [%]	Δ [%]	M_{H} [GeV]	$\delta_{\mathrm{EW}}^{(4)}$ [%]	Δ [%]
100	12.283	0.005	181	8.351	0.006	346	2.361	0.048
110	12.212	0.005	182	8.278	0.006	347	2.327	0.048
120	12.118	0.005	183	8.286	0.008	348	2.356	0.048
130	11.982	0.005	184	8.320	0.009	349	2.470	0.048
140	11.780	0.005	185	8.336	0.009	350	2.570	0.019
145	11.620	0.005	186	8.300	0.009	351	2.629	0.019
150	11.394	0.005	187	8.246	0.007	353	2.721	0.020
151	11.333	0.005	188	8.176	0.009	355	2.834	0.019
152	11.265	0.005	189	8.107	0.010	360	3.049	0.048
153	11.191	0.004	190	8.057	0.010	365	3.300	0.048
154	11.099	0.004	195	7.757	0.010	370	3.405	0.048
155	10.994	0.004	200	7.465	0.010	375	3.492	0.048
156	10.862	0.004	210	7.044	0.010	380	3.589	0.049
157	10.705	0.004	220	6.720	0.018	385	3.521	0.049
158	10.510	0.004	230	6.399	0.019	390	3.463	0.048
159	10.290	0.004	240	6.065	0.020	400	3.260	0.048
160	10.112	0.004	250	5.815	0.019	410	3.020	0.047
161	10.104	0.004	260	5.600	0.019	420	2.680	0.042
162	10.202	0.004	270	5.273	0.020	430	2.211	0.037
163	10.238	0.004	280	5.038	0.020	440	1.710	0.039
164	10.197	0.004	290	4.795	0.019	450	1.139	0.039
165	10.115	0.004	300	4.541	0.020	460	0.444	0.040
166	10.019	0.005	310	4.349	0.019	470	-0.223	0.042
167	9.919	0.005	320	4.106	0.020	480	-1.060	0.047
168	9.822	0.005	325	3.978	0.020	490	-1.740	0.049
169	9.726	0.005	330	3.847	0.020	500	-2.542	0.036
170	9.632	0.005	335	3.688	0.020	550	-7.281	0.048
171	9.531	0.005	336	3.663	0.049	600	-12.708	0.049
172	9.432	0.005	337	3.589	0.049	650	-18.593	0.049
173	9.334	0.005	338	3.539	0.048	700	-24.904	0.049
174	9.234	0.005	339	3.463	0.047	750	-31.227	0.049
175	9.134	0.005	340	3.417	0.049	800	-37.790	0.049
176	9.027	0.005	341	3.317	0.049	850	-44.322	0.049
177	8.907	0.005	342	3.223	0.049	900	-50.768	0.049
178	8.786	0.005	343	3.169	0.049	950	-57.516	0.049
179	8.639	0.005	344	3.048	0.049	1000	-64.187	0.045
180	8.485	0.008	345	2.449	0.049			

remaining uncertainty in the high-mass region and prefer to state that SM4 is in a fully non-perturbative regime which should be approached with extreme caution. For the low-mass region we can do no more than make educated guesses; therefore, assuming a leading 3-loop behaviour of $m_{\mathrm{f}'}^4$, we estimate the remaining uncertainty to be of the order of $(\alpha/\pi)^2(m_{\mathrm{f}'}/M_{\mathrm{W}})^4$ and thus $1-2\,\%$ in the interval $M_{\mathrm{H}} = 100-150$ GeV and almost negligible in the intermediate region, $150-600$ GeV.

14.3 NLO corrections to H $\to$ 4f in SM4

The results of the $\mathrm{H} \to 4\mathrm{f}$ decay channels have been obtained using the Monte Carlo generator PROPHECY4F [18, 20, 435] which has been extended to support the SM4. PROPHECY4F can calculate the EW and QCD NLO corrections to the partial widths for all 4f final states, i.e. leptonic, semi-leptonic, and hadronic final states. Since the vector bosons are kept off shell, the results are valid for Higgs masses below, near, and above the on-shell gauge-boson production thresholds. Moreover, all interferences between WW and ZZ intermediate states are included at LO and NLO.

The additional corrections in SM4 arise from 4th-generation fermion loops in the HWW/HZZ vertices, the gauge-boson self-energies, and the renormalisation constants. For the large 4th-generation masses of $\mathcal{O}(600\text{ GeV})$ considered here, the 4th-generation Yukawa couplings are large, and the total corrections are dominated by the 4th-generation corrections. Numerically the NLO corrections amount to about -85% and depend only weakly on the Higgs-boson mass for not too large M_{H}, since the heavy-fermion masses in the scenario of (102) have only a weak Higgs mass dependence. The corrections from the 4th generation are taken into account at NLO with their full mass dependence, but their behaviour for large masses can be approximated well by the dominant corrections in the heavy-fermion limit. In this limit the leading contribution can be absorbed into effective HWW/HZZ interactions in the G_F renormalisation scheme via the Lagrangian

$$\mathcal{L}_{HVV} = \sqrt{\sqrt{2}G_F}H\left[2M_{\mathrm{W}}^2 W_\mu^\dagger W^\mu(1+\delta_{\mathrm{W}}^{\mathrm{tot}}) + M_{\mathrm{Z}}^2 Z_\mu Z^\mu(1+\delta_{\mathrm{Z}}^{\mathrm{tot}})\right], \tag{107}$$

where W, Z, H denote the fields for the W, Z, and Higgs bosons. The higher-order corrections are contained in the factors δ_V^{tot} whose expansion up to 2-loop order is given by

$$\delta_V^{\mathrm{tot}(1)} = \delta_u^{(1)} + \delta_V^{(1)}, \qquad \delta_V^{\mathrm{tot}(2)} = \delta_u^{(2)} + \delta_V^{(2)} + \delta_u^{(1)}\delta_V^{(1)}. \tag{108}$$

The 1-loop expressions for a single $\mathrm{SU}(2)$ doublet of heavy fermions with masses m_A, m_B are [436]

$$\delta_u^{(1)} = N_c X_A\left[\frac{7}{6}(1+x) + \frac{x}{1-x}\ln x\right], \qquad \delta_V^{(1)} = -2N_c X_A(1+x), \tag{109}$$

where $x = m_B^2/m_A^2$, $X_A = G_F m_A^2/(8\sqrt{2}\pi^2)$, and $N_c = 3$ or 1 for quarks or leptons, respectively. The results for the 2-loop corrections $\delta_V^{\mathrm{tot}(2)}$ can be found in Ref. [437] for the QCD corrections of $\mathcal{O}(\alpha_{\mathrm{s}} G_F m_{\mathrm{f}'}^2)$ and in Ref. [431] for the EW corrections of $\mathcal{O}(G_F^2 m_{\mathrm{f}'}^4)$. The corrected partial decay width is then given by

$$\Gamma_{\mathrm{NLO}} \approx \Gamma_{\mathrm{LO}}\left[1+\delta_\Gamma^{(1)}+\delta_\Gamma^{(2)}\right] = \Gamma_{\mathrm{LO}}\left[1+2\delta_V^{\mathrm{tot}(1)}+(\delta_V^{\mathrm{tot}(1)})^2+2\delta_V^{\mathrm{tot}(2)}\right]. \tag{110}$$

The size of the two-loop corrections $\delta_\Gamma^{(2)}$ is about $+15\%$ for $m_{\mathrm{f}'} = 600\,\mathrm{GeV}$, again depending only very weakly on the Higgs mass. Due to the large 1-loop corrections PROPHECY4F includes the 2-loop QCD and EW corrections in the heavy-fermion limit in addition to the exact 1-loop corrections. Although the asymptotic two-loop corrections are not directly applicable for a heavy Higgs boson, they can be viewed as a qualitative estimate of the 2-loop effects. One should keep in mind that for a Higgs boson heavier than about $600\,\mathrm{GeV}$ many more uncertainties arise owing to the breakdown of perturbation theory.

The leading 2-loop terms can be taken as an estimate of the error from unknown higher-order corrections. This implies an error of 15% relative to the LO for the generic 4th-generation mass scale $m_{\mathrm{f}'} = 600$ GeV on the partial width for all $\mathrm{H} \to 4\mathrm{f}$ decay channels. Assuming a scaling law of this error proportional to X_A^2, the uncertainty is estimated to about $100X_A^2$ relative to the LO prediction. However, since the correction grows large and negative, the relative uncertainty on the corrected width gets enhanced to $100X_A^2/(1 - 23X_A + 100X_A^2)$, where the linear term in X_A parametrises the 1-loop correction and we have assumed the mass splitting given in (102). For $m_{\mathrm{f}'} = 600$ GeV this results roughly in an uncertainty of 50% on the corrected $\mathrm{H} \to 4\mathrm{f}$ decay widths.

14.4 $\mathrm{H} \to \mathrm{f}\bar{\mathrm{f}}$

The decay widths for $\mathrm{H} \to \mathrm{f}\bar{\mathrm{f}}$ are calculated with HDECAY [15–17] which includes the approximate NLO and NNLO EW corrections for the decay channels into SM3 fermion pairs in the heavy SM4 fermion limit according to Ref. [431] and mixed NNLO EW/QCD corrections according to Ref. [437]. These corrections originate from the wave-function renormalisation of the Higgs boson and are thus universal for all fermion species. The leading 1-loop part is given by $\delta_u^{(1)}$ of Eq. (109). Numerically the EW 1-loop correction to the partial decay widths into fermion pairs amounts to about $+40\%$, while the 2-loop correction contributes an additional $+20\%$. The corrections are assumed to factorise from whatever is included in HDECAY, since the approximate expressions emerge as corrections to the effective Lagrangian after integrating out the heavy-fermion species. Thus, HDECAY multiplies the relative SM4 corrections with the full corrected SM3 result including QCD and approximate EW corrections. The scale of the strong coupling α_{s} has been identified with the average mass of the heavy quarks t', b' of the 4th generation. Since for the scenario of Eq. (102), the full SM4 2-loop corrections amount to about $15-20\%$ relative to the LO result, and the NLO QCD and EW corrections amount to about $+60\%$, the remaining theoretical uncertainties can be estimated to be about 10% for the full partial decay widths into fermion pairs for the SM4 part, while the uncertainties of the SM3 EW and QCD parts are negligible with respect to that. The theoretical uncertainties scale with the heavy-fermion masses as $0.1 \times (m_{\mathrm{f}'}/600\,\mathrm{GeV})^4$.

14.5 $\mathrm{H} \to \mathrm{gg}, \gamma\gamma, \gamma\mathrm{Z}$

For the decay modes $\mathrm{H} \to \mathrm{gg}, \gamma\gamma, \gamma\mathrm{Z}$, HDECAY [15–17] is used as well.

For $\mathrm{H} \to \mathrm{gg}$, HDECAY includes the NNNLO QCD corrections of the SM3 in the limit of a heavy top quark [64–68], applied to the results including the heavy-quark loops. While at NNLO the exact QCD corrections in SM4 [429] are included, at NNNLO the relative SM3 corrections are added to the relative NNLO corrections and multiplied by the LO result including the additional quark loops. Since the failure of such an approximation is less than 1% at NNLO, we assume that at NNNLO it is negligible, i.e. much smaller than the residual QCD scale uncertainty of about 3%. In addition the full NLO EW corrections of Section 14.2 have been included in factorised form, since the dominant part of the QCD corrections emerges from the gluonic contributions on top of the corrections to the effective Lagrangian in the limit of heavy quarks. Taking besides the scale uncertainty also the missing quark-mass dependence at NLO and beyond into account, the total theoretical uncertainties can be estimated to about 5%.

HDECAY [15–17] includes the full NLO QCD corrections to the decay mode $\mathrm{H} \to \gamma\gamma$ supplemented by the additional contributions of the 4th-generation quarks and charged leptons according to Refs. [66, 70, 72].

The introduction of EW NLO corrections (2-loop level) to the decay $\mathrm{H} \to \gamma\gamma$ requires particular attention. We write the amplitude as

$$A = A_{\mathrm{LO}} + X_{\mathrm{W}}\, A_{\mathrm{NLO}} + X_{\mathrm{W}}^2\, A_{\mathrm{NNLO}} + \ldots, \qquad X_{\mathrm{W}} = \frac{G_F M_{\mathrm{W}}^2}{8\sqrt{2}\pi^2}. \tag{111}$$

Part of the problem in including the NLO EW term is related to the fact that the cancellation between the W and the fermion loops is stronger in the SM4 than in the SM3 so that the LO result is suppressed more, by about a factor of 2 at the level of the amplitude and thus a factor of 4 at the level of the decay width. Furthermore, the NLO corrections are strongly enhanced for ultra-heavy fermions in the fourth generation; assuming the mass scenario of Eq.(102) for the heavy fermions and a Higgs mass of 100 GeV we get a correction to the decay width (interference of LO with NLO) of -318%; clearly it does not make sense and one should always remember that a badly behaving series should not be used to derive limits on the parameters, i.e., on the heavy-fermion masses.

Extending the same techniques used for $\mathrm{H} \to \mathrm{gg}$ in Ref. [434], we have computed the exact amplitude for $\mathrm{H} \to \gamma\gamma$ up to NLO; assuming for simplicity $m_{\mathrm{b}'} = m_{\mathrm{t}'} = m_Q$ and $m_{\mathrm{l}'} = m_{\nu_{\mathrm{l}}'} = m_L$ (but the calculation gives results for any general setup), the amplitude can be written as follows:

$$A = A_{\mathrm{LO}} \left[1 + X_{\mathrm{W}} \left(C_Q \, \frac{m_Q^2}{M_{\mathrm{W}}^2} + C_L \, \frac{m_L^2}{M_{\mathrm{W}}^2} + R \right) \right], \tag{112}$$

where $C_{Q,L}$ and R depend on masses. In the asymptotic region, $M_{\mathrm{H}} < 2\, M_{\mathrm{W}} \ll m_Q, m_L$ we require R to be a constant and parametrise the C -functions as

$$C_Q = -\,\frac{192}{5}\,(1 + c_Q\,\tau)\,, \qquad C_L = -\,\frac{32}{3}\,(1 + c_L\,\tau)\,, \tag{113}$$

where $C_{Q,L}$ are constant and $\tau^2 = M_{\mathrm{H}}^2/(2\, M_{\mathrm{W}})^2$. Note that for $\tau = R = 0$ this is the leading 2-loop behaviour predicted in Ref. [431] (see also Ref. [432] for the top-dependent contribution which we hide here in R). By performing a fit to our exact result we obtain a good agreement in the asymptotic region, showing that the additional corrections proportional to τ play a relevant role. For instance, with fermions of the fourth generation heavier than 300 GeV we have fit/exact -1 less than 5% in the window $M_{\mathrm{H}} = [80{-}130]$ GeV.

The major part of the NLO corrections emerges from an effective Lagrangian in the heavy-particle limit, therefore we should consider them as correction to the effective Feynman rules and thus to the amplitude. As a result, we define NLO EW corrections to $\mathrm{H} \to \gamma\gamma$ as follows:

$$\Big|A\Big|^2 = \Big|A_{\mathrm{LO}}\Big|^2 \left(1 + \delta_{\mathrm{EW}}^{(4)}\right) = \Big|A_{\mathrm{LO}} + X_{\mathrm{W}}\, A_{\mathrm{NLO}}\Big|^2. \tag{114}$$

This choice is also partially based on the fact that, due to the smallness of the LO amplitude, the interference between LO and NNLO is expected to be suppressed as compared to the squared NLO amplitude. Using Eq. (114), the corrections for $M_{\mathrm{H}} = 100$ GeV and $m_{\mathrm{f}} = 600$ GeV amount to -64.5% as compared to the -318% in the conventional (unrealistic) approach.

To estimate the missing quartic corrections (in the heavy-fermion masses) we assume a leading behaviour of m_Q^4, m_L^4 for NNLO EW, i.e., no accidental cancellations. For a conservative estimate of the uncertainty we use

$$\Big|A\Big|^2 = \Big|A_{\mathrm{LO}} + X_{\mathrm{W}}\, A_{\mathrm{NLO}}\Big|^2 \pm 2\, X_{\mathrm{W}}^2 \Big|A_{\mathrm{LO}}\Big|^2 \Big|C_Q + C_L\Big| \, \frac{m_{\mathrm{f}'}^4}{M_{\mathrm{W}}^4}, \tag{115}$$

where we put $m_Q = m_L = m_{\mathrm{f}'}$ in the last term; given our setup the difference between $m_{\mathrm{t}'}$ and $m_{\mathrm{b}'}$ is irrelevant in estimating the uncertainty. Our educated guess for the error estimate is to use the absolute value of the NLO leading coefficient as the unknown coefficient in the NNLO one.

The effect of including NLO EW corrections is thus better discussed in terms of $|A_{\mathrm{LO}} + X_{\mathrm{W}} A_{\mathrm{NLO}}|^2$; this quantity decreases with increasing values of M_{H} and approaches zero around $M_{\mathrm{H}} = 150\,\mathrm{GeV}$ after which the effect is reversed. The reason for this behaviour is due to the smallness of A_{LO} due to cancellations between bosonic and fermionic loops, while A_{NLO} is relatively large, also due to

absence of the accidental cancellations as the ones observed in the gg channel. Around $M_{\mathrm{H}} = 150$ GeV the credibility of our estimate for the effect of the NNLO corrections becomes more questionable.

It is worth noting that for $\mathrm{H} \to VV$ (see Section 14.3) the situation is different. There is no accidentally small LO (there SM3=SM4 in LO) and the square of A_{NLO} is taken into account by the leading NNLO term taken from Ref. [431], giving the 15% at NNLO, which serves as our error estimate.

The decay mode $\mathrm{H} \to \gamma\mathrm{Z}$ is treated at LO only, since the NLO QCD corrections within the SM3 are known to be small [76] and can thus safely be neglected. The EW corrections in the SM3 as well as the SM4 are unknown. This implies a theoretical uncertainty of the order of 100% in the intermediate Higgs-mass range within the SM4, since large cancellations between the W and fermion loops emerge at LO similar to the decay mode $\mathrm{H} \to \gamma\gamma$.

14.6 Numerical results

The results for the Higgs-boson production cross section via gluon fusion have been obtained by including the NLO QCD corrections with full quark-mass dependence [66] and the NNLO QCD corrections in the limit of heavy quarks [429, 438]. The full EW corrections [434] have been included in factorised from as discussed in Section 14.2. We used the MSTW2008NNLO parton density functions [107] with the strong coupling normalised to $\alpha_{\mathrm{s}}(M_{\mathrm{Z}}) = 0.11707$ at NNLO. The results for the cross sections are displayed in Table 48 for a centre-of-mass energy of $\sqrt{s} = 7$ TeV. The renormalisation and factorisation scales have been chosen as $\mu_{\mathrm{R}} = \mu_{\mathrm{F}} = M_{\mathrm{H}}/2$. These numbers are larger by factors of $4-9$ than the corresponding SM3 cross sections. The QCD uncertainties are about the same as in the SM3 case, while the additional uncertainties due to the EW corrections have been discussed in Section 14.2.

The results for the Higgs branching fractions have been obtained in a similar way as those for the results in SM3 in Refs. [7, 14]. While the partial widths for $\mathrm{H} \to \mathrm{WW/ZZ}$ have been computed with PROPHECY4F, all other partial widths have been calculated with HDECAY[58]. Then, the branching ratios and the total width have been calculated from these partial widths. The full results of the Higgs branching fractions for Higgs masses up to 1 TeV are shown in Tables 49–50 for the 2-fermion final states and in Tables 51–52 for the 2-gauge-boson final states. In the latter table also the total Higgs width is given. Tables 53–54 list the branching fractions for the $\mathrm{e^+e^-e^+e^-}$ and $\mathrm{e^+e^-\mu^+\mu^-}$ final states as well as several combined channels. Apart from the sum of all 4-fermion final states ($\mathrm{H} \to 4\mathrm{f}$) the results for all-leptonic final states $\mathrm{H} \to 4\mathrm{l}$ with $\mathrm{l} = \mathrm{e}, \mu, \tau, \nu_{\mathrm{e}}, \nu_{\mu}, \nu_{\tau}$, the results for all-hadronic final states $\mathrm{H} \to 4\mathrm{q}$ with $\mathrm{q} = \mathrm{u, d, c, s, b}$ and the semi-leptonic final states $\mathrm{H} \to 2\mathrm{l}2\mathrm{q}$ are shown. To compare with the pure SM3, Figure 131 shows the ratios between the SM4 and SM3 branching fractions for the most important channels.

Results for NLO EW corrections to the $\mathrm{H} \to \gamma\gamma$ decay width are shown in Table 55 for the window $[90-150]$ GeV. The effect on the branching fraction is shown in Table 56. The branching ratio for $\mathrm{H} \to \gamma\gamma$ is strongly reduced in SM4.

[58] Note that the EW corrections to the decay width of $H \to \gamma\gamma$ are omitted in the results presented in Tables 51–52. This does practically not influence the other branching ratios.

Table 48: SM4 Higgs-boson production cross section via gluon fusion including NNLO QCD and NLO EW corrections using MSTW2008NNLO PDFs for $\sqrt{s} = 7$ TeV.

$M_{\rm H}$ [GeV]	σ [pb]	$M_{\rm H}$ [GeV]	σ [pb]	$M_{\rm H}$ [GeV]	σ [pb]	$M_{\rm H}$ [GeV]	σ [pb]	$M_{\rm H}$ [GeV]	σ [pb]
100	244	166	77.5	188	56.7	339	13.5	400	9.59
110	199	167	76.3	189	56.0	340	13.5	410	8.80
120	165	168	75.2	190	55.2	341	13.4	420	8.04
130	138	169	74.1	195	51.8	342	13.3	430	7.33
140	117	170	73.0	200	48.6	343	13.3	440	6.67
145	107	171	71.9	210	43.0	344	13.2	450	6.05
150	99.2	172	70.9	220	38.2	345	13.1	460	5.49
151	97.6	173	69.9	230	34.2	346	13.1	470	4.98
152	96.1	174	68.8	240	30.7	347	13.1	480	4.50
153	94.6	175	67.9	250	27.7	348	13.1	490	4.08
154	93.1	176	66.9	260	25.1	349	13.1	500	3.70
155	91.7	177	65.9	270	22.8	350	13.1	550	2.26
156	90.2	178	65.0	280	20.8	351	13.0	600	1.40
157	88.7	179	64.0	290	19.1	352	13.0	650	0.875
158	87.3	180	63.1	300	17.6	353	12.9	700	0.556
159	85.8	181	62.2	310	16.3	354	12.9	750	0.360
160	84.5	182	61.4	320	15.2	355	12.9	800	0.235
161	83.3	183	60.6	330	14.2	360	12.6	850	0.156
162	82.1	184	59.8	335	13.8	370	12.0	900	0.104
163	81.0	185	59.0	336	13.8	375	11.6	950	0.0690
164	79.8	186	58.3	337	13.7	380	11.2	1000	0.0456
165	78.6	187	57.5	338	13.6	390	10.4		

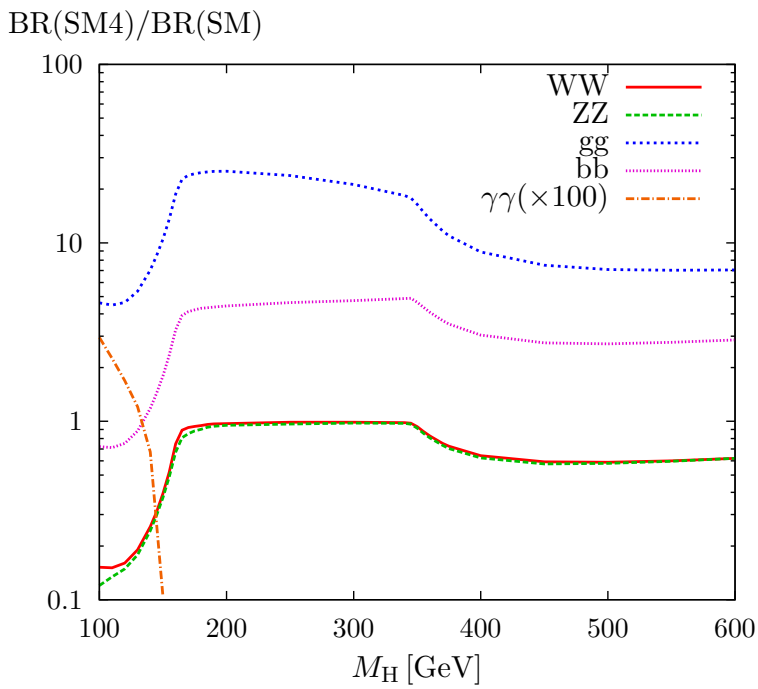

Fig. 131: Ratio of branching fractions in SM4 with respect to SM3 for WW, ZZ, gg, $b\bar{b}$, and $\gamma\gamma$ decay channels ($\gamma\gamma$ ratio multiplied with 100).

Table 49: SM4 Higgs branching fractions for 2-fermion decay channels in the low- and intermediate-mass region.

M_{H} [GeV]	$\mathrm{H} \to \mathrm{bb}$	$\mathrm{H} \to \tau^+\tau^-$	$\mathrm{H} \to \mu^+\mu^-$	$\mathrm{H} \to \mathrm{ss}$	$\mathrm{H} \to \mathrm{c\bar{c}}$	$\mathrm{H} \to \mathrm{t\bar{t}}$
100	$5.70 \cdot 10^{-1}$	$5.98 \cdot 10^{-2}$	$2.08 \cdot 10^{-4}$	$2.44 \cdot 10^{-4}$	$2.88 \cdot 10^{-2}$	0.00
110	$5.30 \cdot 10^{-1}$	$5.67 \cdot 10^{-2}$	$1.97 \cdot 10^{-4}$	$2.26 \cdot 10^{-4}$	$2.68 \cdot 10^{-2}$	0.00
120	$4.87 \cdot 10^{-1}$	$5.29 \cdot 10^{-2}$	$1.84 \cdot 10^{-4}$	$2.08 \cdot 10^{-4}$	$2.46 \cdot 10^{-2}$	0.00
130	$4.36 \cdot 10^{-1}$	$4.82 \cdot 10^{-2}$	$1.67 \cdot 10^{-4}$	$1.86 \cdot 10^{-4}$	$2.20 \cdot 10^{-2}$	0.00
140	$3.72 \cdot 10^{-1}$	$4.17 \cdot 10^{-2}$	$1.45 \cdot 10^{-4}$	$1.59 \cdot 10^{-4}$	$1.88 \cdot 10^{-2}$	0.00
145	$3.33 \cdot 10^{-1}$	$3.75 \cdot 10^{-2}$	$1.30 \cdot 10^{-4}$	$1.42 \cdot 10^{-4}$	$1.68 \cdot 10^{-2}$	0.00
150	$2.83 \cdot 10^{-1}$	$3.20 \cdot 10^{-2}$	$1.11 \cdot 10^{-4}$	$1.21 \cdot 10^{-4}$	$1.42 \cdot 10^{-2}$	0.00
151	$2.71 \cdot 10^{-1}$	$3.08 \cdot 10^{-2}$	$1.07 \cdot 10^{-4}$	$1.16 \cdot 10^{-4}$	$1.37 \cdot 10^{-2}$	0.00
152	$2.59 \cdot 10^{-1}$	$2.94 \cdot 10^{-2}$	$1.02 \cdot 10^{-4}$	$1.11 \cdot 10^{-4}$	$1.31 \cdot 10^{-2}$	0.00
153	$2.46 \cdot 10^{-1}$	$2.80 \cdot 10^{-2}$	$9.70 \cdot 10^{-5}$	$1.05 \cdot 10^{-4}$	$1.24 \cdot 10^{-2}$	0.00
154	$2.32 \cdot 10^{-1}$	$2.64 \cdot 10^{-2}$	$9.16 \cdot 10^{-5}$	$9.89 \cdot 10^{-5}$	$1.17 \cdot 10^{-2}$	0.00
155	$2.17 \cdot 10^{-1}$	$2.47 \cdot 10^{-2}$	$8.57 \cdot 10^{-5}$	$9.24 \cdot 10^{-5}$	$1.09 \cdot 10^{-2}$	0.00
156	$2.01 \cdot 10^{-1}$	$2.29 \cdot 10^{-2}$	$7.94 \cdot 10^{-5}$	$8.56 \cdot 10^{-5}$	$1.01 \cdot 10^{-2}$	0.00
157	$1.83 \cdot 10^{-1}$	$2.09 \cdot 10^{-2}$	$7.25 \cdot 10^{-5}$	$7.80 \cdot 10^{-5}$	$9.22 \cdot 10^{-3}$	0.00
158	$1.61 \cdot 10^{-1}$	$1.84 \cdot 10^{-2}$	$6.39 \cdot 10^{-5}$	$6.87 \cdot 10^{-5}$	$8.12 \cdot 10^{-3}$	0.00
159	$1.38 \cdot 10^{-1}$	$1.58 \cdot 10^{-2}$	$5.49 \cdot 10^{-5}$	$5.90 \cdot 10^{-5}$	$6.97 \cdot 10^{-3}$	0.00
160	$1.13 \cdot 10^{-1}$	$1.29 \cdot 10^{-2}$	$4.48 \cdot 10^{-5}$	$4.80 \cdot 10^{-5}$	$5.67 \cdot 10^{-3}$	0.00
161	$8.91 \cdot 10^{-2}$	$1.02 \cdot 10^{-2}$	$3.55 \cdot 10^{-5}$	$3.80 \cdot 10^{-5}$	$4.49 \cdot 10^{-3}$	0.00
162	$7.15 \cdot 10^{-2}$	$8.22 \cdot 10^{-3}$	$2.85 \cdot 10^{-5}$	$3.05 \cdot 10^{-5}$	$3.60 \cdot 10^{-3}$	0.00
163	$6.00 \cdot 10^{-2}$	$6.91 \cdot 10^{-3}$	$2.40 \cdot 10^{-5}$	$2.56 \cdot 10^{-5}$	$3.02 \cdot 10^{-3}$	0.00
164	$5.23 \cdot 10^{-2}$	$6.03 \cdot 10^{-3}$	$2.09 \cdot 10^{-5}$	$2.23 \cdot 10^{-5}$	$2.64 \cdot 10^{-3}$	0.00
165	$4.68 \cdot 10^{-2}$	$5.39 \cdot 10^{-3}$	$1.87 \cdot 10^{-5}$	$1.99 \cdot 10^{-5}$	$2.36 \cdot 10^{-3}$	0.00
166	$4.26 \cdot 10^{-2}$	$4.92 \cdot 10^{-3}$	$1.71 \cdot 10^{-5}$	$1.82 \cdot 10^{-5}$	$2.15 \cdot 10^{-3}$	0.00
167	$3.94 \cdot 10^{-2}$	$4.55 \cdot 10^{-3}$	$1.58 \cdot 10^{-5}$	$1.68 \cdot 10^{-5}$	$1.98 \cdot 10^{-3}$	0.00
168	$3.67 \cdot 10^{-2}$	$4.25 \cdot 10^{-3}$	$1.47 \cdot 10^{-5}$	$1.57 \cdot 10^{-5}$	$1.85 \cdot 10^{-3}$	0.00
169	$3.45 \cdot 10^{-2}$	$4.00 \cdot 10^{-3}$	$1.39 \cdot 10^{-5}$	$1.47 \cdot 10^{-5}$	$1.74 \cdot 10^{-3}$	0.00
170	$3.26 \cdot 10^{-2}$	$3.78 \cdot 10^{-3}$	$1.31 \cdot 10^{-5}$	$1.39 \cdot 10^{-5}$	$1.64 \cdot 10^{-3}$	0.00
171	$3.10 \cdot 10^{-2}$	$3.60 \cdot 10^{-3}$	$1.25 \cdot 10^{-5}$	$1.32 \cdot 10^{-5}$	$1.56 \cdot 10^{-3}$	0.00
172	$2.95 \cdot 10^{-2}$	$3.43 \cdot 10^{-3}$	$1.19 \cdot 10^{-5}$	$1.26 \cdot 10^{-5}$	$1.49 \cdot 10^{-3}$	0.00
173	$2.83 \cdot 10^{-2}$	$3.29 \cdot 10^{-3}$	$1.14 \cdot 10^{-5}$	$1.20 \cdot 10^{-5}$	$1.42 \cdot 10^{-3}$	0.00
174	$2.71 \cdot 10^{-2}$	$3.15 \cdot 10^{-3}$	$1.09 \cdot 10^{-5}$	$1.15 \cdot 10^{-5}$	$1.36 \cdot 10^{-3}$	0.00
175	$2.60 \cdot 10^{-2}$	$3.03 \cdot 10^{-3}$	$1.05 \cdot 10^{-5}$	$1.11 \cdot 10^{-5}$	$1.31 \cdot 10^{-3}$	0.00
176	$2.50 \cdot 10^{-2}$	$2.92 \cdot 10^{-3}$	$1.01 \cdot 10^{-5}$	$1.07 \cdot 10^{-5}$	$1.26 \cdot 10^{-3}$	0.00
177	$2.41 \cdot 10^{-2}$	$2.81 \cdot 10^{-3}$	$9.75 \cdot 10^{-6}$	$1.03 \cdot 10^{-5}$	$1.21 \cdot 10^{-3}$	0.00
178	$2.32 \cdot 10^{-2}$	$2.71 \cdot 10^{-3}$	$9.41 \cdot 10^{-6}$	$9.89 \cdot 10^{-6}$	$1.17 \cdot 10^{-3}$	0.00
179	$2.23 \cdot 10^{-2}$	$2.62 \cdot 10^{-3}$	$9.07 \cdot 10^{-6}$	$9.52 \cdot 10^{-6}$	$1.13 \cdot 10^{-3}$	0.00
180	$2.15 \cdot 10^{-2}$	$2.52 \cdot 10^{-3}$	$8.74 \cdot 10^{-6}$	$9.17 \cdot 10^{-6}$	$1.08 \cdot 10^{-3}$	0.00
181	$2.06 \cdot 10^{-2}$	$2.42 \cdot 10^{-3}$	$8.40 \cdot 10^{-6}$	$8.80 \cdot 10^{-6}$	$1.04 \cdot 10^{-3}$	0.00
182	$1.97 \cdot 10^{-2}$	$2.31 \cdot 10^{-3}$	$8.01 \cdot 10^{-6}$	$8.38 \cdot 10^{-6}$	$9.90 \cdot 10^{-4}$	0.00
183	$1.86 \cdot 10^{-2}$	$2.19 \cdot 10^{-3}$	$7.60 \cdot 10^{-6}$	$7.95 \cdot 10^{-6}$	$9.38 \cdot 10^{-4}$	0.00
184	$1.77 \cdot 10^{-2}$	$2.08 \cdot 10^{-3}$	$7.21 \cdot 10^{-6}$	$7.53 \cdot 10^{-6}$	$8.90 \cdot 10^{-4}$	0.00
185	$1.68 \cdot 10^{-2}$	$1.98 \cdot 10^{-3}$	$6.87 \cdot 10^{-6}$	$7.17 \cdot 10^{-6}$	$8.47 \cdot 10^{-4}$	0.00
186	$1.61 \cdot 10^{-2}$	$1.89 \cdot 10^{-3}$	$6.57 \cdot 10^{-6}$	$6.85 \cdot 10^{-6}$	$8.09 \cdot 10^{-4}$	0.00
187	$1.54 \cdot 10^{-2}$	$1.82 \cdot 10^{-3}$	$6.31 \cdot 10^{-6}$	$6.57 \cdot 10^{-6}$	$7.76 \cdot 10^{-4}$	0.00
188	$1.48 \cdot 10^{-2}$	$1.75 \cdot 10^{-3}$	$6.07 \cdot 10^{-6}$	$6.31 \cdot 10^{-6}$	$7.46 \cdot 10^{-4}$	0.00
189	$1.43 \cdot 10^{-2}$	$1.69 \cdot 10^{-3}$	$5.86 \cdot 10^{-6}$	$6.09 \cdot 10^{-6}$	$7.20 \cdot 10^{-4}$	0.00
190	$1.39 \cdot 10^{-2}$	$1.64 \cdot 10^{-3}$	$5.69 \cdot 10^{-6}$	$5.91 \cdot 10^{-6}$	$6.98 \cdot 10^{-4}$	0.00
195	$1.20 \cdot 10^{-2}$	$1.43 \cdot 10^{-3}$	$4.94 \cdot 10^{-6}$	$5.10 \cdot 10^{-6}$	$6.03 \cdot 10^{-4}$	0.00
200	$1.06 \cdot 10^{-2}$	$1.27 \cdot 10^{-3}$	$4.41 \cdot 10^{-6}$	$4.53 \cdot 10^{-6}$	$5.35 \cdot 10^{-4}$	0.00
210	$8.71 \cdot 10^{-3}$	$1.05 \cdot 10^{-3}$	$3.64 \cdot 10^{-6}$	$3.71 \cdot 10^{-6}$	$4.38 \cdot 10^{-4}$	0.00
220	$7.33 \cdot 10^{-3}$	$8.93 \cdot 10^{-4}$	$3.09 \cdot 10^{-6}$	$3.12 \cdot 10^{-6}$	$3.69 \cdot 10^{-4}$	0.00

Table 50: SM4 Higgs branching fractions for 2-fermion decay channels in the high-mass region.

M_{H} [GeV]	$\mathrm{H} \to \mathrm{bb}$	$\mathrm{H} \to \tau^+\tau^-$	$\mathrm{H} \to \mu^+\mu^-$	$\mathrm{H} \to \mathrm{ss}$	$\mathrm{H} \to \mathrm{c\bar{c}}$	$\mathrm{H} \to \mathrm{t\bar{t}}$
230	$6.26 \cdot 10^{-3}$	$7.69 \cdot 10^{-4}$	$2.66 \cdot 10^{-6}$	$2.67 \cdot 10^{-6}$	$3.15 \cdot 10^{-4}$	0.00
240	$5.42 \cdot 10^{-3}$	$6.71 \cdot 10^{-4}$	$2.33 \cdot 10^{-6}$	$2.31 \cdot 10^{-6}$	$2.73 \cdot 10^{-4}$	0.00
250	$4.73 \cdot 10^{-3}$	$5.89 \cdot 10^{-4}$	$2.04 \cdot 10^{-6}$	$2.01 \cdot 10^{-6}$	$2.38 \cdot 10^{-4}$	0.00
260	$4.17 \cdot 10^{-3}$	$5.24 \cdot 10^{-4}$	$1.82 \cdot 10^{-6}$	$1.78 \cdot 10^{-6}$	$2.10 \cdot 10^{-4}$	$2.40 \cdot 10^{-7}$
270	$3.71 \cdot 10^{-3}$	$4.69 \cdot 10^{-4}$	$1.62 \cdot 10^{-6}$	$1.58 \cdot 10^{-6}$	$1.86 \cdot 10^{-4}$	$1.07 \cdot 10^{-5}$
280	$3.32 \cdot 10^{-3}$	$4.23 \cdot 10^{-4}$	$1.47 \cdot 10^{-6}$	$1.41 \cdot 10^{-6}$	$1.67 \cdot 10^{-4}$	$5.13 \cdot 10^{-5}$
290	$2.99 \cdot 10^{-3}$	$3.82 \cdot 10^{-4}$	$1.33 \cdot 10^{-6}$	$1.27 \cdot 10^{-6}$	$1.50 \cdot 10^{-4}$	$1.45 \cdot 10^{-4}$
300	$2.70 \cdot 10^{-3}$	$3.48 \cdot 10^{-4}$	$1.21 \cdot 10^{-6}$	$1.15 \cdot 10^{-6}$	$1.36 \cdot 10^{-4}$	$3.26 \cdot 10^{-4}$
310	$2.47 \cdot 10^{-3}$	$3.20 \cdot 10^{-4}$	$1.11 \cdot 10^{-6}$	$1.05 \cdot 10^{-6}$	$1.24 \cdot 10^{-4}$	$6.60 \cdot 10^{-4}$
320	$2.26 \cdot 10^{-3}$	$2.94 \cdot 10^{-4}$	$1.02 \cdot 10^{-6}$	$9.61 \cdot 10^{-7}$	$1.13 \cdot 10^{-4}$	$1.28 \cdot 10^{-3}$
330	$2.07 \cdot 10^{-3}$	$2.72 \cdot 10^{-4}$	$9.41 \cdot 10^{-7}$	$8.83 \cdot 10^{-7}$	$1.04 \cdot 10^{-4}$	$2.52 \cdot 10^{-3}$
335	$1.99 \cdot 10^{-3}$	$2.62 \cdot 10^{-4}$	$9.07 \cdot 10^{-7}$	$8.48 \cdot 10^{-7}$	$1.00 \cdot 10^{-4}$	$3.68 \cdot 10^{-3}$
336	$1.98 \cdot 10^{-3}$	$2.60 \cdot 10^{-4}$	$9.00 \cdot 10^{-7}$	$8.42 \cdot 10^{-7}$	$9.94 \cdot 10^{-5}$	$4.00 \cdot 10^{-3}$
337	$1.96 \cdot 10^{-3}$	$2.58 \cdot 10^{-4}$	$8.94 \cdot 10^{-7}$	$8.36 \cdot 10^{-7}$	$9.86 \cdot 10^{-5}$	$4.36 \cdot 10^{-3}$
338	$1.95 \cdot 10^{-3}$	$2.56 \cdot 10^{-4}$	$8.88 \cdot 10^{-7}$	$8.30 \cdot 10^{-7}$	$9.79 \cdot 10^{-5}$	$4.78 \cdot 10^{-3}$
339	$1.93 \cdot 10^{-3}$	$2.54 \cdot 10^{-4}$	$8.82 \cdot 10^{-7}$	$8.23 \cdot 10^{-7}$	$9.72 \cdot 10^{-5}$	$5.26 \cdot 10^{-3}$
340	$1.92 \cdot 10^{-3}$	$2.53 \cdot 10^{-4}$	$8.76 \cdot 10^{-7}$	$8.18 \cdot 10^{-7}$	$9.64 \cdot 10^{-5}$	$5.83 \cdot 10^{-3}$
345	$1.85 \cdot 10^{-3}$	$2.45 \cdot 10^{-4}$	$8.48 \cdot 10^{-7}$	$7.89 \cdot 10^{-7}$	$9.31 \cdot 10^{-5}$	$1.60 \cdot 10^{-2}$
346	$1.83 \cdot 10^{-3}$	$2.42 \cdot 10^{-4}$	$8.38 \cdot 10^{-7}$	$7.79 \cdot 10^{-7}$	$9.19 \cdot 10^{-5}$	$2.21 \cdot 10^{-2}$
347	$1.80 \cdot 10^{-3}$	$2.38 \cdot 10^{-4}$	$8.24 \cdot 10^{-7}$	$7.65 \cdot 10^{-7}$	$9.03 \cdot 10^{-5}$	$3.08 \cdot 10^{-2}$
348	$1.76 \cdot 10^{-3}$	$2.33 \cdot 10^{-4}$	$8.07 \cdot 10^{-7}$	$7.49 \cdot 10^{-7}$	$8.85 \cdot 10^{-5}$	$4.23 \cdot 10^{-2}$
349	$1.72 \cdot 10^{-3}$	$2.27 \cdot 10^{-4}$	$7.87 \cdot 10^{-7}$	$7.31 \cdot 10^{-7}$	$8.63 \cdot 10^{-5}$	$5.66 \cdot 10^{-2}$
350	$1.67 \cdot 10^{-3}$	$2.21 \cdot 10^{-4}$	$7.67 \cdot 10^{-7}$	$7.12 \cdot 10^{-7}$	$8.40 \cdot 10^{-5}$	$7.25 \cdot 10^{-2}$
351	$1.63 \cdot 10^{-3}$	$2.16 \cdot 10^{-4}$	$7.47 \cdot 10^{-7}$	$6.93 \cdot 10^{-7}$	$8.18 \cdot 10^{-5}$	$8.78 \cdot 10^{-2}$
352	$1.59 \cdot 10^{-3}$	$2.10 \cdot 10^{-4}$	$7.29 \cdot 10^{-7}$	$6.76 \cdot 10^{-7}$	$7.98 \cdot 10^{-5}$	$1.03 \cdot 10^{-1}$
353	$1.55 \cdot 10^{-3}$	$2.05 \cdot 10^{-4}$	$7.11 \cdot 10^{-7}$	$6.59 \cdot 10^{-7}$	$7.77 \cdot 10^{-5}$	$1.18 \cdot 10^{-1}$
354	$1.51 \cdot 10^{-3}$	$2.00 \cdot 10^{-4}$	$6.93 \cdot 10^{-7}$	$6.42 \cdot 10^{-7}$	$7.57 \cdot 10^{-5}$	$1.32 \cdot 10^{-1}$
355	$1.47 \cdot 10^{-3}$	$1.95 \cdot 10^{-4}$	$6.75 \cdot 10^{-7}$	$6.25 \cdot 10^{-7}$	$7.38 \cdot 10^{-5}$	$1.46 \cdot 10^{-1}$
360	$1.29 \cdot 10^{-3}$	$1.72 \cdot 10^{-4}$	$5.97 \cdot 10^{-7}$	$5.51 \cdot 10^{-7}$	$6.50 \cdot 10^{-5}$	$2.09 \cdot 10^{-1}$
370	$1.03 \cdot 10^{-3}$	$1.38 \cdot 10^{-4}$	$4.79 \cdot 10^{-7}$	$4.41 \cdot 10^{-7}$	$5.20 \cdot 10^{-5}$	$3.05 \cdot 10^{-1}$
375	$9.38 \cdot 10^{-4}$	$1.26 \cdot 10^{-4}$	$4.35 \cdot 10^{-7}$	$3.99 \cdot 10^{-7}$	$4.71 \cdot 10^{-5}$	$3.41 \cdot 10^{-1}$
380	$8.57 \cdot 10^{-4}$	$1.15 \cdot 10^{-4}$	$3.99 \cdot 10^{-7}$	$3.65 \cdot 10^{-7}$	$4.30 \cdot 10^{-5}$	$3.71 \cdot 10^{-1}$
390	$7.31 \cdot 10^{-4}$	$9.85 \cdot 10^{-5}$	$3.42 \cdot 10^{-7}$	$3.11 \cdot 10^{-7}$	$3.67 \cdot 10^{-5}$	$4.18 \cdot 10^{-1}$
400	$6.38 \cdot 10^{-4}$	$8.63 \cdot 10^{-5}$	$2.99 \cdot 10^{-7}$	$2.71 \cdot 10^{-7}$	$3.20 \cdot 10^{-5}$	$4.50 \cdot 10^{-1}$
410	$5.66 \cdot 10^{-4}$	$7.69 \cdot 10^{-5}$	$2.67 \cdot 10^{-7}$	$2.41 \cdot 10^{-7}$	$2.84 \cdot 10^{-5}$	$4.73 \cdot 10^{-1}$
420	$5.09 \cdot 10^{-4}$	$6.96 \cdot 10^{-5}$	$2.41 \cdot 10^{-7}$	$2.17 \cdot 10^{-7}$	$2.56 \cdot 10^{-5}$	$4.90 \cdot 10^{-1}$
430	$4.65 \cdot 10^{-4}$	$6.37 \cdot 10^{-5}$	$2.21 \cdot 10^{-7}$	$1.98 \cdot 10^{-7}$	$2.33 \cdot 10^{-5}$	$5.03 \cdot 10^{-1}$
440	$4.28 \cdot 10^{-4}$	$5.88 \cdot 10^{-5}$	$2.04 \cdot 10^{-7}$	$1.82 \cdot 10^{-7}$	$2.15 \cdot 10^{-5}$	$5.11 \cdot 10^{-1}$
450	$3.97 \cdot 10^{-4}$	$5.48 \cdot 10^{-5}$	$1.90 \cdot 10^{-7}$	$1.69 \cdot 10^{-7}$	$1.99 \cdot 10^{-5}$	$5.17 \cdot 10^{-1}$
460	$3.70 \cdot 10^{-4}$	$5.14 \cdot 10^{-5}$	$1.78 \cdot 10^{-7}$	$1.58 \cdot 10^{-7}$	$1.86 \cdot 10^{-5}$	$5.21 \cdot 10^{-1}$
470	$3.48 \cdot 10^{-4}$	$4.84 \cdot 10^{-5}$	$1.68 \cdot 10^{-7}$	$1.48 \cdot 10^{-7}$	$1.75 \cdot 10^{-5}$	$5.24 \cdot 10^{-1}$
480	$3.28 \cdot 10^{-4}$	$4.58 \cdot 10^{-5}$	$1.59 \cdot 10^{-7}$	$1.40 \cdot 10^{-7}$	$1.65 \cdot 10^{-5}$	$5.24 \cdot 10^{-1}$
490	$3.11 \cdot 10^{-4}$	$4.36 \cdot 10^{-5}$	$1.51 \cdot 10^{-7}$	$1.32 \cdot 10^{-7}$	$1.56 \cdot 10^{-5}$	$5.24 \cdot 10^{-1}$
500	$2.96 \cdot 10^{-4}$	$4.16 \cdot 10^{-5}$	$1.44 \cdot 10^{-7}$	$1.26 \cdot 10^{-7}$	$1.48 \cdot 10^{-5}$	$5.22 \cdot 10^{-1}$
550	$2.39 \cdot 10^{-4}$	$3.41 \cdot 10^{-5}$	$1.18 \cdot 10^{-7}$	$1.02 \cdot 10^{-7}$	$1.20 \cdot 10^{-5}$	$5.07 \cdot 10^{-1}$
600	$2.02 \cdot 10^{-4}$	$2.92 \cdot 10^{-5}$	$1.01 \cdot 10^{-7}$	$8.58 \cdot 10^{-8}$	$1.01 \cdot 10^{-5}$	$4.82 \cdot 10^{-1}$
650	$1.74 \cdot 10^{-4}$	$2.55 \cdot 10^{-5}$	$8.84 \cdot 10^{-8}$	$7.39 \cdot 10^{-8}$	$8.72 \cdot 10^{-6}$	$4.52 \cdot 10^{-1}$
700	$1.52 \cdot 10^{-4}$	$2.26 \cdot 10^{-5}$	$7.82 \cdot 10^{-8}$	$6.46 \cdot 10^{-8}$	$7.61 \cdot 10^{-6}$	$4.21 \cdot 10^{-1}$
750	$1.34 \cdot 10^{-4}$	$2.01 \cdot 10^{-5}$	$6.97 \cdot 10^{-8}$	$5.68 \cdot 10^{-8}$	$6.69 \cdot 10^{-6}$	$3.88 \cdot 10^{-1}$
800	$1.18 \cdot 10^{-4}$	$1.80 \cdot 10^{-5}$	$6.24 \cdot 10^{-8}$	$5.02 \cdot 10^{-8}$	$5.91 \cdot 10^{-6}$	$3.56 \cdot 10^{-1}$
1000	$7.37 \cdot 10^{-5}$	$1.17 \cdot 10^{-5}$	$4.06 \cdot 10^{-8}$	$3.13 \cdot 10^{-8}$	$3.69 \cdot 10^{-6}$	$2.43 \cdot 10^{-1}$

Table 51: SM4 Higgs branching fractions for 2-gauge-boson decay channels and total Higgs width in the low- and intermediate-mass region.

M_{H} [GeV]	$\mathrm{H} \to \mathrm{gg}$	$\mathrm{H} \to \gamma\gamma$	$\mathrm{H} \to \mathrm{Z}\gamma$	$\mathrm{H} \to \mathrm{WW}$	$\mathrm{H} \to \mathrm{ZZ}$	Γ_{H} [GeV]
100	$3.39 \cdot 10^{-1}$	$1.31 \cdot 10^{-4}$	$1.70 \cdot 10^{-5}$	$1.67 \cdot 10^{-3}$	$1.35 \cdot 10^{-4}$	$5.52 \cdot 10^{-3}$
110	$3.78 \cdot 10^{-1}$	$1.72 \cdot 10^{-4}$	$1.35 \cdot 10^{-4}$	$7.20 \cdot 10^{-3}$	$5.83 \cdot 10^{-4}$	$6.41 \cdot 10^{-3}$
120	$4.10 \cdot 10^{-1}$	$2.26 \cdot 10^{-4}$	$4.06 \cdot 10^{-4}$	$2.27 \cdot 10^{-2}$	$2.37 \cdot 10^{-3}$	$7.49 \cdot 10^{-3}$
130	$4.28 \cdot 10^{-1}$	$2.95 \cdot 10^{-4}$	$8.51 \cdot 10^{-4}$	$5.77 \cdot 10^{-2}$	$7.12 \cdot 10^{-3}$	$8.92 \cdot 10^{-3}$
140	$4.20 \cdot 10^{-1}$	$3.81 \cdot 10^{-4}$	$1.46 \cdot 10^{-3}$	$1.29 \cdot 10^{-1}$	$1.68 \cdot 10^{-2}$	$1.11 \cdot 10^{-2}$
145	$4.01 \cdot 10^{-1}$	$4.29 \cdot 10^{-4}$	$1.80 \cdot 10^{-3}$	$1.86 \cdot 10^{-1}$	$2.36 \cdot 10^{-2}$	$1.28 \cdot 10^{-2}$
150	$3.63 \cdot 10^{-1}$	$4.74 \cdot 10^{-4}$	$2.13 \cdot 10^{-3}$	$2.75 \cdot 10^{-1}$	$3.09 \cdot 10^{-2}$	$1.55 \cdot 10^{-2}$
151	$3.53 \cdot 10^{-1}$	$4.82 \cdot 10^{-4}$	$2.19 \cdot 10^{-3}$	$2.97 \cdot 10^{-1}$	$3.23 \cdot 10^{-2}$	$1.62 \cdot 10^{-2}$
152	$3.41 \cdot 10^{-1}$	$4.89 \cdot 10^{-4}$	$2.24 \cdot 10^{-3}$	$3.21 \cdot 10^{-1}$	$3.35 \cdot 10^{-2}$	$1.71 \cdot 10^{-2}$
153	$3.28 \cdot 10^{-1}$	$4.95 \cdot 10^{-4}$	$2.29 \cdot 10^{-3}$	$3.48 \cdot 10^{-1}$	$3.46 \cdot 10^{-2}$	$1.81 \cdot 10^{-2}$
154	$3.13 \cdot 10^{-1}$	$4.99 \cdot 10^{-4}$	$2.32 \cdot 10^{-3}$	$3.78 \cdot 10^{-1}$	$3.54 \cdot 10^{-2}$	$1.93 \cdot 10^{-2}$
155	$2.96 \cdot 10^{-1}$	$5.00 \cdot 10^{-4}$	$2.34 \cdot 10^{-3}$	$4.12 \cdot 10^{-1}$	$3.59 \cdot 10^{-2}$	$2.08 \cdot 10^{-2}$
156	$2.77 \cdot 10^{-1}$	$5.00 \cdot 10^{-4}$	$2.34 \cdot 10^{-3}$	$4.52 \cdot 10^{-1}$	$3.59 \cdot 10^{-2}$	$2.25 \cdot 10^{-2}$
157	$2.55 \cdot 10^{-1}$	$4.96 \cdot 10^{-4}$	$2.33 \cdot 10^{-3}$	$4.94 \cdot 10^{-1}$	$3.55 \cdot 10^{-2}$	$2.48 \cdot 10^{-2}$
158	$2.27 \cdot 10^{-1}$	$4.80 \cdot 10^{-4}$	$2.25 \cdot 10^{-3}$	$5.49 \cdot 10^{-1}$	$3.39 \cdot 10^{-2}$	$2.84 \cdot 10^{-2}$
159	$1.97 \cdot 10^{-1}$	$4.61 \cdot 10^{-4}$	$2.15 \cdot 10^{-3}$	$6.09 \cdot 10^{-1}$	$3.15 \cdot 10^{-2}$	$3.32 \cdot 10^{-2}$
160	$1.62 \cdot 10^{-1}$	$4.35 \cdot 10^{-4}$	$2.01 \cdot 10^{-3}$	$6.80 \cdot 10^{-1}$	$2.78 \cdot 10^{-2}$	$4.10 \cdot 10^{-2}$
161	$1.30 \cdot 10^{-1}$	$4.49 \cdot 10^{-4}$	$2.01 \cdot 10^{-3}$	$7.41 \cdot 10^{-1}$	$2.40 \cdot 10^{-2}$	$5.21 \cdot 10^{-2}$
162	$1.06 \cdot 10^{-1}$	$3.65 \cdot 10^{-4}$	$1.65 \cdot 10^{-3}$	$7.89 \cdot 10^{-1}$	$2.11 \cdot 10^{-2}$	$6.52 \cdot 10^{-2}$
163	$8.98 \cdot 10^{-2}$	$3.11 \cdot 10^{-4}$	$1.42 \cdot 10^{-3}$	$8.19 \cdot 10^{-1}$	$1.93 \cdot 10^{-2}$	$7.81 \cdot 10^{-2}$
164	$7.92 \cdot 10^{-2}$	$2.74 \cdot 10^{-4}$	$1.27 \cdot 10^{-3}$	$8.41 \cdot 10^{-1}$	$1.84 \cdot 10^{-2}$	$9.01 \cdot 10^{-2}$
165	$7.15 \cdot 10^{-2}$	$2.48 \cdot 10^{-4}$	$1.16 \cdot 10^{-3}$	$8.56 \cdot 10^{-1}$	$1.80 \cdot 10^{-2}$	$1.01 \cdot 10^{-1}$
166	$6.59 \cdot 10^{-2}$	$2.29 \cdot 10^{-4}$	$1.08 \cdot 10^{-3}$	$8.66 \cdot 10^{-1}$	$1.80 \cdot 10^{-2}$	$1.12 \cdot 10^{-1}$
167	$6.16 \cdot 10^{-2}$	$2.14 \cdot 10^{-4}$	$1.02 \cdot 10^{-3}$	$8.74 \cdot 10^{-1}$	$1.83 \cdot 10^{-2}$	$1.21 \cdot 10^{-1}$
168	$5.81 \cdot 10^{-2}$	$2.02 \cdot 10^{-4}$	$9.71 \cdot 10^{-4}$	$8.81 \cdot 10^{-1}$	$1.87 \cdot 10^{-2}$	$1.31 \cdot 10^{-1}$
169	$5.52 \cdot 10^{-2}$	$1.92 \cdot 10^{-4}$	$9.30 \cdot 10^{-4}$	$8.86 \cdot 10^{-1}$	$1.93 \cdot 10^{-2}$	$1.40 \cdot 10^{-1}$
170	$5.27 \cdot 10^{-2}$	$1.84 \cdot 10^{-4}$	$8.96 \cdot 10^{-4}$	$8.90 \cdot 10^{-1}$	$2.02 \cdot 10^{-2}$	$1.49 \cdot 10^{-1}$
171	$5.06 \cdot 10^{-2}$	$1.76 \cdot 10^{-4}$	$8.66 \cdot 10^{-4}$	$8.92 \cdot 10^{-1}$	$2.15 \cdot 10^{-2}$	$1.57 \cdot 10^{-1}$
172	$4.87 \cdot 10^{-2}$	$1.70 \cdot 10^{-4}$	$8.41 \cdot 10^{-4}$	$8.95 \cdot 10^{-1}$	$2.27 \cdot 10^{-2}$	$1.66 \cdot 10^{-1}$
173	$4.71 \cdot 10^{-2}$	$1.64 \cdot 10^{-4}$	$8.18 \cdot 10^{-4}$	$8.96 \cdot 10^{-1}$	$2.43 \cdot 10^{-2}$	$1.74 \cdot 10^{-1}$
174	$4.56 \cdot 10^{-2}$	$1.59 \cdot 10^{-4}$	$7.98 \cdot 10^{-4}$	$8.97 \cdot 10^{-1}$	$2.62 \cdot 10^{-2}$	$1.83 \cdot 10^{-1}$
175	$4.43 \cdot 10^{-2}$	$1.54 \cdot 10^{-4}$	$7.79 \cdot 10^{-4}$	$8.97 \cdot 10^{-1}$	$2.85 \cdot 10^{-2}$	$1.91 \cdot 10^{-1}$
176	$4.30 \cdot 10^{-2}$	$1.50 \cdot 10^{-4}$	$7.61 \cdot 10^{-4}$	$8.97 \cdot 10^{-1}$	$3.14 \cdot 10^{-2}$	$2.00 \cdot 10^{-1}$
177	$4.18 \cdot 10^{-2}$	$1.46 \cdot 10^{-4}$	$7.44 \cdot 10^{-4}$	$8.96 \cdot 10^{-1}$	$3.50 \cdot 10^{-2}$	$2.08 \cdot 10^{-1}$
178	$4.07 \cdot 10^{-2}$	$1.42 \cdot 10^{-4}$	$7.28 \cdot 10^{-4}$	$8.93 \cdot 10^{-1}$	$3.95 \cdot 10^{-2}$	$2.17 \cdot 10^{-1}$
179	$3.96 \cdot 10^{-2}$	$1.38 \cdot 10^{-4}$	$7.12 \cdot 10^{-4}$	$8.89 \cdot 10^{-1}$	$4.59 \cdot 10^{-2}$	$2.27 \cdot 10^{-1}$
180	$3.85 \cdot 10^{-2}$	$1.34 \cdot 10^{-4}$	$6.95 \cdot 10^{-4}$	$8.82 \cdot 10^{-1}$	$5.43 \cdot 10^{-2}$	$2.37 \cdot 10^{-1}$
181	$3.73 \cdot 10^{-2}$	$1.30 \cdot 10^{-4}$	$6.76 \cdot 10^{-4}$	$8.74 \cdot 10^{-1}$	$6.66 \cdot 10^{-2}$	$2.48 \cdot 10^{-1}$
182	$3.59 \cdot 10^{-2}$	$1.25 \cdot 10^{-4}$	$6.53 \cdot 10^{-4}$	$8.60 \cdot 10^{-1}$	$8.27 \cdot 10^{-2}$	$2.61 \cdot 10^{-1}$
183	$3.44 \cdot 10^{-2}$	$1.20 \cdot 10^{-4}$	$6.27 \cdot 10^{-4}$	$8.43 \cdot 10^{-1}$	$1.02 \cdot 10^{-1}$	$2.77 \cdot 10^{-1}$
184	$3.30 \cdot 10^{-2}$	$1.14 \cdot 10^{-4}$	$6.02 \cdot 10^{-4}$	$8.26 \cdot 10^{-1}$	$1.22 \cdot 10^{-1}$	$2.93 \cdot 10^{-1}$
185	$3.18 \cdot 10^{-2}$	$1.10 \cdot 10^{-4}$	$5.80 \cdot 10^{-4}$	$8.11 \cdot 10^{-1}$	$1.39 \cdot 10^{-1}$	$3.09 \cdot 10^{-1}$
186	$3.07 \cdot 10^{-2}$	$1.06 \cdot 10^{-4}$	$5.61 \cdot 10^{-4}$	$7.97 \cdot 10^{-1}$	$1.54 \cdot 10^{-1}$	$3.25 \cdot 10^{-1}$
187	$2.97 \cdot 10^{-2}$	$1.02 \cdot 10^{-4}$	$5.45 \cdot 10^{-4}$	$7.85 \cdot 10^{-1}$	$1.68 \cdot 10^{-1}$	$3.41 \cdot 10^{-1}$
188	$2.88 \cdot 10^{-2}$	$9.93 \cdot 10^{-5}$	$5.30 \cdot 10^{-4}$	$7.74 \cdot 10^{-1}$	$1.78 \cdot 10^{-1}$	$3.56 \cdot 10^{-1}$
189	$2.81 \cdot 10^{-2}$	$9.66 \cdot 10^{-5}$	$5.17 \cdot 10^{-4}$	$7.66 \cdot 10^{-1}$	$1.88 \cdot 10^{-1}$	$3.70 \cdot 10^{-1}$
190	$2.75 \cdot 10^{-2}$	$9.44 \cdot 10^{-5}$	$5.07 \cdot 10^{-4}$	$7.60 \cdot 10^{-1}$	$1.97 \cdot 10^{-1}$	$3.84 \cdot 10^{-1}$
195	$2.50 \cdot 10^{-2}$	$8.50 \cdot 10^{-5}$	$4.61 \cdot 10^{-4}$	$7.33 \cdot 10^{-1}$	$2.25 \cdot 10^{-1}$	$4.53 \cdot 10^{-1}$
200	$2.33 \cdot 10^{-2}$	$7.84 \cdot 10^{-5}$	$4.28 \cdot 10^{-4}$	$7.18 \cdot 10^{-1}$	$2.43 \cdot 10^{-1}$	$5.21 \cdot 10^{-1}$
210	$2.10 \cdot 10^{-2}$	$6.90 \cdot 10^{-5}$	$3.79 \cdot 10^{-4}$	$7.05 \cdot 10^{-1}$	$2.62 \cdot 10^{-1}$	$6.63 \cdot 10^{-1}$
220	$1.94 \cdot 10^{-2}$	$6.21 \cdot 10^{-5}$	$3.39 \cdot 10^{-4}$	$6.98 \cdot 10^{-1}$	$2.73 \cdot 10^{-1}$	$8.18 \cdot 10^{-1}$

Table 52: SM4 Higgs branching fractions for 2-gauge-boson decay channels and total Higgs width in the high-mass region.

M_{H} [GeV]	$\mathrm{H} \to \mathrm{gg}$	$\mathrm{H} \to \gamma\gamma$	$\mathrm{H} \to \mathrm{Z}\gamma$	$\mathrm{H} \to \mathrm{WW}$	$\mathrm{H} \to \mathrm{ZZ}$	Γ_{H} [GeV]
230	$1.81 \cdot 10^{-2}$	$5.65 \cdot 10^{-5}$	$3.05 \cdot 10^{-4}$	$6.95 \cdot 10^{-1}$	$2.79 \cdot 10^{-1}$	$9.94 \cdot 10^{-1}$
240	$1.71 \cdot 10^{-2}$	$5.20 \cdot 10^{-5}$	$2.75 \cdot 10^{-4}$	$6.92 \cdot 10^{-1}$	$2.84 \cdot 10^{-1}$	1.19
250	$1.62 \cdot 10^{-2}$	$4.80 \cdot 10^{-5}$	$2.48 \cdot 10^{-4}$	$6.93 \cdot 10^{-1}$	$2.86 \cdot 10^{-1}$	1.41
260	$1.56 \cdot 10^{-2}$	$4.49 \cdot 10^{-5}$	$2.26 \cdot 10^{-4}$	$6.91 \cdot 10^{-1}$	$2.90 \cdot 10^{-1}$	1.65
270	$1.50 \cdot 10^{-2}$	$4.22 \cdot 10^{-5}$	$2.05 \cdot 10^{-4}$	$6.88 \cdot 10^{-1}$	$2.93 \cdot 10^{-1}$	1.92
280	$1.46 \cdot 10^{-2}$	$4.00 \cdot 10^{-5}$	$1.88 \cdot 10^{-4}$	$6.88 \cdot 10^{-1}$	$2.95 \cdot 10^{-1}$	2.21
290	$1.42 \cdot 10^{-2}$	$3.81 \cdot 10^{-5}$	$1.72 \cdot 10^{-4}$	$6.86 \cdot 10^{-1}$	$2.97 \cdot 10^{-1}$	2.53
300	$1.39 \cdot 10^{-2}$	$3.65 \cdot 10^{-5}$	$1.58 \cdot 10^{-4}$	$6.84 \cdot 10^{-1}$	$3.00 \cdot 10^{-1}$	2.87
310	$1.38 \cdot 10^{-2}$	$3.55 \cdot 10^{-5}$	$1.46 \cdot 10^{-4}$	$6.80 \cdot 10^{-1}$	$3.02 \cdot 10^{-1}$	3.23
320	$1.36 \cdot 10^{-2}$	$3.45 \cdot 10^{-5}$	$1.35 \cdot 10^{-4}$	$6.79 \cdot 10^{-1}$	$3.03 \cdot 10^{-1}$	3.63
330	$1.36 \cdot 10^{-2}$	$3.39 \cdot 10^{-5}$	$1.25 \cdot 10^{-4}$	$6.78 \cdot 10^{-1}$	$3.03 \cdot 10^{-1}$	4.06
335	$1.37 \cdot 10^{-2}$	$3.39 \cdot 10^{-5}$	$1.20 \cdot 10^{-4}$	$6.77 \cdot 10^{-1}$	$3.03 \cdot 10^{-1}$	4.28
336	$1.37 \cdot 10^{-2}$	$3.39 \cdot 10^{-5}$	$1.20 \cdot 10^{-4}$	$6.77 \cdot 10^{-1}$	$3.03 \cdot 10^{-1}$	4.32
337	$1.37 \cdot 10^{-2}$	$3.39 \cdot 10^{-5}$	$1.19 \cdot 10^{-4}$	$6.77 \cdot 10^{-1}$	$3.02 \cdot 10^{-1}$	4.36
338	$1.38 \cdot 10^{-2}$	$3.39 \cdot 10^{-5}$	$1.18 \cdot 10^{-4}$	$6.76 \cdot 10^{-1}$	$3.02 \cdot 10^{-1}$	4.41
339	$1.38 \cdot 10^{-2}$	$3.39 \cdot 10^{-5}$	$1.17 \cdot 10^{-4}$	$6.76 \cdot 10^{-1}$	$3.02 \cdot 10^{-1}$	4.45
340	$1.38 \cdot 10^{-2}$	$3.40 \cdot 10^{-5}$	$1.17 \cdot 10^{-4}$	$6.76 \cdot 10^{-1}$	$3.02 \cdot 10^{-1}$	4.49
345	$1.39 \cdot 10^{-2}$	$3.44 \cdot 10^{-5}$	$1.13 \cdot 10^{-4}$	$6.69 \cdot 10^{-1}$	$2.99 \cdot 10^{-1}$	4.72
346	$1.39 \cdot 10^{-2}$	$3.42 \cdot 10^{-5}$	$1.11 \cdot 10^{-4}$	$6.65 \cdot 10^{-1}$	$2.97 \cdot 10^{-1}$	4.79
347	$1.38 \cdot 10^{-2}$	$3.38 \cdot 10^{-5}$	$1.10 \cdot 10^{-4}$	$6.59 \cdot 10^{-1}$	$2.94 \cdot 10^{-1}$	4.88
348	$1.37 \cdot 10^{-2}$	$3.33 \cdot 10^{-5}$	$1.07 \cdot 10^{-4}$	$6.51 \cdot 10^{-1}$	$2.90 \cdot 10^{-1}$	5.00
349	$1.36 \cdot 10^{-2}$	$3.26 \cdot 10^{-5}$	$1.05 \cdot 10^{-4}$	$6.41 \cdot 10^{-1}$	$2.86 \cdot 10^{-1}$	5.14
350	$1.34 \cdot 10^{-2}$	$3.19 \cdot 10^{-5}$	$1.02 \cdot 10^{-4}$	$6.31 \cdot 10^{-1}$	$2.81 \cdot 10^{-1}$	5.29
351	$1.32 \cdot 10^{-2}$	$3.12 \cdot 10^{-5}$	$9.91 \cdot 10^{-5}$	$6.21 \cdot 10^{-1}$	$2.76 \cdot 10^{-1}$	5.44
352	$1.30 \cdot 10^{-2}$	$3.05 \cdot 10^{-5}$	$9.66 \cdot 10^{-5}$	$6.11 \cdot 10^{-1}$	$2.71 \cdot 10^{-1}$	5.60
353	$1.28 \cdot 10^{-2}$	$2.98 \cdot 10^{-5}$	$9.41 \cdot 10^{-5}$	$6.01 \cdot 10^{-1}$	$2.66 \cdot 10^{-1}$	5.76
354	$1.26 \cdot 10^{-2}$	$2.91 \cdot 10^{-5}$	$9.16 \cdot 10^{-5}$	$5.92 \cdot 10^{-1}$	$2.61 \cdot 10^{-1}$	5.92
355	$1.24 \cdot 10^{-2}$	$2.84 \cdot 10^{-5}$	$8.91 \cdot 10^{-5}$	$5.82 \cdot 10^{-1}$	$2.57 \cdot 10^{-1}$	6.09
360	$1.15 \cdot 10^{-2}$	$2.53 \cdot 10^{-5}$	$7.82 \cdot 10^{-5}$	$5.39 \cdot 10^{-1}$	$2.38 \cdot 10^{-1}$	7.00
370	$1.01 \cdot 10^{-2}$	$2.04 \cdot 10^{-5}$	$6.18 \cdot 10^{-5}$	$4.73 \cdot 10^{-1}$	$2.10 \cdot 10^{-1}$	8.96
375	$9.46 \cdot 10^{-3}$	$1.85 \cdot 10^{-5}$	$5.56 \cdot 10^{-5}$	$4.49 \cdot 10^{-1}$	$1.99 \cdot 10^{-1}$	$1.00 \cdot 10^{1}$
380	$8.94 \cdot 10^{-3}$	$1.69 \cdot 10^{-5}$	$5.04 \cdot 10^{-5}$	$4.28 \cdot 10^{-1}$	$1.90 \cdot 10^{-1}$	$1.11 \cdot 10^{1}$
390	$8.07 \cdot 10^{-3}$	$1.44 \cdot 10^{-5}$	$4.23 \cdot 10^{-5}$	$3.96 \cdot 10^{-1}$	$1.77 \cdot 10^{-1}$	$1.33 \cdot 10^{1}$
400	$7.40 \cdot 10^{-3}$	$1.25 \cdot 10^{-5}$	$3.63 \cdot 10^{-5}$	$3.74 \cdot 10^{-1}$	$1.68 \cdot 10^{-1}$	$1.55 \cdot 10^{1}$
410	$6.85 \cdot 10^{-3}$	$1.10 \cdot 10^{-5}$	$3.16 \cdot 10^{-5}$	$3.59 \cdot 10^{-1}$	$1.61 \cdot 10^{-1}$	$1.79 \cdot 10^{1}$
420	$6.41 \cdot 10^{-3}$	$9.85 \cdot 10^{-6}$	$2.80 \cdot 10^{-5}$	$3.46 \cdot 10^{-1}$	$1.56 \cdot 10^{-1}$	$2.03 \cdot 10^{1}$
430	$6.00 \cdot 10^{-3}$	$8.93 \cdot 10^{-6}$	$2.51 \cdot 10^{-5}$	$3.38 \cdot 10^{-1}$	$1.53 \cdot 10^{-1}$	$2.27 \cdot 10^{1}$
440	$5.68 \cdot 10^{-3}$	$8.15 \cdot 10^{-6}$	$2.27 \cdot 10^{-5}$	$3.31 \cdot 10^{-1}$	$1.51 \cdot 10^{-1}$	$2.52 \cdot 10^{1}$
450	$5.37 \cdot 10^{-3}$	$7.51 \cdot 10^{-6}$	$2.06 \cdot 10^{-5}$	$3.27 \cdot 10^{-1}$	$1.50 \cdot 10^{-1}$	$2.76 \cdot 10^{1}$
460	$5.10 \cdot 10^{-3}$	$6.97 \cdot 10^{-6}$	$1.89 \cdot 10^{-5}$	$3.24 \cdot 10^{-1}$	$1.49 \cdot 10^{-1}$	$3.02 \cdot 10^{1}$
470	$4.87 \cdot 10^{-3}$	$6.51 \cdot 10^{-6}$	$1.75 \cdot 10^{-5}$	$3.22 \cdot 10^{-1}$	$1.49 \cdot 10^{-1}$	$3.27 \cdot 10^{1}$
480	$4.65 \cdot 10^{-3}$	$6.11 \cdot 10^{-6}$	$1.62 \cdot 10^{-5}$	$3.21 \cdot 10^{-1}$	$1.50 \cdot 10^{-1}$	$3.53 \cdot 10^{1}$
490	$4.47 \cdot 10^{-3}$	$5.76 \cdot 10^{-6}$	$1.51 \cdot 10^{-5}$	$3.21 \cdot 10^{-1}$	$1.51 \cdot 10^{-1}$	$3.80 \cdot 10^{1}$
500	$4.28 \cdot 10^{-3}$	$5.46 \cdot 10^{-6}$	$1.41 \cdot 10^{-5}$	$3.22 \cdot 10^{-1}$	$1.51 \cdot 10^{-1}$	$4.06 \cdot 10^{1}$
550	$3.55 \cdot 10^{-3}$	$4.38 \cdot 10^{-6}$	$1.05 \cdot 10^{-5}$	$3.31 \cdot 10^{-1}$	$1.59 \cdot 10^{-1}$	$5.46 \cdot 10^{1}$
600	$2.99 \cdot 10^{-3}$	$3.74 \cdot 10^{-6}$	$8.21 \cdot 10^{-6}$	$3.46 \cdot 10^{-1}$	$1.69 \cdot 10^{-1}$	$6.99 \cdot 10^{1}$
650	$2.55 \cdot 10^{-3}$	$3.33 \cdot 10^{-6}$	$6.62 \cdot 10^{-6}$	$3.65 \cdot 10^{-1}$	$1.80 \cdot 10^{-1}$	$8.68 \cdot 10^{1}$
700	$2.17 \cdot 10^{-3}$	$3.07 \cdot 10^{-6}$	$5.46 \cdot 10^{-6}$	$3.86 \cdot 10^{-1}$	$1.91 \cdot 10^{-1}$	$1.06 \cdot 10^{2}$
750	$1.86 \cdot 10^{-3}$	$2.89 \cdot 10^{-6}$	$4.57 \cdot 10^{-6}$	$4.06 \cdot 10^{-1}$	$2.03 \cdot 10^{-1}$	$1.27 \cdot 10^{2}$
800	$1.60 \cdot 10^{-3}$	$2.78 \cdot 10^{-6}$	$3.88 \cdot 10^{-6}$	$4.27 \cdot 10^{-1}$	$2.15 \cdot 10^{-1}$	$1.52 \cdot 10^{2}$
1000	$8.08 \cdot 10^{-4}$	$2.85 \cdot 10^{-6}$	$2.28 \cdot 10^{-6}$	$5.02 \cdot 10^{-1}$	$2.54 \cdot 10^{-1}$	$2.88 \cdot 10^{2}$

Table 53: SM4 Higgs branching fractions for 4-fermion final states in the low- and intermediate-mass region with $\mathrm{l} = \mathrm{e}, \mu, \tau, \nu_e, \nu_\mu, \nu_\tau$ and $\mathrm{q} = \mathrm{u}, \mathrm{d}, \mathrm{c}, \mathrm{s}, \mathrm{b}$.

M_H [GeV]	$H \to 4e$	$H \to 2e2\mu$	$H \to 4l$	$H \to 4q$	$H \to 2l2q$	$H \to 4f$
100	$2.26 \cdot 10^{-7}$	$3.31 \cdot 10^{-7}$	$1.67 \cdot 10^{-4}$	$7.48 \cdot 10^{-4}$	$7.85 \cdot 10^{-4}$	$1.70 \cdot 10^{-3}$
110	$7.81 \cdot 10^{-7}$	$1.27 \cdot 10^{-6}$	$7.32 \cdot 10^{-4}$	$3.53 \cdot 10^{-3}$	$3.36 \cdot 10^{-3}$	$7.62 \cdot 10^{-3}$
120	$2.76 \cdot 10^{-6}$	$4.99 \cdot 10^{-6}$	$2.36 \cdot 10^{-3}$	$1.17 \cdot 10^{-2}$	$1.08 \cdot 10^{-2}$	$2.48 \cdot 10^{-2}$
130	$8.00 \cdot 10^{-6}$	$1.48 \cdot 10^{-5}$	$6.12 \cdot 10^{-3}$	$3.05 \cdot 10^{-2}$	$2.78 \cdot 10^{-2}$	$6.44 \cdot 10^{-2}$
140	$1.83 \cdot 10^{-5}$	$3.51 \cdot 10^{-5}$	$1.38 \cdot 10^{-2}$	$6.88 \cdot 10^{-2}$	$6.24 \cdot 10^{-2}$	$1.45 \cdot 10^{-1}$
145	$2.54 \cdot 10^{-5}$	$4.89 \cdot 10^{-5}$	$1.99 \cdot 10^{-2}$	$9.98 \cdot 10^{-2}$	$8.99 \cdot 10^{-2}$	$2.10 \cdot 10^{-1}$
150	$3.33 \cdot 10^{-5}$	$6.42 \cdot 10^{-5}$	$2.91 \cdot 10^{-2}$	$1.45 \cdot 10^{-1}$	$1.31 \cdot 10^{-1}$	$3.05 \cdot 10^{-1}$
151	$3.48 \cdot 10^{-5}$	$6.71 \cdot 10^{-5}$	$3.14 \cdot 10^{-2}$	$1.56 \cdot 10^{-1}$	$1.41 \cdot 10^{-1}$	$3.29 \cdot 10^{-1}$
152	$3.61 \cdot 10^{-5}$	$6.96 \cdot 10^{-5}$	$3.39 \cdot 10^{-2}$	$1.68 \cdot 10^{-1}$	$1.52 \cdot 10^{-1}$	$3.54 \cdot 10^{-1}$
153	$3.71 \cdot 10^{-5}$	$7.11 \cdot 10^{-5}$	$3.66 \cdot 10^{-2}$	$1.82 \cdot 10^{-1}$	$1.64 \cdot 10^{-1}$	$3.82 \cdot 10^{-1}$
154	$3.79 \cdot 10^{-5}$	$7.34 \cdot 10^{-5}$	$3.97 \cdot 10^{-2}$	$1.97 \cdot 10^{-1}$	$1.77 \cdot 10^{-1}$	$4.14 \cdot 10^{-1}$
155	$3.84 \cdot 10^{-5}$	$7.45 \cdot 10^{-5}$	$4.31 \cdot 10^{-2}$	$2.14 \cdot 10^{-1}$	$1.92 \cdot 10^{-1}$	$4.49 \cdot 10^{-1}$
156	$3.85 \cdot 10^{-5}$	$7.42 \cdot 10^{-5}$	$4.66 \cdot 10^{-2}$	$2.30 \cdot 10^{-1}$	$2.10 \cdot 10^{-1}$	$4.86 \cdot 10^{-1}$
157	$3.80 \cdot 10^{-5}$	$7.33 \cdot 10^{-5}$	$5.08 \cdot 10^{-2}$	$2.51 \cdot 10^{-1}$	$2.27 \cdot 10^{-1}$	$5.29 \cdot 10^{-1}$
158	$3.61 \cdot 10^{-5}$	$6.98 \cdot 10^{-5}$	$5.62 \cdot 10^{-2}$	$2.76 \cdot 10^{-1}$	$2.50 \cdot 10^{-1}$	$5.82 \cdot 10^{-1}$
159	$3.34 \cdot 10^{-5}$	$6.47 \cdot 10^{-5}$	$6.18 \cdot 10^{-2}$	$3.02 \cdot 10^{-1}$	$2.75 \cdot 10^{-1}$	$6.39 \cdot 10^{-1}$
160	$2.95 \cdot 10^{-5}$	$5.75 \cdot 10^{-5}$	$6.85 \cdot 10^{-2}$	$3.31 \cdot 10^{-1}$	$3.05 \cdot 10^{-1}$	$7.04 \cdot 10^{-1}$
161	$2.54 \cdot 10^{-5}$	$4.96 \cdot 10^{-5}$	$7.45 \cdot 10^{-2}$	$3.60 \cdot 10^{-1}$	$3.30 \cdot 10^{-1}$	$7.64 \cdot 10^{-1}$
162	$2.23 \cdot 10^{-5}$	$4.32 \cdot 10^{-5}$	$7.90 \cdot 10^{-2}$	$3.81 \cdot 10^{-1}$	$3.49 \cdot 10^{-1}$	$8.09 \cdot 10^{-1}$
163	$2.05 \cdot 10^{-5}$	$3.97 \cdot 10^{-5}$	$8.19 \cdot 10^{-2}$	$3.96 \cdot 10^{-1}$	$3.61 \cdot 10^{-1}$	$8.38 \cdot 10^{-1}$
164	$1.95 \cdot 10^{-5}$	$3.78 \cdot 10^{-5}$	$8.36 \cdot 10^{-2}$	$4.04 \cdot 10^{-1}$	$3.70 \cdot 10^{-1}$	$8.58 \cdot 10^{-1}$
165	$1.91 \cdot 10^{-5}$	$3.70 \cdot 10^{-5}$	$8.50 \cdot 10^{-2}$	$4.11 \cdot 10^{-1}$	$3.76 \cdot 10^{-1}$	$8.73 \cdot 10^{-1}$
166	$1.91 \cdot 10^{-5}$	$3.69 \cdot 10^{-5}$	$8.59 \cdot 10^{-2}$	$4.16 \cdot 10^{-1}$	$3.81 \cdot 10^{-1}$	$8.83 \cdot 10^{-1}$
167	$1.93 \cdot 10^{-5}$	$3.76 \cdot 10^{-5}$	$8.66 \cdot 10^{-2}$	$4.20 \cdot 10^{-1}$	$3.84 \cdot 10^{-1}$	$8.91 \cdot 10^{-1}$
168	$1.98 \cdot 10^{-5}$	$3.85 \cdot 10^{-5}$	$8.72 \cdot 10^{-2}$	$4.23 \cdot 10^{-1}$	$3.87 \cdot 10^{-1}$	$8.98 \cdot 10^{-1}$
169	$2.04 \cdot 10^{-5}$	$3.99 \cdot 10^{-5}$	$8.77 \cdot 10^{-2}$	$4.26 \cdot 10^{-1}$	$3.90 \cdot 10^{-1}$	$9.03 \cdot 10^{-1}$
170	$2.13 \cdot 10^{-5}$	$4.17 \cdot 10^{-5}$	$8.81 \cdot 10^{-2}$	$4.29 \cdot 10^{-1}$	$3.92 \cdot 10^{-1}$	$9.08 \cdot 10^{-1}$
171	$2.24 \cdot 10^{-5}$	$4.35 \cdot 10^{-5}$	$8.84 \cdot 10^{-2}$	$4.31 \cdot 10^{-1}$	$3.93 \cdot 10^{-1}$	$9.12 \cdot 10^{-1}$
172	$2.38 \cdot 10^{-5}$	$4.62 \cdot 10^{-5}$	$8.87 \cdot 10^{-2}$	$4.32 \cdot 10^{-1}$	$3.95 \cdot 10^{-1}$	$9.16 \cdot 10^{-1}$
173	$2.54 \cdot 10^{-5}$	$5.01 \cdot 10^{-5}$	$8.90 \cdot 10^{-2}$	$4.34 \cdot 10^{-1}$	$3.96 \cdot 10^{-1}$	$9.19 \cdot 10^{-1}$
174	$2.74 \cdot 10^{-5}$	$5.40 \cdot 10^{-5}$	$8.92 \cdot 10^{-2}$	$4.35 \cdot 10^{-1}$	$3.97 \cdot 10^{-1}$	$9.22 \cdot 10^{-1}$
175	$2.97 \cdot 10^{-5}$	$5.88 \cdot 10^{-5}$	$8.94 \cdot 10^{-2}$	$4.37 \cdot 10^{-1}$	$3.98 \cdot 10^{-1}$	$9.24 \cdot 10^{-1}$
176	$3.28 \cdot 10^{-5}$	$6.48 \cdot 10^{-5}$	$8.96 \cdot 10^{-2}$	$4.38 \cdot 10^{-1}$	$3.99 \cdot 10^{-1}$	$9.27 \cdot 10^{-1}$
177	$3.65 \cdot 10^{-5}$	$7.21 \cdot 10^{-5}$	$8.97 \cdot 10^{-2}$	$4.39 \cdot 10^{-1}$	$4.00 \cdot 10^{-1}$	$9.29 \cdot 10^{-1}$
178	$4.14 \cdot 10^{-5}$	$8.12 \cdot 10^{-5}$	$8.98 \cdot 10^{-2}$	$4.41 \cdot 10^{-1}$	$4.01 \cdot 10^{-1}$	$9.31 \cdot 10^{-1}$
179	$4.75 \cdot 10^{-5}$	$9.42 \cdot 10^{-5}$	$8.99 \cdot 10^{-2}$	$4.42 \cdot 10^{-1}$	$4.01 \cdot 10^{-1}$	$9.33 \cdot 10^{-1}$
180	$5.64 \cdot 10^{-5}$	$1.11 \cdot 10^{-4}$	$8.98 \cdot 10^{-2}$	$4.44 \cdot 10^{-1}$	$4.02 \cdot 10^{-1}$	$9.36 \cdot 10^{-1}$
181	$6.85 \cdot 10^{-5}$	$1.36 \cdot 10^{-4}$	$9.00 \cdot 10^{-2}$	$4.44 \cdot 10^{-1}$	$4.03 \cdot 10^{-1}$	$9.38 \cdot 10^{-1}$
182	$8.57 \cdot 10^{-5}$	$1.69 \cdot 10^{-4}$	$9.01 \cdot 10^{-2}$	$4.46 \cdot 10^{-1}$	$4.04 \cdot 10^{-1}$	$9.40 \cdot 10^{-1}$
183	$1.06 \cdot 10^{-4}$	$2.09 \cdot 10^{-4}$	$9.02 \cdot 10^{-2}$	$4.48 \cdot 10^{-1}$	$4.05 \cdot 10^{-1}$	$9.43 \cdot 10^{-1}$
184	$1.26 \cdot 10^{-4}$	$2.49 \cdot 10^{-4}$	$9.02 \cdot 10^{-2}$	$4.49 \cdot 10^{-1}$	$4.06 \cdot 10^{-1}$	$9.46 \cdot 10^{-1}$
185	$1.44 \cdot 10^{-4}$	$2.86 \cdot 10^{-4}$	$9.03 \cdot 10^{-2}$	$4.51 \cdot 10^{-1}$	$4.07 \cdot 10^{-1}$	$9.48 \cdot 10^{-1}$
186	$1.59 \cdot 10^{-4}$	$3.18 \cdot 10^{-4}$	$9.05 \cdot 10^{-2}$	$4.52 \cdot 10^{-1}$	$4.07 \cdot 10^{-1}$	$9.50 \cdot 10^{-1}$
187	$1.73 \cdot 10^{-4}$	$3.44 \cdot 10^{-4}$	$9.07 \cdot 10^{-2}$	$4.54 \cdot 10^{-1}$	$4.07 \cdot 10^{-1}$	$9.52 \cdot 10^{-1}$
188	$1.84 \cdot 10^{-4}$	$3.67 \cdot 10^{-4}$	$9.02 \cdot 10^{-2}$	$4.56 \cdot 10^{-1}$	$4.07 \cdot 10^{-1}$	$9.53 \cdot 10^{-1}$
189	$1.94 \cdot 10^{-4}$	$3.87 \cdot 10^{-4}$	$9.03 \cdot 10^{-2}$	$4.57 \cdot 10^{-1}$	$4.07 \cdot 10^{-1}$	$9.55 \cdot 10^{-1}$
190	$2.03 \cdot 10^{-4}$	$4.04 \cdot 10^{-4}$	$9.04 \cdot 10^{-2}$	$4.57 \cdot 10^{-1}$	$4.09 \cdot 10^{-1}$	$9.56 \cdot 10^{-1}$
195	$2.31 \cdot 10^{-4}$	$4.63 \cdot 10^{-4}$	$9.07 \cdot 10^{-2}$	$4.61 \cdot 10^{-1}$	$4.09 \cdot 10^{-1}$	$9.60 \cdot 10^{-1}$
200	$2.49 \cdot 10^{-4}$	$4.99 \cdot 10^{-4}$	$9.06 \cdot 10^{-2}$	$4.63 \cdot 10^{-1}$	$4.10 \cdot 10^{-1}$	$9.64 \cdot 10^{-1}$
210	$2.68 \cdot 10^{-4}$	$5.38 \cdot 10^{-4}$	$9.05 \cdot 10^{-2}$	$4.66 \cdot 10^{-1}$	$4.11 \cdot 10^{-1}$	$9.68 \cdot 10^{-1}$
220	$2.78 \cdot 10^{-4}$	$5.59 \cdot 10^{-4}$	$9.06 \cdot 10^{-2}$	$4.68 \cdot 10^{-1}$	$4.13 \cdot 10^{-1}$	$9.72 \cdot 10^{-1}$

Table 54: SM4 Higgs branching fractions for 4-fermion final states in the high-mass region with $\mathrm{l} = \mathrm{e}, \mu, \tau, \nu_e, \nu_\mu, \nu_\tau$ and $\mathrm{q} = \mathrm{u}, \mathrm{d}, \mathrm{c}, \mathrm{s}, \mathrm{b}$.

M_H [GeV]	$H \to 4e$	$H \to 2e2\mu$	$H \to 4l$	$H \to 4q$	$H \to 2l2q$	$H \to 4f$
230	$2.83 \cdot 10^{-4}$	$5.70 \cdot 10^{-4}$	$9.04 \cdot 10^{-2}$	$4.70 \cdot 10^{-1}$	$4.14 \cdot 10^{-1}$	$9.74 \cdot 10^{-1}$
240	$2.88 \cdot 10^{-4}$	$5.80 \cdot 10^{-4}$	$9.04 \cdot 10^{-2}$	$4.71 \cdot 10^{-1}$	$4.15 \cdot 10^{-1}$	$9.76 \cdot 10^{-1}$
250	$2.90 \cdot 10^{-4}$	$5.86 \cdot 10^{-4}$	$9.05 \cdot 10^{-2}$	$4.71 \cdot 10^{-1}$	$4.16 \cdot 10^{-1}$	$9.78 \cdot 10^{-1}$
260	$2.93 \cdot 10^{-4}$	$5.92 \cdot 10^{-4}$	$9.05 \cdot 10^{-2}$	$4.72 \cdot 10^{-1}$	$4.16 \cdot 10^{-1}$	$9.79 \cdot 10^{-1}$
270	$2.95 \cdot 10^{-4}$	$5.97 \cdot 10^{-4}$	$9.05 \cdot 10^{-2}$	$4.73 \cdot 10^{-1}$	$4.17 \cdot 10^{-1}$	$9.80 \cdot 10^{-1}$
280	$2.98 \cdot 10^{-4}$	$6.02 \cdot 10^{-4}$	$9.06 \cdot 10^{-2}$	$4.73 \cdot 10^{-1}$	$4.17 \cdot 10^{-1}$	$9.81 \cdot 10^{-1}$
290	$2.99 \cdot 10^{-4}$	$6.08 \cdot 10^{-4}$	$9.06 \cdot 10^{-2}$	$4.74 \cdot 10^{-1}$	$4.18 \cdot 10^{-1}$	$9.82 \cdot 10^{-1}$
300	$3.00 \cdot 10^{-4}$	$6.10 \cdot 10^{-4}$	$9.05 \cdot 10^{-2}$	$4.74 \cdot 10^{-1}$	$4.18 \cdot 10^{-1}$	$9.82 \cdot 10^{-1}$
310	$3.03 \cdot 10^{-4}$	$6.14 \cdot 10^{-4}$	$9.07 \cdot 10^{-2}$	$4.75 \cdot 10^{-1}$	$4.17 \cdot 10^{-1}$	$9.82 \cdot 10^{-1}$
320	$3.03 \cdot 10^{-4}$	$6.14 \cdot 10^{-4}$	$9.06 \cdot 10^{-2}$	$4.75 \cdot 10^{-1}$	$4.16 \cdot 10^{-1}$	$9.82 \cdot 10^{-1}$
330	$3.03 \cdot 10^{-4}$	$6.14 \cdot 10^{-4}$	$9.04 \cdot 10^{-2}$	$4.75 \cdot 10^{-1}$	$4.16 \cdot 10^{-1}$	$9.81 \cdot 10^{-1}$
335	$3.03 \cdot 10^{-4}$	$6.13 \cdot 10^{-4}$	$9.02 \cdot 10^{-2}$	$4.74 \cdot 10^{-1}$	$4.15 \cdot 10^{-1}$	$9.80 \cdot 10^{-1}$
336	$3.02 \cdot 10^{-4}$	$6.13 \cdot 10^{-4}$	$9.02 \cdot 10^{-2}$	$4.74 \cdot 10^{-1}$	$4.15 \cdot 10^{-1}$	$9.80 \cdot 10^{-1}$
337	$3.02 \cdot 10^{-4}$	$6.13 \cdot 10^{-4}$	$9.02 \cdot 10^{-2}$	$4.74 \cdot 10^{-1}$	$4.15 \cdot 10^{-1}$	$9.79 \cdot 10^{-1}$
338	$3.02 \cdot 10^{-4}$	$6.12 \cdot 10^{-4}$	$9.01 \cdot 10^{-2}$	$4.74 \cdot 10^{-1}$	$4.15 \cdot 10^{-1}$	$9.79 \cdot 10^{-1}$
339	$3.02 \cdot 10^{-4}$	$6.11 \cdot 10^{-4}$	$9.00 \cdot 10^{-2}$	$4.74 \cdot 10^{-1}$	$4.15 \cdot 10^{-1}$	$9.79 \cdot 10^{-1}$
340	$3.02 \cdot 10^{-4}$	$6.11 \cdot 10^{-4}$	$8.99 \cdot 10^{-2}$	$4.74 \cdot 10^{-1}$	$4.14 \cdot 10^{-1}$	$9.78 \cdot 10^{-1}$
345	$2.98 \cdot 10^{-4}$	$6.02 \cdot 10^{-4}$	$8.88 \cdot 10^{-2}$	$4.69 \cdot 10^{-1}$	$4.10 \cdot 10^{-1}$	$9.68 \cdot 10^{-1}$
346	$2.96 \cdot 10^{-4}$	$5.98 \cdot 10^{-4}$	$8.83 \cdot 10^{-2}$	$4.66 \cdot 10^{-1}$	$4.07 \cdot 10^{-1}$	$9.62 \cdot 10^{-1}$
347	$2.93 \cdot 10^{-4}$	$5.92 \cdot 10^{-4}$	$8.75 \cdot 10^{-2}$	$4.62 \cdot 10^{-1}$	$4.04 \cdot 10^{-1}$	$9.53 \cdot 10^{-1}$
348	$2.90 \cdot 10^{-4}$	$5.85 \cdot 10^{-4}$	$8.65 \cdot 10^{-2}$	$4.57 \cdot 10^{-1}$	$3.99 \cdot 10^{-1}$	$9.42 \cdot 10^{-1}$
349	$2.86 \cdot 10^{-4}$	$5.76 \cdot 10^{-4}$	$8.52 \cdot 10^{-2}$	$4.50 \cdot 10^{-1}$	$3.93 \cdot 10^{-1}$	$9.28 \cdot 10^{-1}$
350	$2.81 \cdot 10^{-4}$	$5.67 \cdot 10^{-4}$	$8.38 \cdot 10^{-2}$	$4.42 \cdot 10^{-1}$	$3.86 \cdot 10^{-1}$	$9.12 \cdot 10^{-1}$
351	$2.76 \cdot 10^{-4}$	$5.53 \cdot 10^{-4}$	$8.24 \cdot 10^{-2}$	$4.35 \cdot 10^{-1}$	$3.80 \cdot 10^{-1}$	$8.97 \cdot 10^{-1}$
352	$2.72 \cdot 10^{-4}$	$5.45 \cdot 10^{-4}$	$8.11 \cdot 10^{-2}$	$4.27 \cdot 10^{-1}$	$3.74 \cdot 10^{-1}$	$8.82 \cdot 10^{-1}$
353	$2.68 \cdot 10^{-4}$	$5.37 \cdot 10^{-4}$	$7.98 \cdot 10^{-2}$	$4.21 \cdot 10^{-1}$	$3.67 \cdot 10^{-1}$	$8.68 \cdot 10^{-1}$
354	$2.64 \cdot 10^{-4}$	$5.28 \cdot 10^{-4}$	$7.83 \cdot 10^{-2}$	$4.14 \cdot 10^{-1}$	$3.61 \cdot 10^{-1}$	$8.54 \cdot 10^{-1}$
355	$2.60 \cdot 10^{-4}$	$5.20 \cdot 10^{-4}$	$7.71 \cdot 10^{-2}$	$4.07 \cdot 10^{-1}$	$3.56 \cdot 10^{-1}$	$8.40 \cdot 10^{-1}$
360	$2.41 \cdot 10^{-4}$	$4.82 \cdot 10^{-4}$	$7.15 \cdot 10^{-2}$	$3.77 \cdot 10^{-1}$	$3.30 \cdot 10^{-1}$	$7.78 \cdot 10^{-1}$
370	$2.13 \cdot 10^{-4}$	$4.25 \cdot 10^{-4}$	$6.30 \cdot 10^{-2}$	$3.31 \cdot 10^{-1}$	$2.90 \cdot 10^{-1}$	$6.83 \cdot 10^{-1}$
375	$2.02 \cdot 10^{-4}$	$4.04 \cdot 10^{-4}$	$5.98 \cdot 10^{-2}$	$3.13 \cdot 10^{-1}$	$2.75 \cdot 10^{-1}$	$6.48 \cdot 10^{-1}$
380	$1.93 \cdot 10^{-4}$	$3.87 \cdot 10^{-4}$	$5.72 \cdot 10^{-2}$	$2.99 \cdot 10^{-1}$	$2.62 \cdot 10^{-1}$	$6.19 \cdot 10^{-1}$
390	$1.80 \cdot 10^{-4}$	$3.60 \cdot 10^{-4}$	$5.31 \cdot 10^{-2}$	$2.77 \cdot 10^{-1}$	$2.43 \cdot 10^{-1}$	$5.73 \cdot 10^{-1}$
400	$1.71 \cdot 10^{-4}$	$3.42 \cdot 10^{-4}$	$5.02 \cdot 10^{-2}$	$2.61 \cdot 10^{-1}$	$2.30 \cdot 10^{-1}$	$5.41 \cdot 10^{-1}$
410	$1.64 \cdot 10^{-4}$	$3.29 \cdot 10^{-4}$	$4.82 \cdot 10^{-2}$	$2.50 \cdot 10^{-1}$	$2.21 \cdot 10^{-1}$	$5.19 \cdot 10^{-1}$
420	$1.60 \cdot 10^{-4}$	$3.19 \cdot 10^{-4}$	$4.67 \cdot 10^{-2}$	$2.42 \cdot 10^{-1}$	$2.14 \cdot 10^{-1}$	$5.03 \cdot 10^{-1}$
430	$1.57 \cdot 10^{-4}$	$3.14 \cdot 10^{-4}$	$4.57 \cdot 10^{-2}$	$2.36 \cdot 10^{-1}$	$2.09 \cdot 10^{-1}$	$4.91 \cdot 10^{-1}$
440	$1.55 \cdot 10^{-4}$	$3.10 \cdot 10^{-4}$	$4.49 \cdot 10^{-2}$	$2.32 \cdot 10^{-1}$	$2.05 \cdot 10^{-1}$	$4.82 \cdot 10^{-1}$
450	$1.54 \cdot 10^{-4}$	$3.07 \cdot 10^{-4}$	$4.44 \cdot 10^{-2}$	$2.30 \cdot 10^{-1}$	$2.03 \cdot 10^{-1}$	$4.77 \cdot 10^{-1}$
460	$1.54 \cdot 10^{-4}$	$3.06 \cdot 10^{-4}$	$4.41 \cdot 10^{-2}$	$2.28 \cdot 10^{-1}$	$2.01 \cdot 10^{-1}$	$4.73 \cdot 10^{-1}$
470	$1.54 \cdot 10^{-4}$	$3.07 \cdot 10^{-4}$	$4.39 \cdot 10^{-2}$	$2.27 \cdot 10^{-1}$	$2.00 \cdot 10^{-1}$	$4.71 \cdot 10^{-1}$
480	$1.54 \cdot 10^{-4}$	$3.09 \cdot 10^{-4}$	$4.39 \cdot 10^{-2}$	$2.27 \cdot 10^{-1}$	$2.00 \cdot 10^{-1}$	$4.71 \cdot 10^{-1}$
490	$1.55 \cdot 10^{-4}$	$3.11 \cdot 10^{-4}$	$4.40 \cdot 10^{-2}$	$2.27 \cdot 10^{-1}$	$2.01 \cdot 10^{-1}$	$4.71 \cdot 10^{-1}$
500	$1.56 \cdot 10^{-4}$	$3.13 \cdot 10^{-4}$	$4.41 \cdot 10^{-2}$	$2.27 \cdot 10^{-1}$	$2.01 \cdot 10^{-1}$	$4.73 \cdot 10^{-1}$
550	$1.63 \cdot 10^{-4}$	$3.29 \cdot 10^{-4}$	$4.57 \cdot 10^{-2}$	$2.35 \cdot 10^{-1}$	$2.08 \cdot 10^{-1}$	$4.89 \cdot 10^{-1}$
600	$1.74 \cdot 10^{-4}$	$3.51 \cdot 10^{-4}$	$4.81 \cdot 10^{-2}$	$2.48 \cdot 10^{-1}$	$2.19 \cdot 10^{-1}$	$5.15 \cdot 10^{-1}$
650	$1.86 \cdot 10^{-4}$	$3.74 \cdot 10^{-4}$	$5.10 \cdot 10^{-2}$	$2.62 \cdot 10^{-1}$	$2.32 \cdot 10^{-1}$	$5.45 \cdot 10^{-1}$
700	$1.99 \cdot 10^{-4}$	$4.00 \cdot 10^{-4}$	$5.41 \cdot 10^{-2}$	$2.77 \cdot 10^{-1}$	$2.46 \cdot 10^{-1}$	$5.77 \cdot 10^{-1}$
750	$2.12 \cdot 10^{-4}$	$4.26 \cdot 10^{-4}$	$5.73 \cdot 10^{-2}$	$2.92 \cdot 10^{-1}$	$2.60 \cdot 10^{-1}$	$6.10 \cdot 10^{-1}$
800	$2.24 \cdot 10^{-4}$	$4.52 \cdot 10^{-4}$	$6.05 \cdot 10^{-2}$	$3.08 \cdot 10^{-1}$	$2.74 \cdot 10^{-1}$	$6.42 \cdot 10^{-1}$
1000	$2.70 \cdot 10^{-4}$	$5.42 \cdot 10^{-4}$	$7.21 \cdot 10^{-2}$	$3.60 \cdot 10^{-1}$	$3.23 \cdot 10^{-1}$	$7.56 \cdot 10^{-1}$

Table 55: NLO EW corrections to the $\mathrm{H} \to \gamma\gamma$ decay width according to Eq.(114) and estimate for the missing higher order (h.o.) corrections from Eq.(115).

M_{H} [GeV]	$\delta_{\mathrm{EW}}^{(4)}$ [%]	missing h.o. [%]
90	-53.9	± 13.9
95	-59.2	± 13.9
100	-64.5	± 13.9
105	-69.5	± 13.9
110	-74.4	± 13.9
115	-79.0	± 13.9
120	-83.3	± 13.9
125	-87.3	$+13.9 -12.7$
130	-90.8	$+13.9 -9.2$
135	-94.0	$+13.9 -6.0$
140	-96.6	$+13.9 -3.4$
145	-98.5	$+13.9 -1.5$
150	-99.7	$+13.9 -0.3$

Table 56: Higgs branching fractions for $\gamma\gamma$ decay channel without and with NLO EW corrections.

M_{H} [GeV]	w/o NLO EW	w/ NLO EW
100	$1.31 \cdot 10^{-4}$	$4.65 \cdot 10^{-5}$
110	$1.72 \cdot 10^{-4}$	$4.40 \cdot 10^{-5}$
120	$2.26 \cdot 10^{-4}$	$3.77 \cdot 10^{-5}$
130	$2.95 \cdot 10^{-4}$	$2.71 \cdot 10^{-5}$
140	$3.81 \cdot 10^{-4}$	$1.30 \cdot 10^{-5}$
150	$4.74 \cdot 10^{-4}$	$1.42 \cdot 10^{-6}$

15 The (heavy) Higgs-boson lineshape[59]

15.1 Introduction

In this section we consider the problem of a consistent definition of the Higgs-boson lineshape at LHC and address the question of optimal presentation of LHC data.

Some preliminary observations are needed: the Higgs system of the Standard Model has almost a non-perturbative behaviour, even at a low scale. Let us consider the traditional on-shell approach and the values for the on-shell decay width of the Higgs boson.

For $M_{\rm H} = 140$ GeV the total width is 8.12×10^{-3} GeV. The process $\rm H \to \overline{b}b$ has a partial with of 2.55×10^{-3} GeV, other two-body decays are almost negligible while $\rm H \to 4f$ has 4.64×10^{-3} GeV, well below the WW threshold. Therefore the four-body decay, even below threshold, is more important than the two-body ones. What are the corresponding implications? Since decay widths are related to the imaginary parts of loop diagrams, the above statement is equivalent to say that, in terms of imaginary parts of the H self-energy, three-loop diagrams are as important as one-loop diagrams.

We realise that most of the people just want to use some well-defined recipe without having to dig any deeper; however, there is no alternative to a complete description of LHC processes which has to include the complete matrix elements for all processes; splitting the whole S-matrix element into components is just conventional wisdom. However, the precise tone and degree of formality must be dictated by gauge invariance.

The framework discussed in this section is general enough and can be used for all processes and for all kinematical regions; however, here the main focus will be on the description of the Higgs-boson lineshape in the heavy-Higgs region, typically above 600 GeV. The general argument is well documented in the literature and, for a complete description of all technical details, we refer to Refs. [222, 439, 440]. Part of the results discussed in this section and concerning a correct implementation of the Higgs-boson lineshape have been summarised in a talk at the BNL meeting of the HXSWG.[60]

One might wonder why considering a SM Higgs boson in such a high-mass range. There are are classic constraints on the Higgs-boson mass coming from unitarity, triviality, and vacuum stability, precision electroweak data and absence of fine-tuning. However, the search for a SM Higgs boson over a mass range from 80 GeV to 1 TeV is clearly indicated as a priority in many experimental papers, e.g., *ATLAS: letter of intent for a general-purpose pp experiment at the large hadron collider at CERN*[61].

Coming back to the framework that we are introducing here, there is another important issue: when working in the on-shell scheme one finds that the two-loop corrections to the on-shell Higgs width exceed the one-loop corrections if the on-shell Higgs mass is larger than 900 GeV, as discussed in Ref. [441]. This fact simply tells you that perturbation theory diverges badly, starting from approximately 1 TeV.

The current recipe to handle theoretical uncertainty for heavy-Higgs-boson lineshape at LHC is to assign a conservative estimate of $150\%\, M_{\rm H}^3$ with $M_{\rm H}$ in TeV [62]. This is equivalent to assume a $\pm 32\%$ at $M_{\rm H} = 600$ GeV and $\pm 77\%$ at $M_{\rm H} = 800$ GeV.

Recently the problem of going beyond the zero-width approximation has received new boost from the work of Ref. [442]: the program IHIXS allows the study of the Higgs-boson lineshape for a finite width of the Higgs boson and computes the cross section sampling over a Breit–Wigner distribution.

To start our discussion we consider the process $ij \to {\rm H}(\to {\rm F}) + {\rm X}$ where $i, j \in$ partons and F is a generic final state (e.g., ${\rm F} = \gamma\gamma, 4{\rm f}$, etc.). For the sake of simplicity we neglect, for a moment, folding the partonic process with parton distribution functions (PDFs). Since the Higgs boson is a scalar resonance we can split the whole process into three parts: *production*, *propagation*, and *decay*.

[59] G. Passarino (ed.), S. Goria and D. Rosco.
[60] http://www.bnl.gov/hcs/
[61] http://atlas.web.cern.ch/Atlas/internal/tdr.html
[62] https://twiki.cern.ch/twiki/bin/view/LHCPhysics/HeavyHiggs

15.2 Propagation

In quantum field theory (QFT) amplitudes are made out of propagators and vertices: the Higgs (Dyson-resummed) propagator reads as follows:

$$\Delta_{\rm H}(s) = \left[s - M_{\rm H}^2 + S_{\rm HH}\left(s, m_{\rm t}^2, M_{\rm H}^2, M_{\rm W}^2, M_{\rm Z}^2\right)\right]^{-1}, \tag{116}$$

where $m_{\rm t}$ and M_i are a renormalised masses and $S_{\rm HH}$ is the renormalised Higgs self-energy (to all orders but with one-particle-irreducible diagrams). The first argument of the self-energy is the external momentum squared, the remaining ones are squared (renormalised) masses in the loops. We define complex poles for unstable particles as the (complex) solutions of the following system:

$$\begin{aligned} s_{\rm H} - M_{\rm H}^2 + S_{\rm HH}\left(s_{\rm H}, m_{\rm t}^2, M_{\rm H}^2, M_{\rm W}^2, M_{\rm Z}^2\right) &= 0, \\ s_{\rm W} - M_{\rm W}^2 + S_{\rm WW}\left(s_{\rm W}, m_{\rm t}^2, M_{\rm H}^2, M_{\rm W}^2, M_{\rm Z}^2\right) &= 0, \end{aligned} \tag{117}$$

etc. To lowest-order accuracy the Higgs propagator is rewritten as

$$\Delta_{\rm H}^{-1} = s - s_{\rm H}. \tag{118}$$

The complex pole describing an unstable particle is conventionally parametrised as

$$s_i = \mu_i^2 - i\,\mu_i\,\gamma_i, \tag{119}$$

where μ_i is an input parameter (similar to the on-shell mass) while γ_i can be computed (as the on-shell total width), say within the Standard Model (SM). Note that the pole of Δ fully embodies the propagation properties of a particle. We know that even in ordinary quantum mechanics the resonances are described as the complex energy poles in the scattering amplitude. The general formalism for describing unstable particles in QFT was developed long ago, see Refs. [443–447]; for an implementation in gauge theories we refer to the work of Refs. [448–451].

Consider the complex-mass scheme (CMS) introduced in Ref. [452] and extended at two-loop level in Ref. [453]: here, at lowest level of accuracy, we use

$$s_{\rm H} - M_{\rm H}^2 + S_{\rm HH}\left(s_{\rm H}, s_{\rm t}, s_{\rm H}, s_{\rm W}, s_{\rm Z}\right) = 0, \tag{120}$$

where now $S_{\rm HH}$ is computed at one-loop level and $s_{\rm W}$ etc. are the experimental complex poles, derived from the corresponding on-shell masses and widths. For the W and Z bosons the input-parameter set (IPS) is defined in terms of pseudo-observables; at first, on-shell quantities are derived by fitting the experimental lineshapes with

$$\Sigma_{\rm VV}(s) = \frac{N}{(s - M_{\rm OS}^2)^2 + s^2\,\Gamma_{\rm OS}^2/M_{\rm OS}^2}, \qquad V = {\rm W}, {\rm Z}, \tag{121}$$

where N is an irrelevant (for our purposes) normalisation constant. Secondly, we define pseudo-observables

$$M_{\rm P} = M_{\rm OS}\,\cos\psi, \qquad \Gamma_{\rm P} = \Gamma_{\rm OS}\,\sin\psi, \qquad \psi = \arctan\frac{\Gamma_{\rm OS}}{M_{\rm OS}}, \tag{122}$$

which are inserted in the IPS.

Renormalisation with complex poles should not be confused with a simple recipe for the replacement of running widths with constant widths; there are many more ingredients in the scheme. It is worth noting that perturbation theory based on $s_{\rm H}$ instead of the on-shell mass has much better convergence properties; indeed, as shown in Ref. [441], the two-loop corrections to the imaginary part of $s_{\rm H}$ become as large as the one-loop ones *only* when $\mu_{\rm H} = 1.74$ TeV. This suggests that the complex pole scheme is preferable also from the point of view of describing the heavy-H-boson production at LHC.

There is a substantial difference between W, Z complex poles and the Higgs complex pole. In the first case W, Z bosons decay predominantly into two (massless) fermions while for the Higgs boson below the WW threshold the decay into four fermions is even larger than the decay into a $\bar{\mathrm{b}}\mathrm{b}$ pair. Therefore we cannot use for the Higgs boson the well-known result, valid for W, Z,

$$\mathrm{Im}\, S_{\mathrm{VV}}(s) \approx \frac{\Gamma_{\mathrm{V}}^{\mathrm{OS}}}{M_{\mathrm{V}}^{\mathrm{OS}}}\, s. \tag{123}$$

As a consequence of this fact we have

$$\mu_{\mathrm{V}}^2 = M_{\mathrm{V\,OS}}^2 - \Gamma_{\mathrm{V\,OS}}^2 + \mathrm{HO}, \quad \gamma_{\mathrm{V}} = \Gamma_{\mathrm{V}}^{\mathrm{OS}} \left[1 - \frac{1}{2}\left(\frac{\Gamma_{\mathrm{V}}^{\mathrm{OS}}}{M_{\mathrm{V}}^{\mathrm{OS}}}\right)^2\right] + \mathrm{HO}, \tag{124}$$

where the perturbative expansion is well under control since $\Gamma_{\mathrm{V}}^{\mathrm{OS}}/M_{\mathrm{V}}^{\mathrm{OS}} \ll 1$. Here "HO" stands for further higher-order contributions. For the Higgs boson we have a different expansion,

$$\begin{aligned}
\gamma_{\mathrm{H}} &= \Gamma_{\mathrm{H}} \left[1 + \sum_n a_n\, \Gamma_{\mathrm{H}}^n\right] + \sum_{\mathrm{V=W,Z}} \Gamma_{\mathrm{V}}\, \frac{M_{\mathrm{V}}}{M_{\mathrm{H}}} \sum_{n,l} b_{nl}^{\mathrm{V}}\, \Gamma_{\mathrm{V}}^n\, \Gamma_{\mathrm{H}}^l, \\
a_1 &= -\left[\mathrm{Im}\; S_{\mathrm{HH,OS}}^h\right]^2, \quad a_2 = \frac{1}{2}\left[\frac{1}{M_{\mathrm{H}}}\; \mathrm{Im}\; S_{\mathrm{HH,OS}}^h - M_{\mathrm{H}}\; \mathrm{Im}\; S_{\mathrm{HH,OS}}^{hh}\right], \\
b_{10}^{\mathrm{V}} &= -\;\mathrm{Re}\; S_{\mathrm{HH,OS}}^v + \mathrm{Re}\; S_{\mathrm{HH,OS}}^v\; \mathrm{Re}\; S_{\mathrm{HH,OS}}^h - \mathrm{Im}\; S_{\mathrm{HH,OS}}^v\; \mathrm{Im}\; S_{\mathrm{HH,OS}}^h, \\
b_{11}^{\mathrm{V}} &= \frac{1}{2\, M_{\mathrm{H}}}\; \mathrm{Im}\; S_{\mathrm{HH,OS}}^v - M_{\mathrm{H}}\; \mathrm{Im}\; S_{\mathrm{HH,OS}}^{hv}, \quad b_{20}^{\mathrm{V}} = -\frac{1}{2}\, \frac{M_{\mathrm{V}}}{M_{\mathrm{H}}}\; \mathrm{Im}\; S_{\mathrm{HH,OS}}^{vv}.
\end{aligned} \tag{125}$$

Here we have $M_i = M_i^{\mathrm{OS}}$, $\Gamma_i = \Gamma_i^{\mathrm{OS}}$ (on-shell quantities) and

$$\begin{aligned}
S_{\mathrm{HH,OS}}^a &= \frac{\partial}{\partial M_a^2}\, S_{\mathrm{HH}}\left(M_{\mathrm{H}}^2, m_{\mathrm{t}}^2, M_{\mathrm{H}}^2, M_{\mathrm{W}}^2, M_{\mathrm{Z}}^2\right), \\
S_{\mathrm{HH,OS}}^{ab} &= \frac{\partial^2}{\partial M_a^2 \partial M_b^2}\, S_{\mathrm{HH}}\left(M_{\mathrm{H}}^2, m_{\mathrm{t}}^2, M_{\mathrm{H}}^2, M_{\mathrm{W}}^2, M_{\mathrm{Z}}^2\right),
\end{aligned} \tag{126}$$

where only the first few terms in the perturbative expansion are given. In Eq.(125) we used the following definition of the on-shell width

$$\Gamma_{\mathrm{H}}^{\mathrm{OS}}\, M_{\mathrm{H}}^{\mathrm{OS}} = \mathrm{Im}\; S_{\mathrm{HH,OS}} + \mathrm{HO}. \tag{127}$$

Only the complex pole is gauge-parameter independent to all orders of perturbation theory while on-shell quantities are ill-defined beyond lowest order. Indeed, in the R_ξ gauge, at lowest order, one has the following expression for the bosonic part:

$$\mathrm{Im}\; S_{\mathrm{HH,bos}} = \frac{g^2}{4\, M_{\mathrm{W}}^2}\, s^2 \left[\left(1 - \frac{M_{\mathrm{H}}^4}{s^2}\right)\left(1 - 4\,\xi_{\mathrm{W}}\, \frac{M_{\mathrm{W}}^2}{s}\right)^{1/2} \theta\left(s - 4\,\xi_{\mathrm{W}} M_{\mathrm{W}}^2\right) + \frac{1}{2}\; (\mathrm{W} \to \mathrm{Z})\right], \tag{128}$$

where ξ_{V} $(\mathrm{V} = \mathrm{W}, \mathrm{Z})$ are gauge parameters. Note that Eq.(125) (the expansion) involves derivatives.

A technical remark: suppose that we use μ_{H} as a *free* input parameter and derive γ_{H} in the SM from the equation

$$\mu_{\mathrm{H}}\, \gamma_{\mathrm{H}} = \mathrm{Im}\; S_{\mathrm{HH}}\left(s_{\mathrm{H}}, s_{\mathrm{t}}, s_{\mathrm{H}}, s_{\mathrm{W}}, s_{\mathrm{Z}}\right). \tag{129}$$

Since the bare W, Z masses are replaced with complex poles also in couplings (to preserve gauge invariance) it follows that γ_{H} (solution of Eq.(129)) is renormalisation scale dependent; while counterterms can be introduced to make the self-energy ultraviolet finite, the μ_{R} dependence drops only in subtracted

Table 57: The Higgs-boson complex pole at fixed values of the W, t complex poles compared with the complete solution for $s_{\mathrm{H}}, s_{\mathrm{W}}$, and s_{t}.

μ_{H} [GeV]	γ_{W} [GeV] fixed	γ_{t} [GeV] fixed	γ_{H} [GeV] derived
200	2.093	1.481	1.264
250			3.369
300			7.721
μ_{H} [GeV]	γ_{W} [GeV] derived	γ_{t} [GeV] derived	γ_{H} [GeV] derived
200	1.932	1.171	1.262
250	1.822	0.923	3.364
300	1.738	0.689	7.711

quantities, i.e., after final renormalisation, something that would require knowledge of the experimental Higgs complex pole. Following our intuition we fix the scale at μ_{H}.

After evaluating the coefficients of Eq.(125) (e.g., in the $\xi = 1$ gauge) it is easily seen that the expanded solution of Eq.(120) is not a good approximation to the exact one, especially for high values of μ_{H}. For instance, for $\mu_{\mathrm{H}} = 500$ GeV we have an exact solution $\gamma_{\mathrm{H}} = 58.85$ GeV and an expanded one of 62.87 GeV with an on-shell with of 68.0 GeV. Therefore, we will use an exact, numerical solution for γ_{H}; details on the structure of the Higgs self-energy to all orders of perturbation theory can be found in Refs. [453, 454].

To compute γ_{H} at the same level of accuracy to which $\Gamma_{\mathrm{H}}^{\mathrm{OS}}$ is known (see Ref. [7]) would require, at least, a three-loop calculation (the first instance where we have a four-fermion cut of the Higgs self-energy).

Complex poles for unstable $\mathrm{W}, \mathrm{Z}, \mathrm{H}$, and t also tell us that it is very difficult for a heavy Higgs boson to come out right within the SM; these complex poles are solutions of a (coupled) system of equations but for W, Z, and (partially) t we can compare with the corresponding experimental quantities. Results are shown in Table 57 and clearly indicate mismatches between predicted and experimental W, t complex poles. Indeed, as soon as μ_{H} increases, it becomes more and more difficult to find complex W, t, and Z poles with an imaginary part compatible with measurements.

This simple fact raises the following question: What is the physical meaning of a heavy-Higgs-boson search? We have the usual and well-known considerations: a Higgs boson above 600 GeV requires new physics at 1 TeV, argument based on partial-wave unitarity (which should not be taken quantitatively nor too literally); violation of unitarity bound possibly implies the presence of $J = 0, 1$ resonances, but there is no way to predict their masses, simply scaling the $\pi-\pi$ system gives resonances in the 1 TeV ballpark. Generally speaking, it would be a good idea to address this search as *search* for $J = 0, 1$ heavy resonances decaying into $\mathrm{VV} \to 4\,\mathrm{f}$.

In a model-independent approach both μ_{H} and γ_{H} should be kept free in order to perform a 2-dimensional scan of the Higgs-boson lineshape. For the high-mass region this remains the recommended strategy. Once the fits are performed it will be left to theorists to struggle with the SM interpretation of the results.

To summarise, we have addressed the following question: What is the common sense definition of mass and width of the Higgs boson? We have several options,

$$s_{\mathrm{H}} = \mu_{\mathrm{H}}^2 - i\,\mu_{\mathrm{H}}\,\gamma_{\mathrm{H}}, \quad s_{\mathrm{H}} = \left(\mu'_{\mathrm{H}} - \frac{i}{2}\,\gamma'_{\mathrm{H}}\right)^2, \quad s_{\mathrm{H}} = \frac{\overline{M}_{\mathrm{H}}^2 - i\,\overline{\Gamma}_{\mathrm{H}}\,\overline{M}_{\mathrm{H}}}{1 + \overline{\Gamma}_{\mathrm{H}}^2/\overline{M}_{\mathrm{H}}^2}. \tag{130}$$

We may ask which one is correct, approximate or closer to the experimental peak. Here we have to distinguish: for $\gamma_{\mathrm{H}} \ll \mu_{\mathrm{H}}$, $\overline{M}_{\mathrm{H}}$ is a good approximation to the on-shell mass and it is closer to the

experimental peak; for instance, for the Z boson $\overline{M}_{\rm Z}$ is equivalent to the mass measured at LEP. However, in the high-mass scenario, where $\gamma_{\rm H} \sim \mu_{\rm H}$, the situation changes and $\overline{O}_{\rm H} \neq O_{\rm H}^{\rm OS}$ for any observable (or pseudo-observable). Therefore, the message is: Do not use the computed on-shell width to estimate $\overline{M}_{\rm H}$.

15.3 Production and decay

Before describing production and decay of an Higgs boson we underline the general structure of any process containing a Higgs-boson intermediate state. The corresponding amplitude is given by

$$A(s) = \frac{f(s)}{s - s_{\rm H}} + N(s), \tag{131}$$

where $N(s)$ denotes the part of the amplitude which is non-resonant. Signal and background are defined as

$$A(s) = S(s) + B(s), \qquad S(s) = \frac{f(s_{\rm H})}{s - s_{\rm H}}, \quad B(s) = \frac{f(s) - f(s_{\rm H})}{s - s_{\rm H}} + N(s). \tag{132}$$

As a first step we will show how to write $f(s)$ in a way such that pseudo-observables make their appearance. Consider the process $ij \to {\rm H} \to {\rm F}$ where $i, j \in$ partons; the complete cross section will be written as follows:

$$\sigma_{ij\to{\rm H}\to{\rm F}}(s) = \frac{1}{2\,s} \int d\Phi_{ij\to{\rm F}} \left[\sum_{s,c} \left|A_{ij\to{\rm H}}\right|^2\right] \frac{1}{\left|s - s_{\rm H}\right|^2} \left[\sum_{s,c} \left|A_{{\rm H}\to{\rm F}}\right|^2\right], \tag{133}$$

where $\sum_{s,c}$ is over spin and colours (averaging on the initial state). Note that the background (e.g., ${\rm gg} \to 4\,{\rm f}$) has not been included and, strictly speaking and for reasons of gauge invariance, one should consider only the residue of the Higgs-resonant amplitude at the complex pole, as described in Eq.(132). For the moment we will argue that the dominant corrections are the QCD ones where we have no problem of gauge-parameter dependence. If we decide to keep the Higgs boson off-shell also in the resonant part of the amplitude (interference signal/background remains unaddressed) then we can write

$$\sum_{s,c} \int d\Phi_{ij\to{\rm H}} \left|A_{ij\to{\rm H}}\right|^2 = s\,\overline{A}_{ij}(s). \tag{134}$$

For instance, we have

$$\overline{A}_{\rm gg}(s) = \frac{\alpha_{\rm s}^2}{\pi^2} \frac{G_F\, s}{288\sqrt{2}} \left|\sum_q f\left(\tau_q\right)\right|^2 \left(1 + \delta_{\rm QCD}\right), \tag{135}$$

where $\tau_q = 4\,m_q^2/s$, $f(\tau_q)$ is defined in Eq.(3) of Ref. [66] and where $\delta_{\rm QCD}$ gives the QCD corrections to ${\rm gg} \to {\rm H}$ up to NNLO + NLL order. Furthermore, we define

$$\Gamma_{{\rm H}\to{\rm F}} = \frac{1}{2\sqrt{s}} \int d\Phi_{{\rm H}\to{\rm F}} \sum_{s,c} \left|A_{{\rm H}\to{\rm F}}\right|^2, \tag{136}$$

which gives the partial decay width of a Higgs boson of virtuality s into a final state F, and

$$\sigma_{ij\to{\rm H}} = \frac{\overline{A}_{ij}(s)}{s}, \tag{137}$$

which gives the production cross section of a Higgs boson of virtuality s. We can write the final result in terms of pseudo-observables

$$\sigma\left(ij \to {\rm H} \to {\rm F}\right) = \frac{1}{\pi}\,\sigma_{ij\to{\rm H}} \frac{s^2}{\left|s - s_{\rm H}\right|^2} \frac{\Gamma_{{\rm H}\to{\rm F}}}{\sqrt{s}}. \tag{138}$$

It is also convenient to rewrite the result as

$$\sigma\,(ij \to \mathrm{H} \to \mathrm{F}) = \frac{1}{\pi}\sigma_{ij\to\mathrm{H}}\,\frac{s^2}{\left|s - s_{\mathrm{H}}\right|^2}\,\frac{\Gamma_{\mathrm{H}}^{\mathrm{tot}}}{\sqrt{s}}\,\mathrm{BR}\,(\mathrm{H} \to \mathrm{F})\,, \tag{139}$$

where we have introduced a sum over all final states,

$$\Gamma_{\mathrm{H}}^{\mathrm{tot}} = \sum_{f\in\mathrm{F}} \Gamma_{\mathrm{H}\to\mathrm{F}}. \tag{140}$$

Note that we have written the phase-space integral for $i(p_1) + j(p_2) \to \mathrm{F}$ as

$$\begin{aligned}\int d\Phi_{ij\to\mathrm{F}} &= \int \left(\prod_f d^4p_f\,\delta^+(p_f^2)\right)\delta^4(p_1 + p_2 - \sum_f p_f)\\ &= \int d^4k\,\delta^4(k - p_1 - p_2)\int \left(\prod_f d^4p_f\,\delta^+(p_f^2)\right)\delta^4(k - \sum_f p_f),\end{aligned} \tag{141}$$

where we assume that all initial and final states (e.g., $\gamma\gamma$, $4\,\mathrm{f}$, etc.) are massless. It is worth noting that the introduction of complex poles does not imply complex kinematics. According to Eq.(132) only the residue of the propagator at the complex pole becomes complex, not any element of the phase-space integral.

<u>Definition:</u> We define an off-shell production cross section (for all channels) as follows:

$$\sigma_{ij\to\mathrm{all}}^{\mathrm{prop}}(s) = \frac{1}{\pi}\,\sigma_{ij\to\mathrm{H}}\,\frac{s^2}{\left|s - s_{\mathrm{H}}\right|^2}\,\frac{\Gamma_{\mathrm{H}}^{\mathrm{tot}}}{\sqrt{s}}. \tag{142}$$

When the cross section $ij \to \mathrm{H}$ refers to an off-shell Higgs boson the choice of the QCD scales should be made according to the virtuality and not to a fixed value. Therefore, always referring to Figure 136, for the PDFs and $\sigma_{ij\to\mathrm{H+X}}$ one should select $\mu_F^2 = \mu_{\mathrm{R}}^2 = z\,s/4$ ($z\,s$ being the invariant mass of the detectable final state). Indeed, beyond LO one must not choose the invariant mass of the incoming partons for the renormalisation and factorisation scales, but an infrared-safe quantity fixed from the detectable final state. The argument is based on minimisation of the universal logarithms (DGLAP) and not the process-dependent ones.

The off-shell Higgs-boson production is currently computed according to the replacement

$$\sigma_{\mathrm{OS}}(\mu_{\mathrm{H}}^2)\,\delta(z\,s - \mu_{\mathrm{H}}^2) \;\longrightarrow\; \sigma_{\mathrm{OFS}}(z\,s)\,\mathrm{BW}(z\,s), \tag{143}$$

(e.g., see Ref. [132]) at least at lowest QCD order, where the so-called modified Breit–Wigner distribution is defined by

$$\mathrm{BW}(s) = \frac{1}{\pi}\,\frac{s\,\Gamma_{\mathrm{H}}^{\mathrm{OS}}/\mu_{\mathrm{H}}}{\left(s - \mu_{\mathrm{H}}^2\right)^2 + \left(s\,\Gamma_{\mathrm{H}}^{\mathrm{OS}}/\mu_{\mathrm{H}}\right)^2}, \tag{144}$$

where now $\mu_{\mathrm{H}} = M_{\mathrm{H}}^{\mathrm{OS}}$. This ad-hoc Breit–Wigner cannot be derived from QFT and also is not normalizable in $[0\,,\,+\infty]$. Note that this Breit–Wigner for a running width comes from the substitution of $\Gamma \to \Gamma(s) = \Gamma\,s/M^2$ in the Breit–Wigner for a fixed width Γ. This substitution is not justifiable. Its practical purpose is to enforce a *physical* behaviour for low virtualities of the Higgs boson, but the usage cannot be justified nor recommended. For instance, if one considers VV scattering and uses this distribution in the s-channel Higgs exchange, the behaviour for large values of s spoils unitarity cancellation with the contact diagram. It is worth noting that the alternative replacement

$$\sigma_{\mathrm{OS}}(\mu_{\mathrm{H}}^2)\,\delta(z\,s - \mu_{\mathrm{H}}^2) \;\longrightarrow\; \sigma_{\mathrm{OFS}}(z\,s)\,\mathrm{BW}(z\,s), \quad \mathrm{BW}(z\,s) = \frac{1}{\pi}\,\frac{\mu_{\mathrm{H}}\,\Gamma_{\mathrm{H}}^{\mathrm{OS}}}{\left(z\,s - \mu_{\mathrm{H}}^2\right)^2 + \left(\mu_{\mathrm{H}}\,\Gamma_{\mathrm{H}}^{\mathrm{OS}}\right)^2}, \tag{145}$$

Table 58: Higgs-boson complex pole; $\Gamma_{\rm H}^{\rm OS}$ is the on-shell width, $\gamma_{\rm H}$ is defined in Eq.(119) and the Bar-scheme in Eq.(146).

$\mu_{\rm H}$[GeV]	$\Gamma_{\rm H}^{\rm OS}$[GeV] (YR)	$\gamma_{\rm H}$ [GeV]	$\overline{M}_{\rm H}$[GeV]	$\overline{\Gamma}_{\rm H}$[GeV]
200	1.43	1.26	200	1.26
400	29.2	24.28	400.7	24.24
600	123	102.17	608.6	100.72
700	199	159.54	717.95	155.55
800	304	228.44	831.98	219.66
900	449	307.63	951.12	291.09

has additional problems at the low-energy tail of the resonance due to the $\rm gg$ luminosity, creating an artificial increase of the lineshape at low virtualities.

Another important issue is that $\gamma_{\rm H}$, which appears in the imaginary part of the inverse Dyson-resummed propagator, is not the on-shell width, since they differ by higher-order terms and their relations becomes non-perturbative when the on-shell width becomes of the same order of the on-shell mass (typically, for on-shell masses above $800\,$GeV).

The complex-mass scheme can be translated into a more familiar language by introducing the Bar-scheme. Using Eq.(118) with the parametrisation of Eq.(119) we perform the well-known transformation

$$\overline{M}_{\rm H}^2 = \mu_{\rm H}^2 + \gamma_{\rm H}^2 \qquad \mu_{\rm H}\,\gamma_{\rm H} = \overline{M}_{\rm H}\,\overline{\Gamma}_{\rm H}. \tag{146}$$

A remarkable identity follows, defining the Bar-scheme:

$$\frac{1}{s - s_{\rm H}} = \Big(1 + i\,\frac{\overline{\Gamma}_{\rm H}}{\overline{M}_{\rm H}}\Big)\Big(s - \overline{M}_{\rm H}^2 + i\,\frac{\overline{\Gamma}_{\rm H}}{\overline{M}_{\rm H}}\,s\Big)^{-1}, \tag{147}$$

showing that the Bar-scheme is equivalent to introducing a running width in the propagator with parameters that are not the on-shell ones. Special attention goes to the numerator in Eq.(147) which is essential in providing the right asymptotic behaviour when $s \to \infty$, as needed for cancellations with contact terms in $\rm VV$ scattering. A sample of numerical results is shown in Table 58 where we compare the Higgs-boson complex pole to the corresponding quantities in the Bar-scheme.

The use of the complex pole is recommended even if the accuracy at which its imaginary part can be computed is not of the same quality as the NLO accuracy of the on-shell width. Nevertheless the use of a solid prediction (from a theoretical point of view) should always be preferred to the introduction of ill-defined quantities (gauge-parameter dependent).

15.3.1 Schemes

We are now in a position to give a more detailed description of the strategy behind Eq.(132). Consider the complete amplitude for a given process, e.g., the one in Figure 136; let $(\hat{s} = zs, \ldots)$ the full list of Mandelstam invariants characterizing the process, then

$$A\,(\hat{s},\,\ldots) \;=\; V_{\rm prod}\,(\hat{s},\,\ldots)\;\Delta_{\rm prop}(\hat{s})\,V_{\rm dec}(\hat{s}) \;+\; N\,(\hat{s},\,\ldots)\,. \tag{148}$$

Here $V_{\rm prod}$ denotes the amplitude for production, e.g., $\rm gg \to H(\hat{s}) + X$, $\Delta_{\rm prop}(\hat{s})$ is the propagation function, $V_{\rm dec}(\hat{s})$ is the amplitude for decay, e.g., $\rm H(\hat{s}) \to 4f$. If no attempt is made to split $A(s)$, no ambiguity arises but, usually, the two components are known at different orders. Ho to define the signal? The following schemes are available:

ONBW

$$S\,(\hat{s},\,\ldots) = V_{\text{prod}}\left(\mu_{\rm H}^2,\,\ldots\right)\,\Delta_{\text{prop}}(\hat{s})\,V_{\text{dec}}(\mu_{\rm H}^2), \qquad \Delta_{\text{prop}}(\hat{s}) = \text{Breit–Wigner}, \tag{149}$$

in general violates gauge invariance, neglects the Higgs off-shellness and introduces the ad hoc Breit–Wigner of Eq.(144).

OFFBW

$$S\,(\hat{s},\,\ldots) = V_{\text{prod}}\,(\hat{s},\,\ldots)\,\Delta_{\text{prop}}(\hat{s})\,V_{\text{dec}}(\hat{s}), \qquad \Delta_{\text{prop}}(\hat{s}) = \text{Breit–Wigner}, \tag{150}$$

in general violates gauge invariance and introduces the ad hoc Breit–Wigner.

ONP

$$S\,(\hat{s},\,\ldots) = V_{\text{prod}}\left(\mu_{\rm H}^2,\,\ldots\right)\,\Delta_{\text{prop}}(\hat{s})\,V_{\text{dec}}(\mu_{\rm H}^2), \qquad \Delta_{\text{prop}}(\hat{s}) = \text{propagator}, \tag{151}$$

in general violates gauge invariance and neglects the Higgs off-shellness.

OFFP

$$S\,(\hat{s},\,\ldots) = V_{\text{prod}}\,(\hat{s},\,\ldots)\,\Delta_{\text{prop}}(\hat{s})\,V_{\text{dec}}(\hat{s}), \qquad \Delta_{\text{prop}}(\hat{s}) = \text{propagator}, \tag{152}$$

in general violates gauge invariance.

CPP

$$S\,(\hat{s},\,\ldots) = V_{\text{prod}}\,(s_{\rm H},\,\ldots)\,\Delta_{\text{prop}}(\hat{s})\,V_{\text{dec}}(s_{\rm H}), \qquad \Delta_{\text{prop}}(\hat{s}) = \text{propagator}. \tag{153}$$

Only the pole, the residue, and the reminder of the amplitude are gauge invariant. Furthermore the CPP-scheme allows to identify POs like the production cross section and any partial decay width by putting in one-to-one correspondence robust theoretical quantities and experimental data.

From the list above it follows that only the CPP-scheme should be used, once the signal/background interference becomes available. However, the largest part of the available calculations is not yet equipped with Feynman integrals on the second Riemann sheet; furthermore the largest corrections in the production are from QCD and we could argue that gauge invariance is not an issue over there, so that the OFFP-scheme remains, at the moment, the most pragmatic alternative.

Implementation of the CPP-scheme requires some care in the presence of four-leg processes (or more). The natural choice is to perform analytical continuation from real kinematics to complex invariants; consider, for instance, the process $\rm gg \to Hj$ where the external H leg is continued from real on-shell mass to $s_{\rm H}$. For the three invariants we use the following continuation:

$$t = -\,\frac{s}{2}\left[1 - \frac{s_{\rm H}}{s} - \left(1 - 4\,\frac{s_{\rm H}}{s}\right)^{1/2}\,\cos\theta\right], \quad u = -\,\frac{s}{2}\left[1 - \frac{s_{\rm H}}{s} + \left(1 - 4\,\frac{s_{\rm H}}{s}\right)^{1/2}\,\cos\theta\right], \tag{154}$$

where θ is the scattering angle and $s = 4\,E^2$, where $2\,E$ is the centre-of-mass energy. To summarise, our proposal aims to support the use of Eq.(139) for producing accurate predictions for the Higgs lineshape in the SM; Eq.(139) can be adapted easily for a large class of extensions of the SM. Similarly Eq.(142) should be used to define the Higgs-boson production cross section instead of $\sigma_{\rm OS}$ or $\sigma_{\rm OFS}$ of Eq.(143).

To repeat an obvious argument the zero-width approximation for the Higgs boson is usually reported in comparing experimental studies and theoretical predictions. The approximation has very low quality in the high-mass region where the Higgs boson has a non negligible width. An integration over some distribution is a more accurate estimate of the signal cross section and we claim that this distribution should be given by the complex propagator and not by some ad hoc Breit–Wigner.

As we have already mentioned, most of this section is devoted to studying the Higgs-boson lineshape in the high-mass region. However, nothing in the formalism is peculiar to that application and the formalism itself forms the basis for extracting pseudo-observables from experimental data. This is a timely contribution to the relevant literature.

15.3.2 Production cross section

Before presenting detailed numerical results and comparisons we give the complete definition of the production cross section,

$$\sigma^{\text{prod}} = \sum_{i,j} \int \text{PDF} \otimes \sigma^{\text{prod}}_{ij\to\text{all}} = \sum_{i,j} \int_{z_0}^{1} dz \int_{z}^{1} \frac{dv}{v}\, \mathcal{L}_{ij}(v) \sigma^{\text{prop}}_{ij\to\text{all}}(zs, vs, \mu_{\rm R}, \mu_{\rm F}), \tag{155}$$

where z_0 is a lower bound on the invariant mass of the H decay products, the luminosity is defined by

$$\mathcal{L}_{ij}(v) = \int_{v}^{1} \frac{dx}{x}\, f_i\left(x, \mu_{\rm F}\right)\, f_j\left(\frac{v}{x}, \mu_{\rm F}\right), \tag{156}$$

where f_i is a parton distribution function and

$$\sigma^{\text{prop}}_{ij\to\text{all}}(zs, vs, \mu_{\rm R}, \mu_{\rm F}) = \frac{1}{\pi}\, \sigma_{ij\to{\rm H+X}}(zs, vs, \mu_{\rm R}, \mu_{\rm F})\, \frac{vzs^2}{\left|zs - s_{\rm H}\right|^2}\, \frac{\Gamma^{\text{tot}}_{\rm H}(zs)}{\sqrt{zs}}. \tag{157}$$

Therefore, $\sigma_{ij\to{\rm H+X}}(zs, vs, \mu_{\rm R})$ is the cross section for two partons of invariant mass vs ($z < v < 1$) to produce a final state containing a H of virtuality zs plus jets (X); it is made of several terms

$$\sum_{ij} \sigma_{ij\to{\rm H+X}}(zs, vs, \mu_{\rm R}, \mu_{\rm F}) = \sigma_{\rm gg\to H}\, \delta\Big(1 - \frac{z}{v}\Big) + \sigma_{\rm gg\to Hg} + \sigma_{\rm qg\to Hq} + \sigma_{\rm \overline{q}q\to Hg} + \text{NNLO}. \tag{158}$$

As a technical remark the complete phase-space integral for the process $\hat{p}_i + \hat{p}_j \to p_k + \{f\}$ ($\hat{p}_i = x_i\, p_i$ etc.) is written as

$$\begin{aligned}\int d\Phi_{ij\to\rm F} &= \int d\Phi_{\text{prod}} \int d\Phi_{\text{dec}} = \int d^4p_k\, \delta^+(p_k^2) \left(\prod_{l=1,n} d^4q_l\, \delta^+(q_l^2)\right) \delta^4\Big(\hat{p}_i + \hat{p}_j - p_k - \sum_l q_l\Big) \\ &= \int d^4k\, d^4Q\, \delta^+(p_k^2)\, \delta^4\Big(\hat{p}_i + \hat{p}_j - p_k - Q\Big) \int \left(\prod_{l=1,n} d^4q_l\, \delta^+(q_l^2)\right) \delta^4\Big(Q - \sum_l q_l\Big),\end{aligned} \tag{159}$$

where $\int d\Phi_{\text{dec}}$ is the phase-space for the process $Q \to \{f\}$ and

$$\begin{aligned}\int d\Phi_{\text{prod}} &= s \int dz \int d^4k\, d^4Q\, \delta^+(p_k^2)\, \delta\left(Q^2 - zs\right)\, \theta(Q_0)\, \delta^4\left(\hat{p}_i + \hat{p}_j - p_k - Q\right) \\ &= s^2 \int dz\, dv\, d\hat{t} \int d^4k\, d^4Q\, \delta^+(p_k^2)\, \delta\left(Q^2 - zs\right)\, \theta(Q_0)\, \delta^4\left(\hat{p}_i + \hat{p}_j - p_k - Q\right) \\ &\quad \times \delta\left((\hat{p}_i + \hat{p}_j)^2 - vs\right)\, \delta\left((\hat{p}_i + Q)^2 - \hat{t}\right).\end{aligned} \tag{160}$$

Eqs.(155) and (157) follow after folding with PDFs of argument x_i and x_j, after using $x_i = x$, $x_j = v/x$ and after integration over $\hat{t}$. At NNLO there is an additional parton in the final state and five invariants are needed to describe the partonic process, plus the H virtuality. However, one should remember that at NNLO use is made of the effective-theory approximation where the Higgs–gluon interaction is described by a local operator. Our variables z, v are related to POWHEG parametrisation [132], Y, ξ, by $Y = \ln(x/\sqrt{z})$ and $v = z/(1-\xi)$.

15.4 Numerical results

In the following we will present numerical results obtained with the program HTO (G. Passarino, unpublished) that allows for the study of the Higgs-boson lineshape using complex poles. HTO is a FORTRAN 95 program that contains a translation of the subroutine `HIGGSNNLO` written by M. Grazzini for computing the total (on-shell) cross section for Higgs-boson production at NLO and NNLO.

The following acronyms will be used:

Table 59: The re-weighting factor w for the (total) integrated Higgs lineshape, $\sigma^{\rm prop}/\sigma^{\rm BW}$ using $\gamma_{\rm H} = \Gamma_{\rm H}^{\rm OS}$ in Eq.(142).

$\mu_{\rm H}$ [GeV]	$\Gamma_{\rm H}^{\rm OS}$ [GeV]	$\sigma^{\rm OS}$ [pb]	$\sigma^{\rm BW}$ [pb]	$\sigma^{\rm prop}$ [pb]	w
200	1.43	5.249	5.674	5.459	0.962
300	8.43	2.418	2.724	2.585	0.949
400	29.2	2.035	1.998	1.927	0.964
500	68.0	0.8497	0.8108	0.7827	0.965
600	123.0	0.3275	0.3231	0.3073	0.951

FW Breit–Wigner Fixed Width (Eq.(145)),

RW Breit–Wigner Running Width (Eq.(144)),

OS parameters in the On-Shell scheme,

Bar parameters in Bar-scheme (Eq.(146)),

FS QCD renormalisation (factorisation) scales fixed,

RS QCD renormalisation (factorisation) scales running.

All results in this section refer to $\sqrt{s} = 7$ TeV and are based on the MSTW2008 PDF sets [107]. For complex $\rm W, Z$ poles we use Eq.(124) with HXSWG standard input.

The integrand in Eq.(155) has several peaks; the most evident is in the propagator and in HTO a change of variable is performed,

$$zs = \frac{1}{1+(\mu_{\rm H}/\gamma_{\rm H})^2}\Big[\mu_{\rm H}^2 + \mu_{\rm H}\,\gamma_{\rm H}\,\tan\big(\mu_{\rm H}\gamma_{\rm H}\,z'\big)\Big],$$
$$z' = \frac{s}{\mu_{\rm H}\gamma_{\rm H}}\Big[(a_m + a_{\rm M})\,\zeta - a_m\Big], \quad a_m = \arctan\frac{\mu_{\rm H}^2 - z_0 s}{\mu_{\rm H}\gamma_{\rm H}}, \quad a_{\rm M} = \arctan\frac{s-\mu_{\rm H}^2}{\mu_{\rm H}\gamma_{\rm H}}. \quad (161)$$

Similarly, another change is performed,

$$v = \exp\{\big(1-u^2\big)\,\ln z\}, \qquad x = \exp\{\big(1-y^2\big)\,\ln v\}. \quad (162)$$

In comparing the OFFBW-scheme with the OFFP-scheme one should realise that there are two sources of difference, the functional form of the distributions and the different numerical values of the parameters in the distributions. To understand the impact of the functional form we have performed a comparison where (unrealistically) $\gamma_{\rm H} = \Gamma_{\rm H}^{\rm OS}$ is used in the Higgs propagator; results are shown in Table 59.

In Table 60 we compare the on-shell production cross section as given in Ref. [7] with the off-shell cross section in the OFFBW-scheme (Eq.(150)) and in the OFFP-scheme (Eq.(152)).

An important question regarding the numerical impact of a calculation where the on-shell Higgs boson is left off-shell and convoluted with some distribution is how much of the effect survives the inclusion of theoretical uncertainties. In the OFFBW-scheme we can compare with the results of Ref. [442], at least for values of the Higgs-boson mass below 300 GeV. We compare with Tables 2–3 of Ref. [7] at 300 GeV and obtain the results shown in Table 61 where only the QCD scale uncertainty is included. At these values of the Higgs-boson mass on-shell production and off-shell production sampled over a Breit–Wigner are compatible within the errors. The OFFP-scheme gives a slightly higher central value of 2.86 pb. The comparison shows drastically different results for high values of the mass where the difference in central values is much bigger than the theoretical uncertainty.

In Table 62 we show a more detailed comparison of the production cross section in the OFFBW-scheme between iHIXS of Ref. [442] and our calculation. Δ is the percentage error due to QCD scale uncertainties, and δ is the percentage ratio HTO/iHIXS.

Table 60: Comparison of the on-shell production cross section as given in Ref. [7] with the off-shell cross section in the OFFBW-scheme (Eq.(150)) and in the OFFP-scheme (Eq.(152)).

$\mu_{\rm H}$[GeV]	$\Gamma_{\rm H}^{\rm OS}$[GeV]	$\gamma_{\rm H}$[GeV]	$\sigma^{\rm OS}$[pb]	$\sigma^{\rm BW}$[pb]	$\sigma^{\rm prop}$[pb]
500	68.0	60.2	0.8497	0.8239	0.9367
550	93.1	82.8	0.5259	0.5161	0.5912
600	123	109	0.3275	0.3287	0.3784
650	158	139	0.2064	0.2154	0.2482
700	199	174	0.1320	0.1456	0.1677
750	248	205	0.0859	0.1013	0.1171
800	304	245	0.0567	0.0733	0.0850
850	371	277	0.0379	0.0545	0.0643
900	449	331	0.0256	0.0417	0.0509

Table 61: The production cross section in pb at $\mu_{\rm H} = 300$ GeV. Results from HTO are computed with running QCD scales.

Tab. 2 of Ref. [7]	Tab. 3 of Ref. [7]	Tab. 5 of Ref. [442]	HTO RS-option
$2.42^{+0.14}_{-0.15}$	$2.45^{+0.16}_{-0.22}$	$2.57^{+0.15}_{-0.22}$	$2.81^{+0.25}_{-0.23}$

Table 62: Comparison of the production cross section in the OFFBW-scheme between iHixs (Table 5 of Ref. [442]) and our calculation. Δ is the percentage error due to QCD scale uncertainties, and δ is the percentage ratio HTO/iHixs.

$\mu_{\rm H}$[GeV]	$\sigma_{\rm iHixs}$[pb]	$\Delta_{\rm iHixs}[\%]$	$\sigma_{\rm HTO}$[pb]	$\Delta_{\rm HTO}[\%]$	$\delta[\%]$
200	5.57	$+7.19\ -9.06$	5.63	$+9.12\ -9.30$	1.08
220	4.54	$+6.92\ -8.99$	4.63	$+8.93\ -8.85$	1.98
240	3.80	$+6.68\ -8.91$	3.91	$+8.76\ -8.51$	2.89
260	3.25	$+6.44\ -8.84$	3.37	$+8.61\ -8.22$	3.69
280	2.85	$+6.18\ -8.74$	2.97	$+8.49\ -7.98$	4.21
300	2.57	$+5.89\ -8.58$	2.69	$+8.36\ -7.75$	4.67

Another quantity that is useful in describing the lineshape is obtained by introducing

$$M_{\rm peak}^2 = \left(M_{\rm H}^{\rm OS}\right)^2 + \left(\Gamma_{\rm H}^{\rm OS}\right)^2, \tag{163}$$

an by considering the following windows in the invariant mass,

$$\left[M_{\rm peak} + \frac{n}{2}\,\Gamma_{\rm H}^{\rm OS}\,,\, M_{\rm peak} + \frac{n+1}{2}\,\Gamma_{\rm H}^{\rm OS}\right], \qquad n = 0, \pm 1, \ldots. \tag{164}$$

In Table 63 we present the ratio OFFP/OFFBW for the invariant mass distribution in the windows of Eq.(164).

In Table 64 we include uncertainties in the comparison; both OFFBW-scheme and OFFP-scheme are used with the RS option, i.e., running QCD scales instead of a fixed one. Note that for $\sigma(\mu)$ we define a central value $\sigma_c = \sigma(\overline{\mu})$ and a scale error as $[\sigma^-\,,\,\sigma^+]$, where

$$\sigma^- = \min_{\mu\in[\overline{\mu}/2,2\overline{\mu}]}\,\sigma(\mu), \qquad \sigma^+ = \max_{\mu\in[\overline{\mu}/2,2\overline{\mu}]}\,\sigma(\mu), \tag{165}$$

and where $\mu = \mu_{\rm R} = \mu_{\rm F}$ and $\overline{\mu}$ is the reference scale, static or dynamic.

Table 63: Scaling factor OFFP/OFFBW schemes (Eqs.(152) and (150)) for the invariant-mass windows of Eq.(164).

$\mu_{\rm H}$[GeV]	$n=-4$	$n=-3$	$n=-2$	$n=-1$	$n=0$	$n=1$	$n=2$	$n=3$
500	1.24	1.13	1.08	1.23	1.32	1.11	0.97	0.88
600	1.39	1.20	1.08	1.27	1.40	1.12	0.94	0.84
650	1.50	1.24	1.08	1.30	1.44	1.13	0.93	0.81
700	1.62	1.28	1.09	1.34	1.49	1.13	0.92	0.79
750	1.78	1.34	1.10	1.41	1.57	1.14	0.90	0.77
800	1.99	1.41	1.12	1.49	1.64	1.14	0.89	0.75

Table 64: Production cross section with errors due to QCD scale variation and PDF uncertainty. First entry is the on-shell cross section of Table 2 of Ref. [7], second entry is OFFBW (Eq.(150)), last entry is OFFP Eq.(152).

$\mu_{\rm H}$[GeV]	σ[pb]	Scale [%]	PDF [%]
600	0.336	$+6.1\ -\ 5.2$	$+6.2\ -\ 5.3$
	0.329	$+11.2\ -\ 11.3$	$+4.7\ -\ 4.8$
	0.378	$+9.7\ -\ 10.0$	$+5.0\ -\ 3.9$
650	0.212	$+6.2\ -\ 5.2$	$+6.5\ -\ 5.5$
	0.215	$+12.4\ -\ 12.2$	$+5.1\ -\ 5.3$
	0.248	$+10.2\ -\ 10.0$	$+5.3\ -\ 4.2$
700	0.136	$+6.3\ -\ 5.3$	$+6.9\ -\ 5.8$
	0.146	$+13.9\ -\ 13.3$	$+5.6\ -\ 5.8$
	0.168	$+11.0\ -\ 11.1$	$+5.5\ -\ 4.6$
750	0.0889	$+6.4\ -\ 5.4$	$+7.2\ -\ 6.1$
	0.101	$+15.8\ -\ 14.5$	$+6.1\ -\ 6.3$
	0.117	$+12.2\ -\ 11.9$	$+5.8\ -\ 5.1$
800	0.0588	$+6.5\ -\ 5.4$	$+7.6\ -\ 6.3$
	0.0733	$+18.0\ -\ 16.0$	$+6.7\ -\ 6.9$
	0.0850	$+13.7\ -\ 13.0$	$+6.1\ -\ 5.5$
850	0.0394	$+6.5\ -\ 5.5$	$+8.0\ -\ 6.6$
	0.0545	$+20.4\ -\ 17.6$	$+7.2\ -\ 7.5$
	0.0643	$+15.7\ -\ 14.3$	$+6.5\ -\ 6.0$
900	0.0267	$+6.7\ -\ 5.6$	$+8.3\ -\ 6.9$
	0.0417	$+22.8\ -\ 19.1$	$+7.7\ -\ 8.0$
	0.0509	$+18.1\ -\ 16.0$	$+7.0\ -\ 6.6$

In Table 65 we compare results from Table 5 of Ref. [442] with our OFFBW results with two options: 1) $\mu_{\rm R}^2, \mu_F^2$ are fixed, 2) they run with $z/4$. For the three values of $\mu_{\rm H}$ reported we find differences of $2.0\%, 3.7\%$, and 4.7%, compatible with the scale uncertainty. Furthermore, we use Ref. [7] for input parameters which differ slightly from the one used in Ref. [442]. Note that also the functional form ot the Breit–Wigner is different since their default value is not the one in Eq.(144) but

$$\mathrm{BW}(s) = \frac{1}{\pi}\,\frac{\sqrt{s}\,\Gamma_{\rm H}(\sqrt{s})}{\left(s-\mu_{\rm H}^2\right)^2 + \mu_{\rm H}^2\,\Gamma_{\rm H}^2(\mu_{\rm H})}, \tag{166}$$

where $\Gamma_{\rm H}(\sqrt{s})$ id the decay width of a Higgs boson at rest with mass $\sqrt{s}$.

In Table 66 we use the OFFP-scheme of Eq.(152) and look for the effect of running QCD scales in the H invariant-mass distribution. Differences are of the order of $2-3\%$ apart from the high-mass side of

Table 65: Comparison of results from Table 5 of Ref. [442] with our OFFBW results (Eq.(150)) with two options: 1) $\mu_{\rm R}^2, \mu_F^2$ are fixed, 2) they run with $z/4$.

	IXIS		HTO			
$\mu_{\rm H}$[GeV]	σ[pb]	Scale [%]	σ_1[pb]	Scale [%]	σ_2[pb]	Scale [%]
220	4.54	$+6.9\ -\ 9.0$	4.63	$+8.9\ -\ 8.9$	4.74	$+7.3\ -\ 8.7$
260	3.25	$+6.4\ -\ 8.8$	3.37	$+8.6\ -\ 8.2$	3.49	$+7.9\ -\ 8.6$
300	2.57	$+5.9\ -\ 8.6$	2.69	$+8.4\ -\ 7.8$	2.81	$+8.4\ -\ 8.5$

Table 66: Scaling factor in the OFFP-scheme (Eq.(152)) running/fixed QCD scales for the invariant-mass distribution. Here $[x, y] = [M_{\rm peak} + x\,\Gamma_{\rm H}^{\rm OS}\,,\ M_{\rm peak} + y\,\Gamma_{\rm H}^{\rm OS}]$.

$\mu_{\rm H}$[GeV]	$[-1\,,\,-\frac{1}{2}]$	$[-\frac{1}{2}\,,\,-\frac{1}{4}]$	$[-\frac{1}{4}\,,\,0]$	$[0\,,\,\frac{1}{4}]$	$[\frac{1}{4}\,,\,\frac{1}{2}]$	$[\frac{1}{2}\,,\,1]$
600	1.023	1.021	1.019	1.018	1.017	1.016
700	1.027	1.023	1.021	1.019	1.018	1.019
800	1.030	1.024	1.021	1.021	1.021	1.136

Table 67: $\gamma_{\rm H}$ and $\Gamma_{\rm H}^{\rm OS}$ as a function of $\mu_{\rm H}$. We also report the ratio between the LO cross sections for $\rm gg \to H$ in the CPP-scheme and in the OS-scheme.

$\mu_{\rm H}$[GeV]	$\gamma_{\rm H}$[GeV]	$\Gamma_{\rm H}^{\rm OS}$[GeV]	$\sigma_{\rm CPP}(s_{\rm H})\,/\,\sigma_{\rm OS}(M_{\rm H}^{\rm OS})$
300	7.58	8.43	0.999
350	14.93	15.20	1.086
400	26.66	29.20	1.155
450	41.18	46.90	1.183
500	58.85	68.00	1.204
550	79.80	93.10	1.221
600	104.16	123.00	1.236
650	131.98	158.00	1.248
700	163.26	199.00	1.256
750	197.96	248.00	1.262
800	235.93	304.00	1.264
850	277.00	371.00	1.263
900	320.96	449.00	1.258
950	367.57	540.00	1.252
1000	416.57	647.00	1.242

the distribution for very high H masses. As we have already mentioned, the only scheme respecting gauge invariance that allows us for a proper definition of pseudo-observables is the CPP-scheme of Eq.(153). It requires analytical continuation of the Feynman integrals into the second Riemann sheet. Once again, the definition of POs is conventional, but should put in one-to-one correspondence well-defined theoretical predictions with derived experimental data. In Table 67 we give a simple example by considering the process $\rm gg \to H$ at lowest order and compare the traditional on-shell production cross section, see the l.h.s. of Eq.(143), with the production cross section as defined in the CPP-scheme. Therefore we only consider $\rm gg \to H$ at LO (i.e., $v = z$) and put H on its real mass shell or on the complex one. Below 300 GeV there is no visible difference, at 300 GeV the two results start to differ with an increasing gap up to 600 GeV after which there is a plateau of about 25% for higher values of $\mu_{\rm H}$.

Table 68: The effect of introducing a cut on the invariant mass of the initial-state partons.

$\mu_{\rm H}$[GeV]	v_c	σ^0[pb]	σ^j[pb]	σ^t[pb]	$\delta[\%]$
600	no cut	0.2677	0.1107	0.3784	
	1.001		0.0127	0.2804	74
	1.01		0.0473	0.3149	83
	1.05		0.0918	0.3595	95
700	no cut	0.1208	0.0469	0.1677	
	1.001		0.0054	0.1262	75
	1.01		0.0201	0.1409	84
	1.05		0.0391	0.1599	95
800	no cut	0.0632	0.0218	0.0850	
	1.001		0.0025	0.0657	77
	1.01		0.0094	0.0726	85
	1.05		0.0182	0.0814	96

Table 69: Comparison of the production cross sections in the OFFP-scheme (Eq.(152)) at 7 TeV and 8 TeV.

$\mu_{\rm H}$[GeV]	σ[pb] 7 TeV	σ[pb] 8 TeV	ratio
600	0.378	0.587	1.55
650	0.248	0.392	1.58
700	0.168	0.271	1.67
750	0.117	0.194	1.67
800	0.0850	0.145	1.77
850	0.0643	0.113	1.77
900	0.0509	0.0922	1.87

The production cross section in Eq.(158) is made of one term corresponding to $\rm gg \to H$ which we denote by σ^0 and terms with at least one additional jet, σ^j. The invariant mass of the two partons in the initial state is vs with $z < v < 1$, zs being the Higgs virtuality. In Table 68 we introduce a cut such that

$$z < v < \min\{v_c\, z\, ,\, 1\} \tag{167}$$

and study the dependence of the result on v_c by considering $\sigma^t = \sigma^0 + \sigma^j$ and $\delta = \sigma^t_c/\sigma^t$. The results show that a cut $z < v < 1.01\, z$ gives already 85% of the total answer.

Although a final decision will only be taken in January 2012 it looks more and more likely that LHC will run at 8 TeV in 2012; in Table 69 we have shown a comparison between production cross sections compute at 7 TeV and 8 TeV.

On the left-hand side of Figure 132 we compare the production cross section as computed with the OFFP-scheme of Eq.(152) or with the OFFBW-scheme of Eq.(150) for $\mu_{\rm H} = 600$ GeV. For the latter we use Breit–Wigner parameters in the OS-scheme (red curve) and in the Bar-scheme of Eq.(146) (blue curve). Deviations from the OFFP-scheme are maximal in the OS-scheme and much less pronounced in the Bar-scheme.

On the right-hand side of Figure 132 we show the effect of using dynamical QCD scales for the $\rm gg \to H + X \to H + \gamma\gamma$ cross section at $\mu_{\rm H} = 400$ GeV.

On the left-hand side of Figure 133 we consider the on-shell production cross section $\sigma^{\rm OS}(\rm pp \to H)$ (black curve) which includes convolution with PDFs. The blue curve gives the off-shell production cross section sampled over the (complex) Higgs propagator while the red curves is sampled over a Breit–Wigner distribution. The observed effect is substantial even in the low-mass region.

On the right-hand side of Figure 133 we show the differential K factor for the process $\mathrm{pp} \to (\mathrm{H} \to 4\,\mathrm{e}) + \mathrm{X}$, comparing the fixed-scale option, $\mu_{\mathrm{R}} = \mu_{\mathrm{F}} = M_{\mathrm{H}}/2$, and the running-scale option, $\mu_{\mathrm{R}} = \mu_{\mathrm{F}} = M(4\,\mathrm{e})/2$. For running QCD scales the K factor is practically constant over a wide range of the Higgs virtuality.

On the left-hand side of Figure 134 we show the normalised invariant-mass distribution in the OFFP-scheme with running QCD scales for 600 GeV (black), 700 GeV (blue), 800 GeV (red) in the windows $M_{\text{peak}} \pm 2\,\Gamma_{\mathrm{OS}}$, where M_{peak} is defined in Eq.(163).

Finally, on the right-hand side of Figure 134 we show the normalised invariant-mass distribution in the OFFP-scheme (blue) and OFFBW-scheme (red) with running QCD scales at 800 GeV in the window $M_{\text{peak}} \pm 2\,\Gamma_{\mathrm{OS}}$. The invariant-mass distribution in the OFFP-scheme with running QCD scales for 800 GeV in the window $M_{\text{peak}} \pm 2\,\Gamma_{\mathrm{OS}}$ is shown in Figure 135. The blue line refers to 8 TeV, the red one to 7 TeV.

15.5 QCD scale error

The conventional theoretical uncertainty associated with QCD scale variation is defined in Eq.(165). Let us consider the production cross section at 800 GeV in the OFFP-scheme with running or fixed QCD scales, we obtain

$$\text{RS} \quad 0.08497\,^{+13.7\%}_{-13.0\%}, \qquad \text{FS} \quad 0.07185\,^{+6.7\%}_{-8.5\%}. \tag{168}$$

The uncertainty with running scales is about twice the one where the scales are kept fixed. One might wonder which is the major source and we have done the following; in estimating the conventional uncertainty in the RS-option we keep $\mu_F^2 = \overline{\mu}^2 = zs/4$ and vary μ_{R} between $\overline{\mu}/2$ and $2\,\overline{\mu}$. The corresponding result is

$$\text{RS} \quad 0.08497\,^{+3.9\%}_{-4.4\%}, \qquad \mu_{\mathrm{R}} \quad \text{only}. \tag{169}$$

Therefore, the main source of uncertainty comes from varying the factorisation scale. However, in the fixed-scale option we obtain

$$\text{FS} \quad 0.07185\,^{+3.6\%}_{-4.4\%}, \qquad \mu_{\mathrm{R}} \quad \text{only} \tag{170}$$

and μ_{F} -variation is less dominant. In any case the question of which variation is dominating depends on the mass range; indeed, in the ONBW-scheme with fixed scales at 140 GeV we have

$$\begin{aligned} &\text{ONBW} \quad 12.27\,^{+11.1\%}_{-10.1\%}, \qquad \mu_{\mathrm{R}} \quad \text{and} \quad \mu_{\mathrm{F}}, \\ &\text{ONBW} \quad 12.27\,^{+8.7\%}_{-9.6\%}, \qquad \mu_{\mathrm{R}} \quad \text{only} \end{aligned} \tag{171}$$

showing μ_{R} dominance.

In order to compare this conventional definition of uncertainty with the work of Ref. [455] we recall their definition of $p\%$ credible interval; given a series

$$\sigma = \sum_{n=l}^{k} c_n\, \alpha_{\mathrm{s}}^n, \tag{172}$$

the $p\%$ credible interval $\sigma \pm \Delta\sigma^p$ is defined as

$$\begin{aligned} \Delta\sigma^p &= \alpha_s^{k+1}\, \max\left(\{c\}\right)\, \frac{n_c+1}{n_c}\, p\%, \qquad p\% < \frac{n_c}{n_c+1}, \\ \Delta\sigma^p &= \alpha_s^{k+1}\, \max\left(\{c\}\right)\, \Big[(n_c+1)\,(1-p\%)\Big]^{-1/n_c}, \qquad p\% > \frac{n_c}{n_c+1}, \end{aligned} \tag{173}$$

with $n_c = k - l + 1$. Using this definition we find that the $68\%(90\%)$ credible interval for μ_{R} uncertainty in the production cross section at 800 GeV is $3.1\%(5.3\%)$ in substantial agreement with the conventional method. For ONBW-scheme at 140 GeV the 90% credible interval for μ_{R} uncertainty is 8.0%. It could be interesting to extend the method of Ref. [455] to cover μ_{F} uncertainty.

15.6 Concluding remarks

In the last two decades many theoretical studies lead to improved estimates of the SM Higgs-boson total cross section at hadron colliders [66, 199, 213, 219, 352, 456] and of Higgs-boson partial decay widths [20]. Less work has been devoted to studying the Higgs-boson invariant-mass distribution (Higgs-boson lineshape).

In this section we made an attempt to resolve the problem by comparing different theoretical inputs to the off-shellness of the Higgs boson. There is no question at all that the zero-width approximation should be avoided, especially in the high-mass region where the on-shell width becomes of the same order as the on-shell mass.

The propagation of the off-shell H is usually parametrised in terms of some Breit–Wigner distribution (several variants are reported in the literature, Eq.(144) and Eq.(166)); we have shown evidence that only the Dyson-resummed propagator should be used, leading to the introduction of the H complex pole, a gauge-invariant property of the S-matrix.

Finally, when one accepts the idea that the Higgs boson is an off-shell intermediate state the question of the most appropriate choice of QCD scales arises. We have shown the effect of including dynamical choices for $\mu_{\rm R}, \mu_{\rm F}$ instead of a static choice.

For many purposes the well-known and convenient machinery of the on-shell approach can be employed, but one should become aware of its limitations and potential pitfalls. Although the basic comparison between different schemes was presented in this section, at this time we are repeating that differences should not be taken as the source of additional theoretical uncertainty; as a consequence, our recommendation is to use the OFFP-scheme described in Section 15.3.1 (see Eq.(152)) with running QCD scales.

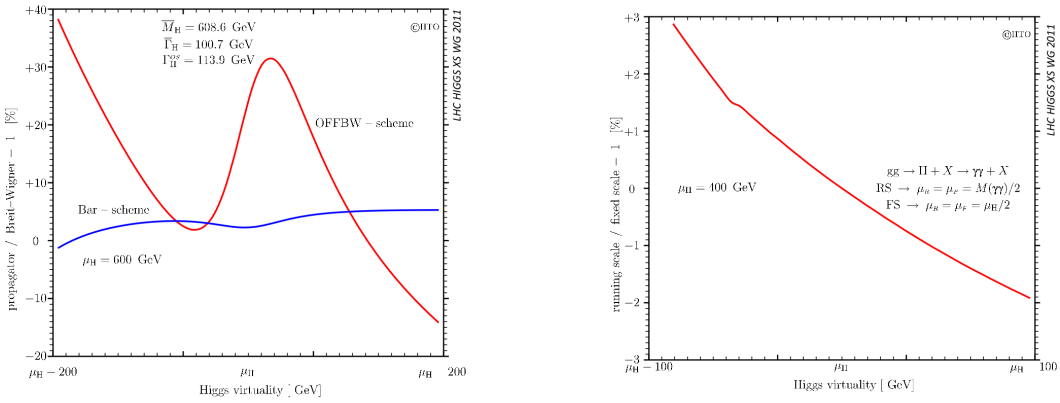

Fig. 132: In the left figure we show a comparison of production cross section as computed with the OFFP-scheme of Eq.(152) or with the OFFBW-scheme of Eq.(150). The red curve gives Breit–Wigner parameters in the OS-scheme and the blue one in the Bar-scheme of Eq.(146). In the right figure we show the effect of using dynamical QCD scales for the production cross section of Eqs.(155)–(157).

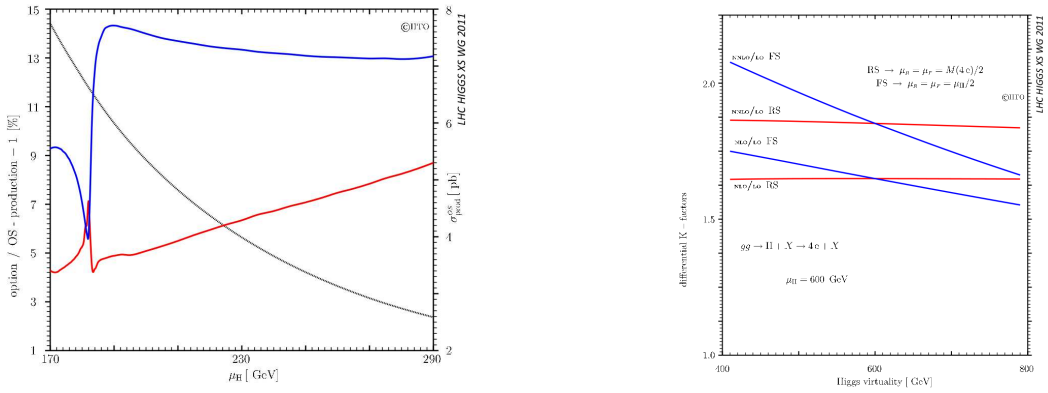

Fig. 133: In the left figure the blue curve gives the off-shell production cross section sampled over the (complex) Higgs propagator while the red curves is sampled over a Breit–Wigner distribution The right figure showes differential K factor for the process $\mathrm{pp} \to (\mathrm{H} \to 4\,\mathrm{e}) + \mathrm{X}$, comparing the fixed scale option, $\mu_\mathrm{R} = \mu_\mathrm{F} = M_\mathrm{H}/2$, and the running scale option, $\mu_\mathrm{R} = \mu_\mathrm{F} = M(4\,\mathrm{e})/2$.

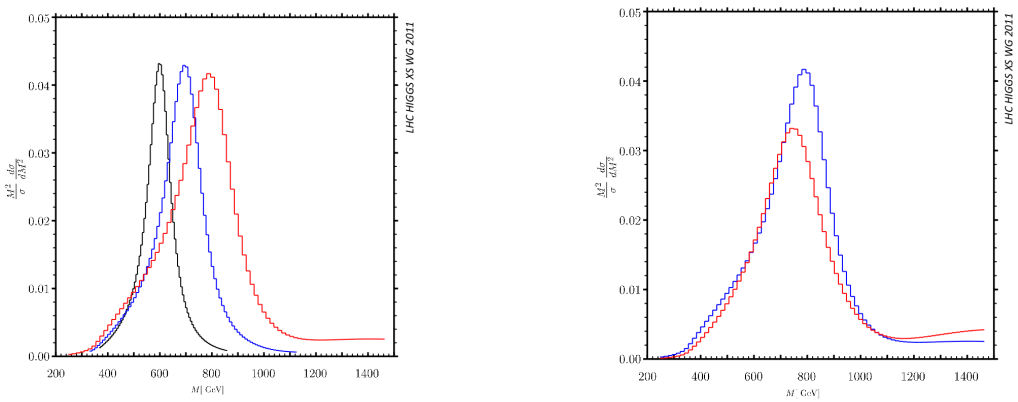

Fig. 134: The normalised invariant-mass distribution in the OFFP-scheme with running QCD scales (left) for 600 GeV (black), 700 GeV (blue), 800 GeV (red) in the windows $M_{\text{peak}} \pm 2\,\Gamma_{\text{OS}}$. The normalised invariant-mass distribution in the OFFP-scheme (blue) and OFFBW-scheme (red) with running QCD scales (right) at 800 GeV in the window $M_{\text{peak}} \pm 2\,\Gamma_{\text{OS}}$.

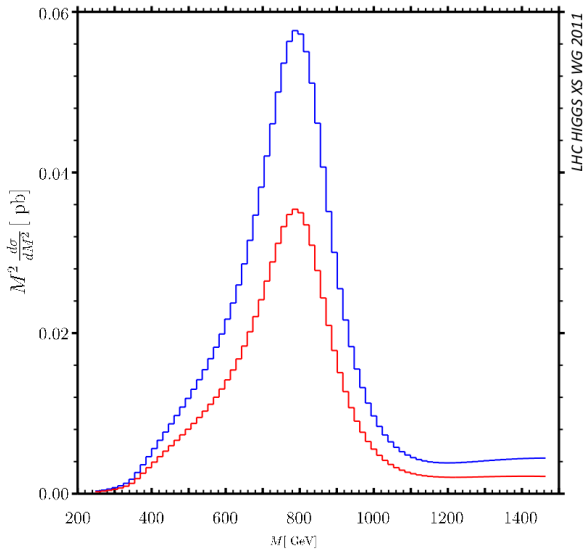

Fig. 135: The invariant-mass distribution in the OFFP-scheme with running QCD scales for 800 GeV in the window $M_{\text{peak}} \pm 2\,\Gamma_{\text{OS}}$. The blue line refers to 8 TeV, the red one to 7 TeV.

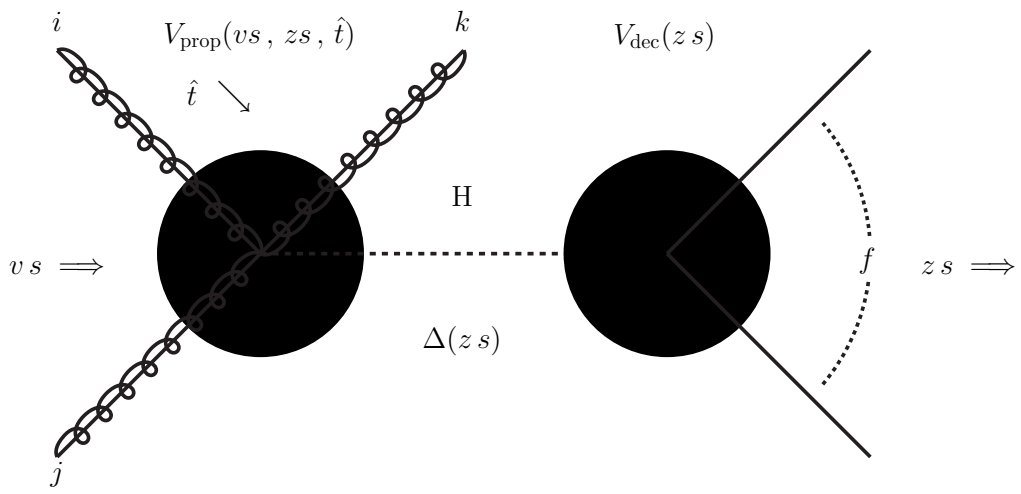

$$\Longrightarrow\ \sigma_{ij\to{\rm H}+k}(vs\,,\,\hat{t}\,,zs)\,\frac{vzs^2}{\left|zs-s_{\rm H}\right|^2}\,\frac{\Gamma_{{\rm H}\to f}(zs)}{(zs)^{1/2}}+{\rm NR}$$

$$=\ \sigma_{ij\to{\rm H}+k}(vs\,,\,\hat{t}\,,s_{\rm H})\,\frac{vs\left|s_{\rm H}\right|^{1/2}}{\left|zs-s_{\rm H}\right|^2}\,\Gamma_{{\rm H}\to f}(s_{\rm H})+{\rm NR}'$$

Fig. 136: The resonant part of the process $ij\to{\rm H}+k$ where i,j and k are partons (g or q). We distinguish between production, propagation and decay, indicating the explicit dependence on Mandelstam invariants. If s denotes the pp invariant mass we distinguish between vs, the ij invariant mass, zs, the Higgs-boson virtuality and $\hat{t}$ which is related to the Higgs-boson transverse momentum. Within NR we include the non-resonant contributions as well as their interference with the signal. NR includes those terms that are of higher order in the Laurent expansion of the signal around the complex pole. At NNLO QCD the parton k is a pair k_1-k_2, and more invariants are needed to characterise the production mechanism.

16 Conclusions[63]

The present document is the result of the activities at the Higgs boson cross section workshops in 2011. The LHC Higgs cross section working group was created in January 2010 as a new joint effort between ATLAS, CMS, and the theory community.

In the previous Report [7] we presented a description of cross sections computed at next-to-next-to-leading order (NNLO) or NLO, for each of the production modes.

Our goal in this second volume is to extend the previous studies to include differential cross sections. The motivation for such investigations is clear: Experimental analyses must impose cuts on the final state in order to extract the signal from background. A precise determination of the corresponding signal acceptance is needed. Hopefully, it is computed to the same order in the perturbative expansion as the inclusive cross section.

Therefore, this Report seeks to answer important questions about the computation of cross sections that include acceptance cuts and differential distributions for all final states that are considered in the Higgs search at the LHC.

The possible distributions of interest in the myriad studies performed at the LHC cover a broad spectrum. Our goal has been to identify and discuss the relevant issues that arise, and to give prescriptions for their solution. We must also stress that such prescriptions are not set in stone, but are subject to change if theoretical advances occur. If new more precise calculations become available, these new results will be incorporated into the relevant experimental investigations. It is our scientific mission and our raison d'être. Updated results will be made available at the TWiki page:
https://twiki.cern.ch/twiki/bin/view/LHCPhysics/CrossSections.

Here is a summary of our guidelines: collecting tools with combined experiment/theory expertise allowing controlled studies of different approaches; stimulate authors to incorporate new features/algorithms into their codes; understand differences between groups, which is even more important than continued improvements within groups; answer the general question 'if a theoretical calculation is done, but it cannot be used by any experimentalists, does it make a sound ?'

If the Higgs boson exists in the simple form invoked by the Standard Model it should start to show up in the data soon, but probably not strongly enough to claim a discovery. If the elusive boson is a mirage, experiments should be able to rule it out completely.

Alternative descriptions, such as some altogether different mechanism, are much more difficult to detect and, perhaps, less attractive. As we know from the history of science, this argument does not suffice to rule out the existence of such alternatives, and we should be ready to cope with the future. But that's another story, for another time, another Report.

Sed fugit interea fugit irreparabile tempus, singula dum capti circumvectamur amore

(But meanwhile it flees: time flees irretrievably, while we wander around, prisoners of our love of detail)

[63] S. Dittmaier, C. Mariotti, G. Passarino and R. Tanaka.

Acknowledgements

We are obliged to Ketevi Assamagan, Albert De Roeck, Eilam Gross, Andrey Korytov, Sandra Kortner, Bill Murray, Aleandro Nisati, Christoph Paus, Gigi Rolandi and Vivek Sharma for their support and encouragement.

We would like to thank Lance Dixon, Pietro Govoni, Andrea Massironi and Adrian Signer for discussions.

We are obliged to CERN, in particular to the IT Department and to the Theory Unit for the support with logistics, especially to Elena Gianolio for technical assistance.

S.Alekin, J. Blümlein and S. Moch have been supported on part by Helmholtz Gemeinschaft under contract VH-HA-101 (*Alliance Physics at the Terascale*), by the Deutsche Forschungsgemeinschaft in Sonderforschungsbereich/Transregio 9, by the European Commission through contract PITN-GA-2010$-$264564 (*LHCPhenoNet*), and by the Russian Foundation for Basic Research under contract RFFI $08-02-91024$ CERN_a.

A. Bagnaschi, G. Degrassi, P. Slavich and A. Vicini are supported by the Research Executive Agency (REA) of the European Union under the Grant Agreement number PITN-GA-2010 $-$ 264564 (LHCPhenoNet).

M.V. Garzelli, A. Kardos, and Z. Trócsány are supported in part by the LHCPhenoNet network PITN-GA-2010 $-$ 264564, the Swiss National Science Foundation Joint Research Project SCOPES IZ73$Z0$_1/28079, and the TÁMOP $4.2.1./B-09/1/$KONV-2010 $-$ 0007 project.

M.V. Garzelli is supported in part by the MEC project FPA $2008-02984$.

S. Heinemeyer is supported in part by CICYT (grant FPA $2010--22163-C02-01$) and by the Spanish MICINN's Consolider-Ingenio 2010 Program under grant MultiDark CSD2009 $-$ 00064.

J. Huston would like to acknowledge National Science Foundation grant PHY-1068318

C.B. Jackson, H. Kim and J. Yu thank the U.S. Department of Energy and the University of Texas at Arlington for the support.

P. Jimenez-Delgado research is supported in part by the Swiss National Science Foundation (SNF) under contract $200020-138206$.

M. Krämer, M. Mühlleitner and M. Ubiali are supported by the DFG SFB/TR9 "Computational Particle Physics".

P. Nadolsky at SMU was supported in part by the U.S. DOE Early Career Research Award DE-SC0003870 and by Lightner-Sams Foundation.

G. Passarino is supported by Ministero dell'Istruzione, dell'Università e della Ricerca Protocollo 2008H8F9RA002.

F. Petriello is supported by the US DOE under contract DE-AC02 $-$ $06CH11357$ and the grant DE-FG02 $-$ $91ER40684$.

L. Reina is partially supported by the US DOE grant DE-FG02 $-$ $97IR41022$.

J. Rojo has been supported by a Marie Curie Intra–European Fellowship of the European Community's 7th Framework Programme under contract number PIEF-GA-2010 $-$ 272515.

G. Salam is supported in part by grant ANR-09-BLAN-0060 from the French Agence Nationale de la Recherche.

M. Schönherr's is supported by the Research Executive Agency (REA) of the European Union under the Grant Agreement number PITN-GA-2010 $-$ 264564 (LHCPhenoNet).

F. Siegert is supported by the German Research Foundation (DFG) via grant DI 784/2-1.

I. Stewart is supported by the Office of Nuclear Physics of the U.S. Department of Energy under the grant DE-FG02 $-$ $94ER40818$.

R. S. Thorne is supported partly by the London Centre for Terauniverse Studies (LCTS), using funding from the European Research Council via the Advanced Investigator Grant 267352, and travel to LHC-Higgs Working Group meetings by an IPPP (Durham) Research Associateship.

T. Vickey is supported by the Oxford Oppenheimer Fund, the Royal Society of the United Kingdom and the National Research Foundation of the Republic of South Africa.

W. Waalewijn is supported by the US DOE grant DE-FG02 $-$ 90ER40546.

D. Wackeroth is partially supported by the National Science Foundation under grants NSF-PHY-0547564 and NSF-PHY-0757691.

M. Warsinsky acknowledges the support of the Initiative and Networking Fund of the Helmholtz Association, contract HA-101 (Physics at the Terascale).

References

[1] F. Englert and R. Brout, *Broken symmetry and the mass of gauge vector mesons*, Phys. Rev. Lett. **13** (1964) 321–323.

[2] P. W. Higgs, *Broken symmetries, massless particles and gauge fields*, Phys. Lett. **12** (1964) 132–133.

[3] P. W. Higgs, *Broken symmetries and the masses of gauge bosons*, Phys. Rev. Lett. **13** (1964) 508–509.

[4] G. Guralnik, C. Hagen, and T. Kibble, *Global conservation laws and massless particles*, Phys. Rev. Lett. **13** (1964) 585–587.

[5] P. W. Higgs, *Spontaneous symmetry breakdown without massless bosons*, Phys. Rev. **145** (1966) 1156–1163.

[6] T. Kibble, *Symmetry breaking in non-Abelian gauge theories*, Phys. Rev. **155** (1967) 1554–1561.

[7] LHC Higgs Cross Section Working Group, S. Dittmaier, C. Mariotti, G. Passarino, and R. Tanaka (Eds.), *Handbook of LHC Higgs Cross Sections: 1. Inclusive Observables*, CERN-2011-002 (CERN, Geneva, 2011) , `arXiv:1101.0593 [hep-ph]`.

[8] *The Standard Model input parameters can be found at LHC Higgs Cross Section Working Group*, `https://twiki.cern.ch/twiki/bin/view/LHCPhysics/SMInputParameter`.

[9] ATLAS and CMS Collaborations, *Combined Standard Model Higgs boson searches with up to* $2.3\,fb^{-1}$ *of* pp *collisions at* $\sqrt{s} = 7$ *TeV at the LHC*, ATLAS-CONF-2011-157, CMS-PAS-HIG-11-023 (2011) .

[10] M. S. Carena, S. Heinemeyer, C. E. M. Wagner, and G. Weiglein, *Suggestions for benchmark scenarios for MSSM Higgs boson searches at hadron colliders*, Eur. Phys. J. **C26** (2003) 601–607, `arXiv:hep-ph/0202167`.

[11] ATLAS Collaboration, G. Aad et al., *Expected Performance of the ATLAS Experiment - Detector, Trigger and Physics*, `arXiv:0901.0512 [hep-ex]`.

[12] CMS Collaboration, G. L. Bayatian et al., *CMS technical design report, volume II: Physics performance*, J. Phys. **G34** (2007) 995–1579.

[13] M. Dührssen et al., *Extracting Higgs boson couplings from LHC data*, Phys. Rev. **D70** (2004) 113009, `arXiv:hep-ph/0406323`.

[14] A. Denner, S. Heinemeyer, I. Puljak, D. Rebuzzi, and M. Spira, *Standard Model Higgs-Boson Branching Ratios with Uncertainties*, Eur.Phys.J. **C71** (2011) 1753, `arXiv:1107.5909 [hep-ph]`.

[15] A. Djouadi, J. Kalinowski, and M. Spira, *HDECAY: A program for Higgs boson decays in the Standard Model and its supersymmetric extension*, Comput. Phys. Commun. **108** (1998) 56–74, `arXiv:hep-ph/9704448`.

[16] M. Spira, *QCD effects in Higgs physics*, Fortschr. Phys. **46** (1998) 203–284, `arXiv:hep-ph/9705337`.

[17] A. Djouadi, J. Kalinowski, M. Mühlleitner, and M. Spira, *An update of the program HDECAY*, in *The Les Houches 2009 workshop on TeV colliders: The tools and Monte Carlo working group summary report*. 2010. `arXiv:1003.1643 [hep-ph]`.

[18] A. Bredenstein, A. Denner, S. Dittmaier, and M. M. Weber, *Precise predictions for the Higgs-boson decay* $H \to WW/ZZ \to 4$ *leptons*, Phys. Rev. **D74** (2006) 013004, `arXiv:hep-ph/0604011`.

[19] A. Bredenstein, A. Denner, S. Dittmaier, and M. Weber, *Radiative corrections to the semileptonic and hadronic Higgs-boson decays* $H \to WW/ZZ \to 4$ *fermions*, JHEP **02** (2007) 080, `arXiv:hep-ph/0611234 [hep-ph]`.

[20] A. Bredenstein, A. Denner, S. Dittmaier, A. Mück, and M. M. Weber, *Prophecy4f: A Monte*

Carlo generator for a proper description of the Higgs decay into 4 fermions, `http://omnibus.uni-freiburg.de/~sd565/programs/prophecy4f/prophecy4f.html`, 2010.

[21] A. Ghinculov, *Two loop heavy Higgs correction to Higgs decay into vector bosons*, Nucl. Phys. **B455** (1995) 21–38, `arXiv:hep-ph/9507240 [hep-ph]`.

[22] A. Frink, B. A. Kniehl, D. Kreimer, and K. Riesselmann, *Heavy Higgs lifetime at two loops*, Phys. Rev. **D54** (1996) 4548–4560, `arXiv:hep-ph/9606310 [hep-ph]`.

[23] U. Aglietti, R. Bonciani, G. Degrassi, and A. Vicini, *Master integrals for the two-loop light fermion contributions to $gg \to H$ and $H \to \gamma\gamma$*, Phys. Lett. **B600** (2004) 57–64, `arXiv:hep-ph/0407162`.

[24] U. Aglietti, R. Bonciani, G. Degrassi, and A. Vicini, *Two-loop light fermion contribution to Higgs production and decays*, Phys. Lett. **B595** (2004) 432–441, `arXiv:hep-ph/0404071`.

[25] U. Aglietti et al., *Tevatron for LHC report: Higgs*, `arXiv:hep-ph/0612172`.

[26] G. Degrassi and F. Maltoni, *Two-loop electroweak corrections to Higgs production at hadron colliders*, Phys. Lett. **B600** (2004) 255–260, `arXiv:hep-ph/0407249`.

[27] G. Degrassi and F. Maltoni, *Two-loop electroweak corrections to the Higgs-boson decay $H\to \gamma\gamma$*, Nucl. Phys. **B724** (2005) 183–196, `arXiv:hep-ph/0504137`.

[28] S. Actis, G. Passarino, C. Sturm, and S. Uccirati, *NLO electroweak corrections to Higgs boson production at hadron colliders*, Phys. Lett. **B670** (2008) 12–17, `arXiv:0809.1301 [hep-ph]`.

[29] S. Actis, G. Passarino, C. Sturm, and S. Uccirati, *NNLO computational techniques: The cases $H \to \gamma\gamma$ and $H \to gg$*, Nucl. Phys. **B811** (2009) 182–273, `arXiv:0809.3667 [hep-ph]`.

[30] S. Narison, *A Fresh look into the heavy quark mass values*, Phys.Lett. **B341** (1994) 73–83, `arXiv:hep-ph/9408376 [hep-ph]`.

[31] S. Bethke, *The 2009 World Average of $\alpha_s(M_Z)$*, Eur. Phys. J. **C64** (2009) 689–703, `arXiv:0908.1135 [hep-ph]`.

[32] Particle Data Group Collaboration, K. Nakamura et al., *Review of particle physics*, J. Phys. **G37** (2010) 075021.

[33] J. H. Kuhn, M. Steinhauser, and C. Sturm, *Heavy quark masses from sum rules in four-loop approximation*, Nucl. Phys. **B778** (2007) 192–215, `arXiv:hep-ph/0702103`.

[34] K. Chetyrkin et al., *Precise charm- and bottom-quark masses: Theoretical and experimental uncertainties*, `arXiv:1010.6157 [hep-ph]`.

[35] A. Signer, private communication.

[36] B. Dehnadi, A. H. Hoang, V. Mateu, and S. M. Zebarjad, *Charm mass determination from QCD charmonium sum rules at order α_s^3*, `arXiv:1102.2264 [hep-ph]`.

[37] CDF and D0 Collaboration, and others, *Combination of CDF and D0 results on the mass of the top quark*, `arXiv:1007.3178 [hep-ex]`.

[38] S. Gorishnii, A. Kataev, S. Larin, and L. Surguladze, *Corrected three loop QCD correction to the correlator of the quark scalar current and $\Gamma_{tot}(H \to hadrons)$*, Mod. Phys. Lett. **A5** (1990) 2703–2712.

[39] S. Gorishnii, A. Kataev, S. Larin, and L. Surguladze, *Scheme dependence of the next to next-to-leading QCD corrections to $\Gamma_{tot}(H \to hadrons)$ and the spurious QCD infrared fixed point*, Phys. Rev. **D43** (1991) 1633–1640.

[40] A. L. Kataev and V. T. Kim, *The effects of the QCD corrections to $\Gamma(H \to \mathrm{b\bar{b}})$*, Mod. Phys. Lett. **A9** (1994) 1309–1326. Revised version of ENSLAPP-A-407-92.

[41] L. R. Surguladze, *Quark mass effects in fermionic decays of the Higgs boson in O (α_s^2) perturbative QCD*, Phys. Lett. **B341** (1994) 60–72, `arXiv:hep-ph/9405325 [hep-ph]`.

[42] S. Larin, T. van Ritbergen, and J. Vermaseren, *The large top quark mass expansion for Higgs*

boson decays into bottom quarks and into gluons, Phys. Lett. **B362** (1995) 134–140, `arXiv:hep-ph/9506465 [hep-ph]`.

[43] K. Chetyrkin and A. Kwiatkowski, *Second order QCD corrections to scalar and pseudoscalar Higgs decays into massive bottom quarks*, Nucl. Phys. **B461** (1996) 3–18, `arXiv:hep-ph/9505358 [hep-ph]`.

[44] K. Chetyrkin, *Correlator of the quark scalar currents and* $\Gamma_{tot}(H \to hadrons)$ *at O* (α_s^3) *in pQCD*, Phys. Lett. **B390** (1997) 309–317, `arXiv:hep-ph/9608318 [hep-ph]`.

[45] P. A. Baikov, K. G. Chetyrkin, and J. H. Kuhn, *Scalar correlator at O*(α_s^4)*, Higgs decay into b-quarks and bounds on the light quark masses*, Phys. Rev. Lett. **96** (2006) 012003, `arXiv:hep-ph/0511063`.

[46] J. Fleischer and F. Jegerlehner, *Radiative corrections to Higgs decays in the extended Weinberg-Salam model*, Phys. Rev. **D23** (1981) 2001–2026.

[47] D. Bardin, B. Vilensky, and P. Khristova, *Calculation of the Higgs boson decay width into fermion pairs*, Sov. J. Nucl. Phys. **53** (1991) 152–158.

[48] A. Dabelstein and W. Hollik, *Electroweak corrections to the fermionic decay width of the standard Higgs boson*, Z. Phys. **C53** (1992) 507–516.

[49] B. A. Kniehl, *Radiative corrections for* $H \to f\bar{f}\,(\gamma)$ *in the Standard Model*, Nucl. Phys. **B376** (1992) 3–28.

[50] A. Djouadi, D. Haidt, B. A. Kniehl, P. M. Zerwas, and B. Mele, *Higgs in the Standard Model*, . In *Munich/Annecy/Hamburg 1991, Proceedings, e^+e^- collisions at 500 GeV, pt. A* 11-30.

[51] E. Braaten and J. P. Leveille, *Higgs boson decay and the running mass*, Phys. Rev. **D22** (1980) 715.

[52] N. Sakai, *Perturbative QCD corrections to the hadronic decay width of the Higgs boson*, Phys. Rev. **D22** (1980) 2220.

[53] T. Inami and T. Kubota, *Renormalization group estimate of the hadronic decay width of the Higgs boson*, Nucl. Phys. **B179** (1981) 171.

[54] S. Gorishnii, A. Kataev, and S. Larin, *The width of Higgs boson decay into hadrons: Three loop corrections of strong interactions*, Sov. J. Nucl. Phys. **40** (1984) 329–334.

[55] M. Drees and K.-i. Hikasa, *Heavy quark thresholds in Higgs physics*, Phys. Rev. **D41** (1990) 1547.

[56] M. Drees and K.-i. Hikasa, *Note on QCD corrections to hadronic Higgs decay*, Phys. Lett. **B240** (1990) 455.

[57] M. Drees and K.-i. Hikasa, *Erratum: Note on QCD corrections to hadronic Higgs decay*, Phys. Lett. **B262** (1991) 497.

[58] A. Ghinculov, *Two loop heavy Higgs corrections to the Higgs fermionic width*, Phys. Lett. **B337** (1994) 137–140, `arXiv:hep-ph/9405394 [hep-ph]`.

[59] A. Ghinculov, *Erratum: Two loop heavy Higgs corrections to the Higgs fermionic width*, Phys. Lett. **B346** (1995) 426, `arXiv:hep-ph/9405394 [hep-ph]`.

[60] L. Durand, K. Riesselmann, and B. A. Kniehl, *Onset of strong interactions in the Higgs sector of the Standard Model:* $H \to f\bar{f}$ *at two loops*, Phys. Rev. Lett. **72** (1994) 2534–2537.

[61] L. Durand, K. Riesselmann, and B. A. Kniehl, *Erratum:Onset of strong interactions in the Higgs sector of the Standard Model:* $H \to f\bar{f}$ *at two loops*, Phys. Rev. Lett. **74** (1995) 1699.

[62] L. Durand, B. A. Kniehl, and K. Riesselmann, *Two loop O*$(G_F^2 M_H^4)$ *corrections to the fermionic decay rates of the Higgs boson*, Phys. Rev. **D51** (1995) 5007–5015, `arXiv:hep-ph/9412311 [hep-ph]`.

[63] V. Borodulin and G. Jikia, *Analytic evaluation of two loop renormalization constants of enhanced electroweak strength in the Higgs sector of the Standard Model*,

Phys. Lett. **B391** (1997) 434–440, arXiv:hep-ph/9609447 [hep-ph].

[64] T. Inami, T. Kubota, and Y. Okada, *Effective gauge theory and the effect of heavy quarks in Higgs boson decay*, Z. Phys. **C18** (1983) 69.

[65] A. Djouadi, M. Spira, and P. Zerwas, *Production of Higgs bosons in proton colliders: QCD corrections*, Phys.Lett. **B264** (1991) 440–446.

[66] M. Spira, A. Djouadi, D. Graudenz, and P. Zerwas, *Higgs boson production at the LHC*, Nucl.Phys. **B453** (1995) 17–82, arXiv:hep-ph/9504378 [hep-ph].

[67] K. Chetyrkin, B. A. Kniehl, and M. Steinhauser, *Hadronic Higgs decay to order α_s^4*, Phys. Rev. Lett. **79** (1997) 353–356, arXiv:hep-ph/9705240 [hep-ph].

[68] P. Baikov and K. Chetyrkin, *Higgs decay into hadrons to order α_s^5*, Phys. Rev. Lett. **97** (2006) 061803, arXiv:hep-ph/0604194 [hep-ph].

[69] H.-Q. Zheng and D.-D. Wu, *First order QCD corrections to the decay of the Higgs boson into two photons*, Phys. Rev. **D42** (1990) 3760–3763.

[70] A. Djouadi, M. Spira, J. van der Bij, and P. Zerwas, *QCD corrections to $\gamma\gamma$ decays of Higgs particles in the intermediate mass range*, Phys. Lett. **B257** (1991) 187–190.

[71] S. Dawson and R. Kauffman, *QCD corrections to $H \to \gamma\gamma$*, Phys. Rev. **D47** (1993) 1264–1267.

[72] A. Djouadi, M. Spira, and P. Zerwas, *Two photon decay widths of Higgs particles*, Phys. Lett. **B311** (1993) 255–260, arXiv:hep-ph/9305335 [hep-ph].

[73] K. Melnikov and O. I. Yakovlev, *Higgs $\to$ two photon decay: QCD radiative correction*, Phys. Lett. **B312** (1993) 179–183, arXiv:hep-ph/9302281 [hep-ph].

[74] M. Inoue, R. Najima, T. Oka, and J. Saito, *QCD corrections to two photon decay of the Higgs boson and its reverse process*, Mod. Phys. Lett. **A9** (1994) 1189–1194.

[75] A. Firan and R. Stroynowski, *Internal conversions in Higgs decays to two photons*, Phys. Rev. **D76** (2007) 057301, arXiv:0704.3987 [hep-ph].

[76] M. Spira, A. Djouadi, and P. M. Zerwas, *QCD corrections to the $HZ\gamma$ coupling*, Phys. Lett. **B276** (1992) 350–353.

[77] S. Heinemeyer, W. Hollik, and G. Weiglein, *FeynHiggs: A program for the calculation of the masses of the neutral CP-even Higgs bosons in the MSSM*, Comput. Phys. Commun. **124** (2000) 76–89, arXiv:hep-ph/9812320.

[78] S. Heinemeyer, W. Hollik, and G. Weiglein, *The masses of the neutral CP-even Higgs bosons in the MSSM: Accurate analysis at the two loop level*, Eur. Phys. J. **C9** (1999) 343–366, arXiv:hep-ph/9812472.

[79] G. Degrassi, S. Heinemeyer, W. Hollik, P. Slavich, and G. Weiglein, *Towards high-precision predictions for the MSSM Higgs sector*, Eur. Phys. J. **C28** (2003) 133–143, arXiv:hep-ph/0212020.

[80] M. Frank, T. Hahn, S. Heinemeyer, W. Hollik, H. Rzehak, et al., *The Higgs boson masses and mixings of the complex MSSM in the Feynman-diagrammatic approach*, JHEP **02** (2007) 047, arXiv:hep-ph/0611326 [hep-ph].

[81] J. S. Lee et al., *CPsuperH: A computational tool for Higgs phenomenology in the minimal supersymmetric Standard Model with explicit CP violation*, Comput. Phys. Commun. **156** (2004) 283–317, arXiv:hep-ph/0307377.

[82] J. S. Lee, M. Carena, J. Ellis, A. Pilaftsis, and C. E. M. Wagner, *CPsuperH2.0: An improved computational tool for Higgs phenomenology in the MSSM with explicit CP violation*, Comput. Phys. Commun. **180** (2009) 312–331, arXiv:0712.2360 [hep-ph].

[83] P. Z. Skands, B. Allanach, H. Baer, C. Balazs, G. Belanger, et al., *SUSY Les Houches accord: Interfacing SUSY spectrum calculators, decay packages, and event generators*, JHEP **07** (2004) 036, arXiv:hep-ph/0311123 [hep-ph].

[84] B. Allanach, C. Balazs, G. Belanger, M. Bernhardt, F. Boudjema, et al., *SUSY Les Houches Accord 2*, Comput.Phys.Commun. **180** (2009) 8–25, arXiv:0801.0045 [hep-ph].

[85] S. AbdusSalam, B. Allanach, H. Dreiner, J. Ellis, U. Ellwanger, et al., *Benchmark models, planes, lines and points for future SUSY searches at the LHC*, arXiv:1109.3859 [hep-ph].

[86] K. E. Williams, H. Rzehak, and G. Weiglein, *Higher order corrections to Higgs boson decays in the MSSM with complex parameters*, Eur.Phys.J. **C71** (2011) 1669, arXiv:1103.1335 [hep-ph].

[87] A. Dabelstein, *Fermionic decays of neutral MSSM Higgs bosons at the one loop level*, Nucl.Phys. **B456** (1995) 25–56, arXiv:hep-ph/9503443 [hep-ph].

[88] J. A. Coarasa Perez, R. A. Jimenez, and J. Sola, *Strong effects on the hadronic widths of the neutral Higgs bosons in the MSSM*, Phys.Lett. **B389** (1996) 312–320, arXiv:hep-ph/9511402 [hep-ph].

[89] H. Eberl, K. Hidaka, S. Kraml, W. Majerotto, and Y. Yamada, *Improved SUSY QCD corrections to Higgs boson decays into quarks and squarks*, Phys.Rev. **D62** (2000) 055006, arXiv:hep-ph/9912463 [hep-ph].

[90] J. Guasch, P. Häfliger, and M. Spira, *MSSM Higgs decays to bottom quark pairs revisited*, Phys. Rev. **D68** (2003) 115001, arXiv:hep-ph/0305101.

[91] D. Noth and M. Spira, *Higgs boson couplings to bottom quarks: Two-loop supersymmetry-QCD corrections*, Phys. Rev. Lett. **101** (2008) 181801, arXiv:0808.0087 [hep-ph].

[92] D. Noth and M. Spira, *Supersymmetric Higgs Yukawa couplings to bottom quarks at next-to-next-to-leading order*, JHEP **06** (2011) 084, arXiv:1001.1935 [hep-ph].

[93] L. Mihaila and C. Reisser, *$O(\alpha_s^2)$ corrections to fermionic Higgs decays in the MSSM*, JHEP **08** (2010) 021, arXiv:arXiv:1007.0693 [hep-ph].

[94] M. Mühlleitner and M. Spira, *Higgs boson production via gluon fusion: squark loops at NLO QCD*, Nucl. Phys. **B790** (2008) 1–27, arXiv:hep-ph/0612254 [hep-ph].

[95] R. D. Ball et al., *Impact of heavy quark masses on parton distributions and LHC phenomenology*, Nucl. Phys. **B849** (2011) 296–363, arXiv:1101.1300 [hep-ph].

[96] R. D. Ball et al., *A first unbiased global NLO determination of parton distributions and their uncertainties*, Nucl. Phys. **B838** (2010) 136–206, arXiv:1002.4407 [hep-ph].

[97] S. Forte, E. Laenen, P. Nason, and J. Rojo, *Heavy quarks in deep-inelastic scattering*, Nucl.Phys. **B834** (2010) 116–162, arXiv:1001.2312 [hep-ph].

[98] The NNPDF Collaboration Collaboration, R. D. Ball et al., *Unbiased global determination of parton distributions and their uncertainties at NNLO and at LO*, Nucl.Phys. **B855** (2012) 153–221, arXiv:1107.2652 [hep-ph].

[99] A. Cooper-Sarkar, *Proton structure from HERA to LHC*, arXiv:1012.1438 [hep-ph].

[100] H1 and ZEUS Collaboration, F. D. Aaron et al., *Combined measurement and QCD analysis of the inclusive ep scattering cross sections at HERA*, JHEP **01** (2010) 109, arXiv:0911.0884 [hep-ex].

[101] M. Botje et al., *The PDF4LHC working group interim recommendations*, arXiv:1101.0538 [hep-ph].

[102] *PDF4LHC steering committee*, http://www.hep.ucl.ac.uk/pdf4lhc/, 2010.

[103] P. M. Nadolsky et al., *Implications of CTEQ global analysis for collider observables*, Phys. Rev. **D78** (2008) 013004, arXiv:0802.0007 [hep-ph].

[104] H.-L. Lai et al., *New parton distributions for collider physics*, arXiv:1007.2241 [hep-ph].

[105] J. M. Campbell and R. K. Ellis, *Radiative corrections to $Zb\bar{b}$ production*, Phys. Rev. **D62** (2000) 114012, arXiv:hep-ph/0006304.

[106] J. Campbell and R. K. Ellis, *Next-to-leading order corrections to W+2jet and Z+2jet production*

at hadron colliders, Phys. Rev. **D65** (2002) 113007, arXiv:hep-ph/0202176.

[107] A. D. Martin, W. J. Stirling, R. S. Thorne, and G. Watt, *Parton distributions for the LHC*, Eur. Phys. J. **C63** (2009) 189–285, arXiv:0901.0002 [hep-ph].

[108] M. Glück, P. Jimenez-Delgado, and E. Reya, *Dynamical parton distributions of the nucleon and very small-x physics*, Eur. Phys. J. **C53** (2008) 355–366, arXiv:0709.0614 [hep-ph].

[109] M. G̈luck, P. Jimenez-Delgado, E. Reya, and C. Schuck, *On the role of heavy flavor parton distributions at high energy colliders*, Phys. Lett. **B664** (2008) 133–138, arXiv:0801.3618 [hep-ph].

[110] S. Alekhin, J. Blümlein, S. Klein, and S. Moch, *The 3-, 4-, and 5-flavor NNLO parton from deep-inelastic-scattering data and at hadron colliders*, Phys. Rev. **D81** (2010) 014032, arXiv:0908.2766 [hep-ph].

[111] J. Pumplin et al., *Uncertainties of predictions from parton distribution functions. 2. The Hessian method*, Phys. Rev. **D65** (2001) 014013, arXiv:hep-ph/0101032.

[112] F. Demartin, S. Forte, E. Mariani, J. Rojo, and A. Vicini, *The impact of PDF and α_s uncertainties on Higgs production in gluon fusion at hadron colliders*, Phys. Rev. **D82** (2010) 014002, arXiv:1004.0962 [hep-ph].

[113] *PDF Correlation Tables*, https://twiki.cern.ch/twiki/bin/view/LHCPhysics/PDFCorrelations.

[114] A. D. Martin, W. J. Stirling, R. S. Thorne, and G. Watt, *Uncertainties on α_s in global PDF analyses and implications for predicted hadronic cross sections*, Eur. Phys. J. **C64** (2009) 653–680, arXiv:0905.3531 [hep-ph].

[115] H.-L. Lai et al., *Uncertainty induced by QCD coupling in the CTEQ global analysis of parton distributions*, arXiv:1004.4624 [hep-ph].

[116] S. Frixione and B. R. Webber, *Matching NLO QCD computations and parton shower simulations*, JHEP **06** (2002) 029, arXiv:hep-ph/0204244.

[117] S. Frixione, P. Nason, and B. R. Webber, *Matching NLO QCD and parton showers in heavy flavour production*, JHEP **08** (2003) 007, arXiv:hep-ph/0305252.

[118] S. Frixione, E. Laenen, P. Motylinski, and B. R. Webber, *Single-top production in MC@NLO*, JHEP **03** (2006) 092, arXiv:hep-ph/0512250.

[119] S. Frixione and B. R. Webber, *The MC@NLO 3.3 event generator*, arXiv:hep-ph/0612272.

[120] S. Frixione, E. Laenen, P. Motylinski, and B. R. Webber, *Angular correlations of lepton pairs from vector boson and top quark decays in Monte Carlo simulations*, JHEP **04** (2007) 081, arXiv:hep-ph/0702198.

[121] S. Frixione, E. Laenen, P. Motylinski, B. R. Webber, and C. D. White, *Single-top hadroproduction in association with a W boson*, JHEP **07** (2008) 029, arXiv:0805.3067 [hep-ph].

[122] O. Latunde-Dada, *Herwig Monte Carlo at next-to-leading order for e^+e^- annihilation and lepton pair production*, JHEP **11** (2007) 040, arXiv:0708.4390 [hep-ph].

[123] P. Nason, *A new method for combining NLO QCD with shower Monte Carlo algorithms*, JHEP **11** (2004) 040, arXiv:hep-ph/0409146.

[124] P. Nason and G. Ridolfi, *A positive-weight next-to-leading-order Monte Carlo for Z pair hadroproduction*, JHEP **08** (2006) 077, arXiv:hep-ph/0606275.

[125] S. Frixione, P. Nason, and G. Ridolfi, *The POWHEG-hvq manual version 1.0*, arXiv:0707.3081 [hep-ph].

[126] S. Frixione, P. Nason, and C. Oleari, *Matching NLO QCD computations with parton shower simulations: The POWHEG method*, JHEP **11** (2007) 070, arXiv:0709.2092 [hep-ph].

[127] S. Frixione, P. Nason, and G. Ridolfi, *A positive-weight next-to-leading-order Monte Carlo for*

heavy flavour hadroproduction, JHEP **09** (2007) 126, arXiv:0707.3088 [hep-ph].

[128] O. Latunde-Dada, S. Gieseke, and B. Webber, *A positive-weight next-to-leading-order Monte Carlo for e^+e^- annihilation to hadrons*, JHEP **02** (2007) 051, arXiv:hep-ph/0612281.

[129] K. Hamilton, P. Richardson, and J. Tully, *A positive-weight next-to-leading order Monte Carlo simulation of Drell-Yan vector boson production*, JHEP **10** (2008) 015, arXiv:0806.0290 [hep-ph].

[130] K. Hamilton, P. Richardson, and J. Tully, *A positive-weight next-to-leading order Monte Carlo simulation for Higgs boson production*, JHEP **04** (2009) 116, arXiv:0903.4345 [hep-ph].

[131] S. Alioli, P. Nason, C. Oleari, and E. Re, *NLO vector-boson production matched with shower in POWHEG*, JHEP **07** (2008) 060, arXiv:0805.4802 [hep-ph].

[132] S. Alioli, P. Nason, C. Oleari, and E. Re, *NLO Higgs boson production via gluon fusion matched with shower in POWHEG*, JHEP **04** (2009) 002, arXiv:0812.0578 [hep-ph].

[133] S. Alioli, P. Nason, C. Oleari, and E. Re, *NLO single-top production matched with shower in POWHEG: s- and t-channel contributions*, JHEP **09** (2009) 111, arXiv:0907.4076 [hep-ph].

[134] O. Latunde-Dada, *Applying the POWHEG method to top pair production and decays at the ILC*, Eur. Phys. J. **C58** (2008) 543–554, arXiv:0806.4560 [hep-ph].

[135] S. Alioli, P. Nason, C. Oleari, and E. Re, *Vector boson plus one jet production in POWHEG*, JHEP **01** (2011) 095, arXiv:1009.5594 [hep-ph].

[136] S. Hoche, F. Krauss, M. Schonherr, and F. Siegert, *NLO matrix elements and truncated showers*, JHEP **08** (2011) 123, arXiv:1009.1127 [hep-ph].

[137] S. Frixione, F. Stoeckli, P. Torrielli, and B. R. Webber, *NLO QCD corrections in Herwig++ with MC@NLO*, JHEP **01** (2011) 053, arXiv:1010.0568 [hep-ph].

[138] P. Torrielli and S. Frixione, *Matching NLO QCD computations with PYTHIA using MC@NLO*, JHEP **04** (2010) 110, arXiv:1002.4293 [hep-ph].

[139] S. Alioli, K. Hamilton, and E. Re, *Practical improvements and merging of POWHEG simulations for vector boson production*, JHEP **09** (2011) 104, arXiv:1108.0909 [hep-ph].

[140] M. L. Mangano, M. Moretti, and R. Pittau, *Multijet matrix elements and shower evolution in hadronic collisions: $Wb\bar{b}$ + n jets as a case study*, Nucl. Phys. **B632** (2002) 343–362, arXiv:hep-ph/0108069.

[141] S. Catani, F. Krauss, R. Kuhn, and B. R. Webber, *QCD matrix elements + parton showers*, JHEP **11** (2001) 063, arXiv:hep-ph/0109231.

[142] L. Lonnblad, *Correcting the colour-dipole cascade model with fixed order matrix elements*, JHEP **05** (2002) 046, arXiv:hep-ph/0112284.

[143] F. Krauss, *Matrix elements and parton showers in hadronic interactions*, JHEP **08** (2002) 015, arXiv:hep-ph/0205283.

[144] S. Mrenna and P. Richardson, *Matching matrix elements and parton showers with HERWIG and PYTHIA*, JHEP **05** (2004) 040, arXiv:hep-ph/0312274 [hep-ph].

[145] A. Schälicke and F. Krauss, *Implementing the ME+PS merging algorithm*, JHEP **07** (2005) 018, arXiv:hep-ph/0503281 [hep-ph].

[146] J. Alwall et al., *Comparative study of various algorithms for the merging of parton showers and matrix elements in hadronic collisions*, Eur. Phys. J. **C53** (2008) 473–500, arXiv:0706.2569 [hep-ph].

[147] S. Höche, F. Krauss, S. Schumann, and F. Siegert, *QCD matrix elements and truncated showers*, JHEP **05** (2009) 053, arXiv:0903.1219 [hep-ph].

[148] K. Hamilton, P. Richardson, and J. Tully, *A modified CKKW matrix element merging approach to angular-ordered parton showers*, JHEP **11** (2009) 038, arXiv:0905.3072 [hep-ph].

[149] F. Siegert, S. Hoche, F. Krauss, and M. Schonherr, *Multi-jet merging with NLO matrix elements*,

PoS **ICHEP2010** (2010) 119, arXiv:1011.6657 [hep-ph].

[150] K. Hamilton and P. Nason, *Improving NLO-parton shower matched simulations with higher order matrix elements*, JHEP **06** (2010) 039, arXiv:1004.1764 [hep-ph].

[151] R. Frederix, S. Frixione, F. Maltoni, and T. Stelzer, *Automation of next-to-leading order computations in QCD: The FKS subtraction*, JHEP **10** (2009) 003, arXiv:0908.4272 [hep-ph].

[152] V. Hirschi et al., *Automation of one-loop QCD corrections*, JHEP **05** (2011) 044, arXiv:1103.0621 [hep-ph].

[153] G. Bevilacqua et al., *HELAC-NLO*, arXiv:1110.1499 [hep-ph].

[154] G. Cullen et al., *GoSam: A program for automated one-loop calculations*, arXiv:1111.6534 [hep-ph].

[155] F. Cascioli, P. Maierhofer, and S. Pozzorini, *Scattering amplitudes with open loops*, arXiv:1111.5206 [hep-ph].

[156] S. Alioli, P. Nason, C. Oleari, and E. Re, *A general framework for implementing NLO calculations in shower Monte Carlo programs: The POWHEG BOX*, JHEP **06** (2010) 043, arXiv:1002.2581 [hep-ph].

[157] S. Hoche, F. Krauss, M. Schonherr, and F. Siegert, *Automating the POWHEG method in SHERPA*, JHEP **04** (2011) 024, arXiv:1008.5399 [hep-ph].

[158] R. Frederix et al., *Scalar and pseudoscalar Higgs production in association with a top-antitop pair*, Phys. Lett. **B701** (2011) 427–433, arXiv:1104.5613 [hep-ph].

[159] S. Hoeche, F. Krauss, M. Schonherr, and F. Siegert, *A critical appraisal of NLO+PS matching methods*, arXiv:1111.1220 [hep-ph].

[160] P. Nason and C. Oleari, *NLO Higgs boson production via vector-boson fusion matched with shower in POWHEG*, JHEP **02** (2010) 037, arXiv:0911.5299 [hep-ph].

[161] L. D'Errico and P. Richardson, *A positive-weight next-to-leading-order Monte Carlo simulation of deep inelastic scattering and Higgs boson production via vector boson fusion in Herwig++*, arXiv:1106.2983 [hep-ph].

[162] M. Garzelli, A. Kardos, C. Papadopoulos, and Z. Trocsanyi, *Standard Model Higgs boson production in association with a top anti-top pair at NLO with parton showering*, Europhys.Lett. **96** (2011) 11001, arXiv:1108.0387 [hep-ph].

[163] K. Hamilton, *A positive-weight next-to-leading order simulation of weak boson pair production*, JHEP **01** (2011) 009, arXiv:1009.5391 [hep-ph].

[164] L. D'Errico and P. Richardson, *Next-to-leading-order Monte Carlo simulation of diphoton production in hadronic collisions*, arXiv:1106.3939 [hep-ph].

[165] C. Oleari and L. Reina, *$W^{\pm}b\bar{b}$ production in POWHEG*, JHEP **08** (2011) 061, arXiv:1105.4488 [hep-ph]. [Erratum-ibid.1111:040,2011].

[166] R. Frederix, S. Frixione, V. Hirschi, F. Maltoni, R. Pittau, et al., *W and Z/γ^* boson production in association with a bottom-antibottom pair*, JHEP **09** (2011) 061, arXiv:1106.6019 [hep-ph].

[167] T. Melia, P. Nason, R. Rontsch, and G. Zanderighi, *W^+W^-, WZ and ZZ production in the POWHEG BOX*, arXiv:1107.5051 [hep-ph].

[168] R. Frederix, S. Frixione, V. Hirschi, F. Maltoni, R. Pittau, et al., *Four-lepton production at hadron colliders: aMC@NLO predictions with theoretical uncertainties*, arXiv:1110.4738 [hep-ph].

[169] R. Frederix, S. Frixione, V. Hirschi, F. Maltoni, R. Pittau, et al., *aMC@NLO predictions for Wjj production at the Tevatron*, arXiv:1110.5502 [hep-ph].

[170] M. Garzelli, A. Kardos, C. Papadopoulos, and Z. Trocsanyi, *Z^0-boson production in association with a top anti-top pair at NLO accuracy with parton shower effects*, arXiv:1111.1444 [hep-ph].

[171] *HqT program*, http://theory.fi.infn.it/grazzini/codes.html.

[172] P. Nason, *Recent developments in POWHEG*, PoS **RADCOR2009** (2010) 018, arXiv:1001.2747 [hep-ph].

[173] M. Grazzini, *NNLO predictions for the Higgs boson signal in the $H \to WW \to l\nu l\nu$ and $H \to ZZ \to 4l$ decay channels*, JHEP **02** (2008) 043, arXiv:0801.3232 [hep-ph].

[174] T. Gleisberg, S. Hoeche, F. Krauss, M. Schonherr, S. Schumann, et al., *Event generation with SHERPA 1.1*, JHEP **02** (2009) 007, arXiv:0811.4622 [hep-ph].

[175] M. Cacciari, G. P. Salam, and G. Soyez, *The anti-k_t jet clustering algorithm*, JHEP **04** (2008) 063, arXiv:0802.1189 [hep-ph].

[176] S. Frixione, Z. Kunszt, and A. Signer, *Three jet cross-sections to next-to-leading order*, Nucl.Phys. **B467** (1996) 399–442, arXiv:hep-ph/9512328 [hep-ph].

[177] S. Catani and M. H. Seymour, *A general algorithm for calculating jet cross sections in NLO QCD*, Nucl. Phys. **B485** (1997) 291–419, arXiv:hep-ph/9605323.

[178] S. Schumann and F. Krauss, *A Parton shower algorithm based on Catani-Seymour dipole factorisation*, JHEP **03** (2008) 038, arXiv:0709.1027 [hep-ph].

[179] Z. Nagy, *Next-to-leading order calculation of three jet observables in hadron hadron collision*, Phys.Rev. **D68** (2003) 094002, arXiv:hep-ph/0307268 [hep-ph].

[180] S. Alekhin, S. Alioli, R. D. Ball, V. Bertone, J. Blümlein, et al., *The PDF4LHC working group interim report*, arXiv:1101.0536 [hep-ph].

[181] J.-C. Winter, F. Krauss, and G. Soff, *A Modified cluster hadronization model*, Eur.Phys.J. **C36** (2004) 381–395, arXiv:hep-ph/0311085 [hep-ph].

[182] B. Andersson, G. Gustafson, G. Ingelman, and T. Sjöstrand, *Parton fragmentation and string dynamics*, Phys.Rept. **97** (1983) 31–145.

[183] T. Sjöstrand, S. Mrenna, and P. Z. Skands, *PYTHIA 6.4 physics and manual*, JHEP **05** (2006) 026, arXiv:hep-ph/0603175 [hep-ph].

[184] T. Sjöstrand and M. van Zijl, *A multiple interaction model for the event structure in hadron collisions*, Phys.Rev. **D36** (1987) 2019.

[185] ATLAS Collaboration, G. Aad et al., *Search for the Higgs boson in the $H \to WW^{(*)} \to \ell^+\nu\ell^-\bar{\nu}$ decay channel in pp collisions at $\sqrt{s} = 7$ TeV with the ATLAS detector*, arXiv:1112.2577 [hep-ex].

[186] A. Buckley, H. Hoeth, H. Lacker, H. Schulz, and J. E. von Seggern, *Systematic event generator tuning for the LHC*, Eur.Phys.J. **C65** (2010) 331–357, arXiv:0907.2973 [hep-ph].

[187] B. Cooper, J. Katzy, M. Mangano, A. Messina, L. Mijovic, et al., *Monte Carlo tuning in the presence of matching*, arXiv:1109.5295 [hep-ph].

[188] S. Frixione and B. R. Webber, *The MC@NLO 3.1 event generator*, arXiv:hep-ph/0506182 [hep-ph].

[189] J. Alwall, Q. Li, and F. Maltoni, *Matched predictions for Higgs production via heavy-quark loops in the SM and beyond*, arXiv:1110.1728 [hep-ph].

[190] E. Bagnaschi, G. Degrassi, P. Slavich, and A. Vicini, *Higgs production via gluon fusion in the POWHEG approach in the SM and in the MSSM*, arXiv:1111.2854 [hep-ph].

[191] J. Alwall, M. Herquet, F. Maltoni, O. Mattelaer, and T. Stelzer, *MadGraph 5: Going beyond*, JHEP **06** (2011) 128, arXiv:1106.0522 [hep-ph].

[192] J. Pumplin et al., *New generation of parton distributions with uncertainties from global QCD analysis*, JHEP **07** (2002) 012, arXiv:hep-ph/0201195.

[193] G. Bozzi, S. Catani, D. de Florian, and M. Grazzini, *Transverse-momentum resummation and the spectrum of the Higgs boson at the LHC*, Nucl. Phys. **B737** (2006) 73–120, arXiv:hep-ph/0508068 [hep-ph].

[194] D. de Florian, G. Ferrera, M. Grazzini, and D. Tommasini, *Transverse-momentum resummation: Higgs boson production at the Tevatron and the LHC*, arXiv:1109.2109 [hep-ph].

[195] C. Anastasiou, K. Melnikov, and F. Petriello, *Higgs boson production at hadron colliders: Differential cross sections through next-to-next-to-leading order*, Phys.Rev.Lett. **93** (2004) 262002, arXiv:hep-ph/0409088 [hep-ph].

[196] C. Anastasiou, K. Melnikov, and F. Petriello, *Fully differential Higgs boson production and the di-photon signal through next-to-next-to-leading order*, Nucl.Phys. **B724** (2005) 197–246, arXiv:hep-ph/0501130 [hep-ph].

[197] S. Catani and M. Grazzini, *An NNLO subtraction formalism in hadron collisions and its application to Higgs boson production at the LHC*, Phys.Rev.Lett. **98** (2007) 222002, arXiv:hep-ph/0703012 [hep-ph].

[198] D. de Florian, M. Grazzini, and Z. Kunszt, *Higgs production with large transverse momentum in hadronic collisions at next-to-leading order*, Phys.Rev.Lett. **82** (1999) 5209–5212, arXiv:hep-ph/9902483 [hep-ph].

[199] V. Ravindran, J. Smith, and W. Van Neerven, *Next-to-leading order QCD corrections to differential distributions of Higgs boson production in hadron hadron collisions*, Nucl.Phys. **B634** (2002) 247–290, arXiv:hep-ph/0201114 [hep-ph].

[200] C. J. Glosser and C. R. Schmidt, *Next-to-leading corrections to the Higgs boson transverse momentum spectrum in gluon fusion*, JHEP **12** (2002) 016, arXiv:hep-ph/0209248 [hep-ph].

[201] Q.-H. Cao, C.-R. Chen, C. Schmidt, and C. P. Yuan, *Improved predictions for Higgs Q_T at the Tevatron and the LHC*, arXiv:0909.2305 [hep-ph].

[202] C. Anastasiou, G. Dissertori, and F. Stöckli, *NNLO QCD predictions for the $H \to WW \to \ell\nu\ell\nu$ signal at the LHC*, JHEP **09** (2007) 018, arXiv:0707.2373 [hep-ph].

[203] C. Anastasiou, G. Dissertori, M. Grazzini, F. Stockli, and B. R. Webber, *Perturbative QCD effects and the search for a $H \to WW \to \ell\nu\ell\nu$ signal at the Tevatron*, JHEP **08** (2009) 099, arXiv:0905.3529 [hep-ph].

[204] I. W. Stewart and F. J. Tackmann, *Theory uncertainties for Higgs and other searches using jet bins*, arXiv:1107.2117 [hep-ph].

[205] I. W. Stewart, F. J. Tackmann, and W. J. Waalewijn, *Factorization at the LHC: From PDFs to initial state jets*, Phys.Rev. **D81** (2010) 094035, arXiv:0910.0467 [hep-ph].

[206] C. F. Berger, C. Marcantonini, I. W. Stewart, F. J. Tackmann, and W. J. Waalewijn, *Higgs production with a central jet veto at NNLL+NNLO*, JHEP **04** (2011) 092, arXiv:1012.4480 [hep-ph].

[207] S. Dawson, *Radiative corrections to Higgs boson production*, Nucl.Phys. **B359** (1991) 283–300.

[208] C. Anastasiou, S. Beerli, S. Bucherer, A. Daleo, and Z. Kunszt, *Two-loop amplitudes and master integrals for the production of a Higgs boson via a massive quark and a scalar-quark loop*, JHEP **01** (2007) 082, arXiv:hep-ph/0611236 [hep-ph].

[209] R. Harlander and P. Kant, *Higgs production and decay: Analytic results at next-to-leading order QCD*, JHEP **12** (2005) 015, arXiv:hep-ph/0509189 [hep-ph].

[210] U. Aglietti, R. Bonciani, G. Degrassi, and A. Vicini, *Analytic results for virtual QCD corrections to Higgs production and decay*, JHEP **01** (2007) 021, arXiv:hep-ph/0611266 [hep-ph].

[211] R. Bonciani, G. Degrassi, and A. Vicini, *Scalar particle contribution to Higgs production via gluon fusion at NLO*, JHEP **11** (2007) 095, arXiv:0709.4227 [hep-ph].

[212] R. V. Harlander and W. B. Kilgore, *Next-to-next-to-leading order Higgs production at hadron colliders*, Phys. Rev. Lett. **88** (2002) 201801, arXiv:hep-ph/0201206.

[213] C. Anastasiou and K. Melnikov, *Higgs boson production at hadron colliders in NNLO QCD*, Nucl. Phys. **B646** (2002) 220–256, arXiv:hep-ph/0207004.

[214] V. Ravindran, J. Smith, and W. L. van Neerven, *NNLO corrections to the total cross section for Higgs boson production in hadron hadron collisions*, Nucl. Phys. **B665** (2003) 325–366, `arXiv:hep-ph/0302135`.

[215] S. Marzani, R. D. Ball, V. Del Duca, S. Forte, and A. Vicini, *Higgs production via gluon-gluon fusion with finite top mass beyond next-to-leading order*, Nucl. Phys. **B800** (2008) 127–145, `arXiv:arXiv:0801.2544 [hep-ph]`.

[216] R. V. Harlander and K. J. Ozeren, *Top mass effects in Higgs production at next-to-next-to-leading order QCD: Virtual corrections*, Phys. Lett. **B679** (2009) 467–472, `arXiv:0907.2997 [hep-ph]`.

[217] R. V. Harlander and K. J. Ozeren, *Finite top mass effects for hadronic Higgs production at next-to-next-to-leading order*, JHEP **11** (2009) 088, `arXiv:0909.3420 [hep-ph]`.

[218] R. V. Harlander, H. Mantler, S. Marzani, and K. J. Ozeren, *Higgs production in gluon fusion at next-to-next-to-leading order QCD for finite top mass*, Eur. Phys. J. **C66** (2010) 359–372, `arXiv:0912.2104 [hep-ph]`.

[219] S. Catani, D. de Florian, M. Grazzini, and P. Nason, *Soft gluon resummation for Higgs boson production at hadron colliders*, JHEP **07** (2003) 028, `arXiv:hep-ph/0306211 [hep-ph]`.

[220] D. de Florian and M. Grazzini, *Higgs production through gluon fusion: Updated cross sections at the Tevatron and the LHC*, Phys. Lett. **B674** (2009) 291–294, `arXiv:0901.2427 [hep-ph]`.

[221] S. Moch and A. Vogt, *Higher-order soft corrections to lepton pair and Higgs boson production*, Phys.Lett. **B631** (2005) 48–57, `arXiv:hep-ph/0508265 [hep-ph]`.

[222] S. Actis, G. Passarino, C. Sturm, and S. Uccirati, *Two-loop threshold singularities, unstable particles and complex masses*, Phys. Lett. **B669** (2008) 62–68, `arXiv:0809.1302 [hep-ph]`.

[223] R. Bonciani, G. Degrassi, and A. Vicini, *On the generalized harmonic polylogarithms of one complex variable*, Comput.Phys.Commun. **182** (2011) 1253–1264, `arXiv:1007.1891 [hep-ph]`.

[224] C. Anastasiou, R. Boughezal, and F. Petriello, *Mixed QCD-electroweak corrections to Higgs boson production in gluon fusion*, JHEP **04** (2009) 003, `arXiv:0811.3458 [hep-ph]`.

[225] W.-Y. Keung and F. J. Petriello, *Electroweak and finite quark-mass effects on the Higgs boson transverse momentum distribution*, Phys. Rev. **D80** (2009) 013007, `arXiv:0905.2775 [hep-ph]`.

[226] O. Brein, *Electroweak and bottom quark contributions to Higgs boson plus jet production*, Phys. Rev. **D81** (2010) 093006, `arXiv:1003.4438 [hep-ph]`.

[227] C. Anastasiou, S. Bucherer, and Z. Kunszt, *HPro: A NLO Monte Carlo for Higgs production via gluon fusion with finite heavy quark masses*, JHEP **10** (2009) 068, `arXiv:0907.2362 [hep-ph]`.

[228] C. Balazs and C. Yuan, *Higgs boson production at the LHC with soft gluon effects*, Phys.Lett. **B478** (2000) 192–198, `arXiv:hep-ph/0001103 [hep-ph]`.

[229] C. Balazs, J. Huston, and I. Puljak, *Higgs production: A Comparison of parton showers and resummation*, Phys.Rev. **D63** (2001) 014021, `arXiv:hep-ph/0002032 [hep-ph]`.

[230] J. M. Campbell, R. Ellis, and C. Williams, *Hadronic production of a Higgs boson and two jets at next-to-leading order*, Phys. Rev. **D81** (2010) 074023, `arXiv:1001.4495 [hep-ph]`.

[231] S. Catani, L. Cieri, G. Ferrera, D. de Florian, and M. Grazzini, *Vector boson production at hadron colliders: A fully exclusive QCD calculation at NNLO*, Phys.Rev.Lett. **103** (2009) 082001, `arXiv:0903.2120 [hep-ph]`.

[232] J. Campbell and K. Ellis, *MCFM-Monte Carlo for FeMtobarn processes*, `http://mcfm.fnal.gov`, 2010.

[233] U. Baur and E. W. N. Glover, *Higgs boson production at large transverse momentum in hadronic*

collisions, Nucl. Phys. **B339** (1990) 38–66.

[234] Y. L. Dokshitzer, D. Diakonov, and S. Troian, *On the transverse momentum distribution of massive lepton pairs*, Phys.Lett. **B79** (1978) 269–272.

[235] Y. L. Dokshitzer, D. Diakonov, and S. Troian, *Hard processes in quantum chromodynamics*, Phys.Rept. **58** (1980) 269–395.

[236] G. Parisi and R. Petronzio, *Small transverse momentum distributions in hard processes*, Nucl.Phys. **B154** (1979) 427.

[237] G. Curci, M. Greco, and Y. Srivastava, *QCD jets from coherent states*, Nucl.Phys. **B159** (1979) 451.

[238] J. C. Collins and D. E. Soper, *Back-to-back jets in QCD*, Nucl.Phys. **B193** (1981) 381.

[239] J. C. Collins and D. E. Soper, *Back-to-back jets: Fourier transform from b to k_t*, Nucl.Phys. **B197** (1982) 446.

[240] J. C. Collins, D. E. Soper, and G. F. Sterman, *Transverse momentum distribution in Drell-Yan pair and W and Z boson production*, Nucl.Phys. **B250** (1985) 199.

[241] J. Kodaira and L. Trentadue, *Summing soft emission in QCD*, Phys.Lett. **B112** (1982) 66.

[242] S. Catani, E. D'Emilio, and L. Trentadue, *The gluon form-factor to higher orders: gluon gluon annihilation at small Q_t*, Phys.Lett. **B211** (1988) 335–342.

[243] S. Catani, D. de Florian, and M. Grazzini, *Universality of nonleading logarithmic contributions in transverse momentum distributions*, Nucl.Phys. **B596** (2001) 299–312, `arXiv:hep-ph/0008184 [hep-ph]`.

[244] S. Catani and M. Grazzini, *QCD transverse-momentum resummation in gluon fusion processes*, Nucl.Phys. **B845** (2011) 297–323, `arXiv:1011.3918 [hep-ph]`.

[245] D. de Florian and M. Grazzini, *Next-to-next-to-leading logarithmic corrections at small transverse momentum in hadronic collisions*, Phys.Rev.Lett. **85** (2000) 4678–4681, `arXiv:hep-ph/0008152 [hep-ph]`.

[246] S. Catani and M. Grazzini, *Higgs boson production at hadron colliders: Hard-collinear coefficients at the NNLO*, `arXiv:1106.4652 [hep-ph]`.

[247] T. Becher and M. Neubert, *Drell-Yan production at small q_T, transverse parton distributions and the collinear anomaly*, Eur.Phys.J. **C71** (2011) 1665, `arXiv:1007.4005 [hep-ph]`.

[248] R. Kauffman, *Higher order corrections to Higgs boson p_T*, Phys.Rev. **D45** (1992) 1512–1517.

[249] G. Bozzi, S. Catani, D. de Florian, and M. Grazzini, *The q_T spectrum of the Higgs boson at the LHC in QCD perturbation theory*, Phys.Lett. **B564** (2003) 65–72, `arXiv:hep-ph/0302104 [hep-ph]`.

[250] E. Laenen, G. F. Sterman, and W. Vogelsang, *Higher order QCD corrections in prompt photon production*, Phys.Rev.Lett. **84** (2000) 4296–4299, `arXiv:hep-ph/0002078 [hep-ph]`.

[251] A. Kulesza, G. F. Sterman, and W. Vogelsang, *Joint resummation in electroweak boson production*, Phys.Rev. **D66** (2002) 014011, `arXiv:hep-ph/0202251 [hep-ph]`.

[252] S. Moch, J. A. M. Vermaseren, and A. Vogt, *The three-loop splitting functions in QCD: The non-singlet case*, Nucl. Phys. **B688** (2004) 101–134, `arXiv:hep-ph/0403192`.

[253] A. Kulesza and W. J. Stirling, *Nonperturbative effects and the resummed Higgs transverse momentum distribution at the LHC*, JHEP **12** (2003) 056, `arXiv:hep-ph/0307208 [hep-ph]`.

[254] G. Watt, *Parton distribution function dependence of benchmark Standard Model total cross sections at the 7 TeV LHC*, JHEP **1109** (2011) 069, `arXiv:1106.5788 [hep-ph]`.

[255] S. Asai et al., *Prospects for the search for a Standard Model Higgs boson in ATLAS using vector boson fusion*, Eur. Phys. J. **C32S2** (2004) 19–54, `arXiv:hep-ph/0402254`.

[256] S. Abdullin et al., *Summary of the CMS potential for the Higgs boson discovery*, Eur. Phys. J. **C39S2** (2005) 41–61.

[257] P. Bolzoni, F. Maltoni, S.-O. Moch, and M. Zaro, *Higgs production via vector-boson fusion at NNLO in QCD*, Phys. Rev. Lett. **105** (2010) 011801, arXiv:1003.4451 [hep-ph].

[258] M. Ciccolini, A. Denner, and S. Dittmaier, *Strong and electroweak corrections to the production of Higgs + 2-jets via weak interactions at the LHC*, Phys. Rev. Lett. **99** (2007) 161803, arXiv:0707.0381 [hep-ph].

[259] M. Ciccolini, A. Denner, and S. Dittmaier, *Electroweak and QCD corrections to Higgs production via vector-boson fusion at the LHC*, Phys. Rev. **D77** (2008) 013002, arXiv:0710.4749 [hep-ph].

[260] A. Denner, S. Dittmaier, and A. Mück, *HAWK: A Monte Carlo generator for the production of Higgs bosons Attached to WeaK bosons at hadron colliders*, http://omnibus.uni-freiburg.de/~sd565/programs/hawk/hawk.html, 2010.

[261] K. Arnold et al., *VBFNLO: A parton level Monte Carlo for processes with electroweak bosons*, http://www-itp.particle.uni-karlsruhe.de/~vbfnloweb, 2009.

[262] T. Figy, S. Palmer, and G. Weiglein, *Higgs production via weak boson fusion in the Standard Model and the MSSM*, arXiv:1012.4789 [hep-ph].

[263] A. Denner, S. Dittmaier, S. Kallweit, and A. Mück, *Electroweak corrections to Higgs-strahlung off W/Z bosons at the Tevatron and the LHC with HAWK*, 2011. arXiv:1112.5142 [hep-ph].

[264] K. Arnold, J. Bellm, G. Bozzi, M. Brieg, F. Campanario, et al., *VBFNLO: A parton level Monte Carlo for processes with electroweak bosons – Manual for Version 2.5.0*, arXiv:arXiv:1107.4038 [hep-ph].

[265] K. Arnold et al., *VBFNLO: A parton level Monte Carlo for processes with electroweak bosons*, Comput. Phys. Commun. **180** (2009) 1661–1670, arXiv:0811.4559 [hep-ph].

[266] T. Figy and D. Zeppenfeld, *QCD corrections to jet correlations in weak boson fusion*, Phys. Lett. **B591** (2004) 297–303, arXiv:hep-ph/0403297 [hep-ph].

[267] P. Govoni, C. Hackstein, and A. Massironi, private communication.

[268] O. Brein, A. Djouadi, and R. Harlander, *NNLO QCD corrections to the Higgs-strahlung processes at hadron colliders*, Phys. Lett. **B579** (2004) 149–156, arXiv:hep-ph/0307206.

[269] M. L. Ciccolini, S. Dittmaier, and M. Krämer, *Electroweak radiative corrections to associated WH and ZH production at hadron colliders*, Phys. Rev. **D68** (2003) 073003, arXiv:hep-ph/0306234.

[270] O. Brein et al., *Precision calculations for associated WH and ZH production at hadron colliders*, arXiv:hep-ph/0402003.

[271] G. Ferrera, M. Grazzini, and F. Tramontano, *Associated WH production at hadron colliders: A fully exclusive QCD calculation at NNLO*, arXiv:1107.1164 [hep-ph].

[272] O. Brein, R. Harlander, M. Wiesemann, and T. Zirke, *Top-quark mediated effects in hadronic Higgs-strahlung*, arXiv:1111.0761 [hep-ph].

[273] ALEPH, CDF, D0, DELPHI, L3, OPAL and SLD Collaborations, LEP Electroweak Working Group, Tevatron Electroweak Working Group, SLD Electroweak and Heavy Flavour Groups, *Precision electroweak measurements and constraints on the Standard Model*, arXiv:1012.2367 [hep-ex].

[274] W. Beenakker et al., *Higgs radiation off top quarks at the Tevatron and the LHC*, Phys. Rev. Lett. **87** (2001) 201805, arXiv:hep-ph/0107081.

[275] W. Beenakker et al., *NLO QCD corrections to $t\bar{t}H$ production in hadron collisions*, Nucl. Phys. **B653** (2003) 151–203, arXiv:hep-ph/0211352.

[276] L. Reina and S. Dawson, *Next-to-leading order results for $t\bar{t}h$ production at the Tevatron*, Phys. Rev. Lett. **87** (2001) 201804, arXiv:hep-ph/0107101.

[277] S. Dawson, L. H. Orr, L. Reina, and D. Wackeroth, *Associated top quark Higgs boson production*

at the LHC, Phys. Rev. **D67** (2003) 071503, arXiv:hep-ph/0211438.

[278] A. Bredenstein, A. Denner, S. Dittmaier, and S. Pozzorini, *NLO QCD corrections to $pp \to t\bar{t}b\bar{b}$ + X at the LHC*, Phys. Rev. Lett. **103** (2009) 012002, arXiv:0905.0110 [hep-ph].

[279] A. Bredenstein, A. Denner, S. Dittmaier, and S. Pozzorini, *NLO QCD corrections to $t\bar{t}b\bar{b}$ production at the LHC: 1. quark-antiquark annihilation*, JHEP **08** (2008) 108, arXiv:0807.1248 [hep-ph].

[280] A. Bredenstein, A. Denner, S. Dittmaier, and S. Pozzorini, *NLO QCD corrections to $t\bar{t}b\bar{b}$ production at the LHC: 2. full hadronic results*, JHEP **03** (2010) 021, arXiv:1001.4006 [hep-ph].

[281] G. Bevilacqua, M. Czakon, C. G. Papadopoulos, R. Pittau, and M. Worek, *Assault on the NLO wishlist: $pp \to t\bar{t}b\bar{b}$*, JHEP **09** (2009) 109, arXiv:0907.4723 [hep-ph].

[282] SM and NLO Multileg Working Group Collaboration, J. R. Andersen et al., *The SM and NLO multileg working group: Summary report*, arXiv:1003.1241 [hep-ph].

[283] F. Cerutti, *The NNPDF2.1 parton set*, arXiv:1107.1095 [hep-ph].

[284] G. Bevilacqua, M. Czakon, M. Garzelli, A. van Hameren, Y. Malamos, et al., *NLO QCD calculations with HELAC-NLO*, Nucl.Phys.Proc.Suppl. **205-206** (2010) 211–217, arXiv:1007.4918 [hep-ph].

[285] A. Kardos, C. Papadopoulos, and Z. Trocsanyi, *Top quark pair production in association with a jet with NLO parton showering*, Phys.Lett. **B705** (2011) 76–81, arXiv:1101.2672 [hep-ph].

[286] M. Garzelli, A. Kardos, and Z. Trocsanyi, *NLO event samples for the LHC*, arXiv:1111.1446 [hep-ph].

[287] G. Corcella et al., *HERWIG 6: An event generator for hadron emission reactions with interfering gluons (including supersymmetric processes)*, JHEP **01** (2001) 010, arXiv:hep-ph/0011363.

[288] G. Corcella, I. Knowles, G. Marchesini, S. Moretti, K. Odagiri, et al., *HERWIG 6.5 release note*, arXiv:hep-ph/0210213 [hep-ph].

[289] P. Z. Skands, *Tuning Monte Carlo generators: The Perugia tunes*, Phys.Rev. **D82** (2010) 074018, arXiv:1005.3457 [hep-ph].

[290] T. Plehn, G. P. Salam, and M. Spannowsky, *Fat jets for a light Higgs*, Phys.Rev.Lett. **104** (2010) 111801, arXiv:0910.5472 [hep-ph].

[291] G. Bevilacqua, M. Czakon, C. G. Papadopoulos, and M. Worek, *Dominant QCD backgrounds in Higgs boson analyses at the LHC: A study of $pp \to t\bar{t}$ + 2 jets at next-to-leading order*, Phys. Rev. Lett. **104** (2010) 162002, arXiv:1002.4009 [hep-ph].

[292] G. Bevilacqua, M. Czakon, C. Papadopoulos, and M. Worek, *Hadronic top-quark pair production in association with two jets at next-to-leading order QCD*, arXiv:1108.2851 [hep-ph].

[293] ATLAS Collaboration, G. Aad et al., *Search for the Standard Model Higgs boson in the two photon decay channel with the ATLAS detector at the LHC*, Phys.Lett. **B705** (2011) 452–470, arXiv:1108.5895 [hep-ex].

[294] ATLAS Collaboration, *Search for a fermiophobic Higgs boson in the diphoton channel with the ATLAS detector*, Tech. Rep. ATLAS-CONF-2011-149, CERN, Geneva, Nov., 2011.

[295] CMS Collaboration, *Search for a Higgs boson decaying into two photons in the CMS detector, CMS-PAS-HIG-11-021*, 2011.

[296] G. Davatz et al., *Combining Monte Carlo generators with next-to-next-to- leading order calculations: Event reweighting for Higgs boson production at the LHC*, JHEP **07** (2006) 037, arXiv:hep-ph/0604077.

[297] N. Chanon, *Observation des photons directs dans les premières données et préparation à la recherche du boson de Higgs dans l'expérience CMS au LHC (CERN).* PhD thesis, Institut de Physique Nucléaire, Université Claude Bernard, Lyon, France, 2010.

[298] L. J. Dixon and M. S. Siu, *Resonance-continuum interference in the di-photon Higgs signal at the LHC*, Phys. Rev. Lett. **90** (2003) 252001, `arXiv:hep-ph/0302233`.

[299] L. Dixon, private communication.

[300] T. Binoth, J. Guillet, E. Pilon, and M. Werlen, *A full next-to-leading order study of direct photon pair production in hadronic collisions*, Eur.Phys.J. **C16** (2000) 311–330, `arXiv:hep-ph/9911340 [hep-ph]`.

[301] C. Balazs, E. L. Berger, S. Mrenna, and C. P. Yuan, *Photon pair production with soft gluon resummation in hadronic interactions*, Phys. Rev. **D57** (1998) 6934–6947, `arXiv:hep-ph/9712471`.

[302] C. Balazs, P. M. Nadolsky, C. Schmidt, and C. P. Yuan, *Diphoton background to Higgs boson production at the LHC with soft gluon effects*, Phys. Lett. **B489** (2000) 157–162, `arXiv:hep-ph/9905551`.

[303] C. Balazs, E. L. Berger, P. M. Nadolsky, and C. P. Yuan, *All-orders resummation for diphoton production at hadron colliders*, Phys. Lett. **B637** (2006) 235–240, `arXiv:hep-ph/0603037`.

[304] C. Balazs, E. L. Berger, P. M. Nadolsky, and C. P. Yuan, *Calculation of prompt diphoton production cross sections at Tevatron and LHC energies*, Phys. Rev. **D76** (2007) 013009, `arXiv:0704.0001 [hep-ph]`.

[305] P. M. Nadolsky, C. Balazs, E. L. Berger, and C. P. Yuan, *Gluon-gluon contributions to the production of continuum diphoton pairs at hadron colliders*, Phys. Rev. **D76** (2007) 013008, `arXiv:hep-ph/0702003`.

[306] Z. Bern, L. J. Dixon, and C. Schmidt, *Isolating a light Higgs boson from the diphoton background at the CERN LHC*, Phys.Rev. **D66** (2002) 074018, `arXiv:hep-ph/0206194 [hep-ph]`.

[307] D. A. Dicus and S. S. D. Willenbrock, *Photon pair production and the intermediate mass Higgs boson*, Phys. Rev. **D37** (1988) 1801.

[308] CDF Collaboration, T. Aaltonen et al., *Measurement of the cross section for prompt isolated diphoton production in $p\bar{p}$ collisions at $\sqrt{s} = 1.96$ TeV*, Phys.Rev. **D84** (2011) 052006, `arXiv:1106.5131 [hep-ex]`.

[309] D0 Collaboration, V. Abazov et al., *Measurement of direct photon pair production cross sections in $p\bar{p}$ collisions at $\sqrt{s} = 1.96$ TeV*, Phys.Lett. **B690** (2010) 108–117, `arXiv:1002.4917 [hep-ex]`.

[310] ATLAS Collaboration, G. Aad et al., *Measurement of the isolated di-photon cross-section in pp collisions at $\sqrt{s} = 7$ TeV with the ATLAS detector*, `arXiv:1107.0581 [hep-ex]`.

[311] CMS Collaboration, S. Chatrchyan et al., *Measurement of the production cross section for pairs of isolated photons in pp collisions at $\sqrt{s} = 7$ TeV*, `arXiv:1110.6461 [hep-ex]`.

[312] S. Catani, L. Cieri, D. de Florian, G. Ferrera, and M. Grazzini, *Diphoton production at hadron colliders: A fully-differential QCD calculation at NNLO*, `arXiv:1110.2375 [hep-ph]`.

[313] S. Frixione, *Isolated photons in perturbative QCD*, Phys.Lett. **B429** (1998) 369–374, `arXiv:hep-ph/9801442 [hep-ph]`.

[314] J. Alwall et al., *MadGraph/MadEvent*, `http://madgraph.hep.uiuc.edu`, 2010.

[315] T. Sjöstrand, S. Ask, R. Corke, S. Mrenna, and P. Skands, *PYTHIA*, `http://home.thep.lu.se/~torbjorn/Pythia.html`, 2010.

[316] ATLAS Collaboration, *Search for the Standard Model Higgs boson in the decay channel $H \to ZZ^{(*)} \to 4\ell$ with 4.8 fb^{-1} of pp collisions at $\sqrt{s} = 7$ TeV*, ATLAS-CONF-2011-162 (2011) .

[317] CMS Collaboration, *Search for a Standard Model Higgs boson produced in the decay channel $H \to ZZ^{(*)} \to 4l$*, CMS-PAS-HIG-11-025 (2011) .

[318] ATLAS Collaboration, G. Aad et al., *Search for a Standard Model Higgs boson in the $H \to ZZ \to \ell^+\ell^-\nu\bar{\nu}$ decay channel with the ATLAS detector*, Phys.Rev.Lett. **107** (2011) 221802, `arXiv:1109.3357 [hep-ex]`.

[319] CMS Collaboration, *Search for the Higgs boson in the $H \to ZZ \to 2l2\nu$ channel in pp collisions at $\sqrt{s} = 7$ TeV*, CMS-PAS-HIG-11-026 (2011) .

[320] ATLAS Collaboration, G. Aad et al., *Search for a heavy Standard Model Higgs boson in the channel $H \to ZZ \to \ell^+\ell^-q\bar{q}$ using the ATLAS detector*, Phys.Lett. **B707** (2012) 27–45, `arXiv:1108.5064 [hep-ex]`.

[321] CMS Collaboration, *Search for the Standard Model Higgs Boson in the decay channel $H \to ZZ^{(*)} \to q\bar{q}\ell^-\ell^+$ at CMS*, CMS-PAS-HIG-11-027 (2011) .

[322] CMS Collaboration, *Search for a Standard Model Higgs boson produced in the decay channel $H \to ZZ \to l^+l^-\tau^+\tau^-$ with CMS detector at $\sqrt{s} = 7$ TeV*, CMS-PAS-HIG-11-028 (2011) .

[323] M. Grazzini, *HNNLO: A MC program for Higgs boson production at hadron colliders*, `arXiv:0806.3336 [hep-ph]`.

[324] J. M. Campbell and R. K. Ellis, *An update on vector boson pair production at hadron colliders*, Phys. Rev. **D60** (1999) 113006, `arXiv:hep-ph/9905386 [hep-ph]`.

[325] J. M. Campbell, R. K. Ellis, and C. Williams, *Vector boson pair production at the LHC*, JHEP **07** (2011) 018, `arXiv:1105.0020 [hep-ph]`.

[326] T. Binoth, N. Kauer, and P. Mertsch, *Gluon-induced QCD corrections to $pp \to ZZ \to \ell\bar{\ell}\ell'\bar{\ell}'$*, Proc. of XVI Int. Workshop on Deep-Inelastic Scattering and Related Topics, London, England, April 2008, `arXiv:0807.0024 [hep-ph]`.

[327] C. Zecher, T. Matsuura, and J. van der Bij, *Leptonic signals from off-shell Z boson pairs at hadron colliders*, Z. Phys. **C64** (1994) 219–226, `arXiv:hep-ph/9404295 [hep-ph]`.

[328] T. Binoth, M. Ciccolini, N. Kauer, and M. Krämer, *Gluon-induced WW background to Higgs boson searches at the LHC*, JHEP **03** (2005) 065, `arXiv:hep-ph/0503094 [hep-ph]`.

[329] T. Binoth, M. Ciccolini, N. Kauer, and M. Krämer, *Gluon-induced W-boson pair production at the LHC*, JHEP **12** (2006) 046, `arXiv:hep-ph/0611170 [hep-ph]`.

[330] P. Fayet, *Supergauge invariant extension of the Higgs mechanism and a model for the electron and its neutrino*, Nucl.Phys. **B90** (1975) 104–124.

[331] P. Fayet, *Spontaneously broken supersymmetric theories of weak, electromagnetic and strong interactions*, Phys.Lett. **B69** (1977) 489.

[332] P. Fayet, *Supersymmetry and weak, electromagnetic and strong interactions*, Phys.Lett. **B64** (1976) 159.

[333] S. Dimopoulos and H. Georgi, *Softly broken supersymmetry and SU(5)*, Nucl.Phys. **B193** (1981) 150.

[334] N. Sakai, *Naturalness in supersymmetric GUTS*, Z.Phys. **C11** (1981) 153.

[335] K. Inoue, A. Kakuto, H. Komatsu, and S. Takeshita, *Low-energy parameters and particle masses in a supersymmetric grand unified model*, Prog.Theor.Phys. **67** (1982) 1889. Revised version.

[336] K. Inoue, A. Kakuto, H. Komatsu, and S. Takeshita, *Aspects of grand unified models with softly broken supersymmetry*, Prog.Theor.Phys. **68** (1982) 927.

[337] K. Inoue, A. Kakuto, H. Komatsu, and S. Takeshita, *Renormalization of supersymmetry breaking parameters revisited*, Prog.Theor.Phys. **71** (1984) 413.

[338] L. J. Hall, R. Rattazzi, and U. Sarid, *The Top quark mass in supersymmetric SO(10) unification*, Phys. Rev. **D50** (1994) 7048–7065, `arXiv:hep-ph/9306309`.

[339] R. Hempfling, *Yukawa coupling unification with supersymmetric threshold corrections*, Phys. Rev. **D49** (1994) 6168–6172.

[340] M. S. Carena, M. Olechowski, S. Pokorski, and C. E. M. Wagner, *Electroweak symmetry*

breaking and bottom-top Yukawa unification, Nucl. Phys. **B426** (1994) 269–300, arXiv:hep-ph/9402253.

[341] D. M. Pierce, J. A. Bagger, K. T. Matchev, and R.-j. Zhang, *Precision corrections in the minimal supersymmetric Standard Model*, Nucl. Phys. **B491** (1997) 3–67, arXiv:hep-ph/9606211.

[342] M. S. Carena, D. Garcia, U. Nierste, and C. E. M. Wagner, *Effective Lagrangian for the $\bar{t}bH^+$ interaction in the MSSM and charged Higgs phenomenology*, Nucl. Phys. **B577** (2000) 88–120, arXiv:hep-ph/9912516.

[343] LEP Working Group for Higgs boson Searches, *Search for the Standard Model Higgs boson at LEP*, Phys. Lett. **B565** (2003) 61–75, arXiv:hep-ex/0306033.

[344] ALEPH, DELPHI, L3 and OPAL Collaborations, LEP Working Group for Higgs Boson Searches, *Search for neutral MSSM Higgs bosons at LEP*, Eur.Phys.J. **C47** (2006) 547–587, arXiv:hep-ex/0602042 [hep-ex].

[345] B. Allanach, *SOFTSUSY: A program for calculating supersymmetric spectra*, Comput.Phys.Commun. **143** (2002) 305–331, arXiv:hep-ph/0104145 [hep-ph].

[346] W. Porod, *SPheno, a program for calculating supersymmetric spectra, SUSY particle decays and SUSY particle production at e^+e^- colliders*, Comput.Phys.Commun. **153** (2003) 275–315, arXiv:hep-ph/0301101 [hep-ph].

[347] W. Porod and F. Staub, *SPheno 3.1: Extensions including flavour, CP-phases and models beyond the MSSM*, arXiv:1104.1573 [hep-ph].

[348] A. Djouadi, J.-L. Kneur, and G. Moultaka, *SuSpect: A Fortran code for the supersymmetric and Higgs particle spectrum in the MSSM*, Comput.Phys.Commun. **176** (2007) 426–455, arXiv:hep-ph/0211331 [hep-ph].

[349] B. Allanach, A. Djouadi, J. Kneur, W. Porod, and P. Slavich, *Precise determination of the neutral Higgs boson masses in the MSSM*, JHEP **09** (2004) 044, arXiv:hep-ph/0406166 [hep-ph].

[350] D. Graudenz, M. Spira, and P. Zerwas, *QCD corrections to Higgs boson production at proton proton colliders*, Phys. Rev. Lett. **70** (1993) 1372–1375.

[351] M. Spira, A. Djouadi, D. Graudenz, and P. Zerwas, *SUSY Higgs production at proton colliders*, Phys. Lett. **B318** (1993) 347–353.

[352] M. Krämer, E. Laenen, and M. Spira, *Soft gluon radiation in Higgs boson production at the LHC*, Nucl. Phys. **B511** (1998) 523–549, arXiv:hep-ph/9611272 [hep-ph].

[353] R. Harlander, *Supersymmetric Higgs production at the Large Hadron Collider*, Eur.Phys.J. **C33** (2004) S454–S456, arXiv:hep-ph/0311005 [hep-ph].

[354] A. Pak, M. Rogal, and M. Steinhauser, *Finite top quark mass effects in NNLO Higgs boson production at LHC*, JHEP **02** (2010) 025, arXiv:0911.4662 [hep-ph].

[355] A. Pak, M. Rogal, and M. Steinhauser, *Production of scalar and pseudo-scalar Higgs bosons to next-to-next-to-leading order at hadron colliders*, JHEP **09** (2011) 088, arXiv:1107.3391 [hep-ph].

[356] R. V. Harlander and M. Steinhauser, *Supersymmetric Higgs production in gluon fusion at next-to-leading order*, JHEP **09** (2004) 066, arXiv:hep-ph/0409010 [hep-ph].

[357] R. V. Harlander and M. Steinhauser, *Hadronic Higgs production and decay in supersymmetry at next-to-leading order*, Phys. Lett. **B574** (2003) 258–268, arXiv:hep-ph/0307346 [hep-ph].

[358] G. Degrassi and P. Slavich, *On the NLO QCD corrections to Higgs production and decay in the MSSM*, Nucl. Phys. **B805** (2008) 267–286, arXiv:0806.1495 [hep-ph].

[359] C. Anastasiou, S. Beerli, and A. Daleo, *The two-loop QCD amplitude $gg \to h, H$ in the minimal supersymmetric Standard Model*, Phys. Rev. Lett. **100** (2008) 241806, arXiv:0803.3065 [hep-ph].

[360] M. Mühlleitner, H. Rzehak, and M. Spira, *SUSY-QCD corrections to MSSM Higgs boson*

production via gluon fusion, PoS **RADCOR2009** (2010) 043, arXiv:1001.3214 [hep-ph].

[361] G. Degrassi and P. Slavich, *NLO QCD bottom corrections to Higgs boson production in the MSSM*, arXiv:1007.3465 [hep-ph].

[362] R. V. Harlander, F. Hofmann, and H. Mantler, *Supersymmetric Higgs production in gluon fusion*, JHEP **02** (2011) 055, arXiv:1012.3361 [hep-ph].

[363] D. L. Rainwater, M. Spira, and D. Zeppenfeld, *Higgs boson production at hadron colliders: Signal and background processes*, arXiv:hep-ph/0203187 [hep-ph].

[364] T. Plehn, *Charged Higgs boson production in bottom gluon fusion*, Phys. Rev. **D67** (2003) 014018, arXiv:hep-ph/0206121.

[365] F. Maltoni, Z. Sullivan, and S. Willenbrock, *Higgs-boson production via bottom-quark fusion*, Phys.Rev. **D67** (2003) 093005, arXiv:hep-ph/0301033 [hep-ph].

[366] S. Dittmaier, M. Krämer, and M. Spira, *Higgs radiation off bottom quarks at the Tevatron and the LHC*, Phys. Rev. **D70** (2004) 074010, arXiv:hep-ph/0309204.

[367] S. Dawson, C. Jackson, L. Reina, and D. Wackeroth, *Exclusive Higgs boson production with bottom quarks at hadron colliders*, Phys. Rev. **D69** (2004) 074027, arXiv:hep-ph/0311067 [hep-ph].

[368] R. V. Harlander and W. B. Kilgore, *Higgs boson production in bottom quark fusion at next-to-next-to leading order*, Phys. Rev. **D68** (2003) 013001, arXiv:hep-ph/0304035 [hep-ph].

[369] S. Dittmaier, M. Krämer, A. Mück, and T. Schluter, *MSSM Higgs-boson production in bottom-quark fusion: electroweak radiative corrections*, JHEP **0703** (2007) 114, arXiv:hep-ph/0611353 [hep-ph].

[370] R. Harlander, M. Krämer, and M. Schumacher, *Bottom-quark associated Higgs-boson production: Reconciling the four- and five-flavour scheme approach*, arXiv:1112.3478 [hep-ph].

[371] S. Dawson, C. Jackson, and P. Jaiswal, *SUSY QCD corrections to Higgs-b production: Is the Δ_b approximation accurate?*, Phys.Rev. **D83** (2011) 115007, arXiv:1104.1631 [hep-ph].

[372] O. Brein and W. Hollik, *MSSM Higgs bosons associated with high-p_T jets at hadron colliders*, Phys.Rev. **D68** (2003) 095006, arXiv:hep-ph/0305321 [hep-ph].

[373] O. Brein and W. Hollik, *Distributions for MSSM Higgs boson + jet production at hadron colliders*, Phys.Rev. **D76** (2007) 035002, arXiv:0705.2744 [hep-ph].

[374] CMS Collaboration, S. Chatrchyan et al., *Search for neutral MSSM Higgs bosons decaying to tau pairs in pp collisions at $\sqrt{s} = 7$ TeV*, Phys. Rev. Lett. **106** (2011) 231801, arXiv:1104.1619 [hep-ex].

[375] ATLAS Collaboration, G. Aad et al., *Search for neutral MSSM Higgs bosons decaying to $\tau^+\tau^-$ pairs in proton-proton collisions at $\sqrt{s} = 7$ TeV with the ATLAS detector*, Phys. Lett. **B705** (2011) 174–192, arXiv:1107.5003 [hep-ex].

[376] U. Langenegger, M. Spira, A. Starodumov, and P. Trueb, *SM and MSSM Higgs boson production: Spectra at large transverse momentum*, JHEP **06** (2006) 035, arXiv:hep-ph/0604156 [hep-ph].

[377] J. Baglio and A. Djouadi, *Higgs production at the LHC*, arXiv:1012.0530 [hep-ph].

[378] T. Figy, C. Oleari, and D. Zeppenfeld, *Next-to-leading order jet distributions for Higgs boson production via weak-boson fusion*, Phys. Rev. **D68** (2003) 073005, arXiv:hep-ph/0306109.

[379] T. Hahn and M. Perez-Victoria, *Automatized one-loop calculations in four and D dimensions*, Comput. Phys. Commun. **118** (1999) 153–165, arXiv:hep-ph/9807565.

[380] G. van Oldenborgh and J. Vermaseren, *New algorithms for one loop integrals*, Z.Phys. **C46** (1990) 425–438.

[381] W. Hollik, T. Plehn, M. Rauch, and H. Rzehak, *Supersymmetric Higgs bosons in weak boson fusion*, Phys. Rev. Lett. **102** (2009) 091802, arXiv:0804.2676 [hep-ph].

[382] M. Rauch, W. Hollik, T. Plehn, and H. Rzehak, *Supersymmetric Higgs production in vector-boson fusion*, PoS **RADCOR2009** (2010) 044, arXiv:1004.2169 [hep-ph].

[383] A. Djouadi and M. Spira, *SUSY-QCD corrections to Higgs boson production at hadron colliders*, Phys. Rev. **D62** (2000) 014004, arXiv:hep-ph/9912476 [hep-ph].

[384] R. V. Harlander, K. J. Ozeren, and M. Wiesemann, *Higgs plus jet production in bottom quark annihilation at next-to-leading order*, Phys.Lett. **B693** (2010) 269–273, arXiv:1007.5411 [hep-ph].

[385] S. Catani, D. de Florian, and M. Grazzini, *Direct Higgs production and jet veto at the Tevatron and the LHC in NNLO QCD*, JHEP **01** (2002) 015, arXiv:hep-ph/0111164 [hep-ph].

[386] R. Harlander and M. Wiesemann, *Jet-veto in bottom-quark induced Higgs production at next-to-next-to-leading order*, arXiv:1111.2182 [hep-ph].

[387] J. M. Campbell, R. Ellis, F. Maltoni, and S. Willenbrock, *Higgs-boson production in association with a single bottom quark*, Phys. Rev. **D67** (2003) 095002, arXiv:hep-ph/0204093 [hep-ph].

[388] A. Djouadi, *The anatomy of electro-weak symmetry breaking. II: The Higgs bosons in the minimal supersymmetric model*, Phys. Rep. **459** (2008) 1–241, arXiv:hep-ph/0503173.

[389] CMS Collaboration, *Search for neutral Higgs bosons decaying to tau pairs in pp collisions at $\sqrt{s} = 7$ TeV*, CMS-PAS-HIG-11-020 (2011) .

[390] R. Kinnunen, S. Lehti, F. Moortgat, A. Nikitenko, and M. Spira, *Measurement of the $H/A \to \tau\tau$ cross section and possible constraints on $\tan\beta$*, Eur. Phys. J. **C40N5** (2005) 23–32, arXiv:hep-ph/0503075.

[391] ALEPH Collaboration, A. Heister et al., *Search for charged Higgs bosons in e^+e^- collisions at energies up to $\sqrt{s}$ = 209-GeV*, Phys. Lett. **B543** (2002) 1–13, arXiv:hep-ex/0207054.

[392] J. F. Gunion and A. Turski, *Renormalization of Higgs boson mass sum rules and screening*, Phys. Rev. **D39** (1989) 2701.

[393] A. Brignole, *Radiative corrections to the supersymmetric charged Higgs boson mass*, Phys. Lett. **B277** (1992) 313–323.

[394] M. A. Diaz and H. E. Haber, *One loop radiative corrections to the charged Higgs mass of the minimal supersymmetric model*, Phys. Rev. **D45** (1992) 4246–4260.

[395] CDF Collaboration, T. Aaltonen et al., *Search for charged Higgs bosons in decays of top quarks in $p\bar{p}$ collisions at $\sqrt{s} = 1.96$ TeV*, Phys. Rev. Lett. **103** (2009) 101803, arXiv:0907.1269 [hep-ex].

[396] D0 Collaboration, V. M. Abazov et al., *Search for charged Higgs bosons in top quark decays*, Phys. Lett. **B682** (2009) 278–286, arXiv:0908.1811 [hep-ex].

[397] S. Dittmaier, G. Hiller, T. Plehn, and M. Spannowsky, *Charged-Higgs collider signals with or without flavor*, Phys. Rev. **D77** (2008) 115001, arXiv:0708.0940 [hep-ph].

[398] D. Eriksson, S. Hesselbach, and J. Rathsman, *Associated charged Higgs and W boson production in the MSSM at the CERN large hadron collider*, Eur. Phys. J. **C53** (2008) 267–280, arXiv:hep-ph/0612198.

[399] A. Krause, T. Plehn, M. Spira, and P. Zerwas, *Production of charged Higgs boson pairs in gluon-gluon collisions*, Nucl.Phys. **B519** (1998) 85–100, arXiv:hep-ph/9707430 [hep-ph].

[400] A. Alves and T. Plehn, *Charged Higgs boson pairs at the LHC*, Phys. Rev. **D71** (2005) 115014, arXiv:hep-ph/0503135.

[401] O. Brein and W. Hollik, *Pair production of charged MSSM Higgs bosons by gluon fusion*, Eur. Phys. J. **C13** (2000) 175–184, arXiv:hep-ph/9908529.

[402] S. Moch and P. Uwer, *Heavy-quark pair production at two loops in QCD*, Nucl. Phys. Proc. Suppl. **183** (2008) 75–80, arXiv:0807.2794 [hep-ph].

[403] U. Langenfeld, S. Moch, and P. Uwer, *New results for $t\bar{t}$ production at hadron colliders*, arXiv:0907.2527 [hep-ph].

[404] ATLAS Collaboration, G. Aad et al., *Measurement of the top quark pair production cross section in pp collisions at $\sqrt{s} = 7$ TeV in dilepton final states with ATLAS*, arXiv:1108.3699 [hep-ex].

[405] M. Spira, *HIGLU and HDECAY: Programs for Higgs boson production at the LHC and Higgs boson decay widths*, Nucl. Instrum. Meth. **A389** (1997) 357–360, arXiv:hep-ph/9610350.

[406] M. S. Carena, S. Heinemeyer, C. E. M. Wagner, and G. Weiglein, *MSSM Higgs boson searches at the Tevatron and the LHC: Impact of different benchmark scenarios*, Eur. Phys. J. **C45** (2006) 797–814, arXiv:hep-ph/0511023.

[407] J. M. Campbell, R. K. Ellis, and F. Tramontano, *Single top production and decay at next-to-leading order*, Phys. Rev. **D70** (2004) 094012, arXiv:hep-ph/0408158.

[408] L. Hofer, U. Nierste, and D. Scherer, *Resummation of $\tan\beta$-enhanced supersymmetric loop corrections beyond the decoupling limit*, JHEP **10** (2009) 081, arXiv:0907.5408 [hep-ph].

[409] A. Czarnecki and S. Davidson, *On the QCD corrections to the charged Higgs decay of a heavy quark*, Phys.Rev. **D47** (1993) 3063–3064, arXiv:hep-ph/9208240 [hep-ph].

[410] R. M. Barnett, H. E. Haber, and D. E. Soper, *Ultraheavy particle production from heavy partons at hadron colliders*, Nucl. Phys. **B306** (1988) 697.

[411] J. M. Campbell et al., *Higgs boson production in association with bottom quarks*, arXiv:hep-ph/0405302.

[412] S. Dawson, C. B. Jackson, L. Reina, and D. Wackeroth, *Higgs production in association with bottom quarks at hadron colliders*, Mod. Phys. Lett. **A21** (2006) 89–110, arXiv:hep-ph/0508293.

[413] C. Buttar et al., *Les Houches physics at TeV colliders 2005, Standard Model and Higgs working group: Summary report*, arXiv:hep-ph/0604120.

[414] S.-h. Zhu, *Complete next-to-leading order QCD corrections to charged Higgs boson associated production with top quark at the CERN Large Hadron Collider*, Phys. Rev. **D67** (2003) 075006, arXiv:hep-ph/0112109.

[415] G.-p. Gao, G.-r. Lu, Z.-h. Xiong, and J. M. Yang, *Loop effects and non-decoupling property of SUSY QCD in $gb \to tH^-$*, Phys. Rev. **D66** (2002) 015007, arXiv:hep-ph/0202016.

[416] E. L. Berger, T. Han, J. Jiang, and T. Plehn, *Associated production of a top quark and a charged Higgs boson*, Phys. Rev. **D71** (2005) 115012, arXiv:hep-ph/0312286.

[417] N. Kidonakis, *Charged Higgs production: Higher-order corrections*, PoS **HEP2005** (2006) 336, arXiv:hep-ph/0511235.

[418] W. Peng et al., *NLO supersymmetric QCD corrections to the $t\bar{b}H^-$ associated production at hadron colliders*, Phys. Rev. **D73** (2006) 015012, arXiv:hep-ph/0601069.

[419] M. Beccaria, G. Macorini, L. Panizzi, F. M. Renard, and C. Verzegnassi, *Associated production of charged Higgs and top at LHC: The role of the complete electroweak supersymmetric contribution*, Phys. Rev. **D80** (2009) 053011, arXiv:0908.1332 [hep-ph].

[420] N. Kidonakis, *Two-loop soft anomalous dimensions for single top quark associated production with a W^- or H^-*, Phys. Rev. **D82** (2010) 054018, arXiv:1005.4451 [hep-ph].

[421] C. Weydert et al., *Charged Higgs boson production in association with a top quark in MC@NLO*, Eur. Phys. J. **C67** (2010) 617–636, arXiv:0912.3430 [hep-ph].

[422] S. Dittmaier, M. Krämer, M. Spira, and M. Walser, *Charged-Higgs-boson production at the LHC: NLO supersymmetric QCD corrections*, arXiv:0906.2648 [hep-ph].

[423] E. Boos and T. Plehn, *Higgs boson production induced by bottom quarks*, Phys.Rev. **D69** (2004) 094005, arXiv:hep-ph/0304034 [hep-ph].

[424] F. Maltoni, T. McElmurry, R. Putman, and S. Willenbrock, *Choosing the factorization scale in perturbative QCD*, arXiv:hep-ph/0703156 [HEP-PH].

[425] J. M. Campbell, R. Frederix, F. Maltoni, and F. Tramontano, *Next-to-leading-order predictions for t-channel single-top production at hadron colliders*, Phys. Rev. Lett. **102** (2009) 182003, arXiv:0903.0005 [hep-ph].

[426] G. D. Kribs, T. Plehn, M. Spannowsky, and T. M. P. Tait, *Four generations and Higgs physics*, Phys. Rev. **D76** (2007) 075016, arXiv:0706.3718 [hep-ph].

[427] M. Hashimoto, *Constraints on mass spectrum of fourth generation fermions and Higgs bosons*, Phys. Rev. **D81** (2010) 075023, arXiv:1001.4335 [hep-ph].

[428] A. Denner, S. Dittmaier, A. Mück, G. Passarino, M. Spira, et al., *Higgs production and decay with a fourth Standard-Model-like fermion generation*, arXiv:1111.6395 [hep-ph].

[429] C. Anastasiou, S. Buehler, E. Furlan, F. Herzog, and A. Lazopoulos, *Higgs production cross-section in a Standard Model with four generations at the LHC*, arXiv:1103.3645 [hep-ph].

[430] A. Djouadi and P. Gambino, *Leading electroweak correction to Higgs boson production at proton colliders*, Phys.Rev.Lett. **73** (1994) 2528–2531, arXiv:hep-ph/9406432 [hep-ph].

[431] A. Djouadi, P. Gambino, and B. A. Kniehl, *Two loop electroweak heavy fermion corrections to Higgs boson production and decay*, Nucl. Phys. **B523** (1998) 17–39, arXiv:hep-ph/9712330.

[432] F. Fugel, B. A. Kniehl, and M. Steinhauser, *Two-loop electroweak correction of O($G_F M_t^2$) to the Higgs-boson decay into photons*, Nucl. Phys. **B702** (2004) 333–345, arXiv:hep-ph/0405232.

[433] H. M. Georgi, S. L. Glashow, M. E. Machacek, and D. V. Nanopoulos, *Higgs bosons from two gluon annihilation in proton proton collisions*, Phys. Rev. Lett. **40** (1978) 692.

[434] G. Passarino, C. Sturm, and S. Uccirati, *Complete electroweak corrections to Higgs production in a Standard Model with four generations at the LHC*, arXiv:1108.2025 [hep-ph].

[435] A. Bredenstein, A. Denner, S. Dittmaier, and M. M. Weber, *Precision calculations for $H \to WW/ZZ \to$ 4fermions with PROPHECY4f*, arXiv:0708.4123 [hep-ph].

[436] M. S. Chanowitz, M. Furman, and I. Hinchliffe, *Weak interactions of ultraheavy fermions*, Phys.Lett. **B78** (1978) 285.

[437] B. A. Kniehl, *Two loop O($\alpha_s G_F M_Q^2$) heavy quark corrections to the interactions between Higgs and intermediate bosons*, Phys.Rev. **D53** (1996) 6477–6485, arXiv:hep-ph/9602304 [hep-ph].

[438] C. Anastasiou, R. Boughezal, and E. Furlan, *The NNLO gluon fusion Higgs production cross-section with many heavy quarks*, JHEP **06** (2010) 101, arXiv:1003.4677 [hep-ph].

[439] G. Passarino, C. Sturm, and S. Uccirati, *Higgs pseudo-observables, second Riemann sheet and all that*, Nucl. Phys. **B834** (2010) 77–115, arXiv:1001.3360 [hep-ph].

[440] S. Goria, G. Passarino, and D. Rosco, *The Higgs boson lineshape*, arXiv:1112.5517 [hep-ph].

[441] A. Ghinculov and T. Binoth, *On the position of a heavy Higgs pole*, Phys.Lett. **B394** (1997) 139–146, arXiv:hep-ph/9611357 [hep-ph].

[442] C. Anastasiou, S. Buhler, F. Herzog, and A. Lazopoulos, *Total cross-section for Higgs boson hadroproduction with anomalous Standard Model interactions*, arXiv:1107.0683 [hep-ph].

[443] M. J. G. Veltman, *Unitarity and causality in a renormalizable field theory with unstable particles*, Physica **29** (1963) 186–207.

[444] R. Jacob and R. Sachs, *Mass and lifetime of unstable particles*, Phys.Rev. **121** (1961) 350–356.

[445] G. Valent, *Renormalization and second sheet poles in unstable particle theory*,

Nucl.Phys. **B65** (1973) 445–459.

[446] J. Lukierski, *Field operator for unstable particle and complex mass description in local QFT*, Fortsch.Phys. **28** (1980) 259.

[447] C. Bollini and L. Oxman, *Unitarity and complex mass fields*, Int.J.Mod.Phys. **A8** (1993) 3185–3198.

[448] P. A. Grassi, B. A. Kniehl, and A. Sirlin, *Width and partial widths of unstable particles in the light of the Nielsen identities*, Phys.Rev. **D65** (2002) 085001, `arXiv:hep-ph/0109228 [hep-ph]`.

[449] P. A. Grassi, B. A. Kniehl, and A. Sirlin, *Width and partial widths of unstable particles*, Phys. Rev. Lett. **86** (2001) 389–392, `arXiv:hep-th/0005149`.

[450] B. A. Kniehl and A. Sirlin, *Mass and width of a heavy Higgs boson*, Phys.Lett. **B440** (1998) 136–140, `arXiv:hep-ph/9807545 [hep-ph]`.

[451] B. A. Kniehl and A. Sirlin, *Differences between the pole and on-shell masses and widths of the Higgs boson*, Phys.Rev.Lett. **81** (1998) 1373–1376, `arXiv:hep-ph/9805390 [hep-ph]`.

[452] A. Denner, S. Dittmaier, M. Roth, and L. Wieders, *Electroweak corrections to charged-current $e^+e^- \to$ 4 fermion processes: Technical details and further results*, Nucl. Phys. **B724** (2005) 247–294, `arXiv:hep-ph/0505042 [hep-ph]`.

[453] S. Actis and G. Passarino, *Two-loop renormalization in the Standard Model. III: Renormalization equations and their solutions*, Nucl. Phys. **B777** (2007) 100–156, `arXiv:hep-ph/0612124`.

[454] S. Actis and G. Passarino, *Two-loop renormalization in the Standard Model Part II: Renormalization procedures and computational techniques*, Nucl.Phys. **B777** (2007) 35–99, `arXiv:hep-ph/0612123 [hep-ph]`.

[455] M. Cacciari and N. Houdeau, *Meaningful characterisation of perturbative theoretical uncertainties*, JHEP **09** (2011) 039, `arXiv:1105.5152 [hep-ph]`.

[456] R. V. Harlander and W. B. Kilgore, *Soft and virtual corrections to $pp \to H + X$ at NNLO*, Phys. Rev. **D64** (2001) 013015, `arXiv:hep-ph/0102241`.

Appendices

A SM Higgs branching ratios

In this appendix we complete the listing of the branching fractions of the Standard Model Higgs boson discussed in Section 2.

Table A.1: SM Higgs branching ratios to two fermions and their total uncertainties (expressed in percentage). Very-low mass range.

M_{H} [GeV]	$\mathrm{H} \to \mathrm{bb}$	$\mathrm{H} \to \tau^+\tau^-$	$\mathrm{H} \to \mu^+\mu^-$	$\mathrm{H} \to \mathrm{c}\overline{\mathrm{c}}$
90.0	$8.10 \cdot 10^{-1}{}^{+1.6\%}_{-1.6\%}$	$8.33 \cdot 10^{-2}{}^{+7.0\%}_{-6.8\%}$	$2.89 \cdot 10^{-4}{}^{+7.3\%}_{-7.1\%}$	$4.10 \cdot 10^{-2}{}^{+12.1\%}_{-12.1\%}$
95.0	$8.02 \cdot 10^{-1}{}^{+1.7\%}_{-1.7\%}$	$8.32 \cdot 10^{-2}{}^{+6.9\%}_{-6.8\%}$	$2.89 \cdot 10^{-4}{}^{+7.3\%}_{-7.1\%}$	$4.05 \cdot 10^{-2}{}^{+12.2\%}_{-12.1\%}$
100.0	$7.89 \cdot 10^{-1}{}^{+1.8\%}_{-1.8\%}$	$8.28 \cdot 10^{-2}{}^{+6.9\%}_{-6.7\%}$	$2.88 \cdot 10^{-4}{}^{+7.2\%}_{-7.0\%}$	$3.99 \cdot 10^{-2}{}^{+12.2\%}_{-12.2\%}$
105.0	$7.71 \cdot 10^{-1}{}^{+1.9\%}_{-2.0\%}$	$8.17 \cdot 10^{-2}{}^{+6.8\%}_{-6.7\%}$	$2.84 \cdot 10^{-4}{}^{+7.1\%}_{-7.0\%}$	$3.90 \cdot 10^{-2}{}^{+12.2\%}_{-12.2\%}$
110.0	$7.44 \cdot 10^{-1}{}^{+2.1\%}_{-2.2\%}$	$7.95 \cdot 10^{-2}{}^{+6.6\%}_{-6.5\%}$	$2.76 \cdot 10^{-4}{}^{+7.0\%}_{-6.8\%}$	$3.75 \cdot 10^{-2}{}^{+12.2\%}_{-12.2\%}$
110.5	$7.40 \cdot 10^{-1}{}^{+2.1\%}_{-2.2\%}$	$7.91 \cdot 10^{-2}{}^{+6.6\%}_{-6.5\%}$	$2.75 \cdot 10^{-4}{}^{+6.9\%}_{-6.8\%}$	$3.74 \cdot 10^{-2}{}^{+12.2\%}_{-12.2\%}$
111.0	$7.37 \cdot 10^{-1}{}^{+2.2\%}_{-2.2\%}$	$7.89 \cdot 10^{-2}{}^{+6.6\%}_{-6.5\%}$	$2.74 \cdot 10^{-4}{}^{+6.9\%}_{-6.8\%}$	$3.72 \cdot 10^{-2}{}^{+12.2\%}_{-12.2\%}$
111.5	$7.33 \cdot 10^{-1}{}^{+2.2\%}_{-2.3\%}$	$7.86 \cdot 10^{-2}{}^{+6.6\%}_{-6.5\%}$	$2.72 \cdot 10^{-4}{}^{+6.9\%}_{-6.8\%}$	$3.70 \cdot 10^{-2}{}^{+12.2\%}_{-12.2\%}$
112.0	$7.29 \cdot 10^{-1}{}^{+2.2\%}_{-2.3\%}$	$7.82 \cdot 10^{-2}{}^{+6.5\%}_{-6.4\%}$	$2.71 \cdot 10^{-4}{}^{+6.9\%}_{-6.7\%}$	$3.68 \cdot 10^{-2}{}^{+12.2\%}_{-12.2\%}$
112.5	$7.25 \cdot 10^{-1}{}^{+2.3\%}_{-2.3\%}$	$7.79 \cdot 10^{-2}{}^{+6.5\%}_{-6.4\%}$	$2.70 \cdot 10^{-4}{}^{+6.8\%}_{-6.7\%}$	$3.66 \cdot 10^{-2}{}^{+12.2\%}_{-12.2\%}$
113.0	$7.21 \cdot 10^{-1}{}^{+2.3\%}_{-2.4\%}$	$7.75 \cdot 10^{-2}{}^{+6.5\%}_{-6.4\%}$	$2.69 \cdot 10^{-4}{}^{+6.8\%}_{-6.7\%}$	$3.64 \cdot 10^{-2}{}^{+12.2\%}_{-12.2\%}$
113.5	$7.17 \cdot 10^{-1}{}^{+2.3\%}_{-2.4\%}$	$7.71 \cdot 10^{-2}{}^{+6.5\%}_{-6.4\%}$	$2.67 \cdot 10^{-4}{}^{+6.8\%}_{-6.7\%}$	$3.62 \cdot 10^{-2}{}^{+12.2\%}_{-12.2\%}$
114.0	$7.12 \cdot 10^{-1}{}^{+2.4\%}_{-2.4\%}$	$7.67 \cdot 10^{-2}{}^{+6.5\%}_{-6.3\%}$	$2.66 \cdot 10^{-4}{}^{+6.8\%}_{-6.7\%}$	$3.59 \cdot 10^{-2}{}^{+12.2\%}_{-12.2\%}$
114.5	$7.08 \cdot 10^{-1}{}^{+2.4\%}_{-2.4\%}$	$7.63 \cdot 10^{-2}{}^{+6.4\%}_{-6.3\%}$	$2.64 \cdot 10^{-4}{}^{+6.8\%}_{-6.6\%}$	$3.57 \cdot 10^{-2}{}^{+12.2\%}_{-12.2\%}$
115.0	$7.03 \cdot 10^{-1}{}^{+2.4\%}_{-2.5\%}$	$7.58 \cdot 10^{-2}{}^{+6.4\%}_{-6.3\%}$	$2.63 \cdot 10^{-4}{}^{+6.7\%}_{-6.6\%}$	$3.55 \cdot 10^{-2}{}^{+12.2\%}_{-12.2\%}$
115.5	$6.98 \cdot 10^{-1}{}^{+2.4\%}_{-2.5\%}$	$7.54 \cdot 10^{-2}{}^{+6.4\%}_{-6.3\%}$	$2.61 \cdot 10^{-4}{}^{+6.7\%}_{-6.6\%}$	$3.52 \cdot 10^{-2}{}^{+12.2\%}_{-12.2\%}$
116.0	$6.93 \cdot 10^{-1}{}^{+2.5\%}_{-2.5\%}$	$7.49 \cdot 10^{-2}{}^{+6.4\%}_{-6.2\%}$	$2.60 \cdot 10^{-4}{}^{+6.7\%}_{-6.6\%}$	$3.50 \cdot 10^{-2}{}^{+12.2\%}_{-12.2\%}$
116.5	$6.88 \cdot 10^{-1}{}^{+2.5\%}_{-2.6\%}$	$7.44 \cdot 10^{-2}{}^{+6.3\%}_{-6.2\%}$	$2.58 \cdot 10^{-4}{}^{+6.6\%}_{-6.5\%}$	$3.48 \cdot 10^{-2}{}^{+12.2\%}_{-12.2\%}$
117.0	$6.83 \cdot 10^{-1}{}^{+2.5\%}_{-2.6\%}$	$7.39 \cdot 10^{-2}{}^{+6.3\%}_{-6.2\%}$	$2.56 \cdot 10^{-4}{}^{+6.6\%}_{-6.5\%}$	$3.44 \cdot 10^{-2}{}^{+12.2\%}_{-12.2\%}$
117.5	$6.77 \cdot 10^{-1}{}^{+2.6\%}_{-2.6\%}$	$7.33 \cdot 10^{-2}{}^{+6.3\%}_{-6.2\%}$	$2.54 \cdot 10^{-4}{}^{+6.6\%}_{-6.5\%}$	$3.42 \cdot 10^{-2}{}^{+12.2\%}_{-12.2\%}$
118.0	$6.72 \cdot 10^{-1}{}^{+2.6\%}_{-2.7\%}$	$7.28 \cdot 10^{-2}{}^{+6.2\%}_{-6.1\%}$	$2.52 \cdot 10^{-4}{}^{+6.5\%}_{-6.4\%}$	$3.40 \cdot 10^{-2}{}^{+12.2\%}_{-12.2\%}$
118.5	$6.66 \cdot 10^{-1}{}^{+2.6\%}_{-2.7\%}$	$7.22 \cdot 10^{-2}{}^{+6.2\%}_{-6.1\%}$	$2.50 \cdot 10^{-4}{}^{+6.5\%}_{-6.4\%}$	$3.37 \cdot 10^{-2}{}^{+12.2\%}_{-12.2\%}$
119.0	$6.60 \cdot 10^{-1}{}^{+2.7\%}_{-2.8\%}$	$7.16 \cdot 10^{-2}{}^{+6.2\%}_{-6.1\%}$	$2.48 \cdot 10^{-4}{}^{+6.5\%}_{-6.4\%}$	$3.33 \cdot 10^{-2}{}^{+12.2\%}_{-12.2\%}$
119.5	$6.54 \cdot 10^{-1}{}^{+2.7\%}_{-2.8\%}$	$7.10 \cdot 10^{-2}{}^{+6.2\%}_{-6.0\%}$	$2.46 \cdot 10^{-4}{}^{+6.4\%}_{-6.3\%}$	$3.31 \cdot 10^{-2}{}^{+12.2\%}_{-12.2\%}$
120.0	$6.48 \cdot 10^{-1}{}^{+2.8\%}_{-2.8\%}$	$7.04 \cdot 10^{-2}{}^{+6.1\%}_{-6.0\%}$	$2.44 \cdot 10^{-4}{}^{+6.4\%}_{-6.3\%}$	$3.27 \cdot 10^{-2}{}^{+12.2\%}_{-12.2\%}$
120.5	$6.41 \cdot 10^{-1}{}^{+2.8\%}_{-2.9\%}$	$6.97 \cdot 10^{-2}{}^{+6.1\%}_{-6.0\%}$	$2.42 \cdot 10^{-4}{}^{+6.4\%}_{-6.3\%}$	$3.24 \cdot 10^{-2}{}^{+12.2\%}_{-12.2\%}$
121.0	$6.35 \cdot 10^{-1}{}^{+2.9\%}_{-2.9\%}$	$6.91 \cdot 10^{-2}{}^{+6.0\%}_{-5.9\%}$	$2.39 \cdot 10^{-4}{}^{+6.3\%}_{-6.2\%}$	$3.21 \cdot 10^{-2}{}^{+12.2\%}_{-12.2\%}$
121.5	$6.28 \cdot 10^{-1}{}^{+2.9\%}_{-3.0\%}$	$6.84 \cdot 10^{-2}{}^{+6.0\%}_{-5.9\%}$	$2.37 \cdot 10^{-4}{}^{+6.3\%}_{-6.2\%}$	$3.17 \cdot 10^{-2}{}^{+12.2\%}_{-12.2\%}$
122.0	$6.21 \cdot 10^{-1}{}^{+2.9\%}_{-3.0\%}$	$6.77 \cdot 10^{-2}{}^{+6.0\%}_{-5.9\%}$	$2.35 \cdot 10^{-4}{}^{+6.2\%}_{-6.1\%}$	$3.14 \cdot 10^{-2}{}^{+12.2\%}_{-12.2\%}$
122.5	$6.14 \cdot 10^{-1}{}^{+3.0\%}_{-3.0\%}$	$6.70 \cdot 10^{-2}{}^{+5.9\%}_{-5.8\%}$	$2.33 \cdot 10^{-4}{}^{+6.2\%}_{-6.1\%}$	$3.10 \cdot 10^{-2}{}^{+12.2\%}_{-12.2\%}$
123.0	$6.07 \cdot 10^{-1}{}^{+3.0\%}_{-3.1\%}$	$6.63 \cdot 10^{-2}{}^{+5.9\%}_{-5.8\%}$	$2.31 \cdot 10^{-4}{}^{+6.2\%}_{-6.0\%}$	$3.07 \cdot 10^{-2}{}^{+12.2\%}_{-12.2\%}$
123.5	$6.00 \cdot 10^{-1}{}^{+3.1\%}_{-3.1\%}$	$6.56 \cdot 10^{-2}{}^{+5.8\%}_{-5.8\%}$	$2.28 \cdot 10^{-4}{}^{+6.1\%}_{-6.0\%}$	$3.03 \cdot 10^{-2}{}^{+12.2\%}_{-12.2\%}$
124.0	$5.92 \cdot 10^{-1}{}^{+3.1\%}_{-3.2\%}$	$6.48 \cdot 10^{-2}{}^{+5.8\%}_{-5.7\%}$	$2.25 \cdot 10^{-4}{}^{+6.1\%}_{-6.0\%}$	$2.99 \cdot 10^{-2}{}^{+12.2\%}_{-12.2\%}$
124.5	$5.84 \cdot 10^{-1}{}^{+3.2\%}_{-3.2\%}$	$6.39 \cdot 10^{-2}{}^{+5.8\%}_{-5.7\%}$	$2.22 \cdot 10^{-4}{}^{+6.0\%}_{-5.9\%}$	$2.95 \cdot 10^{-2}{}^{+12.2\%}_{-12.2\%}$
125.0	$5.77 \cdot 10^{-1}{}^{+3.2\%}_{-3.3\%}$	$6.32 \cdot 10^{-2}{}^{+5.7\%}_{-5.7\%}$	$2.20 \cdot 10^{-4}{}^{+6.0\%}_{-5.9\%}$	$2.91 \cdot 10^{-2}{}^{+12.2\%}_{-12.2\%}$
125.5	$5.69 \cdot 10^{-1}{}^{+3.3\%}_{-3.3\%}$	$6.24 \cdot 10^{-2}{}^{+5.7\%}_{-5.6\%}$	$2.17 \cdot 10^{-4}{}^{+6.0\%}_{-5.8\%}$	$2.87 \cdot 10^{-2}{}^{+12.2\%}_{-12.2\%}$
126.0	$5.61 \cdot 10^{-1}{}^{+3.3\%}_{-3.4\%}$	$6.15 \cdot 10^{-2}{}^{+5.6\%}_{-5.6\%}$	$2.14 \cdot 10^{-4}{}^{+5.9\%}_{-5.8\%}$	$2.83 \cdot 10^{-2}{}^{+12.2\%}_{-12.2\%}$
126.5	$5.53 \cdot 10^{-1}{}^{+3.4\%}_{-3.4\%}$	$6.08 \cdot 10^{-2}{}^{+5.6\%}_{-5.5\%}$	$2.11 \cdot 10^{-4}{}^{+5.9\%}_{-5.7\%}$	$2.79 \cdot 10^{-2}{}^{+12.2\%}_{-12.2\%}$
127.0	$5.45 \cdot 10^{-1}{}^{+3.4\%}_{-3.5\%}$	$5.99 \cdot 10^{-2}{}^{+5.5\%}_{-5.5\%}$	$2.08 \cdot 10^{-4}{}^{+5.8\%}_{-5.7\%}$	$2.75 \cdot 10^{-2}{}^{+12.2\%}_{-12.2\%}$
127.5	$5.37 \cdot 10^{-1}{}^{+3.5\%}_{-3.5\%}$	$5.90 \cdot 10^{-2}{}^{+5.5\%}_{-5.4\%}$	$2.05 \cdot 10^{-4}{}^{+5.8\%}_{-5.6\%}$	$2.71 \cdot 10^{-2}{}^{+12.2\%}_{-12.2\%}$
128.0	$5.28 \cdot 10^{-1}{}^{+3.5\%}_{-3.6\%}$	$5.81 \cdot 10^{-2}{}^{+5.4\%}_{-5.4\%}$	$2.01 \cdot 10^{-4}{}^{+5.7\%}_{-5.6\%}$	$2.67 \cdot 10^{-2}{}^{+12.2\%}_{-12.2\%}$
128.5	$5.19 \cdot 10^{-1}{}^{+3.6\%}_{-3.6\%}$	$5.72 \cdot 10^{-2}{}^{+5.4\%}_{-5.3\%}$	$1.98 \cdot 10^{-4}{}^{+5.7\%}_{-5.5\%}$	$2.63 \cdot 10^{-2}{}^{+12.2\%}_{-12.2\%}$
129.0	$5.11 \cdot 10^{-1}{}^{+3.6\%}_{-3.7\%}$	$5.63 \cdot 10^{-2}{}^{+5.3\%}_{-5.3\%}$	$1.95 \cdot 10^{-4}{}^{+5.6\%}_{-5.5\%}$	$2.58 \cdot 10^{-2}{}^{+12.2\%}_{-12.2\%}$
129.5	$5.02 \cdot 10^{-1}{}^{+3.7\%}_{-3.7\%}$	$5.54 \cdot 10^{-2}{}^{+5.3\%}_{-5.3\%}$	$1.92 \cdot 10^{-4}{}^{+5.6\%}_{-5.5\%}$	$2.54 \cdot 10^{-2}{}^{+12.2\%}_{-12.2\%}$
130.0	$4.94 \cdot 10^{-1}{}^{+3.7\%}_{-3.8\%}$	$5.45 \cdot 10^{-2}{}^{+5.3\%}_{-5.2\%}$	$1.90 \cdot 10^{-4}{}^{+5.5\%}_{-5.4\%}$	$2.49 \cdot 10^{-2}{}^{+12.2\%}_{-12.1\%}$

Table A.2: SM Higgs branching ratios to two fermions and their total uncertainties (expressed in percentage). Low- and intermediate-mass range.

M_{H} [GeV]	$\mathrm{H} \to \mathrm{bb}$	$\mathrm{H} \to \tau^+\tau^-$	$\mathrm{H} \to \mu^+\mu^-$	$\mathrm{H} \to c\overline{c}$
130.5	$4.85 \cdot 10^{-1}{}^{+3.8\%}_{-3.8\%}$	$5.36 \cdot 10^{-2}{}^{+5.2\%}_{-5.2\%}$	$1.86 \cdot 10^{-4}{}^{+5.5\%}_{-5.4\%}$	$2.45 \cdot 10^{-2}{}^{+12.2\%}_{-12.1\%}$
131.0	$4.76 \cdot 10^{-1}{}^{+3.8\%}_{-3.9\%}$	$5.26 \cdot 10^{-2}{}^{+5.2\%}_{-5.1\%}$	$1.82 \cdot 10^{-4}{}^{+5.4\%}_{-5.3\%}$	$2.41 \cdot 10^{-2}{}^{+12.2\%}_{-12.1\%}$
131.5	$4.67 \cdot 10^{-1}{}^{+3.9\%}_{-3.9\%}$	$5.17 \cdot 10^{-2}{}^{+5.1\%}_{-5.1\%}$	$1.80 \cdot 10^{-4}{}^{+5.4\%}_{-5.3\%}$	$2.36 \cdot 10^{-2}{}^{+12.2\%}_{-12.1\%}$
132.0	$4.58 \cdot 10^{-1}{}^{+3.9\%}_{-4.0\%}$	$5.07 \cdot 10^{-2}{}^{+5.1\%}_{-5.0\%}$	$1.77 \cdot 10^{-4}{}^{+5.3\%}_{-5.2\%}$	$2.32 \cdot 10^{-2}{}^{+12.2\%}_{-12.1\%}$
132.5	$4.49 \cdot 10^{-1}{}^{+4.0\%}_{-4.0\%}$	$4.97 \cdot 10^{-2}{}^{+5.0\%}_{-5.0\%}$	$1.72 \cdot 10^{-4}{}^{+5.2\%}_{-5.2\%}$	$2.27 \cdot 10^{-2}{}^{+12.2\%}_{-12.1\%}$
133.0	$4.40 \cdot 10^{-1}{}^{+4.0\%}_{-4.1\%}$	$4.88 \cdot 10^{-2}{}^{+5.0\%}_{-4.9\%}$	$1.69 \cdot 10^{-4}{}^{+5.2\%}_{-5.1\%}$	$2.23 \cdot 10^{-2}{}^{+12.2\%}_{-12.1\%}$
133.5	$4.31 \cdot 10^{-1}{}^{+4.1\%}_{-4.2\%}$	$4.79 \cdot 10^{-2}{}^{+4.9\%}_{-4.9\%}$	$1.67 \cdot 10^{-4}{}^{+5.1\%}_{-5.1\%}$	$2.18 \cdot 10^{-2}{}^{+12.2\%}_{-12.1\%}$
134.0	$4.22 \cdot 10^{-1}{}^{+4.1\%}_{-4.2\%}$	$4.68 \cdot 10^{-2}{}^{+4.8\%}_{-4.8\%}$	$1.63 \cdot 10^{-4}{}^{+5.1\%}_{-5.0\%}$	$2.13 \cdot 10^{-2}{}^{+12.2\%}_{-12.1\%}$
134.5	$4.13 \cdot 10^{-1}{}^{+4.2\%}_{-4.3\%}$	$4.59 \cdot 10^{-2}{}^{+4.8\%}_{-4.8\%}$	$1.60 \cdot 10^{-4}{}^{+5.0\%}_{-5.0\%}$	$2.09 \cdot 10^{-2}{}^{+12.2\%}_{-12.1\%}$
135.0	$4.04 \cdot 10^{-1}{}^{+4.2\%}_{-4.3\%}$	$4.49 \cdot 10^{-2}{}^{+4.8\%}_{-4.8\%}$	$1.55 \cdot 10^{-4}{}^{+5.0\%}_{-4.9\%}$	$2.04 \cdot 10^{-2}{}^{+12.2\%}_{-12.1\%}$
135.5	$3.95 \cdot 10^{-1}{}^{+4.2\%}_{-4.2\%}$	$4.39 \cdot 10^{-2}{}^{+4.6\%}_{-4.6\%}$	$1.52 \cdot 10^{-4}{}^{+4.8\%}_{-4.8\%}$	$2.00 \cdot 10^{-2}{}^{+11.9\%}_{-11.8\%}$
136.0	$3.86 \cdot 10^{-1}{}^{+4.1\%}_{-4.1\%}$	$4.29 \cdot 10^{-2}{}^{+4.5\%}_{-4.5\%}$	$1.49 \cdot 10^{-4}{}^{+4.7\%}_{-4.7\%}$	$1.95 \cdot 10^{-2}{}^{+11.6\%}_{-11.6\%}$
136.5	$3.77 \cdot 10^{-1}{}^{+4.0\%}_{-4.0\%}$	$4.20 \cdot 10^{-2}{}^{+4.4\%}_{-4.4\%}$	$1.45 \cdot 10^{-4}{}^{+4.6\%}_{-4.6\%}$	$1.91 \cdot 10^{-2}{}^{+11.4\%}_{-11.3\%}$
137.0	$3.68 \cdot 10^{-1}{}^{+3.9\%}_{-4.0\%}$	$4.10 \cdot 10^{-2}{}^{+4.3\%}_{-4.3\%}$	$1.42 \cdot 10^{-4}{}^{+4.5\%}_{-4.5\%}$	$1.86 \cdot 10^{-2}{}^{+11.1\%}_{-11.1\%}$
137.5	$3.59 \cdot 10^{-1}{}^{+3.8\%}_{-3.9\%}$	$4.00 \cdot 10^{-2}{}^{+4.2\%}_{-4.2\%}$	$1.39 \cdot 10^{-4}{}^{+4.3\%}_{-4.4\%}$	$1.81 \cdot 10^{-2}{}^{+10.8\%}_{-10.8\%}$
138.0	$3.50 \cdot 10^{-1}{}^{+3.7\%}_{-3.8\%}$	$3.91 \cdot 10^{-2}{}^{+4.1\%}_{-4.1\%}$	$1.35 \cdot 10^{-4}{}^{+4.2\%}_{-4.3\%}$	$1.77 \cdot 10^{-2}{}^{+10.6\%}_{-10.5\%}$
138.5	$3.41 \cdot 10^{-1}{}^{+3.7\%}_{-3.7\%}$	$3.81 \cdot 10^{-2}{}^{+3.9\%}_{-4.0\%}$	$1.32 \cdot 10^{-4}{}^{+4.1\%}_{-4.2\%}$	$1.73 \cdot 10^{-2}{}^{+10.3\%}_{-10.3\%}$
139.0	$3.32 \cdot 10^{-1}{}^{+3.6\%}_{-3.6\%}$	$3.71 \cdot 10^{-2}{}^{+3.8\%}_{-3.8\%}$	$1.29 \cdot 10^{-4}{}^{+4.0\%}_{-4.0\%}$	$1.68 \cdot 10^{-2}{}^{+10.0\%}_{-10.0\%}$
139.5	$3.23 \cdot 10^{-1}{}^{+3.5\%}_{-3.5\%}$	$3.62 \cdot 10^{-2}{}^{+3.7\%}_{-3.7\%}$	$1.25 \cdot 10^{-4}{}^{+3.8\%}_{-3.9\%}$	$1.63 \cdot 10^{-2}{}^{+9.8\%}_{-9.8\%}$
140.0	$3.15 \cdot 10^{-1}{}^{+3.4\%}_{-3.4\%}$	$3.52 \cdot 10^{-2}{}^{+3.6\%}_{-3.6\%}$	$1.22 \cdot 10^{-4}{}^{+3.7\%}_{-3.8\%}$	$1.58 \cdot 10^{-2}{}^{+9.5\%}_{-9.5\%}$
141.0	$2.97 \cdot 10^{-1}{}^{+3.5\%}_{-3.5\%}$	$3.33 \cdot 10^{-2}{}^{+3.5\%}_{-3.5\%}$	$1.15 \cdot 10^{-4}{}^{+3.6\%}_{-3.7\%}$	$1.50 \cdot 10^{-2}{}^{+9.5\%}_{-9.5\%}$
142.0	$2.81 \cdot 10^{-1}{}^{+3.5\%}_{-3.5\%}$	$3.15 \cdot 10^{-2}{}^{+3.5\%}_{-3.5\%}$	$1.09 \cdot 10^{-4}{}^{+3.6\%}_{-3.6\%}$	$1.41 \cdot 10^{-2}{}^{+9.5\%}_{-9.6\%}$
143.0	$2.64 \cdot 10^{-1}{}^{+3.6\%}_{-3.6\%}$	$2.97 \cdot 10^{-2}{}^{+3.4\%}_{-3.4\%}$	$1.03 \cdot 10^{-4}{}^{+3.5\%}_{-3.6\%}$	$1.33 \cdot 10^{-2}{}^{+9.5\%}_{-9.6\%}$
144.0	$2.48 \cdot 10^{-1}{}^{+3.7\%}_{-3.6\%}$	$2.79 \cdot 10^{-2}{}^{+3.4\%}_{-3.4\%}$	$9.67 \cdot 10^{-5}{}^{+3.5\%}_{-3.5\%}$	$1.25 \cdot 10^{-2}{}^{+9.5\%}_{-9.7\%}$
145.0	$2.32 \cdot 10^{-1}{}^{+3.7\%}_{-3.7\%}$	$2.61 \cdot 10^{-2}{}^{+3.3\%}_{-3.3\%}$	$9.06 \cdot 10^{-5}{}^{+3.4\%}_{-3.4\%}$	$1.16 \cdot 10^{-2}{}^{+9.6\%}_{-9.7\%}$
146.0	$2.16 \cdot 10^{-1}{}^{+3.8\%}_{-3.8\%}$	$2.44 \cdot 10^{-2}{}^{+3.3\%}_{-3.3\%}$	$8.46 \cdot 10^{-5}{}^{+3.4\%}_{-3.4\%}$	$1.09 \cdot 10^{-2}{}^{+9.6\%}_{-9.7\%}$
147.0	$2.01 \cdot 10^{-1}{}^{+3.8\%}_{-3.8\%}$	$2.27 \cdot 10^{-2}{}^{+3.2\%}_{-3.2\%}$	$7.87 \cdot 10^{-5}{}^{+3.3\%}_{-3.3\%}$	$1.01 \cdot 10^{-2}{}^{+9.6\%}_{-9.7\%}$
148.0	$1.85 \cdot 10^{-1}{}^{+3.9\%}_{-3.9\%}$	$2.09 \cdot 10^{-2}{}^{+3.1\%}_{-3.2\%}$	$7.26 \cdot 10^{-5}{}^{+3.2\%}_{-3.3\%}$	$9.35 \cdot 10^{-3}{}^{+9.7\%}_{-9.7\%}$
149.0	$1.72 \cdot 10^{-1}{}^{+3.9\%}_{-4.0\%}$	$1.94 \cdot 10^{-2}{}^{+3.1\%}_{-3.1\%}$	$6.74 \cdot 10^{-5}{}^{+3.2\%}_{-3.2\%}$	$8.65 \cdot 10^{-3}{}^{+9.7\%}_{-9.7\%}$
150.0	$1.57 \cdot 10^{-1}{}^{+4.0\%}_{-4.0\%}$	$1.79 \cdot 10^{-2}{}^{+3.0\%}_{-3.1\%}$	$6.19 \cdot 10^{-5}{}^{+3.1\%}_{-3.2\%}$	$7.93 \cdot 10^{-3}{}^{+9.7\%}_{-9.7\%}$
151.0	$1.43 \cdot 10^{-1}{}^{+4.0\%}_{-4.1\%}$	$1.62 \cdot 10^{-2}{}^{+3.0\%}_{-3.0\%}$	$5.65 \cdot 10^{-5}{}^{+3.1\%}_{-3.1\%}$	$7.23 \cdot 10^{-3}{}^{+9.8\%}_{-9.7\%}$
152.0	$1.30 \cdot 10^{-1}{}^{+4.1\%}_{-4.1\%}$	$1.48 \cdot 10^{-2}{}^{+3.0\%}_{-3.0\%}$	$5.13 \cdot 10^{-5}{}^{+3.0\%}_{-3.1\%}$	$6.57 \cdot 10^{-3}{}^{+9.8\%}_{-9.8\%}$
153.0	$1.17 \cdot 10^{-1}{}^{+4.2\%}_{-4.2\%}$	$1.34 \cdot 10^{-2}{}^{+2.9\%}_{-3.0\%}$	$4.63 \cdot 10^{-5}{}^{+3.0\%}_{-3.0\%}$	$5.91 \cdot 10^{-3}{}^{+9.8\%}_{-9.8\%}$
154.0	$1.05 \cdot 10^{-1}{}^{+4.2\%}_{-4.2\%}$	$1.19 \cdot 10^{-2}{}^{+2.9\%}_{-2.9\%}$	$4.14 \cdot 10^{-5}{}^{+2.9\%}_{-3.0\%}$	$5.28 \cdot 10^{-3}{}^{+9.8\%}_{-9.8\%}$
155.0	$9.23 \cdot 10^{-2}{}^{+4.3\%}_{-4.2\%}$	$1.05 \cdot 10^{-2}{}^{+2.8\%}_{-2.9\%}$	$3.65 \cdot 10^{-5}{}^{+2.9\%}_{-2.9\%}$	$4.65 \cdot 10^{-3}{}^{+9.8\%}_{-9.8\%}$
156.0	$8.02 \cdot 10^{-2}{}^{+4.3\%}_{-4.3\%}$	$9.15 \cdot 10^{-3}{}^{+2.8\%}_{-2.8\%}$	$3.17 \cdot 10^{-5}{}^{+2.8\%}_{-2.9\%}$	$4.04 \cdot 10^{-3}{}^{+9.9\%}_{-9.8\%}$
157.0	$6.82 \cdot 10^{-2}{}^{+4.3\%}_{-4.3\%}$	$7.79 \cdot 10^{-3}{}^{+2.8\%}_{-2.8\%}$	$2.71 \cdot 10^{-5}{}^{+2.8\%}_{-2.8\%}$	$3.44 \cdot 10^{-3}{}^{+9.9\%}_{-9.8\%}$
158.0	$5.65 \cdot 10^{-2}{}^{+4.4\%}_{-4.4\%}$	$6.46 \cdot 10^{-3}{}^{+2.7\%}_{-2.8\%}$	$2.25 \cdot 10^{-5}{}^{+2.8\%}_{-2.7\%}$	$2.85 \cdot 10^{-3}{}^{+9.9\%}_{-9.8\%}$
159.0	$4.52 \cdot 10^{-2}{}^{+4.4\%}_{-4.4\%}$	$5.17 \cdot 10^{-3}{}^{+2.7\%}_{-2.7\%}$	$1.80 \cdot 10^{-5}{}^{+2.8\%}_{-2.7\%}$	$2.28 \cdot 10^{-3}{}^{+9.9\%}_{-9.8\%}$
160.0	$3.46 \cdot 10^{-2}{}^{+4.5\%}_{-4.4\%}$	$3.96 \cdot 10^{-3}{}^{+2.6\%}_{-2.7\%}$	$1.38 \cdot 10^{-5}{}^{+2.7\%}_{-2.6\%}$	$1.74 \cdot 10^{-3}{}^{+9.9\%}_{-9.8\%}$
162.0	$1.98 \cdot 10^{-2}{}^{+4.5\%}_{-4.5\%}$	$2.27 \cdot 10^{-3}{}^{+2.6\%}_{-2.7\%}$	$7.87 \cdot 10^{-6}{}^{+2.7\%}_{-2.6\%}$	$9.95 \cdot 10^{-4}{}^{+9.9\%}_{-9.8\%}$
164.0	$1.36 \cdot 10^{-2}{}^{+4.5\%}_{-4.5\%}$	$1.56 \cdot 10^{-3}{}^{+2.6\%}_{-2.7\%}$	$5.43 \cdot 10^{-6}{}^{+2.7\%}_{-2.6\%}$	$6.85 \cdot 10^{-4}{}^{+9.9\%}_{-9.9\%}$
166.0	$1.07 \cdot 10^{-2}{}^{+4.5\%}_{-4.5\%}$	$1.24 \cdot 10^{-3}{}^{+2.6\%}_{-2.6\%}$	$4.30 \cdot 10^{-6}{}^{+2.7\%}_{-2.6\%}$	$5.40 \cdot 10^{-4}{}^{+9.9\%}_{-9.9\%}$
168.0	$9.06 \cdot 10^{-3}{}^{+4.5\%}_{-4.5\%}$	$1.05 \cdot 10^{-3}{}^{+2.6\%}_{-2.6\%}$	$3.63 \cdot 10^{-6}{}^{+2.6\%}_{-2.6\%}$	$4.57 \cdot 10^{-4}{}^{+9.9\%}_{-9.9\%}$
170.0	$7.93 \cdot 10^{-3}{}^{+4.5\%}_{-4.5\%}$	$9.20 \cdot 10^{-4}{}^{+2.6\%}_{-2.6\%}$	$3.19 \cdot 10^{-6}{}^{+2.6\%}_{-2.6\%}$	$4.00 \cdot 10^{-4}{}^{+9.9\%}_{-9.9\%}$

Table A.3: SM Higgs branching ratios to two fermions and their total uncertainties (expressed in percentage). Intermediate-mass range.

$M_{\rm H}$ [GeV]	$\rm H \to bb$	$\rm H \to \tau^+\tau^-$	$\rm H \to \mu^+\mu^-$	$\rm H \to c\overline{c}$
172.0	$7.10\cdot10^{-3}{}^{+4.5\%}_{-4.5\%}$	$8.25\cdot10^{-4}{}^{+2.6\%}_{-2.6\%}$	$2.86\cdot10^{-6}{}^{+2.6\%}_{-2.6\%}$	$3.57\cdot10^{-4}{}^{+9.9\%}_{-9.9\%}$
174.0	$6.45\cdot10^{-3}{}^{+4.5\%}_{-4.5\%}$	$7.51\cdot10^{-4}{}^{+2.6\%}_{-2.6\%}$	$2.60\cdot10^{-6}{}^{+2.6\%}_{-2.6\%}$	$3.25\cdot10^{-4}{}^{+10.0\%}_{-9.9\%}$
176.0	$5.91\cdot10^{-3}{}^{+4.6\%}_{-4.5\%}$	$6.89\cdot10^{-4}{}^{+2.6\%}_{-2.6\%}$	$2.39\cdot10^{-6}{}^{+2.7\%}_{-2.6\%}$	$2.97\cdot10^{-4}{}^{+10.0\%}_{-9.9\%}$
178.0	$5.44\cdot10^{-3}{}^{+4.6\%}_{-4.5\%}$	$6.36\cdot10^{-4}{}^{+2.6\%}_{-2.6\%}$	$2.20\cdot10^{-6}{}^{+2.7\%}_{-2.6\%}$	$2.74\cdot10^{-4}{}^{+10.0\%}_{-9.9\%}$
180.0	$5.01\cdot10^{-3}{}^{+4.6\%}_{-4.5\%}$	$5.87\cdot10^{-4}{}^{+2.6\%}_{-2.6\%}$	$2.04\cdot10^{-6}{}^{+2.7\%}_{-2.6\%}$	$2.52\cdot10^{-4}{}^{+10.0\%}_{-9.9\%}$
182.0	$4.55\cdot10^{-3}{}^{+4.6\%}_{-4.5\%}$	$5.34\cdot10^{-4}{}^{+2.6\%}_{-2.6\%}$	$1.85\cdot10^{-6}{}^{+2.7\%}_{-2.6\%}$	$2.29\cdot10^{-4}{}^{+10.0\%}_{-9.9\%}$
184.0	$4.09\cdot10^{-3}{}^{+4.6\%}_{-4.5\%}$	$4.81\cdot10^{-4}{}^{+2.6\%}_{-2.6\%}$	$1.67\cdot10^{-6}{}^{+2.7\%}_{-2.6\%}$	$2.06\cdot10^{-4}{}^{+10.0\%}_{-9.9\%}$
186.0	$3.70\cdot10^{-3}{}^{+4.6\%}_{-4.5\%}$	$4.37\cdot10^{-4}{}^{+2.6\%}_{-2.6\%}$	$1.52\cdot10^{-6}{}^{+2.6\%}_{-2.5\%}$	$1.87\cdot10^{-4}{}^{+10.0\%}_{-9.9\%}$
188.0	$3.41\cdot10^{-3}{}^{+4.6\%}_{-4.5\%}$	$4.03\cdot10^{-4}{}^{+2.6\%}_{-2.6\%}$	$1.40\cdot10^{-6}{}^{+2.6\%}_{-2.5\%}$	$1.72\cdot10^{-4}{}^{+10.0\%}_{-9.9\%}$
190.0	$3.17\cdot10^{-3}{}^{+4.6\%}_{-4.6\%}$	$3.76\cdot10^{-4}{}^{+2.6\%}_{-2.5\%}$	$1.31\cdot10^{-6}{}^{+2.6\%}_{-2.5\%}$	$1.59\cdot10^{-4}{}^{+10.0\%}_{-9.8\%}$
192.0	$2.97\cdot10^{-3}{}^{+4.6\%}_{-4.6\%}$	$3.53\cdot10^{-4}{}^{+2.6\%}_{-2.6\%}$	$1.23\cdot10^{-6}{}^{+2.6\%}_{-2.5\%}$	$1.50\cdot10^{-4}{}^{+10.0\%}_{-9.9\%}$
194.0	$2.80\cdot10^{-3}{}^{+4.6\%}_{-4.6\%}$	$3.33\cdot10^{-4}{}^{+2.6\%}_{-2.6\%}$	$1.16\cdot10^{-6}{}^{+2.6\%}_{-2.6\%}$	$1.41\cdot10^{-4}{}^{+10.0\%}_{-9.9\%}$
196.0	$2.65\cdot10^{-3}{}^{+4.6\%}_{-4.6\%}$	$3.16\cdot10^{-4}{}^{+2.6\%}_{-2.6\%}$	$1.10\cdot10^{-6}{}^{+2.6\%}_{-2.6\%}$	$1.34\cdot10^{-4}{}^{+10.0\%}_{-9.9\%}$
198.0	$2.52\cdot10^{-3}{}^{+4.6\%}_{-4.6\%}$	$3.01\cdot10^{-4}{}^{+2.6\%}_{-2.6\%}$	$1.05\cdot10^{-6}{}^{+2.6\%}_{-2.6\%}$	$1.27\cdot10^{-4}{}^{+10.0\%}_{-9.9\%}$
200.0	$2.40\cdot10^{-3}{}^{+4.6\%}_{-4.6\%}$	$2.87\cdot10^{-4}{}^{+2.5\%}_{-2.6\%}$	$9.96\cdot10^{-7}{}^{+2.6\%}_{-2.6\%}$	$1.21\cdot10^{-4}{}^{+10.0\%}_{-10.0\%}$
202.0	$2.29\cdot10^{-3}{}^{+4.6\%}_{-4.6\%}$	$2.75\cdot10^{-4}{}^{+2.6\%}_{-2.6\%}$	$9.52\cdot10^{-7}{}^{+2.6\%}_{-2.6\%}$	$1.16\cdot10^{-4}{}^{+10.0\%}_{-10.0\%}$
204.0	$2.19\cdot10^{-3}{}^{+4.6\%}_{-4.6\%}$	$2.63\cdot10^{-4}{}^{+2.6\%}_{-2.6\%}$	$9.13\cdot10^{-7}{}^{+2.6\%}_{-2.6\%}$	$1.11\cdot10^{-4}{}^{+10.0\%}_{-10.0\%}$
206.0	$2.10\cdot10^{-3}{}^{+4.6\%}_{-4.6\%}$	$2.52\cdot10^{-4}{}^{+2.6\%}_{-2.6\%}$	$8.76\cdot10^{-7}{}^{+2.6\%}_{-2.6\%}$	$1.06\cdot10^{-4}{}^{+10.0\%}_{-9.9\%}$
208.0	$2.01\cdot10^{-3}{}^{+4.6\%}_{-4.6\%}$	$2.43\cdot10^{-4}{}^{+2.6\%}_{-2.6\%}$	$8.43\cdot10^{-7}{}^{+2.6\%}_{-2.6\%}$	$1.02\cdot10^{-4}{}^{+10.0\%}_{-9.9\%}$
210.0	$1.93\cdot10^{-3}{}^{+4.6\%}_{-4.6\%}$	$2.34\cdot10^{-4}{}^{+2.6\%}_{-2.6\%}$	$8.11\cdot10^{-7}{}^{+2.6\%}_{-2.6\%}$	$9.75\cdot10^{-5}{}^{+10.0\%}_{-9.9\%}$
212.0	$1.87\cdot10^{-3}{}^{+4.6\%}_{-4.6\%}$	$2.25\cdot10^{-4}{}^{+2.6\%}_{-2.6\%}$	$7.81\cdot10^{-7}{}^{+2.6\%}_{-2.6\%}$	$9.38\cdot10^{-5}{}^{+10.0\%}_{-9.9\%}$
214.0	$1.80\cdot10^{-3}{}^{+4.7\%}_{-4.6\%}$	$2.18\cdot10^{-4}{}^{+2.6\%}_{-2.6\%}$	$7.54\cdot10^{-7}{}^{+2.6\%}_{-2.6\%}$	$9.04\cdot10^{-5}{}^{+10.1\%}_{-9.9\%}$
216.0	$1.73\cdot10^{-3}{}^{+4.7\%}_{-4.6\%}$	$2.10\cdot10^{-4}{}^{+2.6\%}_{-2.6\%}$	$7.29\cdot10^{-7}{}^{+2.6\%}_{-2.6\%}$	$8.71\cdot10^{-5}{}^{+10.1\%}_{-9.9\%}$
218.0	$1.67\cdot10^{-3}{}^{+4.7\%}_{-4.5\%}$	$2.03\cdot10^{-4}{}^{+2.6\%}_{-2.6\%}$	$7.04\cdot10^{-7}{}^{+2.6\%}_{-2.6\%}$	$8.41\cdot10^{-5}{}^{+10.1\%}_{-9.9\%}$
220.0	$1.61\cdot10^{-3}{}^{+4.7\%}_{-4.5\%}$	$1.97\cdot10^{-4}{}^{+2.6\%}_{-2.6\%}$	$6.81\cdot10^{-7}{}^{+2.6\%}_{-2.6\%}$	$8.11\cdot10^{-5}{}^{+10.1\%}_{-9.9\%}$
222.0	$1.56\cdot10^{-3}{}^{+4.7\%}_{-4.5\%}$	$1.90\cdot10^{-4}{}^{+2.6\%}_{-2.6\%}$	$6.59\cdot10^{-7}{}^{+2.6\%}_{-2.6\%}$	$7.84\cdot10^{-5}{}^{+10.1\%}_{-9.9\%}$
224.0	$1.51\cdot10^{-3}{}^{+4.7\%}_{-4.5\%}$	$1.84\cdot10^{-4}{}^{+2.6\%}_{-2.6\%}$	$6.39\cdot10^{-7}{}^{+2.6\%}_{-2.6\%}$	$7.59\cdot10^{-5}{}^{+10.1\%}_{-9.9\%}$
226.0	$1.46\cdot10^{-3}{}^{+4.7\%}_{-4.5\%}$	$1.79\cdot10^{-4}{}^{+2.6\%}_{-2.6\%}$	$6.19\cdot10^{-7}{}^{+2.6\%}_{-2.6\%}$	$7.34\cdot10^{-5}{}^{+10.1\%}_{-10.0\%}$
228.0	$1.41\cdot10^{-3}{}^{+4.7\%}_{-4.5\%}$	$1.73\cdot10^{-4}{}^{+2.6\%}_{-2.6\%}$	$6.00\cdot10^{-7}{}^{+2.6\%}_{-2.6\%}$	$7.10\cdot10^{-5}{}^{+10.1\%}_{-10.0\%}$
230.0	$1.37\cdot10^{-3}{}^{+4.7\%}_{-4.5\%}$	$1.68\cdot10^{-4}{}^{+2.6\%}_{-2.6\%}$	$5.82\cdot10^{-7}{}^{+2.6\%}_{-2.6\%}$	$6.88\cdot10^{-5}{}^{+10.1\%}_{-10.0\%}$
232.0	$1.33\cdot10^{-3}{}^{+4.7\%}_{-4.5\%}$	$1.63\cdot10^{-4}{}^{+2.6\%}_{-2.6\%}$	$5.65\cdot10^{-7}{}^{+2.6\%}_{-2.6\%}$	$6.67\cdot10^{-5}{}^{+10.1\%}_{-10.0\%}$
234.0	$1.29\cdot10^{-3}{}^{+4.7\%}_{-4.5\%}$	$1.58\cdot10^{-4}{}^{+2.6\%}_{-2.6\%}$	$5.49\cdot10^{-7}{}^{+2.6\%}_{-2.6\%}$	$6.46\cdot10^{-5}{}^{+10.1\%}_{-10.0\%}$
236.0	$1.25\cdot10^{-3}{}^{+4.7\%}_{-4.5\%}$	$1.54\cdot10^{-4}{}^{+2.6\%}_{-2.6\%}$	$5.33\cdot10^{-7}{}^{+2.6\%}_{-2.6\%}$	$6.27\cdot10^{-5}{}^{+10.1\%}_{-10.0\%}$
238.0	$1.21\cdot10^{-3}{}^{+4.7\%}_{-4.5\%}$	$1.49\cdot10^{-4}{}^{+2.6\%}_{-2.6\%}$	$5.19\cdot10^{-7}{}^{+2.6\%}_{-2.6\%}$	$6.09\cdot10^{-5}{}^{+10.1\%}_{-10.0\%}$
240.0	$1.17\cdot10^{-3}{}^{+4.7\%}_{-4.5\%}$	$1.45\cdot10^{-4}{}^{+2.6\%}_{-2.6\%}$	$5.05\cdot10^{-7}{}^{+2.6\%}_{-2.6\%}$	$5.92\cdot10^{-5}{}^{+10.1\%}_{-10.0\%}$
242.0	$1.14\cdot10^{-3}{}^{+4.7\%}_{-4.6\%}$	$1.41\cdot10^{-4}{}^{+2.6\%}_{-2.6\%}$	$4.91\cdot10^{-7}{}^{+2.6\%}_{-2.6\%}$	$5.75\cdot10^{-5}{}^{+10.1\%}_{-10.0\%}$
244.0	$1.11\cdot10^{-3}{}^{+4.7\%}_{-4.6\%}$	$1.38\cdot10^{-4}{}^{+2.6\%}_{-2.6\%}$	$4.78\cdot10^{-7}{}^{+2.6\%}_{-2.6\%}$	$5.59\cdot10^{-5}{}^{+10.1\%}_{-10.0\%}$
246.0	$1.08\cdot10^{-3}{}^{+4.7\%}_{-4.6\%}$	$1.34\cdot10^{-4}{}^{+2.6\%}_{-2.6\%}$	$4.66\cdot10^{-7}{}^{+2.6\%}_{-2.6\%}$	$5.43\cdot10^{-5}{}^{+10.1\%}_{-10.0\%}$
248.0	$1.05\cdot10^{-3}{}^{+4.7\%}_{-4.6\%}$	$1.31\cdot10^{-4}{}^{+2.6\%}_{-2.7\%}$	$4.53\cdot10^{-7}{}^{+2.6\%}_{-2.6\%}$	$5.28\cdot10^{-5}{}^{+10.1\%}_{-10.0\%}$
250.0	$1.02\cdot10^{-3}{}^{+4.7\%}_{-4.6\%}$	$1.27\cdot10^{-4}{}^{+2.6\%}_{-2.7\%}$	$4.42\cdot10^{-7}{}^{+2.6\%}_{-2.6\%}$	$5.14\cdot10^{-5}{}^{+10.1\%}_{-10.0\%}$
252.0	$9.95\cdot10^{-4}{}^{+4.7\%}_{-4.6\%}$	$1.24\cdot10^{-4}{}^{+2.6\%}_{-2.7\%}$	$4.31\cdot10^{-7}{}^{+2.6\%}_{-2.6\%}$	$5.00\cdot10^{-5}{}^{+10.1\%}_{-10.0\%}$
254.0	$9.69\cdot10^{-4}{}^{+4.7\%}_{-4.6\%}$	$1.21\cdot10^{-4}{}^{+2.6\%}_{-2.6\%}$	$4.20\cdot10^{-7}{}^{+2.6\%}_{-2.6\%}$	$4.87\cdot10^{-5}{}^{+10.1\%}_{-10.0\%}$
256.0	$9.43\cdot10^{-4}{}^{+4.7\%}_{-4.6\%}$	$1.18\cdot10^{-4}{}^{+2.6\%}_{-2.6\%}$	$4.10\cdot10^{-7}{}^{+2.6\%}_{-2.6\%}$	$4.74\cdot10^{-5}{}^{+10.1\%}_{-10.0\%}$
258.0	$9.19\cdot10^{-4}{}^{+4.7\%}_{-4.6\%}$	$1.15\cdot10^{-4}{}^{+2.6\%}_{-2.6\%}$	$4.00\cdot10^{-7}{}^{+2.6\%}_{-2.6\%}$	$4.62\cdot10^{-5}{}^{+10.1\%}_{-10.0\%}$
260.0	$8.96\cdot10^{-4}{}^{+4.7\%}_{-4.6\%}$	$1.12\cdot10^{-4}{}^{+2.6\%}_{-2.6\%}$	$3.90\cdot10^{-7}{}^{+2.6\%}_{-2.6\%}$	$4.51\cdot10^{-5}{}^{+10.1\%}_{-10.0\%}$

Table A.4: SM Higgs branching ratios to two fermions and their total uncertainties (expressed in percentage). High-mass range.

M_{H} [GeV]	$\mathrm{H} \to \mathrm{bb}$	$\mathrm{H} \to \tau^+\tau^-$	$\mathrm{H} \to \mu^+\mu^-$	$\mathrm{H} \to \mathrm{c}\overline{\mathrm{c}}$	$\mathrm{H} \to \mathrm{t}\overline{\mathrm{t}}$
262.0	$8.74 \cdot 10^{-4}{}^{+4.7\%}_{-4.6\%}$	$1.10 \cdot 10^{-4}{}^{+2.6\%}_{-2.6\%}$	$3.81 \cdot 10^{-7}{}^{+2.6\%}_{-2.6\%}$	$4.39 \cdot 10^{-5}{}^{+10.1\%}_{-10.0\%}$	$1.89 \cdot 10^{-7}{}^{+342.0\%}_{-102.1\%}$
264.0	$8.52 \cdot 10^{-4}{}^{+4.7\%}_{-4.6\%}$	$1.07 \cdot 10^{-4}{}^{+2.6\%}_{-2.6\%}$	$3.72 \cdot 10^{-7}{}^{+2.6\%}_{-2.6\%}$	$4.28 \cdot 10^{-5}{}^{+10.1\%}_{-10.0\%}$	$4.49 \cdot 10^{-7}{}^{+276.1\%}_{-91.5\%}$
266.0	$8.31 \cdot 10^{-4}{}^{+4.7\%}_{-4.6\%}$	$1.05 \cdot 10^{-4}{}^{+2.6\%}_{-2.6\%}$	$3.63 \cdot 10^{-7}{}^{+2.6\%}_{-2.6\%}$	$4.18 \cdot 10^{-5}{}^{+10.1\%}_{-10.0\%}$	$8.63 \cdot 10^{-7}{}^{+210.1\%}_{-80.9\%}$
268.0	$8.11 \cdot 10^{-4}{}^{+4.7\%}_{-4.6\%}$	$1.02 \cdot 10^{-4}{}^{+2.6\%}_{-2.6\%}$	$3.55 \cdot 10^{-7}{}^{+2.6\%}_{-2.6\%}$	$4.08 \cdot 10^{-5}{}^{+10.1\%}_{-10.0\%}$	$1.46 \cdot 10^{-6}{}^{+144.1\%}_{-70.3\%}$
270.0	$7.92 \cdot 10^{-4}{}^{+4.7\%}_{-4.6\%}$	$1.00 \cdot 10^{-4}{}^{+2.6\%}_{-2.6\%}$	$3.47 \cdot 10^{-7}{}^{+2.6\%}_{-2.6\%}$	$3.98 \cdot 10^{-5}{}^{+10.1\%}_{-10.0\%}$	$2.29 \cdot 10^{-6}{}^{+78.1\%}_{-59.7\%}$
272.0	$7.73 \cdot 10^{-4}{}^{+4.7\%}_{-4.6\%}$	$9.80 \cdot 10^{-5}{}^{+2.6\%}_{-2.6\%}$	$3.40 \cdot 10^{-7}{}^{+2.6\%}_{-2.6\%}$	$3.89 \cdot 10^{-5}{}^{+10.1\%}_{-10.0\%}$	$3.37 \cdot 10^{-6}{}^{+72.3\%}_{-56.6\%}$
274.0	$7.55 \cdot 10^{-4}{}^{+4.7\%}_{-4.6\%}$	$9.58 \cdot 10^{-5}{}^{+2.6\%}_{-2.6\%}$	$3.32 \cdot 10^{-7}{}^{+2.6\%}_{-2.6\%}$	$3.80 \cdot 10^{-5}{}^{+10.1\%}_{-10.0\%}$	$4.72 \cdot 10^{-6}{}^{+66.5\%}_{-53.6\%}$
276.0	$7.38 \cdot 10^{-4}{}^{+4.7\%}_{-4.6\%}$	$9.37 \cdot 10^{-5}{}^{+2.6\%}_{-2.6\%}$	$3.25 \cdot 10^{-7}{}^{+2.6\%}_{-2.6\%}$	$3.71 \cdot 10^{-5}{}^{+10.1\%}_{-10.0\%}$	$6.41 \cdot 10^{-6}{}^{+60.7\%}_{-50.6\%}$
278.0	$7.21 \cdot 10^{-4}{}^{+4.7\%}_{-4.7\%}$	$9.17 \cdot 10^{-5}{}^{+2.6\%}_{-2.6\%}$	$3.18 \cdot 10^{-7}{}^{+2.6\%}_{-2.6\%}$	$3.63 \cdot 10^{-5}{}^{+10.1\%}_{-10.0\%}$	$8.45 \cdot 10^{-6}{}^{+54.9\%}_{-47.5\%}$
280.0	$7.05 \cdot 10^{-4}{}^{+4.7\%}_{-4.7\%}$	$8.98 \cdot 10^{-5}{}^{+2.6\%}_{-2.6\%}$	$3.11 \cdot 10^{-7}{}^{+2.6\%}_{-2.6\%}$	$3.55 \cdot 10^{-5}{}^{+10.1\%}_{-10.0\%}$	$1.09 \cdot 10^{-5}{}^{+49.2\%}_{-44.5\%}$
282.0	$6.90 \cdot 10^{-4}{}^{+4.7\%}_{-4.7\%}$	$8.79 \cdot 10^{-5}{}^{+2.6\%}_{-2.6\%}$	$3.05 \cdot 10^{-7}{}^{+2.6\%}_{-2.6\%}$	$3.47 \cdot 10^{-5}{}^{+10.1\%}_{-10.0\%}$	$1.37 \cdot 10^{-5}{}^{+47.2\%}_{-43.2\%}$
284.0	$6.74 \cdot 10^{-4}{}^{+4.7\%}_{-4.7\%}$	$8.61 \cdot 10^{-5}{}^{+2.6\%}_{-2.6\%}$	$2.98 \cdot 10^{-7}{}^{+2.6\%}_{-2.6\%}$	$3.39 \cdot 10^{-5}{}^{+10.1\%}_{-10.0\%}$	$1.72 \cdot 10^{-5}{}^{+45.2\%}_{-41.9\%}$
286.0	$6.60 \cdot 10^{-4}{}^{+4.7\%}_{-4.7\%}$	$8.43 \cdot 10^{-5}{}^{+2.6\%}_{-2.6\%}$	$2.92 \cdot 10^{-7}{}^{+2.6\%}_{-2.6\%}$	$3.32 \cdot 10^{-5}{}^{+10.2\%}_{-10.0\%}$	$2.11 \cdot 10^{-5}{}^{+43.2\%}_{-40.6\%}$
288.0	$6.46 \cdot 10^{-4}{}^{+4.7\%}_{-4.7\%}$	$8.26 \cdot 10^{-5}{}^{+2.6\%}_{-2.6\%}$	$2.86 \cdot 10^{-7}{}^{+2.6\%}_{-2.6\%}$	$3.25 \cdot 10^{-5}{}^{+10.2\%}_{-10.0\%}$	$2.55 \cdot 10^{-5}{}^{+41.3\%}_{-39.4\%}$
290.0	$6.32 \cdot 10^{-4}{}^{+4.7\%}_{-4.7\%}$	$8.09 \cdot 10^{-5}{}^{+2.6\%}_{-2.6\%}$	$2.81 \cdot 10^{-7}{}^{+2.6\%}_{-2.6\%}$	$3.18 \cdot 10^{-5}{}^{+10.2\%}_{-10.0\%}$	$3.06 \cdot 10^{-5}{}^{+39.3\%}_{-38.1\%}$
295.0	$6.00 \cdot 10^{-4}{}^{+4.7\%}_{-4.7\%}$	$7.70 \cdot 10^{-5}{}^{+2.6\%}_{-2.6\%}$	$2.67 \cdot 10^{-7}{}^{+2.6\%}_{-2.6\%}$	$3.01 \cdot 10^{-5}{}^{+10.1\%}_{-10.0\%}$	$4.67 \cdot 10^{-5}{}^{+37.3\%}_{-36.6\%}$
300.0	$5.70 \cdot 10^{-4}{}^{+4.7\%}_{-4.7\%}$	$7.33 \cdot 10^{-5}{}^{+2.6\%}_{-2.6\%}$	$2.55 \cdot 10^{-7}{}^{+2.6\%}_{-2.6\%}$	$2.86 \cdot 10^{-5}{}^{+10.1\%}_{-10.0\%}$	$6.87 \cdot 10^{-5}{}^{+35.3\%}_{-35.1\%}$
305.0	$5.42 \cdot 10^{-4}{}^{+4.7\%}_{-4.7\%}$	$7.00 \cdot 10^{-5}{}^{+2.6\%}_{-2.6\%}$	$2.43 \cdot 10^{-7}{}^{+2.6\%}_{-2.6\%}$	$2.72 \cdot 10^{-5}{}^{+10.2\%}_{-10.0\%}$	$9.83 \cdot 10^{-5}{}^{+35.0\%}_{-34.5\%}$
310.0	$5.15 \cdot 10^{-4}{}^{+4.7\%}_{-4.7\%}$	$6.69 \cdot 10^{-5}{}^{+2.6\%}_{-2.6\%}$	$2.32 \cdot 10^{-7}{}^{+2.6\%}_{-2.6\%}$	$2.60 \cdot 10^{-5}{}^{+10.2\%}_{-10.0\%}$	$1.38 \cdot 10^{-4}{}^{+34.6\%}_{-33.9\%}$
315.0	$4.92 \cdot 10^{-4}{}^{+4.8\%}_{-4.6\%}$	$6.40 \cdot 10^{-5}{}^{+2.6\%}_{-2.5\%}$	$2.22 \cdot 10^{-7}{}^{+2.7\%}_{-2.5\%}$	$2.48 \cdot 10^{-5}{}^{+10.2\%}_{-10.0\%}$	$1.91 \cdot 10^{-4}{}^{+35.7\%}_{-34.1\%}$
320.0	$4.69 \cdot 10^{-4}{}^{+4.8\%}_{-4.6\%}$	$6.11 \cdot 10^{-5}{}^{+2.7\%}_{-2.5\%}$	$2.12 \cdot 10^{-7}{}^{+2.7\%}_{-2.5\%}$	$2.35 \cdot 10^{-5}{}^{+10.2\%}_{-10.0\%}$	$2.65 \cdot 10^{-4}{}^{+36.8\%}_{-34.4\%}$
325.0	$4.49 \cdot 10^{-4}{}^{+4.8\%}_{-4.6\%}$	$5.86 \cdot 10^{-5}{}^{+2.6\%}_{-2.5\%}$	$2.03 \cdot 10^{-7}{}^{+2.6\%}_{-2.5\%}$	$2.25 \cdot 10^{-5}{}^{+10.2\%}_{-10.0\%}$	$3.70 \cdot 10^{-4}{}^{+41.0\%}_{-35.7\%}$
330.0	$4.30 \cdot 10^{-4}{}^{+4.8\%}_{-4.7\%}$	$5.63 \cdot 10^{-5}{}^{+2.6\%}_{-2.5\%}$	$1.95 \cdot 10^{-7}{}^{+2.6\%}_{-2.5\%}$	$2.16 \cdot 10^{-5}{}^{+10.2\%}_{-10.1\%}$	$5.22 \cdot 10^{-4}{}^{+45.1\%}_{-37.1\%}$
335.0	$4.12 \cdot 10^{-4}{}^{+4.8\%}_{-4.7\%}$	$5.41 \cdot 10^{-5}{}^{+2.6\%}_{-2.5\%}$	$1.87 \cdot 10^{-7}{}^{+2.6\%}_{-2.5\%}$	$2.07 \cdot 10^{-5}{}^{+10.2\%}_{-10.1\%}$	$7.61 \cdot 10^{-4}{}^{+110.4\%}_{-41.5\%}$
340.0	$3.95 \cdot 10^{-4}{}^{+4.8\%}_{-4.7\%}$	$5.20 \cdot 10^{-5}{}^{+2.7\%}_{-2.5\%}$	$1.80 \cdot 10^{-7}{}^{+2.7\%}_{-2.5\%}$	$1.98 \cdot 10^{-5}{}^{+10.1\%}_{-10.1\%}$	$1.20 \cdot 10^{-3}{}^{+175.6\%}_{-45.9\%}$
345.0	$3.80 \cdot 10^{-4}{}^{+5.0\%}_{-5.0\%}$	$5.02 \cdot 10^{-5}{}^{+3.5\%}_{-3.7\%}$	$1.74 \cdot 10^{-7}{}^{+3.5\%}_{-3.7\%}$	$1.91 \cdot 10^{-5}{}^{+10.3\%}_{-10.3\%}$	$3.28 \cdot 10^{-3}{}^{+151.7\%}_{-68.6\%}$
350.0	$3.60 \cdot 10^{-4}{}^{+5.2\%}_{-5.3\%}$	$4.77 \cdot 10^{-5}{}^{+4.2\%}_{-4.9\%}$	$1.65 \cdot 10^{-7}{}^{+4.2\%}_{-4.9\%}$	$1.81 \cdot 10^{-5}{}^{+10.5\%}_{-10.4\%}$	$1.56 \cdot 10^{-2}{}^{+127.8\%}_{-91.3\%}$
360.0	$3.18 \cdot 10^{-4}{}^{+6.0\%}_{-5.4\%}$	$4.23 \cdot 10^{-5}{}^{+5.6\%}_{-4.9\%}$	$1.47 \cdot 10^{-7}{}^{+5.6\%}_{-4.9\%}$	$1.60 \cdot 10^{-5}{}^{+11.2\%}_{-10.4\%}$	$5.14 \cdot 10^{-2}{}^{+42.2\%}_{-48.4\%}$
370.0	$2.83 \cdot 10^{-4}{}^{+6.4\%}_{-5.3\%}$	$3.78 \cdot 10^{-5}{}^{+5.8\%}_{-4.7\%}$	$1.31 \cdot 10^{-7}{}^{+5.8\%}_{-4.8\%}$	$1.42 \cdot 10^{-5}{}^{+11.6\%}_{-10.4\%}$	$8.35 \cdot 10^{-2}{}^{+25.4\%}_{-32.1\%}$
380.0	$2.54 \cdot 10^{-4}{}^{+6.6\%}_{-5.4\%}$	$3.41 \cdot 10^{-5}{}^{+5.8\%}_{-4.6\%}$	$1.18 \cdot 10^{-7}{}^{+5.8\%}_{-4.6\%}$	$1.28 \cdot 10^{-5}{}^{+11.8\%}_{-10.6\%}$	$1.10 \cdot 10^{-1}{}^{+18.4\%}_{-24.7\%}$
390.0	$2.30 \cdot 10^{-4}{}^{+6.7\%}_{-5.4\%}$	$3.10 \cdot 10^{-5}{}^{+5.8\%}_{-4.5\%}$	$1.07 \cdot 10^{-7}{}^{+5.9\%}_{-4.5\%}$	$1.16 \cdot 10^{-5}{}^{+12.0\%}_{-10.7\%}$	$1.31 \cdot 10^{-1}{}^{+14.5\%}_{-20.6\%}$
400.0	$2.10 \cdot 10^{-4}{}^{+6.8\%}_{-5.5\%}$	$2.84 \cdot 10^{-5}{}^{+5.8\%}_{-4.3\%}$	$9.83 \cdot 10^{-8}{}^{+5.8\%}_{-4.3\%}$	$1.05 \cdot 10^{-5}{}^{+12.2\%}_{-10.8\%}$	$1.48 \cdot 10^{-1}{}^{+12.2\%}_{-17.8\%}$
410.0	$1.93 \cdot 10^{-4}{}^{+6.9\%}_{-5.5\%}$	$2.62 \cdot 10^{-5}{}^{+5.7\%}_{-4.3\%}$	$9.07 \cdot 10^{-8}{}^{+5.7\%}_{-4.2\%}$	$9.66 \cdot 10^{-6}{}^{+12.3\%}_{-10.8\%}$	$1.61 \cdot 10^{-1}{}^{+10.4\%}_{-16.1\%}$
420.0	$1.78 \cdot 10^{-4}{}^{+7.0\%}_{-5.5\%}$	$2.43 \cdot 10^{-5}{}^{+5.6\%}_{-4.1\%}$	$8.41 \cdot 10^{-8}{}^{+5.6\%}_{-4.1\%}$	$8.93 \cdot 10^{-6}{}^{+12.4\%}_{-10.9\%}$	$1.71 \cdot 10^{-1}{}^{+9.3\%}_{-14.7\%}$
430.0	$1.65 \cdot 10^{-4}{}^{+7.0\%}_{-5.6\%}$	$2.27 \cdot 10^{-5}{}^{+5.5\%}_{-4.0\%}$	$7.84 \cdot 10^{-8}{}^{+5.5\%}_{-4.0\%}$	$8.29 \cdot 10^{-6}{}^{+12.5\%}_{-10.9\%}$	$1.79 \cdot 10^{-1}{}^{+8.4\%}_{-13.8\%}$
440.0	$1.54 \cdot 10^{-4}{}^{+7.1\%}_{-5.6\%}$	$2.12 \cdot 10^{-5}{}^{+5.4\%}_{-3.9\%}$	$7.34 \cdot 10^{-8}{}^{+5.4\%}_{-3.9\%}$	$7.73 \cdot 10^{-6}{}^{+12.5\%}_{-10.9\%}$	$1.84 \cdot 10^{-1}{}^{+7.7\%}_{-13.0\%}$
450.0	$1.44 \cdot 10^{-4}{}^{+7.2\%}_{-5.6\%}$	$2.00 \cdot 10^{-5}{}^{+5.3\%}_{-3.8\%}$	$6.91 \cdot 10^{-8}{}^{+5.3\%}_{-3.8\%}$	$7.25 \cdot 10^{-6}{}^{+12.6\%}_{-11.0\%}$	$1.88 \cdot 10^{-1}{}^{+7.2\%}_{-12.4\%}$
460.0	$1.36 \cdot 10^{-4}{}^{+7.2\%}_{-5.7\%}$	$1.88 \cdot 10^{-5}{}^{+5.2\%}_{-3.7\%}$	$6.52 \cdot 10^{-8}{}^{+5.3\%}_{-3.7\%}$	$6.82 \cdot 10^{-6}{}^{+12.6\%}_{-11.0\%}$	$1.91 \cdot 10^{-1}{}^{+6.8\%}_{-11.9\%}$
470.0	$1.28 \cdot 10^{-4}{}^{+7.2\%}_{-5.6\%}$	$1.78 \cdot 10^{-5}{}^{+5.2\%}_{-3.6\%}$	$6.17 \cdot 10^{-8}{}^{+5.2\%}_{-3.6\%}$	$6.43 \cdot 10^{-6}{}^{+12.6\%}_{-11.0\%}$	$1.92 \cdot 10^{-1}{}^{+6.4\%}_{-11.6\%}$
480.0	$1.21 \cdot 10^{-4}{}^{+7.2\%}_{-5.5\%}$	$1.69 \cdot 10^{-5}{}^{+5.1\%}_{-3.6\%}$	$5.86 \cdot 10^{-8}{}^{+5.1\%}_{-3.5\%}$	$6.08 \cdot 10^{-6}{}^{+12.6\%}_{-11.0\%}$	$1.93 \cdot 10^{-1}{}^{+6.1\%}_{-11.2\%}$
490.0	$1.15 \cdot 10^{-4}{}^{+7.2\%}_{-5.5\%}$	$1.61 \cdot 10^{-5}{}^{+5.0\%}_{-3.5\%}$	$5.57 \cdot 10^{-8}{}^{+5.0\%}_{-3.5\%}$	$5.76 \cdot 10^{-6}{}^{+12.6\%}_{-11.0\%}$	$1.93 \cdot 10^{-1}{}^{+5.9\%}_{-11.0\%}$
500.0	$1.09 \cdot 10^{-4}{}^{+7.2\%}_{-5.4\%}$	$1.53 \cdot 10^{-5}{}^{+5.0\%}_{-3.2\%}$	$5.31 \cdot 10^{-8}{}^{+5.1\%}_{-3.1\%}$	$5.47 \cdot 10^{-6}{}^{+12.8\%}_{-10.7\%}$	$1.92 \cdot 10^{-1}{}^{+4.6\%}_{-9.8\%}$
510.0	$1.04 \cdot 10^{-4}{}^{+7.4\%}_{-5.3\%}$	$1.46 \cdot 10^{-5}{}^{+5.1\%}_{-3.1\%}$	$5.07 \cdot 10^{-8}{}^{+5.1\%}_{-3.1\%}$	$5.21 \cdot 10^{-6}{}^{+12.8\%}_{-10.8\%}$	$1.91 \cdot 10^{-1}{}^{+4.7\%}_{-9.8\%}$
520.0	$9.88 \cdot 10^{-5}{}^{+7.5\%}_{-5.4\%}$	$1.40 \cdot 10^{-5}{}^{+5.1\%}_{-3.2\%}$	$4.85 \cdot 10^{-8}{}^{+5.1\%}_{-3.1\%}$	$4.96 \cdot 10^{-6}{}^{+12.9\%}_{-10.8\%}$	$1.90 \cdot 10^{-1}{}^{+4.8\%}_{-10.1\%}$
530.0	$9.44 \cdot 10^{-5}{}^{+7.5\%}_{-5.5\%}$	$1.34 \cdot 10^{-5}{}^{+5.3\%}_{-3.3\%}$	$4.64 \cdot 10^{-8}{}^{+5.2\%}_{-3.2\%}$	$4.74 \cdot 10^{-6}{}^{+13.0\%}_{-10.9\%}$	$1.88 \cdot 10^{-1}{}^{+5.0\%}_{-10.4\%}$
540.0	$9.02 \cdot 10^{-5}{}^{+7.6\%}_{-5.6\%}$	$1.29 \cdot 10^{-5}{}^{+5.4\%}_{-3.4\%}$	$4.44 \cdot 10^{-8}{}^{+5.4\%}_{-3.4\%}$	$4.52 \cdot 10^{-6}{}^{+13.1\%}_{-11.0\%}$	$1.85 \cdot 10^{-1}{}^{+5.2\%}_{-10.7\%}$

Table A.5: SM Higgs branching ratios to two fermions and their total uncertainties (expressed in percentage). Very-high-mass range.

M_{H} [GeV]	$\mathrm{H} \to \mathrm{bb}$	$\mathrm{H} \to \tau^+\tau^-$	$\mathrm{H} \to \mu^+\mu^-$	$\mathrm{H} \to \mathrm{c}\overline{\mathrm{c}}$	$\mathrm{H} \to \mathrm{t}\overline{\mathrm{t}}$
550.0	$8.64 \cdot 10^{-5}{}^{+7.7\%}_{-5.7\%}$	$1.23 \cdot 10^{-5}{}^{+5.5\%}_{-3.5\%}$	$4.27 \cdot 10^{-8}{}^{+5.5\%}_{-3.5\%}$	$4.33 \cdot 10^{-6}{}^{+13.1\%}_{-11.1\%}$	$1.83 \cdot 10^{-1}{}^{+5.4\%}_{-10.9\%}$
560.0	$8.28 \cdot 10^{-5}{}^{+7.8\%}_{-5.8\%}$	$1.19 \cdot 10^{-5}{}^{+5.6\%}_{-3.7\%}$	$4.10 \cdot 10^{-8}{}^{+5.6\%}_{-3.6\%}$	$4.15 \cdot 10^{-6}{}^{+13.2\%}_{-11.2\%}$	$1.80 \cdot 10^{-1}{}^{+5.6\%}_{-11.3\%}$
570.0	$7.95 \cdot 10^{-5}{}^{+7.8\%}_{-5.9\%}$	$1.14 \cdot 10^{-5}{}^{+5.8\%}_{-3.7\%}$	$3.95 \cdot 10^{-8}{}^{+5.7\%}_{-3.8\%}$	$3.98 \cdot 10^{-6}{}^{+13.3\%}_{-11.3\%}$	$1.78 \cdot 10^{-1}{}^{+5.7\%}_{-11.6\%}$
580.0	$7.64 \cdot 10^{-5}{}^{+7.9\%}_{-6.0\%}$	$1.10 \cdot 10^{-5}{}^{+5.8\%}_{-4.0\%}$	$3.80 \cdot 10^{-8}{}^{+5.8\%}_{-4.0\%}$	$3.83 \cdot 10^{-6}{}^{+13.4\%}_{-11.4\%}$	$1.75 \cdot 10^{-1}{}^{+5.9\%}_{-11.9\%}$
590.0	$7.34 \cdot 10^{-5}{}^{+8.1\%}_{-6.1\%}$	$1.06 \cdot 10^{-5}{}^{+6.0\%}_{-4.0\%}$	$3.67 \cdot 10^{-8}{}^{+6.0\%}_{-4.0\%}$	$3.68 \cdot 10^{-6}{}^{+13.5\%}_{-11.5\%}$	$1.72 \cdot 10^{-1}{}^{+6.2\%}_{-12.2\%}$
600.0	$7.06 \cdot 10^{-5}{}^{+8.2\%}_{-6.3\%}$	$1.02 \cdot 10^{-5}{}^{+6.2\%}_{-4.2\%}$	$3.54 \cdot 10^{-8}{}^{+6.1\%}_{-4.2\%}$	$3.54 \cdot 10^{-6}{}^{+13.7\%}_{-11.6\%}$	$1.69 \cdot 10^{-1}{}^{+6.3\%}_{-12.4\%}$
610.0	$6.81 \cdot 10^{-5}{}^{+8.3\%}_{-6.5\%}$	$9.87 \cdot 10^{-6}{}^{+6.2\%}_{-4.4\%}$	$3.42 \cdot 10^{-8}{}^{+6.2\%}_{-4.4\%}$	$3.41 \cdot 10^{-6}{}^{+13.8\%}_{-11.8\%}$	$1.66 \cdot 10^{-1}{}^{+6.4\%}_{-12.8\%}$
620.0	$6.55 \cdot 10^{-5}{}^{+8.4\%}_{-6.6\%}$	$9.53 \cdot 10^{-6}{}^{+6.3\%}_{-4.5\%}$	$3.30 \cdot 10^{-8}{}^{+6.3\%}_{-4.5\%}$	$3.29 \cdot 10^{-6}{}^{+13.9\%}_{-12.0\%}$	$1.63 \cdot 10^{-1}{}^{+6.6\%}_{-13.2\%}$
630.0	$6.32 \cdot 10^{-5}{}^{+8.6\%}_{-6.7\%}$	$9.22 \cdot 10^{-6}{}^{+6.5\%}_{-4.7\%}$	$3.19 \cdot 10^{-8}{}^{+6.6\%}_{-4.7\%}$	$3.17 \cdot 10^{-6}{}^{+14.0\%}_{-12.1\%}$	$1.59 \cdot 10^{-1}{}^{+6.8\%}_{-13.4\%}$
640.0	$6.10 \cdot 10^{-5}{}^{+8.8\%}_{-6.9\%}$	$8.92 \cdot 10^{-6}{}^{+6.7\%}_{-4.9\%}$	$3.09 \cdot 10^{-8}{}^{+6.7\%}_{-4.9\%}$	$3.06 \cdot 10^{-6}{}^{+14.2\%}_{-12.3\%}$	$1.56 \cdot 10^{-1}{}^{+7.0\%}_{-13.8\%}$
650.0	$5.89 \cdot 10^{-5}{}^{+8.9\%}_{-7.1\%}$	$8.63 \cdot 10^{-6}{}^{+6.8\%}_{-5.0\%}$	$2.99 \cdot 10^{-8}{}^{+6.8\%}_{-5.0\%}$	$2.95 \cdot 10^{-6}{}^{+14.4\%}_{-12.4\%}$	$1.53 \cdot 10^{-1}{}^{+7.1\%}_{-14.2\%}$
660.0	$5.69 \cdot 10^{-5}{}^{+9.1\%}_{-7.2\%}$	$8.36 \cdot 10^{-6}{}^{+7.0\%}_{-5.2\%}$	$2.90 \cdot 10^{-8}{}^{+7.0\%}_{-5.2\%}$	$2.85 \cdot 10^{-6}{}^{+14.5\%}_{-12.6\%}$	$1.50 \cdot 10^{-1}{}^{+7.2\%}_{-14.6\%}$
670.0	$5.50 \cdot 10^{-5}{}^{+9.3\%}_{-7.4\%}$	$8.10 \cdot 10^{-6}{}^{+7.2\%}_{-5.4\%}$	$2.81 \cdot 10^{-8}{}^{+7.2\%}_{-5.4\%}$	$2.76 \cdot 10^{-6}{}^{+14.8\%}_{-12.8\%}$	$1.47 \cdot 10^{-1}{}^{+7.5\%}_{-15.0\%}$
680.0	$5.32 \cdot 10^{-5}{}^{+9.5\%}_{-7.6\%}$	$7.85 \cdot 10^{-6}{}^{+7.4\%}_{-5.5\%}$	$2.72 \cdot 10^{-8}{}^{+7.4\%}_{-5.5\%}$	$2.67 \cdot 10^{-6}{}^{+14.9\%}_{-13.0\%}$	$1.44 \cdot 10^{-1}{}^{+7.7\%}_{-15.4\%}$
690.0	$5.15 \cdot 10^{-5}{}^{+9.7\%}_{-7.8\%}$	$7.61 \cdot 10^{-6}{}^{+7.6\%}_{-5.8\%}$	$2.64 \cdot 10^{-8}{}^{+7.5\%}_{-5.8\%}$	$2.58 \cdot 10^{-6}{}^{+15.1\%}_{-13.2\%}$	$1.41 \cdot 10^{-1}{}^{+7.8\%}_{-15.8\%}$
700.0	$4.98 \cdot 10^{-5}{}^{+9.9\%}_{-8.0\%}$	$7.38 \cdot 10^{-6}{}^{+7.8\%}_{-6.0\%}$	$2.56 \cdot 10^{-8}{}^{+7.8\%}_{-6.0\%}$	$2.50 \cdot 10^{-6}{}^{+15.3\%}_{-13.4\%}$	$1.38 \cdot 10^{-1}{}^{+8.0\%}_{-16.2\%}$
710.0	$4.82 \cdot 10^{-5}{}^{+10.1\%}_{-8.2\%}$	$7.16 \cdot 10^{-6}{}^{+8.0\%}_{-6.2\%}$	$2.48 \cdot 10^{-8}{}^{+8.0\%}_{-6.2\%}$	$2.42 \cdot 10^{-6}{}^{+15.6\%}_{-13.7\%}$	$1.35 \cdot 10^{-1}{}^{+8.2\%}_{-16.7\%}$
720.0	$4.67 \cdot 10^{-5}{}^{+10.4\%}_{-8.4\%}$	$6.94 \cdot 10^{-6}{}^{+8.3\%}_{-6.4\%}$	$2.41 \cdot 10^{-8}{}^{+8.3\%}_{-6.4\%}$	$2.34 \cdot 10^{-6}{}^{+15.8\%}_{-13.8\%}$	$1.32 \cdot 10^{-1}{}^{+8.4\%}_{-17.1\%}$
730.0	$4.53 \cdot 10^{-5}{}^{+10.6\%}_{-8.7\%}$	$6.74 \cdot 10^{-6}{}^{+8.5\%}_{-6.6\%}$	$2.34 \cdot 10^{-8}{}^{+8.5\%}_{-6.7\%}$	$2.27 \cdot 10^{-6}{}^{+16.0\%}_{-14.1\%}$	$1.29 \cdot 10^{-1}{}^{+8.6\%}_{-17.6\%}$
740.0	$4.38 \cdot 10^{-5}{}^{+10.9\%}_{-8.9\%}$	$6.55 \cdot 10^{-6}{}^{+8.8\%}_{-6.9\%}$	$2.27 \cdot 10^{-8}{}^{+8.8\%}_{-6.8\%}$	$2.20 \cdot 10^{-6}{}^{+16.3\%}_{-14.4\%}$	$1.26 \cdot 10^{-1}{}^{+8.7\%}_{-18.2\%}$
750.0	$4.24 \cdot 10^{-5}{}^{+11.2\%}_{-9.2\%}$	$6.36 \cdot 10^{-6}{}^{+9.1\%}_{-7.1\%}$	$2.21 \cdot 10^{-8}{}^{+9.1\%}_{-7.1\%}$	$2.13 \cdot 10^{-6}{}^{+16.6\%}_{-14.6\%}$	$1.23 \cdot 10^{-1}{}^{+8.9\%}_{-18.7\%}$
760.0	$4.11 \cdot 10^{-5}{}^{+11.4\%}_{-9.4\%}$	$6.18 \cdot 10^{-6}{}^{+9.3\%}_{-7.4\%}$	$2.15 \cdot 10^{-8}{}^{+9.3\%}_{-7.3\%}$	$2.07 \cdot 10^{-6}{}^{+16.9\%}_{-14.8\%}$	$1.20 \cdot 10^{-1}{}^{+9.2\%}_{-19.2\%}$
770.0	$3.99 \cdot 10^{-5}{}^{+11.8\%}_{-9.7\%}$	$6.01 \cdot 10^{-6}{}^{+9.6\%}_{-7.6\%}$	$2.09 \cdot 10^{-8}{}^{+9.6\%}_{-7.6\%}$	$2.00 \cdot 10^{-6}{}^{+17.2\%}_{-15.0\%}$	$1.18 \cdot 10^{-1}{}^{+9.4\%}_{-19.8\%}$
780.0	$3.87 \cdot 10^{-5}{}^{+12.1\%}_{-10.0\%}$	$5.84 \cdot 10^{-6}{}^{+10.0\%}_{-7.9\%}$	$2.03 \cdot 10^{-8}{}^{+10.0\%}_{-7.9\%}$	$1.94 \cdot 10^{-6}{}^{+17.6\%}_{-15.3\%}$	$1.15 \cdot 10^{-1}{}^{+9.7\%}_{-20.4\%}$
790.0	$3.75 \cdot 10^{-5}{}^{+12.5\%}_{-10.2\%}$	$5.67 \cdot 10^{-6}{}^{+10.4\%}_{-8.2\%}$	$1.97 \cdot 10^{-8}{}^{+10.3\%}_{-8.1\%}$	$1.89 \cdot 10^{-6}{}^{+17.9\%}_{-15.6\%}$	$1.12 \cdot 10^{-1}{}^{+10.1\%}_{-20.9\%}$
800.0	$3.64 \cdot 10^{-5}{}^{+12.8\%}_{-10.5\%}$	$5.52 \cdot 10^{-6}{}^{+10.7\%}_{-8.5\%}$	$1.92 \cdot 10^{-8}{}^{+10.7\%}_{-8.5\%}$	$1.83 \cdot 10^{-6}{}^{+18.3\%}_{-15.9\%}$	$1.10 \cdot 10^{-1}{}^{+10.6\%}_{-21.6\%}$
810.0	$3.54 \cdot 10^{-5}{}^{+13.2\%}_{-10.8\%}$	$5.37 \cdot 10^{-6}{}^{+11.1\%}_{-8.8\%}$	$1.86 \cdot 10^{-8}{}^{+11.1\%}_{-8.8\%}$	$1.78 \cdot 10^{-6}{}^{+18.7\%}_{-16.2\%}$	$1.07 \cdot 10^{-1}{}^{+11.0\%}_{-22.3\%}$
820.0	$3.43 \cdot 10^{-5}{}^{+13.7\%}_{-11.1\%}$	$5.22 \cdot 10^{-6}{}^{+11.5\%}_{-9.1\%}$	$1.81 \cdot 10^{-8}{}^{+11.5\%}_{-9.1\%}$	$1.73 \cdot 10^{-6}{}^{+19.1\%}_{-16.5\%}$	$1.05 \cdot 10^{-1}{}^{+11.5\%}_{-23.0\%}$
830.0	$3.33 \cdot 10^{-5}{}^{+14.1\%}_{-11.4\%}$	$5.08 \cdot 10^{-6}{}^{+11.9\%}_{-9.4\%}$	$1.76 \cdot 10^{-8}{}^{+11.8\%}_{-9.4\%}$	$1.68 \cdot 10^{-6}{}^{+19.5\%}_{-16.8\%}$	$1.02 \cdot 10^{-1}{}^{+12.0\%}_{-23.6\%}$
840.0	$3.24 \cdot 10^{-5}{}^{+14.5\%}_{-11.8\%}$	$4.94 \cdot 10^{-6}{}^{+12.3\%}_{-9.7\%}$	$1.72 \cdot 10^{-8}{}^{+12.3\%}_{-9.7\%}$	$1.63 \cdot 10^{-6}{}^{+19.9\%}_{-17.2\%}$	$9.99 \cdot 10^{-2}{}^{+12.5\%}_{-24.3\%}$
850.0	$3.14 \cdot 10^{-5}{}^{+15.0\%}_{-12.1\%}$	$4.80 \cdot 10^{-6}{}^{+12.8\%}_{-10.0\%}$	$1.67 \cdot 10^{-8}{}^{+12.8\%}_{-10.1\%}$	$1.58 \cdot 10^{-6}{}^{+20.4\%}_{-17.5\%}$	$9.76 \cdot 10^{-2}{}^{+12.9\%}_{-25.1\%}$
860.0	$3.05 \cdot 10^{-5}{}^{+15.4\%}_{-12.5\%}$	$4.67 \cdot 10^{-6}{}^{+13.3\%}_{-10.4\%}$	$1.62 \cdot 10^{-8}{}^{+13.3\%}_{-10.4\%}$	$1.54 \cdot 10^{-6}{}^{+20.9\%}_{-17.9\%}$	$9.52 \cdot 10^{-2}{}^{+13.5\%}_{-25.8\%}$
870.0	$2.97 \cdot 10^{-5}{}^{+15.9\%}_{-12.9\%}$	$4.55 \cdot 10^{-6}{}^{+13.8\%}_{-10.7\%}$	$1.58 \cdot 10^{-8}{}^{+13.8\%}_{-10.8\%}$	$1.49 \cdot 10^{-6}{}^{+21.4\%}_{-18.3\%}$	$9.29 \cdot 10^{-2}{}^{+14.0\%}_{-26.6\%}$
880.0	$2.88 \cdot 10^{-5}{}^{+16.5\%}_{-13.2\%}$	$4.43 \cdot 10^{-6}{}^{+14.3\%}_{-11.1\%}$	$1.54 \cdot 10^{-8}{}^{+14.3\%}_{-11.1\%}$	$1.45 \cdot 10^{-6}{}^{+22.0\%}_{-18.6\%}$	$9.07 \cdot 10^{-2}{}^{+14.6\%}_{-27.4\%}$
890.0	$2.80 \cdot 10^{-5}{}^{+17.0\%}_{-13.6\%}$	$4.31 \cdot 10^{-6}{}^{+14.9\%}_{-11.5\%}$	$1.50 \cdot 10^{-8}{}^{+14.9\%}_{-11.5\%}$	$1.41 \cdot 10^{-6}{}^{+22.5\%}_{-19.1\%}$	$8.86 \cdot 10^{-2}{}^{+15.1\%}_{-28.3\%}$
900.0	$2.72 \cdot 10^{-5}{}^{+17.6\%}_{-14.0\%}$	$4.19 \cdot 10^{-6}{}^{+15.5\%}_{-11.9\%}$	$1.46 \cdot 10^{-8}{}^{+15.5\%}_{-11.8\%}$	$1.37 \cdot 10^{-6}{}^{+23.1\%}_{-19.4\%}$	$8.65 \cdot 10^{-2}{}^{+15.8\%}_{-29.2\%}$
910.0	$2.64 \cdot 10^{-5}{}^{+18.2\%}_{-14.4\%}$	$4.08 \cdot 10^{-6}{}^{+16.1\%}_{-12.3\%}$	$1.42 \cdot 10^{-8}{}^{+16.0\%}_{-12.3\%}$	$1.33 \cdot 10^{-6}{}^{+23.8\%}_{-19.8\%}$	$8.44 \cdot 10^{-2}{}^{+16.4\%}_{-30.1\%}$
920.0	$2.57 \cdot 10^{-5}{}^{+18.9\%}_{-14.8\%}$	$3.97 \cdot 10^{-6}{}^{+16.7\%}_{-12.7\%}$	$1.38 \cdot 10^{-8}{}^{+16.7\%}_{-12.7\%}$	$1.29 \cdot 10^{-6}{}^{+24.3\%}_{-20.2\%}$	$8.23 \cdot 10^{-2}{}^{+17.0\%}_{-31.0\%}$
930.0	$2.49 \cdot 10^{-5}{}^{+19.6\%}_{-15.2\%}$	$3.87 \cdot 10^{-6}{}^{+17.4\%}_{-13.1\%}$	$1.34 \cdot 10^{-8}{}^{+17.4\%}_{-13.1\%}$	$1.25 \cdot 10^{-6}{}^{+25.1\%}_{-20.6\%}$	$8.03 \cdot 10^{-2}{}^{+17.6\%}_{-32.0\%}$
940.0	$2.42 \cdot 10^{-5}{}^{+20.3\%}_{-15.6\%}$	$3.76 \cdot 10^{-6}{}^{+18.1\%}_{-13.5\%}$	$1.31 \cdot 10^{-8}{}^{+18.1\%}_{-13.5\%}$	$1.22 \cdot 10^{-6}{}^{+25.7\%}_{-21.1\%}$	$7.83 \cdot 10^{-2}{}^{+18.3\%}_{-33.0\%}$
950.0	$2.35 \cdot 10^{-5}{}^{+21.0\%}_{-16.1\%}$	$3.66 \cdot 10^{-6}{}^{+18.8\%}_{-14.0\%}$	$1.27 \cdot 10^{-8}{}^{+18.9\%}_{-13.9\%}$	$1.18 \cdot 10^{-6}{}^{+26.6\%}_{-21.5\%}$	$7.64 \cdot 10^{-2}{}^{+19.0\%}_{-34.0\%}$
960.0	$2.29 \cdot 10^{-5}{}^{+21.9\%}_{-16.6\%}$	$3.56 \cdot 10^{-6}{}^{+19.6\%}_{-14.4\%}$	$1.24 \cdot 10^{-8}{}^{+19.7\%}_{-14.3\%}$	$1.15 \cdot 10^{-6}{}^{+27.3\%}_{-21.9\%}$	$7.45 \cdot 10^{-2}{}^{+19.8\%}_{-35.0\%}$
970.0	$2.23 \cdot 10^{-5}{}^{+22.7\%}_{-17.0\%}$	$3.47 \cdot 10^{-6}{}^{+20.4\%}_{-14.9\%}$	$1.21 \cdot 10^{-8}{}^{+20.5\%}_{-14.8\%}$	$1.12 \cdot 10^{-6}{}^{+28.2\%}_{-22.4\%}$	$7.26 \cdot 10^{-2}{}^{+20.5\%}_{-36.1\%}$
980.0	$2.17 \cdot 10^{-5}{}^{+23.5\%}_{-17.5\%}$	$3.38 \cdot 10^{-6}{}^{+21.3\%}_{-15.3\%}$	$1.17 \cdot 10^{-8}{}^{+21.2\%}_{-15.3\%}$	$1.09 \cdot 10^{-6}{}^{+28.9\%}_{-22.9\%}$	$7.08 \cdot 10^{-2}{}^{+21.2\%}_{-37.2\%}$
990.0	$2.11 \cdot 10^{-5}{}^{+24.4\%}_{-18.0\%}$	$3.28 \cdot 10^{-6}{}^{+22.2\%}_{-15.8\%}$	$1.14 \cdot 10^{-8}{}^{+22.2\%}_{-15.8\%}$	$1.06 \cdot 10^{-6}{}^{+29.9\%}_{-23.4\%}$	$6.90 \cdot 10^{-2}{}^{+22.1\%}_{-38.3\%}$
1000.0	$2.05 \cdot 10^{-5}{}^{+25.3\%}_{-18.5\%}$	$3.20 \cdot 10^{-6}{}^{+23.1\%}_{-16.3\%}$	$1.11 \cdot 10^{-8}{}^{+23.1\%}_{-16.3\%}$	$1.03 \cdot 10^{-6}{}^{+30.9\%}_{-23.8\%}$	$6.73 \cdot 10^{-2}{}^{+22.9\%}_{-39.5\%}$

Table A.6: SM Higgs branching ratios to two gauge bosons and Higgs total width together with their total uncertainties (expressed in percentage). Very-low-mass range.

$M_{\rm H}$ [GeV]	$\rm H \to gg$	$\rm H \to \gamma\gamma$	$\rm H \to Z\gamma$	$\rm H \to WW$	$\rm H \to ZZ$	$\Gamma_{\rm H}$ [GeV]
90.0	$6.12\cdot10^{-2+11.8\%}_{-11.4\%}$	$1.22\cdot10^{-3+6.2\%}_{-6.2\%}$	$0.00^{+0.0\%}_{-0.0\%}$	$2.07\cdot10^{-3+5.8\%}_{-5.7\%}$	$4.17\cdot10^{-4+5.8\%}_{-5.6\%}$	$2.22\cdot10^{-3+5.2\%}_{-5.2\%}$
95.0	$6.74\cdot10^{-2+11.7\%}_{-11.3\%}$	$1.39\cdot10^{-3+6.2\%}_{-6.1\%}$	$4.48\cdot10^{-6+10.2\%}_{-10.1\%}$	$4.67\cdot10^{-3+5.8\%}_{-5.6\%}$	$6.65\cdot10^{-4+5.7\%}_{-5.6\%}$	$2.35\cdot10^{-3+5.2\%}_{-5.1\%}$
100.0	$7.36\cdot10^{-2+11.6\%}_{-11.2\%}$	$1.58\cdot10^{-3+6.2\%}_{-6.1\%}$	$4.93\cdot10^{-5+10.2\%}_{-10.1\%}$	$1.09\cdot10^{-2+5.7\%}_{-5.6\%}$	$1.12\cdot10^{-3+5.7\%}_{-5.5\%}$	$2.49\cdot10^{-3+5.1\%}_{-5.1\%}$
105.0	$7.95\cdot10^{-2+11.4\%}_{-11.1\%}$	$1.77\cdot10^{-3+6.1\%}_{-5.9\%}$	$1.71\cdot10^{-4+10.2\%}_{-9.9\%}$	$2.40\cdot10^{-2+5.6\%}_{-5.5\%}$	$2.13\cdot10^{-3+5.6\%}_{-5.5\%}$	$2.65\cdot10^{-3+5.1\%}_{-5.0\%}$
110.0	$8.45\cdot10^{-2+11.2\%}_{-10.9\%}$	$1.95\cdot10^{-3+5.9\%}_{-5.8\%}$	$3.91\cdot10^{-4+9.9\%}_{-9.8\%}$	$4.77\cdot10^{-2+5.4\%}_{-5.3\%}$	$4.34\cdot10^{-3+5.4\%}_{-5.3\%}$	$2.85\cdot10^{-3+4.9\%}_{-4.9\%}$
110.5	$8.49\cdot10^{-2+11.2\%}_{-10.8\%}$	$1.97\cdot10^{-3+5.9\%}_{-5.8\%}$	$4.18\cdot10^{-4+9.9\%}_{-9.8\%}$	$5.09\cdot10^{-2+5.4\%}_{-5.3\%}$	$4.67\cdot10^{-3+5.4\%}_{-5.3\%}$	$2.87\cdot10^{-3+4.9\%}_{-4.9\%}$
111.0	$8.53\cdot10^{-2+11.2\%}_{-10.8\%}$	$1.98\cdot10^{-3+5.9\%}_{-5.8\%}$	$4.47\cdot10^{-4+9.9\%}_{-9.8\%}$	$5.40\cdot10^{-2+5.4\%}_{-5.2\%}$	$5.00\cdot10^{-3+5.4\%}_{-5.2\%}$	$2.90\cdot10^{-3+4.9\%}_{-4.8\%}$
111.5	$8.56\cdot10^{-2+11.1\%}_{-10.8\%}$	$2.00\cdot10^{-3+5.9\%}_{-5.8\%}$	$4.76\cdot10^{-4+9.9\%}_{-9.8\%}$	$5.75\cdot10^{-2+5.4\%}_{-5.2\%}$	$5.38\cdot10^{-3+5.3\%}_{-5.2\%}$	$2.92\cdot10^{-3+4.8\%}_{-4.8\%}$
112.0	$8.60\cdot10^{-2+11.1\%}_{-10.8\%}$	$2.02\cdot10^{-3+5.8\%}_{-5.8\%}$	$5.07\cdot10^{-4+9.8\%}_{-9.7\%}$	$6.10\cdot10^{-2+5.3\%}_{-5.2\%}$	$5.76\cdot10^{-3+5.3\%}_{-5.2\%}$	$2.95\cdot10^{-3+4.8\%}_{-4.8\%}$
112.5	$8.63\cdot10^{-2+11.1\%}_{-10.8\%}$	$2.03\cdot10^{-3+5.8\%}_{-5.7\%}$	$5.39\cdot10^{-4+9.8\%}_{-9.7\%}$	$6.47\cdot10^{-2+5.3\%}_{-5.2\%}$	$6.17\cdot10^{-3+5.3\%}_{-5.2\%}$	$2.98\cdot10^{-3+4.8\%}_{-4.8\%}$
113.0	$8.66\cdot10^{-2+11.1\%}_{-10.7\%}$	$2.05\cdot10^{-3+5.8\%}_{-5.7\%}$	$5.72\cdot10^{-4+9.8\%}_{-9.7\%}$	$6.87\cdot10^{-2+5.3\%}_{-5.2\%}$	$6.62\cdot10^{-3+5.3\%}_{-5.1\%}$	$3.00\cdot10^{-3+4.8\%}_{-4.8\%}$
113.5	$8.69\cdot10^{-2+11.0\%}_{-10.7\%}$	$2.07\cdot10^{-3+5.8\%}_{-5.7\%}$	$6.05\cdot10^{-4+9.8\%}_{-9.7\%}$	$7.27\cdot10^{-2+5.2\%}_{-5.1\%}$	$7.08\cdot10^{-3+5.2\%}_{-5.1\%}$	$3.03\cdot10^{-3+4.8\%}_{-4.7\%}$
114.0	$8.72\cdot10^{-2+11.0\%}_{-10.7\%}$	$2.08\cdot10^{-3+5.8\%}_{-5.6\%}$	$6.39\cdot10^{-4+9.7\%}_{-9.7\%}$	$7.70\cdot10^{-2+5.2\%}_{-5.1\%}$	$7.58\cdot10^{-3+5.2\%}_{-5.1\%}$	$3.06\cdot10^{-3+4.7\%}_{-4.7\%}$
114.5	$8.74\cdot10^{-2+11.0\%}_{-10.7\%}$	$2.10\cdot10^{-3+5.8\%}_{-5.6\%}$	$6.74\cdot10^{-4+9.7\%}_{-9.6\%}$	$8.14\cdot10^{-2+5.2\%}_{-5.1\%}$	$8.10\cdot10^{-3+5.2\%}_{-5.1\%}$	$3.09\cdot10^{-3+4.7\%}_{-4.7\%}$
115.0	$8.76\cdot10^{-2+10.9\%}_{-10.6\%}$	$2.11\cdot10^{-3+5.7\%}_{-5.6\%}$	$7.10\cdot10^{-4+9.7\%}_{-9.6\%}$	$8.60\cdot10^{-2+5.2\%}_{-5.0\%}$	$8.65\cdot10^{-3+5.2\%}_{-5.0\%}$	$3.12\cdot10^{-3+4.7\%}_{-4.7\%}$
115.5	$8.78\cdot10^{-2+10.9\%}_{-10.6\%}$	$2.12\cdot10^{-3+5.7\%}_{-5.6\%}$	$7.46\cdot10^{-4+9.7\%}_{-9.6\%}$	$9.05\cdot10^{-2+5.1\%}_{-5.0\%}$	$9.21\cdot10^{-3+5.1\%}_{-5.0\%}$	$3.16\cdot10^{-3+4.7\%}_{-4.6\%}$
116.0	$8.80\cdot10^{-2+10.9\%}_{-10.6\%}$	$2.14\cdot10^{-3+5.7\%}_{-5.5\%}$	$7.84\cdot10^{-4+9.6\%}_{-9.6\%}$	$9.55\cdot10^{-2+5.1\%}_{-5.0\%}$	$9.83\cdot10^{-3+5.1\%}_{-5.0\%}$	$3.19\cdot10^{-3+4.6\%}_{-4.6\%}$
116.5	$8.81\cdot10^{-2+10.8\%}_{-10.5\%}$	$2.15\cdot10^{-3+5.6\%}_{-5.5\%}$	$8.22\cdot10^{-4+9.6\%}_{-9.5\%}$	$1.01\cdot10^{-1+5.0\%}_{-4.9\%}$	$1.05\cdot10^{-2+5.0\%}_{-4.9\%}$	$3.23\cdot10^{-3+4.6\%}_{-4.6\%}$
117.0	$8.82\cdot10^{-2+10.8\%}_{-10.5\%}$	$2.16\cdot10^{-3+5.6\%}_{-5.5\%}$	$8.61\cdot10^{-4+9.6\%}_{-9.5\%}$	$1.06\cdot10^{-1+5.0\%}_{-4.9\%}$	$1.12\cdot10^{-2+5.0\%}_{-4.9\%}$	$3.26\cdot10^{-3+4.6\%}_{-4.5\%}$
117.5	$8.83\cdot10^{-2+10.8\%}_{-10.5\%}$	$2.18\cdot10^{-3+5.6\%}_{-5.4\%}$	$9.00\cdot10^{-4+9.5\%}_{-9.5\%}$	$1.11\cdot10^{-1+5.0\%}_{-4.8\%}$	$1.19\cdot10^{-2+5.0\%}_{-4.8\%}$	$3.30\cdot10^{-3+4.5\%}_{-4.5\%}$
118.0	$8.83\cdot10^{-2+10.8\%}_{-10.4\%}$	$2.19\cdot10^{-3+5.5\%}_{-5.4\%}$	$9.40\cdot10^{-4+9.5\%}_{-9.4\%}$	$1.17\cdot10^{-1+4.9\%}_{-4.8\%}$	$1.26\cdot10^{-2+4.9\%}_{-4.8\%}$	$3.34\cdot10^{-3+4.5\%}_{-4.5\%}$
118.5	$8.83\cdot10^{-2+10.7\%}_{-10.4\%}$	$2.20\cdot10^{-3+5.5\%}_{-5.4\%}$	$9.81\cdot10^{-4+9.5\%}_{-9.4\%}$	$1.23\cdot10^{-1+4.9\%}_{-4.8\%}$	$1.34\cdot10^{-2+4.9\%}_{-4.8\%}$	$3.37\cdot10^{-3+4.5\%}_{-4.4\%}$
119.0	$8.83\cdot10^{-2+10.7\%}_{-10.4\%}$	$2.21\cdot10^{-3+5.5\%}_{-5.3\%}$	$1.02\cdot10^{-3+9.4\%}_{-9.4\%}$	$1.29\cdot10^{-1+4.8\%}_{-4.7\%}$	$1.42\cdot10^{-2+4.8\%}_{-4.7\%}$	$3.41\cdot10^{-3+4.4\%}_{-4.4\%}$
119.5	$8.84\cdot10^{-2+10.7\%}_{-10.4\%}$	$2.22\cdot10^{-3+5.4\%}_{-5.3\%}$	$1.06\cdot10^{-3+9.4\%}_{-9.4\%}$	$1.35\cdot10^{-1+4.8\%}_{-4.7\%}$	$1.50\cdot10^{-2+4.8\%}_{-4.7\%}$	$3.46\cdot10^{-3+4.4\%}_{-4.4\%}$
120.0	$8.82\cdot10^{-2+10.6\%}_{-10.3\%}$	$2.23\cdot10^{-3+5.4\%}_{-5.3\%}$	$1.11\cdot10^{-3+9.4\%}_{-9.3\%}$	$1.41\cdot10^{-1+4.8\%}_{-4.7\%}$	$1.59\cdot10^{-2+4.8\%}_{-4.7\%}$	$3.50\cdot10^{-3+4.4\%}_{-4.3\%}$
120.5	$8.82\cdot10^{-2+10.6\%}_{-10.3\%}$	$2.23\cdot10^{-3+5.4\%}_{-5.2\%}$	$1.15\cdot10^{-3+9.3\%}_{-9.3\%}$	$1.48\cdot10^{-1+4.7\%}_{-4.6\%}$	$1.68\cdot10^{-2+4.7\%}_{-4.6\%}$	$3.55\cdot10^{-3+4.3\%}_{-4.3\%}$
121.0	$8.80\cdot10^{-2+10.6\%}_{-10.3\%}$	$2.24\cdot10^{-3+5.3\%}_{-5.2\%}$	$1.19\cdot10^{-3+9.3\%}_{-9.2\%}$	$1.55\cdot10^{-1+4.7\%}_{-4.6\%}$	$1.77\cdot10^{-2+4.7\%}_{-4.6\%}$	$3.60\cdot10^{-3+4.3\%}_{-4.2\%}$
121.5	$8.79\cdot10^{-2+10.5\%}_{-10.2\%}$	$2.25\cdot10^{-3+5.3\%}_{-5.2\%}$	$1.23\cdot10^{-3+9.3\%}_{-9.2\%}$	$1.61\cdot10^{-1+4.6\%}_{-4.5\%}$	$1.87\cdot10^{-2+4.6\%}_{-4.5\%}$	$3.65\cdot10^{-3+4.2\%}_{-4.2\%}$
122.0	$8.77\cdot10^{-2+10.5\%}_{-10.2\%}$	$2.25\cdot10^{-3+5.2\%}_{-5.1\%}$	$1.28\cdot10^{-3+9.2\%}_{-9.1\%}$	$1.69\cdot10^{-1+4.6\%}_{-4.5\%}$	$1.97\cdot10^{-2+4.6\%}_{-4.5\%}$	$3.70\cdot10^{-3+4.2\%}_{-4.2\%}$
122.5	$8.74\cdot10^{-2+10.4\%}_{-10.2\%}$	$2.26\cdot10^{-3+5.2\%}_{-5.1\%}$	$1.32\cdot10^{-3+9.2\%}_{-9.1\%}$	$1.76\cdot10^{-1+4.5\%}_{-4.4\%}$	$2.07\cdot10^{-2+4.5\%}_{-4.4\%}$	$3.76\cdot10^{-3+4.2\%}_{-4.1\%}$
123.0	$8.71\cdot10^{-2+10.4\%}_{-10.1\%}$	$2.27\cdot10^{-3+5.2\%}_{-5.0\%}$	$1.36\cdot10^{-3+9.2\%}_{-9.0\%}$	$1.83\cdot10^{-1+4.5\%}_{-4.4\%}$	$2.18\cdot10^{-2+4.5\%}_{-4.4\%}$	$3.82\cdot10^{-3+4.1\%}_{-4.1\%}$
123.5	$8.68\cdot10^{-2+10.3\%}_{-10.1\%}$	$2.28\cdot10^{-3+5.1\%}_{-5.0\%}$	$1.41\cdot10^{-3+9.1\%}_{-9.0\%}$	$1.91\cdot10^{-1+4.4\%}_{-4.3\%}$	$2.29\cdot10^{-2+4.5\%}_{-4.3\%}$	$3.88\cdot10^{-3+4.1\%}_{-4.0\%}$
124.0	$8.65\cdot10^{-2+10.3\%}_{-10.1\%}$	$2.28\cdot10^{-3+5.1\%}_{-5.0\%}$	$1.45\cdot10^{-3+9.1\%}_{-8.9\%}$	$1.98\cdot10^{-1+4.4\%}_{-4.3\%}$	$2.40\cdot10^{-2+4.4\%}_{-4.3\%}$	$3.94\cdot10^{-3+4.0\%}_{-4.0\%}$
124.5	$8.61\cdot10^{-2+10.3\%}_{-10.0\%}$	$2.28\cdot10^{-3+5.0\%}_{-4.9\%}$	$1.49\cdot10^{-3+9.1\%}_{-8.9\%}$	$2.07\cdot10^{-1+4.3\%}_{-4.2\%}$	$2.52\cdot10^{-2+4.4\%}_{-4.2\%}$	$4.00\cdot10^{-3+4.0\%}_{-4.0\%}$
125.0	$8.57\cdot10^{-2+10.2\%}_{-10.0\%}$	$2.28\cdot10^{-3+5.0\%}_{-4.9\%}$	$1.54\cdot10^{-3+9.0\%}_{-8.8\%}$	$2.15\cdot10^{-1+4.3\%}_{-4.2\%}$	$2.64\cdot10^{-2+4.3\%}_{-4.2\%}$	$4.07\cdot10^{-3+4.0\%}_{-3.9\%}$
125.5	$8.52\cdot10^{-2+10.2\%}_{-9.9\%}$	$2.28\cdot10^{-3+4.9\%}_{-4.8\%}$	$1.58\cdot10^{-3+8.9\%}_{-8.8\%}$	$2.23\cdot10^{-1+4.2\%}_{-4.1\%}$	$2.76\cdot10^{-2+4.3\%}_{-4.1\%}$	$4.14\cdot10^{-3+3.9\%}_{-3.9\%}$
126.0	$8.48\cdot10^{-2+10.1\%}_{-9.9\%}$	$2.28\cdot10^{-3+4.9\%}_{-4.8\%}$	$1.62\cdot10^{-3+8.9\%}_{-8.8\%}$	$2.31\cdot10^{-1+4.1\%}_{-4.1\%}$	$2.89\cdot10^{-2+4.2\%}_{-4.0\%}$	$4.21\cdot10^{-3+3.9\%}_{-3.8\%}$
126.5	$8.42\cdot10^{-2+10.1\%}_{-9.8\%}$	$2.28\cdot10^{-3+4.8\%}_{-4.7\%}$	$1.66\cdot10^{-3+8.8\%}_{-8.7\%}$	$2.39\cdot10^{-1+4.1\%}_{-4.0\%}$	$3.02\cdot10^{-2+4.1\%}_{-4.0\%}$	$4.29\cdot10^{-3+3.8\%}_{-3.8\%}$
127.0	$8.37\cdot10^{-2+10.1\%}_{-9.8\%}$	$2.28\cdot10^{-3+4.8\%}_{-4.7\%}$	$1.70\cdot10^{-3+8.8\%}_{-8.7\%}$	$2.48\cdot10^{-1+4.0\%}_{-4.0\%}$	$3.15\cdot10^{-2+4.1\%}_{-3.9\%}$	$4.37\cdot10^{-3+3.8\%}_{-3.7\%}$
127.5	$8.31\cdot10^{-2+10.0\%}_{-9.8\%}$	$2.28\cdot10^{-3+4.8\%}_{-4.6\%}$	$1.75\cdot10^{-3+8.7\%}_{-8.6\%}$	$2.57\cdot10^{-1+4.0\%}_{-3.9\%}$	$3.28\cdot10^{-2+4.0\%}_{-3.9\%}$	$4.45\cdot10^{-3+3.7\%}_{-3.7\%}$
128.0	$8.25\cdot10^{-2+10.0\%}_{-9.7\%}$	$2.27\cdot10^{-3+4.7\%}_{-4.6\%}$	$1.79\cdot10^{-3+8.7\%}_{-8.6\%}$	$2.66\cdot10^{-1+3.9\%}_{-3.9\%}$	$3.42\cdot10^{-2+3.9\%}_{-3.8\%}$	$4.53\cdot10^{-3+3.7\%}_{-3.6\%}$
128.5	$8.19\cdot10^{-2+9.9\%}_{-9.7\%}$	$2.27\cdot10^{-3+4.7\%}_{-4.5\%}$	$1.83\cdot10^{-3+8.6\%}_{-8.6\%}$	$2.75\cdot10^{-1+3.8\%}_{-3.8\%}$	$3.56\cdot10^{-2+3.9\%}_{-3.8\%}$	$4.62\cdot10^{-3+3.6\%}_{-3.6\%}$
129.0	$8.12\cdot10^{-2+9.9\%}_{-9.6\%}$	$2.26\cdot10^{-3+4.6\%}_{-4.5\%}$	$1.87\cdot10^{-3+8.5\%}_{-8.5\%}$	$2.84\cdot10^{-1+3.8\%}_{-3.7\%}$	$3.70\cdot10^{-2+3.8\%}_{-3.7\%}$	$4.71\cdot10^{-3+3.6\%}_{-3.5\%}$
129.5	$8.05\cdot10^{-2+9.8\%}_{-9.6\%}$	$2.26\cdot10^{-3+4.6\%}_{-4.4\%}$	$1.90\cdot10^{-3+8.5\%}_{-8.5\%}$	$2.93\cdot10^{-1+3.7\%}_{-3.7\%}$	$3.84\cdot10^{-2+3.7\%}_{-3.7\%}$	$4.81\cdot10^{-3+3.5\%}_{-3.5\%}$
130.0	$7.97\cdot10^{-2+9.8\%}_{-9.6\%}$	$2.25\cdot10^{-3+4.5\%}_{-4.4\%}$	$1.95\cdot10^{-3+8.4\%}_{-8.4\%}$	$3.03\cdot10^{-1+3.7\%}_{-3.6\%}$	$3.98\cdot10^{-2+3.7\%}_{-3.6\%}$	$4.91\cdot10^{-3+3.5\%}_{-3.4\%}$

Table A.7: SM Higgs branching ratios to two gauge bosons and Higgs total width together with their total uncertainties (expressed in percentage). Low- and intermediate.mass range.

$M_{\rm H}$ [GeV]	$\rm H \to gg$	$\rm H \to \gamma\gamma$	$\rm H \to Z\gamma$	$\rm H \to WW$	$\rm H \to ZZ$	$\Gamma_{\rm H}$ [GeV]
130.5	$7.90\cdot10^{-2}{}^{+9.8\%}_{-9.5\%}$	$2.24\cdot10^{-3}{}^{+4.5\%}_{-4.3\%}$	$1.99\cdot10^{-3}{}^{+8.4\%}_{-8.4\%}$	$3.12\cdot10^{-1}{}^{+3.6\%}_{-3.5\%}$	$4.13\cdot10^{-2}{}^{+3.6\%}_{-3.5\%}$	$5.01\cdot10^{-3}{}^{+3.4\%}_{-3.4\%}$
131.0	$7.82\cdot10^{-2}{}^{+9.7\%}_{-9.5\%}$	$2.23\cdot10^{-3}{}^{+4.4\%}_{-4.3\%}$	$2.01\cdot10^{-3}{}^{+8.3\%}_{-8.3\%}$	$3.22\cdot10^{-1}{}^{+3.5\%}_{-3.5\%}$	$4.28\cdot10^{-2}{}^{+3.5\%}_{-3.5\%}$	$5.12\cdot10^{-3}{}^{+3.4\%}_{-3.3\%}$
131.5	$7.73\cdot10^{-2}{}^{+9.7\%}_{-9.4\%}$	$2.22\cdot10^{-3}{}^{+4.4\%}_{-4.2\%}$	$2.06\cdot10^{-3}{}^{+8.3\%}_{-8.3\%}$	$3.31\cdot10^{-1}{}^{+3.5\%}_{-3.4\%}$	$4.42\cdot10^{-2}{}^{+3.5\%}_{-3.4\%}$	$5.23\cdot10^{-3}{}^{+3.3\%}_{-3.3\%}$
132.0	$7.65\cdot10^{-2}{}^{+9.6\%}_{-9.4\%}$	$2.21\cdot10^{-3}{}^{+4.3\%}_{-4.2\%}$	$2.09\cdot10^{-3}{}^{+8.2\%}_{-8.2\%}$	$3.41\cdot10^{-1}{}^{+3.4\%}_{-3.4\%}$	$4.57\cdot10^{-2}{}^{+3.4\%}_{-3.4\%}$	$5.35\cdot10^{-3}{}^{+3.2\%}_{-3.2\%}$
132.5	$7.56\cdot10^{-2}{}^{+9.6\%}_{-9.4\%}$	$2.20\cdot10^{-3}{}^{+4.2\%}_{-4.1\%}$	$2.13\cdot10^{-3}{}^{+8.2\%}_{-8.2\%}$	$3.51\cdot10^{-1}{}^{+3.3\%}_{-3.3\%}$	$4.72\cdot10^{-2}{}^{+3.3\%}_{-3.3\%}$	$5.47\cdot10^{-3}{}^{+3.2\%}_{-3.2\%}$
133.0	$7.47\cdot10^{-2}{}^{+9.5\%}_{-9.3\%}$	$2.19\cdot10^{-3}{}^{+4.2\%}_{-4.1\%}$	$2.16\cdot10^{-3}{}^{+8.1\%}_{-8.1\%}$	$3.61\cdot10^{-1}{}^{+3.3\%}_{-3.2\%}$	$4.87\cdot10^{-2}{}^{+3.3\%}_{-3.2\%}$	$5.60\cdot10^{-3}{}^{+3.1\%}_{-3.1\%}$
133.5	$7.37\cdot10^{-2}{}^{+9.5\%}_{-9.3\%}$	$2.17\cdot10^{-3}{}^{+4.1\%}_{-4.0\%}$	$2.19\cdot10^{-3}{}^{+8.1\%}_{-8.1\%}$	$3.70\cdot10^{-1}{}^{+3.2\%}_{-3.2\%}$	$5.02\cdot10^{-2}{}^{+3.2\%}_{-3.2\%}$	$5.74\cdot10^{-3}{}^{+3.1\%}_{-3.1\%}$
134.0	$7.28\cdot10^{-2}{}^{+9.4\%}_{-9.2\%}$	$2.16\cdot10^{-3}{}^{+4.1\%}_{-4.0\%}$	$2.22\cdot10^{-3}{}^{+8.0\%}_{-8.0\%}$	$3.80\cdot10^{-1}{}^{+3.1\%}_{-3.1\%}$	$5.17\cdot10^{-2}{}^{+3.1\%}_{-3.1\%}$	$5.88\cdot10^{-3}{}^{+3.0\%}_{-3.0\%}$
134.5	$7.18\cdot10^{-2}{}^{+9.4\%}_{-9.2\%}$	$2.14\cdot10^{-3}{}^{+4.0\%}_{-3.9\%}$	$2.25\cdot10^{-3}{}^{+8.0\%}_{-7.9\%}$	$3.90\cdot10^{-1}{}^{+3.1\%}_{-3.0\%}$	$5.32\cdot10^{-2}{}^{+3.1\%}_{-3.0\%}$	$6.03\cdot10^{-3}{}^{+3.0\%}_{-3.0\%}$
135.0	$7.08\cdot10^{-2}{}^{+9.3\%}_{-9.2\%}$	$2.13\cdot10^{-3}{}^{+4.0\%}_{-3.9\%}$	$2.27\cdot10^{-3}{}^{+7.9\%}_{-7.9\%}$	$4.00\cdot10^{-1}{}^{+3.0\%}_{-3.0\%}$	$5.47\cdot10^{-2}{}^{+3.0\%}_{-3.0\%}$	$6.18\cdot10^{-3}{}^{+2.9\%}_{-2.9\%}$
135.5	$6.97\cdot10^{-2}{}^{+9.2\%}_{-9.1\%}$	$2.11\cdot10^{-3}{}^{+3.8\%}_{-3.8\%}$	$2.30\cdot10^{-3}{}^{+7.8\%}_{-7.8\%}$	$4.10\cdot10^{-1}{}^{+2.9\%}_{-2.8\%}$	$5.62\cdot10^{-2}{}^{+2.9\%}_{-2.8\%}$	$6.34\cdot10^{-3}{}^{+2.8\%}_{-2.8\%}$
136.0	$6.87\cdot10^{-2}{}^{+9.1\%}_{-9.0\%}$	$2.09\cdot10^{-3}{}^{+3.7\%}_{-3.6\%}$	$2.32\cdot10^{-3}{}^{+7.7\%}_{-7.7\%}$	$4.20\cdot10^{-1}{}^{+2.8\%}_{-2.7\%}$	$5.77\cdot10^{-2}{}^{+2.8\%}_{-2.7\%}$	$6.51\cdot10^{-3}{}^{+2.7\%}_{-2.7\%}$
136.5	$6.76\cdot10^{-2}{}^{+9.0\%}_{-8.9\%}$	$2.08\cdot10^{-3}{}^{+3.6\%}_{-3.5\%}$	$2.34\cdot10^{-3}{}^{+7.5\%}_{-7.5\%}$	$4.30\cdot10^{-1}{}^{+2.6\%}_{-2.6\%}$	$5.91\cdot10^{-2}{}^{+2.6\%}_{-2.6\%}$	$6.69\cdot10^{-3}{}^{+2.6\%}_{-2.6\%}$
137.0	$6.65\cdot10^{-2}{}^{+8.9\%}_{-8.8\%}$	$2.06\cdot10^{-3}{}^{+3.5\%}_{-3.4\%}$	$2.36\cdot10^{-3}{}^{+7.4\%}_{-7.4\%}$	$4.41\cdot10^{-1}{}^{+2.5\%}_{-2.5\%}$	$6.06\cdot10^{-2}{}^{+2.5\%}_{-2.5\%}$	$6.87\cdot10^{-3}{}^{+2.5\%}_{-2.5\%}$
137.5	$6.54\cdot10^{-2}{}^{+8.8\%}_{-8.7\%}$	$2.04\cdot10^{-3}{}^{+3.3\%}_{-3.3\%}$	$2.38\cdot10^{-3}{}^{+7.3\%}_{-7.3\%}$	$4.51\cdot10^{-1}{}^{+2.4\%}_{-2.3\%}$	$6.20\cdot10^{-2}{}^{+2.4\%}_{-2.3\%}$	$7.06\cdot10^{-3}{}^{+2.3\%}_{-2.3\%}$
138.0	$6.43\cdot10^{-2}{}^{+8.7\%}_{-8.5\%}$	$2.02\cdot10^{-3}{}^{+3.2\%}_{-3.2\%}$	$2.40\cdot10^{-3}{}^{+7.2\%}_{-7.2\%}$	$4.61\cdot10^{-1}{}^{+2.2\%}_{-2.2\%}$	$6.34\cdot10^{-2}{}^{+2.2\%}_{-2.2\%}$	$7.27\cdot10^{-3}{}^{+2.2\%}_{-2.2\%}$
138.5	$6.32\cdot10^{-2}{}^{+8.6\%}_{-8.4\%}$	$2.00\cdot10^{-3}{}^{+3.1\%}_{-3.1\%}$	$2.42\cdot10^{-3}{}^{+7.1\%}_{-7.1\%}$	$4.71\cdot10^{-1}{}^{+2.1\%}_{-2.1\%}$	$6.48\cdot10^{-2}{}^{+2.1\%}_{-2.1\%}$	$7.48\cdot10^{-3}{}^{+2.1\%}_{-2.1\%}$
139.0	$6.20\cdot10^{-2}{}^{+8.5\%}_{-8.3\%}$	$1.98\cdot10^{-3}{}^{+3.0\%}_{-3.0\%}$	$2.43\cdot10^{-3}{}^{+6.9\%}_{-7.0\%}$	$4.81\cdot10^{-1}{}^{+1.9\%}_{-1.9\%}$	$6.61\cdot10^{-2}{}^{+2.0\%}_{-1.9\%}$	$7.70\cdot10^{-3}{}^{+2.0\%}_{-2.0\%}$
139.5	$6.08\cdot10^{-2}{}^{+8.4\%}_{-8.2\%}$	$1.95\cdot10^{-3}{}^{+2.9\%}_{-2.9\%}$	$2.45\cdot10^{-3}{}^{+6.8\%}_{-6.8\%}$	$4.91\cdot10^{-1}{}^{+1.8\%}_{-1.8\%}$	$6.75\cdot10^{-2}{}^{+1.8\%}_{-1.8\%}$	$7.93\cdot10^{-3}{}^{+1.9\%}_{-1.9\%}$
140.0	$5.97\cdot10^{-2}{}^{+8.3\%}_{-8.1\%}$	$1.93\cdot10^{-3}{}^{+2.7\%}_{-2.8\%}$	$2.46\cdot10^{-3}{}^{+6.7\%}_{-6.7\%}$	$5.01\cdot10^{-1}{}^{+1.7\%}_{-1.7\%}$	$6.87\cdot10^{-2}{}^{+1.7\%}_{-1.7\%}$	$8.18\cdot10^{-3}{}^{+1.8\%}_{-1.7\%}$
141.0	$5.72\cdot10^{-2}{}^{+8.2\%}_{-8.1\%}$	$1.88\cdot10^{-3}{}^{+2.7\%}_{-2.7\%}$	$2.48\cdot10^{-3}{}^{+6.6\%}_{-6.7\%}$	$5.21\cdot10^{-1}{}^{+1.6\%}_{-1.6\%}$	$7.12\cdot10^{-2}{}^{+1.6\%}_{-1.6\%}$	$8.70\cdot10^{-3}{}^{+1.7\%}_{-1.7\%}$
142.0	$5.48\cdot10^{-2}{}^{+8.2\%}_{-8.1\%}$	$1.84\cdot10^{-3}{}^{+2.6\%}_{-2.6\%}$	$2.49\cdot10^{-3}{}^{+6.6\%}_{-6.6\%}$	$5.41\cdot10^{-1}{}^{+1.5\%}_{-1.5\%}$	$7.35\cdot10^{-2}{}^{+1.5\%}_{-1.5\%}$	$9.28\cdot10^{-3}{}^{+1.6\%}_{-1.6\%}$
143.0	$5.23\cdot10^{-2}{}^{+8.2\%}_{-8.0\%}$	$1.77\cdot10^{-3}{}^{+2.5\%}_{-2.5\%}$	$2.49\cdot10^{-3}{}^{+6.5\%}_{-6.5\%}$	$5.61\cdot10^{-1}{}^{+1.4\%}_{-1.4\%}$	$7.56\cdot10^{-2}{}^{+1.4\%}_{-1.4\%}$	$9.93\cdot10^{-3}{}^{+1.6\%}_{-1.5\%}$
144.0	$4.99\cdot10^{-2}{}^{+8.1\%}_{-8.0\%}$	$1.73\cdot10^{-3}{}^{+2.5\%}_{-2.4\%}$	$2.49\cdot10^{-3}{}^{+6.5\%}_{-6.5\%}$	$5.80\cdot10^{-1}{}^{+1.3\%}_{-1.3\%}$	$7.75\cdot10^{-2}{}^{+1.3\%}_{-1.3\%}$	$1.07\cdot10^{-2}{}^{+1.5\%}_{-1.5\%}$
145.0	$4.74\cdot10^{-2}{}^{+8.1\%}_{-8.0\%}$	$1.68\cdot10^{-3}{}^{+2.4\%}_{-2.4\%}$	$2.48\cdot10^{-3}{}^{+6.4\%}_{-6.4\%}$	$6.00\cdot10^{-1}{}^{+1.2\%}_{-1.3\%}$	$7.91\cdot10^{-2}{}^{+1.2\%}_{-1.3\%}$	$1.15\cdot10^{-2}{}^{+1.4\%}_{-1.4\%}$
146.0	$4.48\cdot10^{-2}{}^{+8.1\%}_{-7.9\%}$	$1.62\cdot10^{-3}{}^{+2.4\%}_{-2.3\%}$	$2.46\cdot10^{-3}{}^{+6.3\%}_{-6.3\%}$	$6.19\cdot10^{-1}{}^{+1.2\%}_{-1.2\%}$	$8.05\cdot10^{-2}{}^{+1.2\%}_{-1.2\%}$	$1.23\cdot10^{-2}{}^{+1.4\%}_{-1.3\%}$
147.0	$4.22\cdot10^{-2}{}^{+8.0\%}_{-7.9\%}$	$1.56\cdot10^{-3}{}^{+2.3\%}_{-2.2\%}$	$2.44\cdot10^{-3}{}^{+6.3\%}_{-6.3\%}$	$6.39\cdot10^{-1}{}^{+1.1\%}_{-1.1\%}$	$8.16\cdot10^{-2}{}^{+1.1\%}_{-1.1\%}$	$1.34\cdot10^{-2}{}^{+1.3\%}_{-1.3\%}$
148.0	$3.96\cdot10^{-2}{}^{+8.0\%}_{-7.9\%}$	$1.49\cdot10^{-3}{}^{+2.2\%}_{-2.2\%}$	$2.39\cdot10^{-3}{}^{+6.2\%}_{-6.3\%}$	$6.58\cdot10^{-1}{}^{+1.0\%}_{-1.0\%}$	$8.24\cdot10^{-2}{}^{+1.0\%}_{-1.0\%}$	$1.45\cdot10^{-2}{}^{+1.2\%}_{-1.2\%}$
149.0	$3.72\cdot10^{-2}{}^{+8.0\%}_{-7.9\%}$	$1.43\cdot10^{-3}{}^{+2.2\%}_{-2.1\%}$	$2.36\cdot10^{-3}{}^{+6.1\%}_{-6.2\%}$	$6.77\cdot10^{-1}{}^{+0.9\%}_{-0.9\%}$	$8.26\cdot10^{-2}{}^{+0.9\%}_{-0.9\%}$	$1.58\cdot10^{-2}{}^{+1.2\%}_{-1.2\%}$
150.0	$3.46\cdot10^{-2}{}^{+7.9\%}_{-7.8\%}$	$1.37\cdot10^{-3}{}^{+2.1\%}_{-2.1\%}$	$2.31\cdot10^{-3}{}^{+6.0\%}_{-6.2\%}$	$6.96\cdot10^{-1}{}^{+0.9\%}_{-0.8\%}$	$8.25\cdot10^{-2}{}^{+0.9\%}_{-0.8\%}$	$1.73\cdot10^{-2}{}^{+1.1\%}_{-1.1\%}$
151.0	$3.20\cdot10^{-2}{}^{+7.9\%}_{-7.8\%}$	$1.29\cdot10^{-3}{}^{+2.1\%}_{-2.0\%}$	$2.24\cdot10^{-3}{}^{+6.0\%}_{-6.1\%}$	$7.16\cdot10^{-1}{}^{+0.8\%}_{-0.8\%}$	$8.19\cdot10^{-2}{}^{+0.8\%}_{-0.8\%}$	$1.91\cdot10^{-2}{}^{+1.1\%}_{-1.1\%}$
152.0	$2.95\cdot10^{-2}{}^{+7.9\%}_{-7.8\%}$	$1.22\cdot10^{-3}{}^{+2.0\%}_{-2.0\%}$	$2.19\cdot10^{-3}{}^{+6.0\%}_{-6.0\%}$	$7.35\cdot10^{-1}{}^{+0.7\%}_{-0.7\%}$	$8.08\cdot10^{-2}{}^{+0.7\%}_{-0.7\%}$	$2.11\cdot10^{-2}{}^{+1.0\%}_{-1.0\%}$
153.0	$2.69\cdot10^{-2}{}^{+7.9\%}_{-7.8\%}$	$1.15\cdot10^{-3}{}^{+2.0\%}_{-1.9\%}$	$2.11\cdot10^{-3}{}^{+6.0\%}_{-6.0\%}$	$7.54\cdot10^{-1}{}^{+0.7\%}_{-0.7\%}$	$7.90\cdot10^{-2}{}^{+0.7\%}_{-0.7\%}$	$2.36\cdot10^{-2}{}^{+1.0\%}_{-1.0\%}$
154.0	$2.44\cdot10^{-2}{}^{+7.9\%}_{-7.7\%}$	$1.07\cdot10^{-3}{}^{+1.9\%}_{-1.9\%}$	$2.02\cdot10^{-3}{}^{+5.9\%}_{-5.9\%}$	$7.74\cdot10^{-1}{}^{+0.6\%}_{-0.6\%}$	$7.66\cdot10^{-2}{}^{+0.6\%}_{-0.6\%}$	$2.66\cdot10^{-2}{}^{+0.9\%}_{-0.9\%}$
155.0	$2.18\cdot10^{-2}{}^{+7.8\%}_{-7.7\%}$	$9.98\cdot10^{-4}{}^{+1.9\%}_{-1.9\%}$	$1.91\cdot10^{-3}{}^{+5.9\%}_{-5.8\%}$	$7.94\cdot10^{-1}{}^{+0.5\%}_{-0.5\%}$	$7.34\cdot10^{-2}{}^{+0.5\%}_{-0.5\%}$	$3.03\cdot10^{-2}{}^{+0.9\%}_{-0.9\%}$
156.0	$1.92\cdot10^{-2}{}^{+7.8\%}_{-7.7\%}$	$9.14\cdot10^{-4}{}^{+1.8\%}_{-1.8\%}$	$1.79\cdot10^{-3}{}^{+5.8\%}_{-5.8\%}$	$8.15\cdot10^{-1}{}^{+0.5\%}_{-0.5\%}$	$6.92\cdot10^{-2}{}^{+0.5\%}_{-0.5\%}$	$3.51\cdot10^{-2}{}^{+0.8\%}_{-0.8\%}$
157.0	$1.65\cdot10^{-2}{}^{+7.8\%}_{-7.7\%}$	$8.23\cdot10^{-4}{}^{+1.8\%}_{-1.8\%}$	$1.65\cdot10^{-3}{}^{+5.8\%}_{-5.8\%}$	$8.37\cdot10^{-1}{}^{+0.4\%}_{-0.4\%}$	$6.40\cdot10^{-2}{}^{+0.4\%}_{-0.4\%}$	$4.14\cdot10^{-2}{}^{+0.8\%}_{-0.8\%}$
158.0	$1.39\cdot10^{-2}{}^{+7.8\%}_{-7.7\%}$	$7.29\cdot10^{-4}{}^{+1.7\%}_{-1.7\%}$	$1.50\cdot10^{-3}{}^{+5.7\%}_{-5.7\%}$	$8.60\cdot10^{-1}{}^{+0.3\%}_{-0.3\%}$	$5.76\cdot10^{-2}{}^{+0.3\%}_{-0.3\%}$	$5.02\cdot10^{-2}{}^{+0.7\%}_{-0.7\%}$
159.0	$1.12\cdot10^{-2}{}^{+7.8\%}_{-7.7\%}$	$6.28\cdot10^{-4}{}^{+1.7\%}_{-1.7\%}$	$1.33\cdot10^{-3}{}^{+5.7\%}_{-5.7\%}$	$8.84\cdot10^{-1}{}^{+0.3\%}_{-0.3\%}$	$4.99\cdot10^{-2}{}^{+0.3\%}_{-0.3\%}$	$6.32\cdot10^{-2}{}^{+0.7\%}_{-0.7\%}$
160.0	$8.65\cdot10^{-3}{}^{+7.8\%}_{-7.7\%}$	$5.32\cdot10^{-4}{}^{+1.6\%}_{-1.6\%}$	$1.16\cdot10^{-3}{}^{+5.6\%}_{-5.7\%}$	$9.08\cdot10^{-1}{}^{+0.2\%}_{-0.2\%}$	$4.15\cdot10^{-2}{}^{+0.2\%}_{-0.2\%}$	$8.31\cdot10^{-2}{}^{+0.6\%}_{-0.6\%}$
162.0	$5.04\cdot10^{-3}{}^{+7.7\%}_{-7.7\%}$	$3.70\cdot10^{-4}{}^{+1.6\%}_{-1.6\%}$	$8.41\cdot10^{-4}{}^{+5.6\%}_{-5.6\%}$	$9.43\cdot10^{-1}{}^{+0.2\%}_{-0.2\%}$	$2.82\cdot10^{-2}{}^{+0.2\%}_{-0.2\%}$	$1.47\cdot10^{-1}{}^{+0.6\%}_{-0.6\%}$
164.0	$3.54\cdot10^{-3}{}^{+7.7\%}_{-7.7\%}$	$2.60\cdot10^{-4}{}^{+1.6\%}_{-1.6\%}$	$6.06\cdot10^{-4}{}^{+5.6\%}_{-5.6\%}$	$9.57\cdot10^{-1}{}^{+0.1\%}_{-0.1\%}$	$2.31\cdot10^{-2}{}^{+0.2\%}_{-0.2\%}$	$2.15\cdot10^{-1}{}^{+0.6\%}_{-0.6\%}$
166.0	$2.85\cdot10^{-3}{}^{+7.7\%}_{-7.7\%}$	$2.08\cdot10^{-4}{}^{+1.6\%}_{-1.6\%}$	$5.00\cdot10^{-4}{}^{+5.6\%}_{-5.6\%}$	$9.62\cdot10^{-1}{}^{+0.1\%}_{-0.1\%}$	$2.18\cdot10^{-2}{}^{+0.1\%}_{-0.1\%}$	$2.76\cdot10^{-1}{}^{+0.6\%}_{-0.6\%}$
168.0	$2.46\cdot10^{-3}{}^{+7.7\%}_{-7.7\%}$	$1.79\cdot10^{-4}{}^{+1.6\%}_{-1.6\%}$	$4.40\cdot10^{-4}{}^{+5.6\%}_{-5.6\%}$	$9.64\cdot10^{-1}{}^{+0.1\%}_{-0.1\%}$	$2.22\cdot10^{-2}{}^{+0.1\%}_{-0.1\%}$	$3.30\cdot10^{-1}{}^{+0.6\%}_{-0.6\%}$
170.0	$2.20\cdot10^{-3}{}^{+7.7\%}_{-7.7\%}$	$1.58\cdot10^{-4}{}^{+1.6\%}_{-1.6\%}$	$4.00\cdot10^{-4}{}^{+5.6\%}_{-5.6\%}$	$9.64\cdot10^{-1}{}^{+0.1\%}_{-0.1\%}$	$2.36\cdot10^{-2}{}^{+0.1\%}_{-0.1\%}$	$3.80\cdot10^{-1}{}^{+0.6\%}_{-0.6\%}$

Table A.8: SM Higgs branching ratios to two gauge bosons and Higgs total width together with their total uncertainties (expressed in percentage). Intermediate-mass range.

$M_{\rm H}$ [GeV]	$\rm H \to gg$	$\rm H \to \gamma\gamma$	$\rm H \to Z\gamma$	$\rm H \to WW$	$\rm H \to ZZ$	$\Gamma_{\rm H}$ [GeV]
172.0	$2.01\cdot10^{-3}{}^{+7.7\%}_{-7.6\%}$	$1.43\cdot10^{-4}{}^{+1.6\%}_{-1.6\%}$	$3.70\cdot10^{-4}{}^{+5.6\%}_{-5.6\%}$	$9.63\cdot10^{-1}{}^{+0.0\%}_{-0.0\%}$	$2.61\cdot10^{-2}{}^{+0.1\%}_{-0.1\%}$	$4.29\cdot10^{-1}{}^{+0.6\%}_{-0.6\%}$
174.0	$1.88\cdot10^{-3}{}^{+7.7\%}_{-7.6\%}$	$1.32\cdot10^{-4}{}^{+1.6\%}_{-1.6\%}$	$3.48\cdot10^{-4}{}^{+5.6\%}_{-5.5\%}$	$9.60\cdot10^{-1}{}^{+0.0\%}_{-0.0\%}$	$2.98\cdot10^{-2}{}^{+0.1\%}_{-0.1\%}$	$4.77\cdot10^{-1}{}^{+0.6\%}_{-0.6\%}$
176.0	$1.76\cdot10^{-3}{}^{+7.7\%}_{-7.6\%}$	$1.22\cdot10^{-4}{}^{+1.6\%}_{-1.6\%}$	$3.29\cdot10^{-4}{}^{+5.6\%}_{-5.5\%}$	$9.55\cdot10^{-1}{}^{+0.0\%}_{-0.0\%}$	$3.54\cdot10^{-2}{}^{+0.1\%}_{-0.1\%}$	$5.25\cdot10^{-1}{}^{+0.6\%}_{-0.6\%}$
178.0	$1.65\cdot10^{-3}{}^{+7.7\%}_{-7.6\%}$	$1.14\cdot10^{-4}{}^{+1.6\%}_{-1.6\%}$	$3.12\cdot10^{-4}{}^{+5.6\%}_{-5.5\%}$	$9.47\cdot10^{-1}{}^{+0.0\%}_{-0.0\%}$	$4.44\cdot10^{-2}{}^{+0.1\%}_{-0.1\%}$	$5.75\cdot10^{-1}{}^{+0.6\%}_{-0.6\%}$
180.0	$1.56\cdot10^{-3}{}^{+7.7\%}_{-7.6\%}$	$1.05\cdot10^{-4}{}^{+1.6\%}_{-1.6\%}$	$2.96\cdot10^{-4}{}^{+5.6\%}_{-5.5\%}$	$9.32\cdot10^{-1}{}^{+0.0\%}_{-0.0\%}$	$6.02\cdot10^{-2}{}^{+0.1\%}_{-0.1\%}$	$6.31\cdot10^{-1}{}^{+0.6\%}_{-0.6\%}$
182.0	$1.44\cdot10^{-3}{}^{+7.7\%}_{-7.6\%}$	$9.69\cdot10^{-5}{}^{+1.6\%}_{-1.6\%}$	$2.76\cdot10^{-4}{}^{+5.6\%}_{-5.5\%}$	$9.03\cdot10^{-1}{}^{+0.0\%}_{-0.0\%}$	$9.00\cdot10^{-2}{}^{+0.1\%}_{-0.1\%}$	$7.00\cdot10^{-1}{}^{+0.6\%}_{-0.6\%}$
184.0	$1.32\cdot10^{-3}{}^{+7.7\%}_{-7.6\%}$	$8.81\cdot10^{-5}{}^{+1.6\%}_{-1.6\%}$	$2.54\cdot10^{-4}{}^{+5.6\%}_{-5.5\%}$	$8.62\cdot10^{-1}{}^{+0.0\%}_{-0.0\%}$	$1.31\cdot10^{-1}{}^{+0.0\%}_{-0.0\%}$	$7.88\cdot10^{-1}{}^{+0.6\%}_{-0.6\%}$
186.0	$1.23\cdot10^{-3}{}^{+7.7\%}_{-7.6\%}$	$8.09\cdot10^{-5}{}^{+1.6\%}_{-1.6\%}$	$2.35\cdot10^{-4}{}^{+5.6\%}_{-5.5\%}$	$8.28\cdot10^{-1}{}^{+0.0\%}_{-0.0\%}$	$1.66\cdot10^{-1}{}^{+0.0\%}_{-0.0\%}$	$8.76\cdot10^{-1}{}^{+0.5\%}_{-0.6\%}$
188.0	$1.16\cdot10^{-3}{}^{+7.7\%}_{-7.6\%}$	$7.52\cdot10^{-5}{}^{+1.6\%}_{-1.5\%}$	$2.22\cdot10^{-4}{}^{+5.6\%}_{-5.5\%}$	$8.03\cdot10^{-1}{}^{+0.0\%}_{-0.0\%}$	$1.91\cdot10^{-1}{}^{+0.0\%}_{-0.0\%}$	$9.60\cdot10^{-1}{}^{+0.5\%}_{-0.5\%}$
190.0	$1.10\cdot10^{-3}{}^{+7.7\%}_{-7.6\%}$	$7.05\cdot10^{-5}{}^{+1.6\%}_{-1.5\%}$	$2.11\cdot10^{-4}{}^{+5.6\%}_{-5.5\%}$	$7.86\cdot10^{-1}{}^{+0.0\%}_{-0.0\%}$	$2.09\cdot10^{-1}{}^{+0.0\%}_{-0.0\%}$	$1.04^{+0.5\%}_{-0.5\%}$
192.0	$1.05\cdot10^{-3}{}^{+7.7\%}_{-7.6\%}$	$6.66\cdot10^{-5}{}^{+1.6\%}_{-1.6\%}$	$2.02\cdot10^{-4}{}^{+5.6\%}_{-5.5\%}$	$7.72\cdot10^{-1}{}^{+0.0\%}_{-0.0\%}$	$2.23\cdot10^{-1}{}^{+0.0\%}_{-0.0\%}$	$1.12^{+0.5\%}_{-0.5\%}$
194.0	$1.01\cdot10^{-3}{}^{+7.7\%}_{-7.6\%}$	$6.32\cdot10^{-5}{}^{+1.6\%}_{-1.6\%}$	$1.94\cdot10^{-4}{}^{+5.6\%}_{-5.5\%}$	$7.61\cdot10^{-1}{}^{+0.0\%}_{-0.0\%}$	$2.34\cdot10^{-1}{}^{+0.0\%}_{-0.0\%}$	$1.20^{+0.5\%}_{-0.5\%}$
196.0	$9.79\cdot10^{-4}{}^{+7.7\%}_{-7.6\%}$	$6.02\cdot10^{-5}{}^{+1.6\%}_{-1.6\%}$	$1.87\cdot10^{-4}{}^{+5.5\%}_{-5.6\%}$	$7.53\cdot10^{-1}{}^{+0.0\%}_{-0.0\%}$	$2.43\cdot10^{-1}{}^{+0.0\%}_{-0.0\%}$	$1.28^{+0.5\%}_{-0.5\%}$
198.0	$9.51\cdot10^{-4}{}^{+7.6\%}_{-7.6\%}$	$5.75\cdot10^{-5}{}^{+1.6\%}_{-1.6\%}$	$1.81\cdot10^{-4}{}^{+5.5\%}_{-5.6\%}$	$7.46\cdot10^{-1}{}^{+0.0\%}_{-0.0\%}$	$2.50\cdot10^{-1}{}^{+0.0\%}_{-0.0\%}$	$1.35^{+0.5\%}_{-0.5\%}$
200.0	$9.26\cdot10^{-4}{}^{+7.6\%}_{-7.6\%}$	$5.51\cdot10^{-5}{}^{+1.6\%}_{-1.6\%}$	$1.75\cdot10^{-4}{}^{+5.5\%}_{-5.6\%}$	$7.41\cdot10^{-1}{}^{+0.0\%}_{-0.0\%}$	$2.55\cdot10^{-1}{}^{+0.0\%}_{-0.0\%}$	$1.43^{+0.5\%}_{-0.5\%}$
202.0	$9.04\cdot10^{-4}{}^{+7.6\%}_{-7.5\%}$	$5.28\cdot10^{-5}{}^{+1.6\%}_{-1.6\%}$	$1.70\cdot10^{-4}{}^{+5.5\%}_{-5.6\%}$	$7.36\cdot10^{-1}{}^{+0.0\%}_{-0.0\%}$	$2.60\cdot10^{-1}{}^{+0.0\%}_{-0.0\%}$	$1.51^{+0.5\%}_{-0.5\%}$
204.0	$8.84\cdot10^{-4}{}^{+7.6\%}_{-7.5\%}$	$5.08\cdot10^{-5}{}^{+1.6\%}_{-1.6\%}$	$1.65\cdot10^{-4}{}^{+5.6\%}_{-5.6\%}$	$7.32\cdot10^{-1}{}^{+0.0\%}_{-0.0\%}$	$2.65\cdot10^{-1}{}^{+0.0\%}_{-0.0\%}$	$1.59^{+0.5\%}_{-0.5\%}$
206.0	$8.66\cdot10^{-4}{}^{+7.6\%}_{-7.5\%}$	$4.89\cdot10^{-5}{}^{+1.6\%}_{-1.6\%}$	$1.61\cdot10^{-4}{}^{+5.6\%}_{-5.6\%}$	$7.28\cdot10^{-1}{}^{+0.0\%}_{-0.0\%}$	$2.68\cdot10^{-1}{}^{+0.0\%}_{-0.0\%}$	$1.68^{+0.5\%}_{-0.5\%}$
208.0	$8.51\cdot10^{-4}{}^{+7.6\%}_{-7.5\%}$	$4.71\cdot10^{-5}{}^{+1.6\%}_{-1.6\%}$	$1.57\cdot10^{-4}{}^{+5.6\%}_{-5.6\%}$	$7.25\cdot10^{-1}{}^{+0.0\%}_{-0.0\%}$	$2.71\cdot10^{-1}{}^{+0.0\%}_{-0.0\%}$	$1.76^{+0.5\%}_{-0.5\%}$
210.0	$8.36\cdot10^{-4}{}^{+7.6\%}_{-7.5\%}$	$4.55\cdot10^{-5}{}^{+1.7\%}_{-1.6\%}$	$1.53\cdot10^{-4}{}^{+5.6\%}_{-5.5\%}$	$7.23\cdot10^{-1}{}^{+0.0\%}_{-0.0\%}$	$2.74\cdot10^{-1}{}^{+0.0\%}_{-0.0\%}$	$1.85^{+0.5\%}_{-0.5\%}$
212.0	$8.22\cdot10^{-4}{}^{+7.6\%}_{-7.5\%}$	$4.39\cdot10^{-5}{}^{+1.6\%}_{-1.6\%}$	$1.49\cdot10^{-4}{}^{+5.6\%}_{-5.5\%}$	$7.20\cdot10^{-1}{}^{+0.0\%}_{-0.0\%}$	$2.76\cdot10^{-1}{}^{+0.0\%}_{-0.0\%}$	$1.93^{+0.5\%}_{-0.5\%}$
214.0	$8.09\cdot10^{-4}{}^{+7.6\%}_{-7.5\%}$	$4.24\cdot10^{-5}{}^{+1.6\%}_{-1.6\%}$	$1.45\cdot10^{-4}{}^{+5.6\%}_{-5.5\%}$	$7.18\cdot10^{-1}{}^{+0.0\%}_{-0.0\%}$	$2.78\cdot10^{-1}{}^{+0.0\%}_{-0.0\%}$	$2.02^{+0.5\%}_{-0.5\%}$
216.0	$7.98\cdot10^{-4}{}^{+7.6\%}_{-7.5\%}$	$4.10\cdot10^{-5}{}^{+1.6\%}_{-1.6\%}$	$1.41\cdot10^{-4}{}^{+5.6\%}_{-5.6\%}$	$7.17\cdot10^{-1}{}^{+0.0\%}_{-0.0\%}$	$2.80\cdot10^{-1}{}^{+0.0\%}_{-0.0\%}$	$2.12^{+0.5\%}_{-0.5\%}$
218.0	$7.87\cdot10^{-4}{}^{+7.6\%}_{-7.5\%}$	$3.96\cdot10^{-5}{}^{+1.6\%}_{-1.6\%}$	$1.38\cdot10^{-4}{}^{+5.6\%}_{-5.6\%}$	$7.15\cdot10^{-1}{}^{+0.0\%}_{-0.0\%}$	$2.82\cdot10^{-1}{}^{+0.0\%}_{-0.0\%}$	$2.21^{+0.5\%}_{-0.5\%}$
220.0	$7.77\cdot10^{-4}{}^{+7.6\%}_{-7.5\%}$	$3.83\cdot10^{-5}{}^{+1.6\%}_{-1.6\%}$	$1.35\cdot10^{-4}{}^{+5.6\%}_{-5.6\%}$	$7.14\cdot10^{-1}{}^{+0.0\%}_{-0.0\%}$	$2.84\cdot10^{-1}{}^{+0.0\%}_{-0.0\%}$	$2.31^{+0.5\%}_{-0.5\%}$
222.0	$7.67\cdot10^{-4}{}^{+7.6\%}_{-7.5\%}$	$3.72\cdot10^{-5}{}^{+1.6\%}_{-1.6\%}$	$1.31\cdot10^{-4}{}^{+5.6\%}_{-5.5\%}$	$7.12\cdot10^{-1}{}^{+0.0\%}_{-0.0\%}$	$2.85\cdot10^{-1}{}^{+0.0\%}_{-0.0\%}$	$2.40^{+0.5\%}_{-0.5\%}$
224.0	$7.59\cdot10^{-4}{}^{+7.6\%}_{-7.5\%}$	$3.60\cdot10^{-5}{}^{+1.6\%}_{-1.6\%}$	$1.28\cdot10^{-4}{}^{+5.6\%}_{-5.5\%}$	$7.11\cdot10^{-1}{}^{+0.0\%}_{-0.0\%}$	$2.86\cdot10^{-1}{}^{+0.0\%}_{-0.0\%}$	$2.50^{+0.5\%}_{-0.5\%}$
226.0	$7.51\cdot10^{-4}{}^{+7.6\%}_{-7.5\%}$	$3.49\cdot10^{-5}{}^{+1.6\%}_{-1.6\%}$	$1.25\cdot10^{-4}{}^{+5.6\%}_{-5.5\%}$	$7.10\cdot10^{-1}{}^{+0.0\%}_{-0.0\%}$	$2.87\cdot10^{-1}{}^{+0.0\%}_{-0.0\%}$	$2.61^{+0.5\%}_{-0.5\%}$
228.0	$7.43\cdot10^{-4}{}^{+7.6\%}_{-7.5\%}$	$3.39\cdot10^{-5}{}^{+1.6\%}_{-1.6\%}$	$1.22\cdot10^{-4}{}^{+5.6\%}_{-5.5\%}$	$7.09\cdot10^{-1}{}^{+0.0\%}_{-0.0\%}$	$2.88\cdot10^{-1}{}^{+0.0\%}_{-0.0\%}$	$2.71^{+0.5\%}_{-0.5\%}$
230.0	$7.35\cdot10^{-4}{}^{+7.6\%}_{-7.5\%}$	$3.28\cdot10^{-5}{}^{+1.6\%}_{-1.6\%}$	$1.19\cdot10^{-4}{}^{+5.6\%}_{-5.5\%}$	$7.08\cdot10^{-1}{}^{+0.0\%}_{-0.0\%}$	$2.89\cdot10^{-1}{}^{+0.0\%}_{-0.0\%}$	$2.82^{+0.5\%}_{-0.5\%}$
232.0	$7.28\cdot10^{-4}{}^{+7.6\%}_{-7.5\%}$	$3.19\cdot10^{-5}{}^{+1.6\%}_{-1.6\%}$	$1.17\cdot10^{-4}{}^{+5.6\%}_{-5.5\%}$	$7.07\cdot10^{-1}{}^{+0.0\%}_{-0.0\%}$	$2.90\cdot10^{-1}{}^{+0.0\%}_{-0.0\%}$	$2.93^{+0.5\%}_{-0.5\%}$
234.0	$7.22\cdot10^{-4}{}^{+7.6\%}_{-7.5\%}$	$3.09\cdot10^{-5}{}^{+1.6\%}_{-1.6\%}$	$1.14\cdot10^{-4}{}^{+5.6\%}_{-5.5\%}$	$7.06\cdot10^{-1}{}^{+0.0\%}_{-0.0\%}$	$2.91\cdot10^{-1}{}^{+0.0\%}_{-0.0\%}$	$3.04^{+0.5\%}_{-0.5\%}$
236.0	$7.16\cdot10^{-4}{}^{+7.6\%}_{-7.5\%}$	$3.00\cdot10^{-5}{}^{+1.6\%}_{-1.6\%}$	$1.11\cdot10^{-4}{}^{+5.5\%}_{-5.6\%}$	$7.06\cdot10^{-1}{}^{+0.0\%}_{-0.0\%}$	$2.92\cdot10^{-1}{}^{+0.0\%}_{-0.0\%}$	$3.16^{+0.5\%}_{-0.5\%}$
238.0	$7.11\cdot10^{-4}{}^{+7.6\%}_{-7.5\%}$	$2.92\cdot10^{-5}{}^{+1.6\%}_{-1.6\%}$	$1.09\cdot10^{-4}{}^{+5.5\%}_{-5.6\%}$	$7.05\cdot10^{-1}{}^{+0.0\%}_{-0.0\%}$	$2.93\cdot10^{-1}{}^{+0.0\%}_{-0.0\%}$	$3.27^{+0.5\%}_{-0.5\%}$
240.0	$7.05\cdot10^{-4}{}^{+7.6\%}_{-7.5\%}$	$2.84\cdot10^{-5}{}^{+1.7\%}_{-1.6\%}$	$1.06\cdot10^{-4}{}^{+5.5\%}_{-5.6\%}$	$7.04\cdot10^{-1}{}^{+0.0\%}_{-0.0\%}$	$2.94\cdot10^{-1}{}^{+0.0\%}_{-0.0\%}$	$3.40^{+0.5\%}_{-0.5\%}$
242.0	$7.00\cdot10^{-4}{}^{+7.6\%}_{-7.5\%}$	$2.76\cdot10^{-5}{}^{+1.7\%}_{-1.6\%}$	$1.04\cdot10^{-4}{}^{+5.5\%}_{-5.6\%}$	$7.04\cdot10^{-1}{}^{+0.0\%}_{-0.0\%}$	$2.94\cdot10^{-1}{}^{+0.0\%}_{-0.0\%}$	$3.52^{+0.5\%}_{-0.5\%}$
244.0	$6.95\cdot10^{-4}{}^{+7.6\%}_{-7.5\%}$	$2.68\cdot10^{-5}{}^{+1.7\%}_{-1.7\%}$	$1.02\cdot10^{-4}{}^{+5.5\%}_{-5.6\%}$	$7.03\cdot10^{-1}{}^{+0.0\%}_{-0.0\%}$	$2.95\cdot10^{-1}{}^{+0.0\%}_{-0.0\%}$	$3.64^{+0.5\%}_{-0.5\%}$
246.0	$6.90\cdot10^{-4}{}^{+7.6\%}_{-7.5\%}$	$2.61\cdot10^{-5}{}^{+1.7\%}_{-1.7\%}$	$9.96\cdot10^{-5}{}^{+5.5\%}_{-5.6\%}$	$7.02\cdot10^{-1}{}^{+0.0\%}_{-0.0\%}$	$2.96\cdot10^{-1}{}^{+0.0\%}_{-0.0\%}$	$3.77^{+0.5\%}_{-0.5\%}$
248.0	$6.86\cdot10^{-4}{}^{+7.6\%}_{-7.5\%}$	$2.54\cdot10^{-5}{}^{+1.7\%}_{-1.7\%}$	$9.75\cdot10^{-5}{}^{+5.6\%}_{-5.6\%}$	$7.02\cdot10^{-1}{}^{+0.0\%}_{-0.0\%}$	$2.96\cdot10^{-1}{}^{+0.0\%}_{-0.0\%}$	$3.91^{+0.5\%}_{-0.5\%}$
250.0	$6.82\cdot10^{-4}{}^{+7.6\%}_{-7.5\%}$	$2.47\cdot10^{-5}{}^{+1.7\%}_{-1.7\%}$	$9.54\cdot10^{-5}{}^{+5.6\%}_{-5.6\%}$	$7.01\cdot10^{-1}{}^{+0.0\%}_{-0.0\%}$	$2.97\cdot10^{-1}{}^{+0.0\%}_{-0.0\%}$	$4.04^{+0.5\%}_{-0.5\%}$
252.0	$6.78\cdot10^{-4}{}^{+7.6\%}_{-7.5\%}$	$2.40\cdot10^{-5}{}^{+1.7\%}_{-1.7\%}$	$9.34\cdot10^{-5}{}^{+5.6\%}_{-5.6\%}$	$7.01\cdot10^{-1}{}^{+0.0\%}_{-0.0\%}$	$2.97\cdot10^{-1}{}^{+0.0\%}_{-0.0\%}$	$4.18^{+0.5\%}_{-0.5\%}$
254.0	$6.75\cdot10^{-4}{}^{+7.6\%}_{-7.5\%}$	$2.34\cdot10^{-5}{}^{+1.7\%}_{-1.7\%}$	$9.14\cdot10^{-5}{}^{+5.6\%}_{-5.6\%}$	$7.00\cdot10^{-1}{}^{+0.0\%}_{-0.0\%}$	$2.98\cdot10^{-1}{}^{+0.0\%}_{-0.0\%}$	$4.32^{+0.5\%}_{-0.5\%}$
256.0	$6.72\cdot10^{-4}{}^{+7.6\%}_{-7.5\%}$	$2.29\cdot10^{-5}{}^{+1.7\%}_{-1.7\%}$	$8.94\cdot10^{-5}{}^{+5.6\%}_{-5.6\%}$	$7.00\cdot10^{-1}{}^{+0.0\%}_{-0.0\%}$	$2.98\cdot10^{-1}{}^{+0.0\%}_{-0.0\%}$	$4.46^{+0.5\%}_{-0.5\%}$
258.0	$6.69\cdot10^{-4}{}^{+7.6\%}_{-7.5\%}$	$2.23\cdot10^{-5}{}^{+1.7\%}_{-1.7\%}$	$8.75\cdot10^{-5}{}^{+5.6\%}_{-5.6\%}$	$6.99\cdot10^{-1}{}^{+0.0\%}_{-0.0\%}$	$2.99\cdot10^{-1}{}^{+0.0\%}_{-0.0\%}$	$4.61^{+0.5\%}_{-0.5\%}$
260.0	$6.66\cdot10^{-4}{}^{+7.7\%}_{-7.5\%}$	$2.17\cdot10^{-5}{}^{+1.7\%}_{-1.7\%}$	$8.57\cdot10^{-5}{}^{+5.6\%}_{-5.6\%}$	$6.99\cdot10^{-1}{}^{+0.0\%}_{-0.0\%}$	$2.99\cdot10^{-1}{}^{+0.0\%}_{-0.0\%}$	$4.76^{+0.5\%}_{-0.5\%}$

Table A.9: SM Higgs branching ratios to two gauge bosons and Higgs total width together with their total uncertainties (expressed in percentage). High-mass range.

$M_{\rm H}$ [GeV]	$\rm H \to gg$	$\rm H \to \gamma\gamma$	$\rm H \to Z\gamma$	$\rm H \to WW$	$\rm H \to ZZ$	$\Gamma_{\rm H}$ [GeV]
262.0	$6.64 \cdot 10^{-4}{}^{+7.7\%}_{-7.5\%}$	$2.11 \cdot 10^{-5}{}^{+1.7\%}_{-1.7\%}$	$8.39 \cdot 10^{-5}{}^{+5.6\%}_{-5.6\%}$	$6.98 \cdot 10^{-1}{}^{+0.0\%}_{-0.0\%}$	$3.00 \cdot 10^{-1}{}^{+0.0\%}_{-0.0\%}$	$4.91^{+0.5\%}_{-0.5\%}$
264.0	$6.61 \cdot 10^{-4}{}^{+7.7\%}_{-7.5\%}$	$2.06 \cdot 10^{-5}{}^{+1.7\%}_{-1.7\%}$	$8.21 \cdot 10^{-5}{}^{+5.6\%}_{-5.6\%}$	$6.98 \cdot 10^{-1}{}^{+0.0\%}_{-0.0\%}$	$3.00 \cdot 10^{-1}{}^{+0.0\%}_{-0.0\%}$	$5.07^{+0.5\%}_{-0.5\%}$
266.0	$6.59 \cdot 10^{-4}{}^{+7.7\%}_{-7.6\%}$	$2.01 \cdot 10^{-5}{}^{+1.7\%}_{-1.7\%}$	$8.04 \cdot 10^{-5}{}^{+5.6\%}_{-5.6\%}$	$6.98 \cdot 10^{-1}{}^{+0.0\%}_{-0.0\%}$	$3.01 \cdot 10^{-1}{}^{+0.0\%}_{-0.0\%}$	$5.23^{+0.5\%}_{-0.5\%}$
268.0	$6.57 \cdot 10^{-4}{}^{+7.7\%}_{-7.6\%}$	$1.96 \cdot 10^{-5}{}^{+1.7\%}_{-1.7\%}$	$7.88 \cdot 10^{-5}{}^{+5.6\%}_{-5.6\%}$	$6.97 \cdot 10^{-1}{}^{+0.0\%}_{-0.0\%}$	$3.01 \cdot 10^{-1}{}^{+0.0\%}_{-0.0\%}$	$5.39^{+0.5\%}_{-0.5\%}$
270.0	$6.55 \cdot 10^{-4}{}^{+7.7\%}_{-7.6\%}$	$1.91 \cdot 10^{-5}{}^{+1.7\%}_{-1.7\%}$	$7.72 \cdot 10^{-5}{}^{+5.6\%}_{-5.6\%}$	$6.97 \cdot 10^{-1}{}^{+0.0\%}_{-0.0\%}$	$3.02 \cdot 10^{-1}{}^{+0.0\%}_{-0.0\%}$	$5.55^{+0.5\%}_{-0.5\%}$
272.0	$6.54 \cdot 10^{-4}{}^{+7.7\%}_{-7.6\%}$	$1.87 \cdot 10^{-5}{}^{+1.7\%}_{-1.7\%}$	$7.56 \cdot 10^{-5}{}^{+5.6\%}_{-5.6\%}$	$6.96 \cdot 10^{-1}{}^{+0.0\%}_{-0.0\%}$	$3.02 \cdot 10^{-1}{}^{+0.0\%}_{-0.0\%}$	$5.72^{+0.5\%}_{-0.5\%}$
274.0	$6.53 \cdot 10^{-4}{}^{+7.7\%}_{-7.6\%}$	$1.82 \cdot 10^{-5}{}^{+1.7\%}_{-1.7\%}$	$7.41 \cdot 10^{-5}{}^{+5.6\%}_{-5.6\%}$	$6.96 \cdot 10^{-1}{}^{+0.0\%}_{-0.0\%}$	$3.02 \cdot 10^{-1}{}^{+0.0\%}_{-0.0\%}$	$5.89^{+0.5\%}_{-0.5\%}$
276.0	$6.51 \cdot 10^{-4}{}^{+7.7\%}_{-7.6\%}$	$1.78 \cdot 10^{-5}{}^{+1.8\%}_{-1.7\%}$	$7.26 \cdot 10^{-5}{}^{+5.6\%}_{-5.6\%}$	$6.96 \cdot 10^{-1}{}^{+0.0\%}_{-0.0\%}$	$3.03 \cdot 10^{-1}{}^{+0.0\%}_{-0.0\%}$	$6.07^{+0.5\%}_{-0.5\%}$
278.0	$6.51 \cdot 10^{-4}{}^{+7.7\%}_{-7.6\%}$	$1.74 \cdot 10^{-5}{}^{+1.8\%}_{-1.7\%}$	$7.12 \cdot 10^{-5}{}^{+5.6\%}_{-5.6\%}$	$6.95 \cdot 10^{-1}{}^{+0.0\%}_{-0.0\%}$	$3.03 \cdot 10^{-1}{}^{+0.0\%}_{-0.0\%}$	$6.25^{+0.5\%}_{-0.5\%}$
280.0	$6.50 \cdot 10^{-4}{}^{+7.7\%}_{-7.6\%}$	$1.68 \cdot 10^{-5}{}^{+1.8\%}_{-1.8\%}$	$6.98 \cdot 10^{-5}{}^{+5.6\%}_{-5.6\%}$	$6.95 \cdot 10^{-1}{}^{+0.0\%}_{-0.0\%}$	$3.04 \cdot 10^{-1}{}^{+0.0\%}_{-0.0\%}$	$6.43^{+0.5\%}_{-0.5\%}$
282.0	$6.49 \cdot 10^{-4}{}^{+7.8\%}_{-7.6\%}$	$1.65 \cdot 10^{-5}{}^{+1.8\%}_{-1.8\%}$	$6.84 \cdot 10^{-5}{}^{+5.6\%}_{-5.6\%}$	$6.95 \cdot 10^{-1}{}^{+0.0\%}_{-0.0\%}$	$3.04 \cdot 10^{-1}{}^{+0.0\%}_{-0.0\%}$	$6.61^{+0.5\%}_{-0.5\%}$
284.0	$6.49 \cdot 10^{-4}{}^{+7.8\%}_{-7.7\%}$	$1.61 \cdot 10^{-5}{}^{+1.8\%}_{-1.8\%}$	$6.71 \cdot 10^{-5}{}^{+5.6\%}_{-5.6\%}$	$6.94 \cdot 10^{-1}{}^{+0.0\%}_{-0.0\%}$	$3.04 \cdot 10^{-1}{}^{+0.0\%}_{-0.0\%}$	$6.80^{+0.5\%}_{-0.5\%}$
286.0	$6.49 \cdot 10^{-4}{}^{+7.8\%}_{-7.7\%}$	$1.57 \cdot 10^{-5}{}^{+1.8\%}_{-1.8\%}$	$6.58 \cdot 10^{-5}{}^{+5.6\%}_{-5.6\%}$	$6.94 \cdot 10^{-1}{}^{+0.0\%}_{-0.0\%}$	$3.05 \cdot 10^{-1}{}^{+0.0\%}_{-0.0\%}$	$6.99^{+0.5\%}_{-0.5\%}$
288.0	$6.49 \cdot 10^{-4}{}^{+7.8\%}_{-7.7\%}$	$1.53 \cdot 10^{-5}{}^{+1.8\%}_{-1.8\%}$	$6.45 \cdot 10^{-5}{}^{+5.6\%}_{-5.6\%}$	$6.93 \cdot 10^{-1}{}^{+0.0\%}_{-0.0\%}$	$3.05 \cdot 10^{-1}{}^{+0.0\%}_{-0.0\%}$	$7.19^{+0.5\%}_{-0.5\%}$
290.0	$6.49 \cdot 10^{-4}{}^{+7.9\%}_{-7.7\%}$	$1.50 \cdot 10^{-5}{}^{+1.8\%}_{-1.8\%}$	$6.32 \cdot 10^{-5}{}^{+5.6\%}_{-5.6\%}$	$6.93 \cdot 10^{-1}{}^{+0.0\%}_{-0.0\%}$	$3.05 \cdot 10^{-1}{}^{+0.0\%}_{-0.0\%}$	$7.39^{+0.5\%}_{-0.5\%}$
295.0	$6.51 \cdot 10^{-4}{}^{+7.9\%}_{-7.8\%}$	$1.42 \cdot 10^{-5}{}^{+1.8\%}_{-1.8\%}$	$6.03 \cdot 10^{-5}{}^{+5.6\%}_{-5.6\%}$	$6.92 \cdot 10^{-1}{}^{+0.0\%}_{-0.0\%}$	$3.06 \cdot 10^{-1}{}^{+0.0\%}_{-0.0\%}$	$7.90^{+0.5\%}_{-0.5\%}$
300.0	$6.54 \cdot 10^{-4}{}^{+8.0\%}_{-7.8\%}$	$1.34 \cdot 10^{-5}{}^{+1.8\%}_{-1.8\%}$	$5.75 \cdot 10^{-5}{}^{+5.6\%}_{-5.6\%}$	$6.92 \cdot 10^{-1}{}^{+0.0\%}_{-0.0\%}$	$3.07 \cdot 10^{-1}{}^{+0.0\%}_{-0.0\%}$	$8.43^{+0.5\%}_{-0.5\%}$
305.0	$6.58 \cdot 10^{-4}{}^{+8.1\%}_{-7.9\%}$	$1.27 \cdot 10^{-5}{}^{+1.8\%}_{-1.8\%}$	$5.49 \cdot 10^{-5}{}^{+5.6\%}_{-5.6\%}$	$6.91 \cdot 10^{-1}{}^{+0.0\%}_{-0.0\%}$	$3.08 \cdot 10^{-1}{}^{+0.0\%}_{-0.0\%}$	$8.99^{+0.5\%}_{-0.5\%}$
310.0	$6.64 \cdot 10^{-4}{}^{+8.2\%}_{-8.0\%}$	$1.20 \cdot 10^{-5}{}^{+1.9\%}_{-1.9\%}$	$5.23 \cdot 10^{-5}{}^{+5.6\%}_{-5.6\%}$	$6.90 \cdot 10^{-1}{}^{+0.0\%}_{-0.0\%}$	$3.08 \cdot 10^{-1}{}^{+0.0\%}_{-0.0\%}$	$9.57^{+0.5\%}_{-0.5\%}$
315.0	$6.71 \cdot 10^{-4}{}^{+8.4\%}_{-8.1\%}$	$1.14 \cdot 10^{-5}{}^{+1.9\%}_{-1.9\%}$	$5.00 \cdot 10^{-5}{}^{+5.6\%}_{-5.6\%}$	$6.90 \cdot 10^{-1}{}^{+0.0\%}_{-0.0\%}$	$3.09 \cdot 10^{-1}{}^{+0.0\%}_{-0.0\%}$	$1.02 \cdot 10^{1}{}^{+0.5\%}_{-0.5\%}$
320.0	$6.80 \cdot 10^{-4}{}^{+8.6\%}_{-8.2\%}$	$1.09 \cdot 10^{-5}{}^{+1.9\%}_{-1.9\%}$	$4.79 \cdot 10^{-5}{}^{+5.7\%}_{-5.5\%}$	$6.89 \cdot 10^{-1}{}^{+0.0\%}_{-0.0\%}$	$3.09 \cdot 10^{-1}{}^{+0.0\%}_{-0.0\%}$	$1.08 \cdot 10^{1}{}^{+0.5\%}_{-0.5\%}$
325.0	$6.92 \cdot 10^{-4}{}^{+8.9\%}_{-8.4\%}$	$1.03 \cdot 10^{-5}{}^{+1.9\%}_{-1.9\%}$	$4.58 \cdot 10^{-5}{}^{+5.7\%}_{-5.5\%}$	$6.88 \cdot 10^{-1}{}^{+0.0\%}_{-0.0\%}$	$3.10 \cdot 10^{-1}{}^{+0.1\%}_{-0.1\%}$	$1.14 \cdot 10^{1}{}^{+0.5\%}_{-0.6\%}$
330.0	$7.07 \cdot 10^{-4}{}^{+9.1\%}_{-8.6\%}$	$9.83 \cdot 10^{-6}{}^{+1.9\%}_{-2.0\%}$	$4.39 \cdot 10^{-5}{}^{+5.6\%}_{-5.5\%}$	$6.88 \cdot 10^{-1}{}^{+0.0\%}_{-0.0\%}$	$3.10 \cdot 10^{-1}{}^{+0.1\%}_{-0.1\%}$	$1.21 \cdot 10^{1}{}^{+0.5\%}_{-0.6\%}$
335.0	$7.26 \cdot 10^{-4}{}^{+10.0\%}_{-9.0\%}$	$9.37 \cdot 10^{-6}{}^{+2.0\%}_{-2.2\%}$	$4.21 \cdot 10^{-5}{}^{+5.6\%}_{-5.5\%}$	$6.87 \cdot 10^{-1}{}^{+0.0\%}_{-0.1\%}$	$3.11 \cdot 10^{-1}{}^{+0.1\%}_{-0.2\%}$	$1.28 \cdot 10^{1}{}^{+0.6\%}_{-0.7\%}$
340.0	$7.51 \cdot 10^{-4}{}^{+10.8\%}_{-9.4\%}$	$8.92 \cdot 10^{-6}{}^{+2.1\%}_{-2.5\%}$	$4.03 \cdot 10^{-5}{}^{+5.6\%}_{-5.5\%}$	$6.87 \cdot 10^{-1}{}^{+0.0\%}_{-0.2\%}$	$3.11 \cdot 10^{-1}{}^{+0.1\%}_{-0.3\%}$	$1.35 \cdot 10^{1}{}^{+0.7\%}_{-0.7\%}$
345.0	$7.83 \cdot 10^{-4}{}^{+10.1\%}_{-9.9\%}$	$8.44 \cdot 10^{-6}{}^{+4.1\%}_{-5.2\%}$	$3.88 \cdot 10^{-5}{}^{+6.7\%}_{-7.1\%}$	$6.85 \cdot 10^{-1}{}^{+0.7\%}_{-1.1\%}$	$3.11 \cdot 10^{-1}{}^{+0.8\%}_{-1.2\%}$	$1.42 \cdot 10^{1}{}^{+1.8\%}_{-1.4\%}$
350.0	$8.14 \cdot 10^{-4}{}^{+9.5\%}_{-10.5\%}$	$7.73 \cdot 10^{-6}{}^{+6.1\%}_{-7.9\%}$	$3.65 \cdot 10^{-5}{}^{+7.7\%}_{-8.6\%}$	$6.76 \cdot 10^{-1}{}^{+1.4\%}_{-2.0\%}$	$3.07 \cdot 10^{-1}{}^{+1.5\%}_{-2.1\%}$	$1.52 \cdot 10^{1}{}^{+2.9\%}_{-2.1\%}$
360.0	$8.51 \cdot 10^{-4}{}^{+8.6\%}_{-8.4\%}$	$6.25 \cdot 10^{-6}{}^{+9.4\%}_{-8.7\%}$	$3.18 \cdot 10^{-5}{}^{+9.5\%}_{-8.8\%}$	$6.51 \cdot 10^{-1}{}^{+2.6\%}_{-2.3\%}$	$2.97 \cdot 10^{-1}{}^{+2.7\%}_{-2.3\%}$	$1.76 \cdot 10^{1}{}^{+2.9\%}_{-3.4\%}$
370.0	$8.64 \cdot 10^{-4}{}^{+8.4\%}_{-7.7\%}$	$5.04 \cdot 10^{-6}{}^{+10.4\%}_{-9.0\%}$	$2.77 \cdot 10^{-5}{}^{+9.8\%}_{-8.7\%}$	$6.28 \cdot 10^{-1}{}^{+2.9\%}_{-2.3\%}$	$2.87 \cdot 10^{-1}{}^{+2.9\%}_{-2.3\%}$	$2.02 \cdot 10^{1}{}^{+2.7\%}_{-3.7\%}$
380.0	$8.61 \cdot 10^{-4}{}^{+8.5\%}_{-7.5\%}$	$4.06 \cdot 10^{-6}{}^{+10.9\%}_{-9.4\%}$	$2.43 \cdot 10^{-5}{}^{+9.9\%}_{-8.6\%}$	$6.09 \cdot 10^{-1}{}^{+3.1\%}_{-2.3\%}$	$2.80 \cdot 10^{-1}{}^{+3.0\%}_{-2.3\%}$	$2.31 \cdot 10^{1}{}^{+2.6\%}_{-3.7\%}$
390.0	$8.50 \cdot 10^{-4}{}^{+8.7\%}_{-7.5\%}$	$3.28 \cdot 10^{-6}{}^{+11.3\%}_{-9.5\%}$	$2.14 \cdot 10^{-5}{}^{+9.9\%}_{-8.5\%}$	$5.94 \cdot 10^{-1}{}^{+3.1\%}_{-2.2\%}$	$2.74 \cdot 10^{-1}{}^{+3.1\%}_{-2.2\%}$	$2.61 \cdot 10^{1}{}^{+2.5\%}_{-3.7\%}$
400.0	$8.32 \cdot 10^{-4}{}^{+8.9\%}_{-7.6\%}$	$2.65 \cdot 10^{-6}{}^{+11.5\%}_{-9.7\%}$	$1.90 \cdot 10^{-5}{}^{+9.9\%}_{-8.4\%}$	$5.82 \cdot 10^{-1}{}^{+3.1\%}_{-2.1\%}$	$2.69 \cdot 10^{-1}{}^{+3.1\%}_{-2.1\%}$	$2.92 \cdot 10^{1}{}^{+2.3\%}_{-3.6\%}$
410.0	$8.11 \cdot 10^{-4}{}^{+9.1\%}_{-7.7\%}$	$2.15 \cdot 10^{-6}{}^{+11.8\%}_{-9.7\%}$	$1.70 \cdot 10^{-5}{}^{+9.8\%}_{-8.2\%}$	$5.72 \cdot 10^{-1}{}^{+3.1\%}_{-2.0\%}$	$2.66 \cdot 10^{-1}{}^{+3.0\%}_{-2.0\%}$	$3.25 \cdot 10^{1}{}^{+2.2\%}_{-3.6\%}$
420.0	$7.89 \cdot 10^{-4}{}^{+9.2\%}_{-7.8\%}$	$1.74 \cdot 10^{-6}{}^{+11.9\%}_{-9.7\%}$	$1.53 \cdot 10^{-5}{}^{+9.6\%}_{-8.1\%}$	$5.65 \cdot 10^{-1}{}^{+3.1\%}_{-1.9\%}$	$2.63 \cdot 10^{-1}{}^{+3.0\%}_{-1.9\%}$	$3.59 \cdot 10^{1}{}^{+2.1\%}_{-3.5\%}$
430.0	$7.65 \cdot 10^{-4}{}^{+9.3\%}_{-7.9\%}$	$1.41 \cdot 10^{-6}{}^{+12.2\%}_{-9.9\%}$	$1.39 \cdot 10^{-5}{}^{+9.5\%}_{-8.0\%}$	$5.59 \cdot 10^{-1}{}^{+3.0\%}_{-1.9\%}$	$2.61 \cdot 10^{-1}{}^{+3.0\%}_{-1.8\%}$	$3.94 \cdot 10^{1}{}^{+1.9\%}_{-3.4\%}$
440.0	$7.41 \cdot 10^{-4}{}^{+9.4\%}_{-8.0\%}$	$1.15 \cdot 10^{-6}{}^{+12.1\%}_{-10.0\%}$	$1.26 \cdot 10^{-5}{}^{+9.4\%}_{-7.8\%}$	$5.55 \cdot 10^{-1}{}^{+3.0\%}_{-1.8\%}$	$2.60 \cdot 10^{-1}{}^{+2.9\%}_{-1.7\%}$	$4.30 \cdot 10^{1}{}^{+1.8\%}_{-3.3\%}$
450.0	$7.18 \cdot 10^{-4}{}^{+9.5\%}_{-8.0\%}$	$9.28 \cdot 10^{-7}{}^{+12.3\%}_{-10.0\%}$	$1.15 \cdot 10^{-5}{}^{+9.2\%}_{-7.6\%}$	$5.51 \cdot 10^{-1}{}^{+2.9\%}_{-1.7\%}$	$2.59 \cdot 10^{-1}{}^{+2.8\%}_{-1.6\%}$	$4.68 \cdot 10^{1}{}^{+1.7\%}_{-3.2\%}$
460.0	$6.94 \cdot 10^{-4}{}^{+9.6\%}_{-8.1\%}$	$7.51 \cdot 10^{-7}{}^{+12.2\%}_{-10.0\%}$	$1.05 \cdot 10^{-5}{}^{+9.1\%}_{-7.4\%}$	$5.49 \cdot 10^{-1}{}^{+2.8\%}_{-1.6\%}$	$2.59 \cdot 10^{-1}{}^{+2.8\%}_{-1.6\%}$	$5.08 \cdot 10^{1}{}^{+1.6\%}_{-3.1\%}$
470.0	$6.71 \cdot 10^{-4}{}^{+9.6\%}_{-8.1\%}$	$6.05 \cdot 10^{-7}{}^{+12.5\%}_{-9.7\%}$	$9.64 \cdot 10^{-6}{}^{+9.0\%}_{-7.4\%}$	$5.47 \cdot 10^{-1}{}^{+2.8\%}_{-1.6\%}$	$2.59 \cdot 10^{-1}{}^{+2.7\%}_{-1.5\%}$	$5.49 \cdot 10^{1}{}^{+1.6\%}_{-3.1\%}$
480.0	$6.48 \cdot 10^{-4}{}^{+9.7\%}_{-8.1\%}$	$4.87 \cdot 10^{-7}{}^{+12.4\%}_{-9.6\%}$	$8.88 \cdot 10^{-6}{}^{+8.8\%}_{-7.2\%}$	$5.46 \cdot 10^{-1}{}^{+2.7\%}_{-1.5\%}$	$2.60 \cdot 10^{-1}{}^{+2.6\%}_{-1.4\%}$	$5.91 \cdot 10^{1}{}^{+1.5\%}_{-3.0\%}$
490.0	$6.26 \cdot 10^{-4}{}^{+9.7\%}_{-8.2\%}$	$3.90 \cdot 10^{-7}{}^{+12.1\%}_{-9.4\%}$	$8.19 \cdot 10^{-6}{}^{+8.7\%}_{-7.1\%}$	$5.46 \cdot 10^{-1}{}^{+2.6\%}_{-1.4\%}$	$2.60 \cdot 10^{-1}{}^{+2.6\%}_{-1.4\%}$	$6.35 \cdot 10^{1}{}^{+1.4\%}_{-2.9\%}$
500.0	$6.04 \cdot 10^{-4}{}^{+9.9\%}_{-7.9\%}$	$3.12 \cdot 10^{-7}{}^{+11.9\%}_{-8.7\%}$	$7.58 \cdot 10^{-6}{}^{+8.7\%}_{-6.7\%}$	$5.46 \cdot 10^{-1}{}^{+2.4\%}_{-1.1\%}$	$2.61 \cdot 10^{-1}{}^{+2.3\%}_{-1.1\%}$	$6.80 \cdot 10^{1}{}^{+1.1\%}_{-3.0\%}$
510.0	$5.83 \cdot 10^{-4}{}^{+9.9\%}_{-8.0\%}$	$2.47 \cdot 10^{-7}{}^{+11.6\%}_{-8.0\%}$	$7.03 \cdot 10^{-6}{}^{+8.7\%}_{-6.6\%}$	$5.46 \cdot 10^{-1}{}^{+2.3\%}_{-1.1\%}$	$2.62 \cdot 10^{-1}{}^{+2.4\%}_{-1.1\%}$	$7.27 \cdot 10^{1}{}^{+1.1\%}_{-3.0\%}$
520.0	$5.62 \cdot 10^{-4}{}^{+10.1\%}_{-8.0\%}$	$1.96 \cdot 10^{-7}{}^{+10.9\%}_{-7.2\%}$	$6.53 \cdot 10^{-6}{}^{+8.6\%}_{-6.5\%}$	$5.47 \cdot 10^{-1}{}^{+2.4\%}_{-1.1\%}$	$2.63 \cdot 10^{-1}{}^{+2.4\%}_{-1.2\%}$	$7.75 \cdot 10^{1}{}^{+1.2\%}_{-3.1\%}$
530.0	$5.42 \cdot 10^{-4}{}^{+10.1\%}_{-8.2\%}$	$1.56 \cdot 10^{-7}{}^{+9.8\%}_{-5.9\%}$	$6.08 \cdot 10^{-6}{}^{+8.6\%}_{-6.5\%}$	$5.48 \cdot 10^{-1}{}^{+2.4\%}_{-1.1\%}$	$2.64 \cdot 10^{-1}{}^{+2.4\%}_{-1.2\%}$	$8.25 \cdot 10^{1}{}^{+1.3\%}_{-3.3\%}$
540.0	$5.24 \cdot 10^{-4}{}^{+10.2\%}_{-8.3\%}$	$1.24 \cdot 10^{-7}{}^{+8.3\%}_{-4.2\%}$	$5.67 \cdot 10^{-6}{}^{+8.6\%}_{-6.5\%}$	$5.49 \cdot 10^{-1}{}^{+2.4\%}_{-1.2\%}$	$2.65 \cdot 10^{-1}{}^{+2.5\%}_{-1.2\%}$	$8.77 \cdot 10^{1}{}^{+1.5\%}_{-3.4\%}$

Table A.10: SM Higgs branching ratios to two gauge bosons and Higgs total width together with their total uncertainties (expressed in percentage). Very-high-mass range.

$M_{\rm H}$ [GeV]	$\rm H \to gg$	$\rm H \to \gamma\gamma$	$\rm H \to Z\gamma$	$\rm H \to WW$	$\rm H \to ZZ$	$\Gamma_{\rm H}$ [GeV]
550.0	$5.05\cdot10^{-4}{}^{+10.4\%}_{-8.4\%}$	$9.90\cdot10^{-8}{}^{+6.1\%}_{-2.7\%}$	$5.30\cdot10^{-6}{}^{+8.6\%}_{-6.6\%}$	$5.50\cdot10^{-1}{}^{+2.4\%}_{-1.2\%}$	$2.66\cdot10^{-1}{}^{+2.5\%}_{-1.2\%}$	$9.30\cdot10^{1}{}^{+1.6\%}_{-3.5\%}$
560.0	$4.88\cdot10^{-4}{}^{+10.5\%}_{-8.6\%}$	$8.10\cdot10^{-8}{}^{+8.7\%}_{-3.2\%}$	$4.95\cdot10^{-6}{}^{+8.6\%}_{-6.6\%}$	$5.52\cdot10^{-1}{}^{+2.5\%}_{-1.2\%}$	$2.67\cdot10^{-1}{}^{+2.5\%}_{-1.2\%}$	$9.86\cdot10^{1}{}^{+1.7\%}_{-3.6\%}$
570.0	$4.71\cdot10^{-4}{}^{+10.6\%}_{-8.7\%}$	$6.83\cdot10^{-8}{}^{+11.5\%}_{-7.2\%}$	$4.64\cdot10^{-6}{}^{+8.6\%}_{-6.7\%}$	$5.53\cdot10^{-1}{}^{+2.5\%}_{-1.2\%}$	$2.68\cdot10^{-1}{}^{+2.5\%}_{-1.3\%}$	$1.04\cdot10^{2}{}^{+1.9\%}_{-3.7\%}$
580.0	$4.55\cdot10^{-4}{}^{+10.7\%}_{-8.9\%}$	$5.91\cdot10^{-8}{}^{+15.2\%}_{-10.3\%}$	$4.35\cdot10^{-6}{}^{+8.7\%}_{-6.9\%}$	$5.55\cdot10^{-1}{}^{+2.5\%}_{-1.2\%}$	$2.70\cdot10^{-1}{}^{+2.5\%}_{-1.3\%}$	$1.10\cdot10^{2}{}^{+2.0\%}_{-3.8\%}$
590.0	$4.39\cdot10^{-4}{}^{+10.9\%}_{-8.9\%}$	$5.33\cdot10^{-8}{}^{+17.8\%}_{-13.5\%}$	$4.08\cdot10^{-6}{}^{+8.9\%}_{-6.9\%}$	$5.57\cdot10^{-1}{}^{+2.5\%}_{-1.3\%}$	$2.71\cdot10^{-1}{}^{+2.5\%}_{-1.3\%}$	$1.16\cdot10^{2}{}^{+2.2\%}_{-3.9\%}$
600.0	$4.24\cdot10^{-4}{}^{+11.1\%}_{-9.1\%}$	$5.03\cdot10^{-8}{}^{+20.7\%}_{-16.0\%}$	$3.84\cdot10^{-6}{}^{+9.2\%}_{-7.1\%}$	$5.58\cdot10^{-1}{}^{+2.5\%}_{-1.3\%}$	$2.72\cdot10^{-1}{}^{+2.5\%}_{-1.3\%}$	$1.23\cdot10^{2}{}^{+2.3\%}_{-4.0\%}$
610.0	$4.10\cdot10^{-4}{}^{+11.0\%}_{-9.3\%}$	$4.86\cdot10^{-8}{}^{+22.0\%}_{-17.2\%}$	$3.61\cdot10^{-6}{}^{+9.3\%}_{-7.5\%}$	$5.60\cdot10^{-1}{}^{+2.5\%}_{-1.3\%}$	$2.74\cdot10^{-1}{}^{+2.6\%}_{-1.3\%}$	$1.29\cdot10^{2}{}^{+2.5\%}_{-4.2\%}$
620.0	$3.96\cdot10^{-4}{}^{+11.2\%}_{-9.4\%}$	$4.82\cdot10^{-8}{}^{+24.2\%}_{-19.1\%}$	$3.40\cdot10^{-6}{}^{+9.4\%}_{-7.6\%}$	$5.62\cdot10^{-1}{}^{+2.6\%}_{-1.3\%}$	$2.75\cdot10^{-1}{}^{+2.6\%}_{-1.3\%}$	$1.36\cdot10^{2}{}^{+2.6\%}_{-4.3\%}$
630.0	$3.82\cdot10^{-4}{}^{+11.4\%}_{-9.5\%}$	$4.93\cdot10^{-8}{}^{+27.1\%}_{-20.8\%}$	$3.21\cdot10^{-6}{}^{+9.7\%}_{-7.8\%}$	$5.64\cdot10^{-1}{}^{+2.5\%}_{-1.3\%}$	$2.76\cdot10^{-1}{}^{+2.6\%}_{-1.3\%}$	$1.43\cdot10^{2}{}^{+2.8\%}_{-4.5\%}$
640.0	$3.69\cdot10^{-4}{}^{+11.6\%}_{-9.8\%}$	$5.29\cdot10^{-8}{}^{+28.1\%}_{-22.8\%}$	$3.03\cdot10^{-6}{}^{+9.9\%}_{-8.1\%}$	$5.66\cdot10^{-1}{}^{+2.6\%}_{-1.3\%}$	$2.77\cdot10^{-1}{}^{+2.6\%}_{-1.3\%}$	$1.50\cdot10^{2}{}^{+3.0\%}_{-4.6\%}$
650.0	$3.57\cdot10^{-4}{}^{+11.8\%}_{-9.9\%}$	$5.82\cdot10^{-8}{}^{+28.0\%}_{-23.9\%}$	$2.86\cdot10^{-6}{}^{+10.1\%}_{-8.3\%}$	$5.68\cdot10^{-1}{}^{+2.6\%}_{-1.3\%}$	$2.79\cdot10^{-1}{}^{+2.6\%}_{-1.3\%}$	$1.58\cdot10^{2}{}^{+3.1\%}_{-4.8\%}$
660.0	$3.45\cdot10^{-4}{}^{+11.9\%}_{-10.2\%}$	$6.60\cdot10^{-8}{}^{+27.1\%}_{-23.1\%}$	$2.70\cdot10^{-6}{}^{+10.3\%}_{-8.5\%}$	$5.70\cdot10^{-1}{}^{+2.6\%}_{-1.3\%}$	$2.80\cdot10^{-1}{}^{+2.6\%}_{-1.3\%}$	$1.65\cdot10^{2}{}^{+3.3\%}_{-4.9\%}$
670.0	$3.33\cdot10^{-4}{}^{+12.1\%}_{-10.3\%}$	$7.56\cdot10^{-8}{}^{+25.1\%}_{-21.7\%}$	$2.56\cdot10^{-6}{}^{+10.6\%}_{-8.7\%}$	$5.71\cdot10^{-1}{}^{+2.6\%}_{-1.3\%}$	$2.81\cdot10^{-1}{}^{+2.6\%}_{-1.3\%}$	$1.73\cdot10^{2}{}^{+3.5\%}_{-5.1\%}$
680.0	$3.22\cdot10^{-4}{}^{+12.4\%}_{-10.5\%}$	$8.65\cdot10^{-8}{}^{+22.7\%}_{-20.2\%}$	$2.42\cdot10^{-6}{}^{+10.8\%}_{-8.9\%}$	$5.73\cdot10^{-1}{}^{+2.6\%}_{-1.3\%}$	$2.82\cdot10^{-1}{}^{+2.6\%}_{-1.3\%}$	$1.82\cdot10^{2}{}^{+3.7\%}_{-5.3\%}$
690.0	$3.12\cdot10^{-4}{}^{+12.5\%}_{-10.8\%}$	$9.86\cdot10^{-8}{}^{+21.2\%}_{-18.5\%}$	$2.30\cdot10^{-6}{}^{+11.1\%}_{-9.2\%}$	$5.75\cdot10^{-1}{}^{+2.6\%}_{-1.3\%}$	$2.84\cdot10^{-1}{}^{+2.6\%}_{-1.3\%}$	$1.90\cdot10^{2}{}^{+3.9\%}_{-5.5\%}$
700.0	$3.01\cdot10^{-4}{}^{+12.7\%}_{-11.0\%}$	$1.11\cdot10^{-7}{}^{+20.1\%}_{-17.1\%}$	$2.18\cdot10^{-6}{}^{+11.4\%}_{-9.5\%}$	$5.77\cdot10^{-1}{}^{+2.6\%}_{-1.3\%}$	$2.85\cdot10^{-1}{}^{+2.6\%}_{-1.3\%}$	$1.99\cdot10^{2}{}^{+4.1\%}_{-5.6\%}$
710.0	$2.91\cdot10^{-4}{}^{+13.0\%}_{-11.2\%}$	$1.24\cdot10^{-7}{}^{+18.8\%}_{-16.0\%}$	$2.07\cdot10^{-6}{}^{+11.6\%}_{-9.8\%}$	$5.79\cdot10^{-1}{}^{+2.6\%}_{-1.3\%}$	$2.86\cdot10^{-1}{}^{+2.6\%}_{-1.3\%}$	$2.08\cdot10^{2}{}^{+4.3\%}_{-5.9\%}$
720.0	$2.81\cdot10^{-4}{}^{+13.3\%}_{-11.5\%}$	$1.38\cdot10^{-7}{}^{+17.6\%}_{-15.3\%}$	$1.96\cdot10^{-6}{}^{+12.0\%}_{-10.0\%}$	$5.81\cdot10^{-1}{}^{+2.6\%}_{-1.3\%}$	$2.87\cdot10^{-1}{}^{+2.6\%}_{-1.3\%}$	$2.17\cdot10^{2}{}^{+4.6\%}_{-6.1\%}$
730.0	$2.73\cdot10^{-4}{}^{+13.6\%}_{-11.7\%}$	$1.52\cdot10^{-7}{}^{+17.0\%}_{-14.4\%}$	$1.87\cdot10^{-6}{}^{+12.2\%}_{-10.3\%}$	$5.83\cdot10^{-1}{}^{+2.6\%}_{-1.3\%}$	$2.88\cdot10^{-1}{}^{+2.6\%}_{-1.3\%}$	$2.27\cdot10^{2}{}^{+4.8\%}_{-6.3\%}$
740.0	$2.63\cdot10^{-4}{}^{+13.9\%}_{-11.9\%}$	$1.65\cdot10^{-7}{}^{+16.4\%}_{-14.0\%}$	$1.77\cdot10^{-6}{}^{+12.5\%}_{-10.6\%}$	$5.84\cdot10^{-1}{}^{+2.6\%}_{-1.3\%}$	$2.89\cdot10^{-1}{}^{+2.6\%}_{-1.3\%}$	$2.37\cdot10^{2}{}^{+5.1\%}_{-6.5\%}$
750.0	$2.54\cdot10^{-4}{}^{+14.1\%}_{-12.2\%}$	$1.79\cdot10^{-7}{}^{+16.0\%}_{-13.6\%}$	$1.69\cdot10^{-6}{}^{+12.9\%}_{-10.9\%}$	$5.86\cdot10^{-1}{}^{+2.6\%}_{-1.3\%}$	$2.90\cdot10^{-1}{}^{+2.6\%}_{-1.3\%}$	$2.47\cdot10^{2}{}^{+5.3\%}_{-6.8\%}$
760.0	$2.46\cdot10^{-4}{}^{+14.4\%}_{-12.4\%}$	$1.92\cdot10^{-7}{}^{+15.6\%}_{-13.2\%}$	$1.61\cdot10^{-6}{}^{+13.2\%}_{-11.2\%}$	$5.88\cdot10^{-1}{}^{+2.6\%}_{-1.3\%}$	$2.91\cdot10^{-1}{}^{+2.6\%}_{-1.3\%}$	$2.58\cdot10^{2}{}^{+5.6\%}_{-7.0\%}$
770.0	$2.38\cdot10^{-4}{}^{+14.7\%}_{-12.8\%}$	$2.05\cdot10^{-7}{}^{+15.6\%}_{-13.0\%}$	$1.53\cdot10^{-6}{}^{+13.6\%}_{-11.4\%}$	$5.89\cdot10^{-1}{}^{+2.6\%}_{-1.3\%}$	$2.93\cdot10^{-1}{}^{+2.6\%}_{-1.2\%}$	$2.69\cdot10^{2}{}^{+5.9\%}_{-7.3\%}$
780.0	$2.30\cdot10^{-4}{}^{+15.1\%}_{-13.0\%}$	$2.18\cdot10^{-7}{}^{+15.1\%}_{-12.9\%}$	$1.46\cdot10^{-6}{}^{+13.9\%}_{-11.8\%}$	$5.91\cdot10^{-1}{}^{+2.6\%}_{-1.3\%}$	$2.94\cdot10^{-1}{}^{+2.6\%}_{-1.3\%}$	$2.80\cdot10^{2}{}^{+6.2\%}_{-7.6\%}$
790.0	$2.23\cdot10^{-4}{}^{+15.5\%}_{-13.3\%}$	$2.31\cdot10^{-7}{}^{+15.0\%}_{-12.7\%}$	$1.40\cdot10^{-6}{}^{+14.4\%}_{-12.2\%}$	$5.93\cdot10^{-1}{}^{+2.7\%}_{-1.3\%}$	$2.95\cdot10^{-1}{}^{+2.6\%}_{-1.3\%}$	$2.92\cdot10^{2}{}^{+6.5\%}_{-7.9\%}$
800.0	$2.16\cdot10^{-4}{}^{+15.8\%}_{-13.6\%}$	$2.44\cdot10^{-7}{}^{+15.2\%}_{-12.7\%}$	$1.33\cdot10^{-6}{}^{+14.8\%}_{-12.5\%}$	$5.94\cdot10^{-1}{}^{+2.7\%}_{-1.3\%}$	$2.96\cdot10^{-1}{}^{+2.7\%}_{-1.3\%}$	$3.04\cdot10^{2}{}^{+6.8\%}_{-8.2\%}$
810.0	$2.09\cdot10^{-4}{}^{+16.3\%}_{-13.9\%}$	$2.57\cdot10^{-7}{}^{+15.0\%}_{-12.7\%}$	$1.27\cdot10^{-6}{}^{+15.1\%}_{-12.8\%}$	$5.96\cdot10^{-1}{}^{+2.7\%}_{-1.3\%}$	$2.96\cdot10^{-1}{}^{+2.7\%}_{-1.3\%}$	$3.17\cdot10^{2}{}^{+7.1\%}_{-8.6\%}$
820.0	$2.02\cdot10^{-4}{}^{+16.8\%}_{-14.2\%}$	$2.69\cdot10^{-7}{}^{+15.3\%}_{-12.6\%}$	$1.22\cdot10^{-6}{}^{+15.6\%}_{-13.2\%}$	$5.98\cdot10^{-1}{}^{+2.7\%}_{-1.4\%}$	$2.97\cdot10^{-1}{}^{+2.7\%}_{-1.3\%}$	$3.30\cdot10^{2}{}^{+7.5\%}_{-8.9\%}$
830.0	$1.96\cdot10^{-4}{}^{+17.1\%}_{-14.6\%}$	$2.82\cdot10^{-7}{}^{+15.3\%}_{-12.6\%}$	$1.16\cdot10^{-6}{}^{+16.2\%}_{-13.5\%}$	$5.99\cdot10^{-1}{}^{+2.7\%}_{-1.4\%}$	$2.98\cdot10^{-1}{}^{+2.7\%}_{-1.4\%}$	$3.43\cdot10^{2}{}^{+7.8\%}_{-9.2\%}$
840.0	$1.90\cdot10^{-4}{}^{+17.6\%}_{-14.9\%}$	$2.93\cdot10^{-7}{}^{+15.4\%}_{-12.8\%}$	$1.12\cdot10^{-6}{}^{+16.6\%}_{-13.9\%}$	$6.01\cdot10^{-1}{}^{+2.7\%}_{-1.4\%}$	$2.99\cdot10^{-1}{}^{+2.7\%}_{-1.4\%}$	$3.57\cdot10^{2}{}^{+8.2\%}_{-9.6\%}$
850.0	$1.84\cdot10^{-4}{}^{+18.1\%}_{-15.2\%}$	$3.03\cdot10^{-7}{}^{+15.7\%}_{-12.8\%}$	$1.07\cdot10^{-6}{}^{+17.1\%}_{-14.2\%}$	$6.02\cdot10^{-1}{}^{+2.7\%}_{-1.4\%}$	$3.00\cdot10^{-1}{}^{+2.7\%}_{-1.4\%}$	$3.71\cdot10^{2}{}^{+8.6\%}_{-10.0\%}$
860.0	$1.78\cdot10^{-4}{}^{+18.6\%}_{-15.7\%}$	$3.15\cdot10^{-7}{}^{+16.1\%}_{-12.9\%}$	$1.02\cdot10^{-6}{}^{+17.6\%}_{-14.7\%}$	$6.04\cdot10^{-1}{}^{+2.7\%}_{-1.4\%}$	$3.01\cdot10^{-1}{}^{+2.7\%}_{-1.4\%}$	$3.86\cdot10^{2}{}^{+9.0\%}_{-10.4\%}$
870.0	$1.72\cdot10^{-4}{}^{+19.1\%}_{-16.0\%}$	$3.27\cdot10^{-7}{}^{+16.2\%}_{-13.2\%}$	$9.83\cdot10^{-7}{}^{+18.1\%}_{-15.1\%}$	$6.05\cdot10^{-1}{}^{+2.7\%}_{-1.4\%}$	$3.02\cdot10^{-1}{}^{+2.7\%}_{-1.4\%}$	$4.01\cdot10^{2}{}^{+9.4\%}_{-10.8\%}$
880.0	$1.67\cdot10^{-4}{}^{+19.7\%}_{-16.3\%}$	$3.38\cdot10^{-7}{}^{+16.6\%}_{-13.3\%}$	$9.44\cdot10^{-7}{}^{+18.7\%}_{-15.4\%}$	$6.06\cdot10^{-1}{}^{+2.8\%}_{-1.5\%}$	$3.03\cdot10^{-1}{}^{+2.7\%}_{-1.4\%}$	$4.16\cdot10^{2}{}^{+9.8\%}_{-11.3\%}$
890.0	$1.62\cdot10^{-4}{}^{+20.2\%}_{-16.9\%}$	$3.48\cdot10^{-7}{}^{+17.0\%}_{-13.5\%}$	$9.06\cdot10^{-7}{}^{+19.3\%}_{-15.9\%}$	$6.08\cdot10^{-1}{}^{+2.8\%}_{-1.5\%}$	$3.03\cdot10^{-1}{}^{+2.7\%}_{-1.5\%}$	$4.32\cdot10^{2}{}^{+10.3\%}_{-11.7\%}$
900.0	$1.57\cdot10^{-4}{}^{+20.9\%}_{-17.1\%}$	$3.58\cdot10^{-7}{}^{+17.1\%}_{-13.8\%}$	$8.71\cdot10^{-7}{}^{+19.9\%}_{-16.3\%}$	$6.09\cdot10^{-1}{}^{+2.8\%}_{-1.5\%}$	$3.04\cdot10^{-1}{}^{+2.8\%}_{-1.5\%}$	$4.49\cdot10^{2}{}^{+10.8\%}_{-12.2\%}$
910.0	$1.52\cdot10^{-4}{}^{+21.4\%}_{-17.6\%}$	$3.67\cdot10^{-7}{}^{+17.9\%}_{-13.8\%}$	$8.39\cdot10^{-7}{}^{+20.6\%}_{-16.7\%}$	$6.10\cdot10^{-1}{}^{+2.8\%}_{-1.5\%}$	$3.05\cdot10^{-1}{}^{+2.8\%}_{-1.5\%}$	$4.66\cdot10^{2}{}^{+11.2\%}_{-12.7\%}$
920.0	$1.48\cdot10^{-4}{}^{+22.1\%}_{-18.0\%}$	$3.77\cdot10^{-7}{}^{+18.8\%}_{-14.1\%}$	$8.07\cdot10^{-7}{}^{+21.2\%}_{-17.2\%}$	$6.12\cdot10^{-1}{}^{+2.8\%}_{-1.5\%}$	$3.06\cdot10^{-1}{}^{+2.8\%}_{-1.5\%}$	$4.84\cdot10^{2}{}^{+11.7\%}_{-13.2\%}$
930.0	$1.44\cdot10^{-4}{}^{+22.8\%}_{-18.5\%}$	$3.86\cdot10^{-7}{}^{+18.9\%}_{-15.0\%}$	$7.77\cdot10^{-7}{}^{+21.9\%}_{-17.6\%}$	$6.13\cdot10^{-1}{}^{+2.8\%}_{-1.6\%}$	$3.06\cdot10^{-1}{}^{+2.8\%}_{-1.5\%}$	$5.02\cdot10^{2}{}^{+12.2\%}_{-13.7\%}$
940.0	$1.39\cdot10^{-4}{}^{+23.4\%}_{-18.9\%}$	$3.93\cdot10^{-7}{}^{+19.5\%}_{-15.0\%}$	$7.49\cdot10^{-7}{}^{+22.7\%}_{-18.1\%}$	$6.14\cdot10^{-1}{}^{+2.8\%}_{-1.6\%}$	$3.07\cdot10^{-1}{}^{+2.8\%}_{-1.5\%}$	$5.21\cdot10^{2}{}^{+12.8\%}_{-14.2\%}$
950.0	$1.35\cdot10^{-4}{}^{+24.3\%}_{-19.3\%}$	$4.00\cdot10^{-7}{}^{+20.1\%}_{-15.3\%}$	$7.22\cdot10^{-7}{}^{+23.4\%}_{-18.5\%}$	$6.16\cdot10^{-1}{}^{+2.8\%}_{-1.6\%}$	$3.08\cdot10^{-1}{}^{+2.8\%}_{-1.6\%}$	$5.40\cdot10^{2}{}^{+13.3\%}_{-14.8\%}$
960.0	$1.31\cdot10^{-4}{}^{+25.1\%}_{-19.8\%}$	$4.09\cdot10^{-7}{}^{+20.9\%}_{-15.6\%}$	$6.97\cdot10^{-7}{}^{+24.3\%}_{-19.0\%}$	$6.17\cdot10^{-1}{}^{+2.8\%}_{-1.6\%}$	$3.09\cdot10^{-1}{}^{+2.8\%}_{-1.6\%}$	$5.60\cdot10^{2}{}^{+13.9\%}_{-15.3\%}$
970.0	$1.27\cdot10^{-4}{}^{+25.8\%}_{-20.3\%}$	$4.17\cdot10^{-7}{}^{+21.5\%}_{-16.0\%}$	$6.74\cdot10^{-7}{}^{+25.1\%}_{-19.5\%}$	$6.18\cdot10^{-1}{}^{+2.8\%}_{-1.6\%}$	$3.09\cdot10^{-1}{}^{+2.8\%}_{-1.6\%}$	$5.81\cdot10^{2}{}^{+14.5\%}_{-15.9\%}$
980.0	$1.23\cdot10^{-4}{}^{+26.8\%}_{-20.8\%}$	$4.26\cdot10^{-7}{}^{+22.3\%}_{-16.3\%}$	$6.51\cdot10^{-7}{}^{+26.0\%}_{-20.0\%}$	$6.19\cdot10^{-1}{}^{+2.9\%}_{-1.6\%}$	$3.10\cdot10^{-1}{}^{+2.8\%}_{-1.6\%}$	$6.02\cdot10^{2}{}^{+15.1\%}_{-16.6\%}$
990.0	$1.19\cdot10^{-4}{}^{+27.7\%}_{-21.3\%}$	$4.33\cdot10^{-7}{}^{+23.0\%}_{-16.8\%}$	$6.29\cdot10^{-7}{}^{+26.9\%}_{-20.5\%}$	$6.20\cdot10^{-1}{}^{+2.9\%}_{-1.6\%}$	$3.10\cdot10^{-1}{}^{+2.8\%}_{-1.6\%}$	$6.24\cdot10^{2}{}^{+15.7\%}_{-17.2\%}$
1000.0	$1.16\cdot10^{-4}{}^{+28.6\%}_{-21.8\%}$	$4.39\cdot10^{-7}{}^{+24.0\%}_{-17.1\%}$	$6.08\cdot10^{-7}{}^{+27.8\%}_{-21.0\%}$	$6.21\cdot10^{-1}{}^{+2.9\%}_{-1.7\%}$	$3.11\cdot10^{-1}{}^{+2.8\%}_{-1.6\%}$	$6.47\cdot10^{2}{}^{+16.3\%}_{-17.8\%}$

Table A.11: SM Higgs branching ratios for the different $\mathrm{H} \to 4\mathrm{l}$ and $\mathrm{H} \to 2\mathrm{l}2\nu$ final states and their total uncertainties (expressed in percentage). Very-low-mass range.

M_{H} [GeV]	$\mathrm{H} \to 4\mathrm{l}$ $\mathrm{l} = \mathrm{e}, \mu, \tau$	$\mathrm{H} \to 4\mathrm{l}$ $\mathrm{l} = \mathrm{e}, \mu$	$\mathrm{H} \to \mathrm{eeee}$	$\mathrm{H} \to \mathrm{ee}\mu\mu$	$\mathrm{H} \to 2\mathrm{l}2\nu$ $\mathrm{l} = \mathrm{e}, \mu, \tau$ $\nu = \mathrm{any}$	$\mathrm{H} \to 2\mathrm{l}2\nu$ $\mathrm{l} = \mathrm{e}, \mu$ $\nu = \mathrm{any}$	$\mathrm{H} \to \mathrm{e}\nu\mathrm{e}\nu$	$\mathrm{H} \to \mathrm{e}\nu\mu\nu$	ΔBR [%]
90.0	$4.89 \cdot 10^{-6}$	$2.33 \cdot 10^{-6}$	$7.01 \cdot 10^{-7}$	$9.30 \cdot 10^{-7}$	$2.10 \cdot 10^{-4}$	$9.12 \cdot 10^{-5}$	$1.75 \cdot 10^{-5}$	$2.43 \cdot 10^{-5}$	± 5.8
95.0	$7.73 \cdot 10^{-6}$	$3.67 \cdot 10^{-6}$	$1.10 \cdot 10^{-6}$	$1.48 \cdot 10^{-6}$	$4.80 \cdot 10^{-4}$	$2.10 \cdot 10^{-4}$	$4.42 \cdot 10^{-5}$	$5.49 \cdot 10^{-5}$	± 5.8
100.0	$1.28 \cdot 10^{-5}$	$6.06 \cdot 10^{-6}$	$1.78 \cdot 10^{-6}$	$2.49 \cdot 10^{-6}$	$1.14 \cdot 10^{-3}$	$5.03 \cdot 10^{-4}$	$1.13 \cdot 10^{-4}$	$1.29 \cdot 10^{-4}$	± 5.7
105.0	$2.37 \cdot 10^{-5}$	$1.11 \cdot 10^{-5}$	$3.18 \cdot 10^{-6}$	$4.74 \cdot 10^{-6}$	$2.53 \cdot 10^{-3}$	$1.12 \cdot 10^{-3}$	$2.59 \cdot 10^{-4}$	$2.83 \cdot 10^{-4}$	± 5.6
110.0	$4.72 \cdot 10^{-5}$	$2.18 \cdot 10^{-5}$	$6.04 \cdot 10^{-6}$	$9.69 \cdot 10^{-6}$	$5.08 \cdot 10^{-3}$	$2.26 \cdot 10^{-3}$	$5.32 \cdot 10^{-4}$	$5.61 \cdot 10^{-4}$	± 5.4
110.5	$5.06 \cdot 10^{-5}$	$2.33 \cdot 10^{-5}$	$6.45 \cdot 10^{-6}$	$1.04 \cdot 10^{-5}$	$5.41 \cdot 10^{-3}$	$2.41 \cdot 10^{-3}$	$5.68 \cdot 10^{-4}$	$5.97 \cdot 10^{-4}$	± 5.4
111.0	$5.42 \cdot 10^{-5}$	$2.49 \cdot 10^{-5}$	$6.88 \cdot 10^{-6}$	$1.12 \cdot 10^{-5}$	$5.76 \cdot 10^{-3}$	$2.57 \cdot 10^{-3}$	$6.06 \cdot 10^{-4}$	$6.35 \cdot 10^{-4}$	± 5.4
111.5	$5.80 \cdot 10^{-5}$	$2.67 \cdot 10^{-5}$	$7.34 \cdot 10^{-6}$	$1.20 \cdot 10^{-5}$	$6.13 \cdot 10^{-3}$	$2.74 \cdot 10^{-3}$	$6.45 \cdot 10^{-4}$	$6.75 \cdot 10^{-4}$	± 5.4
112.0	$6.21 \cdot 10^{-5}$	$2.85 \cdot 10^{-5}$	$7.82 \cdot 10^{-6}$	$1.29 \cdot 10^{-5}$	$6.52 \cdot 10^{-3}$	$2.91 \cdot 10^{-3}$	$6.87 \cdot 10^{-4}$	$7.17 \cdot 10^{-4}$	± 5.3
112.5	$6.64 \cdot 10^{-5}$	$3.05 \cdot 10^{-5}$	$8.34 \cdot 10^{-6}$	$1.38 \cdot 10^{-5}$	$6.92 \cdot 10^{-3}$	$3.09 \cdot 10^{-3}$	$7.31 \cdot 10^{-4}$	$7.61 \cdot 10^{-4}$	± 5.3
113.0	$7.10 \cdot 10^{-5}$	$3.26 \cdot 10^{-5}$	$8.88 \cdot 10^{-6}$	$1.48 \cdot 10^{-5}$	$7.35 \cdot 10^{-3}$	$3.28 \cdot 10^{-3}$	$7.76 \cdot 10^{-4}$	$8.07 \cdot 10^{-4}$	± 5.3
113.5	$7.59 \cdot 10^{-5}$	$3.47 \cdot 10^{-5}$	$9.46 \cdot 10^{-6}$	$1.58 \cdot 10^{-5}$	$7.79 \cdot 10^{-3}$	$3.48 \cdot 10^{-3}$	$8.23 \cdot 10^{-4}$	$8.54 \cdot 10^{-4}$	± 5.2
114.0	$8.10 \cdot 10^{-5}$	$3.71 \cdot 10^{-5}$	$1.01 \cdot 10^{-5}$	$1.69 \cdot 10^{-5}$	$8.25 \cdot 10^{-3}$	$3.69 \cdot 10^{-3}$	$8.73 \cdot 10^{-4}$	$9.04 \cdot 10^{-4}$	± 5.2
114.5	$8.64 \cdot 10^{-5}$	$3.95 \cdot 10^{-5}$	$1.07 \cdot 10^{-5}$	$1.81 \cdot 10^{-5}$	$8.73 \cdot 10^{-3}$	$3.91 \cdot 10^{-3}$	$9.25 \cdot 10^{-4}$	$9.56 \cdot 10^{-4}$	± 5.2
115.0	$9.22 \cdot 10^{-5}$	$4.21 \cdot 10^{-5}$	$1.14 \cdot 10^{-5}$	$1.93 \cdot 10^{-5}$	$9.23 \cdot 10^{-3}$	$4.13 \cdot 10^{-3}$	$9.79 \cdot 10^{-4}$	$1.01 \cdot 10^{-3}$	± 5.2
115.5	$9.82 \cdot 10^{-5}$	$4.48 \cdot 10^{-5}$	$1.21 \cdot 10^{-5}$	$2.06 \cdot 10^{-5}$	$9.74 \cdot 10^{-3}$	$4.36 \cdot 10^{-3}$	$1.03 \cdot 10^{-3}$	$1.06 \cdot 10^{-3}$	± 5.1
116.0	$1.05 \cdot 10^{-4}$	$4.77 \cdot 10^{-5}$	$1.28 \cdot 10^{-5}$	$2.20 \cdot 10^{-5}$	$1.03 \cdot 10^{-2}$	$4.61 \cdot 10^{-3}$	$1.09 \cdot 10^{-3}$	$1.12 \cdot 10^{-3}$	± 5.1
116.5	$1.11 \cdot 10^{-4}$	$5.07 \cdot 10^{-5}$	$1.36 \cdot 10^{-5}$	$2.35 \cdot 10^{-5}$	$1.08 \cdot 10^{-2}$	$4.86 \cdot 10^{-3}$	$1.15 \cdot 10^{-3}$	$1.18 \cdot 10^{-3}$	± 5.0
117.0	$1.18 \cdot 10^{-4}$	$5.38 \cdot 10^{-5}$	$1.44 \cdot 10^{-5}$	$2.50 \cdot 10^{-5}$	$1.14 \cdot 10^{-2}$	$5.12 \cdot 10^{-3}$	$1.22 \cdot 10^{-3}$	$1.24 \cdot 10^{-3}$	± 5.0
117.5	$1.26 \cdot 10^{-4}$	$5.71 \cdot 10^{-5}$	$1.53 \cdot 10^{-5}$	$2.65 \cdot 10^{-5}$	$1.20 \cdot 10^{-2}$	$5.39 \cdot 10^{-3}$	$1.28 \cdot 10^{-3}$	$1.31 \cdot 10^{-3}$	± 5.0
118.0	$1.33 \cdot 10^{-4}$	$6.06 \cdot 10^{-5}$	$1.62 \cdot 10^{-5}$	$2.82 \cdot 10^{-5}$	$1.26 \cdot 10^{-2}$	$5.67 \cdot 10^{-3}$	$1.35 \cdot 10^{-3}$	$1.38 \cdot 10^{-3}$	± 4.9
118.5	$1.41 \cdot 10^{-4}$	$6.42 \cdot 10^{-5}$	$1.71 \cdot 10^{-5}$	$2.99 \cdot 10^{-5}$	$1.33 \cdot 10^{-2}$	$5.96 \cdot 10^{-3}$	$1.42 \cdot 10^{-3}$	$1.44 \cdot 10^{-3}$	± 4.9
119.0	$1.50 \cdot 10^{-4}$	$6.79 \cdot 10^{-5}$	$1.81 \cdot 10^{-5}$	$3.18 \cdot 10^{-5}$	$1.39 \cdot 10^{-2}$	$6.26 \cdot 10^{-3}$	$1.49 \cdot 10^{-3}$	$1.51 \cdot 10^{-3}$	± 4.8
119.5	$1.58 \cdot 10^{-4}$	$7.18 \cdot 10^{-5}$	$1.91 \cdot 10^{-5}$	$3.37 \cdot 10^{-5}$	$1.46 \cdot 10^{-2}$	$6.57 \cdot 10^{-3}$	$1.56 \cdot 10^{-3}$	$1.59 \cdot 10^{-3}$	± 4.8
120.0	$1.67 \cdot 10^{-4}$	$7.59 \cdot 10^{-5}$	$2.01 \cdot 10^{-5}$	$3.56 \cdot 10^{-5}$	$1.53 \cdot 10^{-2}$	$6.89 \cdot 10^{-3}$	$1.64 \cdot 10^{-3}$	$1.66 \cdot 10^{-3}$	± 4.8
120.5	$1.77 \cdot 10^{-4}$	$8.01 \cdot 10^{-5}$	$2.12 \cdot 10^{-5}$	$3.76 \cdot 10^{-5}$	$1.60 \cdot 10^{-2}$	$7.21 \cdot 10^{-3}$	$1.72 \cdot 10^{-3}$	$1.74 \cdot 10^{-3}$	± 4.7
121.0	$1.86 \cdot 10^{-4}$	$8.45 \cdot 10^{-5}$	$2.24 \cdot 10^{-5}$	$3.98 \cdot 10^{-5}$	$1.68 \cdot 10^{-2}$	$7.55 \cdot 10^{-3}$	$1.80 \cdot 10^{-3}$	$1.82 \cdot 10^{-3}$	± 4.7
121.5	$1.96 \cdot 10^{-4}$	$8.90 \cdot 10^{-5}$	$2.35 \cdot 10^{-5}$	$4.19 \cdot 10^{-5}$	$1.75 \cdot 10^{-2}$	$7.90 \cdot 10^{-3}$	$1.88 \cdot 10^{-3}$	$1.90 \cdot 10^{-3}$	± 4.6
122.0	$2.07 \cdot 10^{-4}$	$9.36 \cdot 10^{-5}$	$2.47 \cdot 10^{-5}$	$4.42 \cdot 10^{-5}$	$1.83 \cdot 10^{-2}$	$8.25 \cdot 10^{-3}$	$1.97 \cdot 10^{-3}$	$1.98 \cdot 10^{-3}$	± 4.6
122.5	$2.18 \cdot 10^{-4}$	$9.85 \cdot 10^{-5}$	$2.60 \cdot 10^{-5}$	$4.65 \cdot 10^{-5}$	$1.91 \cdot 10^{-2}$	$8.61 \cdot 10^{-3}$	$2.05 \cdot 10^{-3}$	$2.07 \cdot 10^{-3}$	± 4.5
123.0	$2.29 \cdot 10^{-4}$	$1.03 \cdot 10^{-4}$	$2.72 \cdot 10^{-5}$	$4.90 \cdot 10^{-5}$	$1.99 \cdot 10^{-2}$	$8.99 \cdot 10^{-3}$	$2.14 \cdot 10^{-3}$	$2.16 \cdot 10^{-3}$	± 4.5
123.5	$2.40 \cdot 10^{-4}$	$1.09 \cdot 10^{-4}$	$2.86 \cdot 10^{-5}$	$5.14 \cdot 10^{-5}$	$2.08 \cdot 10^{-2}$	$9.37 \cdot 10^{-3}$	$2.23 \cdot 10^{-3}$	$2.24 \cdot 10^{-3}$	± 4.4
124.0	$2.52 \cdot 10^{-4}$	$1.14 \cdot 10^{-4}$	$2.99 \cdot 10^{-5}$	$5.40 \cdot 10^{-5}$	$2.16 \cdot 10^{-2}$	$9.76 \cdot 10^{-3}$	$2.33 \cdot 10^{-3}$	$2.34 \cdot 10^{-3}$	± 4.4
124.5	$2.64 \cdot 10^{-4}$	$1.19 \cdot 10^{-4}$	$3.13 \cdot 10^{-5}$	$5.66 \cdot 10^{-5}$	$2.25 \cdot 10^{-2}$	$1.02 \cdot 10^{-2}$	$2.42 \cdot 10^{-3}$	$2.43 \cdot 10^{-3}$	± 4.3
125.0	$2.76 \cdot 10^{-4}$	$1.25 \cdot 10^{-4}$	$3.27 \cdot 10^{-5}$	$5.93 \cdot 10^{-5}$	$2.34 \cdot 10^{-2}$	$1.06 \cdot 10^{-2}$	$2.52 \cdot 10^{-3}$	$2.52 \cdot 10^{-3}$	± 4.3
125.5	$2.89 \cdot 10^{-4}$	$1.30 \cdot 10^{-4}$	$3.42 \cdot 10^{-5}$	$6.21 \cdot 10^{-5}$	$2.43 \cdot 10^{-2}$	$1.10 \cdot 10^{-2}$	$2.62 \cdot 10^{-3}$	$2.62 \cdot 10^{-3}$	± 4.2
126.0	$3.02 \cdot 10^{-4}$	$1.36 \cdot 10^{-4}$	$3.56 \cdot 10^{-5}$	$6.49 \cdot 10^{-5}$	$2.53 \cdot 10^{-2}$	$1.14 \cdot 10^{-2}$	$2.72 \cdot 10^{-3}$	$2.72 \cdot 10^{-3}$	± 4.1
126.5	$3.15 \cdot 10^{-4}$	$1.42 \cdot 10^{-4}$	$3.72 \cdot 10^{-5}$	$6.78 \cdot 10^{-5}$	$2.62 \cdot 10^{-2}$	$1.18 \cdot 10^{-2}$	$2.83 \cdot 10^{-3}$	$2.82 \cdot 10^{-3}$	± 4.1
127.0	$3.28 \cdot 10^{-4}$	$1.48 \cdot 10^{-4}$	$3.87 \cdot 10^{-5}$	$7.08 \cdot 10^{-5}$	$2.72 \cdot 10^{-2}$	$1.23 \cdot 10^{-2}$	$2.93 \cdot 10^{-3}$	$2.92 \cdot 10^{-3}$	± 4.0
127.5	$3.42 \cdot 10^{-4}$	$1.54 \cdot 10^{-4}$	$4.03 \cdot 10^{-5}$	$7.38 \cdot 10^{-5}$	$2.81 \cdot 10^{-2}$	$1.27 \cdot 10^{-2}$	$3.04 \cdot 10^{-3}$	$3.02 \cdot 10^{-3}$	± 4.0
128.0	$3.56 \cdot 10^{-4}$	$1.61 \cdot 10^{-4}$	$4.19 \cdot 10^{-5}$	$7.68 \cdot 10^{-5}$	$2.91 \cdot 10^{-2}$	$1.32 \cdot 10^{-2}$	$3.15 \cdot 10^{-3}$	$3.13 \cdot 10^{-3}$	± 3.9
128.5	$3.70 \cdot 10^{-4}$	$1.67 \cdot 10^{-4}$	$4.35 \cdot 10^{-5}$	$8.00 \cdot 10^{-5}$	$3.01 \cdot 10^{-2}$	$1.36 \cdot 10^{-2}$	$3.26 \cdot 10^{-3}$	$3.24 \cdot 10^{-3}$	± 3.8
129.0	$3.85 \cdot 10^{-4}$	$1.73 \cdot 10^{-4}$	$4.52 \cdot 10^{-5}$	$8.31 \cdot 10^{-5}$	$3.12 \cdot 10^{-2}$	$1.41 \cdot 10^{-2}$	$3.37 \cdot 10^{-3}$	$3.34 \cdot 10^{-3}$	± 3.8
129.5	$3.99 \cdot 10^{-4}$	$1.80 \cdot 10^{-4}$	$4.68 \cdot 10^{-5}$	$8.63 \cdot 10^{-5}$	$3.22 \cdot 10^{-2}$	$1.46 \cdot 10^{-2}$	$3.48 \cdot 10^{-3}$	$3.45 \cdot 10^{-3}$	± 3.7
130.0	$4.14 \cdot 10^{-4}$	$1.87 \cdot 10^{-4}$	$4.85 \cdot 10^{-5}$	$8.96 \cdot 10^{-5}$	$3.32 \cdot 10^{-2}$	$1.50 \cdot 10^{-2}$	$3.60 \cdot 10^{-3}$	$3.56 \cdot 10^{-3}$	± 3.7

Table A.12: SM Higgs branching ratios for the different $\mathrm{H} \to 4\mathrm{l}$ and $\mathrm{H} \to 2\mathrm{l}2\nu$ final states and their total uncertainties (expressed in percentage). Low- and intermediate-mass range.

M_{H} [GeV]	$\mathrm{H} \to 4\mathrm{l}$ $\mathrm{l} = \mathrm{e}, \mu, \tau$	$\mathrm{H} \to 4\mathrm{l}$ $\mathrm{l} = \mathrm{e}, \mu$	$\mathrm{H} \to \mathrm{eeee}$	$\mathrm{H} \to \mathrm{ee}\mu\mu$	$\mathrm{H} \to 2\mathrm{l}2\nu$ $\mathrm{l} = \mathrm{e}, \mu, \tau$ $\nu = \mathrm{any}$	$\mathrm{H} \to 2\mathrm{l}2\nu$ $\mathrm{l} = \mathrm{e}, \mu$ $\nu = \mathrm{any}$	$\mathrm{H} \to \mathrm{e}\nu\mathrm{e}\nu$	$\mathrm{H} \to \mathrm{e}\nu\mu\nu$	ΔBR [%]
130.5	$4.29 \cdot 10^{-4}$	$1.93 \cdot 10^{-4}$	$5.02 \cdot 10^{-5}$	$9.29 \cdot 10^{-5}$	$3.43 \cdot 10^{-2}$	$1.55 \cdot 10^{-2}$	$3.71 \cdot 10^{-3}$	$3.67 \cdot 10^{-3}$	± 3.6
131.0	$4.44 \cdot 10^{-4}$	$2.00 \cdot 10^{-4}$	$5.19 \cdot 10^{-5}$	$9.62 \cdot 10^{-5}$	$3.54 \cdot 10^{-2}$	$1.60 \cdot 10^{-2}$	$3.83 \cdot 10^{-3}$	$3.79 \cdot 10^{-3}$	± 3.5
131.5	$4.59 \cdot 10^{-4}$	$2.07 \cdot 10^{-4}$	$5.37 \cdot 10^{-5}$	$9.95 \cdot 10^{-5}$	$3.64 \cdot 10^{-2}$	$1.65 \cdot 10^{-2}$	$3.94 \cdot 10^{-3}$	$3.90 \cdot 10^{-3}$	± 3.5
132.0	$4.75 \cdot 10^{-4}$	$2.14 \cdot 10^{-4}$	$5.54 \cdot 10^{-5}$	$1.03 \cdot 10^{-4}$	$3.75 \cdot 10^{-2}$	$1.70 \cdot 10^{-2}$	$4.06 \cdot 10^{-3}$	$4.01 \cdot 10^{-3}$	± 3.4
132.5	$4.90 \cdot 10^{-4}$	$2.21 \cdot 10^{-4}$	$5.71 \cdot 10^{-5}$	$1.06 \cdot 10^{-4}$	$3.86 \cdot 10^{-2}$	$1.75 \cdot 10^{-2}$	$4.18 \cdot 10^{-3}$	$4.13 \cdot 10^{-3}$	± 3.3
133.0	$5.05 \cdot 10^{-4}$	$2.27 \cdot 10^{-4}$	$5.89 \cdot 10^{-5}$	$1.10 \cdot 10^{-4}$	$3.97 \cdot 10^{-2}$	$1.80 \cdot 10^{-2}$	$4.30 \cdot 10^{-3}$	$4.24 \cdot 10^{-3}$	± 3.3
133.5	$5.21 \cdot 10^{-4}$	$2.34 \cdot 10^{-4}$	$6.06 \cdot 10^{-5}$	$1.13 \cdot 10^{-4}$	$4.08 \cdot 10^{-2}$	$1.85 \cdot 10^{-2}$	$4.43 \cdot 10^{-3}$	$4.36 \cdot 10^{-3}$	± 3.2
134.0	$5.36 \cdot 10^{-4}$	$2.41 \cdot 10^{-4}$	$6.24 \cdot 10^{-5}$	$1.16 \cdot 10^{-4}$	$4.19 \cdot 10^{-2}$	$1.90 \cdot 10^{-2}$	$4.55 \cdot 10^{-3}$	$4.48 \cdot 10^{-3}$	± 3.1
134.5	$5.52 \cdot 10^{-4}$	$2.48 \cdot 10^{-4}$	$6.41 \cdot 10^{-5}$	$1.20 \cdot 10^{-4}$	$4.30 \cdot 10^{-2}$	$1.95 \cdot 10^{-2}$	$4.67 \cdot 10^{-3}$	$4.59 \cdot 10^{-3}$	± 3.1
135.0	$5.67 \cdot 10^{-4}$	$2.55 \cdot 10^{-4}$	$6.58 \cdot 10^{-5}$	$1.23 \cdot 10^{-4}$	$4.41 \cdot 10^{-2}$	$2.00 \cdot 10^{-2}$	$4.79 \cdot 10^{-3}$	$4.71 \cdot 10^{-3}$	± 3.0
135.5	$5.82 \cdot 10^{-4}$	$2.62 \cdot 10^{-4}$	$6.76 \cdot 10^{-5}$	$1.26 \cdot 10^{-4}$	$4.52 \cdot 10^{-2}$	$2.05 \cdot 10^{-2}$	$4.92 \cdot 10^{-3}$	$4.83 \cdot 10^{-3}$	± 2.9
136.0	$5.97 \cdot 10^{-4}$	$2.68 \cdot 10^{-4}$	$6.93 \cdot 10^{-5}$	$1.30 \cdot 10^{-4}$	$4.64 \cdot 10^{-2}$	$2.10 \cdot 10^{-2}$	$5.04 \cdot 10^{-3}$	$4.95 \cdot 10^{-3}$	± 2.8
136.5	$6.12 \cdot 10^{-4}$	$2.75 \cdot 10^{-4}$	$7.10 \cdot 10^{-5}$	$1.33 \cdot 10^{-4}$	$4.75 \cdot 10^{-2}$	$2.15 \cdot 10^{-2}$	$5.16 \cdot 10^{-3}$	$5.07 \cdot 10^{-3}$	± 2.6
137.0	$6.27 \cdot 10^{-4}$	$2.82 \cdot 10^{-4}$	$7.26 \cdot 10^{-5}$	$1.36 \cdot 10^{-4}$	$4.86 \cdot 10^{-2}$	$2.20 \cdot 10^{-2}$	$5.29 \cdot 10^{-3}$	$5.19 \cdot 10^{-3}$	± 2.5
137.5	$6.42 \cdot 10^{-4}$	$2.88 \cdot 10^{-4}$	$7.43 \cdot 10^{-5}$	$1.40 \cdot 10^{-4}$	$4.97 \cdot 10^{-2}$	$2.25 \cdot 10^{-2}$	$5.41 \cdot 10^{-3}$	$5.31 \cdot 10^{-3}$	± 2.4
138.0	$6.56 \cdot 10^{-4}$	$2.94 \cdot 10^{-4}$	$7.59 \cdot 10^{-5}$	$1.43 \cdot 10^{-4}$	$5.09 \cdot 10^{-2}$	$2.31 \cdot 10^{-2}$	$5.54 \cdot 10^{-3}$	$5.42 \cdot 10^{-3}$	± 2.2
138.5	$6.70 \cdot 10^{-4}$	$3.01 \cdot 10^{-4}$	$7.75 \cdot 10^{-5}$	$1.46 \cdot 10^{-4}$	$5.20 \cdot 10^{-2}$	$2.36 \cdot 10^{-2}$	$5.66 \cdot 10^{-3}$	$5.54 \cdot 10^{-3}$	± 2.1
139.0	$6.84 \cdot 10^{-4}$	$3.07 \cdot 10^{-4}$	$7.90 \cdot 10^{-5}$	$1.49 \cdot 10^{-4}$	$5.31 \cdot 10^{-2}$	$2.41 \cdot 10^{-2}$	$5.78 \cdot 10^{-3}$	$5.66 \cdot 10^{-3}$	± 1.9
139.5	$6.97 \cdot 10^{-4}$	$3.13 \cdot 10^{-4}$	$8.05 \cdot 10^{-5}$	$1.52 \cdot 10^{-4}$	$5.42 \cdot 10^{-2}$	$2.46 \cdot 10^{-2}$	$5.91 \cdot 10^{-3}$	$5.78 \cdot 10^{-3}$	± 1.8
140.0	$7.11 \cdot 10^{-4}$	$3.19 \cdot 10^{-4}$	$8.20 \cdot 10^{-5}$	$1.55 \cdot 10^{-4}$	$5.53 \cdot 10^{-2}$	$2.51 \cdot 10^{-2}$	$6.03 \cdot 10^{-3}$	$5.90 \cdot 10^{-3}$	± 1.7
141.0	$7.36 \cdot 10^{-4}$	$3.30 \cdot 10^{-4}$	$8.48 \cdot 10^{-5}$	$1.60 \cdot 10^{-4}$	$5.76 \cdot 10^{-2}$	$2.61 \cdot 10^{-2}$	$6.28 \cdot 10^{-3}$	$6.14 \cdot 10^{-3}$	± 1.6
142.0	$7.59 \cdot 10^{-4}$	$3.41 \cdot 10^{-4}$	$8.75 \cdot 10^{-5}$	$1.66 \cdot 10^{-4}$	$5.98 \cdot 10^{-2}$	$2.71 \cdot 10^{-2}$	$6.52 \cdot 10^{-3}$	$6.37 \cdot 10^{-3}$	± 1.5
143.0	$7.81 \cdot 10^{-4}$	$3.50 \cdot 10^{-4}$	$8.99 \cdot 10^{-5}$	$1.70 \cdot 10^{-4}$	$6.20 \cdot 10^{-2}$	$2.81 \cdot 10^{-2}$	$6.76 \cdot 10^{-3}$	$6.61 \cdot 10^{-3}$	± 1.4
144.0	$8.00 \cdot 10^{-4}$	$3.59 \cdot 10^{-4}$	$9.20 \cdot 10^{-5}$	$1.75 \cdot 10^{-4}$	$6.41 \cdot 10^{-2}$	$2.91 \cdot 10^{-2}$	$7.00 \cdot 10^{-3}$	$6.84 \cdot 10^{-3}$	± 1.3
145.0	$8.17 \cdot 10^{-4}$	$3.66 \cdot 10^{-4}$	$9.38 \cdot 10^{-5}$	$1.78 \cdot 10^{-4}$	$6.63 \cdot 10^{-2}$	$3.00 \cdot 10^{-2}$	$7.24 \cdot 10^{-3}$	$7.07 \cdot 10^{-3}$	± 1.2
146.0	$8.31 \cdot 10^{-4}$	$3.72 \cdot 10^{-4}$	$9.53 \cdot 10^{-5}$	$1.82 \cdot 10^{-4}$	$6.84 \cdot 10^{-2}$	$3.10 \cdot 10^{-2}$	$7.48 \cdot 10^{-3}$	$7.30 \cdot 10^{-3}$	± 1.2
147.0	$8.41 \cdot 10^{-4}$	$3.77 \cdot 10^{-4}$	$9.65 \cdot 10^{-5}$	$1.84 \cdot 10^{-4}$	$7.05 \cdot 10^{-2}$	$3.20 \cdot 10^{-2}$	$7.72 \cdot 10^{-3}$	$7.53 \cdot 10^{-3}$	± 1.1
148.0	$8.48 \cdot 10^{-4}$	$3.80 \cdot 10^{-4}$	$9.72 \cdot 10^{-5}$	$1.86 \cdot 10^{-4}$	$7.26 \cdot 10^{-2}$	$3.29 \cdot 10^{-2}$	$7.95 \cdot 10^{-3}$	$7.75 \cdot 10^{-3}$	± 1.0
149.0	$8.51 \cdot 10^{-4}$	$3.81 \cdot 10^{-4}$	$9.75 \cdot 10^{-5}$	$1.86 \cdot 10^{-4}$	$7.46 \cdot 10^{-2}$	$3.38 \cdot 10^{-2}$	$8.18 \cdot 10^{-3}$	$7.98 \cdot 10^{-3}$	± 0.9
150.0	$8.50 \cdot 10^{-4}$	$3.81 \cdot 10^{-4}$	$9.72 \cdot 10^{-5}$	$1.86 \cdot 10^{-4}$	$7.67 \cdot 10^{-2}$	$3.47 \cdot 10^{-2}$	$8.41 \cdot 10^{-3}$	$8.20 \cdot 10^{-3}$	± 0.9
151.0	$8.43 \cdot 10^{-4}$	$3.78 \cdot 10^{-4}$	$9.64 \cdot 10^{-5}$	$1.85 \cdot 10^{-4}$	$7.87 \cdot 10^{-2}$	$3.56 \cdot 10^{-2}$	$8.64 \cdot 10^{-3}$	$8.43 \cdot 10^{-3}$	± 0.8
152.0	$8.31 \cdot 10^{-4}$	$3.72 \cdot 10^{-4}$	$9.50 \cdot 10^{-5}$	$1.82 \cdot 10^{-4}$	$8.07 \cdot 10^{-2}$	$3.65 \cdot 10^{-2}$	$8.86 \cdot 10^{-3}$	$8.66 \cdot 10^{-3}$	± 0.7
153.0	$8.13 \cdot 10^{-4}$	$3.64 \cdot 10^{-4}$	$9.29 \cdot 10^{-5}$	$1.78 \cdot 10^{-4}$	$8.27 \cdot 10^{-2}$	$3.74 \cdot 10^{-2}$	$9.10 \cdot 10^{-3}$	$8.89 \cdot 10^{-3}$	± 0.7
154.0	$7.88 \cdot 10^{-4}$	$3.53 \cdot 10^{-4}$	$8.99 \cdot 10^{-5}$	$1.73 \cdot 10^{-4}$	$8.48 \cdot 10^{-2}$	$3.83 \cdot 10^{-2}$	$9.33 \cdot 10^{-3}$	$9.12 \cdot 10^{-3}$	± 0.6
155.0	$7.55 \cdot 10^{-4}$	$3.38 \cdot 10^{-4}$	$8.60 \cdot 10^{-5}$	$1.65 \cdot 10^{-4}$	$8.69 \cdot 10^{-2}$	$3.92 \cdot 10^{-2}$	$9.57 \cdot 10^{-3}$	$9.36 \cdot 10^{-3}$	± 0.5
156.0	$7.11 \cdot 10^{-4}$	$3.18 \cdot 10^{-4}$	$8.11 \cdot 10^{-5}$	$1.56 \cdot 10^{-4}$	$8.90 \cdot 10^{-2}$	$4.01 \cdot 10^{-2}$	$9.81 \cdot 10^{-3}$	$9.61 \cdot 10^{-3}$	± 0.5
157.0	$6.57 \cdot 10^{-4}$	$2.94 \cdot 10^{-4}$	$7.49 \cdot 10^{-5}$	$1.44 \cdot 10^{-4}$	$9.11 \cdot 10^{-2}$	$4.10 \cdot 10^{-2}$	$1.01 \cdot 10^{-2}$	$9.87 \cdot 10^{-3}$	± 0.4
158.0	$5.91 \cdot 10^{-4}$	$2.64 \cdot 10^{-4}$	$6.73 \cdot 10^{-5}$	$1.30 \cdot 10^{-4}$	$9.33 \cdot 10^{-2}$	$4.19 \cdot 10^{-2}$	$1.03 \cdot 10^{-2}$	$1.01 \cdot 10^{-2}$	± 0.3
159.0	$5.12 \cdot 10^{-4}$	$2.29 \cdot 10^{-4}$	$5.82 \cdot 10^{-5}$	$1.12 \cdot 10^{-4}$	$9.56 \cdot 10^{-2}$	$4.29 \cdot 10^{-2}$	$1.06 \cdot 10^{-2}$	$1.04 \cdot 10^{-2}$	± 0.3
160.0	$4.25 \cdot 10^{-4}$	$1.90 \cdot 10^{-4}$	$4.83 \cdot 10^{-5}$	$9.34 \cdot 10^{-5}$	$9.79 \cdot 10^{-2}$	$4.38 \cdot 10^{-2}$	$1.08 \cdot 10^{-2}$	$1.07 \cdot 10^{-2}$	± 0.2
162.0	$2.89 \cdot 10^{-4}$	$1.29 \cdot 10^{-4}$	$3.28 \cdot 10^{-5}$	$6.35 \cdot 10^{-5}$	$1.01 \cdot 10^{-1}$	$4.52 \cdot 10^{-2}$	$1.12 \cdot 10^{-2}$	$1.11 \cdot 10^{-2}$	± 0.2
164.0	$2.37 \cdot 10^{-4}$	$1.06 \cdot 10^{-4}$	$2.69 \cdot 10^{-5}$	$5.21 \cdot 10^{-5}$	$1.02 \cdot 10^{-1}$	$4.57 \cdot 10^{-2}$	$1.14 \cdot 10^{-2}$	$1.13 \cdot 10^{-2}$	± 0.1
166.0	$2.23 \cdot 10^{-4}$	$9.98 \cdot 10^{-5}$	$2.53 \cdot 10^{-5}$	$4.92 \cdot 10^{-5}$	$1.03 \cdot 10^{-1}$	$4.59 \cdot 10^{-2}$	$1.14 \cdot 10^{-2}$	$1.13 \cdot 10^{-2}$	± 0.1
168.0	$2.27 \cdot 10^{-4}$	$1.01 \cdot 10^{-4}$	$2.57 \cdot 10^{-5}$	$5.00 \cdot 10^{-5}$	$1.03 \cdot 10^{-1}$	$4.60 \cdot 10^{-2}$	$1.15 \cdot 10^{-2}$	$1.14 \cdot 10^{-2}$	± 0.1
170.0	$2.41 \cdot 10^{-4}$	$1.08 \cdot 10^{-4}$	$2.73 \cdot 10^{-5}$	$5.32 \cdot 10^{-5}$	$1.03 \cdot 10^{-1}$	$4.61 \cdot 10^{-2}$	$1.15 \cdot 10^{-2}$	$1.14 \cdot 10^{-2}$	± 0.1

Table A.13: SM Higgs branching ratios for the different $\mathrm{H} \to 4\mathrm{l}$ and $\mathrm{H} \to 2\mathrm{l}2\nu$ final states and their total uncertainties (expressed in percentage). Intermediate-mass range.

M_{H} [GeV]	$\mathrm{H} \to 4\mathrm{l}$ $\mathrm{l} = \mathrm{e}, \mu, \tau$	$\mathrm{H} \to 4\mathrm{l}$ $\mathrm{l} = \mathrm{e}, \mu$	$\mathrm{H} \to \mathrm{eeee}$	$\mathrm{H} \to \mathrm{ee}\mu\mu$	$\mathrm{H} \to 2\mathrm{l}2\nu$ $\mathrm{l} = \mathrm{e}, \mu, \tau$ $\nu = \mathrm{any}$	$\mathrm{H} \to 2\mathrm{l}2\nu$ $\mathrm{l} = \mathrm{e}, \mu$ $\nu = \mathrm{any}$	$\mathrm{H} \to \mathrm{e}\nu\mathrm{e}\nu$	$\mathrm{H} \to \mathrm{e}\nu\mu\nu$	ΔBR [%]
172.0	$2.66 \cdot 10^{-4}$	$1.19 \cdot 10^{-4}$	$3.00 \cdot 10^{-5}$	$5.87 \cdot 10^{-5}$	$1.03 \cdot 10^{-1}$	$4.61 \cdot 10^{-2}$	$1.15 \cdot 10^{-2}$	$1.14 \cdot 10^{-2}$	± 0.0
174.0	$3.04 \cdot 10^{-4}$	$1.36 \cdot 10^{-4}$	$3.42 \cdot 10^{-5}$	$6.71 \cdot 10^{-5}$	$1.03 \cdot 10^{-1}$	$4.61 \cdot 10^{-2}$	$1.14 \cdot 10^{-2}$	$1.13 \cdot 10^{-2}$	± 0.0
176.0	$3.61 \cdot 10^{-4}$	$1.61 \cdot 10^{-4}$	$4.06 \cdot 10^{-5}$	$7.98 \cdot 10^{-5}$	$1.03 \cdot 10^{-1}$	$4.60 \cdot 10^{-2}$	$1.14 \cdot 10^{-2}$	$1.13 \cdot 10^{-2}$	± 0.0
178.0	$4.52 \cdot 10^{-4}$	$2.01 \cdot 10^{-4}$	$5.07 \cdot 10^{-5}$	$9.99 \cdot 10^{-5}$	$1.02 \cdot 10^{-1}$	$4.58 \cdot 10^{-2}$	$1.13 \cdot 10^{-2}$	$1.12 \cdot 10^{-2}$	± 0.0
180.0	$6.12 \cdot 10^{-4}$	$2.73 \cdot 10^{-4}$	$6.85 \cdot 10^{-5}$	$1.36 \cdot 10^{-4}$	$1.01 \cdot 10^{-1}$	$4.55 \cdot 10^{-2}$	$1.12 \cdot 10^{-2}$	$1.10 \cdot 10^{-2}$	± 0.0
182.0	$9.14 \cdot 10^{-4}$	$4.07 \cdot 10^{-4}$	$1.02 \cdot 10^{-4}$	$2.03 \cdot 10^{-4}$	$9.94 \cdot 10^{-2}$	$4.50 \cdot 10^{-2}$	$1.10 \cdot 10^{-2}$	$1.06 \cdot 10^{-2}$	± 0.0
184.0	$1.33 \cdot 10^{-3}$	$5.93 \cdot 10^{-4}$	$1.49 \cdot 10^{-4}$	$2.96 \cdot 10^{-4}$	$9.67 \cdot 10^{-2}$	$4.42 \cdot 10^{-2}$	$1.07 \cdot 10^{-2}$	$1.02 \cdot 10^{-2}$	± 0.0
186.0	$1.69 \cdot 10^{-3}$	$7.50 \cdot 10^{-4}$	$1.88 \cdot 10^{-4}$	$3.75 \cdot 10^{-4}$	$9.45 \cdot 10^{-2}$	$4.35 \cdot 10^{-2}$	$1.05 \cdot 10^{-2}$	$9.76 \cdot 10^{-3}$	± 0.0
188.0	$1.94 \cdot 10^{-3}$	$8.62 \cdot 10^{-4}$	$2.16 \cdot 10^{-4}$	$4.31 \cdot 10^{-4}$	$9.29 \cdot 10^{-2}$	$4.30 \cdot 10^{-2}$	$1.03 \cdot 10^{-2}$	$9.47 \cdot 10^{-3}$	± 0.0
190.0	$2.12 \cdot 10^{-3}$	$9.44 \cdot 10^{-4}$	$2.36 \cdot 10^{-4}$	$4.72 \cdot 10^{-4}$	$9.18 \cdot 10^{-2}$	$4.27 \cdot 10^{-2}$	$1.02 \cdot 10^{-2}$	$9.26 \cdot 10^{-3}$	± 0.0
192.0	$2.26 \cdot 10^{-3}$	$1.01 \cdot 10^{-3}$	$2.52 \cdot 10^{-4}$	$5.03 \cdot 10^{-4}$	$9.09 \cdot 10^{-2}$	$4.24 \cdot 10^{-2}$	$1.01 \cdot 10^{-2}$	$9.10 \cdot 10^{-3}$	± 0.0
194.0	$2.37 \cdot 10^{-3}$	$1.05 \cdot 10^{-3}$	$2.64 \cdot 10^{-4}$	$5.27 \cdot 10^{-4}$	$9.02 \cdot 10^{-2}$	$4.22 \cdot 10^{-2}$	$1.00 \cdot 10^{-2}$	$8.98 \cdot 10^{-3}$	± 0.0
196.0	$2.46 \cdot 10^{-3}$	$1.09 \cdot 10^{-3}$	$2.74 \cdot 10^{-4}$	$5.46 \cdot 10^{-4}$	$8.97 \cdot 10^{-2}$	$4.20 \cdot 10^{-2}$	$9.96 \cdot 10^{-3}$	$8.88 \cdot 10^{-3}$	± 0.0
198.0	$2.53 \cdot 10^{-3}$	$1.12 \cdot 10^{-3}$	$2.81 \cdot 10^{-4}$	$5.62 \cdot 10^{-4}$	$8.92 \cdot 10^{-2}$	$4.19 \cdot 10^{-2}$	$9.91 \cdot 10^{-3}$	$8.80 \cdot 10^{-3}$	± 0.0
200.0	$2.59 \cdot 10^{-3}$	$1.15 \cdot 10^{-3}$	$2.88 \cdot 10^{-4}$	$5.75 \cdot 10^{-4}$	$8.89 \cdot 10^{-2}$	$4.18 \cdot 10^{-2}$	$9.87 \cdot 10^{-3}$	$8.73 \cdot 10^{-3}$	± 0.0
202.0	$2.64 \cdot 10^{-3}$	$1.17 \cdot 10^{-3}$	$2.93 \cdot 10^{-4}$	$5.86 \cdot 10^{-4}$	$8.86 \cdot 10^{-2}$	$4.17 \cdot 10^{-2}$	$9.84 \cdot 10^{-3}$	$8.67 \cdot 10^{-3}$	± 0.0
204.0	$2.68 \cdot 10^{-3}$	$1.19 \cdot 10^{-3}$	$2.98 \cdot 10^{-4}$	$5.96 \cdot 10^{-4}$	$8.83 \cdot 10^{-2}$	$4.16 \cdot 10^{-2}$	$9.81 \cdot 10^{-3}$	$8.62 \cdot 10^{-3}$	± 0.0
206.0	$2.72 \cdot 10^{-3}$	$1.21 \cdot 10^{-3}$	$3.02 \cdot 10^{-4}$	$6.04 \cdot 10^{-4}$	$8.81 \cdot 10^{-2}$	$4.16 \cdot 10^{-2}$	$9.78 \cdot 10^{-3}$	$8.58 \cdot 10^{-3}$	± 0.0
208.0	$2.75 \cdot 10^{-3}$	$1.22 \cdot 10^{-3}$	$3.05 \cdot 10^{-4}$	$6.11 \cdot 10^{-4}$	$8.79 \cdot 10^{-2}$	$4.15 \cdot 10^{-2}$	$9.76 \cdot 10^{-3}$	$8.55 \cdot 10^{-3}$	± 0.0
210.0	$2.78 \cdot 10^{-3}$	$1.23 \cdot 10^{-3}$	$3.08 \cdot 10^{-4}$	$6.17 \cdot 10^{-4}$	$8.77 \cdot 10^{-2}$	$4.14 \cdot 10^{-2}$	$9.74 \cdot 10^{-3}$	$8.52 \cdot 10^{-3}$	± 0.0
212.0	$2.80 \cdot 10^{-3}$	$1.24 \cdot 10^{-3}$	$3.11 \cdot 10^{-4}$	$6.22 \cdot 10^{-4}$	$8.76 \cdot 10^{-2}$	$4.14 \cdot 10^{-2}$	$9.73 \cdot 10^{-3}$	$8.49 \cdot 10^{-3}$	± 0.0
214.0	$2.82 \cdot 10^{-3}$	$1.25 \cdot 10^{-3}$	$3.13 \cdot 10^{-4}$	$6.27 \cdot 10^{-4}$	$8.74 \cdot 10^{-2}$	$4.14 \cdot 10^{-2}$	$9.71 \cdot 10^{-3}$	$8.47 \cdot 10^{-3}$	± 0.0
216.0	$2.84 \cdot 10^{-3}$	$1.26 \cdot 10^{-3}$	$3.16 \cdot 10^{-4}$	$6.31 \cdot 10^{-4}$	$8.73 \cdot 10^{-2}$	$4.13 \cdot 10^{-2}$	$9.70 \cdot 10^{-3}$	$8.45 \cdot 10^{-3}$	± 0.0
218.0	$2.86 \cdot 10^{-3}$	$1.27 \cdot 10^{-3}$	$3.17 \cdot 10^{-4}$	$6.35 \cdot 10^{-4}$	$8.72 \cdot 10^{-2}$	$4.13 \cdot 10^{-2}$	$9.69 \cdot 10^{-3}$	$8.43 \cdot 10^{-3}$	± 0.0
220.0	$2.87 \cdot 10^{-3}$	$1.28 \cdot 10^{-3}$	$3.19 \cdot 10^{-4}$	$6.38 \cdot 10^{-4}$	$8.71 \cdot 10^{-2}$	$4.13 \cdot 10^{-2}$	$9.68 \cdot 10^{-3}$	$8.41 \cdot 10^{-3}$	± 0.0
222.0	$2.89 \cdot 10^{-3}$	$1.28 \cdot 10^{-3}$	$3.21 \cdot 10^{-4}$	$6.41 \cdot 10^{-4}$	$8.70 \cdot 10^{-2}$	$4.12 \cdot 10^{-2}$	$9.67 \cdot 10^{-3}$	$8.39 \cdot 10^{-3}$	± 0.0
224.0	$2.90 \cdot 10^{-3}$	$1.29 \cdot 10^{-3}$	$3.22 \cdot 10^{-4}$	$6.44 \cdot 10^{-4}$	$8.70 \cdot 10^{-2}$	$4.12 \cdot 10^{-2}$	$9.66 \cdot 10^{-3}$	$8.38 \cdot 10^{-3}$	± 0.0
226.0	$2.91 \cdot 10^{-3}$	$1.29 \cdot 10^{-3}$	$3.24 \cdot 10^{-4}$	$6.47 \cdot 10^{-4}$	$8.69 \cdot 10^{-2}$	$4.12 \cdot 10^{-2}$	$9.65 \cdot 10^{-3}$	$8.36 \cdot 10^{-3}$	± 0.0
228.0	$2.92 \cdot 10^{-3}$	$1.30 \cdot 10^{-3}$	$3.25 \cdot 10^{-4}$	$6.49 \cdot 10^{-4}$	$8.68 \cdot 10^{-2}$	$4.12 \cdot 10^{-2}$	$9.65 \cdot 10^{-3}$	$8.35 \cdot 10^{-3}$	± 0.0
230.0	$2.93 \cdot 10^{-3}$	$1.30 \cdot 10^{-3}$	$3.26 \cdot 10^{-4}$	$6.52 \cdot 10^{-4}$	$8.68 \cdot 10^{-2}$	$4.12 \cdot 10^{-2}$	$9.64 \cdot 10^{-3}$	$8.34 \cdot 10^{-3}$	± 0.0
232.0	$2.94 \cdot 10^{-3}$	$1.31 \cdot 10^{-3}$	$3.27 \cdot 10^{-4}$	$6.54 \cdot 10^{-4}$	$8.67 \cdot 10^{-2}$	$4.11 \cdot 10^{-2}$	$9.63 \cdot 10^{-3}$	$8.33 \cdot 10^{-3}$	± 0.0
234.0	$2.95 \cdot 10^{-3}$	$1.31 \cdot 10^{-3}$	$3.28 \cdot 10^{-4}$	$6.56 \cdot 10^{-4}$	$8.67 \cdot 10^{-2}$	$4.11 \cdot 10^{-2}$	$9.63 \cdot 10^{-3}$	$8.32 \cdot 10^{-3}$	± 0.0
236.0	$2.96 \cdot 10^{-3}$	$1.32 \cdot 10^{-3}$	$3.29 \cdot 10^{-4}$	$6.58 \cdot 10^{-4}$	$8.66 \cdot 10^{-2}$	$4.11 \cdot 10^{-2}$	$9.62 \cdot 10^{-3}$	$8.31 \cdot 10^{-3}$	± 0.0
238.0	$2.97 \cdot 10^{-3}$	$1.32 \cdot 10^{-3}$	$3.30 \cdot 10^{-4}$	$6.59 \cdot 10^{-4}$	$8.66 \cdot 10^{-2}$	$4.11 \cdot 10^{-2}$	$9.62 \cdot 10^{-3}$	$8.30 \cdot 10^{-3}$	± 0.0
240.0	$2.97 \cdot 10^{-3}$	$1.32 \cdot 10^{-3}$	$3.31 \cdot 10^{-4}$	$6.61 \cdot 10^{-4}$	$8.65 \cdot 10^{-2}$	$4.11 \cdot 10^{-2}$	$9.61 \cdot 10^{-3}$	$8.29 \cdot 10^{-3}$	± 0.0
242.0	$2.98 \cdot 10^{-3}$	$1.32 \cdot 10^{-3}$	$3.31 \cdot 10^{-4}$	$6.62 \cdot 10^{-4}$	$8.65 \cdot 10^{-2}$	$4.11 \cdot 10^{-2}$	$9.61 \cdot 10^{-3}$	$8.29 \cdot 10^{-3}$	± 0.0
244.0	$2.99 \cdot 10^{-3}$	$1.33 \cdot 10^{-3}$	$3.32 \cdot 10^{-4}$	$6.64 \cdot 10^{-4}$	$8.64 \cdot 10^{-2}$	$4.11 \cdot 10^{-2}$	$9.60 \cdot 10^{-3}$	$8.28 \cdot 10^{-3}$	± 0.0
246.0	$2.99 \cdot 10^{-3}$	$1.33 \cdot 10^{-3}$	$3.33 \cdot 10^{-4}$	$6.65 \cdot 10^{-4}$	$8.64 \cdot 10^{-2}$	$4.10 \cdot 10^{-2}$	$9.60 \cdot 10^{-3}$	$8.27 \cdot 10^{-3}$	± 0.0
248.0	$3.00 \cdot 10^{-3}$	$1.33 \cdot 10^{-3}$	$3.33 \cdot 10^{-4}$	$6.67 \cdot 10^{-4}$	$8.64 \cdot 10^{-2}$	$4.10 \cdot 10^{-2}$	$9.59 \cdot 10^{-3}$	$8.27 \cdot 10^{-3}$	± 0.0
250.0	$3.01 \cdot 10^{-3}$	$1.34 \cdot 10^{-3}$	$3.34 \cdot 10^{-4}$	$6.68 \cdot 10^{-4}$	$8.63 \cdot 10^{-2}$	$4.10 \cdot 10^{-2}$	$9.59 \cdot 10^{-3}$	$8.26 \cdot 10^{-3}$	± 0.0
252.0	$3.01 \cdot 10^{-3}$	$1.34 \cdot 10^{-3}$	$3.35 \cdot 10^{-4}$	$6.69 \cdot 10^{-4}$	$8.63 \cdot 10^{-2}$	$4.10 \cdot 10^{-2}$	$9.59 \cdot 10^{-3}$	$8.25 \cdot 10^{-3}$	± 0.0
254.0	$3.02 \cdot 10^{-3}$	$1.34 \cdot 10^{-3}$	$3.35 \cdot 10^{-4}$	$6.70 \cdot 10^{-4}$	$8.62 \cdot 10^{-2}$	$4.10 \cdot 10^{-2}$	$9.58 \cdot 10^{-3}$	$8.25 \cdot 10^{-3}$	± 0.0
256.0	$3.02 \cdot 10^{-3}$	$1.34 \cdot 10^{-3}$	$3.36 \cdot 10^{-4}$	$6.71 \cdot 10^{-4}$	$8.62 \cdot 10^{-2}$	$4.10 \cdot 10^{-2}$	$9.58 \cdot 10^{-3}$	$8.24 \cdot 10^{-3}$	± 0.0
258.0	$3.03 \cdot 10^{-3}$	$1.35 \cdot 10^{-3}$	$3.37 \cdot 10^{-4}$	$6.73 \cdot 10^{-4}$	$8.62 \cdot 10^{-2}$	$4.10 \cdot 10^{-2}$	$9.58 \cdot 10^{-3}$	$8.24 \cdot 10^{-3}$	± 0.0
260.0	$3.03 \cdot 10^{-3}$	$1.35 \cdot 10^{-3}$	$3.37 \cdot 10^{-4}$	$6.74 \cdot 10^{-4}$	$8.62 \cdot 10^{-2}$	$4.10 \cdot 10^{-2}$	$9.57 \cdot 10^{-3}$	$8.23 \cdot 10^{-3}$	± 0.0

Table A.14: SM Higgs branching ratios for the different $\mathrm{H} \to 4\mathrm{l}$ and $\mathrm{H} \to 2\mathrm{l}2\nu$ final states and their total uncertainties (expressed in percentage). High-mass range.

M_{H} [GeV]	$\mathrm{H} \to 4\mathrm{l}$ $\mathrm{l} = \mathrm{e}, \mu, \tau$	$\mathrm{H} \to 4\mathrm{l}$ $\mathrm{l} = \mathrm{e}, \mu$	$\mathrm{H} \to \mathrm{eeee}$	$\mathrm{H} \to \mathrm{ee}\mu\mu$	$\mathrm{H} \to 2\mathrm{l}2\nu$ $\mathrm{l} = \mathrm{e}, \mu, \tau$ $\nu = \mathrm{any}$	$\mathrm{H} \to 2\mathrm{l}2\nu$ $\mathrm{l} = \mathrm{e}, \mu$ $\nu = \mathrm{any}$	$\mathrm{H} \to \mathrm{e}\nu\mathrm{e}\nu$	$\mathrm{H} \to \mathrm{e}\nu\mu\nu$	ΔBR [%]
262.0	$3.04 \cdot 10^{-3}$	$1.35 \cdot 10^{-3}$	$3.38 \cdot 10^{-4}$	$6.75 \cdot 10^{-4}$	$8.61 \cdot 10^{-2}$	$4.10 \cdot 10^{-2}$	$9.57 \cdot 10^{-3}$	$8.22 \cdot 10^{-3}$	± 0.0
264.0	$3.04 \cdot 10^{-3}$	$1.35 \cdot 10^{-3}$	$3.38 \cdot 10^{-4}$	$6.76 \cdot 10^{-4}$	$8.61 \cdot 10^{-2}$	$4.10 \cdot 10^{-2}$	$9.57 \cdot 10^{-3}$	$8.22 \cdot 10^{-3}$	± 0.0
266.0	$3.05 \cdot 10^{-3}$	$1.35 \cdot 10^{-3}$	$3.39 \cdot 10^{-4}$	$6.77 \cdot 10^{-4}$	$8.61 \cdot 10^{-2}$	$4.09 \cdot 10^{-2}$	$9.56 \cdot 10^{-3}$	$8.21 \cdot 10^{-3}$	± 0.0
268.0	$3.05 \cdot 10^{-3}$	$1.36 \cdot 10^{-3}$	$3.39 \cdot 10^{-4}$	$6.78 \cdot 10^{-4}$	$8.60 \cdot 10^{-2}$	$4.09 \cdot 10^{-2}$	$9.56 \cdot 10^{-3}$	$8.21 \cdot 10^{-3}$	± 0.0
270.0	$3.05 \cdot 10^{-3}$	$1.36 \cdot 10^{-3}$	$3.40 \cdot 10^{-4}$	$6.79 \cdot 10^{-4}$	$8.60 \cdot 10^{-2}$	$4.09 \cdot 10^{-2}$	$9.56 \cdot 10^{-3}$	$8.21 \cdot 10^{-3}$	± 0.0
272.0	$3.06 \cdot 10^{-3}$	$1.36 \cdot 10^{-3}$	$3.40 \cdot 10^{-4}$	$6.80 \cdot 10^{-4}$	$8.60 \cdot 10^{-2}$	$4.09 \cdot 10^{-2}$	$9.55 \cdot 10^{-3}$	$8.20 \cdot 10^{-3}$	± 0.0
274.0	$3.06 \cdot 10^{-3}$	$1.36 \cdot 10^{-3}$	$3.40 \cdot 10^{-4}$	$6.80 \cdot 10^{-4}$	$8.60 \cdot 10^{-2}$	$4.09 \cdot 10^{-2}$	$9.55 \cdot 10^{-3}$	$8.20 \cdot 10^{-3}$	± 0.0
276.0	$3.07 \cdot 10^{-3}$	$1.36 \cdot 10^{-3}$	$3.41 \cdot 10^{-4}$	$6.81 \cdot 10^{-4}$	$8.59 \cdot 10^{-2}$	$4.09 \cdot 10^{-2}$	$9.55 \cdot 10^{-3}$	$8.19 \cdot 10^{-3}$	± 0.0
278.0	$3.07 \cdot 10^{-3}$	$1.36 \cdot 10^{-3}$	$3.41 \cdot 10^{-4}$	$6.82 \cdot 10^{-4}$	$8.59 \cdot 10^{-2}$	$4.09 \cdot 10^{-2}$	$9.55 \cdot 10^{-3}$	$8.19 \cdot 10^{-3}$	± 0.0
280.0	$3.07 \cdot 10^{-3}$	$1.37 \cdot 10^{-3}$	$3.42 \cdot 10^{-4}$	$6.83 \cdot 10^{-4}$	$8.59 \cdot 10^{-2}$	$4.09 \cdot 10^{-2}$	$9.54 \cdot 10^{-3}$	$8.18 \cdot 10^{-3}$	± 0.0
282.0	$3.08 \cdot 10^{-3}$	$1.37 \cdot 10^{-3}$	$3.42 \cdot 10^{-4}$	$6.84 \cdot 10^{-4}$	$8.59 \cdot 10^{-2}$	$4.09 \cdot 10^{-2}$	$9.54 \cdot 10^{-3}$	$8.18 \cdot 10^{-3}$	± 0.0
284.0	$3.08 \cdot 10^{-3}$	$1.37 \cdot 10^{-3}$	$3.43 \cdot 10^{-4}$	$6.85 \cdot 10^{-4}$	$8.59 \cdot 10^{-2}$	$4.09 \cdot 10^{-2}$	$9.54 \cdot 10^{-3}$	$8.18 \cdot 10^{-3}$	± 0.0
286.0	$3.08 \cdot 10^{-3}$	$1.37 \cdot 10^{-3}$	$3.43 \cdot 10^{-4}$	$6.85 \cdot 10^{-4}$	$8.58 \cdot 10^{-2}$	$4.09 \cdot 10^{-2}$	$9.54 \cdot 10^{-3}$	$8.17 \cdot 10^{-3}$	± 0.0
288.0	$3.09 \cdot 10^{-3}$	$1.37 \cdot 10^{-3}$	$3.43 \cdot 10^{-4}$	$6.86 \cdot 10^{-4}$	$8.58 \cdot 10^{-2}$	$4.09 \cdot 10^{-2}$	$9.53 \cdot 10^{-3}$	$8.17 \cdot 10^{-3}$	± 0.0
290.0	$3.09 \cdot 10^{-3}$	$1.37 \cdot 10^{-3}$	$3.44 \cdot 10^{-4}$	$6.87 \cdot 10^{-4}$	$8.58 \cdot 10^{-2}$	$4.09 \cdot 10^{-2}$	$9.53 \cdot 10^{-3}$	$8.16 \cdot 10^{-3}$	± 0.0
295.0	$3.10 \cdot 10^{-3}$	$1.38 \cdot 10^{-3}$	$3.45 \cdot 10^{-4}$	$6.88 \cdot 10^{-4}$	$8.57 \cdot 10^{-2}$	$4.08 \cdot 10^{-2}$	$9.53 \cdot 10^{-3}$	$8.15 \cdot 10^{-3}$	± 0.0
300.0	$3.11 \cdot 10^{-3}$	$1.38 \cdot 10^{-3}$	$3.45 \cdot 10^{-4}$	$6.90 \cdot 10^{-4}$	$8.57 \cdot 10^{-2}$	$4.08 \cdot 10^{-2}$	$9.52 \cdot 10^{-3}$	$8.15 \cdot 10^{-3}$	± 0.0
305.0	$3.11 \cdot 10^{-3}$	$1.38 \cdot 10^{-3}$	$3.46 \cdot 10^{-4}$	$6.92 \cdot 10^{-4}$	$8.56 \cdot 10^{-2}$	$4.08 \cdot 10^{-2}$	$9.52 \cdot 10^{-3}$	$8.14 \cdot 10^{-3}$	± 0.0
310.0	$3.12 \cdot 10^{-3}$	$1.39 \cdot 10^{-3}$	$3.47 \cdot 10^{-4}$	$6.93 \cdot 10^{-4}$	$8.56 \cdot 10^{-2}$	$4.08 \cdot 10^{-2}$	$9.51 \cdot 10^{-3}$	$8.13 \cdot 10^{-3}$	± 0.0
315.0	$3.13 \cdot 10^{-3}$	$1.39 \cdot 10^{-3}$	$3.48 \cdot 10^{-4}$	$6.94 \cdot 10^{-4}$	$8.56 \cdot 10^{-2}$	$4.08 \cdot 10^{-2}$	$9.51 \cdot 10^{-3}$	$8.12 \cdot 10^{-3}$	± 0.0
320.0	$3.13 \cdot 10^{-3}$	$1.39 \cdot 10^{-3}$	$3.48 \cdot 10^{-4}$	$6.96 \cdot 10^{-4}$	$8.55 \cdot 10^{-2}$	$4.08 \cdot 10^{-2}$	$9.50 \cdot 10^{-3}$	$8.11 \cdot 10^{-3}$	± 0.0
325.0	$3.14 \cdot 10^{-3}$	$1.39 \cdot 10^{-3}$	$3.49 \cdot 10^{-4}$	$6.97 \cdot 10^{-4}$	$8.55 \cdot 10^{-2}$	$4.08 \cdot 10^{-2}$	$9.49 \cdot 10^{-3}$	$8.11 \cdot 10^{-3}$	± 0.0
330.0	$3.14 \cdot 10^{-3}$	$1.40 \cdot 10^{-3}$	$3.49 \cdot 10^{-4}$	$6.98 \cdot 10^{-4}$	$8.54 \cdot 10^{-2}$	$4.07 \cdot 10^{-2}$	$9.49 \cdot 10^{-3}$	$8.10 \cdot 10^{-3}$	± 0.0
335.0	$3.14 \cdot 10^{-3}$	$1.40 \cdot 10^{-3}$	$3.50 \cdot 10^{-4}$	$6.99 \cdot 10^{-4}$	$8.54 \cdot 10^{-2}$	$4.07 \cdot 10^{-2}$	$9.48 \cdot 10^{-3}$	$8.09 \cdot 10^{-3}$	± 0.0
340.0	$3.15 \cdot 10^{-3}$	$1.40 \cdot 10^{-3}$	$3.50 \cdot 10^{-4}$	$6.99 \cdot 10^{-4}$	$8.53 \cdot 10^{-2}$	$4.07 \cdot 10^{-2}$	$9.48 \cdot 10^{-3}$	$8.08 \cdot 10^{-3}$	± 0.0
345.0	$3.14 \cdot 10^{-3}$	$1.40 \cdot 10^{-3}$	$3.49 \cdot 10^{-4}$	$6.98 \cdot 10^{-4}$	$8.51 \cdot 10^{-2}$	$4.06 \cdot 10^{-2}$	$9.45 \cdot 10^{-3}$	$8.06 \cdot 10^{-3}$	± 0.7
350.0	$3.11 \cdot 10^{-3}$	$1.38 \cdot 10^{-3}$	$3.45 \cdot 10^{-4}$	$6.90 \cdot 10^{-4}$	$8.40 \cdot 10^{-2}$	$4.01 \cdot 10^{-2}$	$9.33 \cdot 10^{-3}$	$7.96 \cdot 10^{-3}$	± 1.4
360.0	$3.00 \cdot 10^{-3}$	$1.33 \cdot 10^{-3}$	$3.34 \cdot 10^{-4}$	$6.67 \cdot 10^{-4}$	$8.09 \cdot 10^{-2}$	$3.86 \cdot 10^{-2}$	$8.99 \cdot 10^{-3}$	$7.66 \cdot 10^{-3}$	± 2.6
370.0	$2.91 \cdot 10^{-3}$	$1.29 \cdot 10^{-3}$	$3.23 \cdot 10^{-4}$	$6.46 \cdot 10^{-4}$	$7.82 \cdot 10^{-2}$	$3.73 \cdot 10^{-2}$	$8.68 \cdot 10^{-3}$	$7.40 \cdot 10^{-3}$	± 2.9
380.0	$2.83 \cdot 10^{-3}$	$1.26 \cdot 10^{-3}$	$3.15 \cdot 10^{-4}$	$6.29 \cdot 10^{-4}$	$7.59 \cdot 10^{-2}$	$3.62 \cdot 10^{-2}$	$8.43 \cdot 10^{-3}$	$7.18 \cdot 10^{-3}$	± 3.1
390.0	$2.77 \cdot 10^{-3}$	$1.23 \cdot 10^{-3}$	$3.08 \cdot 10^{-4}$	$6.16 \cdot 10^{-4}$	$7.40 \cdot 10^{-2}$	$3.54 \cdot 10^{-2}$	$8.23 \cdot 10^{-3}$	$7.00 \cdot 10^{-3}$	± 3.1
400.0	$2.73 \cdot 10^{-3}$	$1.21 \cdot 10^{-3}$	$3.03 \cdot 10^{-4}$	$6.06 \cdot 10^{-4}$	$7.26 \cdot 10^{-2}$	$3.47 \cdot 10^{-2}$	$8.06 \cdot 10^{-3}$	$6.86 \cdot 10^{-3}$	± 3.1
410.0	$2.69 \cdot 10^{-3}$	$1.20 \cdot 10^{-3}$	$2.99 \cdot 10^{-4}$	$5.98 \cdot 10^{-4}$	$7.14 \cdot 10^{-2}$	$3.41 \cdot 10^{-2}$	$7.94 \cdot 10^{-3}$	$6.75 \cdot 10^{-3}$	± 3.1
420.0	$2.67 \cdot 10^{-3}$	$1.19 \cdot 10^{-3}$	$2.96 \cdot 10^{-4}$	$5.93 \cdot 10^{-4}$	$7.06 \cdot 10^{-2}$	$3.37 \cdot 10^{-2}$	$7.84 \cdot 10^{-3}$	$6.66 \cdot 10^{-3}$	± 3.1
430.0	$2.65 \cdot 10^{-3}$	$1.18 \cdot 10^{-3}$	$2.94 \cdot 10^{-4}$	$5.89 \cdot 10^{-4}$	$6.99 \cdot 10^{-2}$	$3.34 \cdot 10^{-2}$	$7.76 \cdot 10^{-3}$	$6.59 \cdot 10^{-3}$	± 3.0
440.0	$2.64 \cdot 10^{-3}$	$1.17 \cdot 10^{-3}$	$2.93 \cdot 10^{-4}$	$5.86 \cdot 10^{-4}$	$6.94 \cdot 10^{-2}$	$3.32 \cdot 10^{-2}$	$7.71 \cdot 10^{-3}$	$6.54 \cdot 10^{-3}$	± 3.0
450.0	$2.63 \cdot 10^{-3}$	$1.17 \cdot 10^{-3}$	$2.92 \cdot 10^{-4}$	$5.85 \cdot 10^{-4}$	$6.90 \cdot 10^{-2}$	$3.30 \cdot 10^{-2}$	$7.67 \cdot 10^{-3}$	$6.50 \cdot 10^{-3}$	± 2.9
460.0	$2.63 \cdot 10^{-3}$	$1.17 \cdot 10^{-3}$	$2.92 \cdot 10^{-4}$	$5.84 \cdot 10^{-4}$	$6.88 \cdot 10^{-2}$	$3.29 \cdot 10^{-2}$	$7.64 \cdot 10^{-3}$	$6.48 \cdot 10^{-3}$	± 2.8
470.0	$2.63 \cdot 10^{-3}$	$1.17 \cdot 10^{-3}$	$2.92 \cdot 10^{-4}$	$5.84 \cdot 10^{-4}$	$6.86 \cdot 10^{-2}$	$3.28 \cdot 10^{-2}$	$7.62 \cdot 10^{-3}$	$6.46 \cdot 10^{-3}$	± 2.8
480.0	$2.63 \cdot 10^{-3}$	$1.17 \cdot 10^{-3}$	$2.93 \cdot 10^{-4}$	$5.85 \cdot 10^{-4}$	$6.85 \cdot 10^{-2}$	$3.28 \cdot 10^{-2}$	$7.61 \cdot 10^{-3}$	$6.45 \cdot 10^{-3}$	± 2.7
490.0	$2.64 \cdot 10^{-3}$	$1.17 \cdot 10^{-3}$	$2.93 \cdot 10^{-4}$	$5.87 \cdot 10^{-4}$	$6.85 \cdot 10^{-2}$	$3.28 \cdot 10^{-2}$	$7.61 \cdot 10^{-3}$	$6.44 \cdot 10^{-3}$	± 2.6
500.0	$2.65 \cdot 10^{-3}$	$1.18 \cdot 10^{-3}$	$2.94 \cdot 10^{-4}$	$5.88 \cdot 10^{-4}$	$6.85 \cdot 10^{-2}$	$3.28 \cdot 10^{-2}$	$7.61 \cdot 10^{-3}$	$6.44 \cdot 10^{-3}$	± 2.4
510.0	$2.66 \cdot 10^{-3}$	$1.18 \cdot 10^{-3}$	$2.95 \cdot 10^{-4}$	$5.90 \cdot 10^{-4}$	$6.86 \cdot 10^{-2}$	$3.28 \cdot 10^{-2}$	$7.62 \cdot 10^{-3}$	$6.45 \cdot 10^{-3}$	± 2.3
520.0	$2.67 \cdot 10^{-3}$	$1.18 \cdot 10^{-3}$	$2.96 \cdot 10^{-4}$	$5.92 \cdot 10^{-4}$	$6.87 \cdot 10^{-2}$	$3.29 \cdot 10^{-2}$	$7.64 \cdot 10^{-3}$	$6.46 \cdot 10^{-3}$	± 2.4
530.0	$2.68 \cdot 10^{-3}$	$1.19 \cdot 10^{-3}$	$2.97 \cdot 10^{-4}$	$5.95 \cdot 10^{-4}$	$6.89 \cdot 10^{-2}$	$3.30 \cdot 10^{-2}$	$7.65 \cdot 10^{-3}$	$6.47 \cdot 10^{-3}$	± 2.4
540.0	$2.69 \cdot 10^{-3}$	$1.19 \cdot 10^{-3}$	$2.99 \cdot 10^{-4}$	$5.97 \cdot 10^{-4}$	$6.90 \cdot 10^{-2}$	$3.31 \cdot 10^{-2}$	$7.67 \cdot 10^{-3}$	$6.48 \cdot 10^{-3}$	± 2.4

Table A.15: SM Higgs branching ratios for the different $\mathrm{H} \to 4\mathrm{l}$ and $\mathrm{H} \to 2\mathrm{l}2\nu$ final states and their total uncertainties (expressed in percentage). Very-high-mass range.

M_{H} [GeV]	$\mathrm{H} \to 4\mathrm{l}$ $\mathrm{l} = \mathrm{e}, \mu, \tau$	$\mathrm{H} \to 4\mathrm{l}$ $\mathrm{l} = \mathrm{e}, \mu$	$\mathrm{H} \to \mathrm{eeee}$	$\mathrm{H} \to \mathrm{ee}\mu\mu$	$\mathrm{H} \to 2\mathrm{l}2\nu$ $\mathrm{l} = \mathrm{e}, \mu, \tau$ $\nu = \mathrm{any}$	$\mathrm{H} \to 2\mathrm{l}2\nu$ $\mathrm{l} = \mathrm{e}, \mu$ $\nu = \mathrm{any}$	$\mathrm{H} \to \mathrm{e}\nu\mathrm{e}\nu$	$\mathrm{H} \to \mathrm{e}\nu\mu\nu$	ΔBR [%]
550.0	$2.70 \cdot 10^{-3}$	$1.20 \cdot 10^{-3}$	$3.00 \cdot 10^{-4}$	$6.00 \cdot 10^{-4}$	$6.92 \cdot 10^{-2}$	$3.32 \cdot 10^{-2}$	$7.69 \cdot 10^{-3}$	$6.50 \cdot 10^{-3}$	± 2.4
560.0	$2.71 \cdot 10^{-3}$	$1.21 \cdot 10^{-3}$	$3.01 \cdot 10^{-4}$	$6.03 \cdot 10^{-4}$	$6.94 \cdot 10^{-2}$	$3.33 \cdot 10^{-2}$	$7.71 \cdot 10^{-3}$	$6.51 \cdot 10^{-3}$	± 2.5
570.0	$2.73 \cdot 10^{-3}$	$1.21 \cdot 10^{-3}$	$3.03 \cdot 10^{-4}$	$6.06 \cdot 10^{-4}$	$6.96 \cdot 10^{-2}$	$3.34 \cdot 10^{-2}$	$7.74 \cdot 10^{-3}$	$6.53 \cdot 10^{-3}$	± 2.5
580.0	$2.74 \cdot 10^{-3}$	$1.22 \cdot 10^{-3}$	$3.04 \cdot 10^{-4}$	$6.09 \cdot 10^{-4}$	$6.99 \cdot 10^{-2}$	$3.35 \cdot 10^{-2}$	$7.76 \cdot 10^{-3}$	$6.55 \cdot 10^{-3}$	± 2.5
590.0	$2.75 \cdot 10^{-3}$	$1.22 \cdot 10^{-3}$	$3.06 \cdot 10^{-4}$	$6.12 \cdot 10^{-4}$	$7.01 \cdot 10^{-2}$	$3.36 \cdot 10^{-2}$	$7.79 \cdot 10^{-3}$	$6.57 \cdot 10^{-3}$	± 2.5
600.0	$2.77 \cdot 10^{-3}$	$1.23 \cdot 10^{-3}$	$3.07 \cdot 10^{-4}$	$6.15 \cdot 10^{-4}$	$7.03 \cdot 10^{-2}$	$3.37 \cdot 10^{-2}$	$7.82 \cdot 10^{-3}$	$6.59 \cdot 10^{-3}$	± 2.5
610.0	$2.78 \cdot 10^{-3}$	$1.24 \cdot 10^{-3}$	$3.09 \cdot 10^{-4}$	$6.18 \cdot 10^{-4}$	$7.06 \cdot 10^{-2}$	$3.38 \cdot 10^{-2}$	$7.84 \cdot 10^{-3}$	$6.61 \cdot 10^{-3}$	± 2.5
620.0	$2.79 \cdot 10^{-3}$	$1.24 \cdot 10^{-3}$	$3.10 \cdot 10^{-4}$	$6.21 \cdot 10^{-4}$	$7.08 \cdot 10^{-2}$	$3.40 \cdot 10^{-2}$	$7.87 \cdot 10^{-3}$	$6.64 \cdot 10^{-3}$	± 2.6
630.0	$2.81 \cdot 10^{-3}$	$1.25 \cdot 10^{-3}$	$3.12 \cdot 10^{-4}$	$6.24 \cdot 10^{-4}$	$7.11 \cdot 10^{-2}$	$3.41 \cdot 10^{-2}$	$7.90 \cdot 10^{-3}$	$6.66 \cdot 10^{-3}$	± 2.5
640.0	$2.82 \cdot 10^{-3}$	$1.25 \cdot 10^{-3}$	$3.13 \cdot 10^{-4}$	$6.27 \cdot 10^{-4}$	$7.14 \cdot 10^{-2}$	$3.42 \cdot 10^{-2}$	$7.93 \cdot 10^{-3}$	$6.68 \cdot 10^{-3}$	± 2.6
650.0	$2.83 \cdot 10^{-3}$	$1.26 \cdot 10^{-3}$	$3.15 \cdot 10^{-4}$	$6.29 \cdot 10^{-4}$	$7.16 \cdot 10^{-2}$	$3.43 \cdot 10^{-2}$	$7.96 \cdot 10^{-3}$	$6.71 \cdot 10^{-3}$	± 2.6
660.0	$2.85 \cdot 10^{-3}$	$1.26 \cdot 10^{-3}$	$3.16 \cdot 10^{-4}$	$6.32 \cdot 10^{-4}$	$7.19 \cdot 10^{-2}$	$3.45 \cdot 10^{-2}$	$7.99 \cdot 10^{-3}$	$6.73 \cdot 10^{-3}$	± 2.6
670.0	$2.86 \cdot 10^{-3}$	$1.27 \cdot 10^{-3}$	$3.18 \cdot 10^{-4}$	$6.35 \cdot 10^{-4}$	$7.21 \cdot 10^{-2}$	$3.46 \cdot 10^{-2}$	$8.02 \cdot 10^{-3}$	$6.75 \cdot 10^{-3}$	± 2.6
680.0	$2.87 \cdot 10^{-3}$	$1.28 \cdot 10^{-3}$	$3.19 \cdot 10^{-4}$	$6.38 \cdot 10^{-4}$	$7.24 \cdot 10^{-2}$	$3.47 \cdot 10^{-2}$	$8.04 \cdot 10^{-3}$	$6.77 \cdot 10^{-3}$	± 2.6
690.0	$2.88 \cdot 10^{-3}$	$1.28 \cdot 10^{-3}$	$3.20 \cdot 10^{-4}$	$6.41 \cdot 10^{-4}$	$7.26 \cdot 10^{-2}$	$3.48 \cdot 10^{-2}$	$8.07 \cdot 10^{-3}$	$6.80 \cdot 10^{-3}$	± 2.6
700.0	$2.90 \cdot 10^{-3}$	$1.29 \cdot 10^{-3}$	$3.22 \cdot 10^{-4}$	$6.44 \cdot 10^{-4}$	$7.29 \cdot 10^{-2}$	$3.50 \cdot 10^{-2}$	$8.10 \cdot 10^{-3}$	$6.82 \cdot 10^{-3}$	± 2.6
710.0	$2.91 \cdot 10^{-3}$	$1.29 \cdot 10^{-3}$	$3.23 \cdot 10^{-4}$	$6.46 \cdot 10^{-4}$	$7.31 \cdot 10^{-2}$	$3.51 \cdot 10^{-2}$	$8.13 \cdot 10^{-3}$	$6.84 \cdot 10^{-3}$	± 2.6
720.0	$2.92 \cdot 10^{-3}$	$1.30 \cdot 10^{-3}$	$3.24 \cdot 10^{-4}$	$6.49 \cdot 10^{-4}$	$7.34 \cdot 10^{-2}$	$3.52 \cdot 10^{-2}$	$8.16 \cdot 10^{-3}$	$6.86 \cdot 10^{-3}$	± 2.6
730.0	$2.93 \cdot 10^{-3}$	$1.30 \cdot 10^{-3}$	$3.26 \cdot 10^{-4}$	$6.52 \cdot 10^{-4}$	$7.37 \cdot 10^{-2}$	$3.53 \cdot 10^{-2}$	$8.18 \cdot 10^{-3}$	$6.89 \cdot 10^{-3}$	± 2.6
740.0	$2.94 \cdot 10^{-3}$	$1.31 \cdot 10^{-3}$	$3.27 \cdot 10^{-4}$	$6.54 \cdot 10^{-4}$	$7.39 \cdot 10^{-2}$	$3.54 \cdot 10^{-2}$	$8.21 \cdot 10^{-3}$	$6.91 \cdot 10^{-3}$	± 2.6
750.0	$2.95 \cdot 10^{-3}$	$1.31 \cdot 10^{-3}$	$3.28 \cdot 10^{-4}$	$6.57 \cdot 10^{-4}$	$7.41 \cdot 10^{-2}$	$3.56 \cdot 10^{-2}$	$8.24 \cdot 10^{-3}$	$6.93 \cdot 10^{-3}$	± 2.6
760.0	$2.97 \cdot 10^{-3}$	$1.32 \cdot 10^{-3}$	$3.30 \cdot 10^{-4}$	$6.59 \cdot 10^{-4}$	$7.44 \cdot 10^{-2}$	$3.57 \cdot 10^{-2}$	$8.26 \cdot 10^{-3}$	$6.95 \cdot 10^{-3}$	± 2.6
770.0	$2.98 \cdot 10^{-3}$	$1.32 \cdot 10^{-3}$	$3.31 \cdot 10^{-4}$	$6.62 \cdot 10^{-4}$	$7.46 \cdot 10^{-2}$	$3.58 \cdot 10^{-2}$	$8.29 \cdot 10^{-3}$	$6.97 \cdot 10^{-3}$	± 2.6
780.0	$2.99 \cdot 10^{-3}$	$1.33 \cdot 10^{-3}$	$3.32 \cdot 10^{-4}$	$6.64 \cdot 10^{-4}$	$7.48 \cdot 10^{-2}$	$3.59 \cdot 10^{-2}$	$8.32 \cdot 10^{-3}$	$6.99 \cdot 10^{-3}$	± 2.6
790.0	$3.00 \cdot 10^{-3}$	$1.33 \cdot 10^{-3}$	$3.33 \cdot 10^{-4}$	$6.67 \cdot 10^{-4}$	$7.51 \cdot 10^{-2}$	$3.60 \cdot 10^{-2}$	$8.34 \cdot 10^{-3}$	$7.02 \cdot 10^{-3}$	± 2.7
800.0	$3.01 \cdot 10^{-3}$	$1.34 \cdot 10^{-3}$	$3.34 \cdot 10^{-4}$	$6.69 \cdot 10^{-4}$	$7.53 \cdot 10^{-2}$	$3.61 \cdot 10^{-2}$	$8.37 \cdot 10^{-3}$	$7.04 \cdot 10^{-3}$	± 2.7
810.0	$3.02 \cdot 10^{-3}$	$1.34 \cdot 10^{-3}$	$3.35 \cdot 10^{-4}$	$6.71 \cdot 10^{-4}$	$7.55 \cdot 10^{-2}$	$3.62 \cdot 10^{-2}$	$8.39 \cdot 10^{-3}$	$7.06 \cdot 10^{-3}$	± 2.7
820.0	$3.03 \cdot 10^{-3}$	$1.35 \cdot 10^{-3}$	$3.37 \cdot 10^{-4}$	$6.73 \cdot 10^{-4}$	$7.57 \cdot 10^{-2}$	$3.63 \cdot 10^{-2}$	$8.42 \cdot 10^{-3}$	$7.08 \cdot 10^{-3}$	± 2.7
830.0	$3.04 \cdot 10^{-3}$	$1.35 \cdot 10^{-3}$	$3.38 \cdot 10^{-4}$	$6.75 \cdot 10^{-4}$	$7.60 \cdot 10^{-2}$	$3.64 \cdot 10^{-2}$	$8.44 \cdot 10^{-3}$	$7.10 \cdot 10^{-3}$	± 2.7
840.0	$3.05 \cdot 10^{-3}$	$1.36 \cdot 10^{-3}$	$3.39 \cdot 10^{-4}$	$6.78 \cdot 10^{-4}$	$7.62 \cdot 10^{-2}$	$3.65 \cdot 10^{-2}$	$8.46 \cdot 10^{-3}$	$7.12 \cdot 10^{-3}$	± 2.7
850.0	$3.06 \cdot 10^{-3}$	$1.36 \cdot 10^{-3}$	$3.40 \cdot 10^{-4}$	$6.80 \cdot 10^{-4}$	$7.64 \cdot 10^{-2}$	$3.67 \cdot 10^{-2}$	$8.49 \cdot 10^{-3}$	$7.13 \cdot 10^{-3}$	± 2.7
860.0	$3.07 \cdot 10^{-3}$	$1.36 \cdot 10^{-3}$	$3.41 \cdot 10^{-4}$	$6.82 \cdot 10^{-4}$	$7.66 \cdot 10^{-2}$	$3.67 \cdot 10^{-2}$	$8.51 \cdot 10^{-3}$	$7.15 \cdot 10^{-3}$	± 2.7
870.0	$3.08 \cdot 10^{-3}$	$1.37 \cdot 10^{-3}$	$3.42 \cdot 10^{-4}$	$6.84 \cdot 10^{-4}$	$7.68 \cdot 10^{-2}$	$3.68 \cdot 10^{-2}$	$8.53 \cdot 10^{-3}$	$7.17 \cdot 10^{-3}$	± 2.7
880.0	$3.09 \cdot 10^{-3}$	$1.37 \cdot 10^{-3}$	$3.43 \cdot 10^{-4}$	$6.86 \cdot 10^{-4}$	$7.70 \cdot 10^{-2}$	$3.69 \cdot 10^{-2}$	$8.55 \cdot 10^{-3}$	$7.19 \cdot 10^{-3}$	± 2.8
890.0	$3.09 \cdot 10^{-3}$	$1.38 \cdot 10^{-3}$	$3.44 \cdot 10^{-4}$	$6.88 \cdot 10^{-4}$	$7.72 \cdot 10^{-2}$	$3.70 \cdot 10^{-2}$	$8.58 \cdot 10^{-3}$	$7.21 \cdot 10^{-3}$	± 2.8
900.0	$3.10 \cdot 10^{-3}$	$1.38 \cdot 10^{-3}$	$3.45 \cdot 10^{-4}$	$6.89 \cdot 10^{-4}$	$7.74 \cdot 10^{-2}$	$3.71 \cdot 10^{-2}$	$8.60 \cdot 10^{-3}$	$7.23 \cdot 10^{-3}$	± 2.8
910.0	$3.11 \cdot 10^{-3}$	$1.38 \cdot 10^{-3}$	$3.46 \cdot 10^{-4}$	$6.91 \cdot 10^{-4}$	$7.76 \cdot 10^{-2}$	$3.72 \cdot 10^{-2}$	$8.62 \cdot 10^{-3}$	$7.24 \cdot 10^{-3}$	± 2.8
920.0	$3.12 \cdot 10^{-3}$	$1.39 \cdot 10^{-3}$	$3.47 \cdot 10^{-4}$	$6.93 \cdot 10^{-4}$	$7.78 \cdot 10^{-2}$	$3.73 \cdot 10^{-2}$	$8.64 \cdot 10^{-3}$	$7.26 \cdot 10^{-3}$	± 2.8
930.0	$3.13 \cdot 10^{-3}$	$1.39 \cdot 10^{-3}$	$3.48 \cdot 10^{-4}$	$6.95 \cdot 10^{-4}$	$7.79 \cdot 10^{-2}$	$3.74 \cdot 10^{-2}$	$8.66 \cdot 10^{-3}$	$7.28 \cdot 10^{-3}$	± 2.8
940.0	$3.14 \cdot 10^{-3}$	$1.39 \cdot 10^{-3}$	$3.48 \cdot 10^{-4}$	$6.97 \cdot 10^{-4}$	$7.81 \cdot 10^{-2}$	$3.75 \cdot 10^{-2}$	$8.68 \cdot 10^{-3}$	$7.29 \cdot 10^{-3}$	± 2.8
950.0	$3.14 \cdot 10^{-3}$	$1.40 \cdot 10^{-3}$	$3.49 \cdot 10^{-4}$	$6.98 \cdot 10^{-4}$	$7.83 \cdot 10^{-2}$	$3.76 \cdot 10^{-2}$	$8.70 \cdot 10^{-3}$	$7.31 \cdot 10^{-3}$	± 2.8
960.0	$3.15 \cdot 10^{-3}$	$1.40 \cdot 10^{-3}$	$3.50 \cdot 10^{-4}$	$7.00 \cdot 10^{-4}$	$7.85 \cdot 10^{-2}$	$3.77 \cdot 10^{-2}$	$8.72 \cdot 10^{-3}$	$7.33 \cdot 10^{-3}$	± 2.8
970.0	$3.16 \cdot 10^{-3}$	$1.40 \cdot 10^{-3}$	$3.51 \cdot 10^{-4}$	$7.02 \cdot 10^{-4}$	$7.86 \cdot 10^{-2}$	$3.77 \cdot 10^{-2}$	$8.74 \cdot 10^{-3}$	$7.34 \cdot 10^{-3}$	± 2.8
980.0	$3.17 \cdot 10^{-3}$	$1.41 \cdot 10^{-3}$	$3.52 \cdot 10^{-4}$	$7.04 \cdot 10^{-4}$	$7.88 \cdot 10^{-2}$	$3.78 \cdot 10^{-2}$	$8.76 \cdot 10^{-3}$	$7.36 \cdot 10^{-3}$	± 2.9
990.0	$3.17 \cdot 10^{-3}$	$1.41 \cdot 10^{-3}$	$3.53 \cdot 10^{-4}$	$7.05 \cdot 10^{-4}$	$7.90 \cdot 10^{-2}$	$3.79 \cdot 10^{-2}$	$8.78 \cdot 10^{-3}$	$7.37 \cdot 10^{-3}$	± 2.9
1000.0	$3.18 \cdot 10^{-3}$	$1.41 \cdot 10^{-3}$	$3.53 \cdot 10^{-4}$	$7.07 \cdot 10^{-4}$	$7.91 \cdot 10^{-2}$	$3.80 \cdot 10^{-2}$	$8.80 \cdot 10^{-3}$	$7.39 \cdot 10^{-3}$	± 2.9

Table A.16: SM Higgs branching ratios for the different four-fermion final states and their total uncertainties (expressed in percentage). Very-low-mass range.

M_{H} [GeV]	$\mathrm{H} \to 2l2q$ $l = e, \mu, \tau$ $q = udcsb$	$\mathrm{H} \to 2l2q$ $l = e, \mu$ $q = udcsb$	$\mathrm{H} \to l\nu_l qq$ $l = e, \mu$ $q = udcsb$	$\mathrm{H} \to \nu\nu qq$ $\nu =$ any $q = udcsb$	$\mathrm{H} \to 4q$ $q = udcsb$	$\mathrm{H} \to 4f$ $f =$ any fermion	ΔBR [%]
90.0	$5.87 \cdot 10^{-5}$	$3.91 \cdot 10^{-5}$	$3.03 \cdot 10^{-4}$	$1.18 \cdot 10^{-4}$	$1.05 \cdot 10^{-3}$	$2.37 \cdot 10^{-3}$	± 5.8
95.0	$9.31 \cdot 10^{-5}$	$6.21 \cdot 10^{-5}$	$6.85 \cdot 10^{-4}$	$1.87 \cdot 10^{-4}$	$2.32 \cdot 10^{-3}$	$5.17 \cdot 10^{-3}$	± 5.8
100.0	$1.57 \cdot 10^{-4}$	$1.04 \cdot 10^{-4}$	$1.61 \cdot 10^{-3}$	$3.14 \cdot 10^{-4}$	$5.34 \cdot 10^{-3}$	$1.18 \cdot 10^{-2}$	± 5.7
105.0	$2.97 \cdot 10^{-4}$	$1.98 \cdot 10^{-4}$	$3.52 \cdot 10^{-3}$	$5.95 \cdot 10^{-4}$	$1.17 \cdot 10^{-2}$	$2.58 \cdot 10^{-2}$	± 5.6
110.0	$6.06 \cdot 10^{-4}$	$4.04 \cdot 10^{-4}$	$6.99 \cdot 10^{-3}$	$1.21 \cdot 10^{-3}$	$2.34 \cdot 10^{-2}$	$5.15 \cdot 10^{-2}$	± 5.4
110.5	$6.50 \cdot 10^{-4}$	$4.34 \cdot 10^{-4}$	$7.44 \cdot 10^{-3}$	$1.30 \cdot 10^{-3}$	$2.50 \cdot 10^{-2}$	$5.49 \cdot 10^{-2}$	± 5.4
111.0	$6.98 \cdot 10^{-4}$	$4.66 \cdot 10^{-4}$	$7.92 \cdot 10^{-3}$	$1.40 \cdot 10^{-3}$	$2.66 \cdot 10^{-2}$	$5.85 \cdot 10^{-2}$	± 5.4
111.5	$7.50 \cdot 10^{-4}$	$5.00 \cdot 10^{-4}$	$8.42 \cdot 10^{-3}$	$1.50 \cdot 10^{-3}$	$2.83 \cdot 10^{-2}$	$6.23 \cdot 10^{-2}$	± 5.4
112.0	$8.04 \cdot 10^{-4}$	$5.36 \cdot 10^{-4}$	$8.94 \cdot 10^{-3}$	$1.61 \cdot 10^{-3}$	$3.01 \cdot 10^{-2}$	$6.62 \cdot 10^{-2}$	± 5.3
112.5	$8.62 \cdot 10^{-4}$	$5.75 \cdot 10^{-4}$	$9.48 \cdot 10^{-3}$	$1.72 \cdot 10^{-3}$	$3.20 \cdot 10^{-2}$	$7.03 \cdot 10^{-2}$	± 5.3
113.0	$9.23 \cdot 10^{-4}$	$6.16 \cdot 10^{-4}$	$1.01 \cdot 10^{-2}$	$1.85 \cdot 10^{-3}$	$3.40 \cdot 10^{-2}$	$7.46 \cdot 10^{-2}$	± 5.3
113.5	$9.89 \cdot 10^{-4}$	$6.59 \cdot 10^{-4}$	$1.06 \cdot 10^{-2}$	$1.98 \cdot 10^{-3}$	$3.60 \cdot 10^{-2}$	$7.91 \cdot 10^{-2}$	± 5.2
114.0	$1.06 \cdot 10^{-3}$	$7.05 \cdot 10^{-4}$	$1.13 \cdot 10^{-2}$	$2.11 \cdot 10^{-3}$	$3.81 \cdot 10^{-2}$	$8.38 \cdot 10^{-2}$	± 5.2
114.5	$1.13 \cdot 10^{-3}$	$7.54 \cdot 10^{-4}$	$1.19 \cdot 10^{-2}$	$2.26 \cdot 10^{-3}$	$4.04 \cdot 10^{-2}$	$8.87 \cdot 10^{-2}$	± 5.2
115.0	$1.21 \cdot 10^{-3}$	$8.05 \cdot 10^{-4}$	$1.26 \cdot 10^{-2}$	$2.41 \cdot 10^{-3}$	$4.27 \cdot 10^{-2}$	$9.38 \cdot 10^{-2}$	± 5.2
115.5	$1.29 \cdot 10^{-3}$	$8.59 \cdot 10^{-4}$	$1.33 \cdot 10^{-2}$	$2.58 \cdot 10^{-3}$	$4.51 \cdot 10^{-2}$	$9.90 \cdot 10^{-2}$	± 5.1
116.0	$1.37 \cdot 10^{-3}$	$9.16 \cdot 10^{-4}$	$1.40 \cdot 10^{-2}$	$2.75 \cdot 10^{-3}$	$4.76 \cdot 10^{-2}$	$1.05 \cdot 10^{-1}$	± 5.1
116.5	$1.46 \cdot 10^{-3}$	$9.76 \cdot 10^{-4}$	$1.47 \cdot 10^{-2}$	$2.93 \cdot 10^{-3}$	$5.03 \cdot 10^{-2}$	$1.10 \cdot 10^{-1}$	± 5.0
117.0	$1.56 \cdot 10^{-3}$	$1.04 \cdot 10^{-3}$	$1.55 \cdot 10^{-2}$	$3.11 \cdot 10^{-3}$	$5.30 \cdot 10^{-2}$	$1.16 \cdot 10^{-1}$	± 5.0
117.5	$1.66 \cdot 10^{-3}$	$1.10 \cdot 10^{-3}$	$1.63 \cdot 10^{-2}$	$3.31 \cdot 10^{-3}$	$5.58 \cdot 10^{-2}$	$1.22 \cdot 10^{-1}$	± 5.0
118.0	$1.76 \cdot 10^{-3}$	$1.17 \cdot 10^{-3}$	$1.71 \cdot 10^{-2}$	$3.52 \cdot 10^{-3}$	$5.87 \cdot 10^{-2}$	$1.29 \cdot 10^{-1}$	± 4.9
118.5	$1.87 \cdot 10^{-3}$	$1.25 \cdot 10^{-3}$	$1.80 \cdot 10^{-2}$	$3.73 \cdot 10^{-3}$	$6.17 \cdot 10^{-2}$	$1.35 \cdot 10^{-1}$	± 4.9
119.0	$1.98 \cdot 10^{-3}$	$1.32 \cdot 10^{-3}$	$1.89 \cdot 10^{-2}$	$3.96 \cdot 10^{-3}$	$6.48 \cdot 10^{-2}$	$1.42 \cdot 10^{-1}$	± 4.8
119.5	$2.10 \cdot 10^{-3}$	$1.40 \cdot 10^{-3}$	$1.98 \cdot 10^{-2}$	$4.19 \cdot 10^{-3}$	$6.80 \cdot 10^{-2}$	$1.49 \cdot 10^{-1}$	± 4.8
120.0	$2.22 \cdot 10^{-3}$	$1.48 \cdot 10^{-3}$	$2.07 \cdot 10^{-2}$	$4.44 \cdot 10^{-3}$	$7.13 \cdot 10^{-2}$	$1.56 \cdot 10^{-1}$	± 4.8
120.5	$2.35 \cdot 10^{-3}$	$1.57 \cdot 10^{-3}$	$2.16 \cdot 10^{-2}$	$4.69 \cdot 10^{-3}$	$7.47 \cdot 10^{-2}$	$1.64 \cdot 10^{-1}$	± 4.7
121.0	$2.48 \cdot 10^{-3}$	$1.65 \cdot 10^{-3}$	$2.26 \cdot 10^{-2}$	$4.95 \cdot 10^{-3}$	$7.82 \cdot 10^{-2}$	$1.71 \cdot 10^{-1}$	± 4.7
121.5	$2.62 \cdot 10^{-3}$	$1.74 \cdot 10^{-3}$	$2.36 \cdot 10^{-2}$	$5.22 \cdot 10^{-3}$	$8.18 \cdot 10^{-2}$	$1.79 \cdot 10^{-1}$	± 4.6
122.0	$2.76 \cdot 10^{-3}$	$1.84 \cdot 10^{-3}$	$2.47 \cdot 10^{-2}$	$5.50 \cdot 10^{-3}$	$8.55 \cdot 10^{-2}$	$1.87 \cdot 10^{-1}$	± 4.6
122.5	$2.90 \cdot 10^{-3}$	$1.94 \cdot 10^{-3}$	$2.57 \cdot 10^{-2}$	$5.80 \cdot 10^{-3}$	$8.92 \cdot 10^{-2}$	$1.95 \cdot 10^{-1}$	± 4.5
123.0	$3.06 \cdot 10^{-3}$	$2.04 \cdot 10^{-3}$	$2.68 \cdot 10^{-2}$	$6.10 \cdot 10^{-3}$	$9.31 \cdot 10^{-2}$	$2.04 \cdot 10^{-1}$	± 4.5
123.5	$3.21 \cdot 10^{-3}$	$2.14 \cdot 10^{-3}$	$2.79 \cdot 10^{-2}$	$6.40 \cdot 10^{-3}$	$9.71 \cdot 10^{-2}$	$2.13 \cdot 10^{-1}$	± 4.4
124.0	$3.37 \cdot 10^{-3}$	$2.25 \cdot 10^{-3}$	$2.91 \cdot 10^{-2}$	$6.72 \cdot 10^{-3}$	$1.01 \cdot 10^{-1}$	$2.21 \cdot 10^{-1}$	± 4.4
124.5	$3.53 \cdot 10^{-3}$	$2.36 \cdot 10^{-3}$	$3.02 \cdot 10^{-2}$	$7.05 \cdot 10^{-3}$	$1.05 \cdot 10^{-1}$	$2.30 \cdot 10^{-1}$	± 4.3
125.0	$3.70 \cdot 10^{-3}$	$2.47 \cdot 10^{-3}$	$3.14 \cdot 10^{-2}$	$7.38 \cdot 10^{-3}$	$1.10 \cdot 10^{-1}$	$2.40 \cdot 10^{-1}$	± 4.3
125.5	$3.87 \cdot 10^{-3}$	$2.58 \cdot 10^{-3}$	$3.26 \cdot 10^{-2}$	$7.73 \cdot 10^{-3}$	$1.14 \cdot 10^{-1}$	$2.49 \cdot 10^{-1}$	± 4.2
126.0	$4.05 \cdot 10^{-3}$	$2.70 \cdot 10^{-3}$	$3.38 \cdot 10^{-2}$	$8.08 \cdot 10^{-3}$	$1.18 \cdot 10^{-1}$	$2.59 \cdot 10^{-1}$	± 4.1
126.5	$4.23 \cdot 10^{-3}$	$2.82 \cdot 10^{-3}$	$3.51 \cdot 10^{-2}$	$8.44 \cdot 10^{-3}$	$1.23 \cdot 10^{-1}$	$2.68 \cdot 10^{-1}$	± 4.1
127.0	$4.42 \cdot 10^{-3}$	$2.94 \cdot 10^{-3}$	$3.64 \cdot 10^{-2}$	$8.81 \cdot 10^{-3}$	$1.27 \cdot 10^{-1}$	$2.78 \cdot 10^{-1}$	± 4.0
127.5	$4.60 \cdot 10^{-3}$	$3.07 \cdot 10^{-3}$	$3.76 \cdot 10^{-2}$	$9.18 \cdot 10^{-3}$	$1.32 \cdot 10^{-1}$	$2.89 \cdot 10^{-1}$	± 4.0
128.0	$4.79 \cdot 10^{-3}$	$3.20 \cdot 10^{-3}$	$3.89 \cdot 10^{-2}$	$9.56 \cdot 10^{-3}$	$1.37 \cdot 10^{-1}$	$2.99 \cdot 10^{-1}$	± 3.9
128.5	$4.99 \cdot 10^{-3}$	$3.32 \cdot 10^{-3}$	$4.03 \cdot 10^{-2}$	$9.94 \cdot 10^{-3}$	$1.41 \cdot 10^{-1}$	$3.09 \cdot 10^{-1}$	± 3.8
129.0	$5.18 \cdot 10^{-3}$	$3.46 \cdot 10^{-3}$	$4.16 \cdot 10^{-2}$	$1.03 \cdot 10^{-2}$	$1.46 \cdot 10^{-1}$	$3.20 \cdot 10^{-1}$	± 3.8
129.5	$5.38 \cdot 10^{-3}$	$3.59 \cdot 10^{-3}$	$4.30 \cdot 10^{-2}$	$1.07 \cdot 10^{-2}$	$1.51 \cdot 10^{-1}$	$3.30 \cdot 10^{-1}$	± 3.7
130.0	$5.59 \cdot 10^{-3}$	$3.72 \cdot 10^{-3}$	$4.43 \cdot 10^{-2}$	$1.11 \cdot 10^{-2}$	$1.56 \cdot 10^{-1}$	$3.41 \cdot 10^{-1}$	± 3.7

Table A.17: SM Higgs branching ratios for the different four-fermion final states and their total uncertainties (expressed in percentage). Low- and intermediate-mass range.

M_{H} [GeV]	$\mathrm{H} \to 2l2q$ $l = e, \mu, \tau$ $q = udcsb$	$\mathrm{H} \to 2l2q$ $l = e, \mu$ $q = udcsb$	$\mathrm{H} \to l\nu_l qq$ $l = e, \mu$ $q = udcsb$	$\mathrm{H} \to \nu\nu qq$ $\nu = \mathrm{any}$ $q = udcsb$	$\mathrm{H} \to 4q$ $q = udcsb$	$\mathrm{H} \to 4f$ $f = \mathrm{any}$ fermion	ΔBR [%]
130.5	$5.79 \cdot 10^{-3}$	$3.86 \cdot 10^{-3}$	$4.57 \cdot 10^{-2}$	$1.15 \cdot 10^{-2}$	$1.61 \cdot 10^{-1}$	$3.52 \cdot 10^{-1}$	± 3.6
131.0	$6.00 \cdot 10^{-3}$	$4.00 \cdot 10^{-3}$	$4.71 \cdot 10^{-2}$	$1.20 \cdot 10^{-2}$	$1.66 \cdot 10^{-1}$	$3.63 \cdot 10^{-1}$	± 3.5
131.5	$6.21 \cdot 10^{-3}$	$4.14 \cdot 10^{-3}$	$4.85 \cdot 10^{-2}$	$1.24 \cdot 10^{-2}$	$1.71 \cdot 10^{-1}$	$3.74 \cdot 10^{-1}$	± 3.5
132.0	$6.41 \cdot 10^{-3}$	$4.28 \cdot 10^{-3}$	$4.99 \cdot 10^{-2}$	$1.28 \cdot 10^{-2}$	$1.76 \cdot 10^{-1}$	$3.85 \cdot 10^{-1}$	± 3.4
132.5	$6.62 \cdot 10^{-3}$	$4.42 \cdot 10^{-3}$	$5.14 \cdot 10^{-2}$	$1.32 \cdot 10^{-2}$	$1.81 \cdot 10^{-1}$	$3.96 \cdot 10^{-1}$	± 3.3
133.0	$6.83 \cdot 10^{-3}$	$4.56 \cdot 10^{-3}$	$5.28 \cdot 10^{-2}$	$1.36 \cdot 10^{-2}$	$1.87 \cdot 10^{-1}$	$4.08 \cdot 10^{-1}$	± 3.3
133.5	$7.05 \cdot 10^{-3}$	$4.70 \cdot 10^{-3}$	$5.42 \cdot 10^{-2}$	$1.40 \cdot 10^{-2}$	$1.92 \cdot 10^{-1}$	$4.19 \cdot 10^{-1}$	± 3.2
134.0	$7.26 \cdot 10^{-3}$	$4.84 \cdot 10^{-3}$	$5.57 \cdot 10^{-2}$	$1.45 \cdot 10^{-2}$	$1.97 \cdot 10^{-1}$	$4.31 \cdot 10^{-1}$	± 3.1
134.5	$7.47 \cdot 10^{-3}$	$4.98 \cdot 10^{-3}$	$5.72 \cdot 10^{-2}$	$1.49 \cdot 10^{-2}$	$2.02 \cdot 10^{-1}$	$4.42 \cdot 10^{-1}$	± 3.1
135.0	$7.68 \cdot 10^{-3}$	$5.12 \cdot 10^{-3}$	$5.86 \cdot 10^{-2}$	$1.53 \cdot 10^{-2}$	$2.08 \cdot 10^{-1}$	$4.53 \cdot 10^{-1}$	± 3.0
135.5	$7.89 \cdot 10^{-3}$	$5.26 \cdot 10^{-3}$	$6.01 \cdot 10^{-2}$	$1.57 \cdot 10^{-2}$	$2.13 \cdot 10^{-1}$	$4.65 \cdot 10^{-1}$	± 2.9
136.0	$8.09 \cdot 10^{-3}$	$5.39 \cdot 10^{-3}$	$6.16 \cdot 10^{-2}$	$1.61 \cdot 10^{-2}$	$2.18 \cdot 10^{-1}$	$4.76 \cdot 10^{-1}$	± 2.8
136.5	$8.30 \cdot 10^{-3}$	$5.53 \cdot 10^{-3}$	$6.30 \cdot 10^{-2}$	$1.65 \cdot 10^{-2}$	$2.23 \cdot 10^{-1}$	$4.88 \cdot 10^{-1}$	± 2.6
137.0	$8.50 \cdot 10^{-3}$	$5.67 \cdot 10^{-3}$	$6.45 \cdot 10^{-2}$	$1.69 \cdot 10^{-2}$	$2.29 \cdot 10^{-1}$	$4.99 \cdot 10^{-1}$	± 2.5
137.5	$8.70 \cdot 10^{-3}$	$5.80 \cdot 10^{-3}$	$6.60 \cdot 10^{-2}$	$1.73 \cdot 10^{-2}$	$2.34 \cdot 10^{-1}$	$5.11 \cdot 10^{-1}$	± 2.4
138.0	$8.90 \cdot 10^{-3}$	$5.93 \cdot 10^{-3}$	$6.75 \cdot 10^{-2}$	$1.77 \cdot 10^{-2}$	$2.39 \cdot 10^{-1}$	$5.22 \cdot 10^{-1}$	± 2.2
138.5	$9.10 \cdot 10^{-3}$	$6.06 \cdot 10^{-3}$	$6.90 \cdot 10^{-2}$	$1.81 \cdot 10^{-2}$	$2.45 \cdot 10^{-1}$	$5.34 \cdot 10^{-1}$	± 2.1
139.0	$9.29 \cdot 10^{-3}$	$6.19 \cdot 10^{-3}$	$7.04 \cdot 10^{-2}$	$1.85 \cdot 10^{-2}$	$2.50 \cdot 10^{-1}$	$5.45 \cdot 10^{-1}$	± 1.9
139.5	$9.47 \cdot 10^{-3}$	$6.31 \cdot 10^{-3}$	$7.19 \cdot 10^{-2}$	$1.89 \cdot 10^{-2}$	$2.55 \cdot 10^{-1}$	$5.57 \cdot 10^{-1}$	± 1.8
140.0	$9.65 \cdot 10^{-3}$	$6.44 \cdot 10^{-3}$	$7.34 \cdot 10^{-2}$	$1.92 \cdot 10^{-2}$	$2.60 \cdot 10^{-1}$	$5.68 \cdot 10^{-1}$	± 1.7
141.0	$1.00 \cdot 10^{-2}$	$6.67 \cdot 10^{-3}$	$7.63 \cdot 10^{-2}$	$1.99 \cdot 10^{-2}$	$2.70 \cdot 10^{-1}$	$5.91 \cdot 10^{-1}$	± 1.6
142.0	$1.03 \cdot 10^{-2}$	$6.89 \cdot 10^{-3}$	$7.92 \cdot 10^{-2}$	$2.06 \cdot 10^{-2}$	$2.81 \cdot 10^{-1}$	$6.13 \cdot 10^{-1}$	± 1.5
143.0	$1.06 \cdot 10^{-2}$	$7.08 \cdot 10^{-3}$	$8.21 \cdot 10^{-2}$	$2.11 \cdot 10^{-2}$	$2.91 \cdot 10^{-1}$	$6.35 \cdot 10^{-1}$	± 1.4
144.0	$1.09 \cdot 10^{-2}$	$7.26 \cdot 10^{-3}$	$8.50 \cdot 10^{-2}$	$2.17 \cdot 10^{-2}$	$3.00 \cdot 10^{-1}$	$6.56 \cdot 10^{-1}$	± 1.3
145.0	$1.11 \cdot 10^{-2}$	$7.42 \cdot 10^{-3}$	$8.79 \cdot 10^{-2}$	$2.21 \cdot 10^{-2}$	$3.10 \cdot 10^{-1}$	$6.77 \cdot 10^{-1}$	± 1.2
146.0	$1.13 \cdot 10^{-2}$	$7.55 \cdot 10^{-3}$	$9.07 \cdot 10^{-2}$	$2.25 \cdot 10^{-2}$	$3.20 \cdot 10^{-1}$	$6.98 \cdot 10^{-1}$	± 1.2
147.0	$1.15 \cdot 10^{-2}$	$7.65 \cdot 10^{-3}$	$9.36 \cdot 10^{-2}$	$2.28 \cdot 10^{-2}$	$3.29 \cdot 10^{-1}$	$7.19 \cdot 10^{-1}$	± 1.1
148.0	$1.16 \cdot 10^{-2}$	$7.71 \cdot 10^{-3}$	$9.64 \cdot 10^{-2}$	$2.30 \cdot 10^{-2}$	$3.38 \cdot 10^{-1}$	$7.39 \cdot 10^{-1}$	± 1.0
149.0	$1.16 \cdot 10^{-2}$	$7.74 \cdot 10^{-3}$	$9.92 \cdot 10^{-2}$	$2.31 \cdot 10^{-2}$	$3.47 \cdot 10^{-1}$	$7.58 \cdot 10^{-1}$	± 0.9
150.0	$1.16 \cdot 10^{-2}$	$7.73 \cdot 10^{-3}$	$1.02 \cdot 10^{-1}$	$2.31 \cdot 10^{-2}$	$3.56 \cdot 10^{-1}$	$7.77 \cdot 10^{-1}$	± 0.9
151.0	$1.15 \cdot 10^{-2}$	$7.68 \cdot 10^{-3}$	$1.05 \cdot 10^{-1}$	$2.29 \cdot 10^{-2}$	$3.64 \cdot 10^{-1}$	$7.96 \cdot 10^{-1}$	± 0.8
152.0	$1.14 \cdot 10^{-2}$	$7.57 \cdot 10^{-3}$	$1.08 \cdot 10^{-1}$	$2.26 \cdot 10^{-2}$	$3.72 \cdot 10^{-1}$	$8.14 \cdot 10^{-1}$	± 0.7
153.0	$1.11 \cdot 10^{-2}$	$7.41 \cdot 10^{-3}$	$1.10 \cdot 10^{-1}$	$2.21 \cdot 10^{-2}$	$3.80 \cdot 10^{-1}$	$8.32 \cdot 10^{-1}$	± 0.7
154.0	$1.08 \cdot 10^{-2}$	$7.18 \cdot 10^{-3}$	$1.13 \cdot 10^{-1}$	$2.14 \cdot 10^{-2}$	$3.88 \cdot 10^{-1}$	$8.49 \cdot 10^{-1}$	± 0.6
155.0	$1.03 \cdot 10^{-2}$	$6.88 \cdot 10^{-3}$	$1.16 \cdot 10^{-1}$	$2.05 \cdot 10^{-2}$	$3.96 \cdot 10^{-1}$	$8.67 \cdot 10^{-1}$	± 0.5
156.0	$9.73 \cdot 10^{-3}$	$6.49 \cdot 10^{-3}$	$1.19 \cdot 10^{-1}$	$1.94 \cdot 10^{-2}$	$4.04 \cdot 10^{-1}$	$8.84 \cdot 10^{-1}$	± 0.5
157.0	$9.00 \cdot 10^{-3}$	$6.00 \cdot 10^{-3}$	$1.23 \cdot 10^{-1}$	$1.79 \cdot 10^{-2}$	$4.11 \cdot 10^{-1}$	$9.01 \cdot 10^{-1}$	± 0.4
158.0	$8.09 \cdot 10^{-3}$	$5.39 \cdot 10^{-3}$	$1.26 \cdot 10^{-1}$	$1.61 \cdot 10^{-2}$	$4.18 \cdot 10^{-1}$	$9.17 \cdot 10^{-1}$	± 0.3
159.0	$7.01 \cdot 10^{-3}$	$4.68 \cdot 10^{-3}$	$1.30 \cdot 10^{-1}$	$1.39 \cdot 10^{-2}$	$4.25 \cdot 10^{-1}$	$9.33 \cdot 10^{-1}$	± 0.3
160.0	$5.83 \cdot 10^{-3}$	$3.88 \cdot 10^{-3}$	$1.33 \cdot 10^{-1}$	$1.16 \cdot 10^{-2}$	$4.32 \cdot 10^{-1}$	$9.49 \cdot 10^{-1}$	± 0.2
162.0	$3.96 \cdot 10^{-3}$	$2.64 \cdot 10^{-3}$	$1.38 \cdot 10^{-1}$	$7.88 \cdot 10^{-3}$	$4.42 \cdot 10^{-1}$	$9.70 \cdot 10^{-1}$	± 0.2
164.0	$3.25 \cdot 10^{-3}$	$2.17 \cdot 10^{-3}$	$1.40 \cdot 10^{-1}$	$6.47 \cdot 10^{-3}$	$4.46 \cdot 10^{-1}$	$9.79 \cdot 10^{-1}$	± 0.1
166.0	$3.07 \cdot 10^{-3}$	$2.04 \cdot 10^{-3}$	$1.41 \cdot 10^{-1}$	$6.11 \cdot 10^{-3}$	$4.48 \cdot 10^{-1}$	$9.84 \cdot 10^{-1}$	± 0.1
168.0	$3.12 \cdot 10^{-3}$	$2.08 \cdot 10^{-3}$	$1.41 \cdot 10^{-1}$	$6.21 \cdot 10^{-3}$	$4.49 \cdot 10^{-1}$	$9.86 \cdot 10^{-1}$	± 0.1
170.0	$3.32 \cdot 10^{-3}$	$2.21 \cdot 10^{-3}$	$1.41 \cdot 10^{-1}$	$6.61 \cdot 10^{-3}$	$4.50 \cdot 10^{-1}$	$9.88 \cdot 10^{-1}$	± 0.1

Table A.18: SM Higgs branching ratios for the different four-fermion final states and their total uncertainties (expressed in percentage). Intermediate-mass range.

M_{H} [GeV]	$\mathrm{H} \to 2\mathrm{l}2\mathrm{q}$ $\mathrm{l} = \mathrm{e}, \mu, \tau$ $\mathrm{q} = \mathrm{udcsb}$	$\mathrm{H} \to 2\mathrm{l}2\mathrm{q}$ $\mathrm{l} = \mathrm{e}, \mu$ $\mathrm{q} = \mathrm{udcsb}$	$\mathrm{H} \to \mathrm{l}\nu_l\mathrm{qq}$ $\mathrm{l} = \mathrm{e}, \mu$ $\mathrm{q} = \mathrm{udcsb}$	$\mathrm{H} \to \nu\nu\mathrm{qq}$ $\nu = \mathrm{any}$ $\mathrm{q} = \mathrm{udcsb}$	$\mathrm{H} \to 4\mathrm{q}$ $\mathrm{q} = \mathrm{udcsb}$	$\mathrm{H} \to 4\mathrm{f}$ $f = \mathrm{any}$ fermion	ΔBR [%]
172.0	$3.67 \cdot 10^{-3}$	$2.44 \cdot 10^{-3}$	$1.41 \cdot 10^{-1}$	$7.30 \cdot 10^{-3}$	$4.50 \cdot 10^{-1}$	$9.89 \cdot 10^{-1}$	± 0.0
174.0	$4.19 \cdot 10^{-3}$	$2.79 \cdot 10^{-3}$	$1.41 \cdot 10^{-1}$	$8.34 \cdot 10^{-3}$	$4.51 \cdot 10^{-1}$	$9.90 \cdot 10^{-1}$	± 0.0
176.0	$4.98 \cdot 10^{-3}$	$3.32 \cdot 10^{-3}$	$1.40 \cdot 10^{-1}$	$9.92 \cdot 10^{-3}$	$4.51 \cdot 10^{-1}$	$9.91 \cdot 10^{-1}$	± 0.0
178.0	$6.24 \cdot 10^{-3}$	$4.16 \cdot 10^{-3}$	$1.39 \cdot 10^{-1}$	$1.24 \cdot 10^{-2}$	$4.52 \cdot 10^{-1}$	$9.91 \cdot 10^{-1}$	± 0.0
180.0	$8.47 \cdot 10^{-3}$	$5.65 \cdot 10^{-3}$	$1.37 \cdot 10^{-1}$	$1.69 \cdot 10^{-2}$	$4.53 \cdot 10^{-1}$	$9.92 \cdot 10^{-1}$	± 0.0
182.0	$1.27 \cdot 10^{-2}$	$8.44 \cdot 10^{-3}$	$1.32 \cdot 10^{-1}$	$2.52 \cdot 10^{-2}$	$4.54 \cdot 10^{-1}$	$9.93 \cdot 10^{-1}$	± 0.0
184.0	$1.85 \cdot 10^{-2}$	$1.23 \cdot 10^{-2}$	$1.26 \cdot 10^{-1}$	$3.69 \cdot 10^{-2}$	$4.56 \cdot 10^{-1}$	$9.93 \cdot 10^{-1}$	± 0.0
186.0	$2.34 \cdot 10^{-2}$	$1.56 \cdot 10^{-2}$	$1.21 \cdot 10^{-1}$	$4.66 \cdot 10^{-2}$	$4.57 \cdot 10^{-1}$	$9.94 \cdot 10^{-1}$	± 0.0
188.0	$2.69 \cdot 10^{-2}$	$1.79 \cdot 10^{-2}$	$1.18 \cdot 10^{-1}$	$5.36 \cdot 10^{-2}$	$4.58 \cdot 10^{-1}$	$9.94 \cdot 10^{-1}$	± 0.0
190.0	$2.95 \cdot 10^{-2}$	$1.97 \cdot 10^{-2}$	$1.15 \cdot 10^{-1}$	$5.87 \cdot 10^{-2}$	$4.59 \cdot 10^{-1}$	$9.95 \cdot 10^{-1}$	± 0.0
192.0	$3.14 \cdot 10^{-2}$	$2.09 \cdot 10^{-2}$	$1.13 \cdot 10^{-1}$	$6.26 \cdot 10^{-2}$	$4.60 \cdot 10^{-1}$	$9.95 \cdot 10^{-1}$	± 0.0
194.0	$3.29 \cdot 10^{-2}$	$2.20 \cdot 10^{-2}$	$1.12 \cdot 10^{-1}$	$6.56 \cdot 10^{-2}$	$4.60 \cdot 10^{-1}$	$9.95 \cdot 10^{-1}$	± 0.0
196.0	$3.42 \cdot 10^{-2}$	$2.28 \cdot 10^{-2}$	$1.10 \cdot 10^{-1}$	$6.80 \cdot 10^{-2}$	$4.61 \cdot 10^{-1}$	$9.96 \cdot 10^{-1}$	± 0.0
198.0	$3.51 \cdot 10^{-2}$	$2.34 \cdot 10^{-2}$	$1.09 \cdot 10^{-1}$	$7.00 \cdot 10^{-2}$	$4.61 \cdot 10^{-1}$	$9.96 \cdot 10^{-1}$	± 0.0
200.0	$3.60 \cdot 10^{-2}$	$2.40 \cdot 10^{-2}$	$1.08 \cdot 10^{-1}$	$7.16 \cdot 10^{-2}$	$4.61 \cdot 10^{-1}$	$9.96 \cdot 10^{-1}$	± 0.0
202.0	$3.67 \cdot 10^{-2}$	$2.44 \cdot 10^{-2}$	$1.08 \cdot 10^{-1}$	$7.30 \cdot 10^{-2}$	$4.61 \cdot 10^{-1}$	$9.96 \cdot 10^{-1}$	± 0.0
204.0	$3.72 \cdot 10^{-2}$	$2.48 \cdot 10^{-2}$	$1.07 \cdot 10^{-1}$	$7.42 \cdot 10^{-2}$	$4.62 \cdot 10^{-1}$	$9.96 \cdot 10^{-1}$	± 0.0
206.0	$3.77 \cdot 10^{-2}$	$2.52 \cdot 10^{-2}$	$1.07 \cdot 10^{-1}$	$7.52 \cdot 10^{-2}$	$4.62 \cdot 10^{-1}$	$9.96 \cdot 10^{-1}$	± 0.0
208.0	$3.82 \cdot 10^{-2}$	$2.55 \cdot 10^{-2}$	$1.06 \cdot 10^{-1}$	$7.61 \cdot 10^{-2}$	$4.62 \cdot 10^{-1}$	$9.97 \cdot 10^{-1}$	± 0.0
210.0	$3.86 \cdot 10^{-2}$	$2.57 \cdot 10^{-2}$	$1.06 \cdot 10^{-1}$	$7.68 \cdot 10^{-2}$	$4.62 \cdot 10^{-1}$	$9.97 \cdot 10^{-1}$	± 0.0
212.0	$3.89 \cdot 10^{-2}$	$2.59 \cdot 10^{-2}$	$1.06 \cdot 10^{-1}$	$7.75 \cdot 10^{-2}$	$4.62 \cdot 10^{-1}$	$9.97 \cdot 10^{-1}$	± 0.0
214.0	$3.92 \cdot 10^{-2}$	$2.61 \cdot 10^{-2}$	$1.05 \cdot 10^{-1}$	$7.81 \cdot 10^{-2}$	$4.62 \cdot 10^{-1}$	$9.97 \cdot 10^{-1}$	± 0.0
216.0	$3.95 \cdot 10^{-2}$	$2.63 \cdot 10^{-2}$	$1.05 \cdot 10^{-1}$	$7.86 \cdot 10^{-2}$	$4.63 \cdot 10^{-1}$	$9.97 \cdot 10^{-1}$	± 0.0
218.0	$3.97 \cdot 10^{-2}$	$2.65 \cdot 10^{-2}$	$1.05 \cdot 10^{-1}$	$7.91 \cdot 10^{-2}$	$4.63 \cdot 10^{-1}$	$9.97 \cdot 10^{-1}$	± 0.0
220.0	$3.99 \cdot 10^{-2}$	$2.66 \cdot 10^{-2}$	$1.05 \cdot 10^{-1}$	$7.95 \cdot 10^{-2}$	$4.63 \cdot 10^{-1}$	$9.97 \cdot 10^{-1}$	± 0.0
222.0	$4.01 \cdot 10^{-2}$	$2.67 \cdot 10^{-2}$	$1.04 \cdot 10^{-1}$	$7.99 \cdot 10^{-2}$	$4.63 \cdot 10^{-1}$	$9.97 \cdot 10^{-1}$	± 0.0
224.0	$4.03 \cdot 10^{-2}$	$2.69 \cdot 10^{-2}$	$1.04 \cdot 10^{-1}$	$8.02 \cdot 10^{-2}$	$4.63 \cdot 10^{-1}$	$9.97 \cdot 10^{-1}$	± 0.0
226.0	$4.04 \cdot 10^{-2}$	$2.70 \cdot 10^{-2}$	$1.04 \cdot 10^{-1}$	$8.06 \cdot 10^{-2}$	$4.63 \cdot 10^{-1}$	$9.97 \cdot 10^{-1}$	± 0.0
228.0	$4.06 \cdot 10^{-2}$	$2.71 \cdot 10^{-2}$	$1.04 \cdot 10^{-1}$	$8.09 \cdot 10^{-2}$	$4.63 \cdot 10^{-1}$	$9.97 \cdot 10^{-1}$	± 0.0
230.0	$4.07 \cdot 10^{-2}$	$2.72 \cdot 10^{-2}$	$1.04 \cdot 10^{-1}$	$8.12 \cdot 10^{-2}$	$4.63 \cdot 10^{-1}$	$9.98 \cdot 10^{-1}$	± 0.0
232.0	$4.09 \cdot 10^{-2}$	$2.73 \cdot 10^{-2}$	$1.04 \cdot 10^{-1}$	$8.14 \cdot 10^{-2}$	$4.63 \cdot 10^{-1}$	$9.98 \cdot 10^{-1}$	± 0.0
234.0	$4.10 \cdot 10^{-2}$	$2.73 \cdot 10^{-2}$	$1.03 \cdot 10^{-1}$	$8.17 \cdot 10^{-2}$	$4.63 \cdot 10^{-1}$	$9.98 \cdot 10^{-1}$	± 0.0
236.0	$4.11 \cdot 10^{-2}$	$2.74 \cdot 10^{-2}$	$1.03 \cdot 10^{-1}$	$8.19 \cdot 10^{-2}$	$4.63 \cdot 10^{-1}$	$9.98 \cdot 10^{-1}$	± 0.0
238.0	$4.12 \cdot 10^{-2}$	$2.75 \cdot 10^{-2}$	$1.03 \cdot 10^{-1}$	$8.21 \cdot 10^{-2}$	$4.63 \cdot 10^{-1}$	$9.98 \cdot 10^{-1}$	± 0.0
240.0	$4.13 \cdot 10^{-2}$	$2.76 \cdot 10^{-2}$	$1.03 \cdot 10^{-1}$	$8.23 \cdot 10^{-2}$	$4.63 \cdot 10^{-1}$	$9.98 \cdot 10^{-1}$	± 0.0
242.0	$4.14 \cdot 10^{-2}$	$2.76 \cdot 10^{-2}$	$1.03 \cdot 10^{-1}$	$8.25 \cdot 10^{-2}$	$4.63 \cdot 10^{-1}$	$9.98 \cdot 10^{-1}$	± 0.0
244.0	$4.15 \cdot 10^{-2}$	$2.77 \cdot 10^{-2}$	$1.03 \cdot 10^{-1}$	$8.27 \cdot 10^{-2}$	$4.64 \cdot 10^{-1}$	$9.98 \cdot 10^{-1}$	± 0.0
246.0	$4.16 \cdot 10^{-2}$	$2.77 \cdot 10^{-2}$	$1.03 \cdot 10^{-1}$	$8.29 \cdot 10^{-2}$	$4.64 \cdot 10^{-1}$	$9.98 \cdot 10^{-1}$	± 0.0
248.0	$4.17 \cdot 10^{-2}$	$2.78 \cdot 10^{-2}$	$1.03 \cdot 10^{-1}$	$8.30 \cdot 10^{-2}$	$4.64 \cdot 10^{-1}$	$9.98 \cdot 10^{-1}$	± 0.0
250.0	$4.18 \cdot 10^{-2}$	$2.78 \cdot 10^{-2}$	$1.03 \cdot 10^{-1}$	$8.32 \cdot 10^{-2}$	$4.64 \cdot 10^{-1}$	$9.98 \cdot 10^{-1}$	± 0.0
252.0	$4.18 \cdot 10^{-2}$	$2.79 \cdot 10^{-2}$	$1.03 \cdot 10^{-1}$	$8.34 \cdot 10^{-2}$	$4.64 \cdot 10^{-1}$	$9.98 \cdot 10^{-1}$	± 0.0
254.0	$4.19 \cdot 10^{-2}$	$2.79 \cdot 10^{-2}$	$1.03 \cdot 10^{-1}$	$8.35 \cdot 10^{-2}$	$4.64 \cdot 10^{-1}$	$9.98 \cdot 10^{-1}$	± 0.0
256.0	$4.20 \cdot 10^{-2}$	$2.80 \cdot 10^{-2}$	$1.02 \cdot 10^{-1}$	$8.37 \cdot 10^{-2}$	$4.64 \cdot 10^{-1}$	$9.98 \cdot 10^{-1}$	± 0.0
258.0	$4.21 \cdot 10^{-2}$	$2.80 \cdot 10^{-2}$	$1.02 \cdot 10^{-1}$	$8.38 \cdot 10^{-2}$	$4.64 \cdot 10^{-1}$	$9.98 \cdot 10^{-1}$	± 0.0
260.0	$4.21 \cdot 10^{-2}$	$2.81 \cdot 10^{-2}$	$1.02 \cdot 10^{-1}$	$8.39 \cdot 10^{-2}$	$4.64 \cdot 10^{-1}$	$9.98 \cdot 10^{-1}$	± 0.0

Table A.19: SM Higgs branching ratios for the different four-fermion final states and their total uncertainties (expressed in percentage). High-mass range.

M_{H} [GeV]	$\mathrm{H} \to 2\mathrm{l}2\mathrm{q}$ $\mathrm{l} = \mathrm{e}, \mu, \tau$ $\mathrm{q} = \mathrm{udcsb}$	$\mathrm{H} \to 2\mathrm{l}2\mathrm{q}$ $\mathrm{l} = \mathrm{e}, \mu$ $\mathrm{q} = \mathrm{udcsb}$	$\mathrm{H} \to \mathrm{l}\nu_l\mathrm{qq}$ $\mathrm{l} = \mathrm{e}, \mu$ $\mathrm{q} = \mathrm{udcsb}$	$\mathrm{H} \to \nu\nu\mathrm{qq}$ $\nu = \mathrm{any}$ $\mathrm{q} = \mathrm{udcsb}$	$\mathrm{H} \to 4\mathrm{q}$ $\mathrm{q} = \mathrm{udcsb}$	$\mathrm{H} \to 4\mathrm{f}$ $f = \mathrm{any}$ fermion	ΔBR [%]
262.0	$4.22 \cdot 10^{-2}$	$2.81 \cdot 10^{-2}$	$1.02 \cdot 10^{-1}$	$8.41 \cdot 10^{-2}$	$4.64 \cdot 10^{-1}$	$9.98 \cdot 10^{-1}$	± 0.0
264.0	$4.23 \cdot 10^{-2}$	$2.82 \cdot 10^{-2}$	$1.02 \cdot 10^{-1}$	$8.42 \cdot 10^{-2}$	$4.64 \cdot 10^{-1}$	$9.98 \cdot 10^{-1}$	± 0.0
266.0	$4.23 \cdot 10^{-2}$	$2.82 \cdot 10^{-2}$	$1.02 \cdot 10^{-1}$	$8.43 \cdot 10^{-2}$	$4.64 \cdot 10^{-1}$	$9.98 \cdot 10^{-1}$	± 0.0
268.0	$4.24 \cdot 10^{-2}$	$2.83 \cdot 10^{-2}$	$1.02 \cdot 10^{-1}$	$8.44 \cdot 10^{-2}$	$4.64 \cdot 10^{-1}$	$9.98 \cdot 10^{-1}$	± 0.0
270.0	$4.24 \cdot 10^{-2}$	$2.83 \cdot 10^{-2}$	$1.02 \cdot 10^{-1}$	$8.45 \cdot 10^{-2}$	$4.64 \cdot 10^{-1}$	$9.98 \cdot 10^{-1}$	± 0.0
272.0	$4.25 \cdot 10^{-2}$	$2.83 \cdot 10^{-2}$	$1.02 \cdot 10^{-1}$	$8.47 \cdot 10^{-2}$	$4.64 \cdot 10^{-1}$	$9.98 \cdot 10^{-1}$	± 0.0
274.0	$4.26 \cdot 10^{-2}$	$2.84 \cdot 10^{-2}$	$1.02 \cdot 10^{-1}$	$8.48 \cdot 10^{-2}$	$4.64 \cdot 10^{-1}$	$9.98 \cdot 10^{-1}$	± 0.0
276.0	$4.26 \cdot 10^{-2}$	$2.84 \cdot 10^{-2}$	$1.02 \cdot 10^{-1}$	$8.49 \cdot 10^{-2}$	$4.64 \cdot 10^{-1}$	$9.98 \cdot 10^{-1}$	± 0.0
278.0	$4.27 \cdot 10^{-2}$	$2.84 \cdot 10^{-2}$	$1.02 \cdot 10^{-1}$	$8.50 \cdot 10^{-2}$	$4.64 \cdot 10^{-1}$	$9.98 \cdot 10^{-1}$	± 0.0
280.0	$4.27 \cdot 10^{-2}$	$2.85 \cdot 10^{-2}$	$1.02 \cdot 10^{-1}$	$8.51 \cdot 10^{-2}$	$4.64 \cdot 10^{-1}$	$9.98 \cdot 10^{-1}$	± 0.0
282.0	$4.28 \cdot 10^{-2}$	$2.85 \cdot 10^{-2}$	$1.02 \cdot 10^{-1}$	$8.52 \cdot 10^{-2}$	$4.64 \cdot 10^{-1}$	$9.98 \cdot 10^{-1}$	± 0.0
284.0	$4.28 \cdot 10^{-2}$	$2.85 \cdot 10^{-2}$	$1.02 \cdot 10^{-1}$	$8.53 \cdot 10^{-2}$	$4.64 \cdot 10^{-1}$	$9.98 \cdot 10^{-1}$	± 0.0
286.0	$4.29 \cdot 10^{-2}$	$2.86 \cdot 10^{-2}$	$1.02 \cdot 10^{-1}$	$8.54 \cdot 10^{-2}$	$4.64 \cdot 10^{-1}$	$9.98 \cdot 10^{-1}$	± 0.0
288.0	$4.29 \cdot 10^{-2}$	$2.86 \cdot 10^{-2}$	$1.02 \cdot 10^{-1}$	$8.55 \cdot 10^{-2}$	$4.64 \cdot 10^{-1}$	$9.98 \cdot 10^{-1}$	± 0.0
290.0	$4.30 \cdot 10^{-2}$	$2.86 \cdot 10^{-2}$	$1.02 \cdot 10^{-1}$	$8.56 \cdot 10^{-2}$	$4.64 \cdot 10^{-1}$	$9.98 \cdot 10^{-1}$	± 0.0
295.0	$4.31 \cdot 10^{-2}$	$2.87 \cdot 10^{-2}$	$1.01 \cdot 10^{-1}$	$8.58 \cdot 10^{-2}$	$4.64 \cdot 10^{-1}$	$9.98 \cdot 10^{-1}$	± 0.0
300.0	$4.32 \cdot 10^{-2}$	$2.88 \cdot 10^{-2}$	$1.01 \cdot 10^{-1}$	$8.60 \cdot 10^{-2}$	$4.64 \cdot 10^{-1}$	$9.99 \cdot 10^{-1}$	± 0.0
305.0	$4.33 \cdot 10^{-2}$	$2.88 \cdot 10^{-2}$	$1.01 \cdot 10^{-1}$	$8.62 \cdot 10^{-2}$	$4.64 \cdot 10^{-1}$	$9.99 \cdot 10^{-1}$	± 0.0
310.0	$4.34 \cdot 10^{-2}$	$2.89 \cdot 10^{-2}$	$1.01 \cdot 10^{-1}$	$8.64 \cdot 10^{-2}$	$4.64 \cdot 10^{-1}$	$9.99 \cdot 10^{-1}$	± 0.0
315.0	$4.34 \cdot 10^{-2}$	$2.90 \cdot 10^{-2}$	$1.01 \cdot 10^{-1}$	$8.66 \cdot 10^{-2}$	$4.64 \cdot 10^{-1}$	$9.99 \cdot 10^{-1}$	± 0.0
320.0	$4.35 \cdot 10^{-2}$	$2.90 \cdot 10^{-2}$	$1.01 \cdot 10^{-1}$	$8.67 \cdot 10^{-2}$	$4.64 \cdot 10^{-1}$	$9.98 \cdot 10^{-1}$	± 0.0
325.0	$4.36 \cdot 10^{-2}$	$2.91 \cdot 10^{-2}$	$1.01 \cdot 10^{-1}$	$8.68 \cdot 10^{-2}$	$4.64 \cdot 10^{-1}$	$9.98 \cdot 10^{-1}$	± 0.0
330.0	$4.37 \cdot 10^{-2}$	$2.91 \cdot 10^{-2}$	$1.01 \cdot 10^{-1}$	$8.70 \cdot 10^{-2}$	$4.64 \cdot 10^{-1}$	$9.98 \cdot 10^{-1}$	± 0.0
335.0	$4.37 \cdot 10^{-2}$	$2.91 \cdot 10^{-2}$	$1.01 \cdot 10^{-1}$	$8.71 \cdot 10^{-2}$	$4.64 \cdot 10^{-1}$	$9.98 \cdot 10^{-1}$	± 0.0
340.0	$4.37 \cdot 10^{-2}$	$2.92 \cdot 10^{-2}$	$1.01 \cdot 10^{-1}$	$8.72 \cdot 10^{-2}$	$4.64 \cdot 10^{-1}$	$9.98 \cdot 10^{-1}$	± 0.0
345.0	$4.37 \cdot 10^{-2}$	$2.91 \cdot 10^{-2}$	$1.00 \cdot 10^{-1}$	$8.71 \cdot 10^{-2}$	$4.63 \cdot 10^{-1}$	$9.95 \cdot 10^{-1}$	± 0.7
350.0	$4.32 \cdot 10^{-2}$	$2.88 \cdot 10^{-2}$	$9.90 \cdot 10^{-2}$	$8.61 \cdot 10^{-2}$	$4.57 \cdot 10^{-1}$	$9.83 \cdot 10^{-1}$	± 1.4
360.0	$4.17 \cdot 10^{-2}$	$2.78 \cdot 10^{-2}$	$9.53 \cdot 10^{-2}$	$8.31 \cdot 10^{-2}$	$4.41 \cdot 10^{-1}$	$9.47 \cdot 10^{-1}$	± 2.6
370.0	$4.04 \cdot 10^{-2}$	$2.69 \cdot 10^{-2}$	$9.20 \cdot 10^{-2}$	$8.05 \cdot 10^{-2}$	$4.26 \cdot 10^{-1}$	$9.15 \cdot 10^{-1}$	± 2.9
380.0	$3.93 \cdot 10^{-2}$	$2.62 \cdot 10^{-2}$	$8.92 \cdot 10^{-2}$	$7.84 \cdot 10^{-2}$	$4.14 \cdot 10^{-1}$	$8.89 \cdot 10^{-1}$	± 3.1
390.0	$3.85 \cdot 10^{-2}$	$2.57 \cdot 10^{-2}$	$8.70 \cdot 10^{-2}$	$7.67 \cdot 10^{-2}$	$4.04 \cdot 10^{-1}$	$8.68 \cdot 10^{-1}$	± 3.1
400.0	$3.79 \cdot 10^{-2}$	$2.52 \cdot 10^{-2}$	$8.52 \cdot 10^{-2}$	$7.54 \cdot 10^{-2}$	$3.96 \cdot 10^{-1}$	$8.51 \cdot 10^{-1}$	± 3.1
410.0	$3.74 \cdot 10^{-2}$	$2.49 \cdot 10^{-2}$	$8.38 \cdot 10^{-2}$	$7.44 \cdot 10^{-2}$	$3.90 \cdot 10^{-1}$	$8.38 \cdot 10^{-1}$	± 3.1
420.0	$3.70 \cdot 10^{-2}$	$2.47 \cdot 10^{-2}$	$8.27 \cdot 10^{-2}$	$7.37 \cdot 10^{-2}$	$3.85 \cdot 10^{-1}$	$8.28 \cdot 10^{-1}$	± 3.1
430.0	$3.68 \cdot 10^{-2}$	$2.45 \cdot 10^{-2}$	$8.19 \cdot 10^{-2}$	$7.32 \cdot 10^{-2}$	$3.82 \cdot 10^{-1}$	$8.20 \cdot 10^{-1}$	± 3.0
440.0	$3.66 \cdot 10^{-2}$	$2.44 \cdot 10^{-2}$	$8.12 \cdot 10^{-2}$	$7.29 \cdot 10^{-2}$	$3.79 \cdot 10^{-1}$	$8.15 \cdot 10^{-1}$	± 3.0
450.0	$3.65 \cdot 10^{-2}$	$2.44 \cdot 10^{-2}$	$8.08 \cdot 10^{-2}$	$7.27 \cdot 10^{-2}$	$3.77 \cdot 10^{-1}$	$8.11 \cdot 10^{-1}$	± 2.9
460.0	$3.65 \cdot 10^{-2}$	$2.43 \cdot 10^{-2}$	$8.04 \cdot 10^{-2}$	$7.27 \cdot 10^{-2}$	$3.76 \cdot 10^{-1}$	$8.08 \cdot 10^{-1}$	± 2.8
470.0	$3.65 \cdot 10^{-2}$	$2.43 \cdot 10^{-2}$	$8.02 \cdot 10^{-2}$	$7.27 \cdot 10^{-2}$	$3.75 \cdot 10^{-1}$	$8.07 \cdot 10^{-1}$	± 2.8
480.0	$3.65 \cdot 10^{-2}$	$2.44 \cdot 10^{-2}$	$8.01 \cdot 10^{-2}$	$7.28 \cdot 10^{-2}$	$3.75 \cdot 10^{-1}$	$8.06 \cdot 10^{-1}$	± 2.7
490.0	$3.66 \cdot 10^{-2}$	$2.44 \cdot 10^{-2}$	$8.00 \cdot 10^{-2}$	$7.29 \cdot 10^{-2}$	$3.75 \cdot 10^{-1}$	$8.06 \cdot 10^{-1}$	± 2.6
500.0	$3.67 \cdot 10^{-2}$	$2.45 \cdot 10^{-2}$	$8.00 \cdot 10^{-2}$	$7.31 \cdot 10^{-2}$	$3.75 \cdot 10^{-1}$	$8.07 \cdot 10^{-1}$	± 2.4
510.0	$3.68 \cdot 10^{-2}$	$2.46 \cdot 10^{-2}$	$8.01 \cdot 10^{-2}$	$7.33 \cdot 10^{-2}$	$3.76 \cdot 10^{-1}$	$8.08 \cdot 10^{-1}$	± 2.3
520.0	$3.70 \cdot 10^{-2}$	$2.47 \cdot 10^{-2}$	$8.02 \cdot 10^{-2}$	$7.36 \cdot 10^{-2}$	$3.77 \cdot 10^{-1}$	$8.10 \cdot 10^{-1}$	± 2.4
530.0	$3.71 \cdot 10^{-2}$	$2.48 \cdot 10^{-2}$	$8.03 \cdot 10^{-2}$	$7.39 \cdot 10^{-2}$	$3.78 \cdot 10^{-1}$	$8.12 \cdot 10^{-1}$	± 2.4
540.0	$3.73 \cdot 10^{-2}$	$2.49 \cdot 10^{-2}$	$8.05 \cdot 10^{-2}$	$7.42 \cdot 10^{-2}$	$3.79 \cdot 10^{-1}$	$8.14 \cdot 10^{-1}$	± 2.4

Table A.20: SM Higgs branching ratios for the different four-fermion final states and their total uncertainties (expressed in percentage). Very-high-mass range.

M_{H} [GeV]	$\mathrm{H} \to 2l2q$ $l = e, \mu, \tau$ $q = udcsb$	$\mathrm{H} \to 2l2q$ $l = e, \mu$ $q = udcsb$	$\mathrm{H} \to l\nu_l qq$ $l = e, \mu$ $q = udcsb$	$\mathrm{H} \to \nu\nu qq$ $\nu =$ any $q = udcsb$	$\mathrm{H} \to 4q$ $q = udcsb$	$\mathrm{H} \to 4f$ $f =$ any fermion	ΔBR [%]
550.0	$3.75 \cdot 10^{-2}$	$2.50 \cdot 10^{-2}$	$8.06 \cdot 10^{-2}$	$7.45 \cdot 10^{-2}$	$3.80 \cdot 10^{-1}$	$8.16 \cdot 10^{-1}$	± 2.4
560.0	$3.76 \cdot 10^{-2}$	$2.51 \cdot 10^{-2}$	$8.09 \cdot 10^{-2}$	$7.49 \cdot 10^{-2}$	$3.81 \cdot 10^{-1}$	$8.19 \cdot 10^{-1}$	± 2.5
570.0	$3.78 \cdot 10^{-2}$	$2.52 \cdot 10^{-2}$	$8.11 \cdot 10^{-2}$	$7.52 \cdot 10^{-2}$	$3.82 \cdot 10^{-1}$	$8.22 \cdot 10^{-1}$	± 2.5
580.0	$3.80 \cdot 10^{-2}$	$2.53 \cdot 10^{-2}$	$8.13 \cdot 10^{-2}$	$7.56 \cdot 10^{-2}$	$3.84 \cdot 10^{-1}$	$8.25 \cdot 10^{-1}$	± 2.5
590.0	$3.82 \cdot 10^{-2}$	$2.54 \cdot 10^{-2}$	$8.16 \cdot 10^{-2}$	$7.60 \cdot 10^{-2}$	$3.85 \cdot 10^{-1}$	$8.28 \cdot 10^{-1}$	± 2.5
600.0	$3.83 \cdot 10^{-2}$	$2.56 \cdot 10^{-2}$	$8.18 \cdot 10^{-2}$	$7.63 \cdot 10^{-2}$	$3.87 \cdot 10^{-1}$	$8.31 \cdot 10^{-1}$	± 2.5
610.0	$3.85 \cdot 10^{-2}$	$2.57 \cdot 10^{-2}$	$8.21 \cdot 10^{-2}$	$7.67 \cdot 10^{-2}$	$3.88 \cdot 10^{-1}$	$8.34 \cdot 10^{-1}$	± 2.5
620.0	$3.87 \cdot 10^{-2}$	$2.58 \cdot 10^{-2}$	$8.24 \cdot 10^{-2}$	$7.70 \cdot 10^{-2}$	$3.89 \cdot 10^{-1}$	$8.37 \cdot 10^{-1}$	± 2.6
630.0	$3.89 \cdot 10^{-2}$	$2.59 \cdot 10^{-2}$	$8.27 \cdot 10^{-2}$	$7.74 \cdot 10^{-2}$	$3.91 \cdot 10^{-1}$	$8.40 \cdot 10^{-1}$	± 2.5
640.0	$3.91 \cdot 10^{-2}$	$2.61 \cdot 10^{-2}$	$8.29 \cdot 10^{-2}$	$7.78 \cdot 10^{-2}$	$3.92 \cdot 10^{-1}$	$8.43 \cdot 10^{-1}$	± 2.6
650.0	$3.93 \cdot 10^{-2}$	$2.62 \cdot 10^{-2}$	$8.32 \cdot 10^{-2}$	$7.81 \cdot 10^{-2}$	$3.94 \cdot 10^{-1}$	$8.46 \cdot 10^{-1}$	± 2.6
660.0	$3.94 \cdot 10^{-2}$	$2.63 \cdot 10^{-2}$	$8.35 \cdot 10^{-2}$	$7.85 \cdot 10^{-2}$	$3.95 \cdot 10^{-1}$	$8.50 \cdot 10^{-1}$	± 2.6
670.0	$3.96 \cdot 10^{-2}$	$2.64 \cdot 10^{-2}$	$8.38 \cdot 10^{-2}$	$7.88 \cdot 10^{-2}$	$3.97 \cdot 10^{-1}$	$8.53 \cdot 10^{-1}$	± 2.6
680.0	$3.98 \cdot 10^{-2}$	$2.65 \cdot 10^{-2}$	$8.40 \cdot 10^{-2}$	$7.92 \cdot 10^{-2}$	$3.98 \cdot 10^{-1}$	$8.56 \cdot 10^{-1}$	± 2.6
690.0	$4.00 \cdot 10^{-2}$	$2.66 \cdot 10^{-2}$	$8.43 \cdot 10^{-2}$	$7.95 \cdot 10^{-2}$	$3.99 \cdot 10^{-1}$	$8.59 \cdot 10^{-1}$	± 2.6
700.0	$4.01 \cdot 10^{-2}$	$2.68 \cdot 10^{-2}$	$8.46 \cdot 10^{-2}$	$7.98 \cdot 10^{-2}$	$4.01 \cdot 10^{-1}$	$8.62 \cdot 10^{-1}$	± 2.6
710.0	$4.03 \cdot 10^{-2}$	$2.69 \cdot 10^{-2}$	$8.48 \cdot 10^{-2}$	$8.02 \cdot 10^{-2}$	$4.02 \cdot 10^{-1}$	$8.65 \cdot 10^{-1}$	± 2.6
720.0	$4.05 \cdot 10^{-2}$	$2.70 \cdot 10^{-2}$	$8.51 \cdot 10^{-2}$	$8.05 \cdot 10^{-2}$	$4.04 \cdot 10^{-1}$	$8.68 \cdot 10^{-1}$	± 2.6
730.0	$4.06 \cdot 10^{-2}$	$2.71 \cdot 10^{-2}$	$8.54 \cdot 10^{-2}$	$8.08 \cdot 10^{-2}$	$4.05 \cdot 10^{-1}$	$8.71 \cdot 10^{-1}$	± 2.6
740.0	$4.08 \cdot 10^{-2}$	$2.72 \cdot 10^{-2}$	$8.56 \cdot 10^{-2}$	$8.11 \cdot 10^{-2}$	$4.06 \cdot 10^{-1}$	$8.74 \cdot 10^{-1}$	± 2.6
750.0	$4.09 \cdot 10^{-2}$	$2.73 \cdot 10^{-2}$	$8.59 \cdot 10^{-2}$	$8.14 \cdot 10^{-2}$	$4.08 \cdot 10^{-1}$	$8.76 \cdot 10^{-1}$	± 2.6
760.0	$4.11 \cdot 10^{-2}$	$2.74 \cdot 10^{-2}$	$8.62 \cdot 10^{-2}$	$8.17 \cdot 10^{-2}$	$4.09 \cdot 10^{-1}$	$8.79 \cdot 10^{-1}$	± 2.6
770.0	$4.12 \cdot 10^{-2}$	$2.75 \cdot 10^{-2}$	$8.64 \cdot 10^{-2}$	$8.20 \cdot 10^{-2}$	$4.10 \cdot 10^{-1}$	$8.82 \cdot 10^{-1}$	± 2.6
780.0	$4.14 \cdot 10^{-2}$	$2.76 \cdot 10^{-2}$	$8.67 \cdot 10^{-2}$	$8.23 \cdot 10^{-2}$	$4.11 \cdot 10^{-1}$	$8.85 \cdot 10^{-1}$	± 2.6
790.0	$4.15 \cdot 10^{-2}$	$2.77 \cdot 10^{-2}$	$8.69 \cdot 10^{-2}$	$8.26 \cdot 10^{-2}$	$4.13 \cdot 10^{-1}$	$8.87 \cdot 10^{-1}$	± 2.7
800.0	$4.17 \cdot 10^{-2}$	$2.78 \cdot 10^{-2}$	$8.72 \cdot 10^{-2}$	$8.29 \cdot 10^{-2}$	$4.14 \cdot 10^{-1}$	$8.90 \cdot 10^{-1}$	± 2.7
810.0	$4.18 \cdot 10^{-2}$	$2.79 \cdot 10^{-2}$	$8.74 \cdot 10^{-2}$	$8.31 \cdot 10^{-2}$	$4.15 \cdot 10^{-1}$	$8.93 \cdot 10^{-1}$	± 2.7
820.0	$4.19 \cdot 10^{-2}$	$2.80 \cdot 10^{-2}$	$8.76 \cdot 10^{-2}$	$8.34 \cdot 10^{-2}$	$4.16 \cdot 10^{-1}$	$8.95 \cdot 10^{-1}$	± 2.7
830.0	$4.21 \cdot 10^{-2}$	$2.80 \cdot 10^{-2}$	$8.79 \cdot 10^{-2}$	$8.37 \cdot 10^{-2}$	$4.17 \cdot 10^{-1}$	$8.98 \cdot 10^{-1}$	± 2.7
840.0	$4.22 \cdot 10^{-2}$	$2.81 \cdot 10^{-2}$	$8.81 \cdot 10^{-2}$	$8.39 \cdot 10^{-2}$	$4.18 \cdot 10^{-1}$	$9.00 \cdot 10^{-1}$	± 2.7
850.0	$4.23 \cdot 10^{-2}$	$2.82 \cdot 10^{-2}$	$8.83 \cdot 10^{-2}$	$8.42 \cdot 10^{-2}$	$4.19 \cdot 10^{-1}$	$9.02 \cdot 10^{-1}$	± 2.7
860.0	$4.24 \cdot 10^{-2}$	$2.83 \cdot 10^{-2}$	$8.85 \cdot 10^{-2}$	$8.44 \cdot 10^{-2}$	$4.20 \cdot 10^{-1}$	$9.05 \cdot 10^{-1}$	± 2.7
870.0	$4.26 \cdot 10^{-2}$	$2.84 \cdot 10^{-2}$	$8.87 \cdot 10^{-2}$	$8.46 \cdot 10^{-2}$	$4.21 \cdot 10^{-1}$	$9.07 \cdot 10^{-1}$	± 2.7
880.0	$4.27 \cdot 10^{-2}$	$2.85 \cdot 10^{-2}$	$8.90 \cdot 10^{-2}$	$8.49 \cdot 10^{-2}$	$4.22 \cdot 10^{-1}$	$9.09 \cdot 10^{-1}$	± 2.8
890.0	$4.28 \cdot 10^{-2}$	$2.85 \cdot 10^{-2}$	$8.92 \cdot 10^{-2}$	$8.51 \cdot 10^{-2}$	$4.23 \cdot 10^{-1}$	$9.11 \cdot 10^{-1}$	± 2.8
900.0	$4.29 \cdot 10^{-2}$	$2.86 \cdot 10^{-2}$	$8.94 \cdot 10^{-2}$	$8.53 \cdot 10^{-2}$	$4.24 \cdot 10^{-1}$	$9.13 \cdot 10^{-1}$	± 2.8
910.0	$4.30 \cdot 10^{-2}$	$2.87 \cdot 10^{-2}$	$8.96 \cdot 10^{-2}$	$8.55 \cdot 10^{-2}$	$4.25 \cdot 10^{-1}$	$9.16 \cdot 10^{-1}$	± 2.8
920.0	$4.31 \cdot 10^{-2}$	$2.88 \cdot 10^{-2}$	$8.98 \cdot 10^{-2}$	$8.57 \cdot 10^{-2}$	$4.26 \cdot 10^{-1}$	$9.18 \cdot 10^{-1}$	± 2.8
930.0	$4.32 \cdot 10^{-2}$	$2.88 \cdot 10^{-2}$	$9.00 \cdot 10^{-2}$	$8.59 \cdot 10^{-2}$	$4.27 \cdot 10^{-1}$	$9.20 \cdot 10^{-1}$	± 2.8
940.0	$4.33 \cdot 10^{-2}$	$2.89 \cdot 10^{-2}$	$9.02 \cdot 10^{-2}$	$8.62 \cdot 10^{-2}$	$4.28 \cdot 10^{-1}$	$9.22 \cdot 10^{-1}$	± 2.8
950.0	$4.34 \cdot 10^{-2}$	$2.90 \cdot 10^{-2}$	$9.03 \cdot 10^{-2}$	$8.64 \cdot 10^{-2}$	$4.29 \cdot 10^{-1}$	$9.24 \cdot 10^{-1}$	± 2.8
960.0	$4.35 \cdot 10^{-2}$	$2.90 \cdot 10^{-2}$	$9.05 \cdot 10^{-2}$	$8.65 \cdot 10^{-2}$	$4.30 \cdot 10^{-1}$	$9.25 \cdot 10^{-1}$	± 2.8
970.0	$4.36 \cdot 10^{-2}$	$2.91 \cdot 10^{-2}$	$9.07 \cdot 10^{-2}$	$8.67 \cdot 10^{-2}$	$4.31 \cdot 10^{-1}$	$9.27 \cdot 10^{-1}$	± 2.8
980.0	$4.37 \cdot 10^{-2}$	$2.92 \cdot 10^{-2}$	$9.09 \cdot 10^{-2}$	$8.69 \cdot 10^{-2}$	$4.31 \cdot 10^{-1}$	$9.29 \cdot 10^{-1}$	± 2.9
990.0	$4.38 \cdot 10^{-2}$	$2.92 \cdot 10^{-2}$	$9.10 \cdot 10^{-2}$	$8.71 \cdot 10^{-2}$	$4.32 \cdot 10^{-1}$	$9.31 \cdot 10^{-1}$	± 2.9
1000.0	$4.39 \cdot 10^{-2}$	$2.93 \cdot 10^{-2}$	$9.12 \cdot 10^{-2}$	$8.73 \cdot 10^{-2}$	$4.33 \cdot 10^{-1}$	$9.33 \cdot 10^{-1}$	± 2.9

B Weights for POWHEG by HQT program

Table B.1 completes the studies on $\mathrm{H} \to \mathrm{ZZ}$ in Section 11 by the explicit factor for the POWHEG/HQT reweighting of the Higgs-p_{T} spectrum for several Higgs-boson masses.

C 2D K-factors for gluon-fusion Higgs signal production and prompt diphoton backgrounds

Tables C.1–C.5 show the doubly-differential K-factors for the $\mathrm{gg} \to \mathrm{H} \to \gamma\gamma$ discussed in Section 9.3.2.

Table B.1: Relative weights HQT vs. POWHEG for several Higgs-boson masses and p_{T} values.

	M_{H} [GeV]																		
p_{T} [GeV]	115	120	130	140	150	160	170	180	190	200	220	250	300	350	400	450	500	550	600
1.0	0.81	0.74	0.91	0.94	1.01	1.02	0.92	0.80	0.82	0.87	0.83	0.68	0.60	0.47	0.50	0.36	0.23	0.16	0.14
5.0	1.27	1.26	1.25	1.25	1.22	1.24	1.23	1.22	1.21	1.22	1.18	1.18	1.14	1.12	1.10	1.06	1.03	1.00	0.97
10.0	1.22	1.21	1.21	1.21	1.20	1.20	1.19	1.19	1.18	1.18	1.16	1.16	1.13	1.11	1.09	1.06	1.03	1.01	0.98
15.0	1.16	1.16	1.16	1.16	1.16	1.16	1.16	1.16	1.16	1.15	1.14	1.14	1.12	1.10	1.09	1.06	1.04	1.01	0.99
20.0	1.11	1.11	1.12	1.12	1.12	1.13	1.13	1.13	1.13	1.13	1.12	1.12	1.11	1.09	1.09	1.06	1.04	1.02	1.00
25.0	1.06	1.07	1.08	1.08	1.09	1.09	1.10	1.10	1.10	1.10	1.10	1.10	1.09	1.09	1.08	1.06	1.04	1.03	1.01
30.0	1.02	1.03	1.04	1.04	1.05	1.06	1.07	1.07	1.07	1.08	1.08	1.08	1.08	1.08	1.07	1.06	1.05	1.03	1.02
35.0	0.98	0.98	1.00	1.01	1.02	1.03	1.04	1.04	1.05	1.05	1.06	1.07	1.07	1.07	1.07	1.06	1.05	1.04	1.03
40.0	0.94	0.95	0.96	0.97	0.99	1.00	1.01	1.02	1.02	1.03	1.05	1.05	1.06	1.06	1.06	1.05	1.05	1.04	1.03
45.0	0.90	0.91	0.93	0.94	0.96	0.97	0.98	0.99	1.00	1.01	1.03	1.03	1.04	1.05	1.06	1.05	1.05	1.05	1.04
50.0	0.87	0.88	0.90	0.91	0.93	0.94	0.95	0.96	0.98	0.98	1.01	1.01	1.03	1.04	1.05	1.05	1.05	1.05	1.04
55.0	0.83	0.85	0.87	0.88	0.90	0.91	0.93	0.94	0.95	0.96	0.99	0.99	1.02	1.04	1.04	1.04	1.05	1.05	1.05
60.0	0.80	0.82	0.84	0.85	0.87	0.89	0.90	0.91	0.93	0.94	0.97	0.98	1.01	1.03	1.04	1.04	1.05	1.05	1.05
65.0	0.78	0.79	0.81	0.83	0.85	0.86	0.88	0.89	0.91	0.92	0.95	0.96	0.99	1.02	1.03	1.04	1.04	1.06	1.05
70.0	0.75	0.76	0.79	0.80	0.82	0.84	0.86	0.87	0.89	0.90	0.93	0.94	0.98	1.01	1.02	1.03	1.04	1.06	1.05
75.0	0.73	0.74	0.76	0.78	0.80	0.82	0.84	0.85	0.87	0.88	0.91	0.93	0.97	1.00	1.01	1.03	1.04	1.06	1.06
80.0	0.71	0.72	0.74	0.76	0.78	0.79	0.82	0.83	0.85	0.86	0.89	0.91	0.95	0.99	1.01	1.02	1.04	1.05	1.06
85.0	0.69	0.70	0.72	0.74	0.76	0.77	0.80	0.81	0.83	0.84	0.87	0.89	0.94	0.98	1.00	1.01	1.03	1.05	1.06
90.0	0.67	0.68	0.70	0.72	0.74	0.75	0.78	0.79	0.81	0.82	0.85	0.88	0.93	0.96	0.99	1.01	1.03	1.05	1.06
95.0	0.66	0.67	0.69	0.70	0.72	0.74	0.76	0.77	0.79	0.81	0.83	0.86	0.91	0.95	0.98	1.00	1.02	1.05	1.05
100.0	0.64	0.65	0.67	0.69	0.71	0.72	0.74	0.75	0.77	0.79	0.81	0.85	0.90	0.94	0.97	0.99	1.02	1.04	1.05
105.0	0.63	0.64	0.65	0.67	0.69	0.70	0.72	0.74	0.76	0.77	0.80	0.83	0.89	0.93	0.96	0.99	1.01	1.04	1.05
110.0	0.62	0.63	0.64	0.66	0.68	0.69	0.71	0.72	0.74	0.76	0.78	0.82	0.87	0.92	0.95	0.98	1.01	1.03	1.05
115.0	0.61	0.62	0.63	0.64	0.66	0.67	0.69	0.71	0.72	0.74	0.76	0.80	0.86	0.91	0.94	0.97	1.00	1.03	1.04
120.0	0.60	0.61	0.62	0.63	0.65	0.66	0.68	0.69	0.71	0.73	0.75	0.79	0.85	0.89	0.93	0.96	0.99	1.02	1.04
125.0	0.59	0.60	0.61	0.62	0.64	0.65	0.67	0.68	0.70	0.71	0.73	0.77	0.83	0.88	0.92	0.95	0.98	1.01	1.03
130.0	0.59	0.59	0.60	0.61	0.63	0.64	0.65	0.67	0.68	0.70	0.72	0.76	0.82	0.87	0.90	0.94	0.97	1.00	1.03
135.0	0.58	0.59	0.59	0.61	0.62	0.63	0.64	0.66	0.67	0.69	0.70	0.75	0.81	0.85	0.89	0.93	0.97	1.00	1.02
140.0	0.58	0.58	0.59	0.60	0.61	0.62	0.63	0.65	0.66	0.68	0.69	0.73	0.79	0.84	0.88	0.92	0.96	0.99	1.01
145.0	0.58	0.58	0.58	0.59	0.60	0.61	0.62	0.64	0.65	0.66	0.67	0.72	0.78	0.83	0.87	0.91	0.95	0.98	1.01
150.0	0.57	0.57	0.57	0.59	0.60	0.60	0.61	0.63	0.64	0.65	0.66	0.71	0.76	0.81	0.86	0.90	0.93	0.97	1.00
155.0	0.57	0.57	0.57	0.58	0.59	0.59	0.61	0.62	0.63	0.64	0.65	0.69	0.75	0.80	0.84	0.89	0.92	0.95	0.99
160.0	0.57	0.57	0.57	0.58	0.59	0.59	0.60	0.61	0.62	0.63	0.64	0.68	0.74	0.79	0.83	0.88	0.91	0.94	0.98
165.0	0.57	0.57	0.57	0.58	0.58	0.58	0.59	0.61	0.61	0.63	0.63	0.67	0.72	0.77	0.82	0.86	0.90	0.93	0.97
170.0	0.57	0.57	0.56	0.57	0.58	0.58	0.59	0.60	0.60	0.62	0.62	0.66	0.71	0.76	0.80	0.85	0.89	0.92	0.96
175.0	0.57	0.57	0.56	0.57	0.58	0.58	0.58	0.60	0.60	0.61	0.61	0.65	0.69	0.74	0.79	0.84	0.87	0.90	0.94
180.0	0.57	0.57	0.56	0.57	0.57	0.57	0.58	0.59	0.59	0.60	0.61	0.63	0.68	0.72	0.77	0.82	0.86	0.89	0.93
185.0	0.57	0.57	0.56	0.57	0.57	0.57	0.57	0.59	0.59	0.60	0.60	0.62	0.66	0.71	0.76	0.81	0.85	0.87	0.92
190.0	0.57	0.58	0.56	0.57	0.57	0.57	0.57	0.59	0.58	0.59	0.60	0.61	0.65	0.69	0.74	0.80	0.83	0.85	0.91
195.0	0.57	0.58	0.57	0.57	0.57	0.57	0.57	0.58	0.58	0.59	0.59	0.60	0.63	0.68	0.73	0.78	0.81	0.84	0.89
200.0	0.57	0.58	0.57	0.57	0.57	0.57	0.57	0.58	0.58	0.58	0.59	0.59	0.62	0.66	0.71	0.77	0.80	0.82	0.88
205.0	0.57	0.59	0.57	0.58	0.57	0.58	0.57	0.58	0.57	0.58	0.59	0.61	0.65	0.63	0.68	0.76	0.80	0.85	0.89
210.0	0.57	0.59	0.57	0.58	0.57	0.58	0.57	0.59	0.57	0.58	0.59	0.61	0.64	0.63	0.67	0.75	0.79	0.84	0.88
215.0	0.57	0.59	0.58	0.58	0.58	0.58	0.57	0.59	0.57	0.57	0.59	0.60	0.64	0.63	0.67	0.75	0.79	0.83	0.87
220.0	0.57	0.59	0.58	0.58	0.58	0.59	0.57	0.59	0.57	0.57	0.59	0.60	0.64	0.63	0.67	0.74	0.78	0.82	0.86
225.0	0.56	0.60	0.58	0.59	0.58	0.59	0.58	0.59	0.57	0.57	0.59	0.60	0.63	0.63	0.66	0.73	0.77	0.81	0.85
230.0	0.56	0.60	0.59	0.59	0.59	0.60	0.58	0.60	0.57	0.57	0.60	0.60	0.63	0.63	0.66	0.73	0.76	0.80	0.84
235.0	0.56	0.60	0.59	0.59	0.59	0.60	0.58	0.60	0.58	0.57	0.61	0.60	0.63	0.63	0.66	0.72	0.76	0.79	0.83
240.0	0.55	0.61	0.59	0.60	0.59	0.61	0.59	0.61	0.58	0.58	0.61	0.59	0.62	0.63	0.66	0.72	0.75	0.79	0.82
245.0	0.55	0.61	0.60	0.60	0.60	0.62	0.59	0.62	0.58	0.58	0.62	0.59	0.62	0.63	0.65	0.71	0.74	0.78	0.81
250.0	0.54	0.61	0.60	0.60	0.60	0.63	0.60	0.62	0.59	0.58	0.63	0.59	0.62	0.63	0.65	0.71	0.74	0.77	0.80
255.0	0.54	0.61	0.60	0.60	0.60	0.62	0.60	0.62	0.58	0.58	0.63	0.59	0.61	0.63	0.65	0.70	0.73	0.76	0.79
260.0	0.54	0.60	0.60	0.60	0.60	0.62	0.60	0.62	0.58	0.58	0.63	0.59	0.61	0.63	0.65	0.70	0.72	0.76	0.79
265.0	0.53	0.60	0.60	0.60	0.60	0.62	0.59	0.62	0.58	0.58	0.63	0.59	0.61	0.62	0.64	0.69	0.72	0.75	0.78
270.0	0.53	0.60	0.59	0.60	0.59	0.62	0.59	0.62	0.58	0.57	0.63	0.58	0.61	0.62	0.64	0.69	0.71	0.74	0.77
275.0	0.53	0.60	0.59	0.59	0.59	0.62	0.59	0.61	0.58	0.57	0.62	0.58	0.61	0.62	0.64	0.68	0.70	0.74	0.76
280.0	0.53	0.60	0.59	0.59	0.59	0.61	0.59	0.61	0.57	0.57	0.62	0.58	0.60	0.62	0.64	0.68	0.70	0.73	0.76
285.0	0.53	0.59	0.59	0.59	0.59	0.61	0.59	0.61	0.57	0.57	0.62	0.58	0.60	0.62	0.63	0.67	0.69	0.72	0.75
290.0	0.52	0.59	0.59	0.59	0.59	0.61	0.58	0.61	0.57	0.57	0.62	0.58	0.60	0.62	0.63	0.67	0.69	0.72	0.74
295.0	0.52	0.59	0.58	0.59	0.58	0.61	0.58	0.61	0.57	0.56	0.62	0.58	0.60	0.62	0.63	0.66	0.68	0.71	0.74
300.0	0.52	0.59	0.58	0.58	0.58	0.61	0.58	0.60	0.57	0.56	0.61	0.58	0.60	0.62	0.63	0.66	0.68	0.71	0.73
305.0	0.52	0.59	0.58	0.58	0.58	0.60	0.58	0.60	0.56	0.56	0.61	0.57	0.59	0.62	0.63	0.66	0.67	0.70	0.73
310.0	0.52	0.58	0.58	0.58	0.58	0.60	0.58	0.60	0.56	0.56	0.61	0.57	0.59	0.62	0.62	0.65	0.67	0.70	0.72
315.0	0.51	0.58	0.58	0.58	0.58	0.60	0.57	0.60	0.56	0.56	0.61	0.57	0.59	0.62	0.62	0.65	0.66	0.69	0.72
320.0	0.51	0.58	0.57	0.58	0.57	0.60	0.57	0.60	0.56	0.55	0.61	0.57	0.59	0.61	0.62	0.65	0.66	0.69	0.71
325.0	0.51	0.58	0.57	0.57	0.57	0.60	0.57	0.59	0.56	0.55	0.60	0.57	0.59	0.61	0.62	0.64	0.66	0.68	0.71
330.0	0.51	0.58	0.57	0.57	0.57	0.59	0.57	0.59	0.55	0.55	0.60	0.57	0.59	0.61	0.62	0.64	0.65	0.68	0.70
335.0	0.51	0.57	0.57	0.57	0.57	0.59	0.57	0.59	0.55	0.55	0.60	0.57	0.59	0.61	0.61	0.64	0.65	0.67	0.70
340.0	0.50	0.57	0.57	0.57	0.57	0.59	0.56	0.59	0.55	0.55	0.60	0.57	0.59	0.61	0.61	0.63	0.65	0.67	0.70
345.0	0.50	0.57	0.56	0.57	0.56	0.59	0.56	0.59	0.55	0.54	0.60	0.57	0.59	0.61	0.61	0.63	0.64	0.67	0.69
350.0	0.50	0.57	0.56	0.56	0.56	0.59	0.56	0.58	0.55	0.54	0.59	0.57	0.58	0.61	0.61	0.63	0.64	0.66	0.69
355.0	0.50	0.57	0.56	0.56	0.56	0.58	0.56	0.58	0.54	0.54	0.59	0.57	0.58	0.61	0.61	0.63	0.64	0.66	0.69
360.0	0.50	0.56	0.56	0.56	0.56	0.58	0.56	0.58	0.54	0.54	0.59	0.57	0.58	0.60	0.61	0.62	0.64	0.66	0.68
365.0	0.49	0.56	0.56	0.56	0.56	0.58	0.55	0.58	0.54	0.54	0.59	0.56	0.58	0.60	0.60	0.62	0.63	0.65	0.68
370.0	0.49	0.56	0.55	0.56	0.55	0.58	0.55	0.58	0.54	0.53	0.59	0.56	0.58	0.60	0.60	0.62	0.63	0.65	0.68
375.0	0.49	0.56	0.55	0.55	0.55	0.58	0.55	0.57	0.54	0.53	0.58	0.56	0.58	0.60	0.60	0.62	0.63	0.65	0.68
380.0	0.49	0.56	0.55	0.55	0.55	0.57	0.55	0.57	0.53	0.53	0.58	0.56	0.58	0.60	0.60	0.61	0.63	0.65	0.68
385.0	0.49	0.55	0.55	0.55	0.55	0.57	0.55	0.57	0.53	0.53	0.58	0.56	0.58	0.60	0.60	0.61	0.63	0.64	0.68
390.0	0.48	0.55	0.55	0.55	0.55	0.57	0.54	0.57	0.53	0.53	0.58	0.56	0.58	0.59	0.60	0.61	0.62	0.64	0.68
395.0	0.48	0.55	0.54	0.55	0.54	0.57	0.54	0.57	0.53	0.52	0.58	0.56	0.58	0.59	0.60	0.61	0.62	0.64	0.68
400.0	0.48	0.55	0.54	0.54	0.54	0.57	0.54	0.56	0.53	0.52	0.57	0.56	0.58	0.59	0.60	0.61	0.62	0.64	0.68
405.0	0.48	0.55	0.54	0.54	0.54	0.56	0.54	0.56	0.52	0.52	0.57	0.56	0.58	0.59	0.59	0.61	0.62	0.64	0.68
410.0	0.48	0.54	0.54	0.54	0.54	0.56	0.54	0.56	0.52	0.52	0.57	0.56	0.59	0.59	0.59	0.60	0.62	0.64	0.68
415.0	0.47	0.54	0.54	0.54	0.54	0.56	0.53	0.56	0.52	0.52	0.57	0.56	0.59	0.59	0.59	0.60	0.62	0.64	0.68
420.0	0.47	0.54	0.53	0.54	0.53	0.56	0.53	0.56	0.52	0.51	0.57	0.56	0.59	0.58	0.59	0.60	0.62	0.63	0.68
425.0	0.47	0.54	0.53	0.53	0.53	0.56	0.53	0.55	0.52	0.51	0.56	0.56	0.59	0.58	0.59	0.60	0.62	0.63	0.68
430.0	0.47	0.54	0.53	0.53	0.53	0.55	0.53	0.55	0.51	0.51	0.56	0.56	0.59	0.58	0.59	0.60	0.62	0.63	0.68
435.0	0.47	0.53	0.53	0.53	0.53	0.55	0.53	0.55	0.51	0.51	0.56	0.56	0.59	0.58	0.59	0.60	0.62	0.63	0.68
440.0	0.46	0.53	0.53	0.53	0.53	0.55	0.52	0.55	0.51	0.51	0.56	0.56	0.59	0.58	0.59	0.60	0.62	0.63	0.68
445.0	0.46	0.53	0.52	0.53	0.52	0.55	0.52	0.55	0.51	0.50	0.56	0.56	0.58	0.58	0.59	0.60	0.62	0.63	0.68
450.0	0.46	0.53	0.52	0.52	0.52	0.55	0.52	0.54	0.51	0.50	0.55	0.56	0.58	0.58	0.59	0.60	0.62	0.63	0.68
455.0	0.46	0.53	0.52	0.52	0.52	0.54	0.52	0.54	0.50	0.50	0.55	0.56	0.58	0.58	0.59	0.60	0.62	0.63	0.68
460.0	0.46	0.52	0.52	0.52	0.52	0.54	0.52	0.54	0.50	0.50	0.55	0.56	0.58	0.58	0.59	0.60	0.61	0.63	0.67
465.0	0.45	0.52	0.52	0.52	0.52	0.54	0.51	0.54	0.50	0.50	0.55	0.56	0.58	0.58	0.58	0.60	0.61	0.63	0.67
470.0	0.45	0.52	0.51	0.52	0.51	0.54	0.51	0.54	0.50	0.49	0.55	0.56	0.58	0.57	0.58	0.60	0.61	0.63	0.67
475.0	0.45	0.52	0.51	0.51	0.51	0.54	0.51	0.53	0.50	0.49	0.54	0.55	0.58	0.57	0.58	0.59	0.61	0.63	0.67
480.0	0.45	0.52	0.51	0.51	0.51	0.53	0.51	0.53	0.49	0.49	0.54	0.55	0.58	0.57	0.58	0.59	0.61	0.63	0.67
485.0	0.45	0.51	0.51	0.51	0.51	0.53	0.51	0.53	0.49	0.49	0.54	0.55	0.58	0.57	0.58	0.59	0.61	0.62	0.67
490.0	0.44	0.51	0.51	0.51	0.51	0.53	0.50	0.53	0.49	0.49	0.54	0.55	0.58	0.57	0.58	0.59	0.61	0.62	0.67
495.0	0.44	0.51	0.50	0.51	0.50	0.53	0.50	0.53	0.49	0.48	0.54	0.55	0.58	0.57	0.58	0.59	0.61	0.62	0.67
500.0	0.44	0.51	0.50	0.50	0.50	0.53	0.50	0.52	0.49	0.48	0.53	0.55	0.58	0.57	0.58	0.59	0.61	0.62	0.67
499.0	0.44	0.51	0.50	0.50	0.50	0.53	0.50	0.53	0.49	0.48	0.53	0.55	0.58	0.57	0.58	0.59	0.61	0.62	0.67

Table C.1: Relative weights HNNLO vs POWHEG for a Higgs-boson mass $M_{\mathrm{H}} = 110$ GeV.

q_T [GeV] / $\lvert Y_{\gamma\gamma}\rvert$	0.00	0.25	0.50	0.75	1.00	1.25	1.50	1.75	2.00	2.25
0.00	1.62	1.74	1.58	1.75	1.80	1.79	2.06	2.06	2.06	2.06
4.00	1.62	1.74	1.58	1.75	1.80	1.79	2.06	2.06	2.06	2.06
8.00	1.62	1.74	1.58	1.75	1.80	1.79	2.06	2.06	2.06	2.06
12.00	1.62	1.74	1.58	1.75	1.80	1.79	2.06	2.06	2.06	2.06
16.00	1.39	1.39	1.31	1.31	1.38	1.38	1.44	1.44	1.34	1.34
20.00	1.23	1.23	1.29	1.29	1.27	1.27	1.11	1.11	1.34	1.34
24.00	1.04	1.04	1.16	1.16	1.26	1.26	1.19	1.19	1.11	1.11
28.00	1.04	1.04	1.19	1.19	0.97	0.97	1.16	1.16	1.11	1.11
32.00	0.96	0.96	0.94	0.94	1.02	1.02	1.06	1.06	1.01	1.01
36.00	0.93	0.93	0.96	0.96	0.94	0.94	0.96	0.96	1.01	1.01
40.00	0.88	0.88	1.08	1.08	1.01	1.01	0.92	0.92	1.00	1.00
44.00	0.96	0.96	0.89	0.89	0.91	0.91	0.91	0.91	1.00	1.00
48.00	0.88	0.88	0.93	0.93	1.07	1.07	0.95	0.95	0.90	0.90
52.00	0.81	0.81	0.85	0.85	0.96	0.96	0.86	0.86	0.90	0.90
56.00	0.88	0.88	0.87	0.87	0.91	0.91	0.96	0.96	0.70	0.70
60.00	0.85	0.85	0.90	0.90	0.87	0.87	0.92	0.92	0.70	0.70
64.00	0.89	0.89	0.89	0.89	0.93	0.93	0.80	0.80	0.70	0.70
68.00	0.92	0.92	0.90	0.90	0.96	0.96	1.01	1.01	1.08	1.08
72.00	0.83	0.83	0.90	0.90	1.01	1.01	0.77	0.77	1.08	1.08
76.00	0.81	0.81	0.95	0.95	0.92	0.92	0.76	0.76	1.08	1.08
80.00	0.83	0.83	0.83	0.83	0.83	0.83	0.82	0.82	0.82	0.82
84.00	0.83	0.83	0.83	0.83	0.83	0.83	0.82	0.82	0.82	0.82
88.00	0.83	0.83	0.83	0.83	0.83	0.83	0.82	0.82	0.82	0.82
92.00	0.83	0.83	0.83	0.83	0.83	0.83	0.82	0.82	0.82	0.82
96.00	0.83	0.83	0.83	0.83	0.83	0.83	0.82	0.82	0.82	0.82
100.00	0.84	0.84	0.81	0.81	0.81	0.81	0.69	0.69	0.69	0.69
104.00	0.84	0.84	0.81	0.81	0.81	0.81	0.69	0.69	0.69	0.69
108.00	0.84	0.84	0.81	0.81	0.81	0.81	0.69	0.69	0.69	0.69
112.00	0.84	0.84	0.81	0.81	0.81	0.81	0.69	0.69	0.69	0.69
116.00	0.84	0.84	0.81	0.81	0.81	0.81	0.69	0.69	0.69	0.69
120.00	0.82	0.82	0.82	0.82	0.82	0.82	0.82	0.82	0.82	0.82
124.00	0.82	0.82	0.82	0.82	0.82	0.82	0.82	0.82	0.82	0.82
128.00	0.82	0.82	0.82	0.82	0.82	0.82	0.82	0.82	0.82	0.82
132.00	0.82	0.82	0.82	0.82	0.82	0.82	0.82	0.82	0.82	0.82
136.00	0.86	0.86	0.86	0.86	0.86	0.86	0.86	0.86	0.86	0.86
140.00	0.86	0.86	0.86	0.86	0.86	0.86	0.86	0.86	0.86	0.86
144.00	0.86	0.86	0.86	0.86	0.86	0.86	0.86	0.86	0.86	0.86
148.00	0.86	0.86	0.86	0.86	0.86	0.86	0.86	0.86	0.86	0.86
152.00	0.86	0.86	0.86	0.86	0.86	0.86	0.86	0.86	0.86	0.86
156.00	0.86	0.86	0.86	0.86	0.86	0.86	0.86	0.86	0.86	0.86
160.00	0.86	0.86	0.86	0.86	0.86	0.86	0.86	0.86	0.86	0.86
164.00	0.86	0.86	0.86	0.86	0.86	0.86	0.86	0.86	0.86	0.86
168.00	0.86	0.86	0.86	0.86	0.86	0.86	0.86	0.86	0.86	0.86
172.00	0.86	0.86	0.86	0.86	0.86	0.86	0.86	0.86	0.86	0.86
176.00	0.86	0.86	0.86	0.86	0.86	0.86	0.86	0.86	0.86	0.86
180.00	0.86	0.86	0.86	0.86	0.86	0.86	0.86	0.86	0.86	0.86
184.00	0.86	0.86	0.86	0.86	0.86	0.86	0.86	0.86	0.86	0.86
188.00	0.86	0.86	0.86	0.86	0.86	0.86	0.86	0.86	0.86	0.86
192.00	0.86	0.86	0.86	0.86	0.86	0.86	0.86	0.86	0.86	0.86
196.00	0.86	0.86	0.86	0.86	0.86	0.86	0.86	0.86	0.86	0.86

Table C.2: Relative weights HNNLO vs POWHEG for a Higgs-boson mass $M_{\mathrm{H}} = 120$ GeV.

q_T [GeV] / $\lvert Y_{\gamma\gamma}\rvert$	0.00	0.25	0.50	0.75	1.00	1.25	1.50	1.75	2.00	2.25
0.00	1.51	1.53	1.68	1.96	1.90	1.77	1.75	1.75	1.75	1.75
4.00	1.51	1.53	1.68	1.96	1.90	1.77	1.75	1.75	1.75	1.75
8.00	1.51	1.53	1.68	1.96	1.90	1.77	1.75	1.75	1.75	1.75
12.00	1.51	1.53	1.68	1.96	1.90	1.77	1.75	1.75	1.75	1.75
16.00	1.48	1.48	1.43	1.43	1.40	1.40	1.49	1.49	1.30	1.30
20.00	1.24	1.24	1.31	1.31	1.25	1.25	1.18	1.18	1.30	1.30
24.00	1.17	1.17	1.24	1.24	1.26	1.26	1.28	1.28	1.29	1.29
28.00	1.08	1.08	1.12	1.12	1.14	1.14	1.27	1.27	1.29	1.29
32.00	0.96	0.96	1.03	1.03	1.01	1.01	0.92	0.92	1.04	1.04
36.00	0.99	0.99	0.95	0.95	1.01	1.01	1.11	1.11	1.04	1.04
40.00	1.06	1.06	0.99	0.99	1.00	1.00	1.01	1.01	1.03	1.03
44.00	0.99	0.99	0.96	0.96	0.91	0.91	0.91	0.91	1.03	1.03
48.00	0.92	0.92	1.16	1.16	0.94	0.94	0.98	0.98	0.79	0.79
52.00	0.89	0.89	0.65	0.65	0.93	0.93	0.94	0.94	0.79	0.79
56.00	0.97	0.97	0.92	0.92	0.97	0.97	0.96	0.96	0.87	0.87
60.00	0.84	0.84	0.91	0.91	0.98	0.98	1.02	1.02	0.87	0.87
64.00	0.95	0.95	0.91	0.91	0.98	0.98	0.66	0.66	0.87	0.87
68.00	0.82	0.82	0.85	0.85	0.79	0.79	1.06	1.06	0.98	0.98
72.00	0.85	0.85	0.86	0.86	0.91	0.91	0.92	0.92	0.98	0.98
76.00	0.83	0.83	0.82	0.82	1.03	1.03	0.84	0.84	0.98	0.98
80.00	0.91	0.91	0.88	0.88	0.88	0.88	0.75	0.75	0.75	0.75
84.00	0.91	0.91	0.88	0.88	0.88	0.88	0.75	0.75	0.75	0.75
88.00	0.91	0.91	0.88	0.88	0.88	0.88	0.75	0.75	0.75	0.75
92.00	0.91	0.91	0.88	0.88	0.88	0.88	0.75	0.75	0.75	0.75
96.00	0.91	0.91	0.88	0.88	0.88	0.88	0.75	0.75	0.75	0.75
100.00	0.85	0.85	0.87	0.87	0.87	0.87	0.75	0.75	0.75	0.75
104.00	0.85	0.85	0.87	0.87	0.87	0.87	0.75	0.75	0.75	0.75
108.00	0.85	0.85	0.87	0.87	0.87	0.87	0.75	0.75	0.75	0.75
112.00	0.85	0.85	0.87	0.87	0.87	0.87	0.75	0.75	0.75	0.75
116.00	0.85	0.85	0.87	0.87	0.87	0.87	0.75	0.75	0.75	0.75
120.00	0.88	0.88	0.88	0.88	0.88	0.88	0.88	0.88	0.88	0.88
124.00	0.88	0.88	0.88	0.88	0.88	0.88	0.88	0.88	0.88	0.88
128.00	0.88	0.88	0.88	0.88	0.88	0.88	0.88	0.88	0.88	0.88
132.00	0.88	0.88	0.88	0.88	0.88	0.88	0.88	0.88	0.88	0.88
136.00	0.83	0.83	0.83	0.83	0.83	0.83	0.83	0.83	0.83	0.83
140.00	0.83	0.83	0.83	0.83	0.83	0.83	0.83	0.83	0.83	0.83
144.00	0.83	0.83	0.83	0.83	0.83	0.83	0.83	0.83	0.83	0.83
148.00	0.83	0.83	0.83	0.83	0.83	0.83	0.83	0.83	0.83	0.83
152.00	0.83	0.83	0.83	0.83	0.83	0.83	0.83	0.83	0.83	0.83
156.00	0.83	0.83	0.83	0.83	0.83	0.83	0.83	0.83	0.83	0.83
160.00	0.83	0.83	0.83	0.83	0.83	0.83	0.83	0.83	0.83	0.83
164.00	0.83	0.83	0.83	0.83	0.83	0.83	0.83	0.83	0.83	0.83
168.00	0.83	0.83	0.83	0.83	0.83	0.83	0.83	0.83	0.83	0.83
172.00	0.83	0.83	0.83	0.83	0.83	0.83	0.83	0.83	0.83	0.83
176.00	0.83	0.83	0.83	0.83	0.83	0.83	0.83	0.83	0.83	0.83
180.00	0.83	0.83	0.83	0.83	0.83	0.83	0.83	0.83	0.83	0.83
184.00	0.83	0.83	0.83	0.83	0.83	0.83	0.83	0.83	0.83	0.83
188.00	0.83	0.83	0.83	0.83	0.83	0.83	0.83	0.83	0.83	0.83
192.00	0.83	0.83	0.83	0.83	0.83	0.83	0.83	0.83	0.83	0.83
196.00	0.83	0.83	0.83	0.83	0.83	0.83	0.83	0.83	0.83	0.83

Table C.3: Relative weights HNNLO vs POWHEG for a Higgs-boson mass $M_{\mathrm{H}} = 130$ GeV.

q_T [GeV] / $\lvert Y_{\gamma\gamma}\rvert$	0.00	0.25	0.50	0.75	1.00	1.25	1.50	1.75	2.00	2.25
0.00	1.60	1.66	1.61	1.61	1.75	1.80	1.81	1.81	1.81	1.81
4.00	1.60	1.66	1.61	1.61	1.75	1.80	1.81	1.81	1.81	1.81
8.00	1.60	1.66	1.61	1.61	1.75	1.80	1.81	1.81	1.81	1.81
12.00	1.60	1.66	1.61	1.61	1.75	1.80	1.81	1.81	1.81	1.81
16.00	1.40	1.40	1.57	1.57	1.47	1.47	1.36	1.36	1.28	1.28
20.00	1.31	1.31	1.31	1.31	1.09	1.09	1.17	1.17	1.28	1.28
24.00	1.21	1.21	1.19	1.19	1.51	1.51	1.31	1.31	1.13	1.13
28.00	1.07	1.07	1.06	1.06	1.13	1.13	1.30	1.30	1.13	1.13
32.00	1.14	1.14	1.17	1.17	1.10	1.10	1.06	1.06	0.91	0.91
36.00	0.90	0.90	0.98	0.98	0.98	0.98	0.96	0.96	0.91	0.91
40.00	0.94	0.94	1.03	1.03	0.99	0.99	1.10	1.10	0.81	0.81
44.00	0.97	0.97	0.97	0.97	0.96	0.96	0.99	0.99	0.81	0.81
48.00	0.96	0.96	0.97	0.97	0.85	0.85	0.80	0.80	0.82	0.82
52.00	0.97	0.97	0.92	0.92	1.00	1.00	0.91	0.91	0.82	0.82
56.00	0.94	0.94	0.85	0.85	0.98	0.98	1.03	1.03	0.84	0.84
60.00	0.89	0.89	1.02	1.02	1.03	1.03	0.95	0.95	0.84	0.84
64.00	0.88	0.88	0.95	0.95	1.01	1.01	0.82	0.82	0.84	0.84
68.00	0.81	0.81	0.89	0.89	0.91	0.91	0.91	0.91	0.80	0.80
72.00	0.90	0.90	0.82	0.82	0.84	0.84	0.74	0.74	0.80	0.80
76.00	0.84	0.84	0.91	0.91	0.97	0.97	0.87	0.87	0.80	0.80
80.00	0.83	0.83	0.84	0.84	0.84	0.84	0.79	0.79	0.79	0.79
84.00	0.83	0.83	0.84	0.84	0.84	0.84	0.79	0.79	0.79	0.79
88.00	0.83	0.83	0.84	0.84	0.84	0.84	0.79	0.79	0.79	0.79
92.00	0.83	0.83	0.84	0.84	0.84	0.84	0.79	0.79	0.79	0.79
96.00	0.83	0.83	0.84	0.84	0.84	0.84	0.79	0.79	0.79	0.79
100.00	0.84	0.84	0.83	0.83	0.83	0.83	0.83	0.83	0.83	0.83
104.00	0.84	0.84	0.83	0.83	0.83	0.83	0.83	0.83	0.83	0.83
108.00	0.84	0.84	0.83	0.83	0.83	0.83	0.83	0.83	0.83	0.83
112.00	0.84	0.84	0.83	0.83	0.83	0.83	0.83	0.83	0.83	0.83
116.00	0.84	0.84	0.83	0.83	0.83	0.83	0.83	0.83	0.83	0.83
120.00	0.85	0.85	0.85	0.85	0.85	0.85	0.85	0.85	0.85	0.85
124.00	0.85	0.85	0.85	0.85	0.85	0.85	0.85	0.85	0.85	0.85
128.00	0.85	0.85	0.85	0.85	0.85	0.85	0.85	0.85	0.85	0.85
132.00	0.85	0.85	0.85	0.85	0.85	0.85	0.85	0.85	0.85	0.85
136.00	0.81	0.81	0.81	0.81	0.81	0.81	0.81	0.81	0.81	0.81
140.00	0.81	0.81	0.81	0.81	0.81	0.81	0.81	0.81	0.81	0.81
144.00	0.81	0.81	0.81	0.81	0.81	0.81	0.81	0.81	0.81	0.81
148.00	0.81	0.81	0.81	0.81	0.81	0.81	0.81	0.81	0.81	0.81
152.00	0.81	0.81	0.81	0.81	0.81	0.81	0.81	0.81	0.81	0.81
156.00	0.81	0.81	0.81	0.81	0.81	0.81	0.81	0.81	0.81	0.81
160.00	0.81	0.81	0.81	0.81	0.81	0.81	0.81	0.81	0.81	0.81
164.00	0.81	0.81	0.81	0.81	0.81	0.81	0.81	0.81	0.81	0.81
168.00	0.81	0.81	0.81	0.81	0.81	0.81	0.81	0.81	0.81	0.81
172.00	0.81	0.81	0.81	0.81	0.81	0.81	0.81	0.81	0.81	0.81
176.00	0.81	0.81	0.81	0.81	0.81	0.81	0.81	0.81	0.81	0.81
180.00	0.81	0.81	0.81	0.81	0.81	0.81	0.81	0.81	0.81	0.81
184.00	0.81	0.81	0.81	0.81	0.81	0.81	0.81	0.81	0.81	0.81
188.00	0.81	0.81	0.81	0.81	0.81	0.81	0.81	0.81	0.81	0.81
192.00	0.81	0.81	0.81	0.81	0.81	0.81	0.81	0.81	0.81	0.81
196.00	0.81	0.81	0.81	0.81	0.81	0.81	0.81	0.81	0.81	0.81

Table C.4: Relative weights HNNLO vs POWHEG for a Higgs-boson mass $M_{\mathrm{H}} = 140$ GeV.

q_T [GeV] / $\lvert Y_{\gamma\gamma}\rvert$	0.00	0.25	0.50	0.75	1.00	1.25	1.50	1.75	2.00	2.25
0.00	1.63	1.53	1.69	1.59	1.98	1.72	1.76	1.76	1.76	1.76
4.00	1.63	1.53	1.69	1.59	1.98	1.72	1.76	1.76	1.76	1.76
8.00	1.63	1.53	1.69	1.59	1.98	1.72	1.76	1.76	1.76	1.76
12.00	1.63	1.53	1.69	1.59	1.98	1.72	1.76	1.76	1.76	1.76
16.00	1.51	1.51	1.44	1.44	1.49	1.49	1.41	1.41	1.43	1.43
20.00	1.32	1.32	1.28	1.28	1.16	1.16	1.21	1.21	1.43	1.43
24.00	1.11	1.11	1.19	1.19	1.30	1.30	1.28	1.28	0.99	0.99
28.00	1.13	1.13	1.24	1.24	1.03	1.03	1.18	1.18	0.99	0.99
32.00	1.17	1.17	1.11	1.11	1.18	1.18	1.05	1.05	1.01	1.01
36.00	1.01	1.01	1.07	1.07	1.03	1.03	1.04	1.04	1.01	1.01
40.00	1.02	1.02	1.08	1.08	1.05	1.05	0.99	0.99	0.95	0.95
44.00	0.93	0.93	0.96	0.96	1.00	1.00	0.93	0.93	0.95	0.95
48.00	0.90	0.90	0.99	0.99	0.92	0.92	1.14	1.14	0.85	0.85
52.00	0.88	0.88	0.93	0.93	0.98	0.98	1.68	1.68	0.85	0.85
56.00	0.94	0.94	0.86	0.86	1.08	1.08	0.32	0.32	0.73	0.73
60.00	0.93	0.93	1.02	1.02	0.83	0.83	0.21	0.21	0.73	0.73
64.00	0.88	0.88	0.91	0.91	1.09	1.09	1.42	1.42	0.73	0.73
68.00	0.89	0.89	1.05	1.05	0.86	0.86	0.84	0.84	0.90	0.90
72.00	1.06	1.06	0.93	0.93	1.00	1.00	0.61	0.61	0.90	0.90
76.00	0.72	0.72	0.87	0.87	0.84	0.84	0.99	0.99	0.90	0.90
80.00	0.85	0.85	0.90	0.90	0.90	0.90	0.82	0.82	0.82	0.82
84.00	0.85	0.85	0.90	0.90	0.90	0.90	0.82	0.82	0.82	0.82
88.00	0.85	0.85	0.90	0.90	0.90	0.90	0.82	0.82	0.82	0.82
92.00	0.85	0.85	0.90	0.90	0.90	0.90	0.82	0.82	0.82	0.82
96.00	0.85	0.85	0.90	0.90	0.90	0.90	0.82	0.82	0.82	0.82
100.00	0.84	0.84	0.85	0.85	0.85	0.85	0.80	0.80	0.80	0.80
104.00	0.84	0.84	0.85	0.85	0.85	0.85	0.80	0.80	0.80	0.80
108.00	0.84	0.84	0.85	0.85	0.85	0.85	0.80	0.80	0.80	0.80
112.00	0.84	0.84	0.85	0.85	0.85	0.85	0.80	0.80	0.80	0.80
116.00	0.84	0.84	0.85	0.85	0.85	0.85	0.80	0.80	0.80	0.80
120.00	0.84	0.84	0.84	0.84	0.84	0.84	0.84	0.84	0.84	0.84
124.00	0.84	0.84	0.84	0.84	0.84	0.84	0.84	0.84	0.84	0.84
128.00	0.84	0.84	0.84	0.84	0.84	0.84	0.84	0.84	0.84	0.84
132.00	0.84	0.84	0.84	0.84	0.84	0.84	0.84	0.84	0.84	0.84
136.00	0.84	0.84	0.84	0.84	0.84	0.84	0.84	0.84	0.84	0.84
140.00	0.84	0.84	0.84	0.84	0.84	0.84	0.84	0.84	0.84	0.84
144.00	0.84	0.84	0.84	0.84	0.84	0.84	0.84	0.84	0.84	0.84
148.00	0.84	0.84	0.84	0.84	0.84	0.84	0.84	0.84	0.84	0.84
152.00	0.84	0.84	0.84	0.84	0.84	0.84	0.84	0.84	0.84	0.84
156.00	0.84	0.84	0.84	0.84	0.84	0.84	0.84	0.84	0.84	0.84
160.00	0.84	0.84	0.84	0.84	0.84	0.84	0.84	0.84	0.84	0.84
164.00	0.84	0.84	0.84	0.84	0.84	0.84	0.84	0.84	0.84	0.84
168.00	0.84	0.84	0.84	0.84	0.84	0.84	0.84	0.84	0.84	0.84
172.00	0.84	0.84	0.84	0.84	0.84	0.84	0.84	0.84	0.84	0.84
176.00	0.84	0.84	0.84	0.84	0.84	0.84	0.84	0.84	0.84	0.84
180.00	0.84	0.84	0.84	0.84	0.84	0.84	0.84	0.84	0.84	0.84
184.00	0.84	0.84	0.84	0.84	0.84	0.84	0.84	0.84	0.84	0.84
188.00	0.84	0.84	0.84	0.84	0.84	0.84	0.84	0.84	0.84	0.84
192.00	0.84	0.84	0.84	0.84	0.84	0.84	0.84	0.84	0.84	0.84
196.00	0.84	0.84	0.84	0.84	0.84	0.84	0.84	0.84	0.84	0.84

Table C.5: Relative weights DIPHOX + GAMMA2MC vs MADGRAPH $\gamma\gamma$+jets + PYTHIA box.

q_{T} [GeV] / $M_{\gamma\gamma}$ [GeV]	100	105	110	115	120	125	130	135	140	145	150	155
0.00	2.12	1.66	1.69	1.96	2.16	1.61	1.79	2.25	2.12	1.36	1.69	1.69
4.00	1.45	1.26	1.21	1.33	1.53	1.20	1.20	1.48	1.33	0.95	1.69	1.69
8.00	1.58	1.56	1.52	1.56	1.64	1.59	1.52	1.54	1.47	1.68	1.37	1.37
12.00	1.12	1.19	1.17	1.14	1.17	1.06	1.30	1.19	1.22	1.18	1.37	1.37
16.00	0.95	0.94	0.94	1.01	0.95	1.00	1.05	1.03	1.00	1.04	1.05	1.05
20.00	0.90	0.93	0.90	0.96	0.94	0.93	0.91	0.96	0.91	0.98	1.05	1.05
24.00	0.83	0.83	0.86	0.83	0.86	0.79	0.85	0.87	0.94	0.93	0.85	0.85
28.00	0.86	0.80	0.87	0.80	0.84	0.91	0.84	0.81	0.94	0.97	0.85	0.85
32.00	0.84	0.75	0.78	0.77	0.80	0.74	0.85	0.87	0.98	0.85	0.77	0.77
36.00	0.90	0.83	0.87	0.76	0.78	0.76	0.69	0.76	0.68	0.74	0.77	0.77
40.00	0.79	0.79	0.86	0.86	0.78	0.78	0.76	0.76	0.80	0.80	0.75	0.75
44.00	0.79	0.79	0.86	0.86	0.78	0.78	0.76	0.76	0.80	0.80	0.75	0.75
48.00	0.84	0.84	0.72	0.72	0.94	0.94	0.78	0.78	0.79	0.79	0.69	0.69
52.00	0.84	0.84	0.72	0.72	0.94	0.94	0.78	0.78	0.79	0.79	0.69	0.69
56.00	0.99	0.99	0.79	0.79	0.81	0.81	0.88	0.88	0.78	0.78	0.85	0.85
60.00	0.99	0.99	0.79	0.79	0.81	0.81	0.88	0.88	0.78	0.78	0.85	0.85
64.00	0.97	0.97	0.76	0.76	0.86	0.86	0.82	0.82	0.83	0.83	0.77	0.77
68.00	0.97	0.97	0.76	0.76	0.86	0.86	0.82	0.82	0.83	0.83	0.77	0.77
72.00	0.88	0.88	0.93	0.93	1.07	1.07	0.97	0.97	0.83	0.83	1.13	1.13
76.00	0.88	0.88	0.93	0.93	1.07	1.07	0.97	0.97	0.83	0.83	1.13	1.13
80.00	1.02	1.02	0.84	0.84	1.17	1.17	1.03	1.03	1.30	1.30	0.65	0.65
84.00	1.02	1.02	0.84	0.84	1.17	1.17	1.03	1.03	1.30	1.30	0.65	0.65
88.00	0.89	0.89	0.78	0.78	0.79	0.79	1.00	1.00	0.73	0.73	0.70	0.70
92.00	0.89	0.89	0.78	0.78	0.79	0.79	1.00	1.00	0.73	0.73	0.70	0.70
96.00	1.16	1.16	0.81	0.81	1.14	1.14	1.13	1.13	0.90	0.90	1.43	1.43
100.00	1.16	1.16	0.81	0.81	1.14	1.14	1.13	1.13	0.90	0.90	1.43	1.43
104.00	0.97	0.97	0.98	0.98	1.02	1.02	1.04	1.04	1.30	1.30	0.91	0.91
108.00	0.97	0.97	0.98	0.98	1.02	1.02	1.04	1.04	1.30	1.30	0.91	0.91
112.00	0.90	0.90	0.94	0.94	0.90	0.90	1.36	1.36	1.06	1.06	0.74	0.74
116.00	0.90	0.90	0.94	0.94	0.90	0.90	1.36	1.36	1.06	1.06	0.74	0.74
120.00	1.06	1.06	1.06	1.06	1.27	1.27	1.27	1.27	1.34	1.34	1.34	1.34
124.00	1.06	1.06	1.06	1.06	1.27	1.27	1.27	1.27	1.34	1.34	1.34	1.34
128.00	1.06	1.06	1.06	1.06	1.27	1.27	1.27	1.27	1.34	1.34	1.34	1.34
132.00	1.06	1.06	1.06	1.06	1.27	1.27	1.27	1.27	1.34	1.34	1.34	1.34
136.00	1.71	1.71	1.71	1.71	1.49	1.49	1.49	1.49	1.18	1.18	1.18	1.18
140.00	1.71	1.71	1.71	1.71	1.49	1.49	1.49	1.49	1.18	1.18	1.18	1.18
144.00	1.71	1.71	1.71	1.71	1.49	1.49	1.49	1.49	1.18	1.18	1.18	1.18
148.00	1.71	1.71	1.71	1.71	1.49	1.49	1.49	1.49	1.18	1.18	1.18	1.18
152.00	0.80	0.80	0.80	0.80	1.03	1.03	1.03	1.03	1.39	1.39	1.39	1.39
156.00	0.80	0.80	0.80	0.80	1.03	1.03	1.03	1.03	1.39	1.39	1.39	1.39
160.00	0.80	0.80	0.80	0.80	1.03	1.03	1.03	1.03	1.39	1.39	1.39	1.39
164.00	0.80	0.80	0.80	0.80	1.03	1.03	1.03	1.03	1.39	1.39	1.39	1.39
168.00	1.23	1.23	1.23	1.23	1.83	1.83	1.83	1.83	1.54	1.54	1.54	1.54
172.00	1.23	1.23	1.23	1.23	1.83	1.83	1.83	1.83	1.54	1.54	1.54	1.54
176.00	1.23	1.23	1.23	1.23	1.83	1.83	1.83	1.83	1.54	1.54	1.54	1.54
180.00	1.23	1.23	1.23	1.23	1.83	1.83	1.83	1.83	1.54	1.54	1.54	1.54
184.00	0.87	0.87	0.87	0.87	2.09	2.09	2.09	2.09	2.23	2.23	2.23	2.23
188.00	0.87	0.87	0.87	0.87	2.09	2.09	2.09	2.09	2.23	2.23	2.23	2.23
192.00	0.87	0.87	0.87	0.87	2.09	2.09	2.09	2.09	2.23	2.23	2.23	2.23
196.00	0.87	0.87	0.87	0.87	2.09	2.09	2.09	2.09	2.23	2.23	2.23	2.23